COMPREHENSIVE TECHNICAL REPORT

DIRECT AIR CYCLE | AIRCRAFT NUCLEAR PROPULSION PROGRAM

APEX 908

PART C

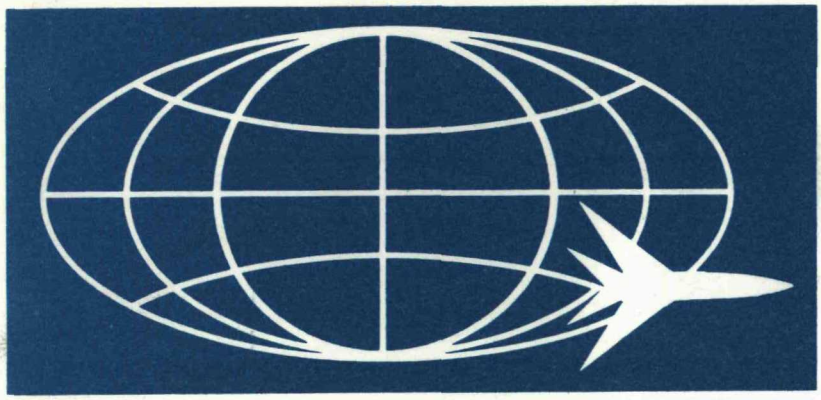

XNJ 140E NUCLEAR TURBOJET

FLIGHT PROPULSION LABORATORY DEPARTMENT

GENERAL ELECTRIC

DISCLAIMER

[redacted] CONFIDENTIAL

APEX-908
PART C

UNCLASSIFIED

COMPREHENSIVE TECHNICAL REPORT GENERAL ELECTRIC DIRECT-AIR-CYCLE AIRCRAFT NUCLEAR PROPULSION PROGRAM

XNJ 140E NUCLEAR TURBOJET

SECTION 5. SHIELD
SECTION 6. TURBOMACHINERY
SECTION 7. CONTROL SYSTEM

Author: D. C. LAYMAN
Contributors: T. A. DeROSIER
K. F. MERTEN
J. W. TENHUNDFELD
Editor: D. C. LAYMAN

MAY 25, 1962

United States Air Force — Contract No AF33(600)—38062
United States Atomic Energy Commission — Contract No. AT(11-1)—171

UNCLASSIFIED

GENERAL ELECTRIC
NUCLEAR MATERIALS AND PROPULSION OPERATION
(Formerly Aircraft Nuclear Propulsion Department)
FLIGHT PROPULSION LABORATORY DEPARTMENT
Cincinnati 15, Ohio

AEC RESEARCH AND DEVELOPMENT REPORT

[redacted] CONFIDENTIAL

DISTRIBUTION

INTERNAL

C. L. Chase
D. Cochran
E. B. Delson
M. C. Leverett
W. H. Long
H. F. Matthiesen
A. J. Rothstein (6)
D. R. Shoults
G. Thornton
Library (6)

EXTERNAL DISTRIBUTION

Col. Ola P. Thorne
Pentagon, Washington 25, D. C.

Capt. Hendricks
Andrews AFB, Md.

Lt. Col. Stanley Valcik (2)
A. S. D.
Wright-Patterson AFB, Ohio

Dr. Frank Pittman
AEC
Washington 25, D. C.

DTIE (14) plus reproducible master
Oak Ridge, Tennessee

ABSTRACT

This volume is one of twenty-one summarizing the Aircraft Nuclear Propulsion Program of the General Electric Company. It is a comprehensive technical report of the design and development activities of the XNJ140E Project. Included are a presentation of the design objectives and requirements, an engineering description of the XNJ140E-1 nuclear turbojet engine, supporting analytical design data and methods of calculation, and a brief review of three design studies preceding, and directly applicable to the XNJ-140E program.

Beginning early in 1960, a major phase of the national effort leading to the achievement of nuclear powered flight was the design and development of the XNJ140E-1 nuclear turbojet engine to be utilized in an Advanced Core Test program. This program was to demonstrate the capabilities of a ceramic reactor coupled with the appropriate associated components of a direct-air-cycle nuclear turbojet engine. Descriptive material contained in this report is based upon the status of the XNJ140E Project at the time of contract termination.

The XNJ140E-1 engine was designed with a reactor of sufficient capability to provide engine performance equivalent to that specified in Department of Defense guidance, which required a speed of Mach 0.8 at an altitude of approximately 35,000 feet in a Convair Model NX 2 aircraft, or equivalent, and an engine life potential of 1000 hours. During this flight condition, the estimated minimum net thrust of the engine was 8120 pounds.

The engine contained a reactor-shield assembly coupled with a single set of X211 turbomachinery and arranged in an integral, in-line configuration. The compressor and turbine were separated, but connected by a long coupling shaft. An annular combustor system, using JP-4 jet fuel, was placed in-line between the reactor rear shield and the turbine inlet, and was arranged concentrically around the coupling shaft.

The reactor-shield assembly was a prototype of comparable components to be used in subsequently planned flight versions of the engine. Turbomachinery components of improved design and an operational afterburner also would have been used.

The reactor fuel elements were made of a beryllium oxide matrix impregnated with enriched uranium dioxide (~93% U^{235}); the uranium dioxide was stabilized with yttrium oxide to limit the conversion of uranium dioxide to higher states of oxidation. Fuel element surfaces exposed to high velocity

cooling air were coated with zirconium oxide stabilized with yttrium oxide; this coating eliminated water vapor corrosion of the beryllium oxide. The maximum operating temperature was 2530°F.

Beryllium oxide was used in the front, rear, and outer reflectors. Aluminum oxide was used as the inner reflector and served as thermal insulation between the core and the coupling shaft. Beryllium and stainless steel were used as shielding material in the end shields; each material was used both borated and unborated. Lithium hydride, sealed in stainless steel cans, was used as shielding material in the side shield.

This over-all report is divided into four parts. Part A contains section 1., a summary of the report and significant terminology; section 2., precedent studies leading to the selection of the XNJ140E power plant; and section 3., a description of the over-all power plant. Part B contains section 4., a description of the reactor. Part C contains section 5., a description of the shield; section 6., a description of the turbomachinery; and section 7., a description of the control system. Part D contains section 8., a description of test planning, special engineering data instrumentation, and test installations for the Advanced Core Test program; section 9., a discussion of remote handling and maintenance; and section 10., a discussion of on-site and off-site hazards associated with the operation of the engine during the Advanced Core Test program.

ACKNOWLEDGEMENTS

Acknowledgement is made of technical contributions from many members of the Department's engineering staff and of the many reviews and suggestions of J. I. Trussell.

CONTENTS

Page

Page

An abridged table of contents for other parts of this volume is presented below to establish the relationship of this part to the total volume.

PART A

PART B

PART D

FIGURES*

*Each part of this volume contains its own list of figures.

Page

Page

TABLES*

*Each part of this volume contains its own list of tables.

5. SHIELD

5.1 INTRODUCTION

The radiation shield for the XNJ140E-1 engine was a prototype of flight-type radiation shields to be used on subsequent flight versions of the XNJ140E power plant. It was based on the divided-shield concept wherein shield material was used to surround both the reactor and the crew compartment, and distributed so that the weight of the total shield was minimized and the radiation level in the crew compartment did not exceed 0.02 rem per hour at the cruise-flight condition. It reduced radiation levels external to the engine so that induced radioactivity of parts not mounted on the engine did not hamper subsequent maintenance and so that radiation damage did not unnecessarily limit the life of engine-mounted parts.

The shield assembly was located between the compressor rear frame and the turbine front frame and had an over-all length of approximately 140 inches. The outer envelope of the side shield, located outside the pressure vessel, was contained within a circle 108.8 inches in diameter. End shields were located within the pressure vessel forward and aft of the reactor. Figure 5.1 is an isometric cutaway view of the shield assembly.

Flight-type XNJ140E engines were intended for three-abreast installation in the aft end of the Convair NX2 airframe. When engines were installed in this close array, an 83.00-inch separation was maintained between engine centerlines and the side shield was shared on the side (or sides) adjacent to another engine. On the nonshared side an additional piece of shielding (corresponding to the cheek that had been removed) was attached to the aircraft structure to complete the side-shield contour. In this shared-shield design, the portion of the side shield permanently mounted on the engine was symmetrical and the engines were interchangeable in the array.

Materials within the reactor and surrounding the active core also served as neutron shielding and, to a certain extent, as gamma shielding. In addition, the thick outer reflector and the borated steel pressure pads enclosing the reflector served in combination as a thermal shield and limited energy deposition in the side shield. Some neutrons were slowed down in the reflector and, subsequently, were absorbed in the borated pads. Zones of high energy deposition were confined to regions where the heat could be dissipated by primary air.

Air bled from the primary airstream was used to cool the front and rear shields. Facility-supplied (FET) air was used to cool the side shield (ram air would be used in flight versions of the XNJ140E engine). Primary air ducts and air-cooling passages were designed to permit airflow through the system without excessive pressure loss and, at the same time, to prevent escape of excessive radiation from the system.

The nuclear design of the shield was based upon meeting the objective external dose rates shown in Figure 5.2 (neutron) and Figure 5.3 (gamma). These objective dose rates, the result of over-all shield optimization studies, were established jointly with Convair, Fort Worth.

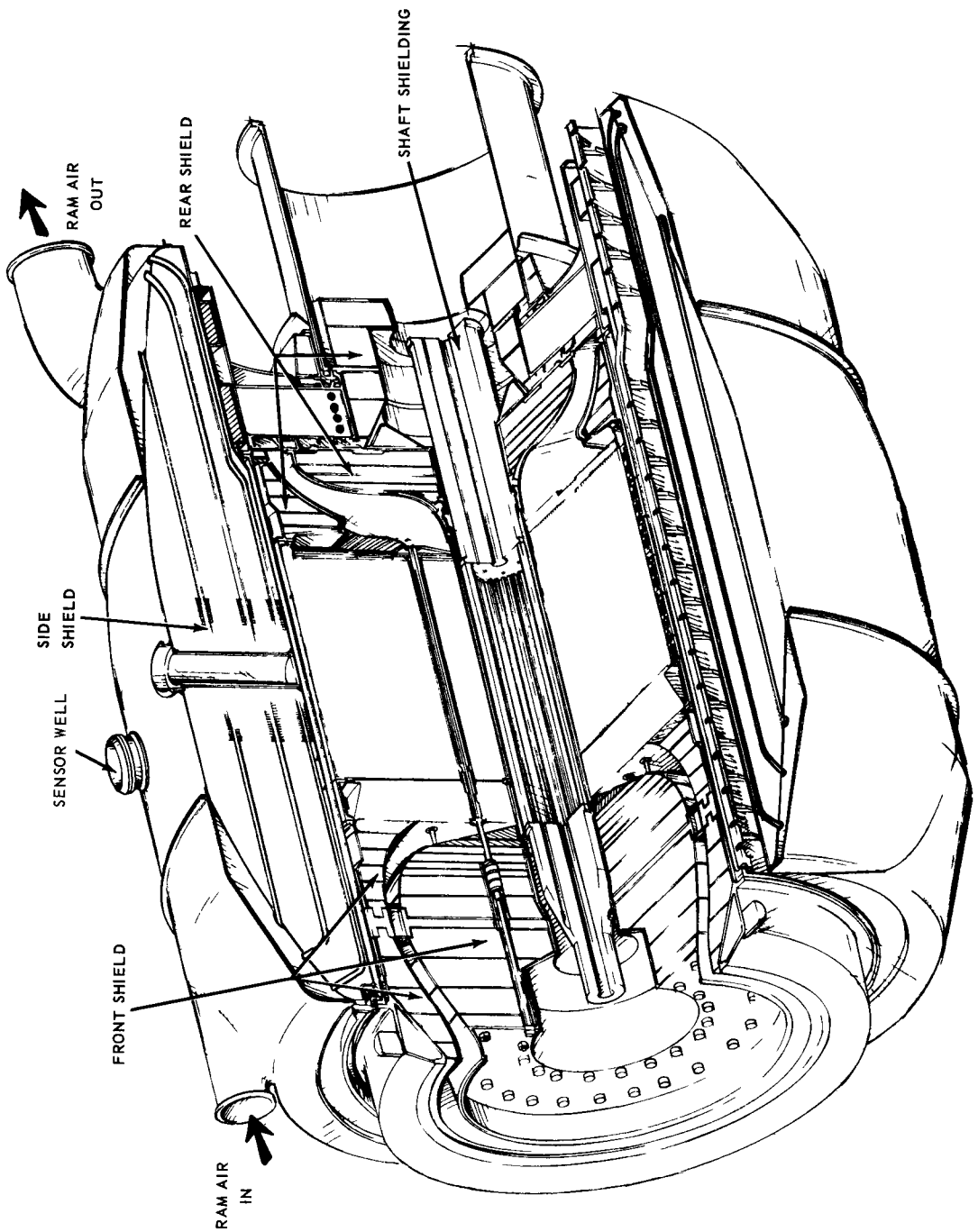

Fig. 5.1 – XNJ140E-1 shield assembly

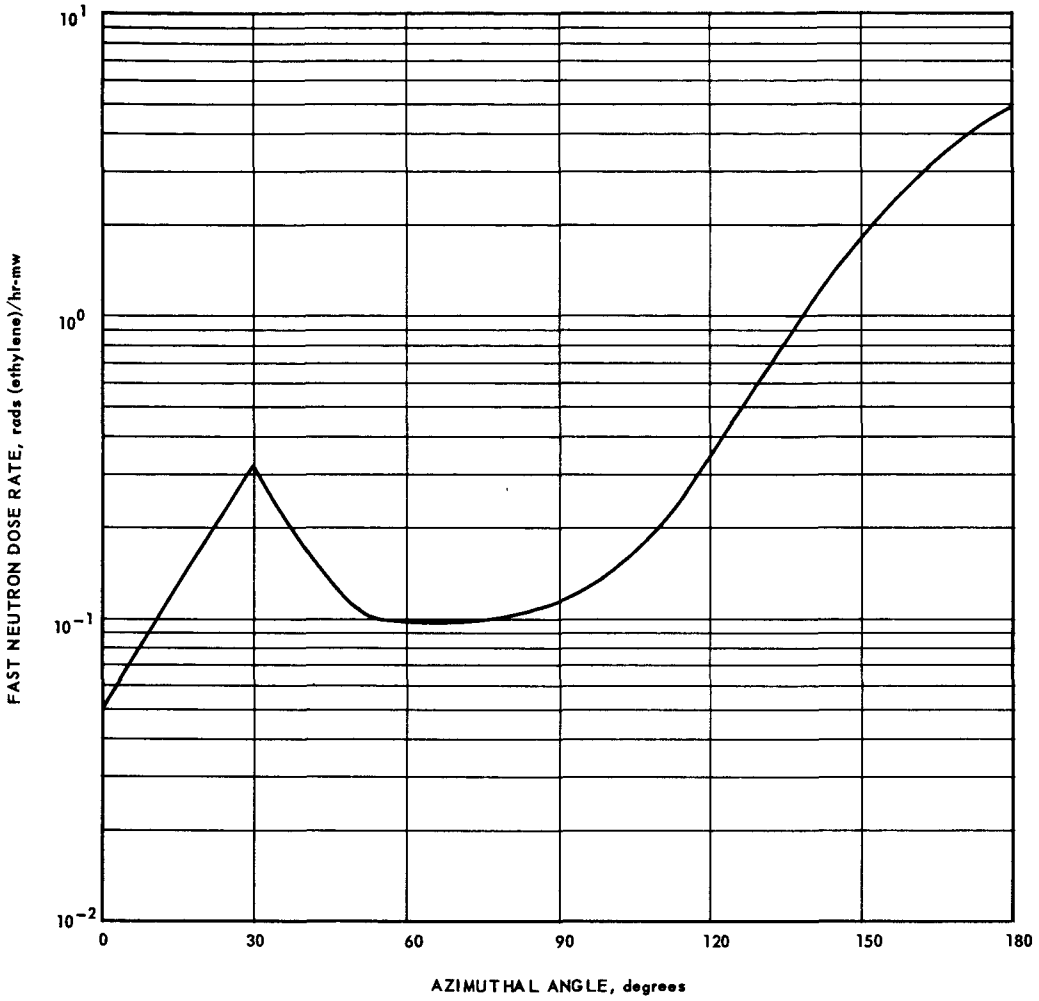

Fig. 5.2—Objective fast neutron dose rates per megawatt of reactor power 50 feet from reactor midpoint

5.2 OVER-ALL SHIELD

5.2.1 DESCRIPTION

The over-all shield assembly contained five major design assemblies; front shield, rear shield, side shield, coupling shaft inserts, and pressure vessel. Although the pressure vessel was not a nuclear-shielding component, it formed the structural tie between the front and rear shields, and was designed and treated as a shield system component. The configuration control dimensions are shown in Figure 5.4.

The primary shielding materials were canned lithium hydride (LiH_X) castings for the side shield and beryllium (Be) and stainless steel with boron (B) additive for the end shields.

Estimated weights of the various components are given in Table 5.1.

5.2.1.1 Front Shield

The front shield assembly provided the nuclear radiation shielding in front of the reactor. In addition, it formed the annular duct for the compressor discharge-air and

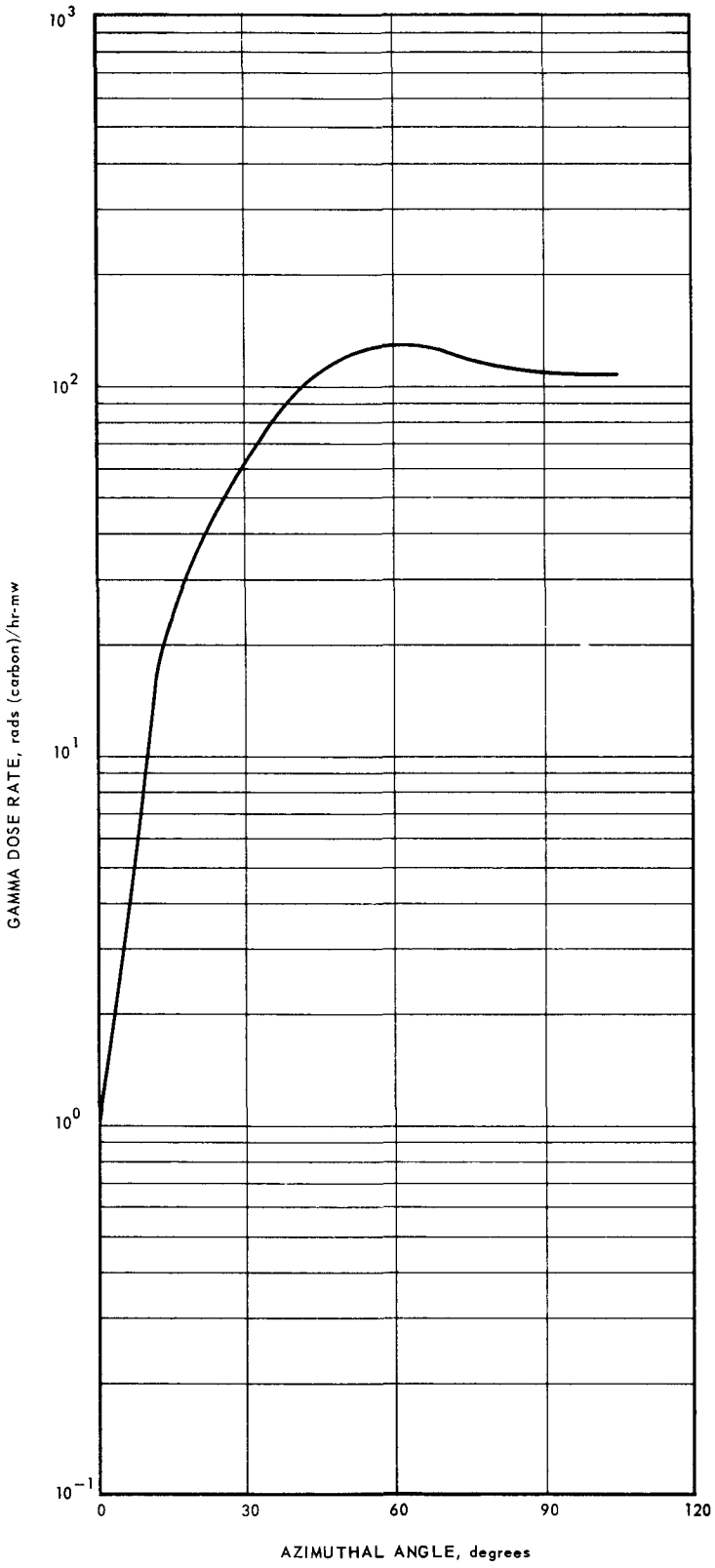

Fig. 5.3 – Objective gamma dose rates per megawatt of reactor power 50 feet from reactor midpoint

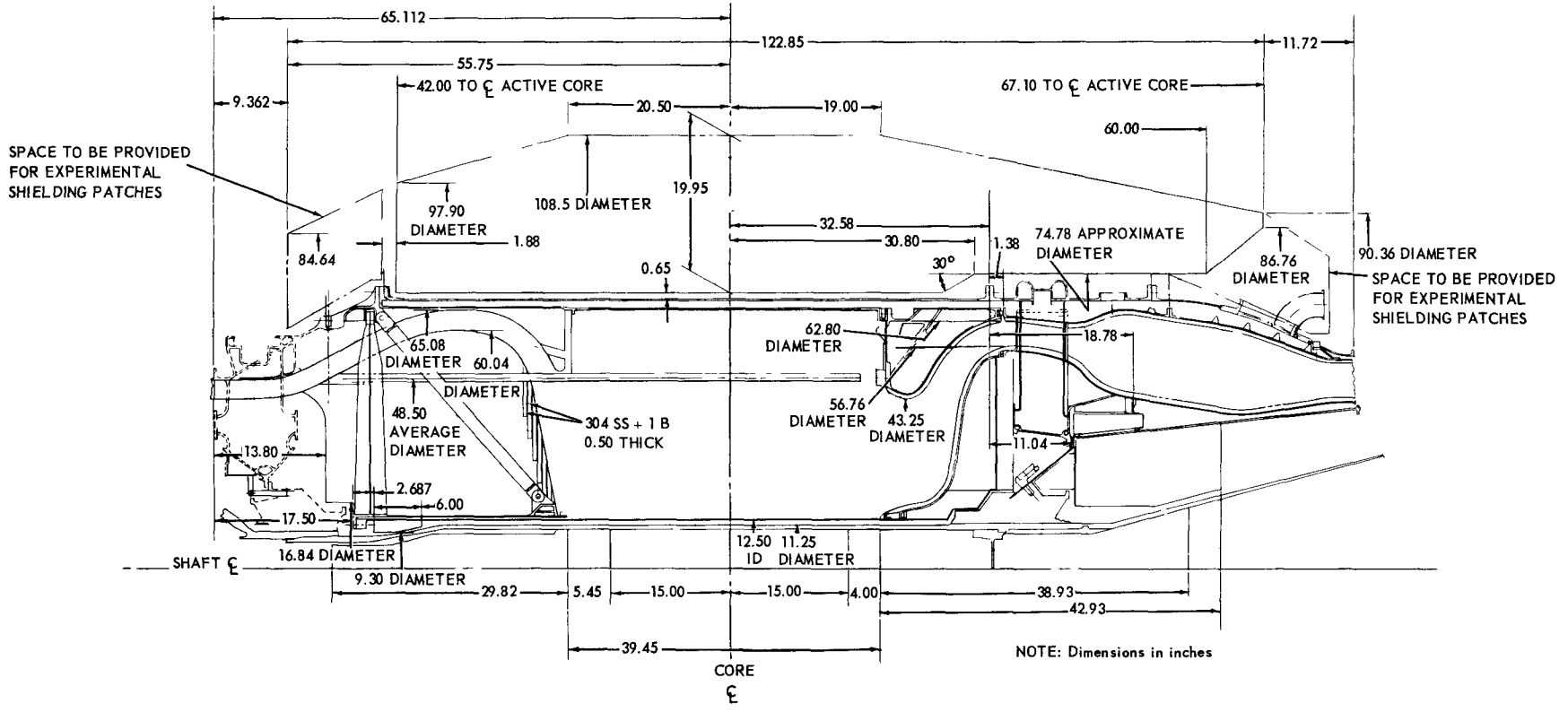

Fig. 5.4 – Control dimensions of XNJ140E-1 shield assembly

TABLE 5.1

ESTIMATED SHIELD WEIGHT

Component	Weight, lb	
Front Shield		
Structure	1,000	
Shielding material	4,650	
Total		5,650
Rear Shield		
Structure	1,550	
Shielding material	2,800	
Total		4,350
Side Shield		
Structure	5,700	
Shielding material	10,100	
Total		15,800
Pressure Vessel		1,100
Test Instrumentation		800
Total Shield		27,900

provided the structural tie between the compressor rear frame and the pressure vessel. The three primary subassemblies, outer section, central island, and support structure, are shown in Figure 5.5. An isometric view of the support structure is shown in Figure 5.6.

The outer section consisted of annular rings of borated Be attached to the inner surface of the reactor structural shell. This shell supported the front shield and the reactor and was cantilevered from the front flange of the pressure vessel.

The central island consisted of sectored discs of shielding material supported by the support structure. The discs were made of both borated 304 stainless steel and borated Be; each material contained 1 weight percent of natural boron. They were held together by axial tie rods, and contained a pattern of axial holes in the region of the outer reflector for the control rods.

Structural materials used were Inconel and Inconel X. Inconel was used where stiffness requirements resulted in low stress conditions. Inconel X was used to obtain high strength-to-weight ratio.

Cooling-air removed the secondary heat generated within the shield. Most of this cooling was accomplished by bleeding primary-air from the annular duct into passages between the shield discs. This air was then collected, bypassed the reactor, and was used further to cool other components. Air bled radially outward was collected in the bleed-speed duct and used for bleed-speed control as well as for cooling other components. Air bled radially inward was collected outside the shaft tunnel and flowed rearward.

5.2.1.2 Rear Shield

The rear shield was located between the reactor and the turbine rotor, and partially within the turbine front frame. Figure 5.7 is an isometric cutaway view of the rear shield assembly. The assembly consisted of an outer section, a forward central island, and an aft central island. Figure 5.8 is an exploded isometric view of the rear shield.

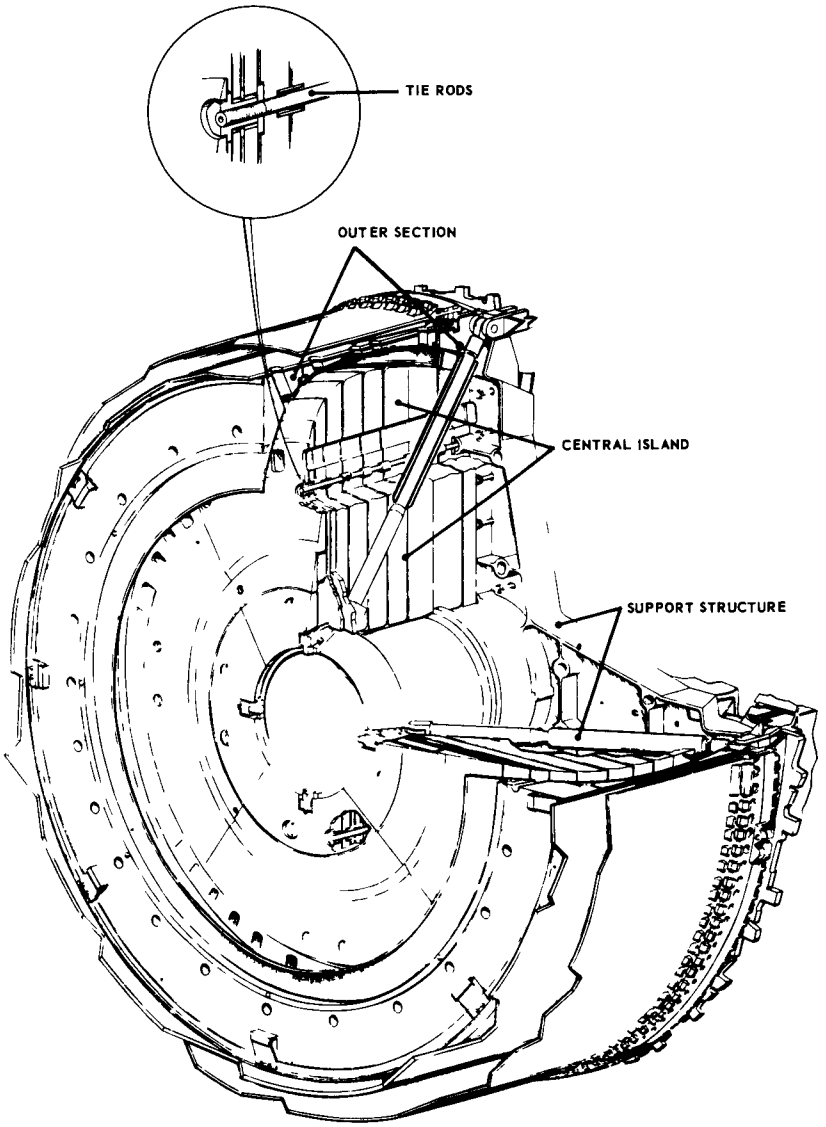

Fig. 5.5 – Isometric cutaway view of XNJ140E-1 front shield assembly

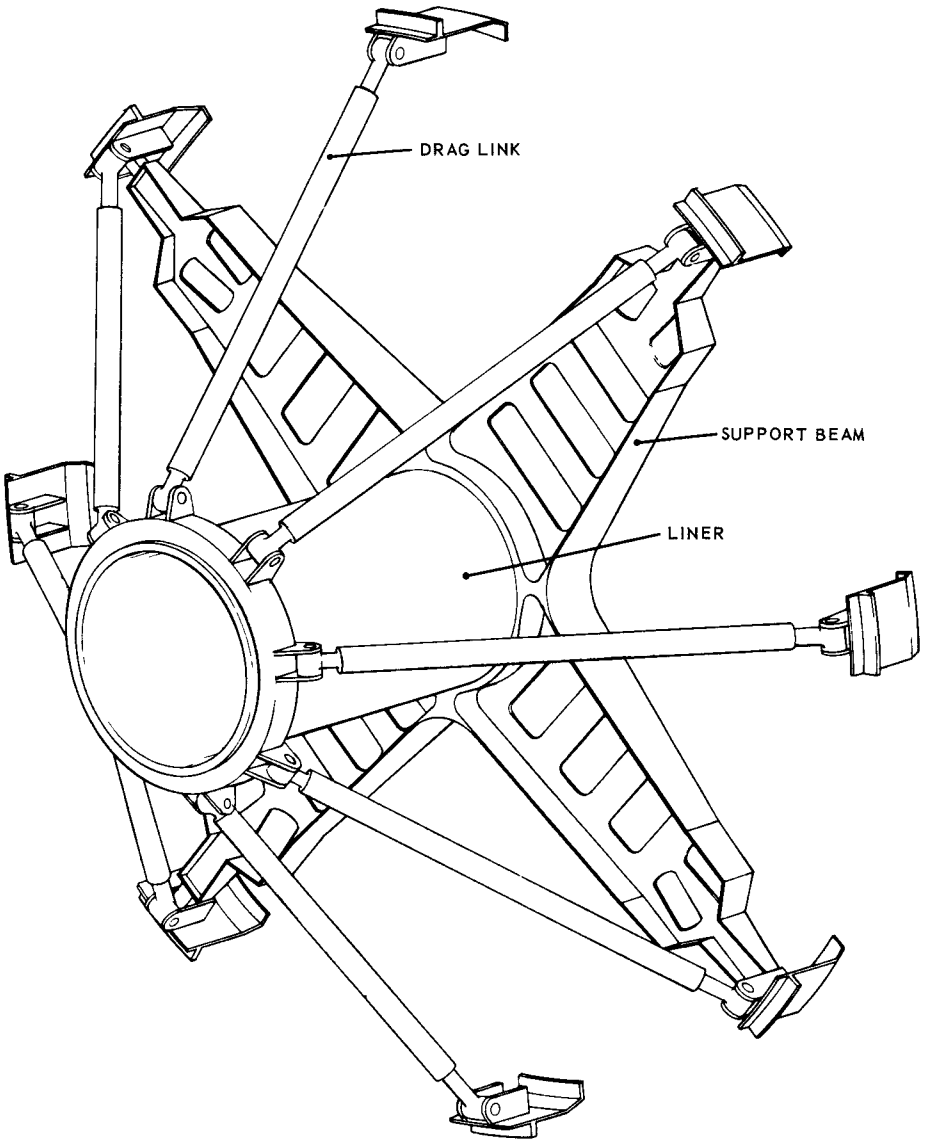

Fig. 5.6 – Isometric cutaway view of XNJ140E-1 front shield support structure

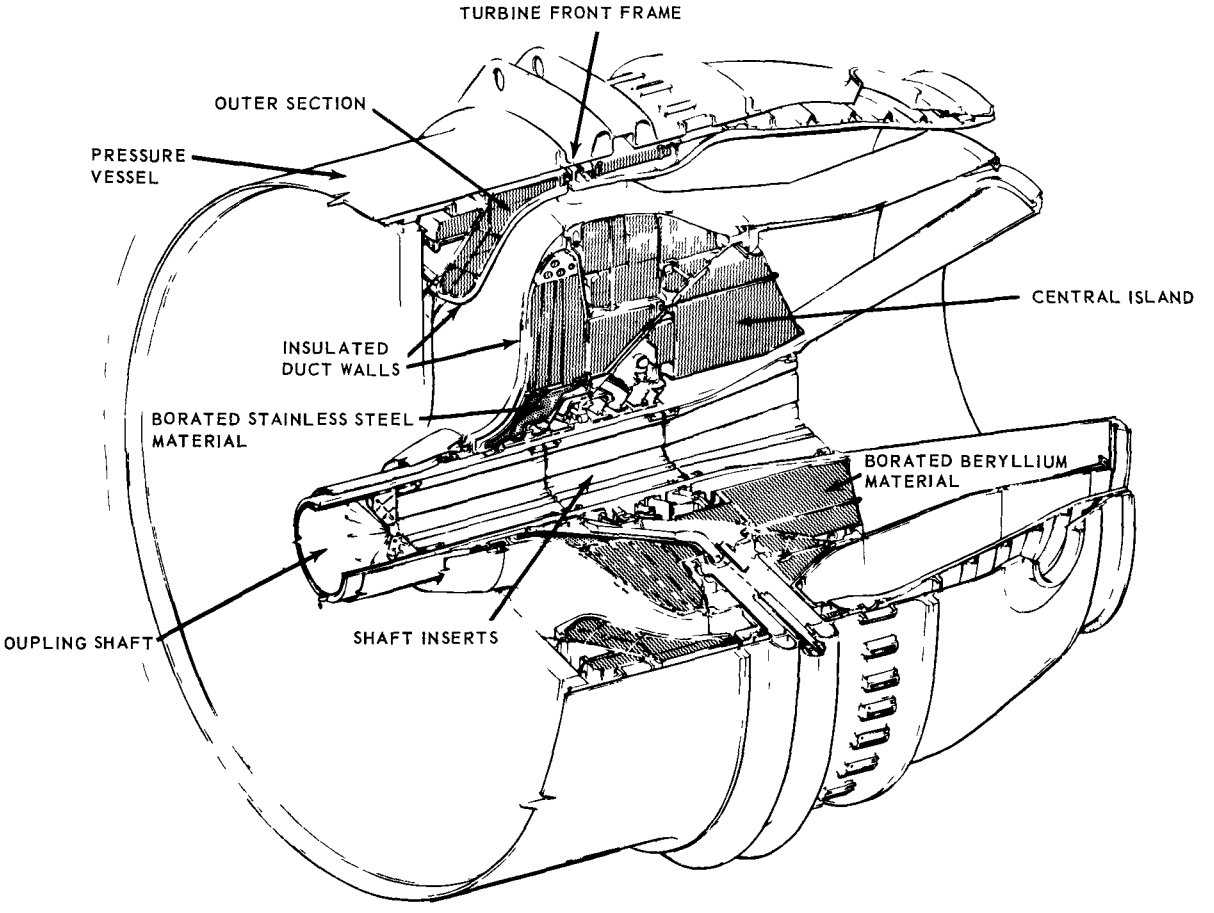

Fig. 5.7 – Isometric cutaway view of XNJ140E-1 rear shield assembly

The rear shield performed the following functions:

1. Provided the nuclear radiation shielding to the rear of the reactor
2. Provided the annular duct for passage of the core discharge air to the turbine inlet
3. Provided most of the axial support of the reactor aft-retainer assembly to react against the core pressure drop and inertial loading.

The primary shielding material was Be with an additive of 1 percent boron by weight. The primary structural material was heat-treated Inconel X.

The outer section consisted of a ring of shielding material, the main support cone, and a removable insulated duct wall. It was attached to the reactor structural shell and supported axial loads on the aft-retainer assembly. It was air-cooled by compressor discharge-air which was diverted from the bleed-speed annulus and directed into cooling channels around the structural walls and shielding blocks. This same air was used further to cool the duct wall insulation before being discharged into the primary-air stream.

The central island consisted of several annular subassemblies attached to the turbine front frame and the combustor structural walls. Shielding contained either forward of, or within the turbine rear frame was called the forward central island; shielding behind the turbine frame was called the aft central island. These parts were attached to the turbine front frame. Shielding material was in the form of discs, blocks, and rings that were arranged to form air-cooling channels as required. Cooling-air was obtained from com-

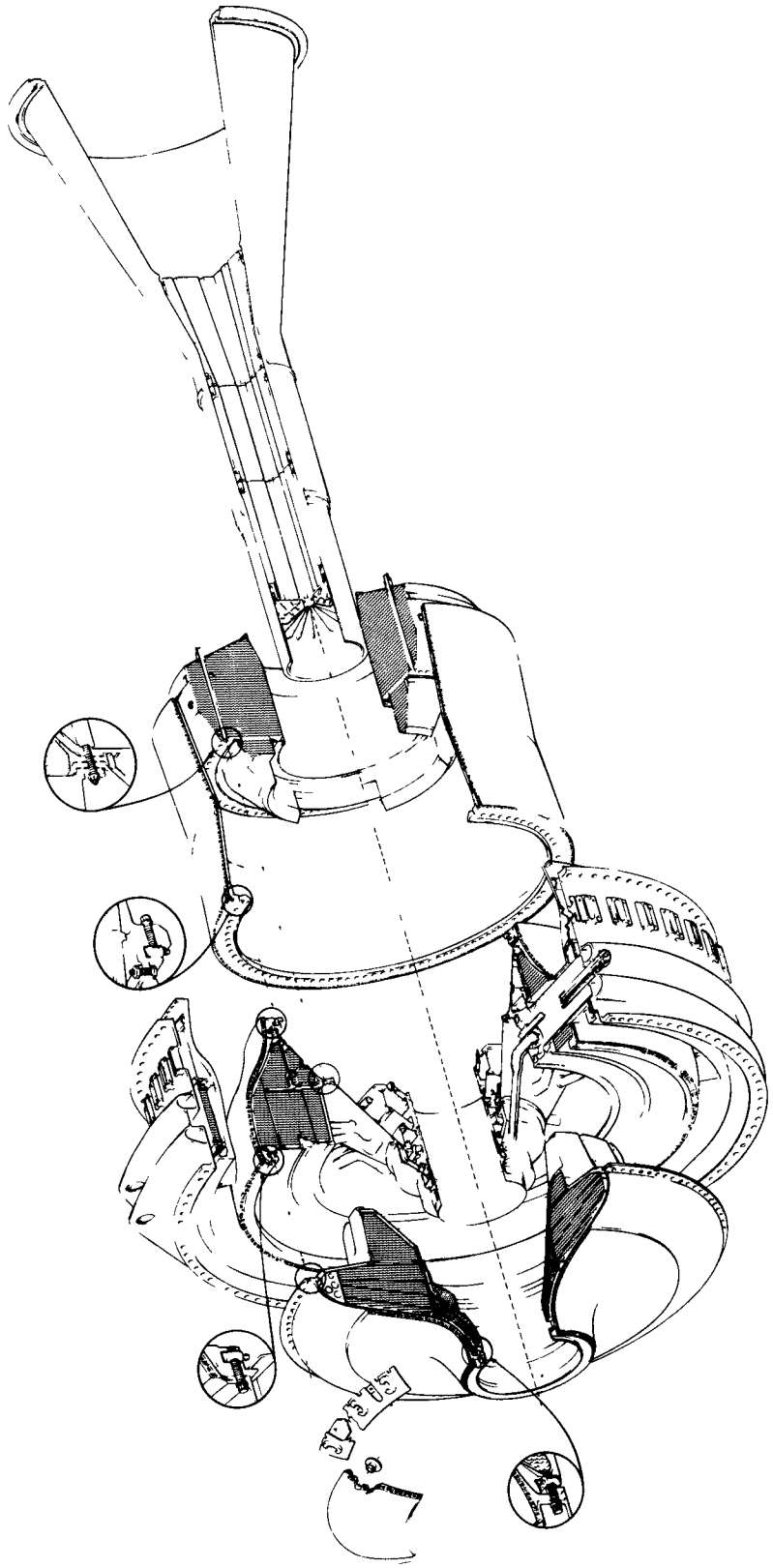

Fig. 5.8 – Rear shield exploded isometric cutaway view (Dwg. DI444)

pressor discharge-air that was used to cool the front shield and then flowed rearward through the shaft tunnel annulus.

The duct-wall insulation was a 0.5-inch-thick sandwich of fibrous alumina silica, a layer of metallic foil, and a corrugated sheet of Hastelloy X which was attached to a cover sheet of 0.050-inch-thick Hastelloy X. This sandwich was fabricated into pads that were held in place by retainers attached to the structural wall.

5.2.1.3 Side Shield

The side shield provided radiation shielding around the reactor in the radial direction. The assembly, shown in Figures 5.9 and 5.10, consisted of top and bottom halves which were built up from segments. The segments were made of LiH_x cast and sealed in 19-9 DL stainless steel cans as shown in Figure 5.11. When the two halves were assembled, the resultant configuration was an annular ring with flattened sides. Side-cheek assemblies, not shown in Figure 5.10, were provided to complete the side-shield outer contour at the flattened sides.

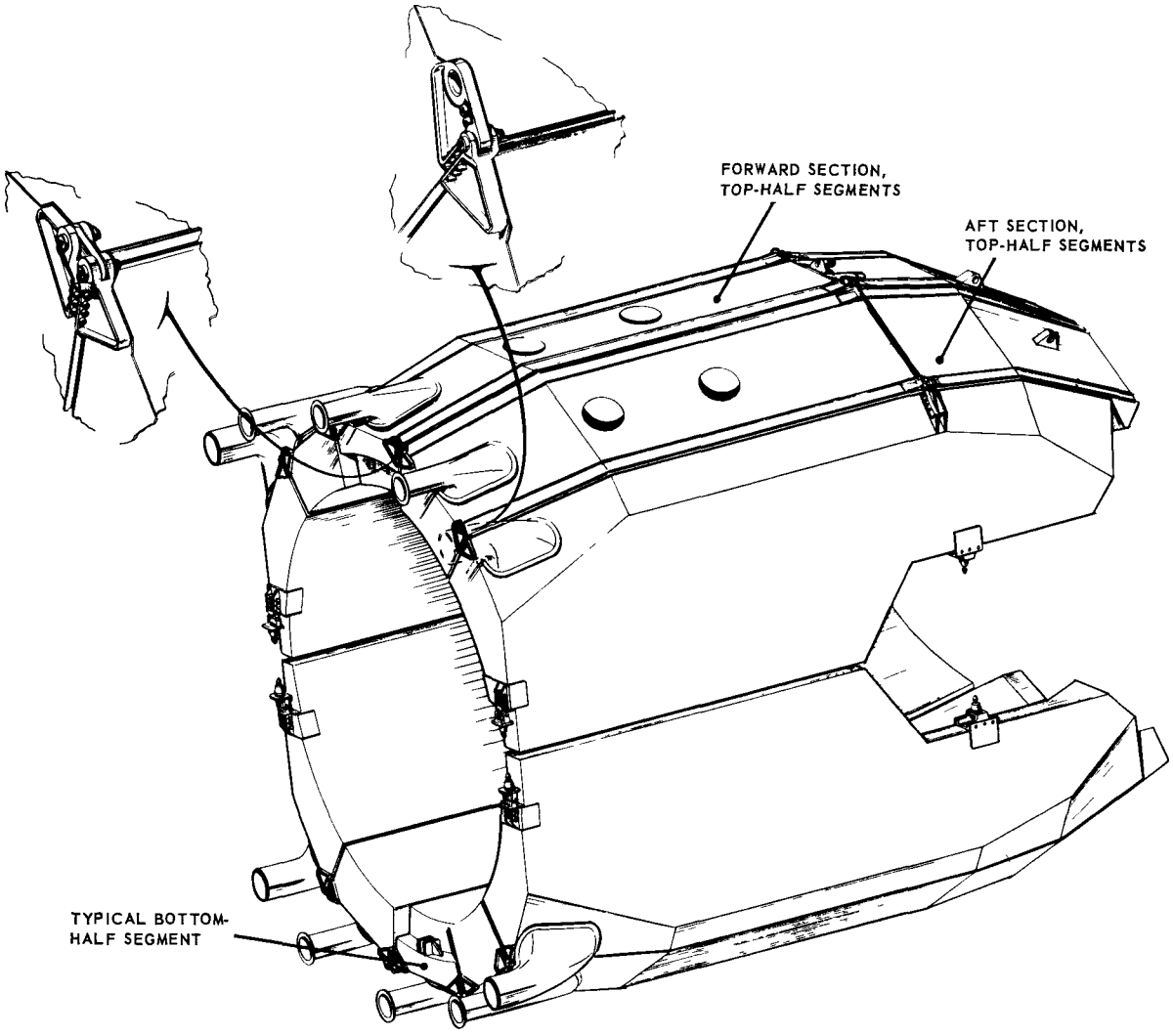

Fig. 5.9 – Cutaway view of XNJ140E-1 side shield assembly

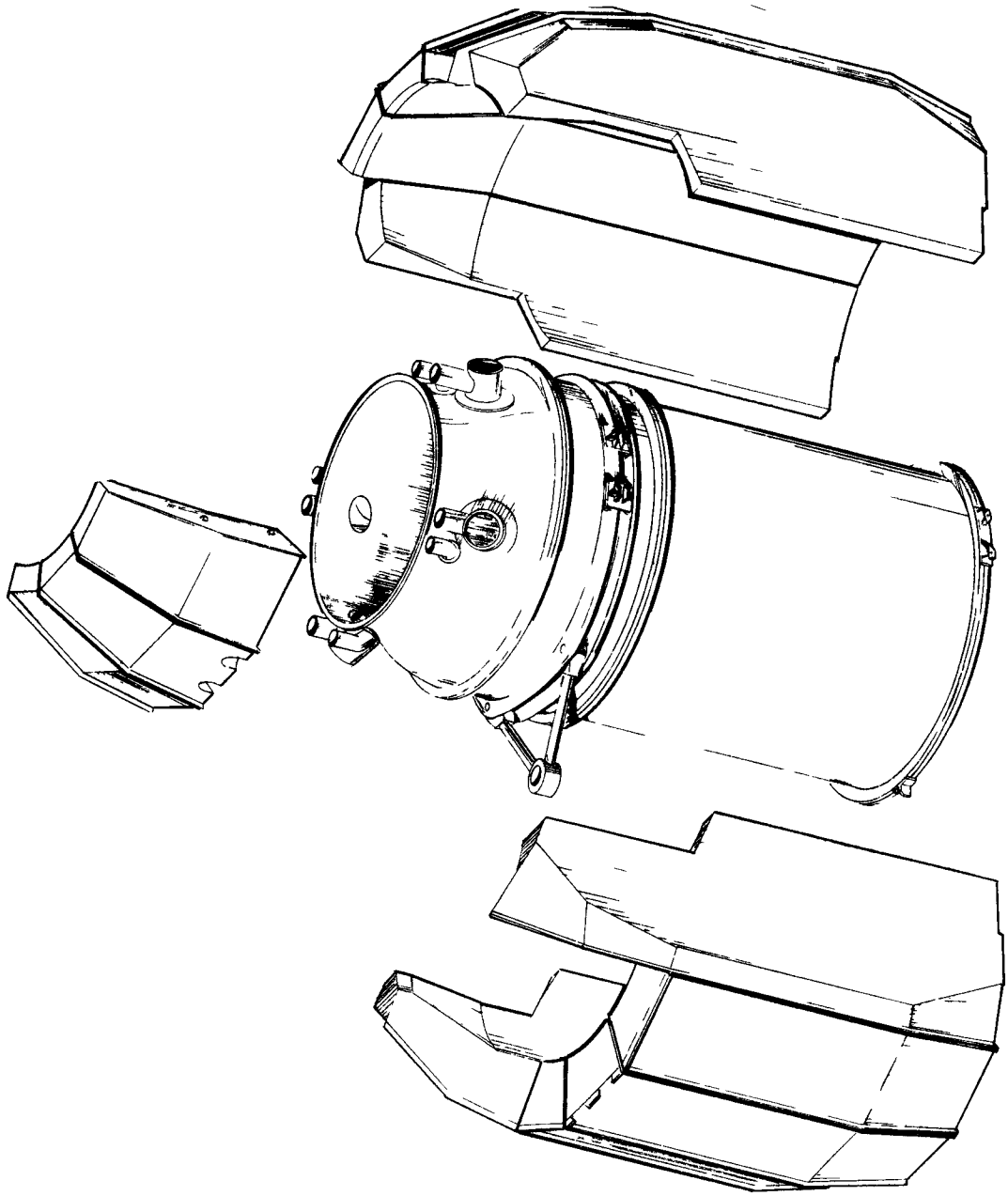

Fig. 5.10 – XNJ140E-1 side shield assembly with major components separated, exploded view

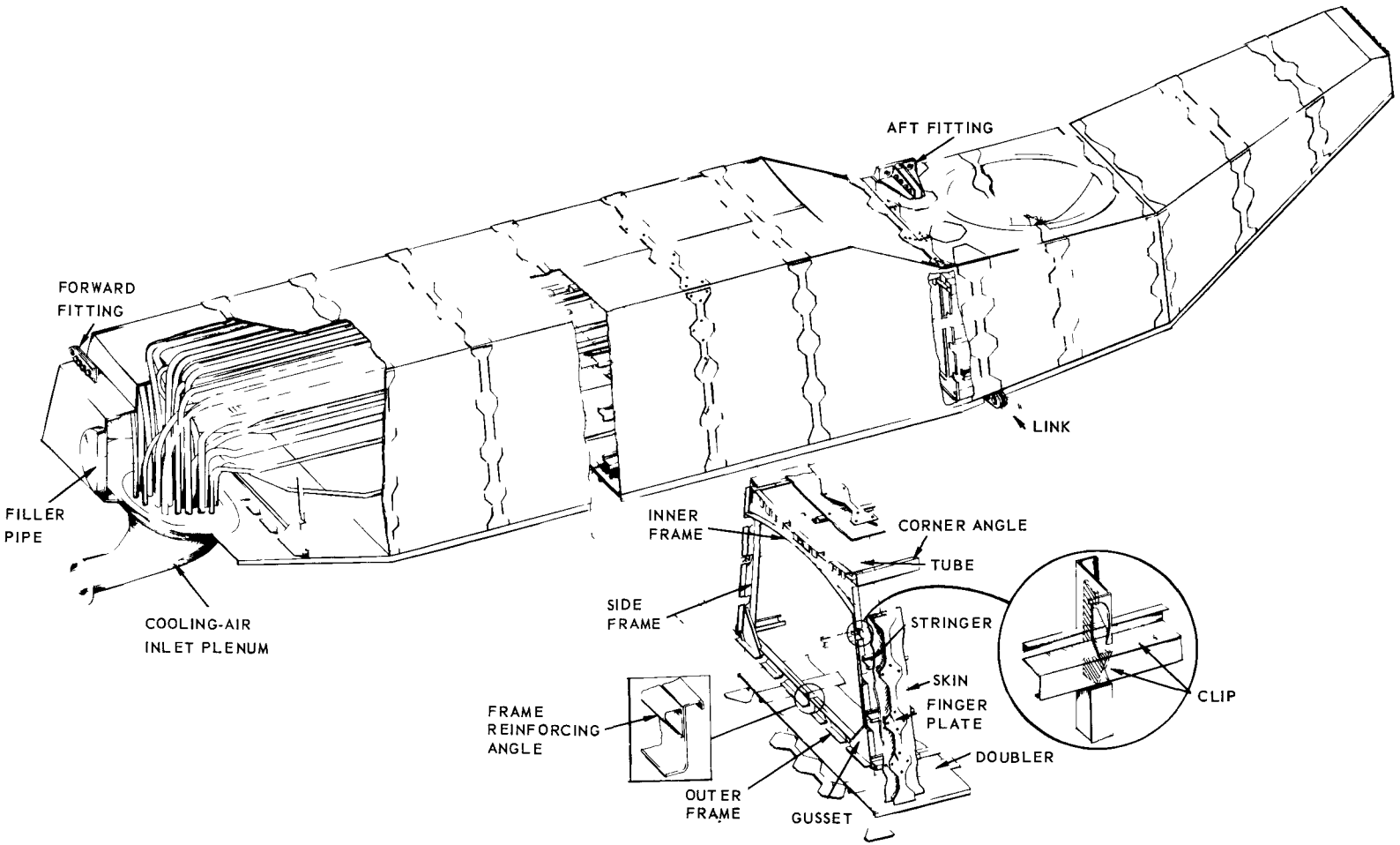

Fig. 5.11 – Lower-half side shield segment

The assembly was supported by fittings that were attached to the pressure vessel and the aft trunnion ring on the turbine. The outer diameter was 108.8 inches, and the shield thickness was 17.0 inches.

The shield segments were cooled by passing ram air through thin-walled cooling tubes in the LiH_x castings. Figure 5.11 shows the cooling tubes in a typical segment.

5.2.1.4 Coupling Shaft Shield Inserts

Five inserts were mounted within the coupling shaft, as shown in Figure 5.12. The inner inserts were made of unborated Be and were aligned radially with the reactor forward and aft reflectors; they acted as reflectors. The remaining inserts were made of Be containing 1 weight percent natural boron and served as shielding to reduce the direct-line radiation.

Since Be has a lower coefficient of expansion than the shaft material (A-286), the inserts were mounted on torsional springs. The natural frequencies of these parts were above the operating range of frequencies. Cooling was accomplished by ninth-stage compressor bleed-air passing through axial holes machined into the inserts.

Design of the inserts was not complete at the time of contract termination.

5.2.1.5 Pressure Vessel

The pressure vessel was a cylindrical shell, flanged at each end and made of age-hardened Inconel X. Over-all length was approximately 76 inches and the diameter was approximately 68 inches. The aft flange was of conventional design, but the forward flange was designed to utilize captive nuts. Adjacent to the forward flange, external support lugs were provided around the periphery for location of a remote-handling fixture. Provision was made inside the forward end of the vessel for permanent attachment of the ring of Be shielding blocks that constituted the front shield outer section. Figure 5.13 shows the pressure vessel and includes a detail of the captive-nut locations.

The pressure vessel contained the system primary-air, connected the turbine section to the forward portion of the engine, and provided part of the support for the side shield. During operation, the vessel was cooled on its inside surface by bleed-speed air which flowed aft in the annulus between the vessel and the reactor structural shell.

5.2.2 DESIGN REQUIREMENTS

5.2.2.1 Mechanical

Requirements imposed on the mechanical design of shield components were as follows:

1. Design criteria defined in section 3.2.3.
2. Performance requirements defined in section 3.2.1
3. Wherever possible, the shield was designed in accordance with standard aircraft practice.
4. All removable or replaceable assemblies, components, and parts were dimensionally and functionally interchangeable. Subassemblies and components had dimensional tolerances no more stringent than necessary to achieve required performance, interchangeability, and replaceability throughout the test and operational life.
5. Insofar as practicable, parts of the shield requiring routine service checking, adjustment, or replacement were made readily accessible for servicing without major teardown of the engine.
6. The maximum deflections of the front and rear shield central islands were held within 0.125 inch in the axial direction and 0.08 inch in the vertical and side directions.

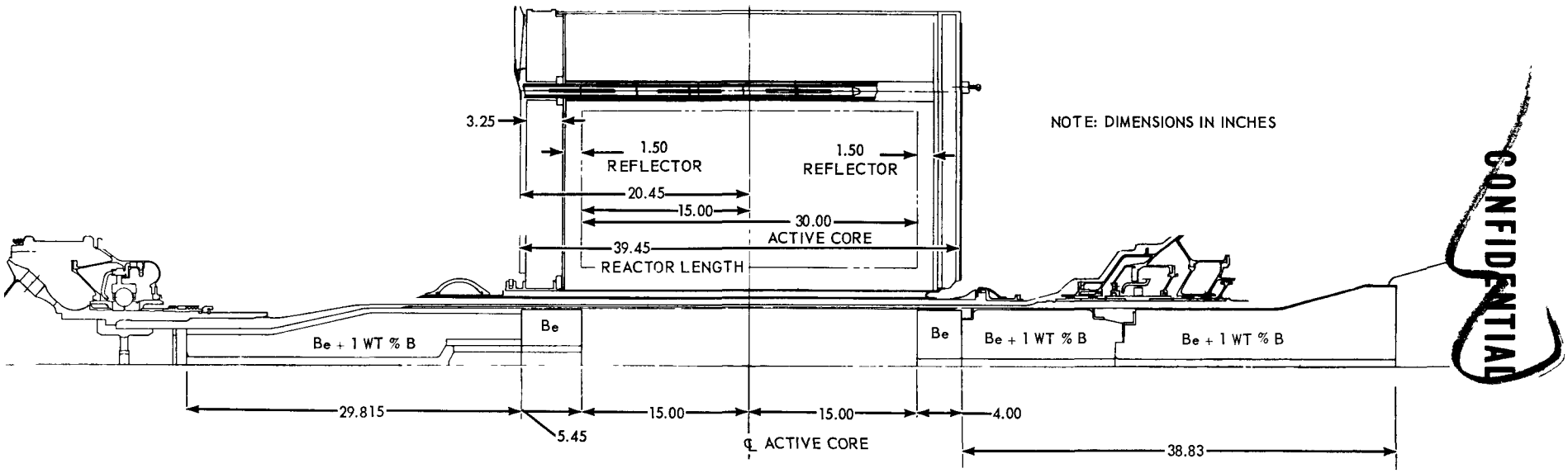

Fig. 5.12 – Coupling shaft shield inserts

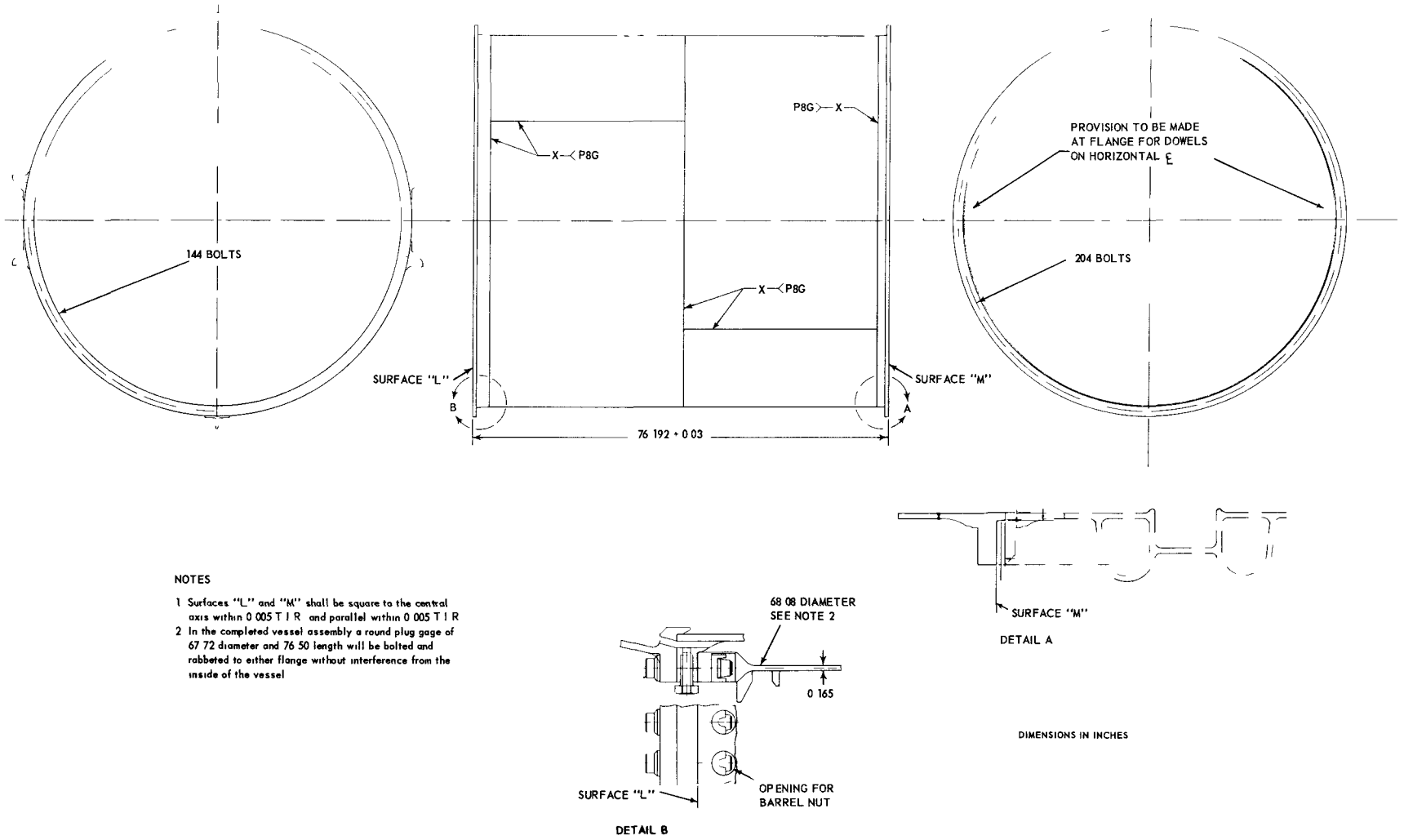

Fig. 5.13 – XNJ140E-1 pressure vessel

7. The side shield segment cans were vented so that no significant internal bursting pressures developed.
8. The side shield segments did not deflect in a manner permitting contact with the pressure vessel under any operating condition.

5. 2. 2. 2 Aerothermal

Requirements imposed on the aerothermal design of shield components were as follows:

1. The maximum allowable material temperatures were as follows:

Stainless steel	1200°F
Beryllium	1000°F, surface
	1200°F, internal
Insulation covers	1700°F
Lithium hydride	850°F, long term
	1050°F, short term
19-DL stainless steel	1000°F

2. Nominal nuclear-heating-rate distribution and twice nominal calculated values of heating rates were used in the analysis of the front and rear shields.
3. Nominal heating rates and heating-rate distributions were used in the analysis of the side shield.
4. Ram air was utilized for cooling the side shield, keeping to a minimum the ram drag of the over-all system.
5. Transient and steady-state temperature distributions did not produce excessive thermal gradients.
6. The pressure ratio ($P_{3.7}/P_{3.6}$) across the rear shield of 0. 975 was to be met during the cruise flight condition.
7. The design was based on developing maximum material temperatures during steady-state operation.

Detailed aerothermal design requirements are contained in references 1 through 10.*

5. 2. 2. 3 Nuclear

Shield optimization studies were performed considering three reactor-shield assemblies operating at 50 megawatts each, with a dose rate in the crew compartment of 0. 02 rem per hour. The studies also considered constraints on neutron leakage from the reactor shield in order to limit aircraft activation. The results of these studies were shown in Figures 5. 2 and 5. 3 as objective neutron- and gamma-dose patterns, respectively, for a single engine. These patterns were used as a guide in establishing the nuclear design.

Although these dose-rate patterns were established as objectives, they were not interpreted as such, in the strict sense, because of the dependence of an optimized over-all shield system design on a combination of criteria not adequately described by the simplified dose-rate patterns. Considerations of the number, angular distribution, and energy of particles or photons as a function of position on the shield surface were factored into the detailed analyses.

Nuclear design requirements are contained in reference 11.

*Reference lists appear at the end of each section.

5.3 OVER-ALL DESIGN DATA

5. 3. 1 MECHANICAL DESIGN

The engine assembly drawing, Figure 3. 7 in section 3. 3. 1, served as the over-all assembly drawing of the shield. Mechanical design data for components of the shield are presented in subsequent sections dealing with each particular component.

5. 3. 2 AEROTHERMAL DESIGN

5. 3. 2. 1 Primary-Air Ducts

The primary-cycle airflow ducting in the end shields was designed to provide flat velocity distribution with minimum loss into both the reactor core and the series chemical interburner. The forward duct consisted of an annular passage that delivered the air from the compressor-discharge annulus to the reactor in such a way as to decelerate the flow to the desired Mach number. Heated reactor cooling-air was discharged into an aft header and delivered to the series interburner by means of an annular duct designed to provide the designated velocity distribution.

5. 3. 2. 2 Primary-Air Cooling

Cooling airflow distribution is shown schematically in Figure 5. 14.

The front- and rear-shield central islands were cooled in series by 3. 2 percent $W_{a2.\,0}$. This air was extracted from the forward annular duct through cooling slots between the discs that comprised the front shield central island. This air then was collected at the inner radius of the front shield and ducted aft between the core liner and the shaft tunnel to the rear shield. In the rear shield, 1. 32 percent of $W_{a2.\,0}$ was bled off in four places in each of two circumferential locations to cool the insulating pads. The remainder (1.88%) cooled the rear-shield forward central island and was delivered to the connecting flange at the outer radius of the central island just forward of the rear shield support struts. After cooling the rear shield central island, this air passed to the turbine section and was used for further cooling in the turbine front frame.

The forward portion of the front shield outer section was cooled by core bypass air (1% $W_{a2.\,0}$) routed into the annulus between the reactor structural shell and the pressure vessel. The aft portion of the front shield outer section was cooled by bleed-speed control air that passed through holes leading to the annulus between the reactor structural shell and the pressure vessel.

The rear shield outer section was cooled by 1. 1 percent of $W_{a2.\,0}$ extracted from the annulus between the reactor structural shell and the pressure vessel. After cooling the shielding material and structure, the air passed through the insulation pads and mixed with the primary-air.

A portion (1% $W_{a2.\,0}$) of the core bypass air that flowed through the bleed-speed annulus was extracted from the annulus through holes in each of the ten turbine-rear-frame support struts. At the inner radius of each strut, the air was directed into the aft section of the rear shield through holes in the turbine front frame. The air was routed through shielding material before it leaked, through seals, back into the primary-air stream or into the No. 3 bearing housing.

5. 3. 2. 3 Ram-Air Cooling

Ram-air was used for in-flight cooling of the side shield and passed through internal cooling tubes extending the full length of the segments. These cooling tubes (which were finned in the area of highest heat generation) were installed prior to the casting process.

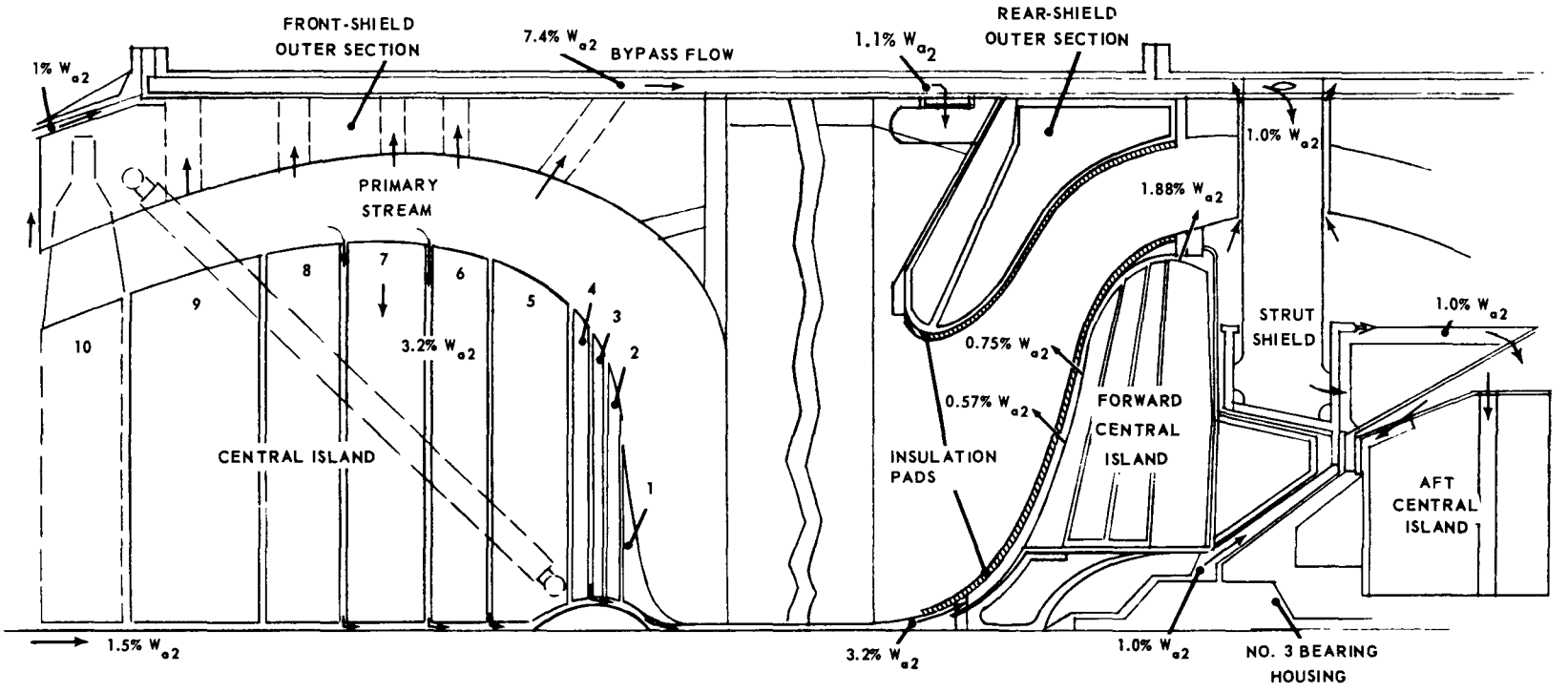

Fig. 5.14 – Flow distribution of cooling air in XNJ140E-1 end shields

The ram-air was brought on board and ducted to the individual segments. Each segment had a forward plenum to decelerate the flow before entering the individual cooling tubes. After passing the length of the segment, the air was collected in a rear plenum and discharged. For ACT operation, facility-supplied cooling air was used and then dumped directly from the tubes after cooling the segments.

Cooling tube patterns were selected on the basis of cooling requirements at the most critical flight point, the emergency power setting. Since the cooling was accomplished by ram-air, the flight condition having the worst combination of low flight speed, high inlet-air temperature, and high core power was the limiting case for steady-state operation. Cooling designed for this critical flight point was over-adequate at other flight points. Table 5. 2 illustrates significant cooling characteristics of the side shield using ram-air during several flight conditions.

Materials within the reactor surrounding the active core also served as neutron shielding and, to a certain extent, as gamma shielding. In addition, the outer reflector and the borated-steel pressure pads enclosing the reflector served in combination as a thermal shield and limited energy deposition in the side shield. Some neutrons were slowed down in the reflector and were subsequently absorbed in the borated pads. Zones of high-energy deposition thus were confined to regions where the heat could be dissipated by primary-air.

TABLE 5. 2

COOLING CHARACTERISTICS[a] OF SIDE SHIELD
DURING STEADY-STATE OPERATION

Flight Condition	c	d	e	f	Emergency
Altitude, ft	20, 000	35, 000	35, 000	10, 000	5, 000
Type of day	Std	Std	Std	Std	Hot
M_n	0. 7	0. 8	0. 8	0. 6	0. 43
$\Delta P_t/P_{t_{inside\ shield}}$	0. 161	0. 213	0. 213	0. 122	0. 080
W_{ram}, lb/sec	1. 7	1. 05	1. 05	2. 2	1. 72
Tt_{in}, °F	31	-16	-16	58	103
Tt_{out}, °F	348	316	335	372	533
$T_{LiHx_{max}}$, °F	621	574	610	650	911
Q_{core}, mw	78. 1	50. 5	53. 6	98. 5	109

[a]Based on ram-air cooling designs adequate for the emergency flight condition.

5. 3. 3 MATERIAL SELECTION

The choice of shielding materials was based upon a combination of nuclear, aerothermodynamic, and mechanical design considerations.

The neutron shielding materials were LiH_X and Be plus 1 weight percent boron. LiH_X was selected for the side shield because ram-air was used for cooling purposes. Where compressor discharge-air was used to dissipate the secondary heat, i. e. , in the front and rear shields, borated Be was chosen. The gamma-ray shielding material was 304 stainless steel plus 1 weight percent boron.

In addition to radiation shielding for biological purposes, thermal shields were used as an integral part of the reactor assembly in order to reduce secondary heat generation in

surrounding components. These shields were borated stainless steel placed around the outer reflector and forward of the front reflector. Radially, the thermal shield served to absorb neutrons, thereby suppressing thermal neutron absorption and subsequent alpha particle emission in the LiH_X of the side shield. Thermal shielding in the forward direction served a dual purpose in that it suppressed the thermal neutron flux, and also absorbed gamma rays in sufficient amounts to limit gamma-ray heating to handleable levels in the front shield. Shielding provided by the reflectors and reactor structure augmented the thermal shield.

Boron was used in all shielding materials with the exception of LiH_X which, in itself, contained a good thermal neutron absorber, lithium 6. The purpose was twofold: (1) to suppress thermal neutron absorption in structural materials and reduce the production of gamma rays which, in turn, led to photoneutron production in Be, and (2) to minimize induced radioactivity in engine components and aircraft structures.

5. 3. 4 NUCLEAR DESIGN

5. 3. 4. 1 Optimization and Constraints

The divided-shield concept entailed the use of radiation shielding around both the reactor and crew compartments. Shield system optimization was realized by distributing the shielding between each in a manner that minimized the over-all system weight and yet limited radiation to tolerable levels within the crew compartment as well as around the reactor-shield assembly. The maximum radiation leakage was determined by tolerable radiation levels incident on engine and aircraft systems and structures and therefore established minimum shield thicknesses. The additional shielding required to attain the allowable biological dose rate was distributed between reactor shield and crew shield in a manner that obtained minimum over-all shield system weight.

Optimization studies were conducted by Convair - Fort Worth under General Electric subcontract. These studies[12*] were based on a crew dose rate of 0. 02 rem per hour within a Convair five-man crew compartment located approximately 100 feet forward of the core midpoint. A gamma-ray dose rate of 1. 0 rad (carbon) per hour per megawatt of reactor power at 50 feet in the forward direction closely approximated the optimum division of gamma-ray shielding between reactor shield and crew shield. Furthermore, the effect of air-scattered gamma rays on crew dose diminished rapidly with increasing scattering angles to the extent that gamma-ray shielding along the side or rear of the reactor was virtually ineffective in reducing the gamma-ray dose in the crew compartment. Consequently, gamma-ray shielding was used only in the forward part of the reactor shield and no specific provisions were made for reducing gamma-ray leakage at other angles. The effects of the resultant gamma-ray levels in regard to radiation damage of engine components and aircraft systems were not factored fully into the study.

The desired engine life was set at 1000 hours. However, certain organic components or items required replacement every 120-hour mission because of radiation damage. Based on reference 13, the bearing-oil dose constraint was assumed to be 7.2×10^8 ergs per gram per hour for a duration of 120 hours at an oil-in temperature of 250°F. The gamma-ray radiation damage constraint for elastomers (organic seals, O rings, tubing, insulation) was approximately 5×10^7 rads (carbon) integrated dose.

The shield was designed to meet external neutron dose levels based upon considerations of aircraft activation constraints together with optimum weight division between reactor shield and crew shield. Aircraft maintenance considerations established desirable limits of neutron-induced radioactivity in aircraft structures and, therefore, established activa-

*Superscripts refer to the reference lists that appear at the end of each section.

tion constraints. In order to meet these constraints neutron shielding over and above that required for optimum weight division was added along the horizontal sides of the external engines (shield cheeks) in order to limit activation of the aircraft wings.

5. 3. 4. 2 Shield Sharing

The reduction in external radiation levels in the horizontal plane, resulting from the shadow-shielding effect of one engine by the other, was taken into account in establishing the desired levels to which the reactor shield was designed.[11]

Furthermore, the shields on adjacent engines were shared to a certain extent; that is, the engines were placed in close proximity, as shown in Figure 5. 15. A slice was removed from each side shield, and a net weight saving resulted.

For the sake of simplicity and expediency in performing calculations using computer programs, the basic nuclear analysis of the reactor shield assumed an unshared, cylindrically symmetric shield for one engine.

5. 3. 4. 3 Dose Rates

Direct-beam fast-neutron and gamma-ray dose rate predictions were based upon point kernel computations for line-of-sight paths through the shield from numerous reactor source points to each receiver point. Shielding Computer Program 14-0[14] was used for these computations. In addition, the effects of radiation scattering along the annular ducts were estimated. Neutron and gamma radiation emitted from the fissioning of uranium in the active core, and neutron-capture gamma rays from core and shield materials were the sources of radiation taken into account.

Dose rates outside the shield did not include effects of scattering or attenuation in air, unless specifically noted. These effects were taken into account in the design of the crew shield and in the optimization calculations; however, the objective dose-rate patterns were given in terms of a direct-beam dose including shield-secondary and shield-scattered contributions, but excluding air-scattered contributions.

The radiation patterns presented in subsequent sections were computed for a nuclear model simulating an unshared cylindrically symmetric shield, and operating at a reactor power of 1 megawatt. Dose-rate patterns at a specific distance from the active core midpoint are presented as a function of azimuthal angle, α , from front to rear as defined in Figure 5. 16. For the assumed cylindrically symmetric shield, these patterns applied to any polar angle, ϕ, measured in a plane perpendicular to the engine centerline, Figure 5. 16. However, for combinations of engines the shielding of adjacent engines perturbed these patterns and variations occurred as a function of polar angle as well as azimuthal angle.

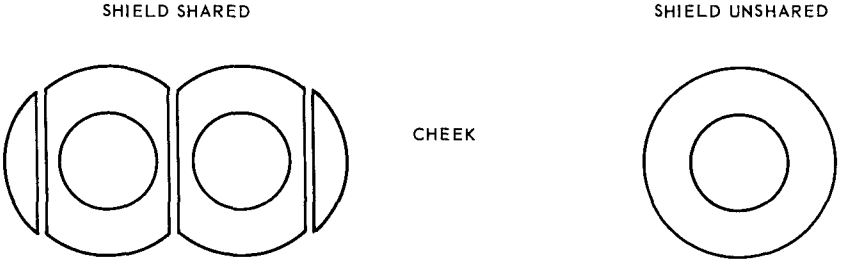

Fig. 5.15 – Shield sharing concept

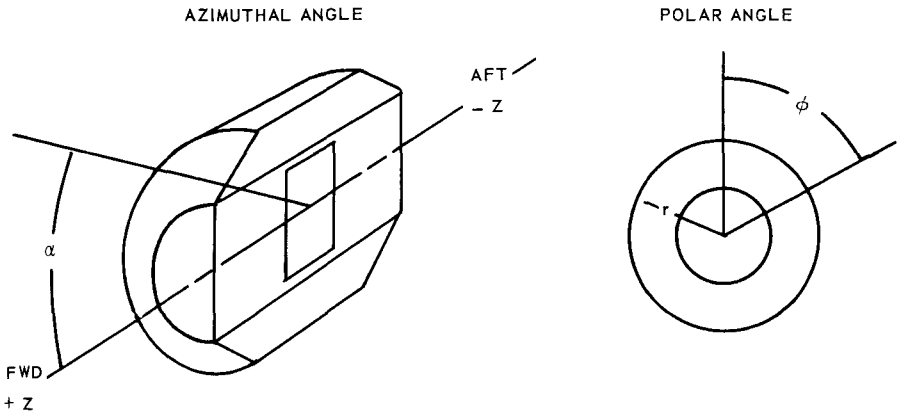

Fig. 5.16 – Definition of angles for shield nuclear data

The radiation patterns shown in this section were applicable to the shield-shared case only at remote locations in the vertical plane (polar angle $\phi = 0$ degree and 180 degrees), where the power in each engine produced roughly the same effect and, therefore, the total dose was directly proportional to the combined power. In the horizontal plane (polar angle $\phi = 90$ degrees and 270 degrees) at an azimuthal angle of 90 degrees, the total dose equalled that from one outboard engine, since the outboard engine served as a shadow shield for adjacent engines. At other locations around a multi-engine system the total dose rate varied between the two cases mentioned.

Figures 5.17 and 5.18 show the calculated environmental dose rates for fast neutrons and gammas, respectively. These dose rates are shown as the radiation pattern at a distance of 50 feet from the center of the reactor in the vertical plane through a typical side shield segment, and included the effects of the shield pads surrounding the control rod actuators.

Figures 5.19 and 5.20 show external isodose patterns for fast-neutron and gamma-ray dose rates, respectively, during nuclear operation. Figure 5.21 presents an external isodose pattern for after-shutdown gamma rays. The isodose patterns presented in Figures 5.19, 5.20, and 5.21 lay in a horizontal plane through the reactor midpoint and are shown as a function of azimuthal angle and radii from the reactor midpoint.

The isodose pattern shown in Figure 5.19 included the calculated contributions of direct-beam penetration, single air-scattering, and scattering through the rear-shield annular duct. The gamma-ray isodose patterns shown in Figures 5.20 and 5.21 included the contribution of direct-beam penetration and single air-scattering, and are based upon core-originated gamma rays only. An operating history of 100 hours of equilibrium operation, followed by 10 hours of shutdown, was assumed in the calculations for Figure 5.21.

Figure 5.22 is a plot of factors to be used in converting the after-shutdown isodose pattern shown in Figure 5.21 to other operating and shutdown histories.

Figure 5.23 shows neutron isodoses within the shield based on calculations of direct-beam penetration (line-of-sight penetration from numerous core source points to each receiver point). The data pertained to the horizontal plane ($\phi = 0$ degree) through the reactor centerline, and were based on a reactor operating power of 1 megawatt. Dose rates at other power levels were in direct proportion to the power.

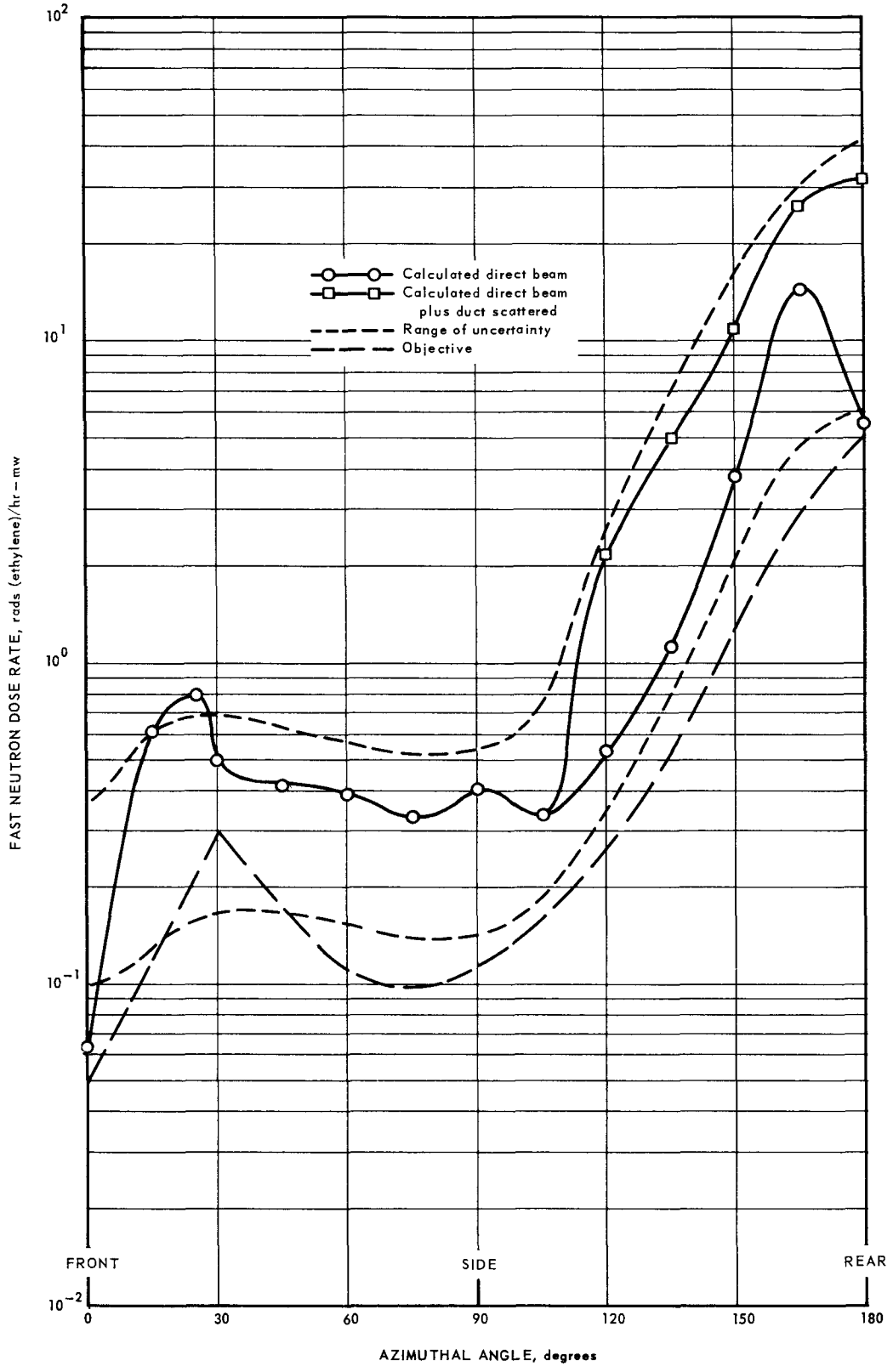

Fig. 5.17 – Calculated fast neutron dose rates per megawatt of reactor power 50 feet from XNJ140E-1 reactor midpoint

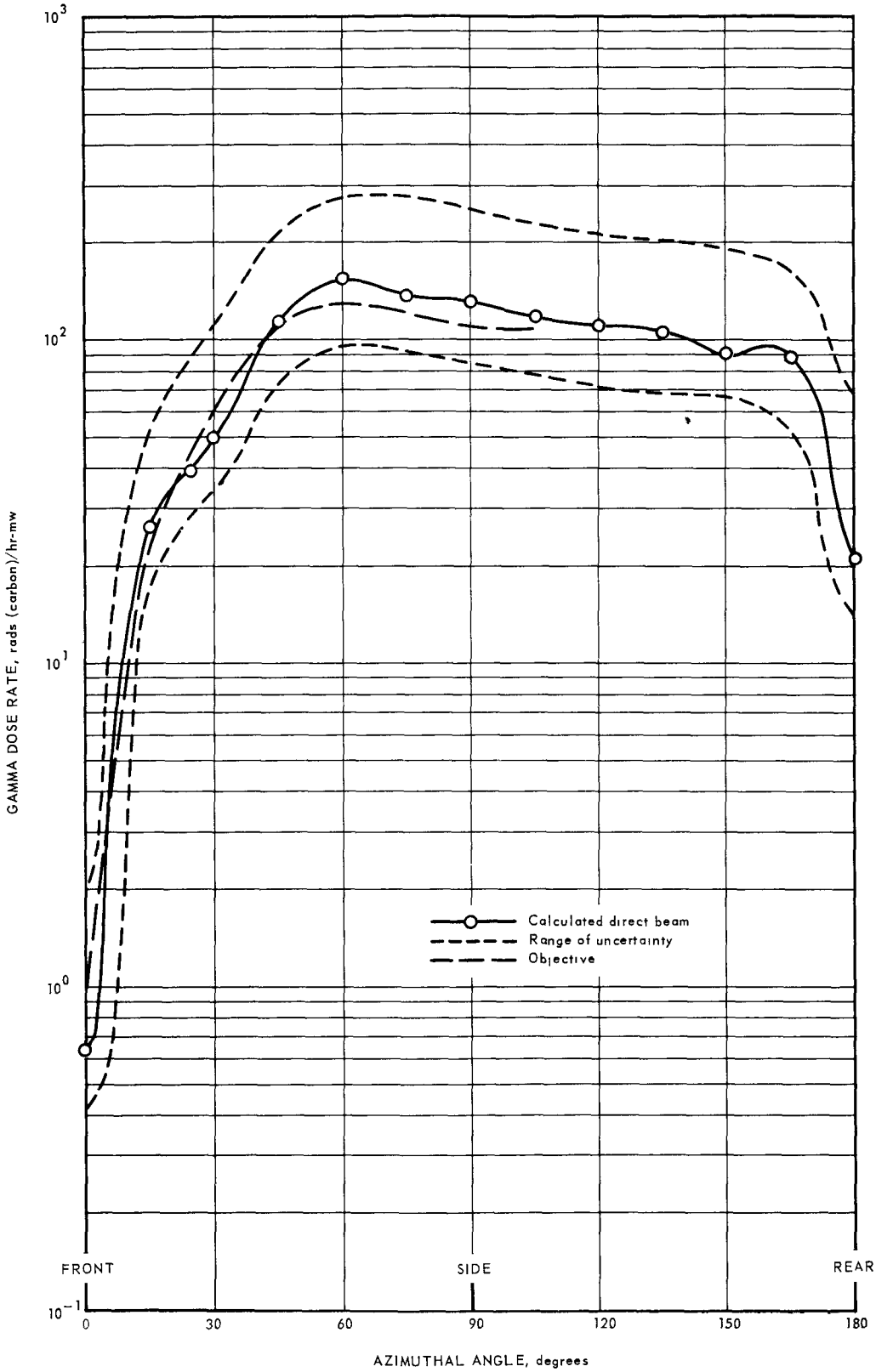

Fig. 5.18 – Calculated gamma dose rate per megawatt of reactor power 50 feet from XNJ140E-1 reactor midpoint

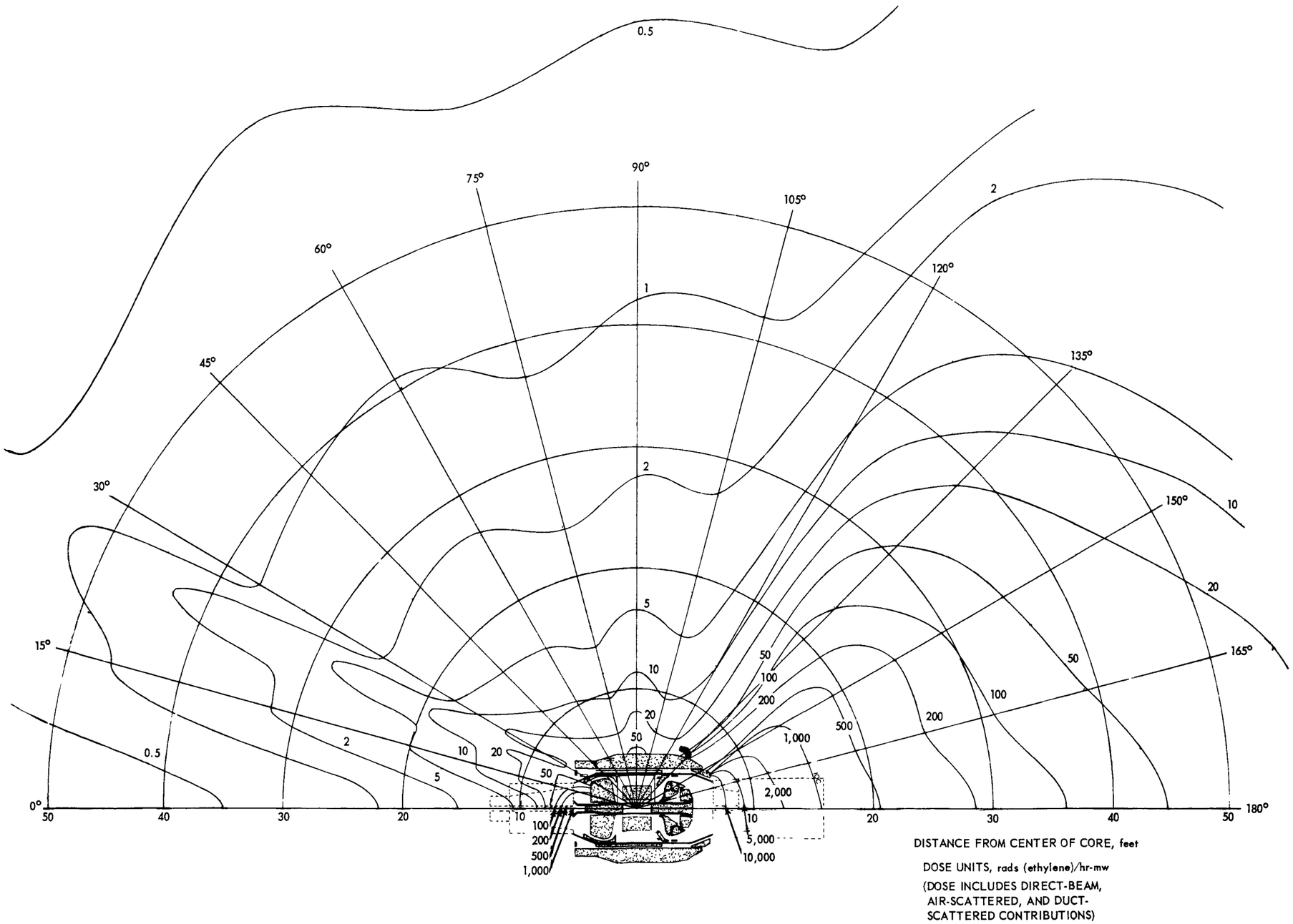

Fig. 5.19 – External fast neutron isodose pattern during nuclear operation, XNJ140E-1 engine

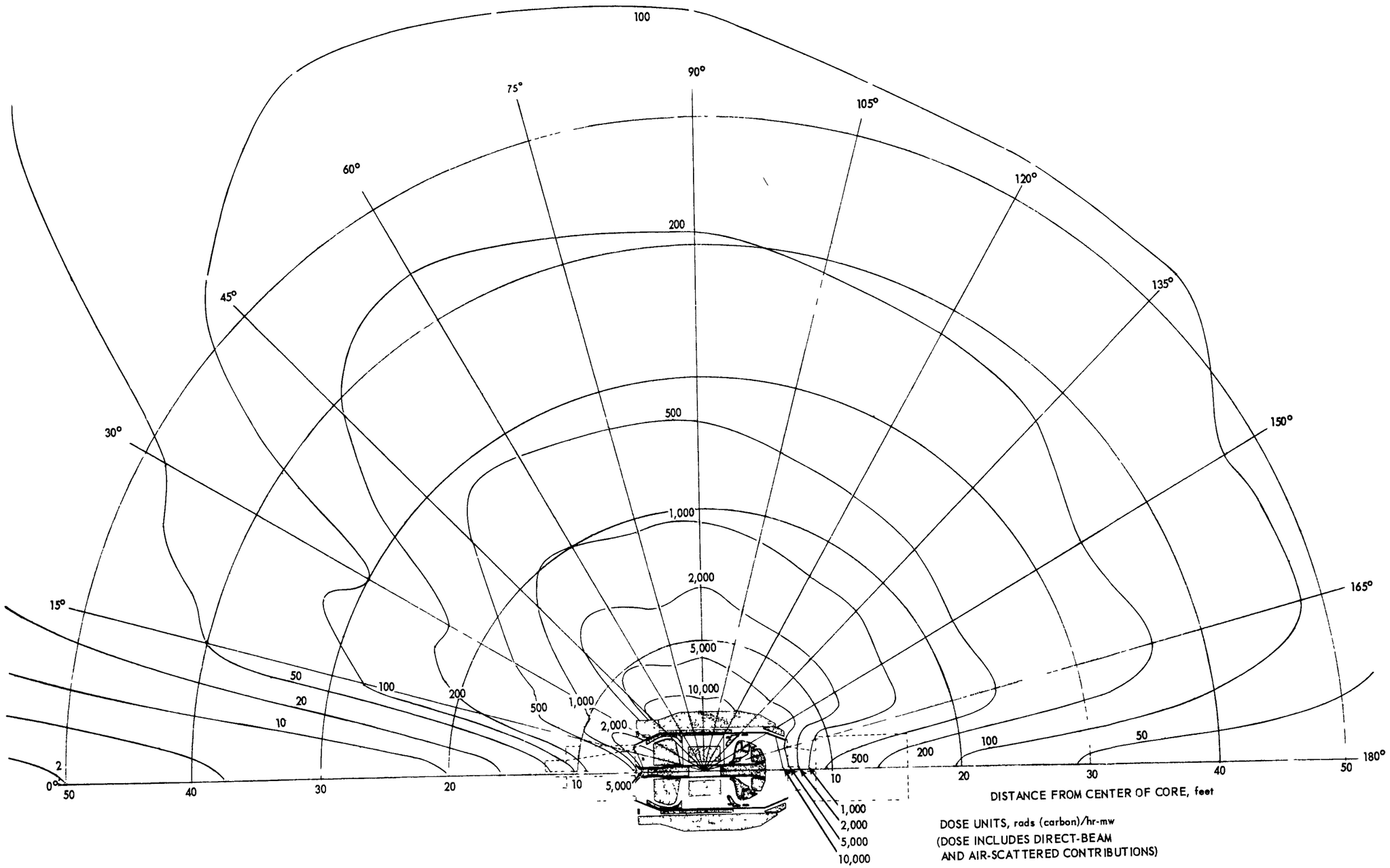

Fig. 5.20 – External gamma isodose pattern during nuclear operation, XNJ140E-1 engine

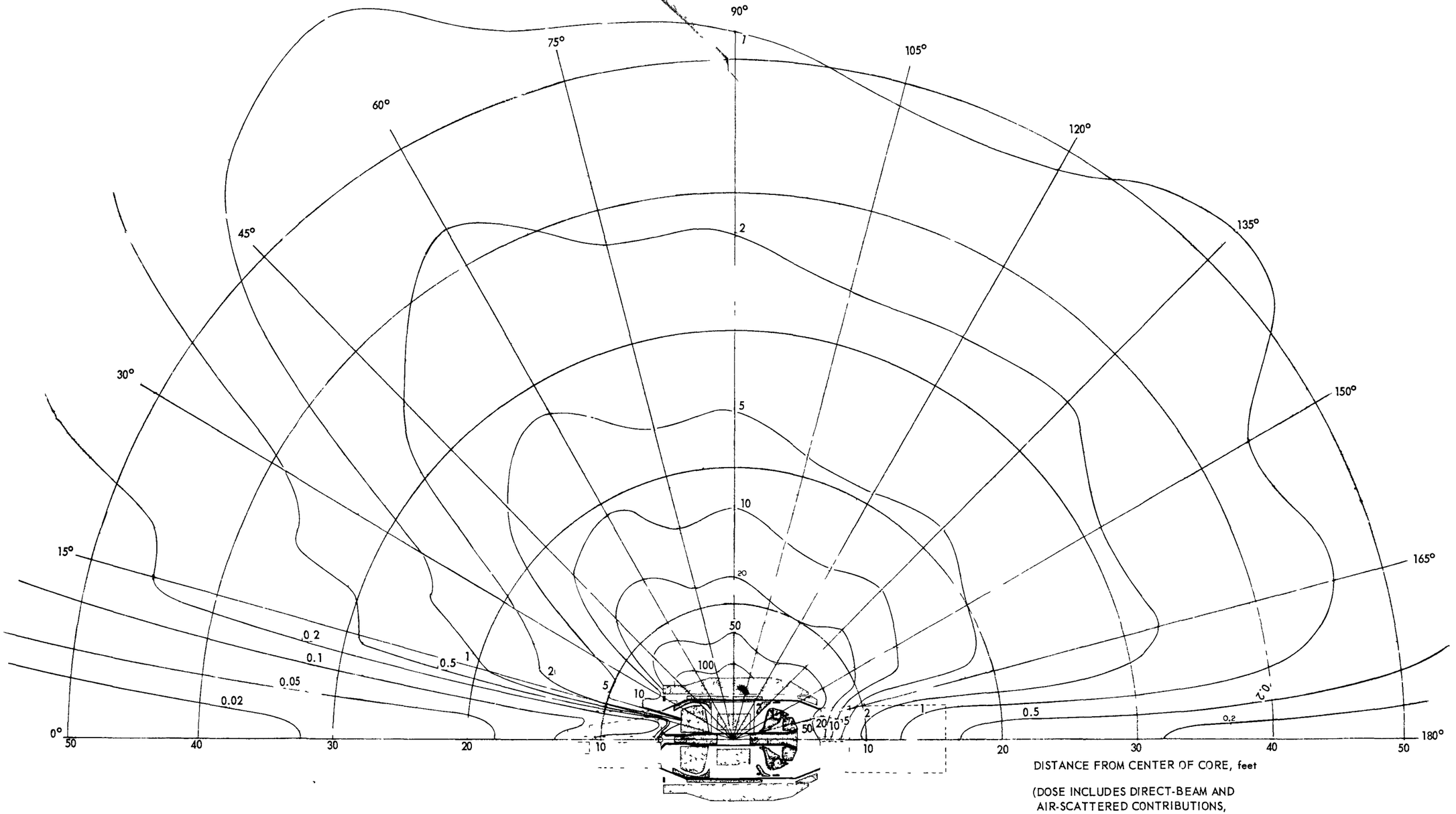

Fig. 5.21 – External gamma isodose pattern following shutdown from nuclear operation, XNJ140E-1 engine

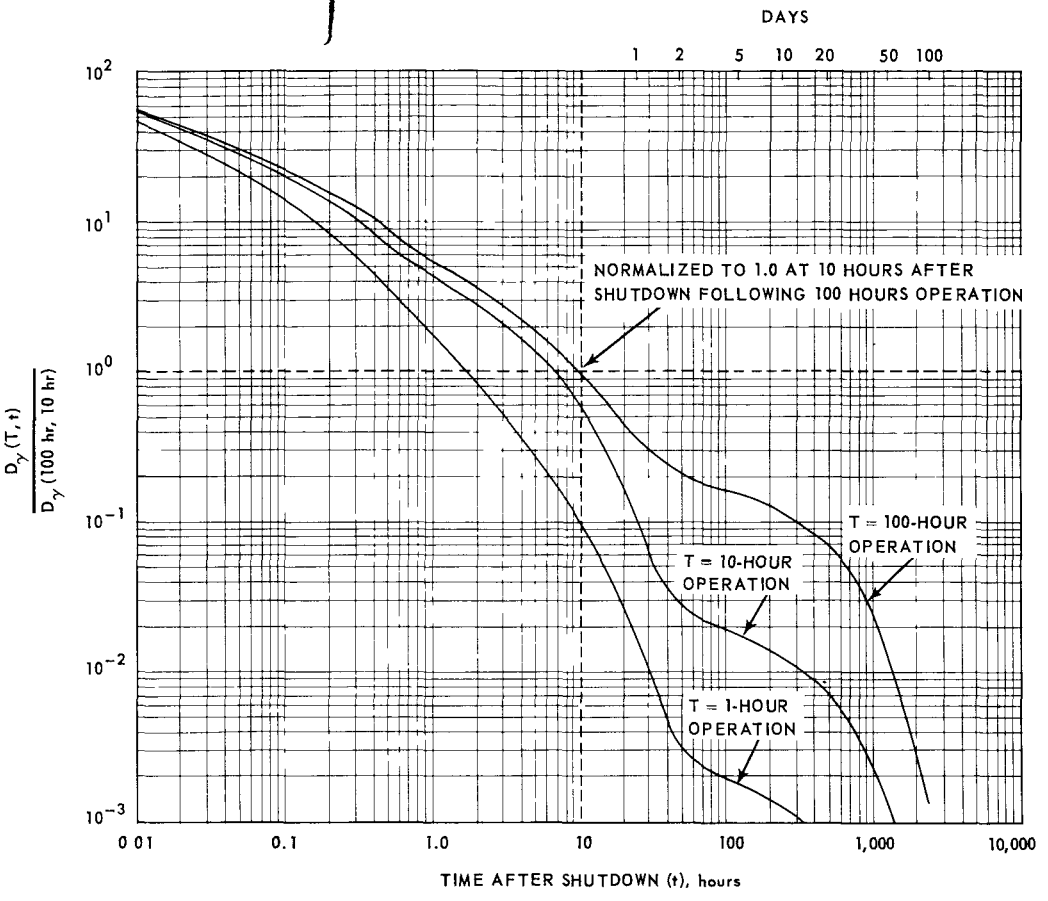

Fig. 5.22 – Relative after-shutdown gamma dose rates as a function of operating and shutdown history

5.3.4.4 Secondary Heating Rates

Nuclear heat generation rates in the shield were computed on the basis of energy deposition by four processes:

1. Absorption of core gamma rays
2. Kinetic energy loss, or moderation, of fast neutrons
3. Kinetic energy deposition due to the $(n - \alpha)$ reaction in B^{10} or Li^6
4. Absorption of gamma rays caused by neutron captures.

The contribution of gamma-ray heating due to inelastic scattering of neutrons was not included; however, it was expected to be small. Calculations of gamma-ray heating due to neutron captures throughout the reactor-shield assembly showed that this contribution was approximately 10 percent of the core gamma-ray heating in the front shield, 35 percent of the core gamma-ray heating in the side shield, and point values as high as 50 percent of the core gamma-ray heating in the rear shield.

All the data presented herein are nominal or "as calculated" values. Refinements based on measurements made in critical experiments or resulting from improved calculational techniques, such as Monte Carlo, were planned, but were not completed at the time of contract termination. Initial critical experiment data obtained prior to the termination of the program were insufficient to determine the validity of the heating-rate calculations. However, when combined with some metallic core experimental data, the experimental

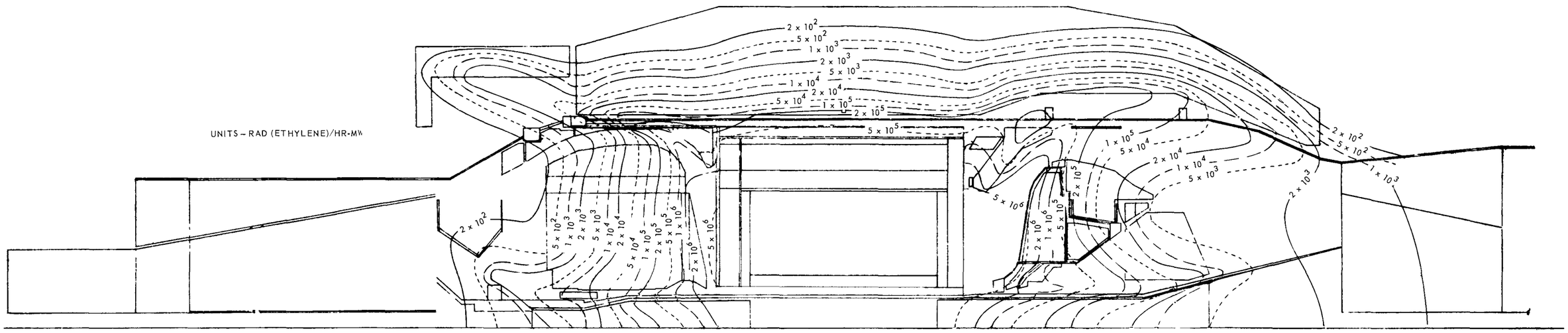

Fig. 5.23 – Fast neutron isodose pattern in the shield assembly (Dwg. SK207R873)

data indicated that the analytical data, in general, were (1) within a factor of two for neutron-induced reactions, and (2) within a factor of 1.5 for gamma-ray heating.

Monte Carlo calculations were being performed at the time of contract termination which showed good agreement with point kernel calculations. A Monte Carlo computer program for neutrons was being prepared but was not completed. A preliminary comparison of the core-originated gamma-ray heating is presented in Table 5.3.

TABLE 5.3

COMPARISON OF GAMMA RAY ENERGY DEPOSITION DUE TO CORE-ORIGINATED GAMMA RAYS USING MONTE CARLO AND POINT KERNEL METHODS

	Gamma Ray Energy Deposition, watts/mw		
Shield Region	Point Kernel	Monte Carlo	Monte Carlo / Point Kernel
Front	1.265×10^3	1.279×10^3	1.011
Side	3.269×10^2	3.788×10^2	1.159
Rear	6.80×10^2	5.688×10^2	0.836

Secondary Gamma Production - Gamma-ray dose rates and heating rates resulting from neutron capture in the shielding and structural materials were based on the combined use of programs G-2,[15,16] CURE, and 14-0. Program G-2 and 14-0 are explained in section 5.9. Program CURE was a two-dimensional multi-group multi-region code based on diffusion theory. Program G-2 was employed to obtain the distribution of neutron captures along a radial traverse at the core midplane. Normalization of Program G-2 results was obtained by comparison of G-2 calculated fast-neutron dose rates with those calculated by Program 14-0. The longitudinal distribution of neutron captures in all side-shield and outer-reflector source regions, with the exception of the control rods, was assumed to follow the longitudinal variation in fast-neutron dose rate at the pressure pads. The longitudinal distribution for the front- and rear-shield source regions was obtained from Program G-2, assuming a centerline located at a radius of 17.74 inches. Since the neutron spectral information obtained from G-2 was limited to locations along a radial traverse at the core midplane and an axial traverse at the core centerline, the distribution of neutron flux in the rods and the rear-shield stainless steel regions was determined by reference to the results of Program CURE computations. The capture distribution and capture gamma-ray spectra were used in Program 14-0 to obtain capture-gamma dose rates and heating rates.

5.3.4.5 Induced Radioactivity

The radiation environment, following shutdown from nuclear operation, surrounding the engine or its components, necessitated special handling techniques. These techniques involved (1) limited manual maintenance, (2) semi-remote maintenance requiring shielded approach vehicles, and (3) remote handling in a hot cell. The category into which any operation fell was determined by the intensity of the radiation environment.

Residual gamma-ray dose rates from radioactive decay of induced activation were negligible compared to the fission-product-decay gamma rays in the core. Following disassembly and removal of the reactor, however, induced radioactivity usually determined the kind of maintenance required.

The analytical method used to evaluate induced radioactivity involved the computation of nuclear reaction rates in the various components due to an impinging neutron flux, the conversion of the resulting radioactive decay to gamma-ray dose rates, and the summing up of such dosages at various field points for various times of interest. The method and techniques used are described in references 17 and 18.

Figures 5.24 and 5.25 show the neutron spectra assumed in computing the induced-activation reaction rates. The spectra shown were semi-empirical in nature, having been determined by correlating program G-2 diffusion theory calculations with experimental results obtained from nuclear emulsion track plates exposed behind shield mockups. The spectra were normalized so that exposure of a phantom dosimeter to the differential neutron flux would read 1 rad (tissue) per hour. The integral neutron flux is shown in Figure 5.26.

For calculation purposes, the shape of the neutron spectra was assumed invariant and the magnitude was solely dependent upon the neutron dose rate evaluated at the point of interest. These neutron dose rates were evaluated using GE-ANPD Shielding Computer Code 14-0. A typical calculated fast neutron dose rate pattern was shown in Figure 5.17.

The predicted levels of induced radioactivity given below were based on a history of 100 hours operation at reactor power of 50 megawatts followed by a 100-hour decay time.

Compressor Section - The compressor rear frame was estimated to be the critical component because of its large mass and proximity to the reactor. A simplified calculation of the compressor rear frame activation was completed and the results were as follows:

Dose rate at No. 2 bearing, r/hr	2.1
Dose rate at 3-foot radius in the plane of the frame front flange, mr/hr	680
Dose rate at 4-foot radius in the plane of the frame front flange, mr/hr	330
Dose rate at 5-foot radius in the plane of the frame front flange, mr/hr	220

Approximately 92 percent of the residual gamma-ray dose rate was due to Co^{58} (half-life, 72 days), and approximately 6 percent was due to Co^{60} (half-life, 5.3 years). These values were preliminary and were being refined at the time of contract termination.

Reactor-Shield Assembly - Calculations involving components of the reactor-shield assembly had been initiated, but no significant data had been generated.

Turbine Section - The turbine assembly was expected to be extremely radioactive because of the high neutron radiation levels encountered in the reactor aft direction and the high absorption cross sections of the structural materials. Figure 5.27 shows the calculated residual gamma-ray dose rates for the turbine assembly. Shield material and duct structure was not included, and only part of the combustor assembly was accounted for. Dose rates were calculated at 3-foot and 5-foot radii at the planes of the stator front flange, stator rear flange, and rear-frame rear flange. The study showed that induced radioactivity of the turbine front frame was the major contributor to the calculated dose rates; its contribution never was less than 93 percent of the total dose at any field point considered. Table 5.4 summarizes the calculated dose rates and provides some additional information concerning the contributions of nozzles, discs, and buckets.

Induced Activity in the Coupling Shaft - The coupling shaft passed through the center of the reactor and, as a result, became highly activated. Preliminary estimates of the dose rate yielded 11,000 r/hr per lineal foot of shaft passing through the active core.

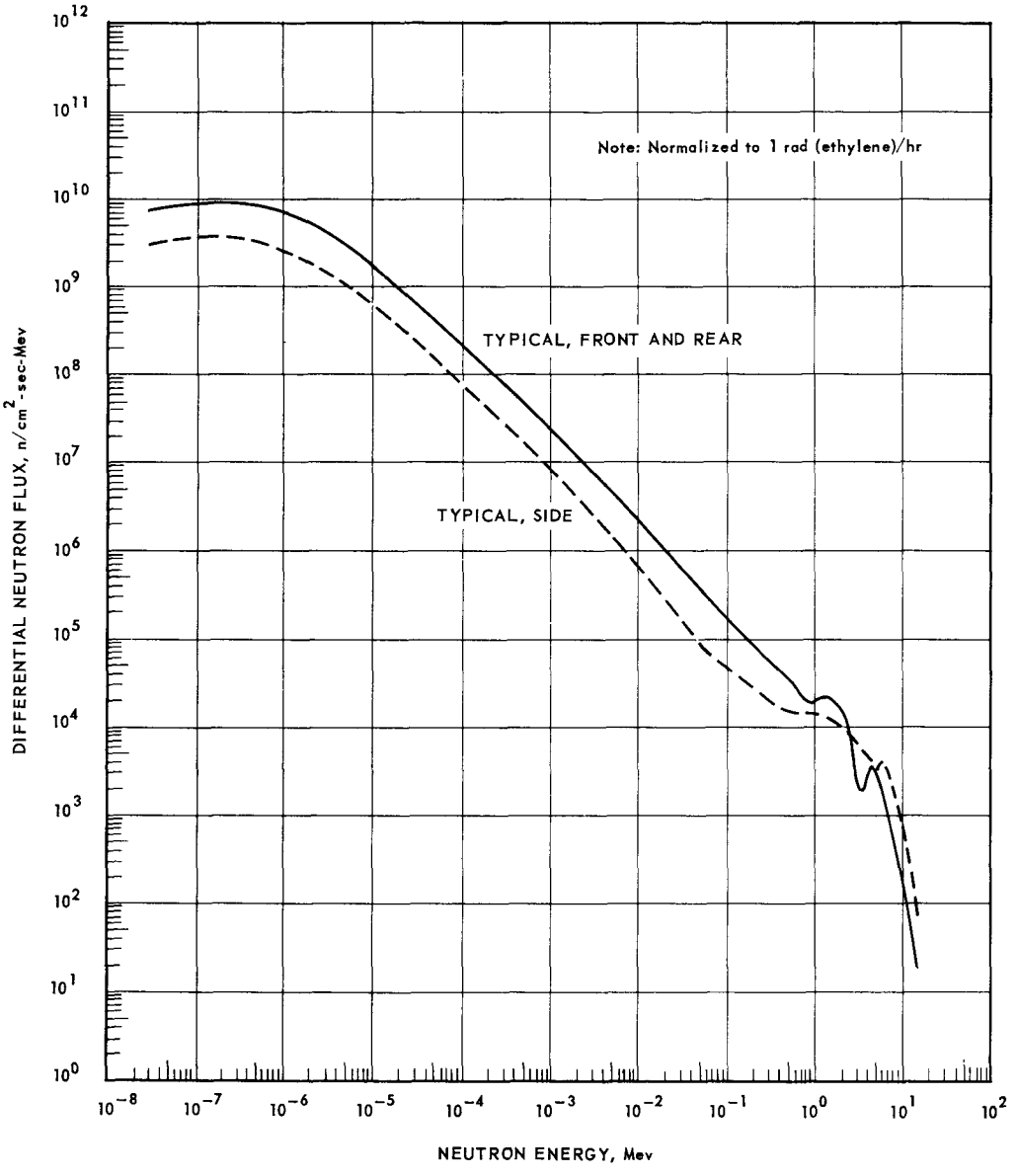

Fig. 5.24 – Collimated differential neutron flux leaving front, side, and rear of XNJ140E-1 engine, low-energy range

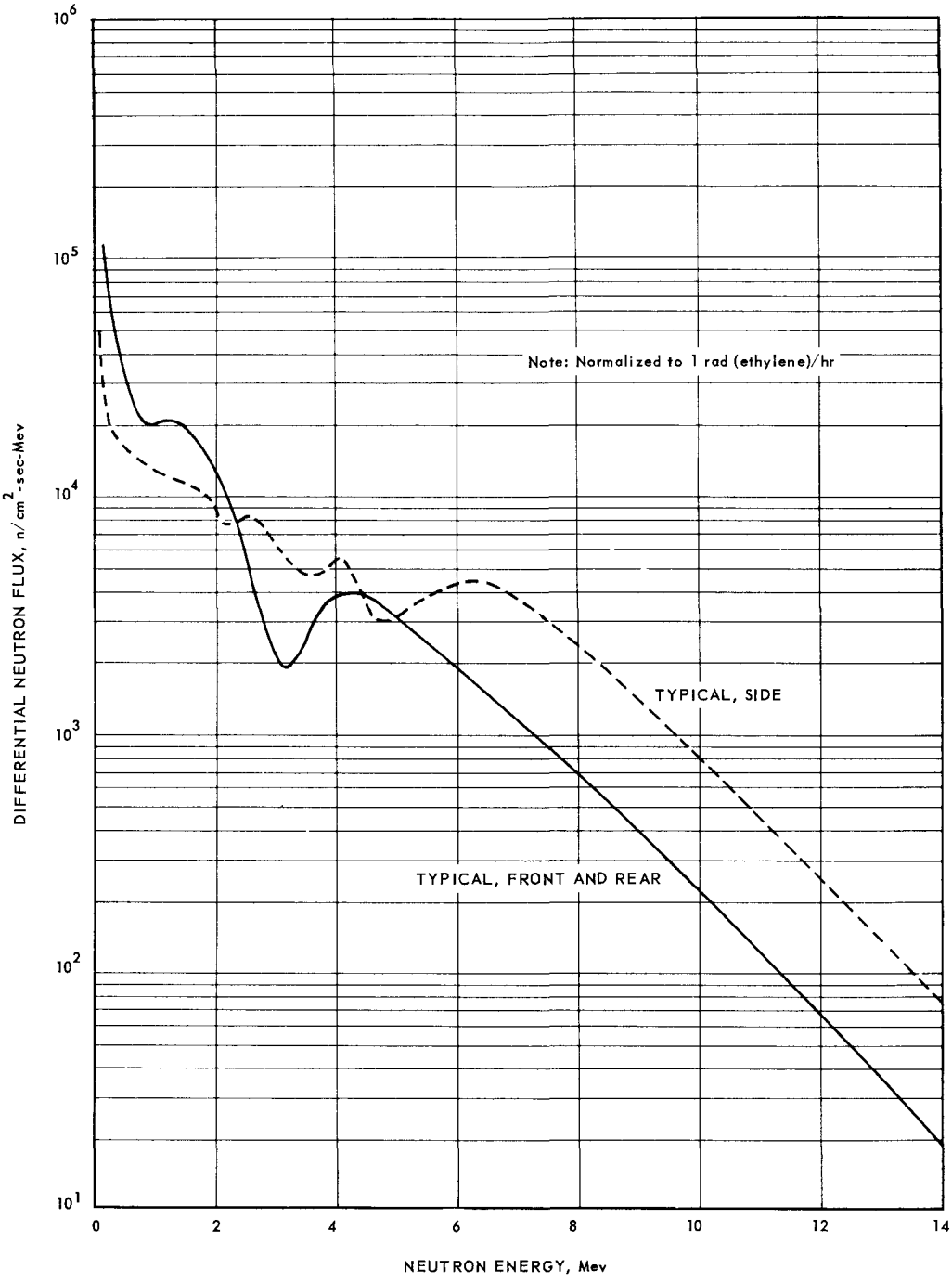

Fig. 5.25 – Collimated differential neutron flux leaving front, side, and rear of XNJ140E-1 engine, high-energy range

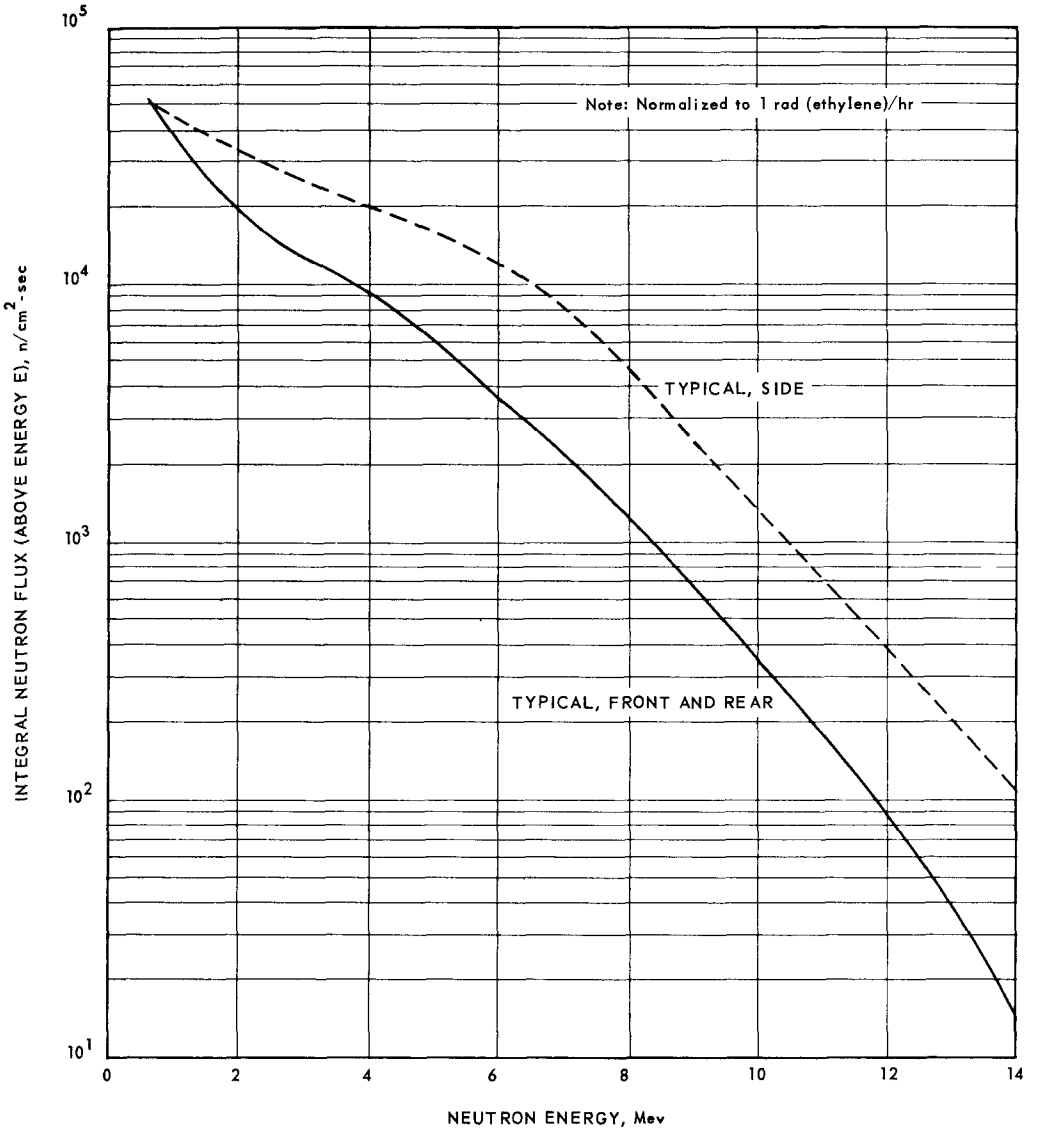

Fig. 5.26 – Collimated integral neutron flux leaving the front, rear, and side of the XNJ140E-1 engine

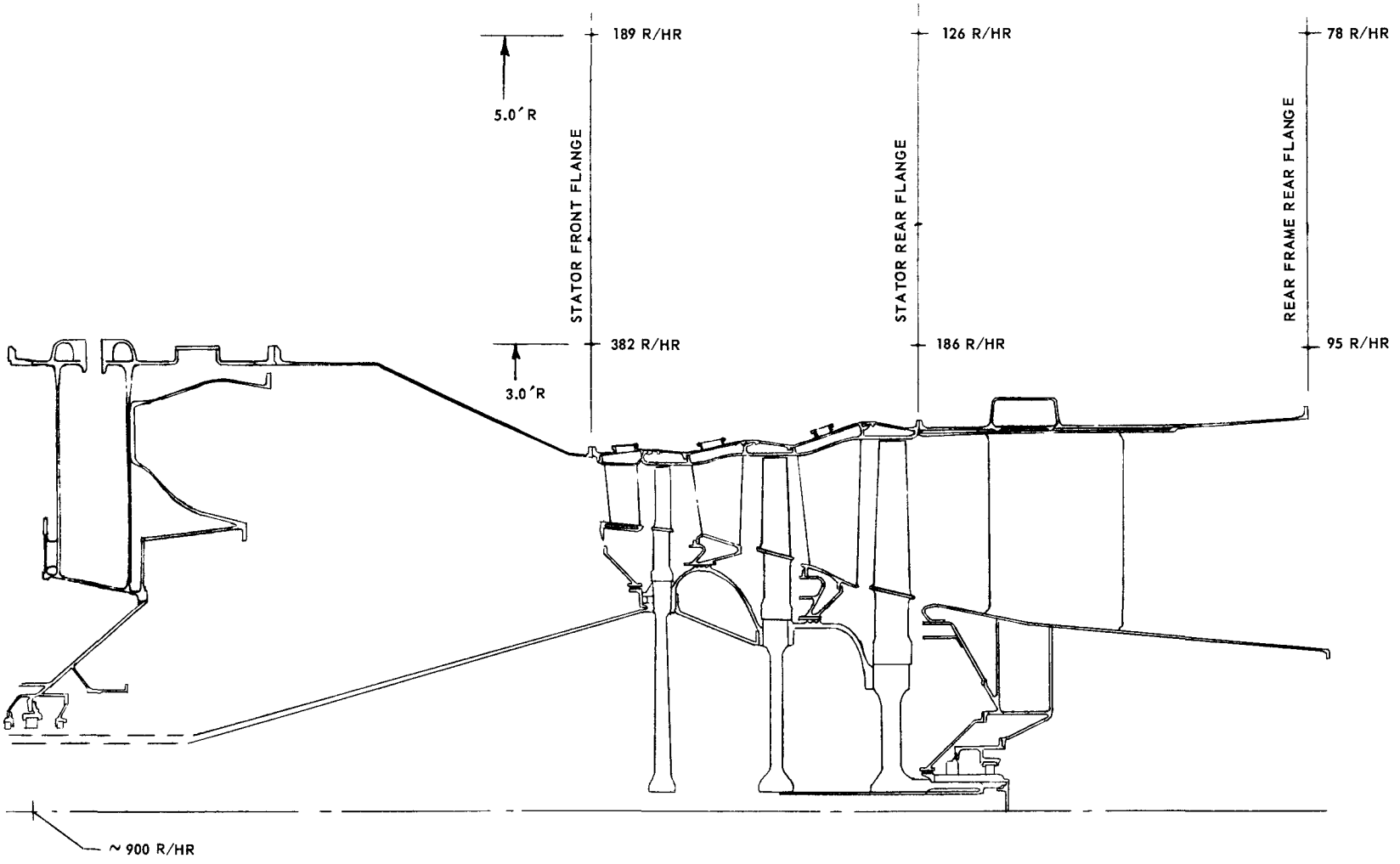

Fig. 5.27 – Residual gamma-ray dose rates due to radioactivity in the turbine section

TABLE 5.4

INDUCED RADIOACTIVITY[a] IN TURBINE SECTION

	Stator Front Flange		Stator Rear Flange		Rear Frame	Rear Flange
	3 ft[b]	5 ft[b]	3 ft[b]	5 ft[b]	3 ft[b]	5 ft[b]
Turbine Front Frame	357	182	170	120	90	74
Combustor Casing	16.7	5.05	8.95	3.62	3.38	2.27
Stator Assembly	3.8	0.8	2.5	0.8	0.7	0.6
Nozzles	2.9	0.6	1.8	0.6	0.5	0.3
Rotor Assembly	4.5	1.5	4.0	1.3	1.3	0.8
Discs, spacers, shaft	0.9	0.3	0.7	0.3	0.3	0.2
Buckets	3.6	1.2	3.3	1.0	1.0	0.6
Turbine Rear Frame	0.049		0.171		0.090	
Total, Turbine Assembly	382	189	186	126	95	78

[a]All dose rates in r/hr 100 hours after shutdown from 100 hour operation at reactor power 50 mw.

[b]Radial distance from engine axis.

The methods used for calculating these dose rates were used to calculate comparable dose rates of a J79 jet engine. The calculated results then were compared to the dose rates from an irradiated J79 jet engine. For shutdown times greater than 50 hours, the method predicted the resulting gamma-ray dose rates within a factor of two at distances in the order of one diameter from the activated surface. This factor should be applied as a generalization to the data reported above.

5.3.5 STRESS AND WEIGHTS

Detailed information relative to over-all shield stresses are contained in references 19 and 20. The magnitudes of the calculated loads indicated that the over-all structural design was feasible within the power plant design criteria.

Shield component weights are summarized in section 3.3.2 and reference 21, and were listed in Table 5.1.

5.4 FRONT SHIELD COMPONENT DESIGN DATA

5.4.1 MECHANICAL DESIGN

The maximum compressor discharge pressure affecting the front shield assembly design occurred during Condition 2; maximum acceleration to "q" limit - maximum power limit - cold day. For this condition $P_{t_{3.2}} = 230$ psia, $T_{3.2} = 505^{\circ}F$, $W_{a_{3.2}} = 546$ lb/sec and $Q = 150$ megawatts. The maximum material temperatures occurred during Condition 4; emergency power at $M_n = 0.43$ hot day when $P_{3.2} = 173$ psia, $T_{3.2} = 778^{\circ}F$, $W_{a_{3.2}} = 364$ lb/sec, and $Q = 109$ megawatts.

The layout of the front shield is shown in Figure 5.28. The outer section consisted of blocks of borated Be and borated stainless steel mounted inside the compressor rear frame, the front shield cone, the forward portion of the reactor structural shell, and in the vicinity of the forward flange of the pressure vessel. The front shield cone was a conical shell flanged at both ends. The forward flange of the front shield cone was attached

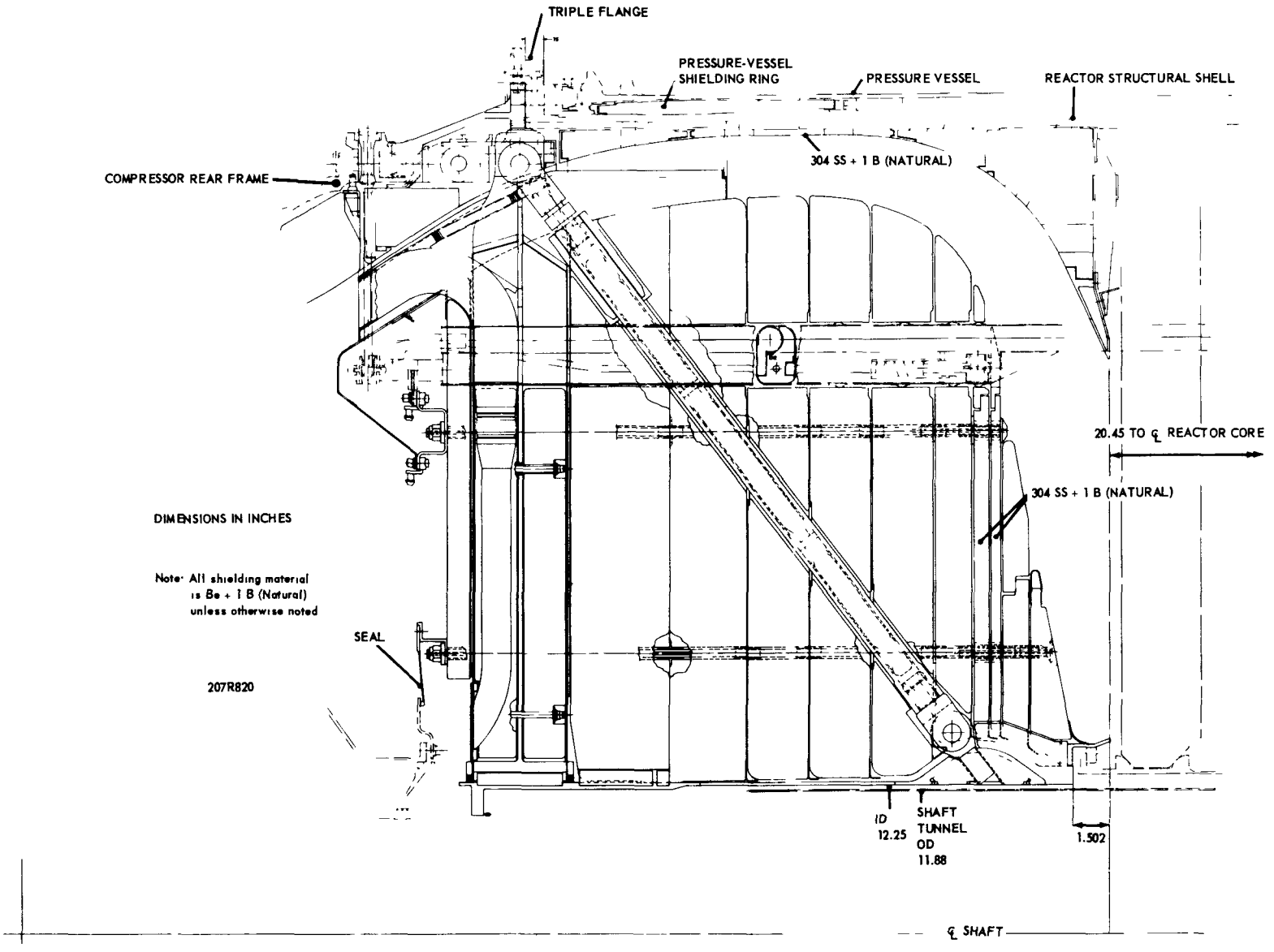

Fig. 5.28 – XNJ140E-1 front shield layout

to the compressor rear frame. The aft flange was bolted between the pressure vessel flange and reactor structural shell flange. This assembly of flanges constituted the triple flange. The central island was supported through its support structure, the support structure was bolted to the cone. The control rod actuators were mounted externally on the triple flange.

Structural materials in the front shield were Inconel and Inconel X. In addition, shielding materials were used judiciously as structural materials wherever possible. Inconel was used where stiffness requirements resulted in moderate stress levels. Age-hardened Inconel X was used to obtain a maximum strength-to-weight ratio.

Nuclear heat generated within the central island shield material was dissipated by air bled from the primary-air stream through gaps provided between shielding discs and sectors. Cooling-air entered radially, flowed inward, and then was collected in the annulus around the tunnel. In the outer section, cooling-air flowed radially outward between shield blocks. This cooling-air then was collected in the bleed-speed annulus.

A number of nuclear heat-rate sensors, static pressure taps, and thermocouples were located within the front shield. Instrumentation leads were gathered at the forward end of the front shield and carried through holes in the cone aft flange to the outside.

5.4.1.1 Central Island

The central island consisted of the support structure and shielding. The support structure was made up of a truss framework with four drag links, four radial support beams, and an inner cylinder. The shielding consisted of borated Be and borated stainless steel discs and sectors acting as a single unit.

The support structure, Figure 5.29, was an indeterminate truss system. The cylinder was 19.32 inches long with a 12.50-inch outside diameter and a 12.25-inch inside diameter. The inner diameter was governed by the coupling shaft (which passed through the cylinder) and the cooling-air annulus requirement. The cylinder was made of age-hardened Inconel X and was internally flanged at the forward end for attachment to the shaft tunnel. The flange was a machined ring and an integral part of the cylinder. An aft support ring was welded to the outside aft surface of the cylinder. This ring served as a means of attaching the drag links. The drag links transmitted axial vertical and side loads from the central island and the reactor core to the front shield cone.

Figure 5.30 shows the layout of the cylinder. The cross section of the aft support ring was shaped similar to a segment of a circle, with the cylinder wall forming the chord of the segment. The arc thickness was 3/16 inch and the radius of the arc was 2.31 inches. It was a hollow ring except for four circumferentially equidistant solid fittings which formed the drag link attachments. Attached to the front end of these fittings were four machined keys that fitted into machined keyways in the stainless steel shielding discs and transmitted shield loads to the aft support ring. Four keys, bolted around the front end of the cylinder, fitted into keyways machined in the inner ring of the support beam. Directly aft of these keys was another set of four keys that fitted inside machined keyways in the Be shielding discs. Aft of the second set of keys was a piston-type seal ring that fitted in a groove around the cylinder.

Four drag links were tied to the cylinder aft ring at the rear and to the radial support beams at the front outer radius. These drag links were age-hardened Inconel X, 31.80 inches in length with an outside diameter of 1.25 inches and an inside diameter of 0.94 inches. Figure 5.31 shows design details on the drag links and their fittings. The drag links were spaced 90 degrees apart and were oriented at 45 degrees from the horizontal and vertical centerlines.

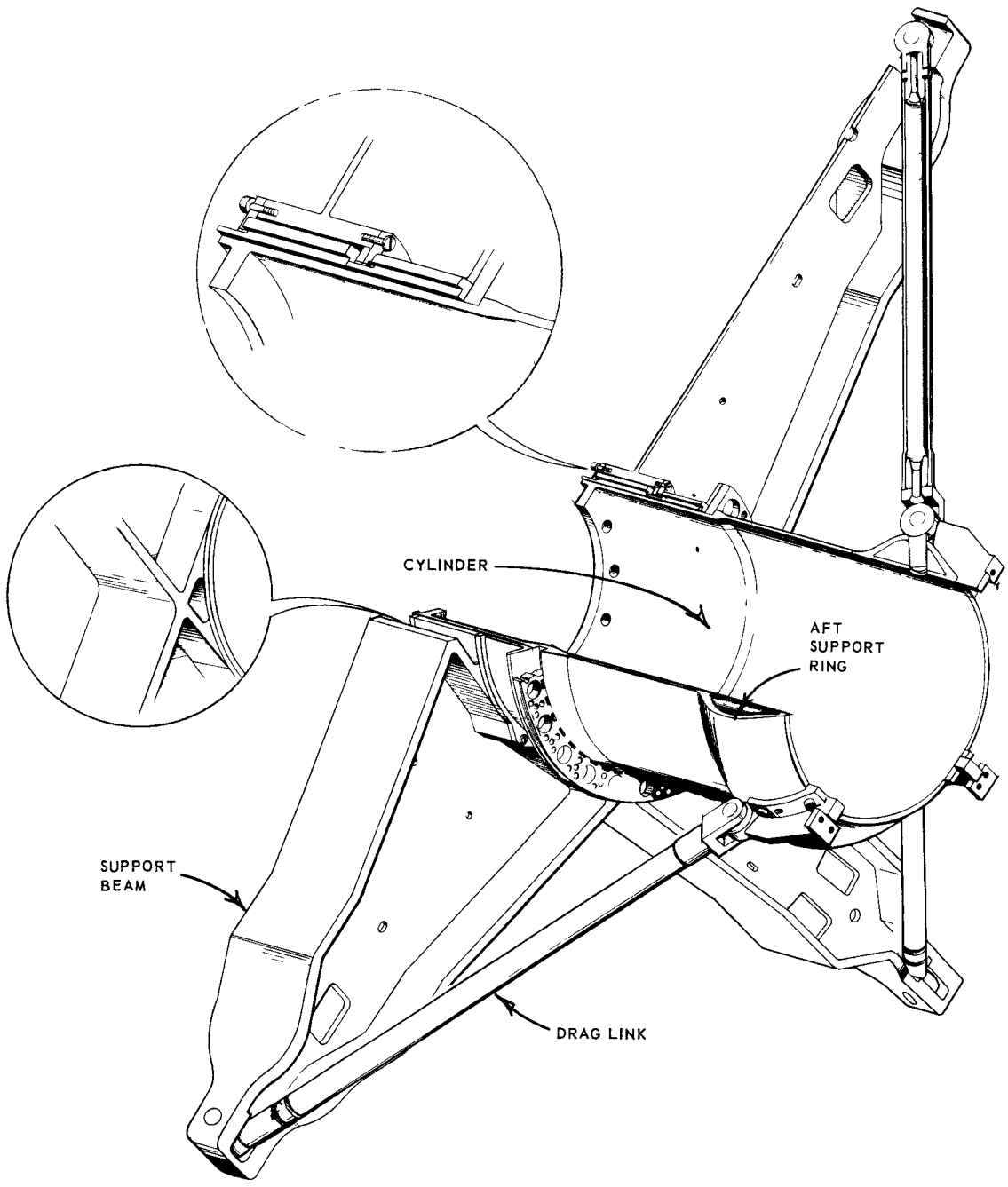

Fig. 5.29 – Front shield support structure

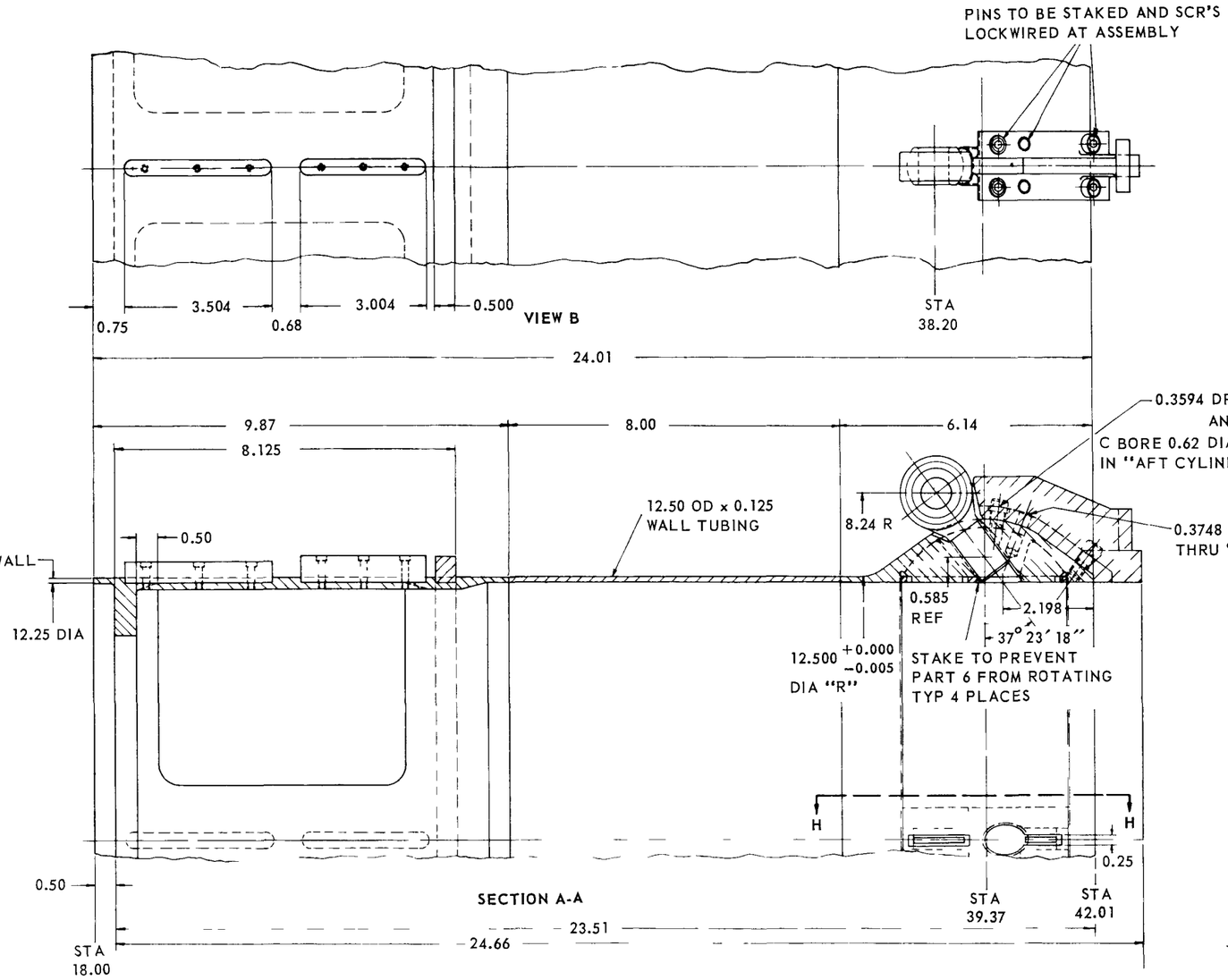

NOTE: STATION NUMBERS ARE INCHES AFT
OF THE PRESSURE VESSEL FRONT FACE

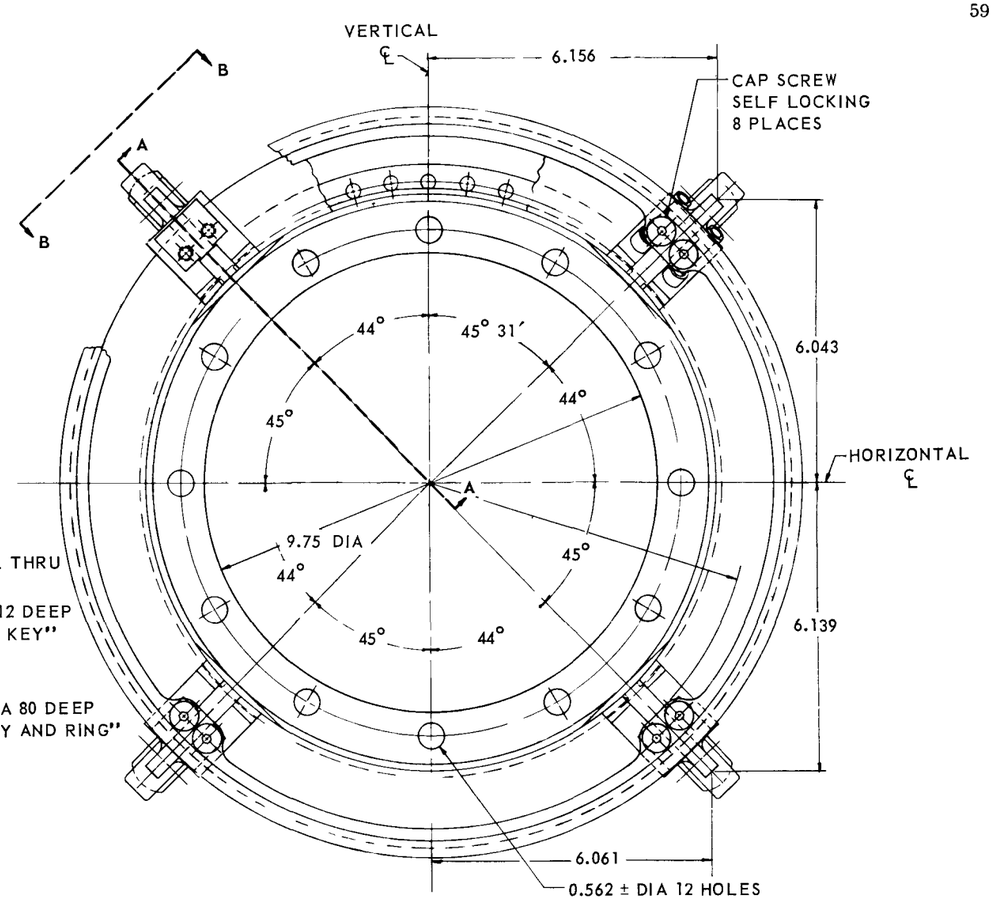

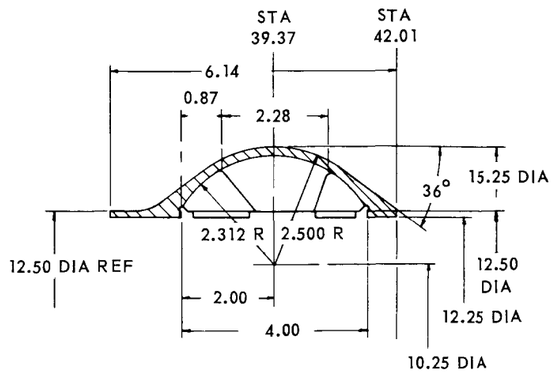

SECTION H-H
(INSIDE RING REMOVED)

SPHERICAL BALL JOINT

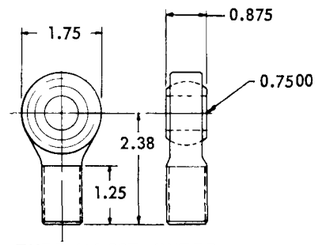

BALL-TYPE 416 SST. OUTER
RACE-TYPE 347 SST. HOUSING – INCONEL X

NOTE: LINEAR DIMENSIONS IN INCHES

Fig. 5.30 – Support structure cylinder (Dwg. 207R829)

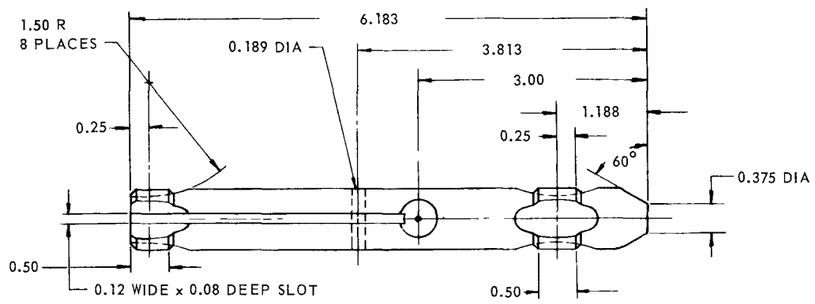

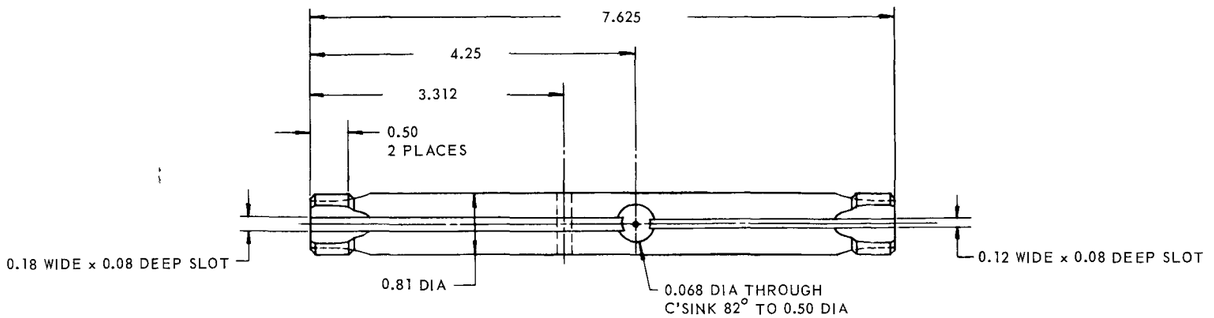

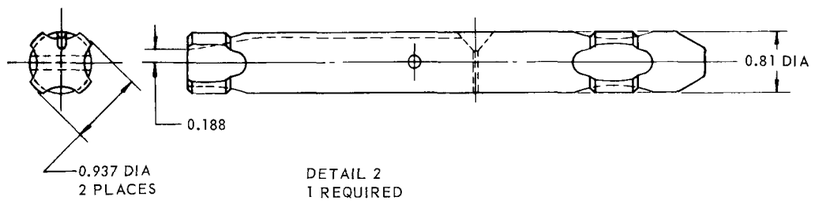

DETAIL 2
1 REQUIRED

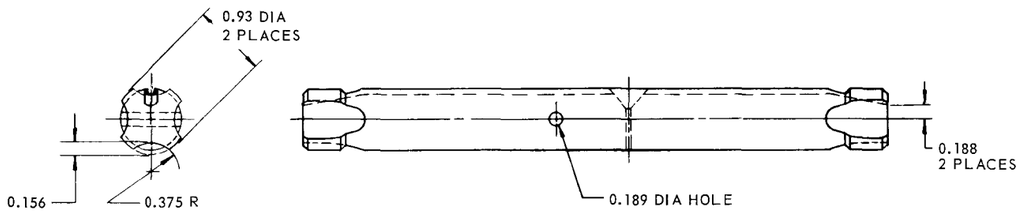

DETAIL 4
1 REQUIRED

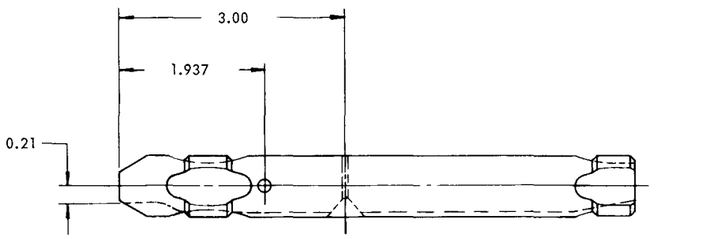

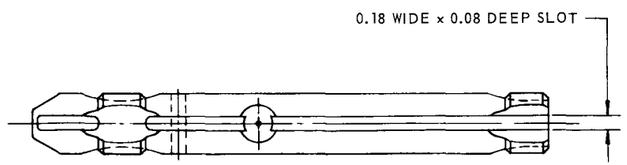

DETAIL 1
1 REQUIRED
SAME AS DETAIL 2
EXCEPT AS SHOWN

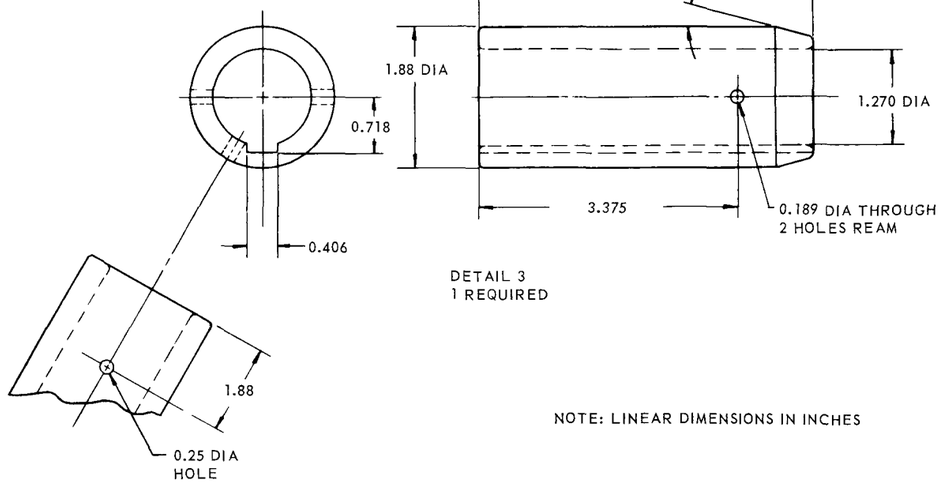

DETAIL 3
1 REQUIRED

NOTE: LINEAR DIMENSIONS IN INCHES

Fig. 5.31 – Support structure drag links and fittings

The four radial support beams were I-beam-shaped structural members that transmitted all inertial and pressure loads from the center island, and certain core loads to the shield cone. The radial length of each beam was approximately 24.75 inches and the flange thickness was 3/16 inch. They were tapered from a 3.87-inch web and a 10.4-inch flange height at the hub to a 2.0-inch web and a 1.25-inch flange height at the tip. The web thickness varied from 0.312 inch near the hub to 0.50 inch near the midpoint of the beam length. Since deflection, and not stress, was the limiting design parameter, Inconel was used as the structural material.

The shielding material consisted of borated Be and borated stainless steel circular slabs, which were used in both disc and sector form. The outer radius of the shielding slabs served as the inner wall for the forward primary-air duct. A circular hole, large enough to enable assembling these slabs around the inner cylinder, was located in the center of each slab. However, only the slabs at the front and aft end of the central island contacted the cylinder. Figures 5.32a and 5.32b show the layout of the shielding slabs in the central island and identify the slab nomenclature. Figure 5.33 shows the details of a typical slab (Slab I-3).

The shielding was divided axially into 12 slabs, ten of which were borated Be. Starting from the front, the first row of slabs ahead of the support beam, slab I-3, was made of pie-shaped borated Be sectors fitted between the support beams. These were as thick as the beams and were located in the same plane. Two solid Be discs of unequal width, slabs I-1 and I-2, were immediately adjacent to the beam. These discs had keyways machined at their inner radii to absorb inertial and pressure loads on the entire assembly. The disc immediately aft of the support beams had four axial keyways to absorb vertical and side loads, and one tangential keyway to absorb aft loads. The second disc had a tangential keyway to absorb forward loading only.

Slabs I-4 through I-9 consisted of 90-degree borated Be sectors. Sectors were used to minimize the thermal stress levels that would be encountered in complete discs. Slabs I-10 through I-14 were 90-degree sectors of borated stainless steel tied together by connecting links to form complete discs. The philosophy was to minimize the effects of thermal gradients. Axial keyways were machined at the inner radius of slabs I-11 and I-13 to absorb the inertial and pressure loads. Slabs I-15 and I-17 were made of 90-degree sectors of borated Be. Slab I-14 was a stainless steel slab used to complete the primary-air duct contour of slab I-15. The contour of slab I-17 was completed by the use of a stainless steel fairing.

A set of six shear collars was used to connect axially each of the shielding slabs to the adjacent slab. Four of these collars were located at the same radius and were equally spaced. The other two were placed at a smaller radius 180 degrees apart. These collars, together with the pre-loaded tension rods, Figure 5.34, that passed through the collars, maintained the assembly as an integral unit. The collars transmitted side and vertical inertial loads through adjacent slabs to the front and aft discs. These discs transmitted the loads through their keys. Axial gaps between slabs were maintained by means of spacers machined on the shear collars. The spacing of axial gaps between the slabs and the axial widths of the slabs was determined by the aerothermal requirements.

5.4.1.2 Outer Section

The outer section consisted of borated Be and borated stainless steel slabs, and the structural arrangement required to support these slabs. An isometric cutaway view of the outer section is shown in Figure 5.35. The aft-assembly shielding and front-cone shielding are shown in Figures 5.36 and 5.37, respectively. The slabs were shaped as 45-degree annular sections and used in an arrangement forming complete annular rings.

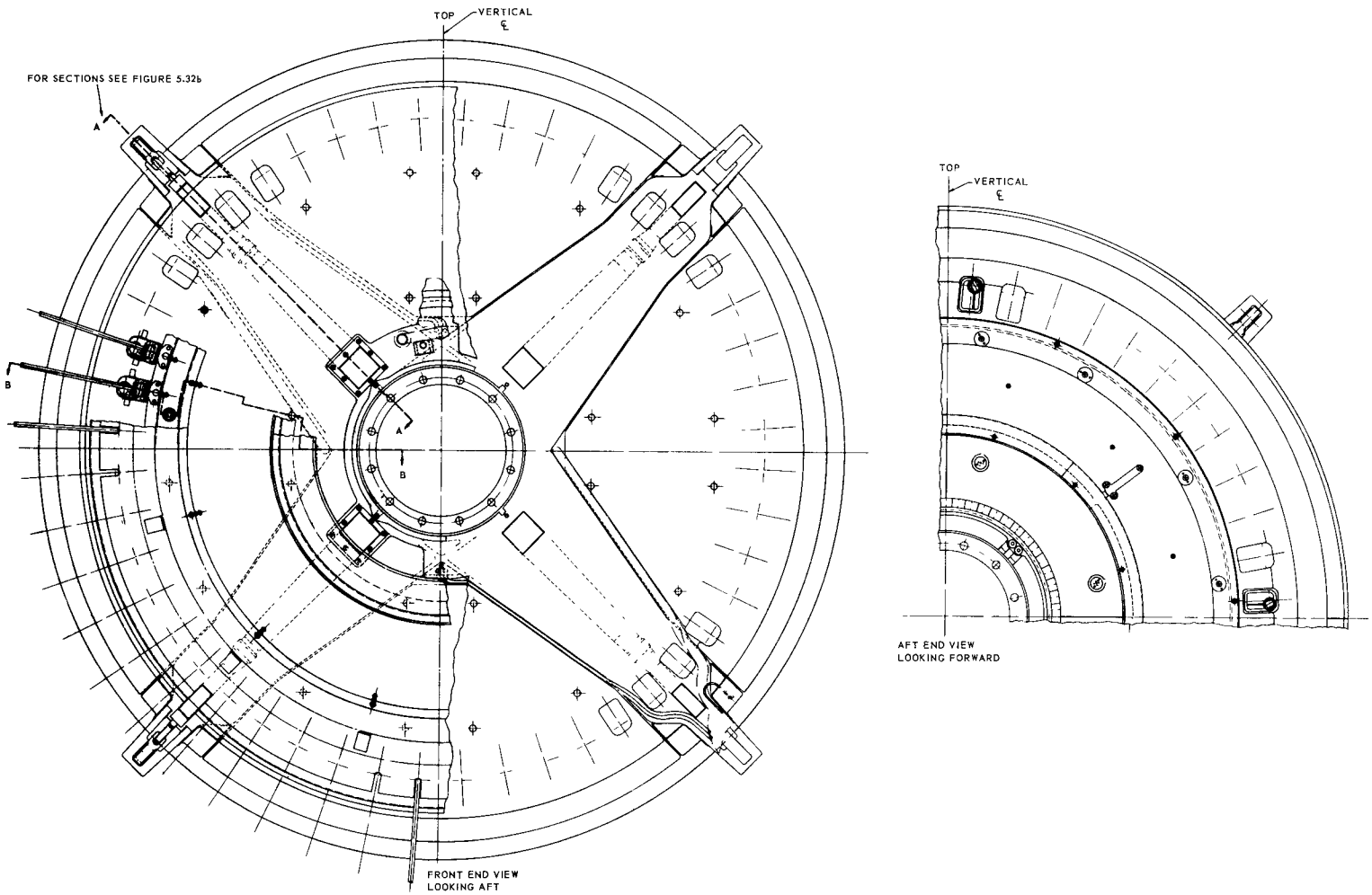

Fig. 5.32a – XNJ140E-1 front shield central island layout (Dwg. 207R828, Sh. 1)

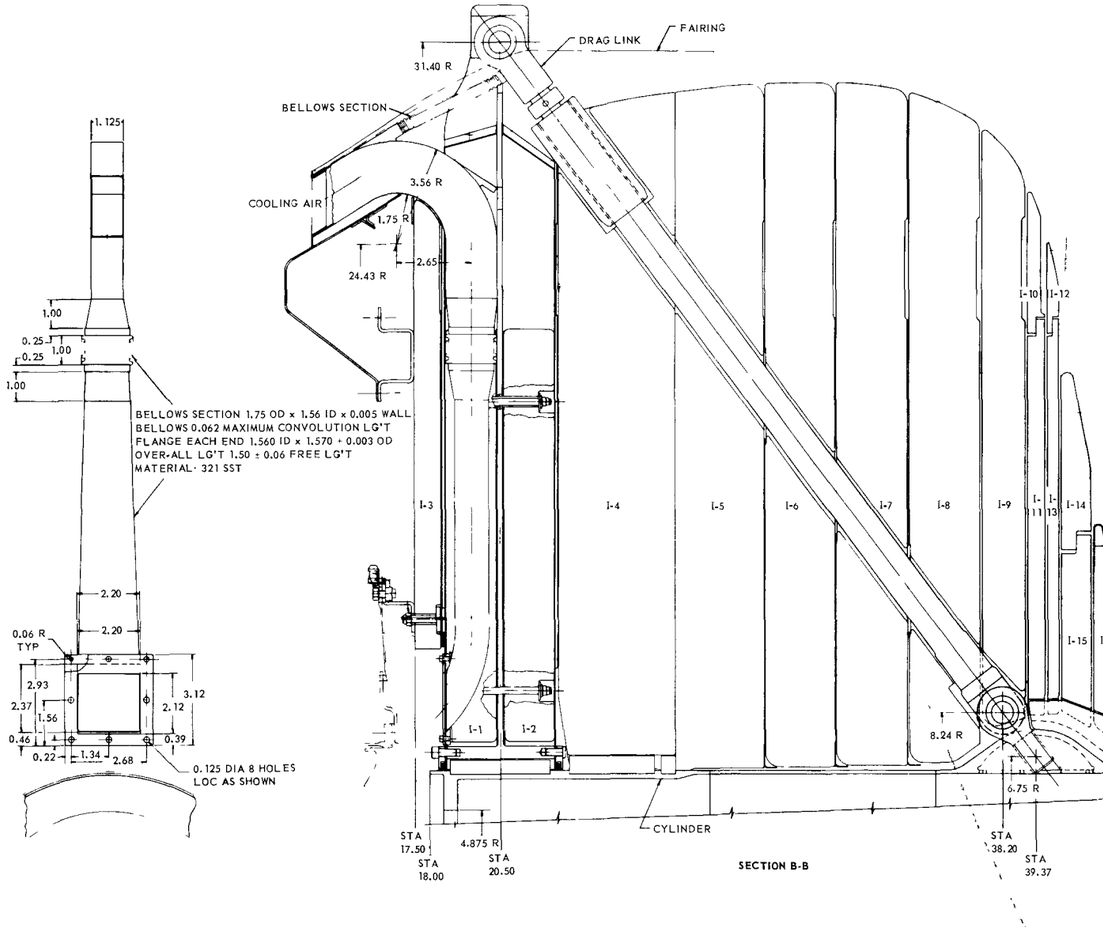

TABLE

SHIELDING DIMENSIONS

DISC NUMBER	STATION FORWARD FACE	THICK	AIR GAP
I-3	17.50	0.970	0.03
I-1	18.50	4.000	0.03
I-4	22.53	4.095	–
I-5	26.62	3.165	0.03
I-6	29.82	2.500	0.04
I-7	32.36	2.500	0.07
I-8	34.93	2.500	0.09
I-9	37.52	1.500	0.09
I-10 and -11	39.11	0.600	0.10
I-12 and -13	39.81	0.400	0.08
I-14 and -15	40.29	1.060	0.08
I-17	41.43	–	–

STATION	CONTOUR RADIUS
13.00	23.76
14.00	24.36
15.00	24.95
16.00	25.55
17.00	26.14
18.00	26.74
19.00	27.33
20.00	27.85
21.00	28.30
22.00	28.67
23.00	28.97
24.00	29.21
25.00	29.41
26.00	29.57
27.00	29.70
28.00	29.82
29.00	29.92
30.00	29.98
31.00	30.01
32.00	30.02
33.00	30.00
34.00	29.89
35.00	29.60
36.00	29.36
37.00	28.88
38.00	28.14
39.00	26.87
40.00	24.22
40.25	23.00
40.50	21.54
40.75	20.00
41.00	18.58
42.00	13.50
43.00	8.50

NOTE· DIMENSIONS IN INCHES

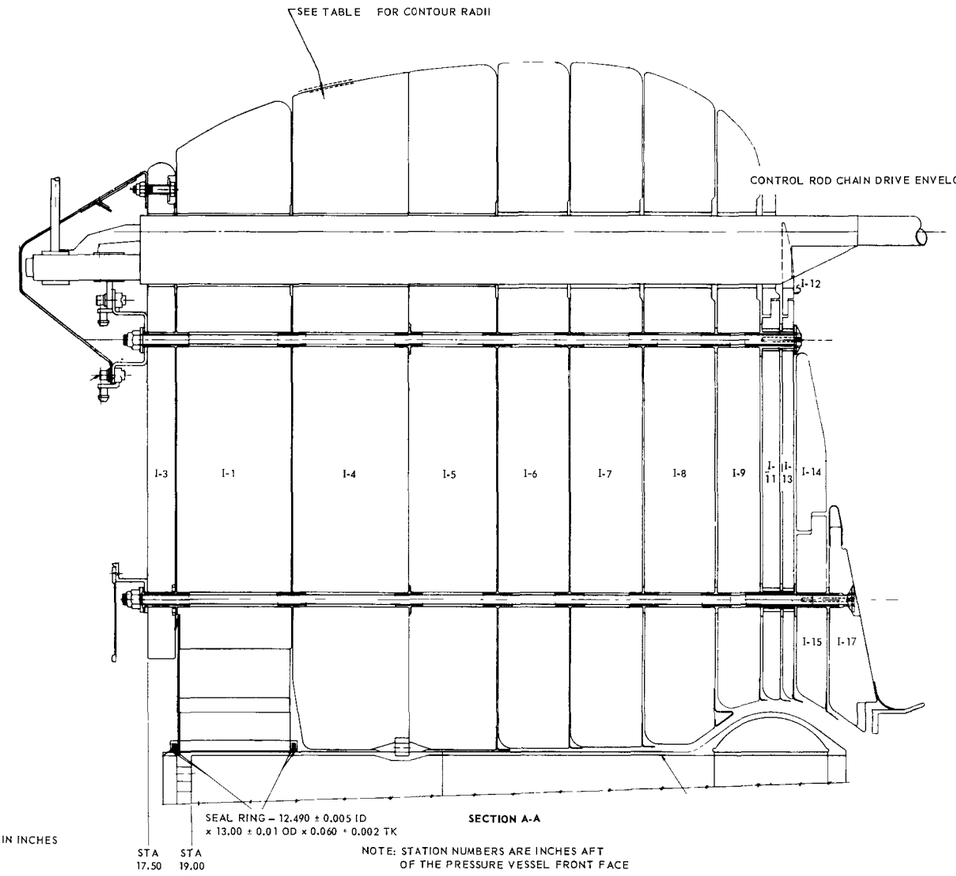

Fig. 5.32b – XNJ140E-1 front shield central island layout (Dwg. 207R828, Sh. 2)

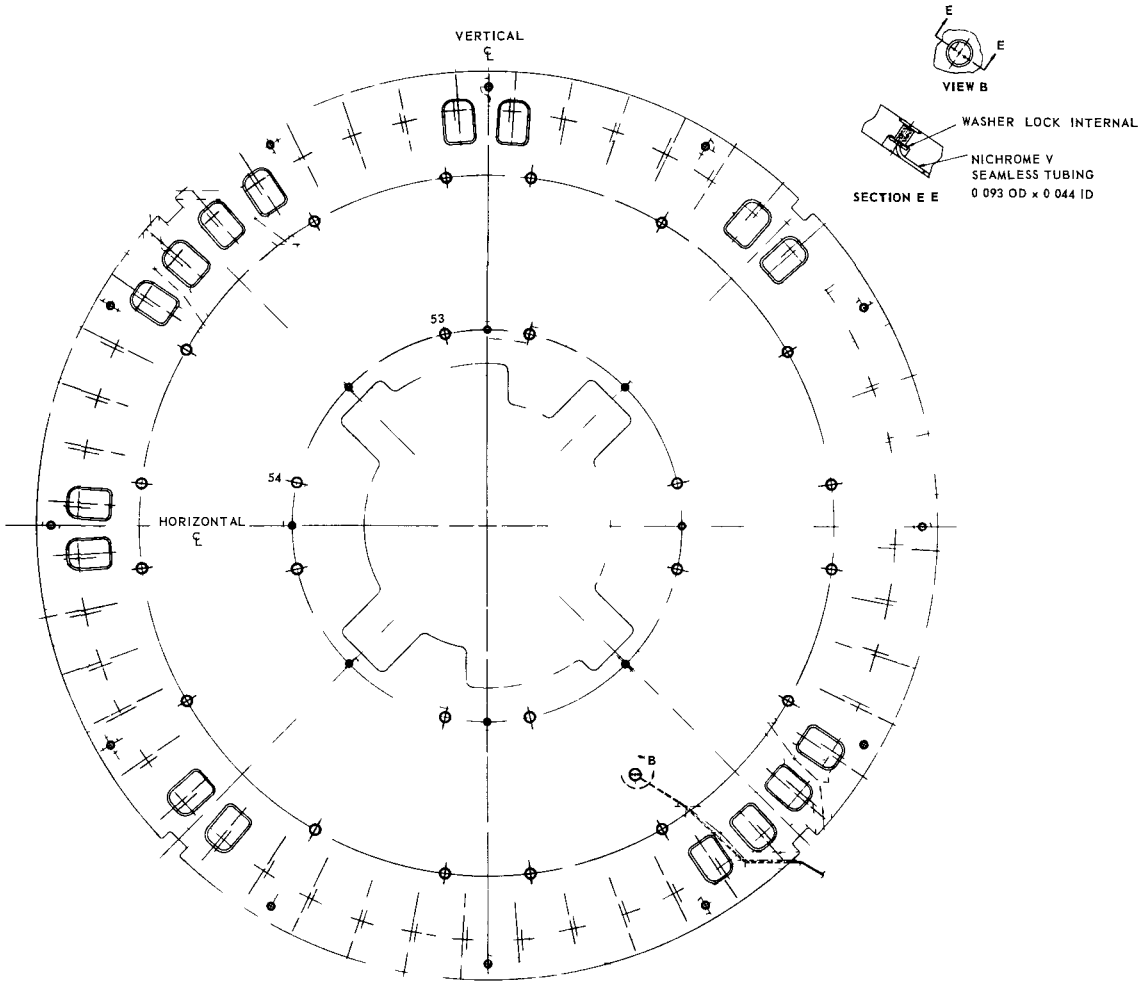

Fig. 5.33 – Front shield central island, slab I-3 (656E785)

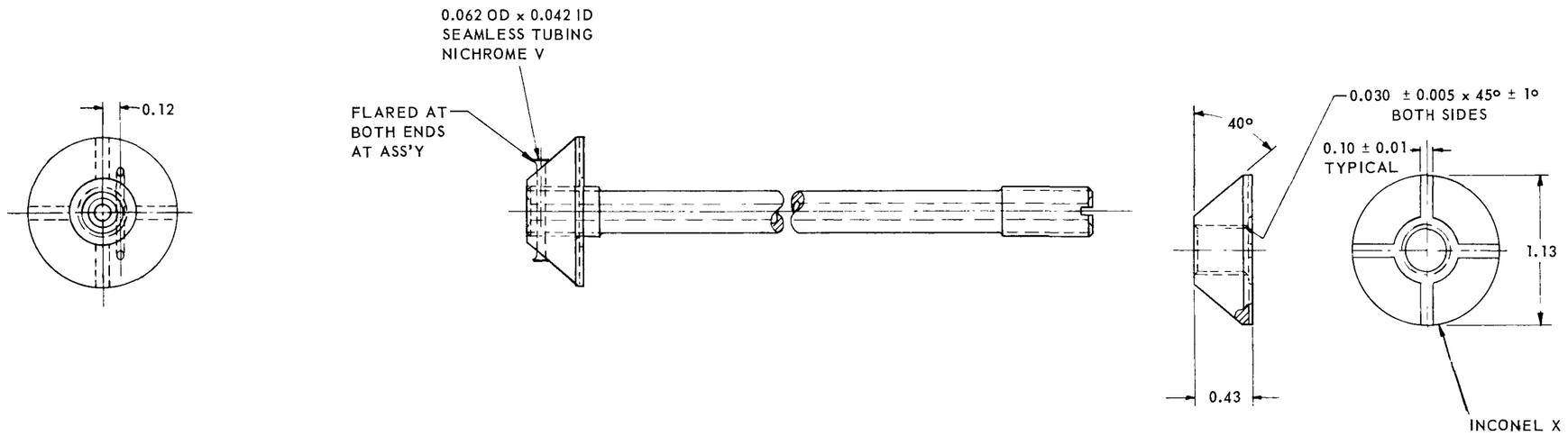

Fig. 5.34 – Front shield central island tension rod (Dwg. 736D237)

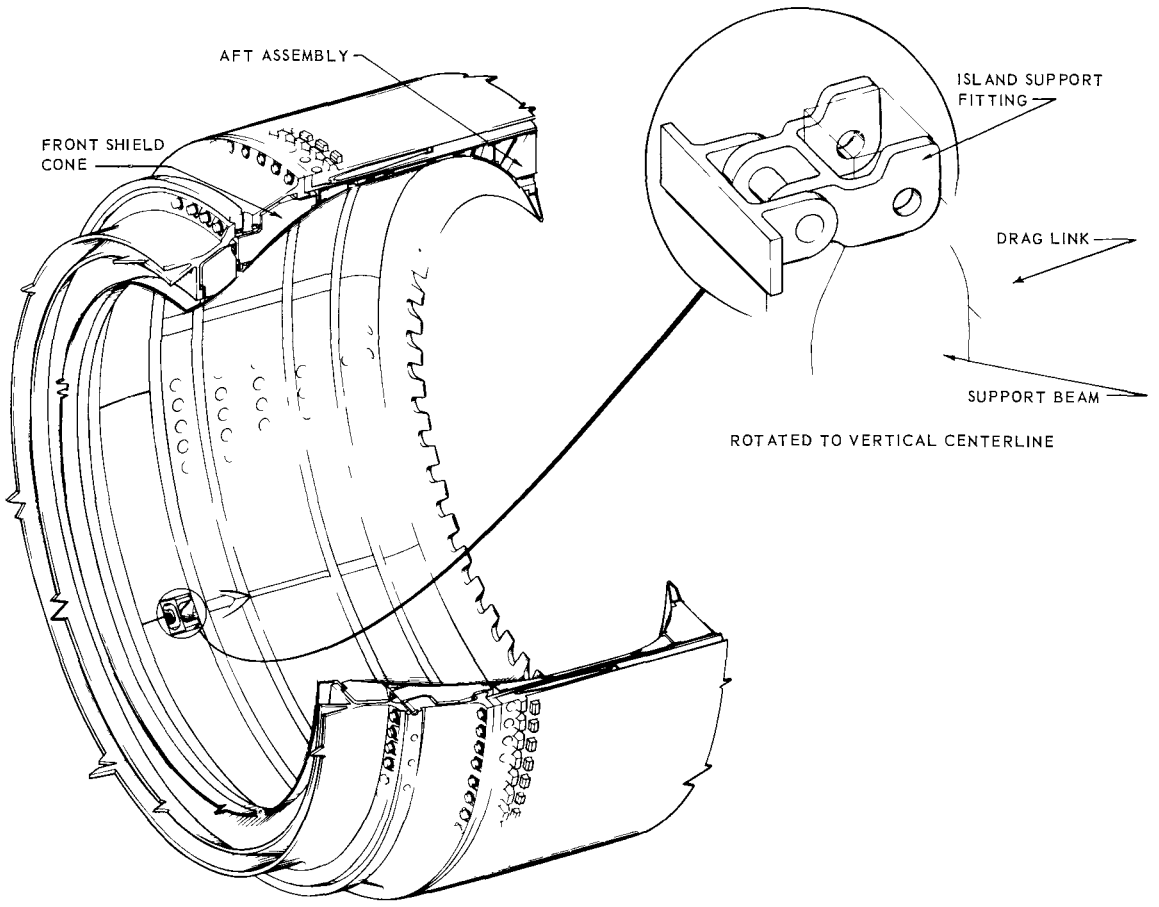

Fig. 5.35 – Front shield outer section isometric cutaway view (Dwg. DI549)

The inner radius of shielding within the structural shell formed the outer wall of the primary-air duct between the compressor discharge and the reactor. This shielding consisted of borated Be slabs at the front and aft ends, and slabs of borated stainless steel in the thin central portion. The widths and the inner contour of each row of slabs were varied to form the duct geometry and, at the same time, satisfy nuclear considerations and thermal stress requirements.

The slabs were supported axially through a series of radial coil springs located on the flanges of continuous rings with I-shaped cross sections. Axial leaf springs were placed between the shielding sectors to provide the tangential force required to constrain the shielding blocks. Eight rectangular beams passed circumferentially through the edges of the slabs, and were spaced at 45-degree increments around the mating surfaces of two adjacent blocks. Beams at the 45-degree locations from the horizontal and vertical centerlines served as tangential spring supports and did not carry external loads. However, the beams located at the horizontal and vertical centerlines were larger in size and absorbed the vertical and side loads of the outer section. Inconel was used in the beams and the radial spring support rings. The tangential leaf springs were Rene' 41.

The outer section was assembled as a unit, inserted within the reactor structural shell, and attached to the inside of the structural shell flange. A radial gap of 1/8 inch was maintained between the shield and the structural shell during assembly at room temperature. This gap accommodated relative thermal expansions between the shield assembly

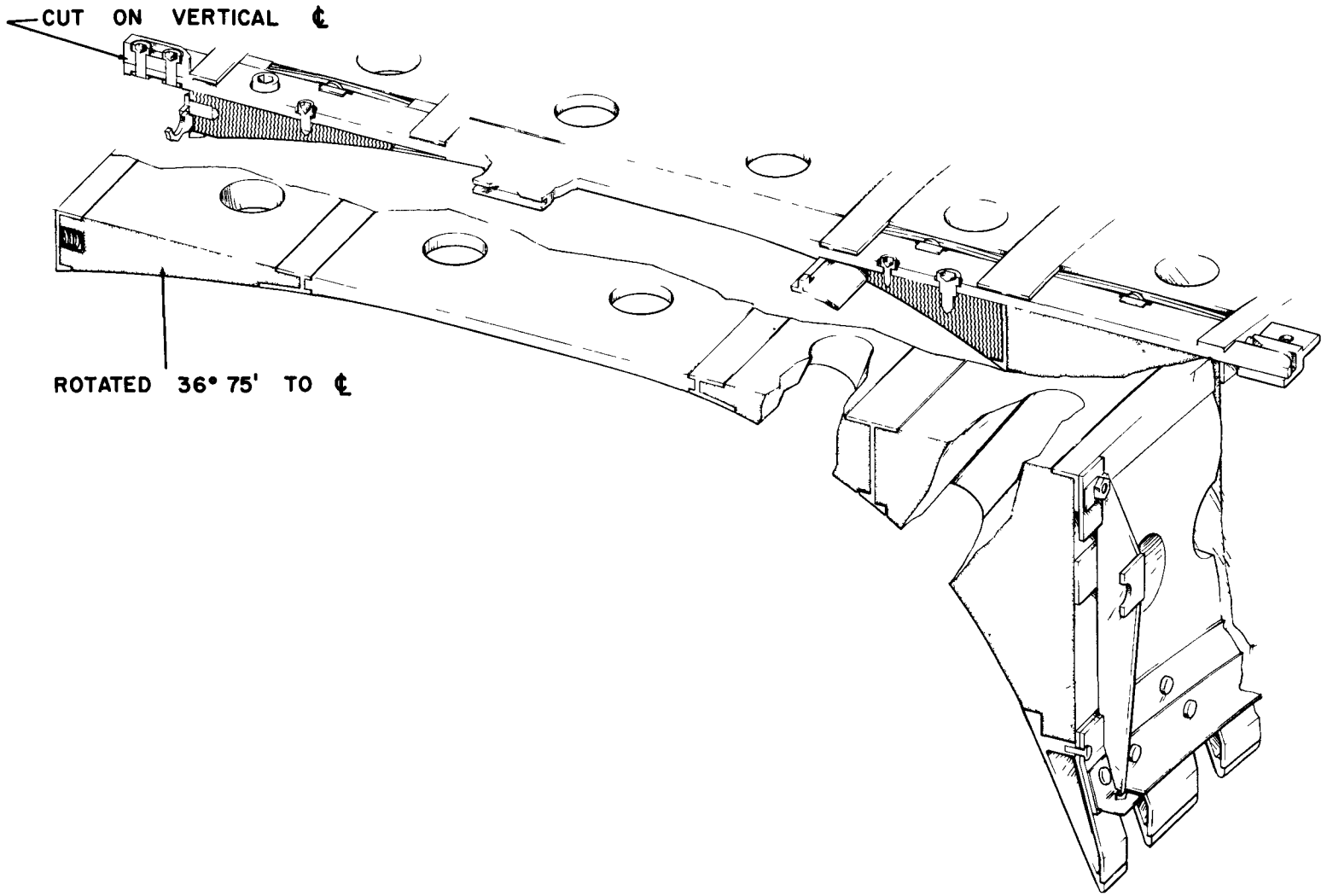

Fig. 5.36 – Front shield outer section, aft assembly (Dwg. DI546)

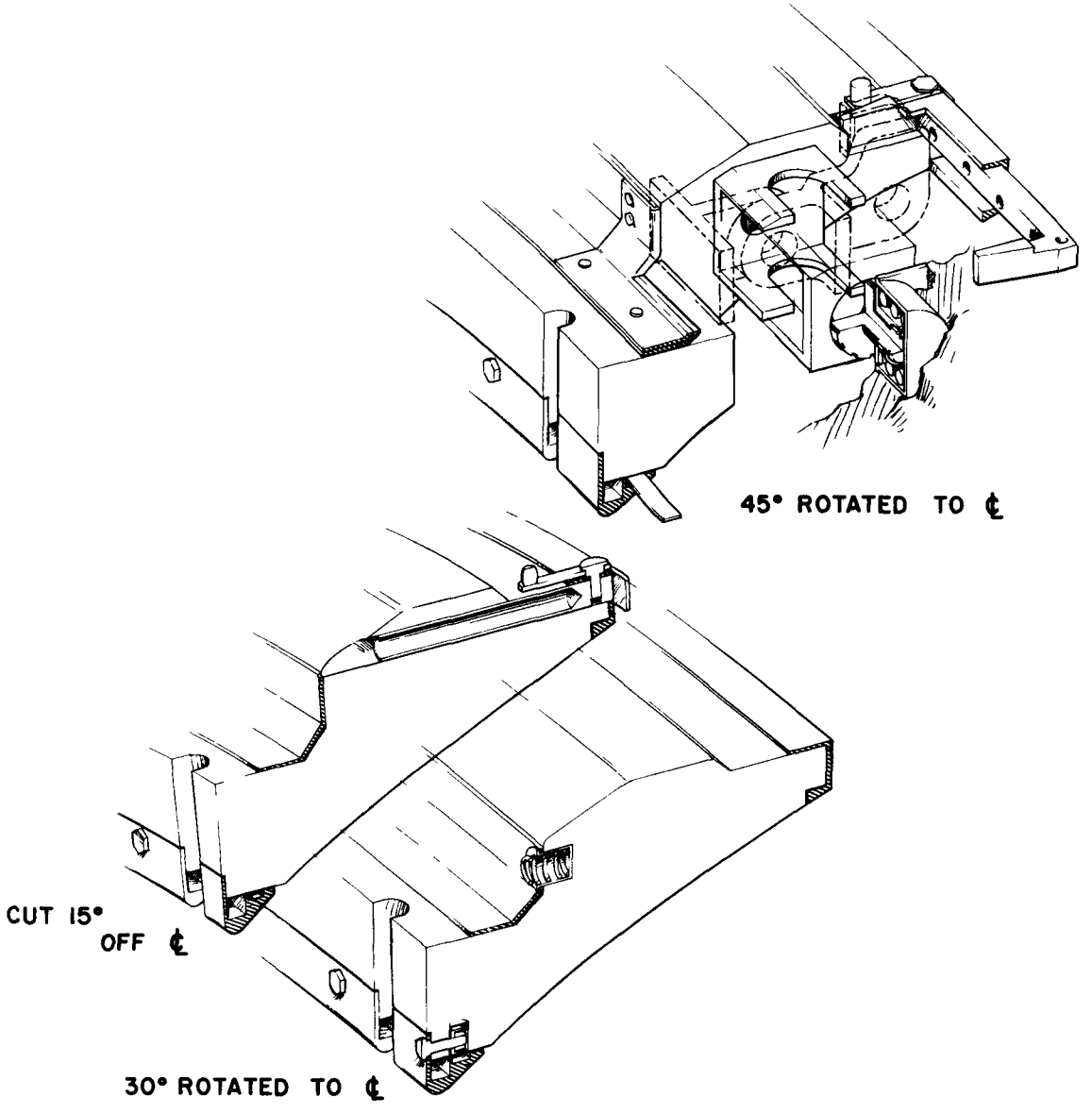

Fig. 5.37 – Front shield outer section, front shield cone (Dwg. DI553)

and the structural shell under operating conditions. The front fitting was the only tie through which loads from the outer section were transmitted.

Figure 5. 38 shows the layout of the front shield outer section, and includes details of the radial springs. The layout of the front shield cone is shown in Figure 5. 39.

5. 4. 2 AEROTHERMAL DESIGN

5. 4. 2. 1 Central Island

Spacing of the discs was governed by the need to provide coolant flow in the radial direction adequate to yield satisfactory internal temperature levels and temperature distributions. The cooling-air was bled radially inward from the primary-air duct. Flow extraction was similar in nature to boundary layer bleed, with the points of extraction being positioned for optimum flow dispersion. After passing radially inward, the cooling-air was collected and bled aft through the shaft tunnel annulus. It then was used further to cool rear-shield components.

Three and two-tenths percent of the compressor discharge-air was used for cooling the shield material and associated structure. Cooling-air distribution was dictated by the temperature limits of 1200°F and 1000°F permitted for stainless steel and Be, respectively.

Rapid changes in compressor discharge-air temperature, associated with transient engine performance, tended to cause radial temperature differentials in the slabs and induce thermal stresses. This effect resulted from the large amount of heat transferred into the slabs at the outer radial periphery along the duct wall. Since the gap spacing was designed for the lesser amount of flow necessary to meet steady-state cooling requirements, there was a temperature lag at the inner radii with respect to the outer radii because of geometry, thermal inertia, and thermal conductivity of the system. This effect was less pronounced in those slabs closest to the core since the duct geometry provided a higher ratio of cooled surface area (exposed to the primary-air stream) – to – volume than in the forward slabs. Since the radial temperature gradients and profiles had a pronounced effect on thermal stresses, these gradients were minimized. Transient conditions determined the limiting aerothermal design restraints.

Two methods were used to alleviate transient thermal gradients. The forward Be discs (where the allowable radial gradients were small) were insulated from the primary-air stream by an outer radial metallic cover of sheet metal which provided a stagnant air gap serving as a thermal insulation barrier. Those slabs toward the rear (closest to the core) were segmented into four quadrants to allow higher radial temperature differentials.

Transient temperature gradients were most severe in the forward slabs during a chemical start. Steady-state gradients were most pronounced in those slabs closest to the core during nuclear operation. Figure 5. 40 is a schematic showing nomenclature used in the aerothermal analysis of the central island. Slabs S3 and S4 were borated stainless steel; all other slabs were borated Be. The secondary heating rate decreased rapidly with distance from the core. Those slabs closest to the core, of necessity, received the majority of coolant flow during steady-state operation. Thermal differentials through the slabs, for a nuclear start during ITS hot-day ambient conditions, were calculated and are contained in reference 4. These calculations showed that the initial effect of nuclear heating was small compared to the heat addition from primary-air. The rear portions of the shield (slabs S1 through S4) responded to temperature transients without developing large radial temperature gradients. Slab S11, typical of the large forward slabs, had radial temperature differentials in the order of 150°F. Figure 5. 41a shows the transient temperature distribution through slab S11 following engine startup on NHO. The maximum radial tem-

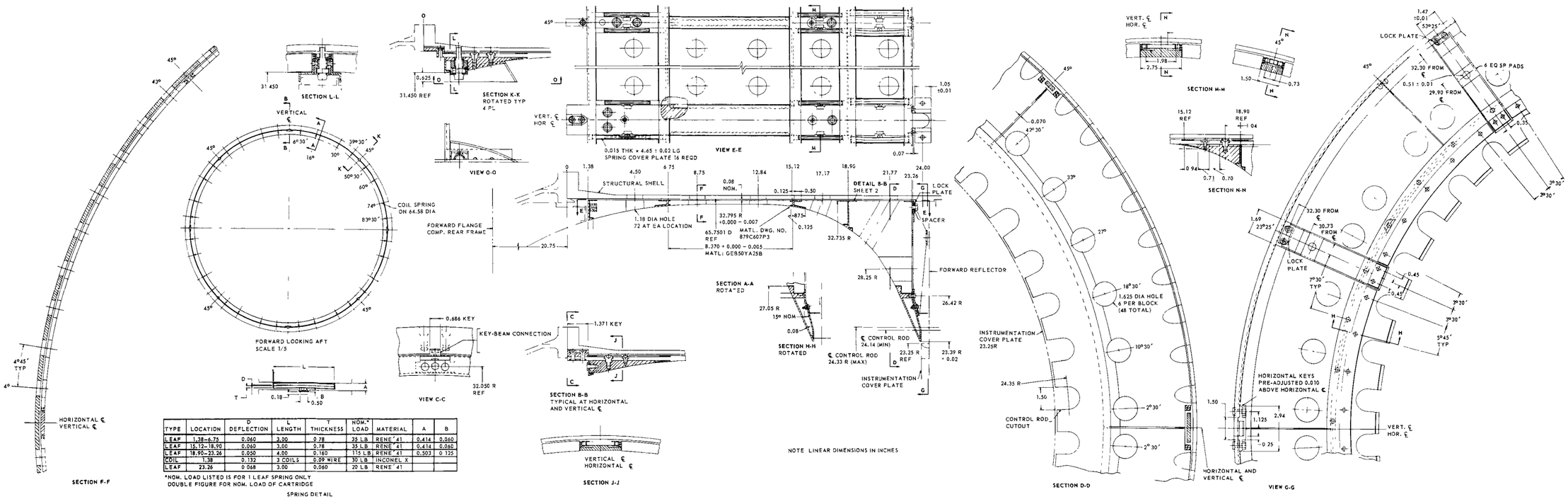

TYPE	LOCATION	D DEFLECTION	L LENGTH	T THICKNESS	NOM.* LOAD	MATERIAL	A	B
LEAF	1.38–6.75	0.060	3.00	0.78	35 LB	RENE´41	0.414	0.060
LEAF	15.12–18.90	0.060	3.00	0.78	35 LB	RENE´41	0.414	0.060
LEAF	18.90–23.26	0.050	4.00	0.160	115 LB	RENE´41	0.503	0.125
COIL	1.38	0.132	2 COILS	0.09 WIRE	30 LB	INCONEL X		
LEAF	23.26	0.068	3.00	0.060	20 LB	RENE´41		

*NOM. LOAD LISTED IS FOR 1 LEAF SPRING ONLY
DOUBLE FIGURE FOR NOM. LOAD OF CARTRIDGE

SPRING DETAIL

Fig. 5.38 – Front shield outer section layout (Dwg. 207R821, Rev. A)

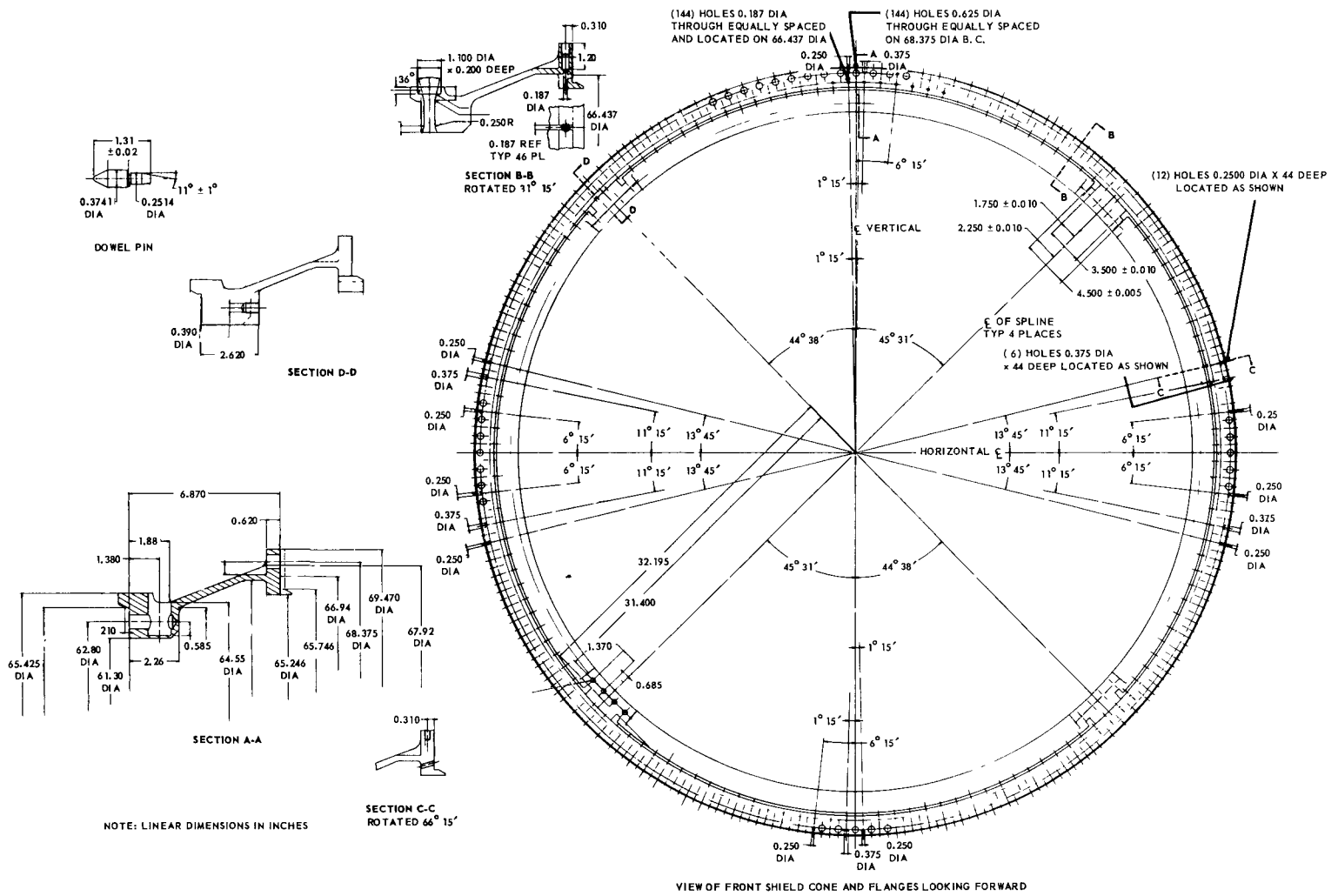

Fig. 5.39 – Front shield cone (Dwg. 207R823)

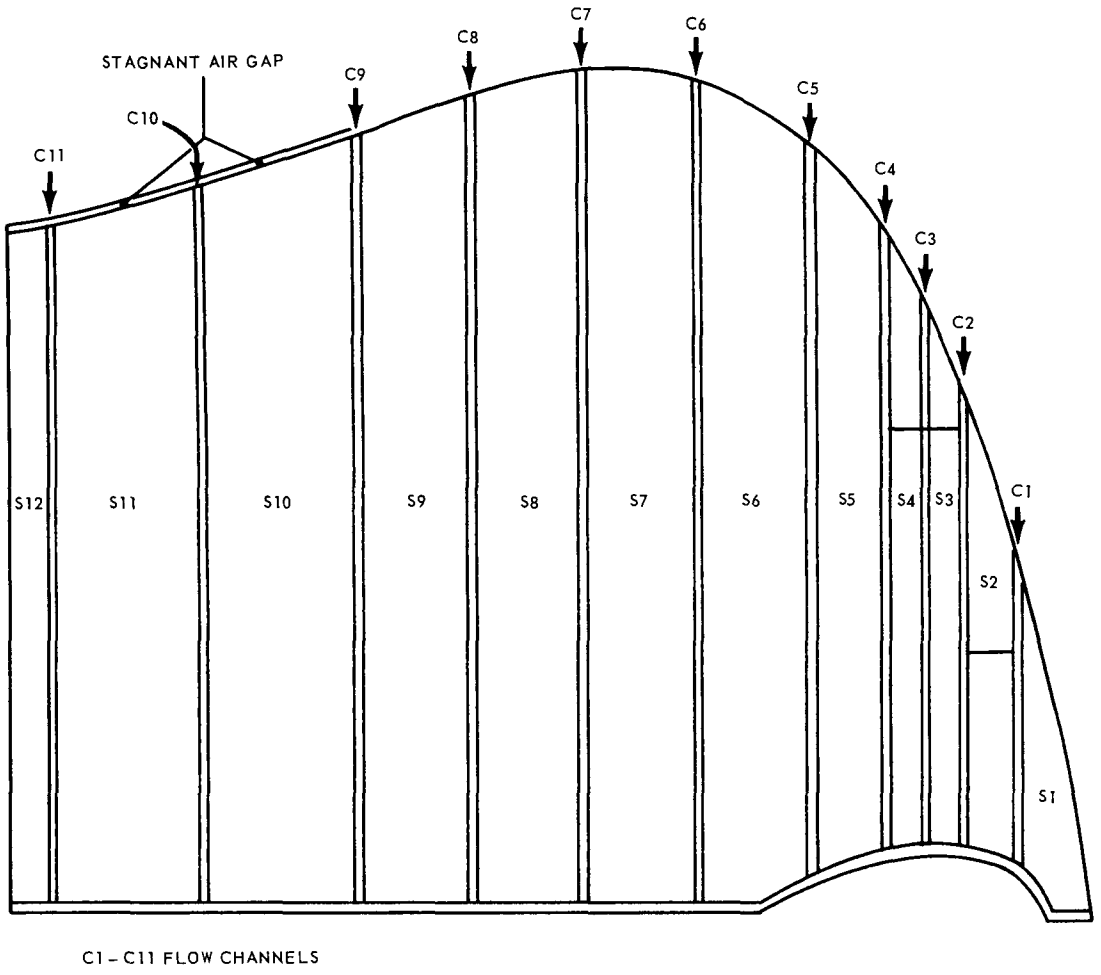

Fig. 5.40 – Aerothermal nomenclature, front shield central island

perature differential occurred approximately 2000 seconds after startup. The resulting thermal stresses were excessive. Insulation in the form of a dead air gap was added to the outer contours of slabs S10, S11, and S12. The temperature differentials through slab S11 for the same startup transient are shown in Figure 5.41b when the insulating effect of the dead air gap was included in the calculations. As shown in Figure 5.41b, the maximum temperature differential was reduced to 115°F and caused acceptable thermal stress levels.

Temperature responses to chemical startup transients were very similar to those for nuclear starts because of the minor contribution of secondary heat to the total heat input during nuclear starts. The maximum temperatures reached the compressor discharge-air temperature, 710°F during hot-day operation. Detailed data for this transient condition are contained in reference 4.

The effects of temperature transients due to engine shutdowns also were analyzed. Again, the major restraints were the radial temperature differences in the shield slabs. Chemical shutdown, with low afterheating because of the initial decay of secondary heat, posed no problem. The effects of nuclear scrams during ACT operation were determined by the mode of aftercooling. Two modes were studied:

1. Motoring the engine by means of the starting motor.
2. Cooling with air from the external auxiliary blower system.

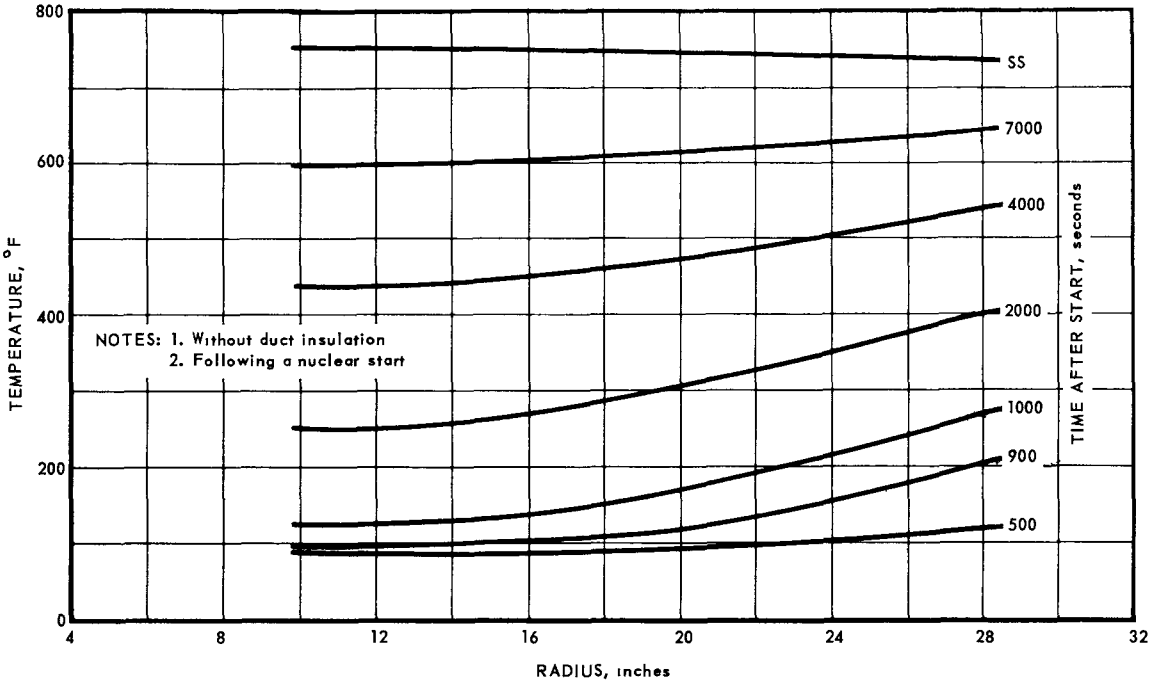

Fig. 5.41a – Temperature distribution through slab S11

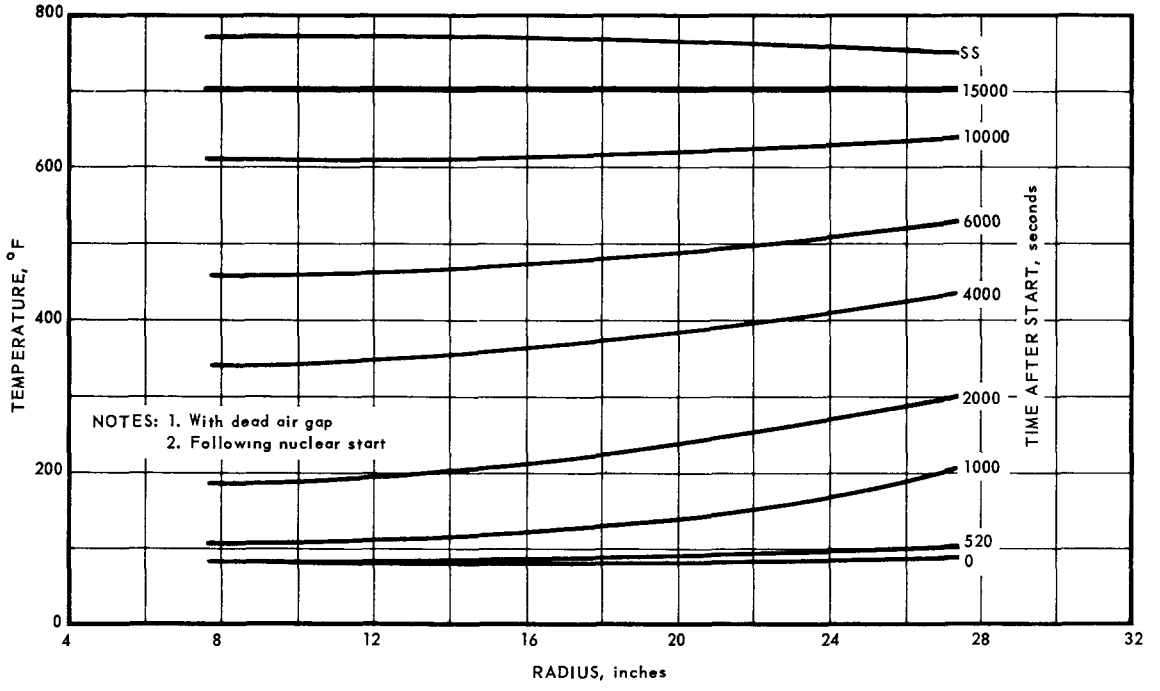

Fig. 5.41b – Temperature distribution through slab S11

For the mode of a normal shutdown with starter motoring, it was assumed that 3.2 percent of total compressor airflow passed through the central island at a compressor discharge-air temperature of 125°F. It was also assumed that motoring occurred at high-torque starter speed. For the second mode, the engine was assumed to be inoperative. Aftercooling-air was introduced into the external bleed-speed ducting with the bleed-speed valves closed. The aftercooling-air entered the bleed-speed annulus, flowed forward, entered the primary-air stream through the front shield outer section, and flowed rearward through the reactor. The air was introduced into the primary-air ducts at a temperature of 300°F.

The second mode of aftercooling, based on the inoperative engine, led to more severe temperature gradients. These gradients, however, were not as severe as those encountered during nuclear starts because the rapid change in primary-air temperature was coupled with a decrease in heat transfer coefficient along the duct wall. This heat transfer coefficient increased during engine startup. The rapid decrease in mass flow was the predominant factor in decreasing the heat transfer coefficient.

The following conditions and assumptions were used for the analysis of the inoperative engine transient:

1. Hot day, 5000 feet, Mach = 0, scram from military power setting
2. Aftercooling-air supply temperature = 300°F
3. Total aftercooling-air flow = 25 pounds per second
4. Aftercooling-air flow initiated at 100 seconds after scram
5. A short interval of airflow at a higher temperature (405°F) entering the forward primary duct was used to simulate initial heat input to the air stream as it flowed forward in the bleed-speed annulus.
6. Three and two-tenths percent of the compressor airflow passed through the central island.

Temperature gradients through all slabs following scram are shown in reference 4. In all cases, they were less than those occurring during nuclear starts. Reference 4 also contains the detailed temperature gradients for the engine coastdown condition followed by motoring with the starter.

During steady-state operation, the maximum temperatures and gradients occurred in slabs S3 and S4. These slabs were borated stainless steel and, because of their high density, had a high rate of heat generation per unit volume. The maximum temperature was about 960°F. Since they were relatively thin, the temperatures at the outer radii were approximately 830°F when the primary-air temperature was 710°F. The maximum temperature gradient was 130°F in slab S4.

The support beam was a structural member located well forward in the central island in an area of low secondary heating rates. During steady-state nuclear operation, a small amount of cooling-air was sufficient to cool this member. Flow was directed radially inward and the flow path was determined by the physical placement of shield slabs within the flange webs.

During engine startup or shutdown, two thermal gradients were produced within the support beam. A radial gradient existed due to the nature of the cooling-air flow paths, with the inner radius always lagging. A second gradient occurred between the beam flange and beam web due to the difference in thickness (and mass) of these parts.

Cooling methods of the support structure were designed to eliminate web-to-flange temperature gradients in the beam. The air gap was kept constant to insure even flow distribution along the flange. Large temperature gradients during transient operation

were developed in the structural members and the shield slabs, but method of attachment ensured that mechanical loads developed between these parts were small. Analytical data describing the greatest flange-to-web temperature variation and the associated coolant flow are presented in reference 4.

The aft support ring, located at the aft end of the cylinder, provided the anchor points for the four drag links. Its thermal performance was affected by two circumstances; it was cooled by air discharged from the island, and it was located in a region of high secondary heating rates. Because of the high heating rate, the temperature response of the support ring was different during nuclear starts and chemical starts. In fact, during nuclear starts it tended to extend beyond the forward part of the inner cylinder to which it was attached.

During nuclear steady-state operation, the support ring temperature was substantially above the primary-air temperature. Detailed temperature profiles are shown in reference 4.

The tension rods served to hold the shield slabs in longitudinal restraint. They were cooled by air bled from the primary-air stream and entering the hollow rods at the aft face of the central island. The cooling-air supply continued whenever the compressor was in operation, and adequately cooled the rod. Thermal analysis of the rods during the locked-rotor transient showed that the rod temperature then was largely dependent upon radiative heat transfer to the surrounding slabs to keep it cool. Figure 5.42 shows the axial temperature distribution of a typical rod and the adjacent shield slabs 300 seconds after a locked-rotor scram. Because of the small amount of secondary heat generated in the rod and its favorable radiation view factor to the shield, the rod was within $60^{\circ}F$ of the surrounding shield slabs during the entire transient.

The drag link, supporting the inner cylinder from the front support beam, was cooled by its own cooling channels, and, in general, was within $50^{\circ}F$ of the compressor discharge-air temperature. The temperature was always well below the material limit of $1200^{\circ}F$. A temperature plot of the link is shown in Figure 5.43 with the temperature increasing in the direction of fluid flow. The hot end was the anchor point on the aft support cylinder. Figure 5.43 was plotted for ITS operation at the emergency power setting. Temperature values for

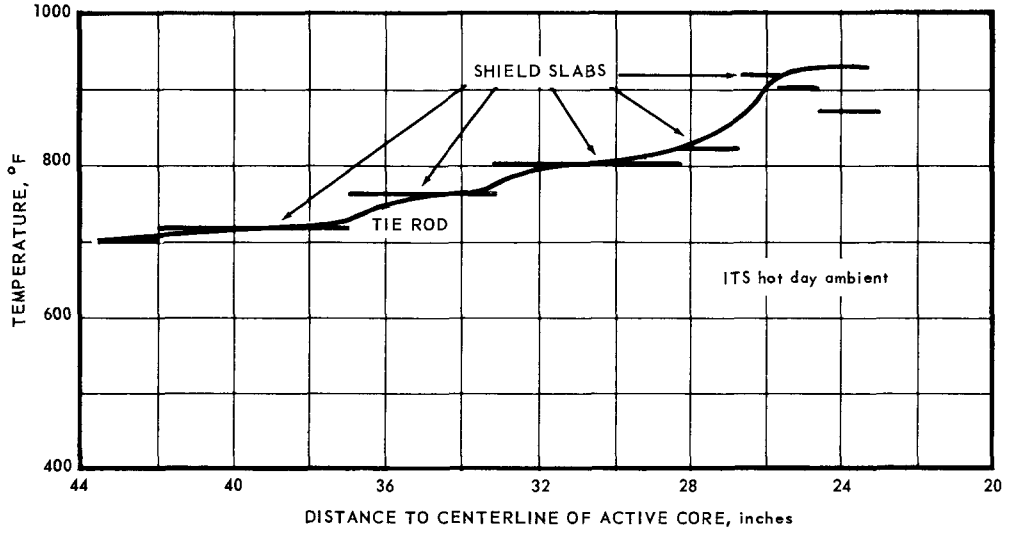

Fig. 5.42 – Axial temperature distribution of a typical tension rod and the adjacent shield slabs 300 seconds after a locked rotor scram

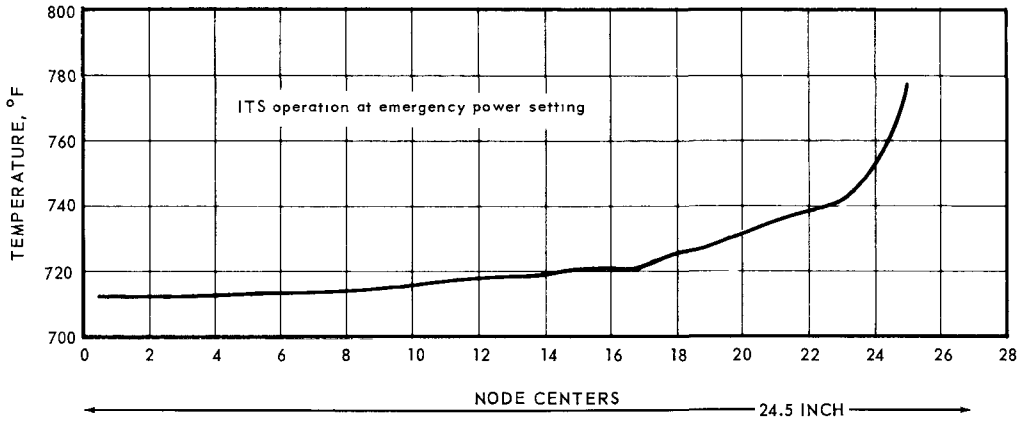

Fig. 5.43 – Drag link temperature as a function of length

other operating conditions varied almost directly with the compressor discharge-air temperature.

Figure 5.44 shows the transient average temperature of the drag link during a chemical start. The temperature response of the drag link closely followed the compressor discharge-air temperature transient.

5.4.2.2 Outer Section

Aerothermal analysis of the outer section included the triple-flange assembly. Analysis was concentrated on the triple-flange assembly for three reasons. First, the thermal conductivity of Be was high, 60 to 70 Btu/hr-ft per ^{o}F, and transient engine operation resulted in easily handleable temperature gradients. Second, the materials in the triple-flange assembly had relatively low thermal conductivities ranging around 12 Btu/hr-ft per ^{o}F, and relatively high densities with resultant high volumetric secondary heating rates. Third, the triple-flange assembly was a key structural member critically sensitive to high thermal stresses.

As was the case in the central-island aerothermal analyses, the non-nuclear transients were the most significant conditions analyzed. The cooling-air flow schematic and nodal patterns used for transient analysis of the outer section are shown in Figures 5.45 and 5.46 respectively. Typical data for the analysis of a chemical start are shown on Figure 5.47 for nodal positions 608, 726, 712, 722, and 728 shown in Figure 5.46. Corresponding data for other nodal points are contained in reference 4.

The steady-state temperature distribution during nuclear operation, sea level static, military setting, standard day, is presented in Figure 5.48. Temperatures and temperature differentials were within allowable limits.

5.4.3 NUCLEAR DESIGN

Assumptions and methods of calculating secondary heating rates are described in section 5.9. Typical results of nuclear calculations are shown in Figures 5.49 and 5.50. Figure 5.49 is a plot of the longitudinal secondary heating rates, expressed as watts per gram per megawatt of reactor power, at a radial distance of 12.4 inches from the engine centerline. Figure 5.50 is a radial traverse of secondary heating rates through a longitudinal plane 23.95 inches forward of the core midpoint. Other data are contained in reference 4.

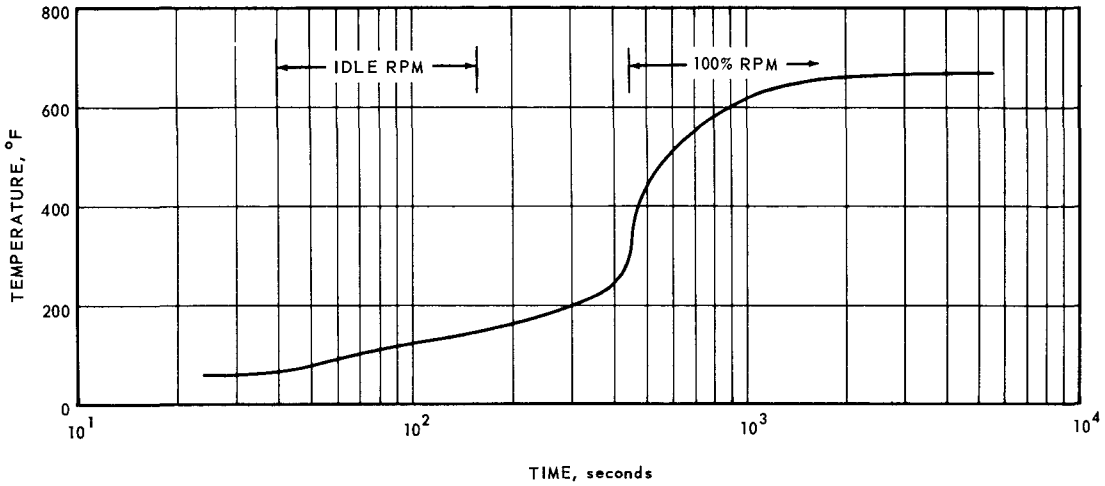

Fig. 5.44 – Drag link average temperature during chemical start

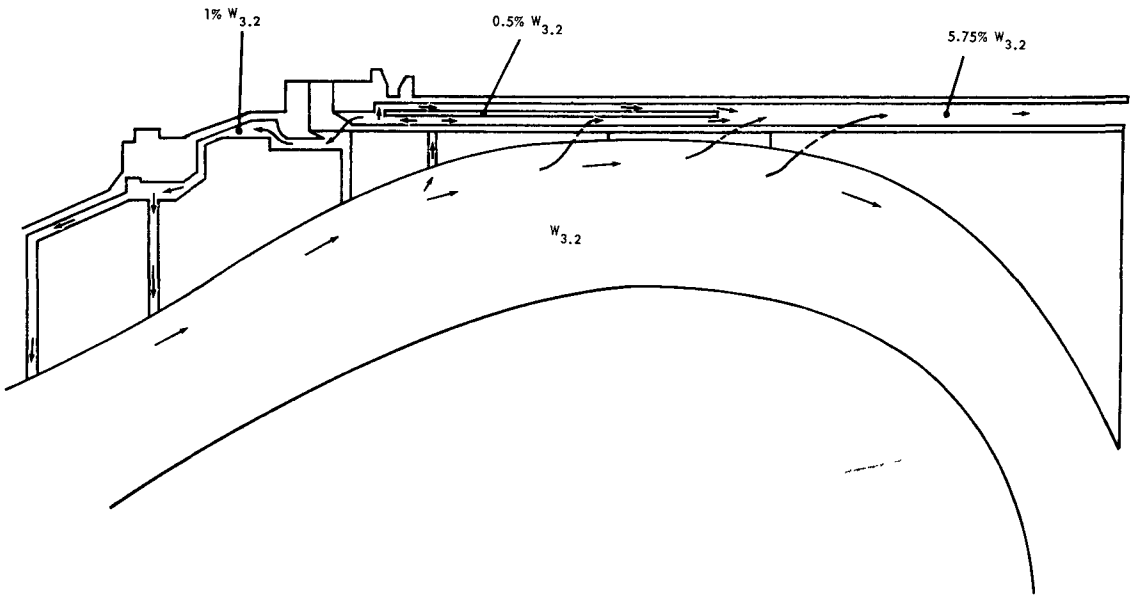

Fig. 5.45 – Cooling-air flow schematic, front shield outer section

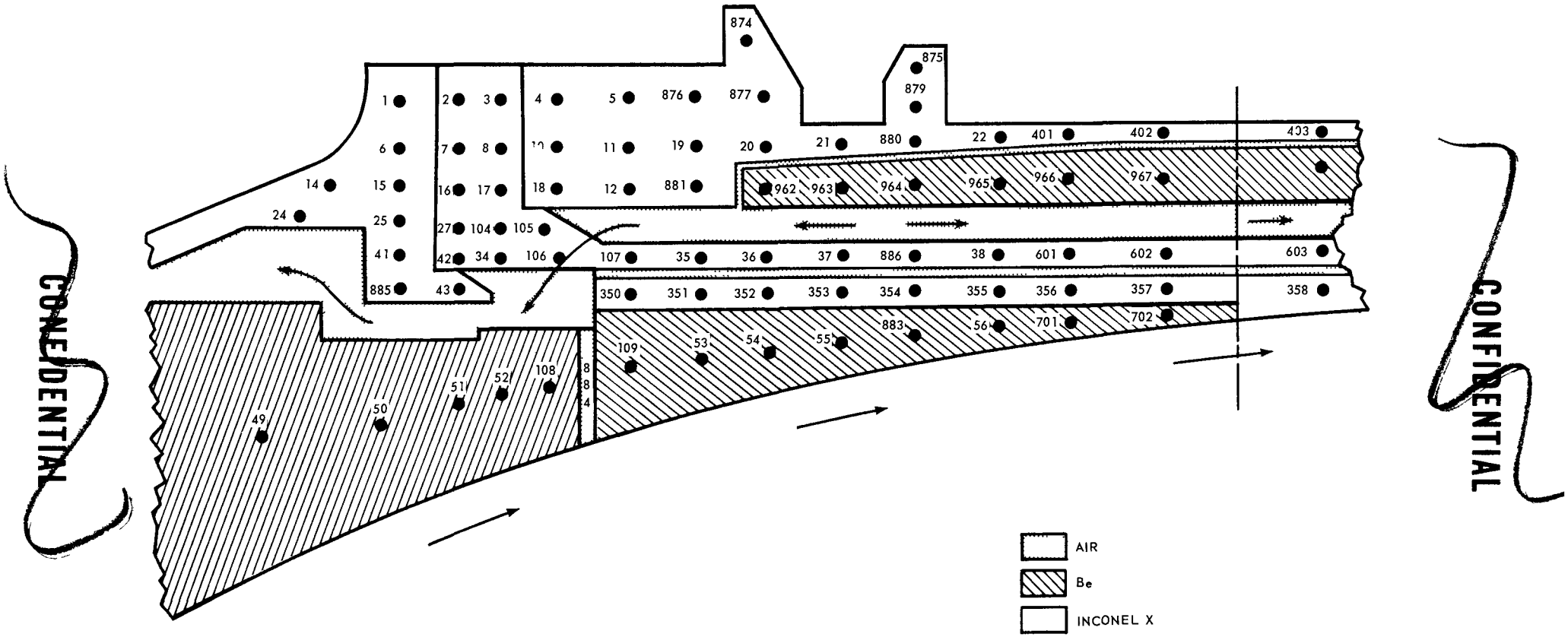

Fig 5 46 – Front shield outer section nodal pattern for aerothermal analyses

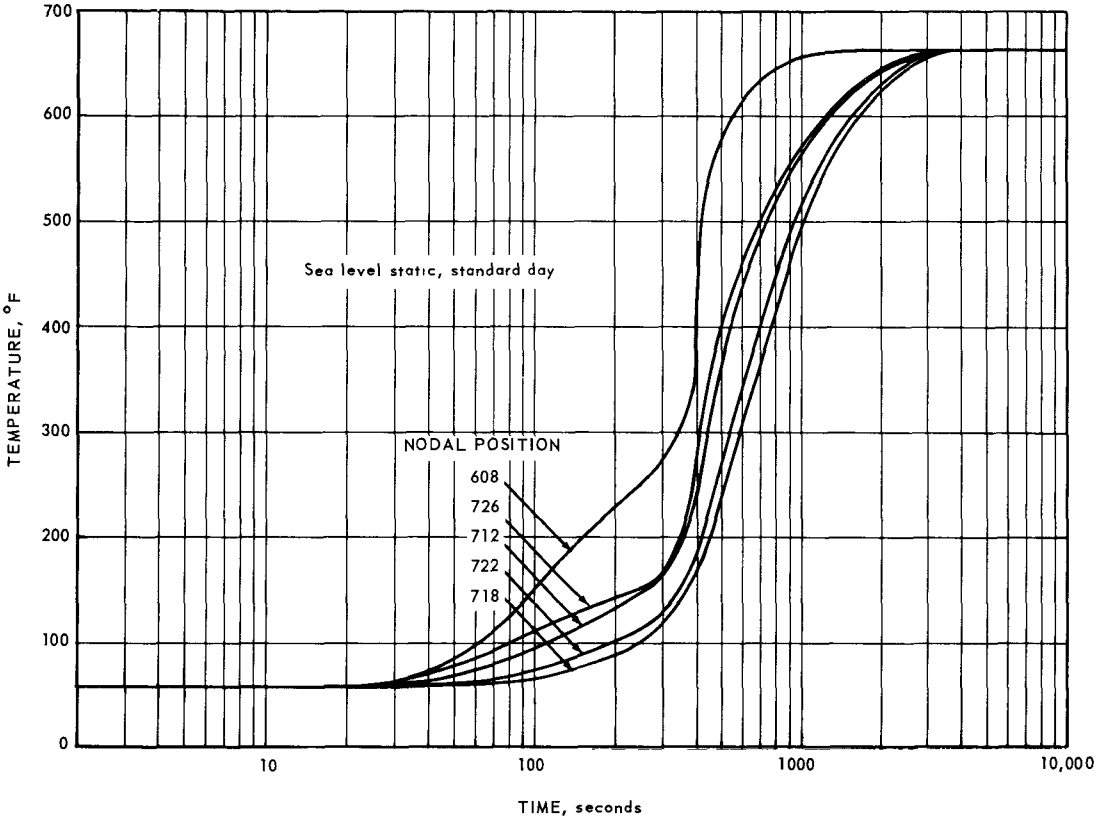

Fig. 5.47 – Temperature response during chemical start, front shield outer section

5.4.4 STRESS AND WEIGHT

5.4.4.1 Central Island

Load paths through the primary support structure were as follows:

1. Vertical and side loads acting on the slabs were transmitted axially through adjacent slabs to the front and aft discs by means of shear collars. Approximately one-half the load was absorbed at the forward end by the Be circular discs and the remaining portion was absorbed at the aft end by stainless steel sectors connected together to form a circular disc. Loads from the Be discs were transferred to the inner cylinder and then forward into the support beams by means of shear keys.

   The load from the stainless steel disc was transmitted to the aft support ring by a system of shear keys. A small portion of this load was carried along the inner cylinder to the support beams. The larger portion was picked up by the drag links and transferred to the support fittings of the support beams. Since the ends of the support beams were splined into the support fittings and permitted radial movement, beam loads could be absorbed by the support fittings only in a tangential direction and normal to the plane of the beams.
2. The axial load acting on the central island was carried entirely by the forward Be circular disc and was transmitted to the inner cylinder by means of a piston ring around the cylinder. Since the forward end of the cylinder was free to slide fore and aft within the support beams, the only path for this load was through the aft support ring to the drag links and then to the support beams.

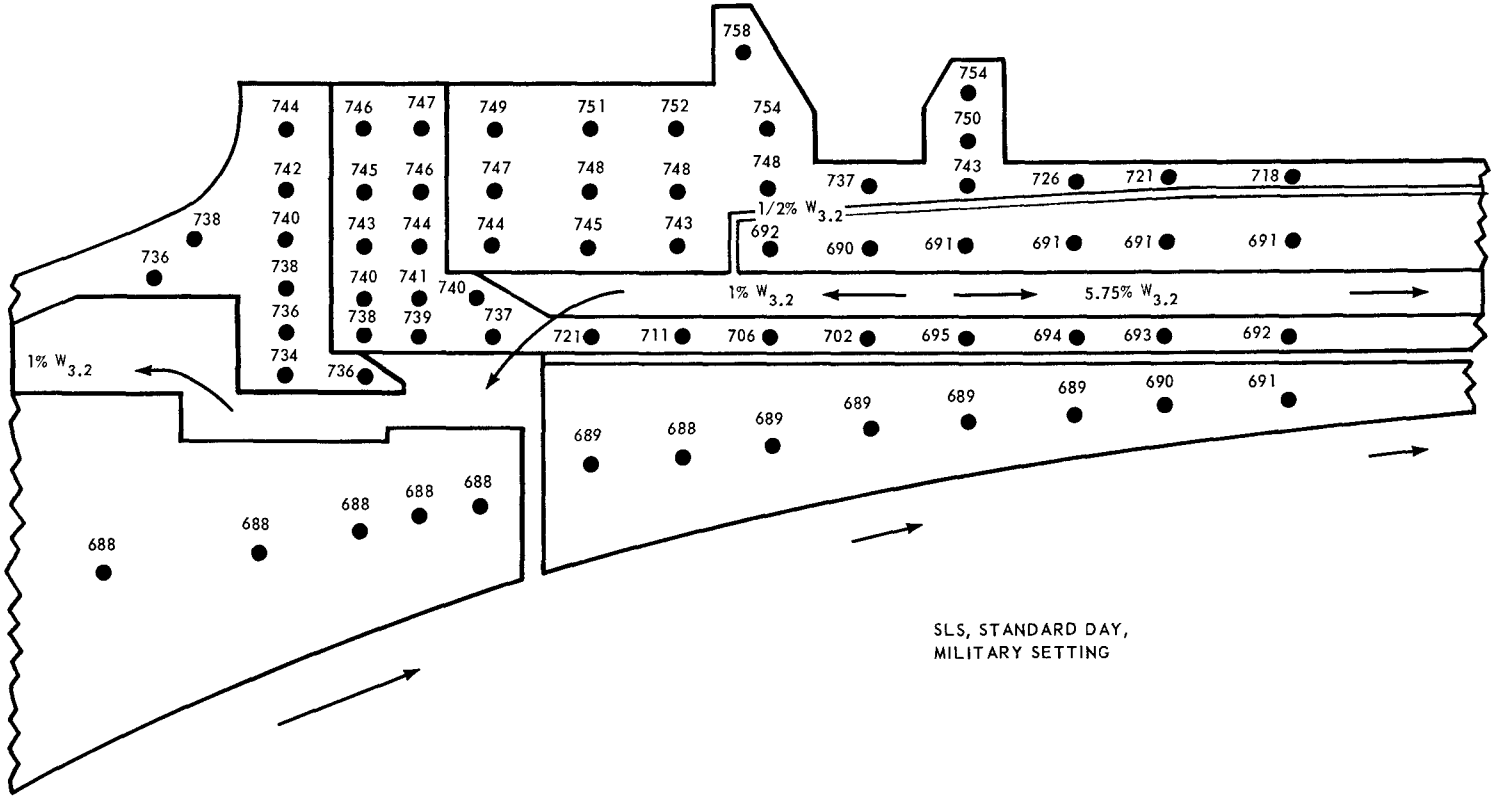

Fig. 5.48 – Temperature distribution during steady state nuclear operation, front shield outer section

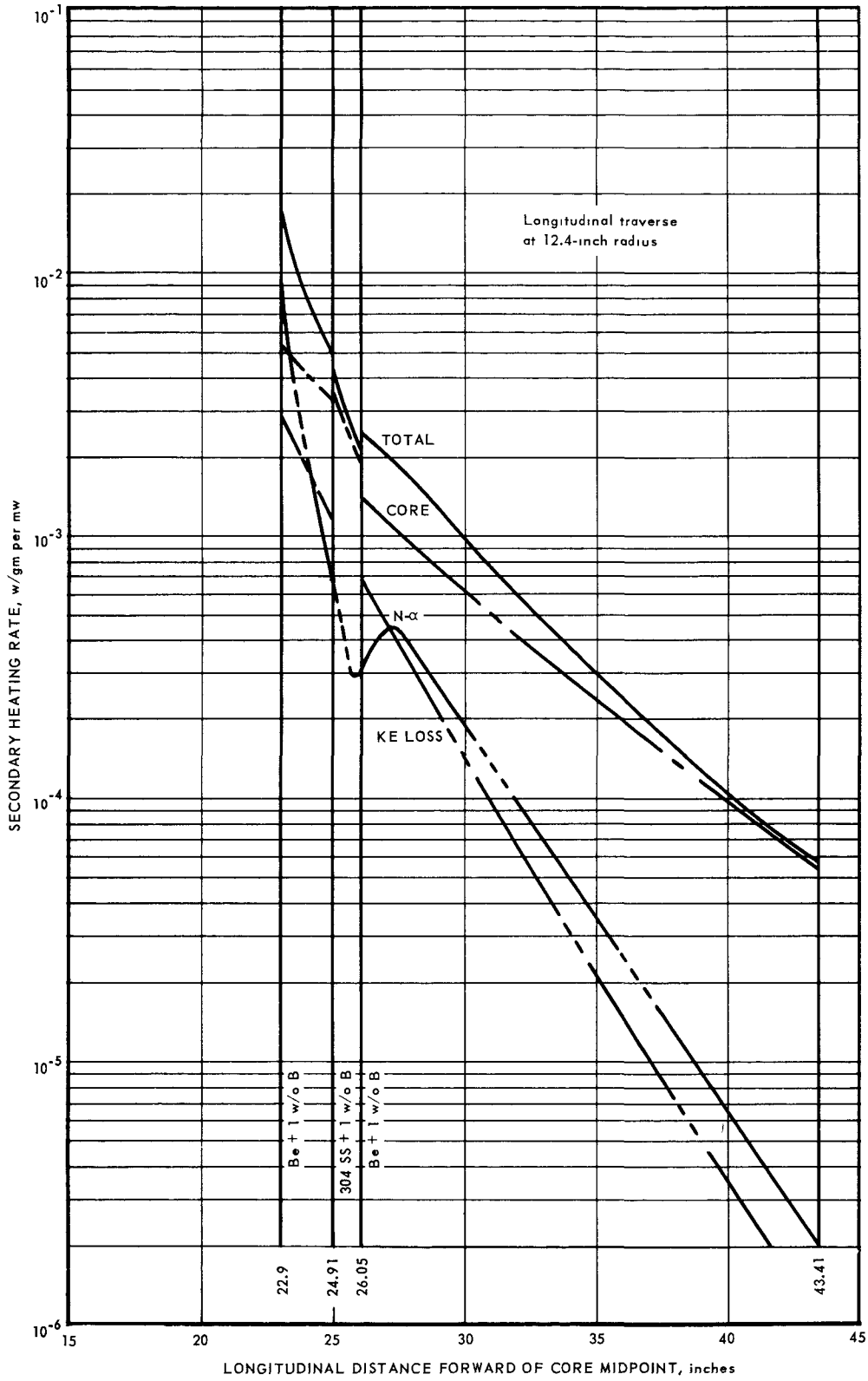

Fig. 5.49 – Front shield secondary heating rates, longitudinal traverse

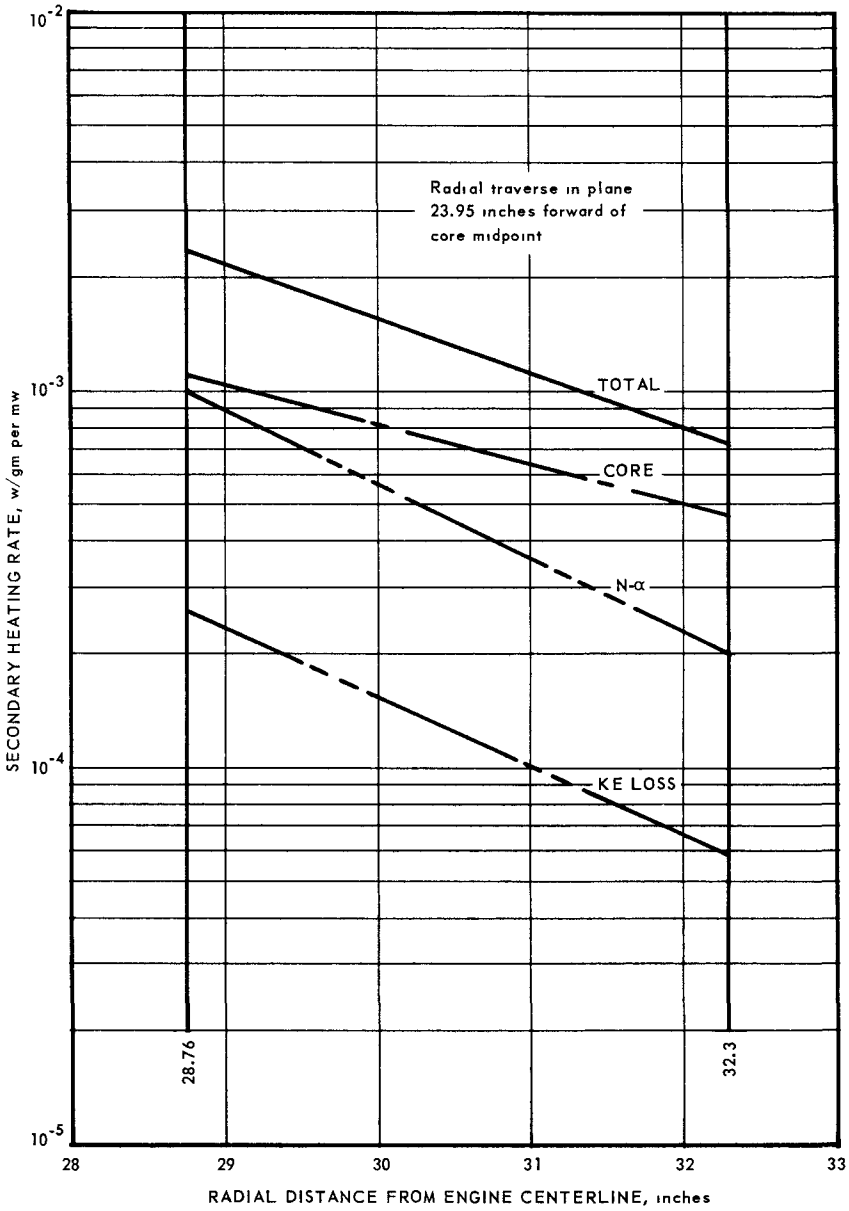

Fig. 5.50 – Front shield secondary heating rates, radial traverse

3. The vertical and side shaft tunnel loads, due to tunnel deflection, were absorbed at the connecting flange of the inner cylinder as a concentrated load and a moment. The concentrated load passed directly into the support beams and then to the support fittings. The moment was transmitted through the inner cylinder to the aft support ring where it was picked up by the drag links, carried to the support beams, and absorbed by the support fittings in the fore-aft direction (normal to the plane of the beams).
4. The fore-aft load applied to the tunnel was transmitted through the tunnel to the flange connection at the forward end of the inner cylinder. Since the inner cylinder was free to slide fore and aft in the support beams, the load moved down the inner cylinder into the aft support ring. Here it was absorbed by the drag links, carried to the support beams, and picked up by the support fittings in the fore-aft direction (normal to the plane of the beams).

A chart of the deflections throughout the primary support structure due to flight-maneuver and ground-operation loading conditions is given in Figure 5.51. These deflections were due to loads which followed the load paths described above.

Other detailed stress analysis results are contained in references 4 and 22.

5.4.4.2 Outer Section

The front shield cone was a vital structural member. It formed the main load path between the pressure vessel and the compressor section. In addition, a major portion of the reactor-shield assembly side and vertical inertial loads, and the system pressure loads were absorbed through the front shield cone. The cone was the tie between the pressure vessel and the compressor rear frame. The compressor rear frame contained the forward trunnion ring. The cone consisted of a forward flange, an aft flange, and an intermediate 0.2-inch-thick cone. The forward flange mated with the compressor rear-frame aft flange; these flanges were analyzed as an integral unit. The aft flange was analyzed as a member of the triple-flange assembly. The entire cone was analyzed for pressure and inertial loads and found to be structurally satisfactory.

The structural support of the shielding material acted to make the whole unit respond as an integral unit independent of the structural shell, except for (1) a tie-in in the front flange,

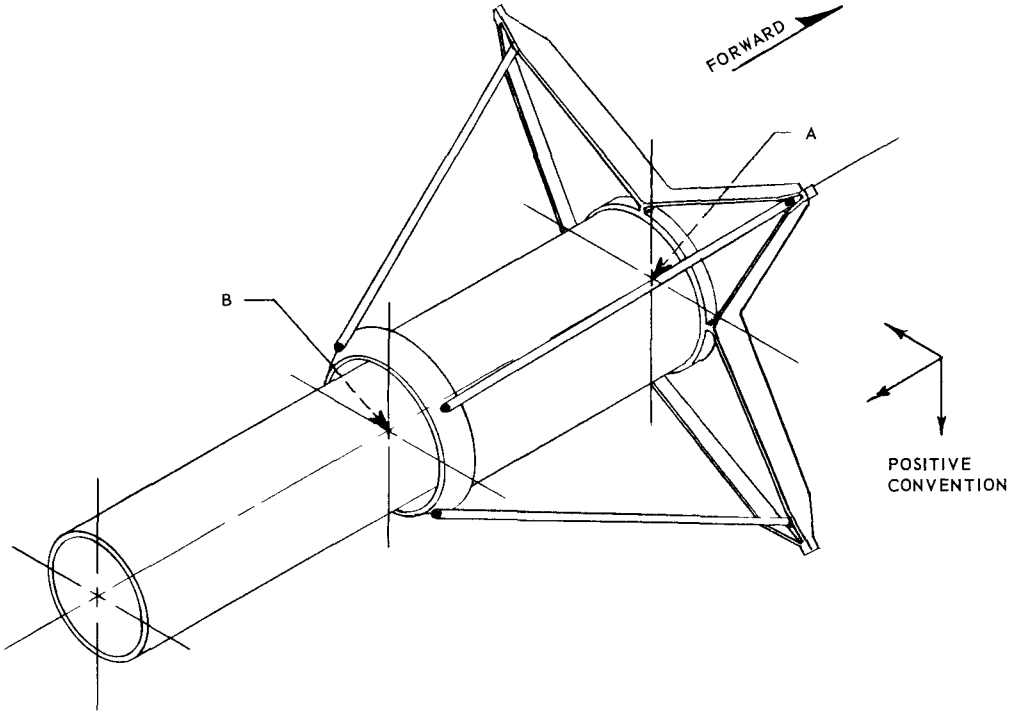

PT.	LOAD CONDITION	VERTICAL DEFLECTION, inch	AXIAL DEFLECTION, inch	SIDE DEFLECTION, inch
A	FLIGHT MANEUVER	+ 0.0572 - 0.0286	+ 0.0856 - 0.0105	+ 0.0143 - 0.0143
	GROUND OPERATION	+ 0.0286 - 0.0286	+ 0.0960 - 0.0210	+ 0.0143 - 0.0143
B	FLIGHT MANEUVER	+ 0.0677 - 0.0338	+ 0.0765 - 0.0094	+ 0.0169 - 0.0169
	GROUND OPERATION	+ 0.0338 - 0.0338	+ 0.0860 - 0.0189	+ 0.0169 - 0.0169

Fig. 5.51 – Primary support structure deflections (Dwg. 207R820)

and (2) a stop at the aft end of the shielding which absorbed aft inertial and pressure loads. The outer section could be assembled separately, and remotely inserted or removed from the structural shell. However, structural feasibility had not been fully evaluated at the time of contract termination. The cross section of the four support beams at the horizontal and vertical centerlines was larger than the cross section of the four located at 45 degrees from the horizontal and vertical centerlines. The horizontal beams carried the vertical load, and the vertical beams carried the side inertial loads. In addition, all four of these beams transmitted axial inertial loads from the shielding to the structural shell forward flange. At the forward end these beams were bolted into a ring which contained a lock-pin assembly inserted in the shell forward flange. At the aft end, these beams passed through the support ring and were free to slide under axial loads. The aft inertial and pressure loads on the shielding were transmitted through the four beams, the bolts at the forward end, and the shear pins. The forward inertial loads were carried into the stop furnished by the front-shield-cone flange in the triple-flange assembly.

The lighter beams at locations 45 degrees from the horizontal and vertical centerlines were used to restrain the tangential springs system and provide static equilibrium. Five structural rings were used as a means of providing pressure-type circumferential loading through their outer flanges.

Steady-state and transient stress analysis data are contained in references 4, 19, 21, 23, and 24.

5.4.4.3 Weight

The calculated weight of the front shield was 5695 pounds, distributed as shown in Table 5.5.[25]

TABLE 5.5

WEIGHT BREAKDOWN[a] OF FRONT SHIELD

Part	Weight, lb
Structure	
Outer section	590
Central island	425
Total	1,015
Be Shielding Material	
Outer section	715
Central island	3,370
Total	4,085
Stainless Steel Shielding Material	
Outer section	120
Central island	425
Total	545
Total Front Shield	5,645
Data Instrumentation[b]	50

[a]Based on drawings completed during contract termination. The weight of structure may have increased by 150 lbs (estimated) during final design.

[b]Estimated.

The center of gravity of the front shield was 28.29 inches from the forward flange of the compressor rear frame. The center of gravity of the central island was 29.40 inches from the forward flange of the compressor rear frame. The center of gravity of the outer section, including the front shield cone, was 24.96 inches from the forward flange of the compressor rear frame.

5.5 REAR SHIELD COMPONENT DESIGN DATA

5.5.1 MECHANICAL

The rear shield, shown in Figures 5.52a and 5.52b, consisted of an outer section, a forward central island, and an aft central island. The central island consisted of several annular subassemblies attached to the turbine front frame and the combustor structural walls. Shielding included either forward of, or within, the turbine rear-frame area was called the forward central island; shielding behind the turbine frame was called the aft central island.

The outer section was cantilevered from the reactor structural shell and was isolated completely from the central island. This assembly could be remotely disassembled and assembled with the reactor section. The forward and aft central islands were flanged to the turbine front frame as shown in Figure 5.53, and could be remotely disassembled and assembled. The over-all assembly had an outside diameter of 66 inches and a length of 38 inches.

Barrel nuts were used in all flanges requiring remote-handling capabilities. The use of barrel nuts eliminated voids in the shielding which otherwise would have been required for remote-handling tool clearance.

Beryllium material in all sections was mechanically attached to adjacent structure. Relative thermal movement between parts was permitted by the attachment devices.

5.5.1.1 Insulation

The walls of the primary-air annular duct were covered by thermal insulation that limited the maximum temperature of the structure to 1000°F. An insulation sandwich, made up of a layer of fibrous insulation next to the structural wall and an air-cooled hot-cover-sheet assembly to protect the fibrous insulation, was used. The hot cover sheet was cooled by air passing through numerous discrete passages formed by a corrugated sheet welded to the hot cover sheet. The insulation sandwich was attached to the structural wall by fasteners formed by a spacer welded to the cover sheet and a washer welded to the structural wall. The spacers were trapped in the washers and permitted differential thermal growth between the cover sheet and the structural wall.

Figure 5.54 illustrates a typical cross section of the insulation sandwich. It shows the cover sheet with the corrugated sheet spot-welded to it, a layer of foil over the fibrous insulation, and a fastener holding the insulation sandwich to the structural wall. Figure 5.54 also shows a cross section of a corrugation entering the cooling-air manifold and shows the metering orifices in the manifold side wall. The cover sheet was 0.050-inch-thick Hastelloy X. The corrugation sheet was 0.040-inch-thick Hastelloy X. The fibrous insulation was alumina silica with a density of 12 pounds per cubic foot and approximately 0.25 inch thick. The over-all sandwich thickness was nominally 0.050 inch. Fasteners were spaced approximately 6 to 8 inches apart in all directions, and as close to the pad edges as possible.

Compressor discharge-air was used to cool the cover sheet. This air was introduced into each pad through a manifold inlet which connected shield cooling-air passages behind the structural wall to a manifold on each insulation pad. The manifold was a common air supply

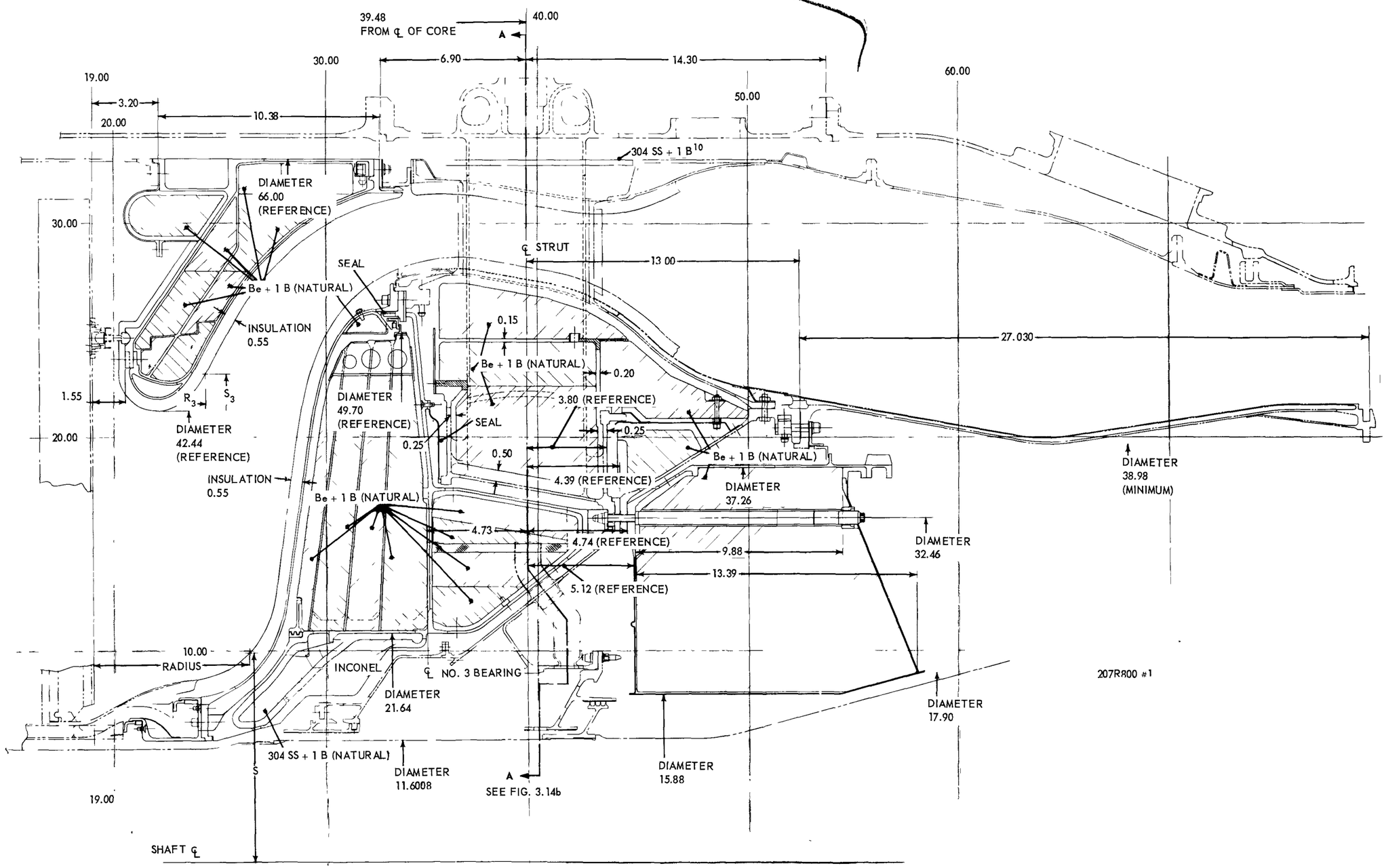

Fig. 5.52a – XNJ140E-1 rear shield layout

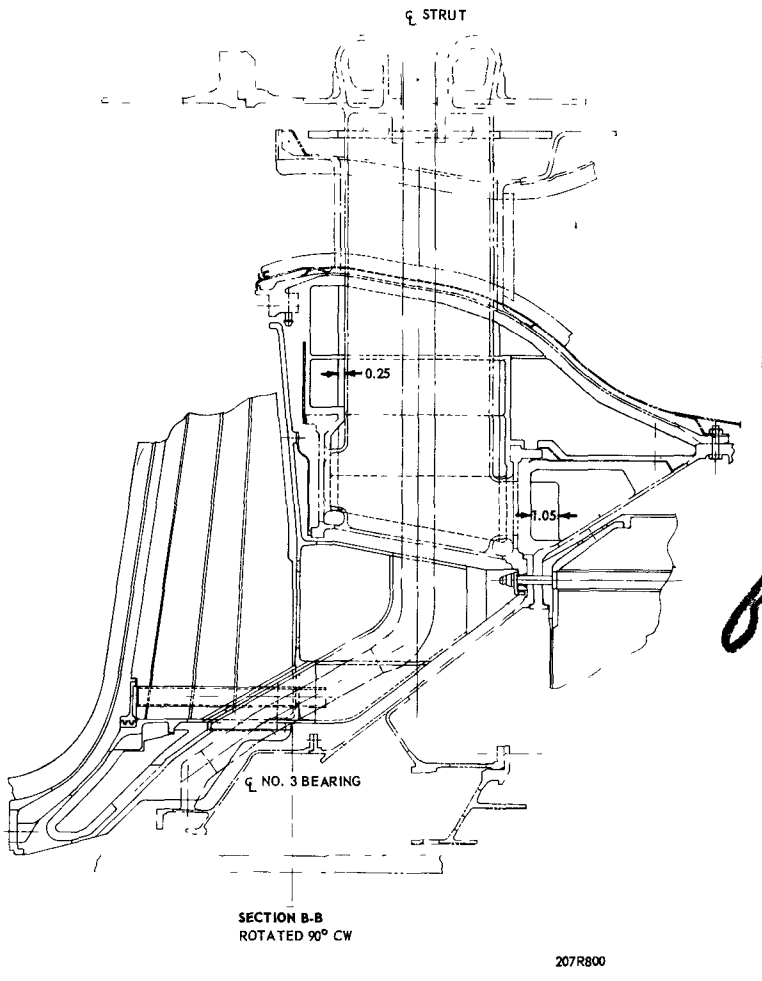

Fig. 5.52b – XNJ140E-1 rear-shield layout

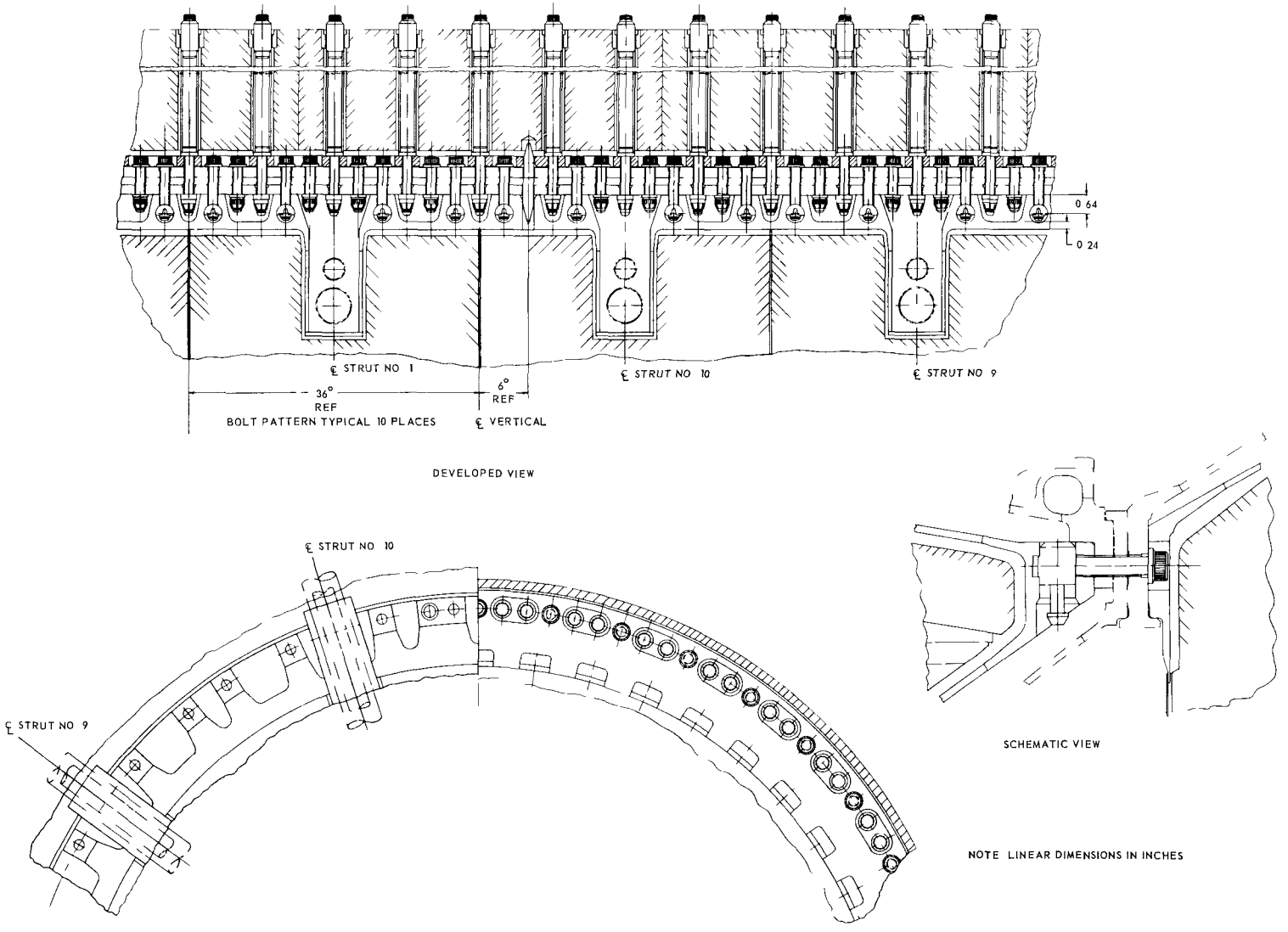

Fig. 5.53 – Attachment of rear shield central island to turbine front frame (Dwg. 207R800)

CONFIDENTIAL

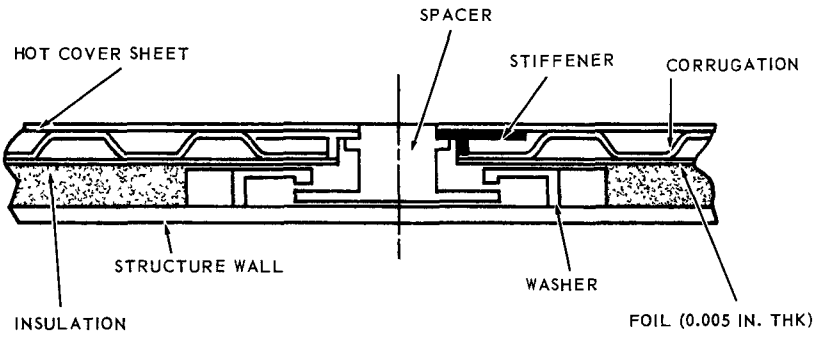

FASTENER ASSEMBLY

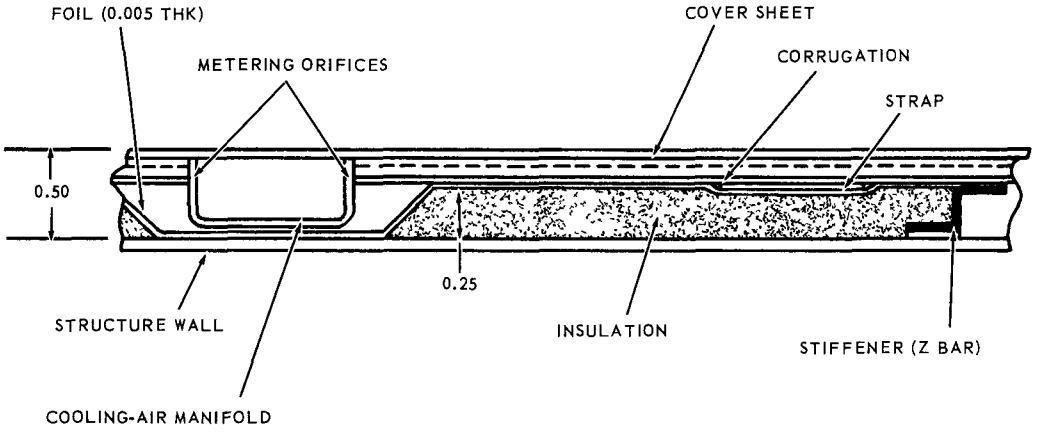

CORRUGATION AND MANIFOLD

Fig. 5.54 – Insulation sandwich

for all corrugations of each insulation pad. Cooling-air was metered through an orifice at the entrance to each corrugation and discharged to the primary-air stream at a point of relatively low static pressure.

The edges of each pad were baffled to restrict the flow of primary-air into the voids between the insulation sandwich and the structural wall. These baffles were Z bars welded to the underside of the corrugations and resting on the structural wall. The void between the structural wall and the sandwich was vented to a point of low static pressure. A pressure differential was set up on the cover sheet which tended to push the cover sheet against the structural wall under steady-state conditions. The imploding pressure reached a maximum of approximately 5-1/2 psi and was taken up by the Z bars.

During severe transients such as compressor stall or rotor lock, the pressure in the void could have reached a static pressure higher than the main stream static pressure. The differential between these pressures was fixed by the vent areas in each pad; these vent areas were sized to limit the transient differential pressure to a maximum of 0.85 psi. This differential pressure tended to blow the hot cover sheet-corrugation sheet assembly away from the structural wall and was restrained by the fasteners. This exploding load also was transmitted across corrugations to the fasteners by means of straps welded to the bottom of each corrugation. These straps permitted wider spacing of the fasteners.

The insulation was divided into pads to facilitate assembly and to limit the differential thermal expansion. The pads were approximately rectangular in shape, with a maximum dimension of approximately 20 inches. Each pad was fixed on the structural wall at one point and guided at a second point. Some pads, due to the extremely sharp curvature, did not have fixed points of attachment. All pad leading edges were overlapped in the direction of airflow to eliminate edges protruding into the primary-air stream. Pad edges were lapped circumferentially in the axial direction to facilitate remote assembly.

Figure 5.55 is a schematic diagram describing the location and types of the rear shield insulation pads. The outer-section insulation pads and structural wall were remotely separable from the rest of the shield structure. Similarly, the forward-central-island structural wall and insulation pads were remotely separable from the remainder of the central-island structure. All rear shield insulation pads could be replaced if damaged. However, replacing them necessitated new insulation pads and new structural walls for both the outer section and the central island.

5.5.1.2 Central Island

Forward Central Island - The details of this subassembly are shown in Figure 5.56. It consisted of four discs and three rings of borated Be and borated 304 stainless-steel shielding material, an Inconel and heat-treated Inconel X main support structure, and a heat-treated insulated Inconel X duct wall. It was flanged to, and supported by, the forward side of the turbine front frame as illustrated in Figure 5.57. The support structure supported and contained the four discs and two of the rings of Be shielding material. The other ring of shielding material was attached to the inner surface of the duct wall at the outer flange. The duct wall formed the inner wall of the annular primary-air duct through the rear shield and was thermally insulated from the primary airstream. Details of the duct wall are shown in Figure 5.58.

As shown in Figure 5.56, the four discs were mechanically attached as a unit by 0.25-inch-diameter age-hardened Inconel X bolts extending through all four discs to the supporting structure. To insure that the specified close tolerance on the cooling passageways between the discs was held, special washers were inserted between the discs and retained by the bolts. Each segment of a disc was supported by bolts at three points. The outermost bolt and washer combination fitted into a keyway at the inner surface and was used as a shear tie to fix the segment in true position. The other two bolt-and-washer combinations were designed to absorb only axial loads and allowed for growth due to differential thermal expansions. Segments of the two rings also were mechanically attached by 0.25-inch Inconel X bolts. Each ring segment was independently attached to the supporting structure. All bolts were pre-torqued so that the shielding blocks were held firmly in place.

The borated stainless steel ring, was continuous and keyed to the support structure in four places. A flanged lip, machined on the outer surface, was restrained between the support structure and allowed for differential thermal expansions during operation.

Each of the shield blocks was restrained from closing the cooling passageways by metallic spacers. The forward central island cooling-air was supplied from the front shield through the annulus between the shaft tunnel and core liner. After passing through slots in the support structure flange, part of this air was used to cool the duct wall and insulation while the remaining portion cooled the material and structure. It then was exhausted into the turbine front frame insulation and was used for additional cooling.

Segments of the forward central island were contained within the turbine-front-frame struts. This subassembly consisted of a series of borated shield blocks, 304 stainless steel shield pads, and hardware for attaching the shield blocks to the turbine front frame. The blocks were mounted in the void areas between, and in the rear of, the ten turbine-front-frame struts.

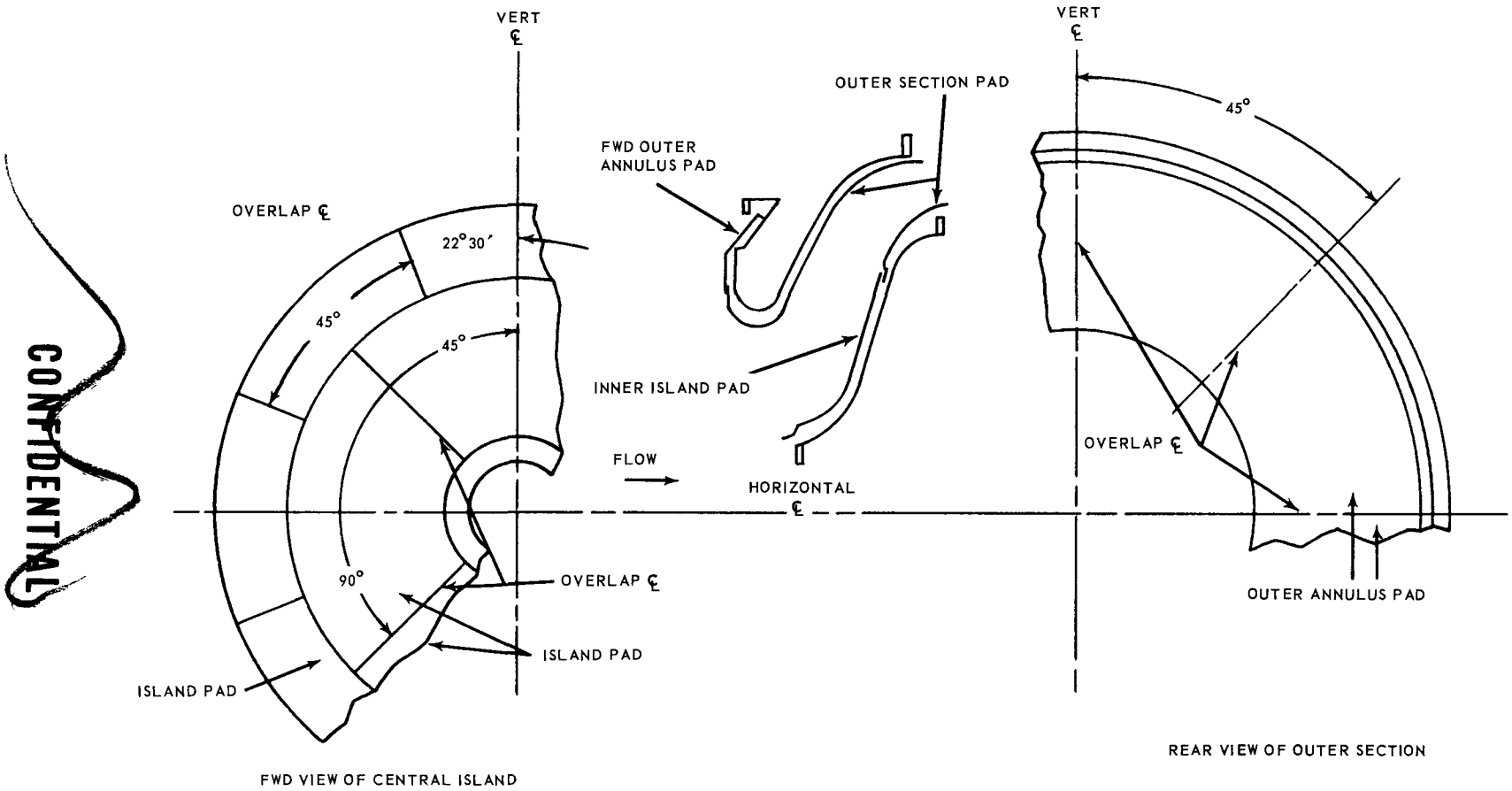

Fig. 5.55 – Schematic diagram of rear shield insulation pads

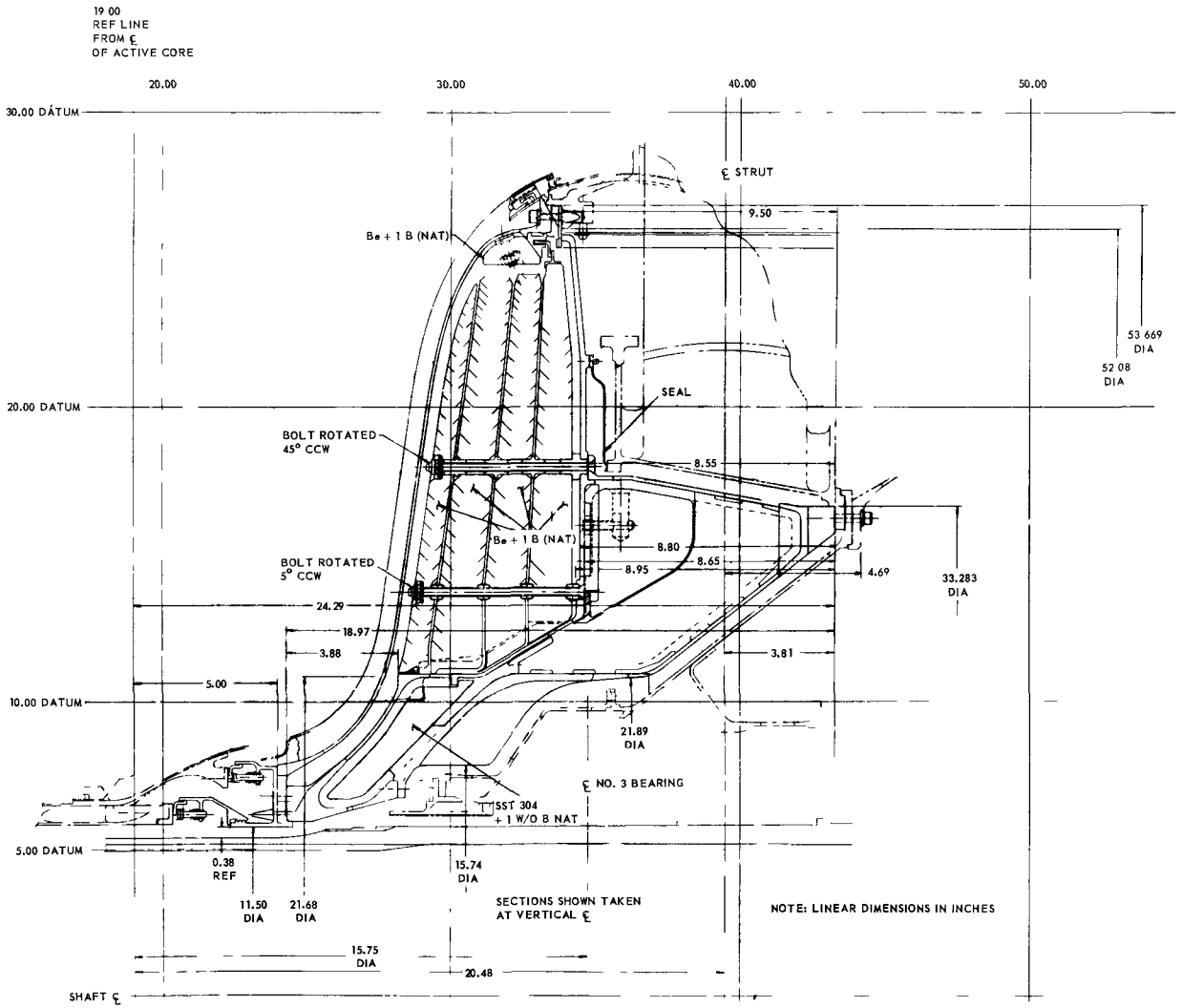

Fig. 5.56 – Rear shield forward central island (Dwg. 207R803 Rev. A Sh. 1)

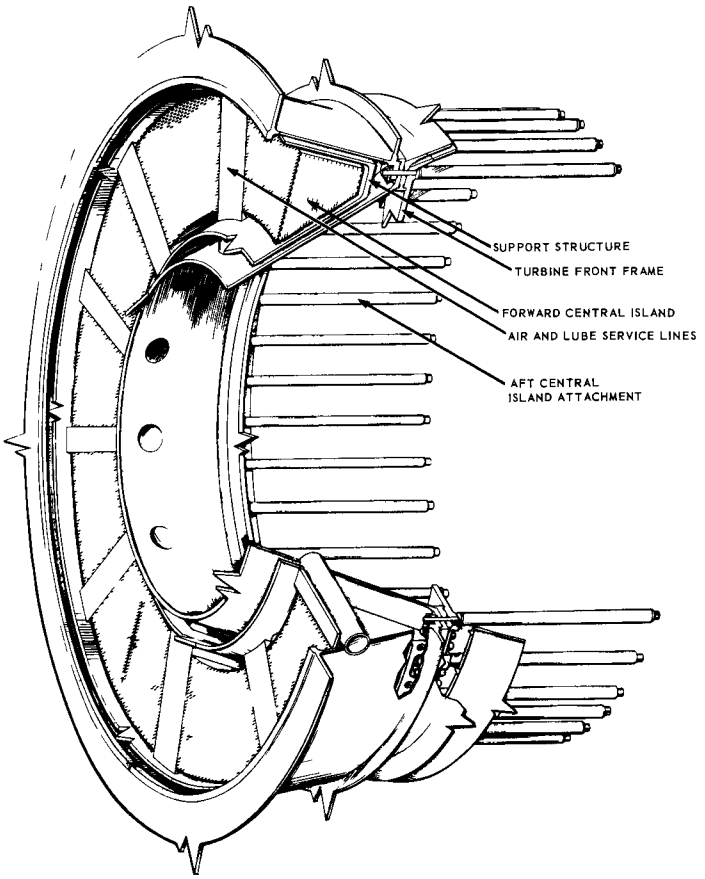

Fig. 5.57 – Forward and aft central island attachment to turbine front frame (Dwg. DI442)

The inner-strut segments, Figure 5.59, were blocks of Be containing 1 weight percent natural boron. Each bay of shield blocks was attached mechanically to the turbine front frame by long 0.25-inch age-hardened Inconel X bolts that incorporated metallic spacers to permit cooling-air flow. Cooling-air flowing through these passageways was used further to cool other rear shield parts and turbine-front-frame structure. Afterwards, the air passed through voids between the struts and strut collar and finally into the bleed-speed annulus.

The outer-strut segments were 0.25-inch-thick 304 stainless steel containing 1 weight percent B^{10} and were used to reduce secondary heating in the side shield. A segment of this shielding was placed between each of the ten struts and was bolted to the turbine front frame. These segments were cooled by air flowing through the bleed-speed annulus.

Aft Central Island - Details of this subassembly are shown in Figures 5.60a and 5.60b. It consisted of a ring of Be shielding material and an age-hardened Inconel X supporting structure. The support structure was used to support and contain the segments of shield material that made up the shield ring. It was flanged to, and supported by, the aft side of the turbine front frame.

Shielding material consisted of segments of Be containing 1 weight percent natural boron. Each segment had a series of holes that aligned with the structure and were used as one of several parallel paths for cooling-air from the turbine-front-frame struts. The forward outer face of each segment was notched in order that cooling-air, passing through slots in

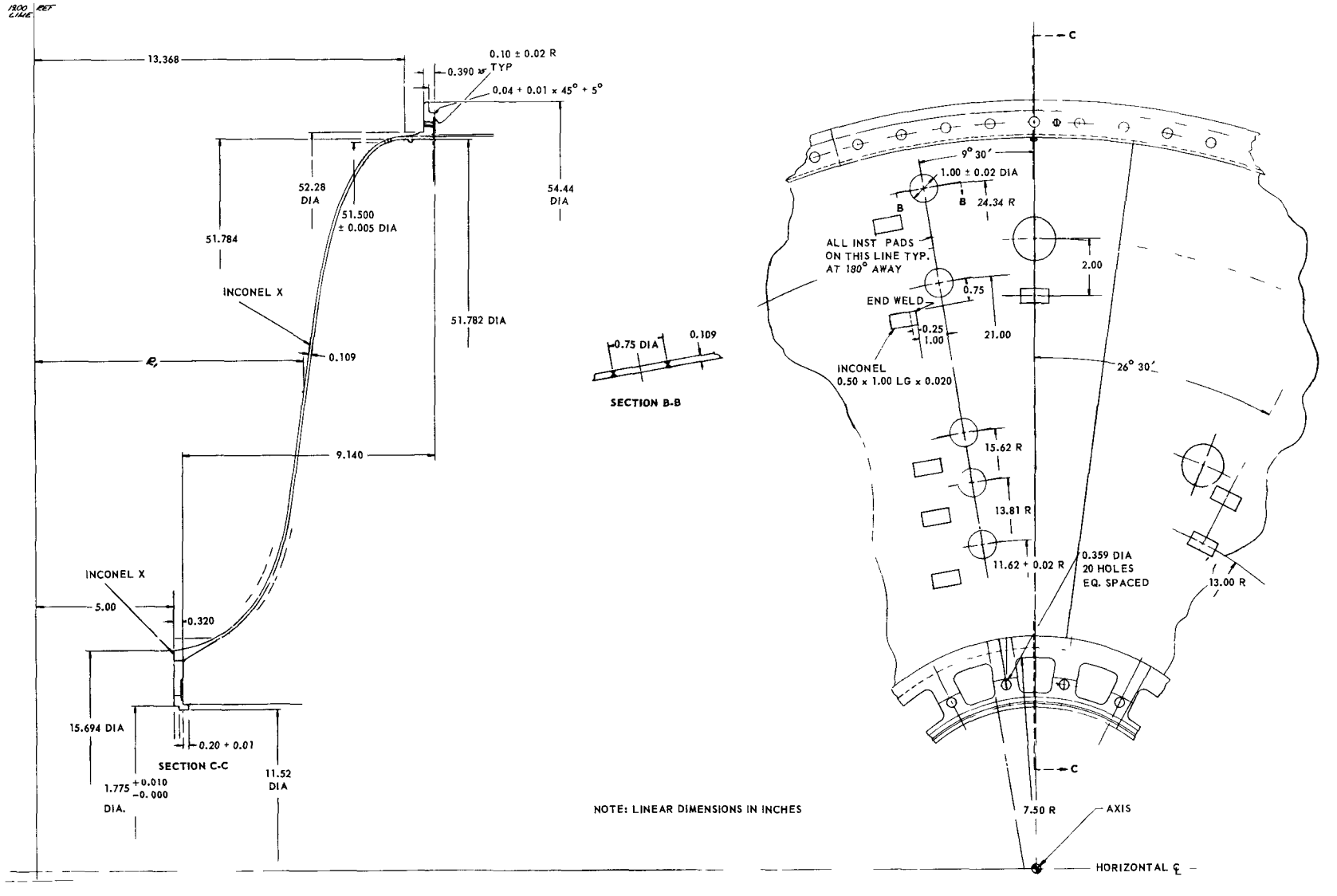

Fig. 5.58 – Forward central island duct wall (Dwg. 207R803 Rev. A Sh. 2)

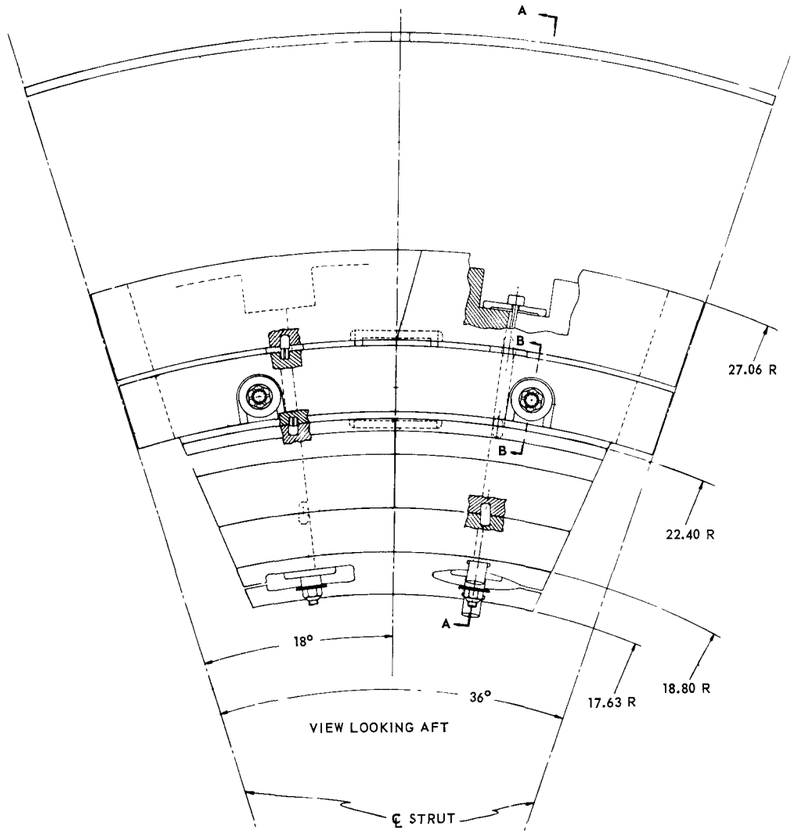

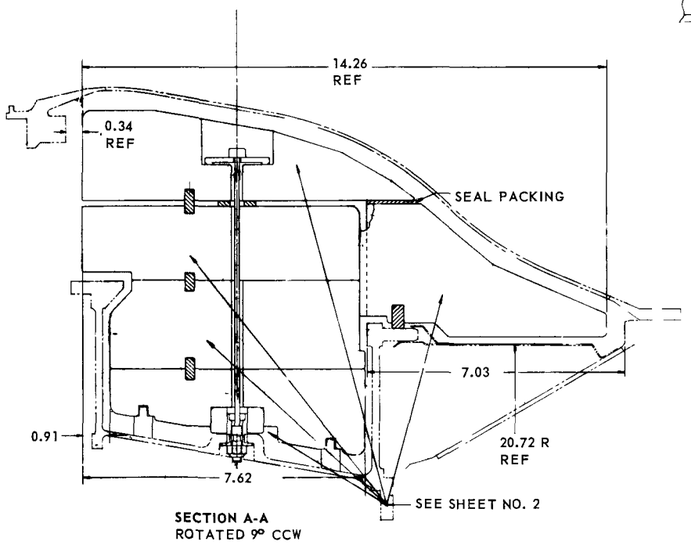

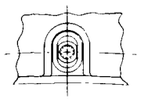

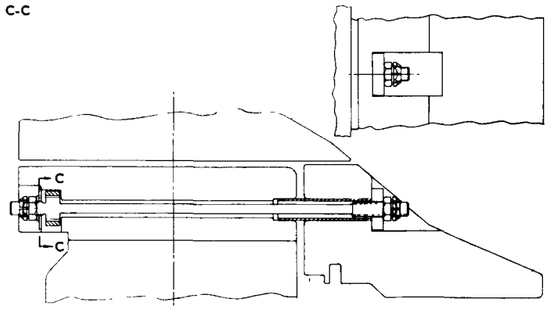

NOTE: LINEAR DIMENSIONS IN INCHES

Fig. 5.59 – Inner strut segments, rear shield forward central island (Dwg. 207R804 Sh. 1)

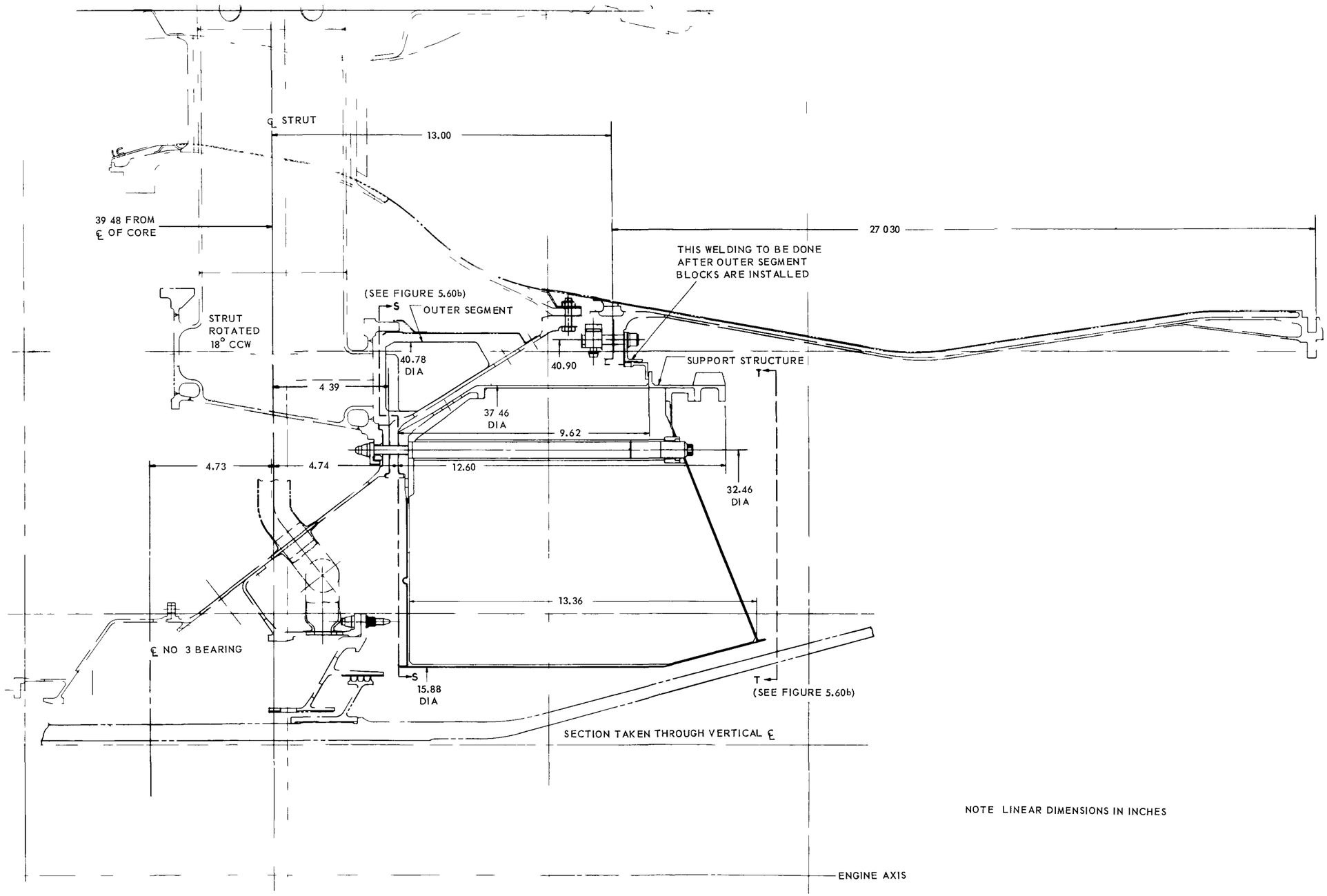

NOTE LINEAR DIMENSIONS IN INCHES

Fig. 5.60a – Rear shield aft central island (Dwg 207R805 Sh. 1)

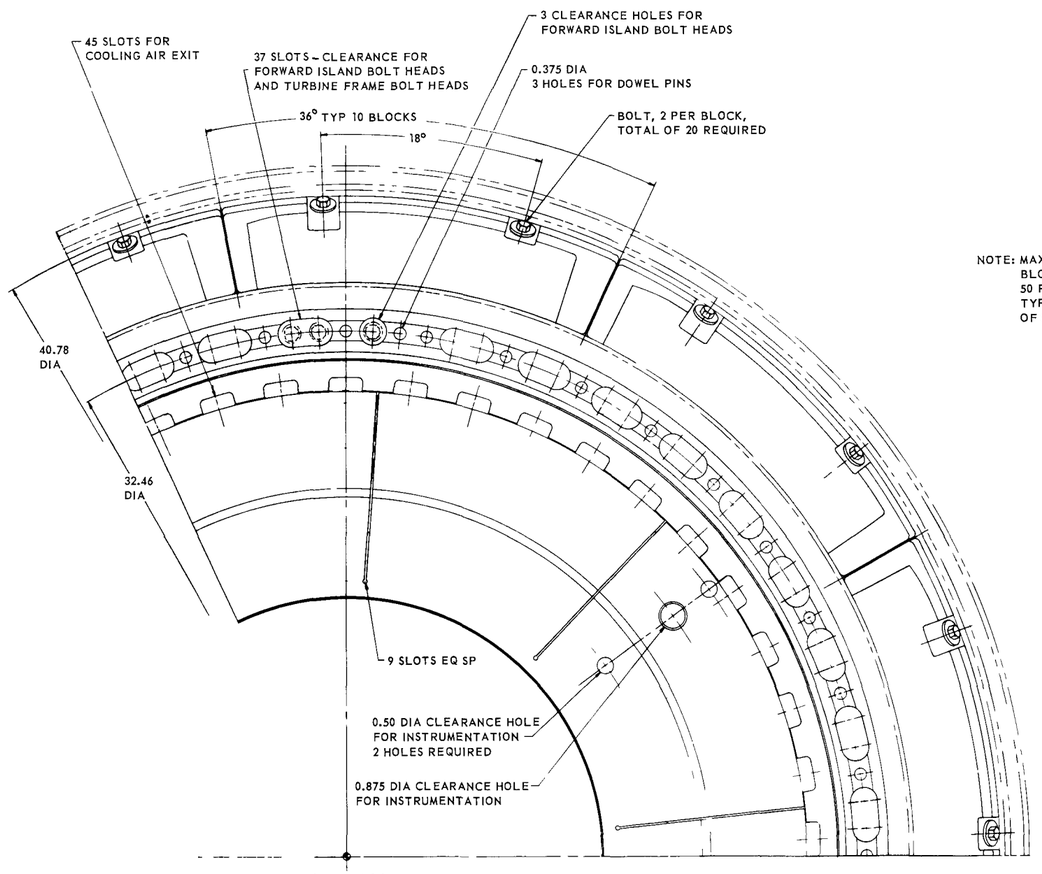

NOTE: MAXIMUM GAP 0.005 BETWEEN SHIELD BLOCKS, 0.000 GAP MUST BE MAINTAINED ON 50 PERCENT OF THE SURFACE AREAS. TYPICAL FOR ALL BUTTING SURFACES OF SHIELD BLOCKS.

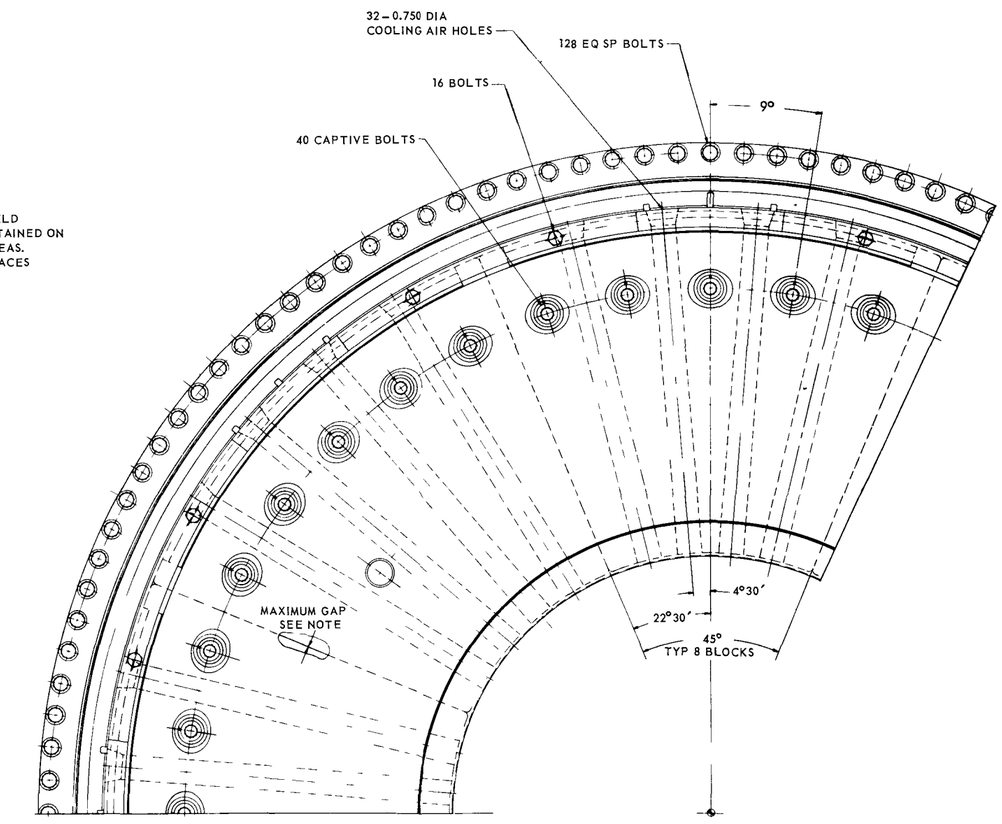

NOTE: LINEAR DIMENSIONS IN INCHES

Fig. 5.60b – Rear shield aft central island (Dwg. 207R805 Sh. 2)

the cone of the structure, further could cool the flange area of the structure and shield material. All cooling-air exhausted into the turbine-front-frame seal-leakage plenum.

5.5.1.3 Outer Section

A cutaway view of the rear shield outer section is shown in Figure 5.61. The layout drawing is shown in Figure 5.62.

It consisted of a ring of shielding material, an age-hardened Inconel X support cone, and a thermally insulated duct wall. The subassembly was flanged to, and supported by, the structural shell as shown in Figure 5.61. The support cone supported a large portion of the aft-retainer assembly load, and the forward portion of the shielding. The remaining shield material was supported by the duct wall. The innermost surface of the duct wall formed the outer wall of the annular primary-air duct through the rear shield and was thermally insulated from the primary airstream. This insulation consisted of pads attached to the duct wall and the support cone by fasteners designed to provide differential expansion between the pads and the supporting surface.

The shield ring consisted of 30-degree segments of Be containing 1 weight percent natural boron. Each segment was mechanically attached to the adjacent structure by 0.25-inch-diameter age-hardened Inconel X bolts. These bolts were pre-torqued at assembly. Each block also was restrained from closing the cooling-air passageway by Inconel spacers inserted into the blocks. The shield material and supporting structure were cooled by bleed-speed bypass air flowing through slots in the forward end of the main support structure. This air then flowed through cooling channels, exited through holes in the duct wall, cooled the duct-wall insulation cover sheet, and was dumped into the primary airstream.

5.5.2 AEROTHERMAL

Detailed steady-state analyses were performed for several flight conditions. The selection of conditions to be analyzed was based on an attempt to determine limiting aspects of the over-all design relative to reliability and performance. The emergency-power-set-

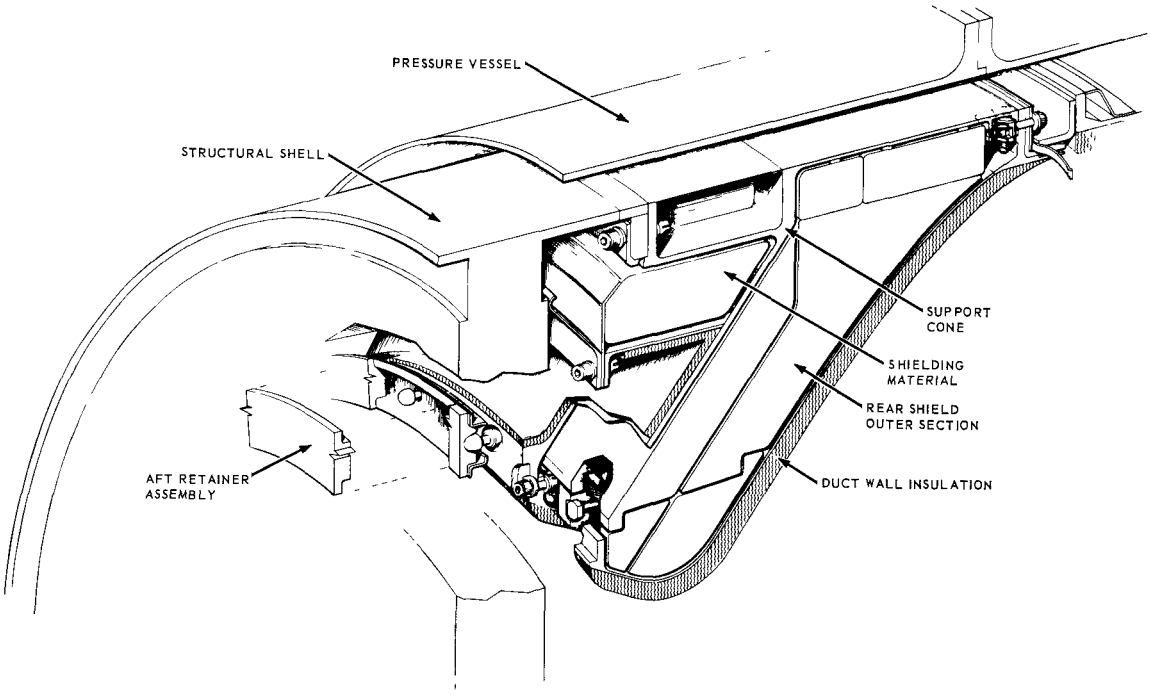

Fig. 5.61 – View of rear shield outer section (Dwg. DI449)

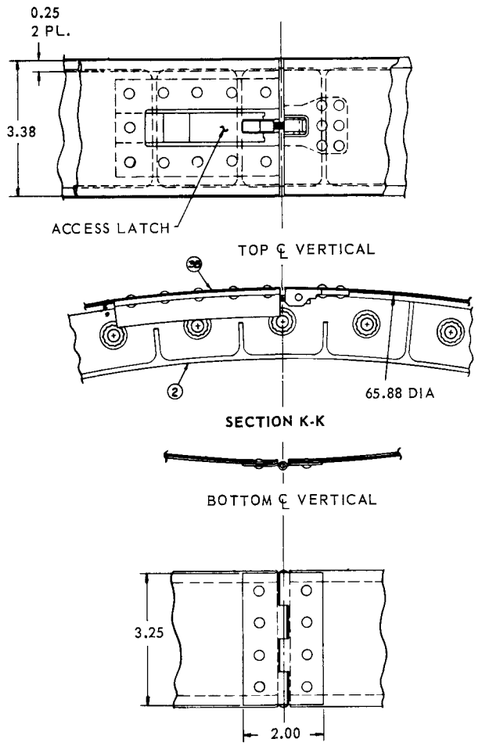

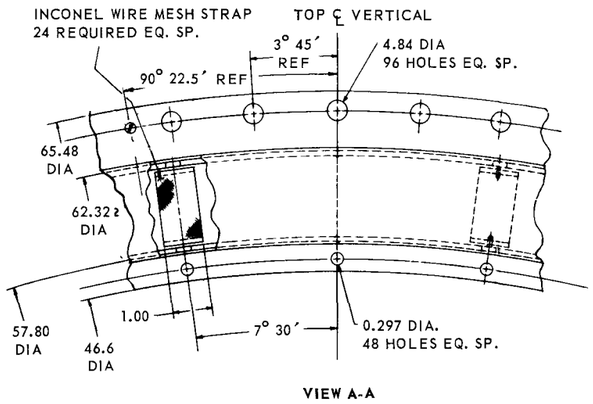

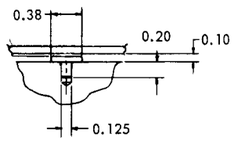

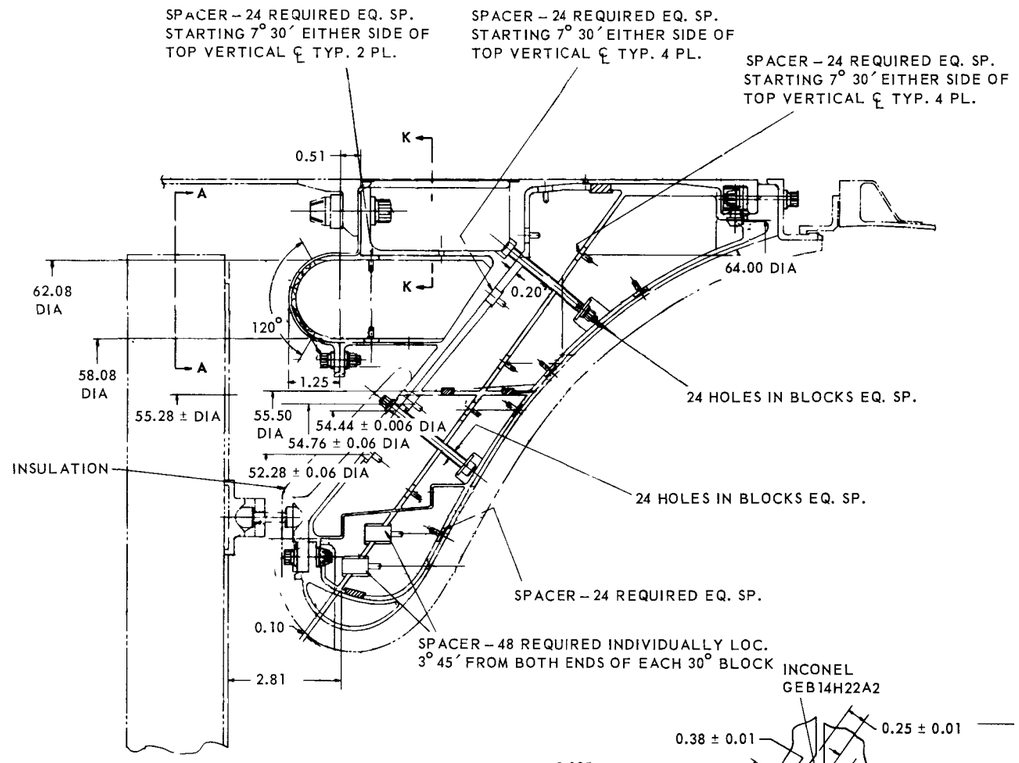

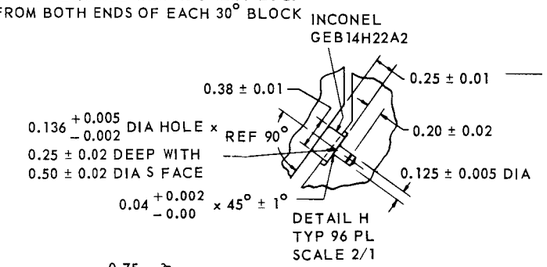

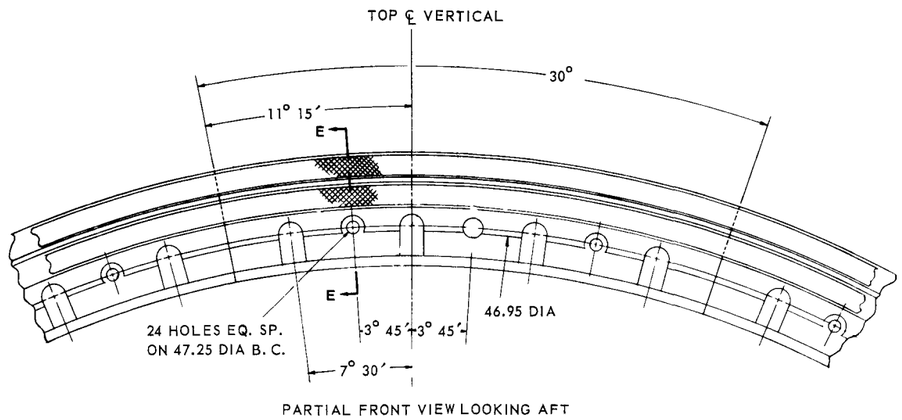

NOTE: LINEAR DIMENSIONS IN INCHES

Fig. 5.62 – Rear shield outer section (Dwg. 207R801 Rev. A Sh. 1)

ting flight condition resulted in the highest temperature levels, and, in general, the most severe aerothermal limitations. Where pressure levels or pressure differentials were a critical design factor, maximum acceleration to "q" limit, cold day was the critical condition. For long-term operational reliability, the cruise flight condition was the design point. In several instances, it was necessary to evaluate flight points which gave the most severe combination of temperature, pressure, and design life. Transient analyses were based on ambient conditions of 5000-foot altitude, hot-day, static.

The following transients were analyzed:

1. Chemical start
2. Nuclear start
3. Scram, followed by a rotor lock at 40 percent speed and 25 pounds per second of aftercooling-air
4. Scram, followed by engine coastdown with subsequent starter engagement.

Temperature differentials usually were the critical design parameter. Chemical start resulted in the most severe temperature differentials since it resulted in the most rapid change in compressor discharge-air temperature. Most of the transient analysis was concentrated on this mode of operation. Nuclear heating helped alleviate the temperature differentials, and analysis of the nuclear start showed lesser differentials. Temperature differentials resulting from shutdown transients also were less severe than those during the chemical start.

5.5.2.1 Central Island

Forward Central Island - The forward central island was cooled by air which had passed between the core liner and shaft tunnel before entering the rear-shield area. This cooling-air equaled 3.2 percent W_{a_2}. Of the 3.2 percent W_{a_2}, 1.17 percent W_{a_2} was extracted at two radial locations on the forward-island duct wall; 0.49 percent W_{a_2} at a 16.5 inch radius; and 0.68 percent W_{a_2} at a 22.8 inch radius. The 1.17 percent W_{a_2} was used to cool the insulation cover sheet. The remainder of the 3.2 percent W_{a_2} was used to cool the shielding material and subsequently was used for cooling the combustor liner prior to being mixed with the primary-air.

Thermal analysis showed that the maximum allowable surface temperature of 1000°F was exceeded in the forward island for all flight conditions wherein T_{a_3} exceeded 730°F. Raising the surface temperature limit from 1000° to 1100°F allowed acceptable performance during all flight and test conditions. All standard day flight and test conditions resulted in Be surface temperatures less than 1000°F.

Results of detailed aerothermal analyses are contained in reference 4, and include data pertaining to the insulation pads and the strut segments.

Aft Central Island - Figure 5.63 shows the steady-state temperature distribution through this subassembly during the emergency power setting condition. The maximum indicated temperature was 850°F; cooling was adequate. Detailed results of steady-state and transient analyses are contained in reference 4.

5.5.2.2 Outer Section

Bleed-speed air was introduced into this subassembly and distributed by two flow circuits, one containing 0.25 percent W_{a_2} and the other 0.85 percent W_{a_2} as shown in Figure 5.64. This figure also shows the temperature distribution in this subassembly during steady-state operation equivalent to the emergency power setting. The maximum Be temperature was 996°F; that in the stainless steel was 1206°F. Twice the nominal heating rate was used for these analyses.

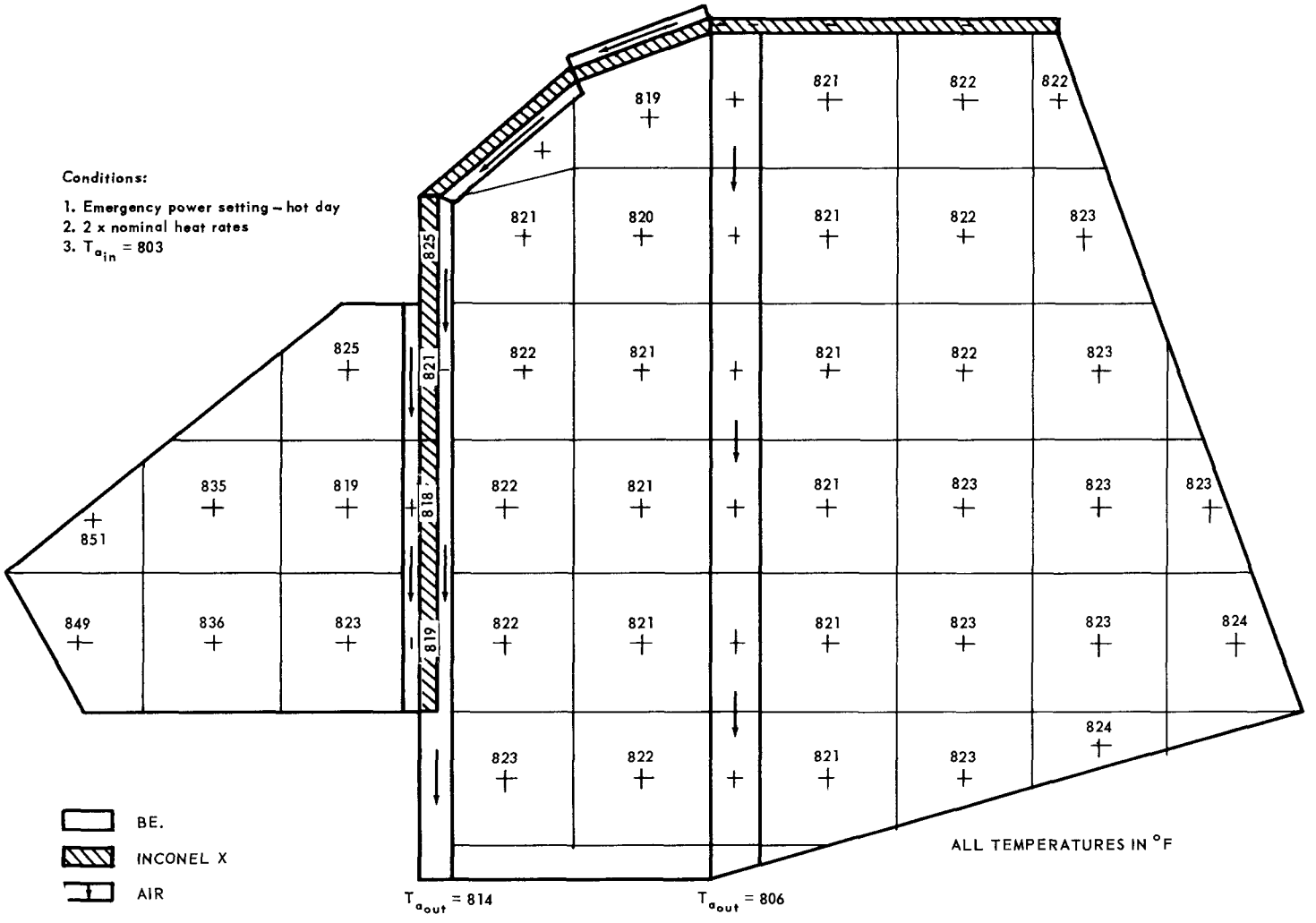

Fig. 5.63 – Temperature distribution through the aft central island

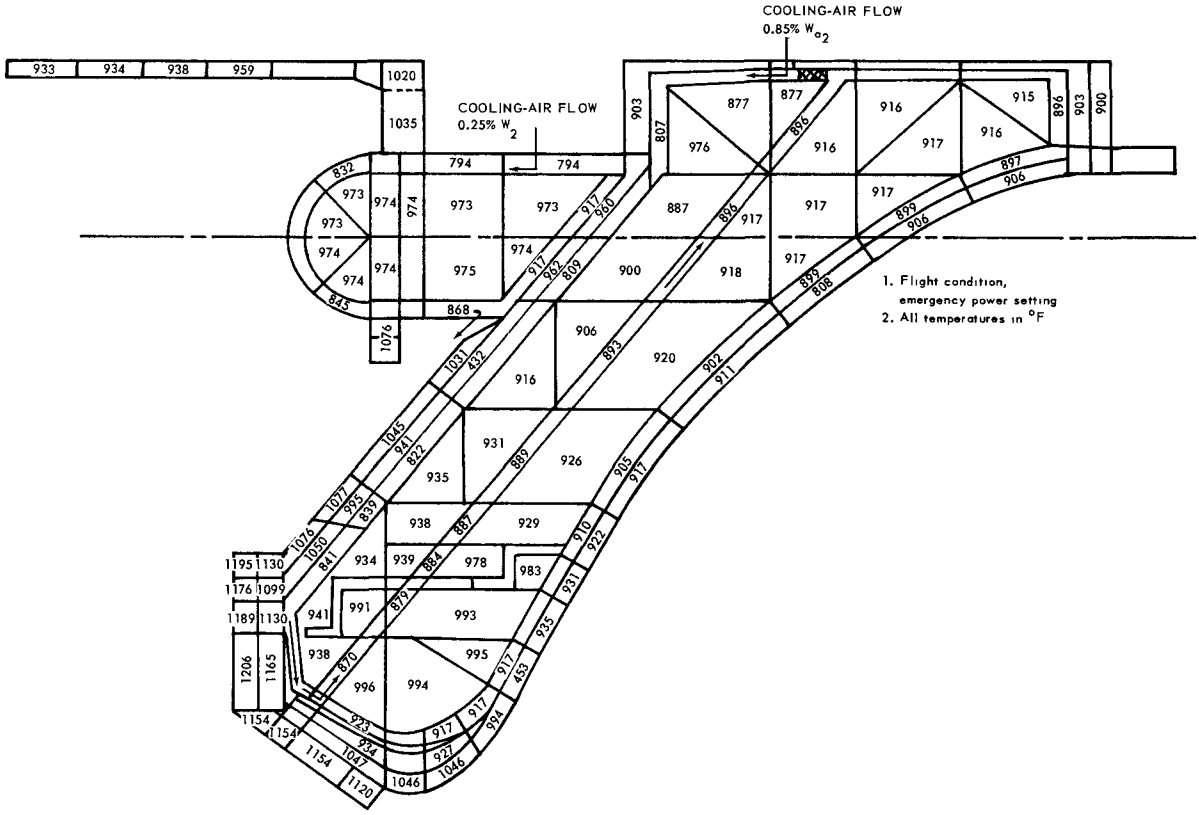

Fig. 5.64 – Aerothermal characteristics of rear shield outer section

Further steady-state and transient analysis data are contained in reference 4.

5.5.3 NUCLEAR

Secondary heating rates were calculated by the methods described in section 5.9. Detailed plots of the secondary heating-rate distribution through the rear shield are contained in reference 4.

5.5.4 STRESS AND WEIGHTS

Two distinct load paths were utilized for transmitting the rear-shield loads. Outer section pressure, inertial, and thermal loads, together with the core aft loads were transferred to the reactor structural shell through the mating flange of the outer section. The central island loads consisted of inertial, pressure, and internal thermal gradients, together with loads imposed due to temperature differentials between the mating flanges of the turbine forward frame and the central island. All loads on the aft central island were transmitted to the turbine forward frame.

5.5.4.1 Central Island

Forward Central Island - The size of most of the structural components in the forward island, especially the duct structural wall, was governed by allowable deflection and not by stress requirements. The maximum thermal gradient along the duct structural wall was less than $100^{\circ}F$ and the maximum temperature level was less than $1000^{\circ}F$. These conditions produced less than 10,000 psi stress in the wall.

The structural wall, however, was exposed to high pressure loads which made it susceptible to buckling. An equation for critical buckling pressure was developed using the strain energy due to deflection, and the potential energy of the pressure. The basic relationship used was

$$P_{cr} = \frac{U}{\Delta V}$$

where P_{cr} = critical buckling pressure
U = strain energy associated with deflection
ΔV = volume between deflected position and initial position.

The bending energy in the circumferential direction was neglected and radial bending only was considered. It was assumed that the buckling pattern in the circumferential direction was an ellipse, and the volumetric change of the deflected surface was determined by integrating the difference in area between an ellipse and a circle.

The following equation was developed:

$$P_{cr} = \left[\frac{\pi^3 E}{36(1-\nu^2)\sin^3 p}\right] \quad x \quad \left[\frac{t^3}{S^3}\left(\frac{4R_i}{S} + 2\right)\right]$$

where P_{cr} = critical buckling pressure
E = modulus of elasticity
t = thickness of the structural wall
S = total length along the mean generatrix
B = semi-apex angle of the (cone) structural wall
R_i = inside radius of the structural wall.

The major mechanical loads on the supporting rods in the strut-segment subassembly were the inertial-load and the thermal-load peaks during startup before they settled down to the steady-state value. The thermal load decreased rapidly during shutdown, reached zero, and then increased to a new value. Thermal stresses resulted from three sources: (1) temperature difference between the tie rod and the beryllium shielding (2) thermal

gradients within the tie rod during startup or shutdown (3) thermal gradients between the turbine frame strut and the tie rod. Detailed results of this stress analysis are contained in reference 4 and 26.

Aft Central Island - Two structural concepts were studied for the support of the shielding material. One was the cylinder-cone support concept, and the other was the bolted support concept. Details of comparative stress analysis of the two concepts are presented in reference 4 and 26. The design problems inherent in each concept had not been fully resolved at the time of program termination.

5.5.4.2 Outer Section

The structural elements were made up of a main support structure and a secondary structure. The main support structure consisted of a flanged cone with the flange at its aft end at the outer radius. This flange was an integral part of a gussetted flange assembly called the transition ring. The transition ring consisted of a flanged cylinder. Its forward flange mated with the aft flange of the reactor structural shell. Its aft flange was an integral part of the cone and an outer cylinder. A series of axial gussets were arranged equidistant circumferentially on the short cylinder of the transition ring. A flanged inner ring was located on the inside radius of the cone. The secondary structure consisted of a small torus flanged to the inner ring of the cone at its front end. Connected to the aft end of the torus was a duct wall with a flanged ring at its outer end. The outer cylinder was attached to the transition ring at its front end, mated with the aft end of the duct wall at its aft end. Another torus was located forward of the main support cone and consisted of a semicircular arc and a cylinder with a ring section between the two. Both the main support structure and the secondary structure were made of Inconel X.

Detailed results of the stress analysis are presented in references 4 and 26. The design was not structurally feasible for all operating conditions and required either (1) a reduction in core axial loads, or (2) decreased thermal gradients in the structure and decreased temperature differentials between the shielding and the tie bolts. The required design changes were of a minor nature and were being resolved.

5.5.4.3 Weights

The weight of the rear shield, based on drawings completed as a part of contract termination, was 4405 pounds, distributed as shown in Table 5.6. The total weight of the structural materials, 1535 pounds, could have varied ±75 pounds during final design.

5.6 SIDE SHIELD COMPONENT DESIGN DATA

5.6.1 MECHANICAL

An isometric cutaway view of the side shield without cheeks was shown in Figure 5.9. Over-all control dimensions were shown in Figure 5.4. The assembly consisted of annular sectors of LiH_x shielding cast in 19-9DL stainless steel cans. These sectors were called segments. Shielding material was removed to form flattened horizontal sides and to permit spacing individual engines on an 83.00-inch centerline separation distance. During test operation of the XNJ140E-1 engine, side-shield cheeks and actuator shielding pads were added to the assembled engine to complete the external shielding. The design layout is shown in Figures 5.65a and 5.65b. The assembly was an annular ring with flattened sides on the horizontal centerline, an outer diameter of 108.8 inches, and a major thickness of 17.0 inches. The cylindrical contour was completed by adding the shield cheeks, Figure 5.66.

TABLE 5.6

WEIGHT BREAKDOWN OF REAR SHIELD

Part	Weight, lb
Structure	
Outer section	555
Forward central island	415
Strut segments	35
Aft central island	120
Outer section insulation	170
Central island insulation	145
Seals	95
Total	1,535
Be Shielding Material	
Outer section	485
Forward central island	660
Strut segments	620
Aft central island	670
Total	2,435
Stainless Steel Shielding Material	
Forward central island	70
Strut segments	120
Total	190
Inconel X Shielding Material	
Forward central island	195
Total	195
Total Rear Shield	4,355
Data Instrumentation[a]	50

[a]Estimated.

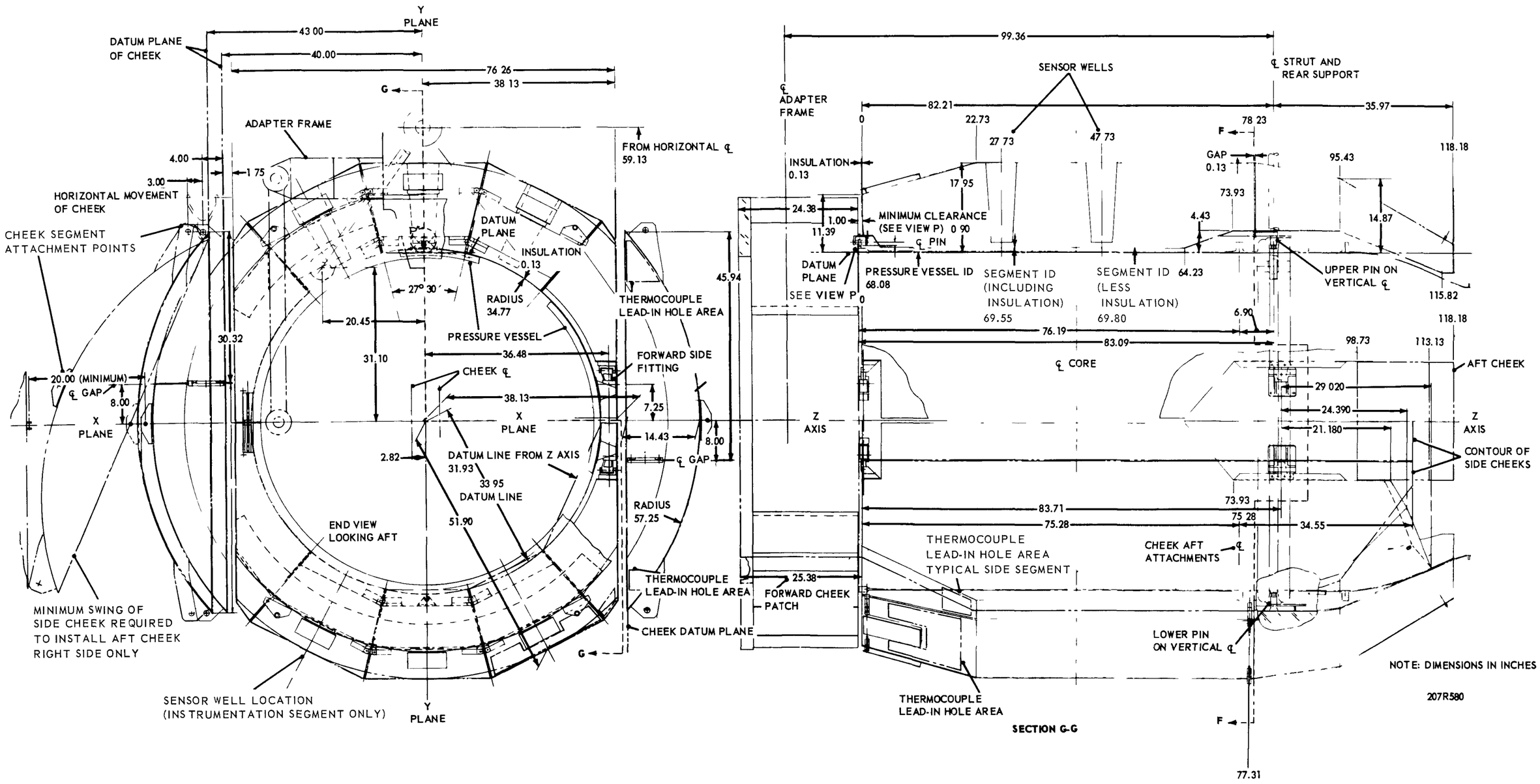

Fig. 5.65a – XNJ140E-1 side shield layout (Dwg. 207R580)

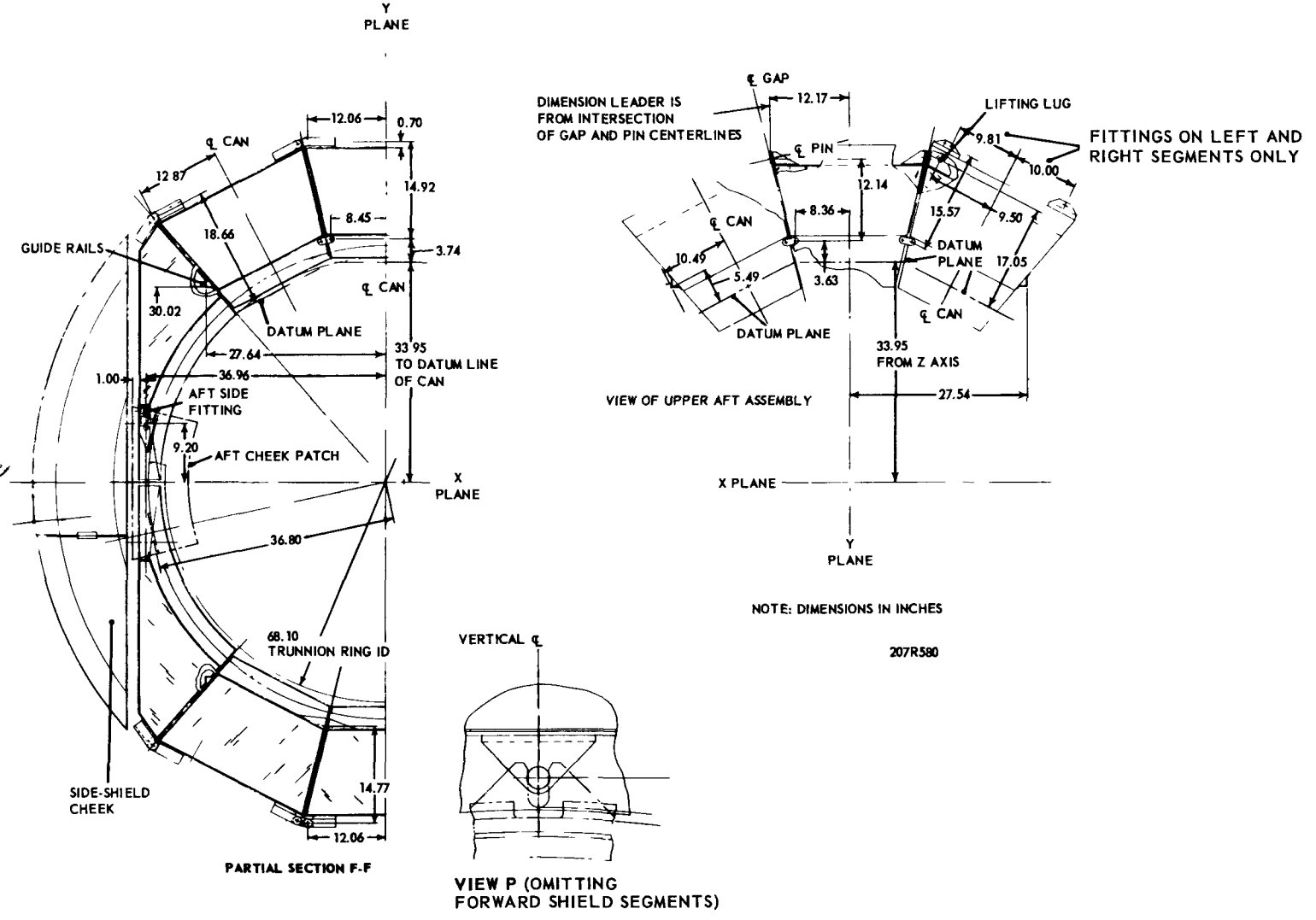

Fig. 5.65b – XNJ140E-1 side shield layout (Dwg. 207R580)

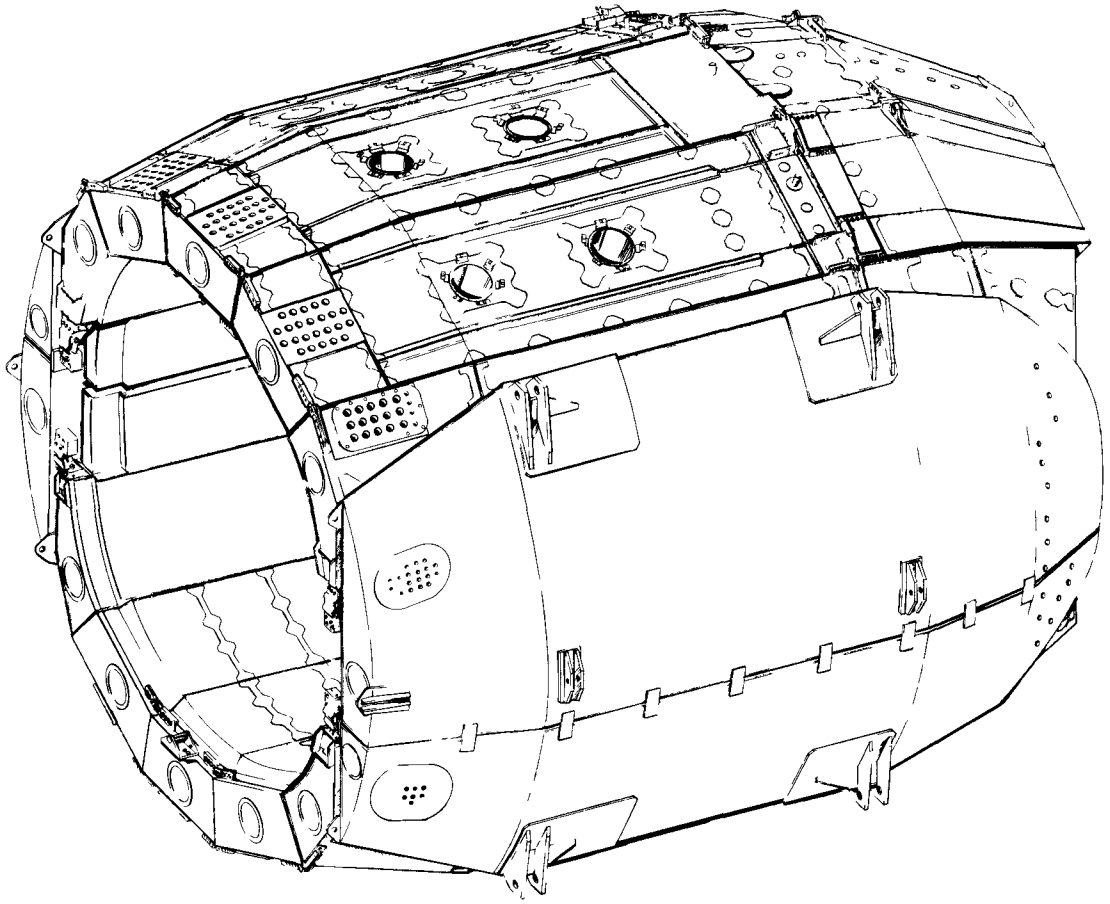

Fig. 5.66 – XNJ140E-1 side shield and cheeks (Dwg. DI568 Rev. A)

A cutaway isometric view of a typical lower-half side-shield segment was shown in Figure 5.11. It consisted of a sheet-metal can supported internally by a stringer-frame structure and contained the cooling-tube assembly. The sheet-metal can was closed by resistance welds along the exposed outer flanges and a fusion-seal weld at the outer edge. Each individual segment had provisions for an inlet cooling-air plenum at the forward end.

The assembly was built up of upper and lower halves. The two halves were attached to the engine at the forward flange of the pressure vessel and at the aft trunnion ring on the turbine front frame, as shown in Figure 5.67. Vertical and side loads were reacted at the forward attachments. Fore, aft, and side loads were reacted at the vertical centerline of the aft attachment points. Vertical, axial, and side loads were reacted at the horizontal aft attachment points. Side-shield inertial loads were carried by the cans, which acted as thin-skinned semi-monocoque structure around the shield-material castings.

The three inner segments of both the top and bottom halves were interconnected at frame points in the forward and aft sections to form a complete structure as shown in Figure 5.68. Keys at the plane of separation between the forward and aft sections of the upper-half segments provided assembly and air-cooling-channel alignment. The side segments that completed each half-assembly were hinged from the assembly of the upper- and lower-half inner segments, Figure 5.69. For removal, each half-section of the shield was freed by disengaging four pins. Since the aft attachment of the engine to the adapter frame pierced the upper half of the side shield, the aft section of the three inner segments

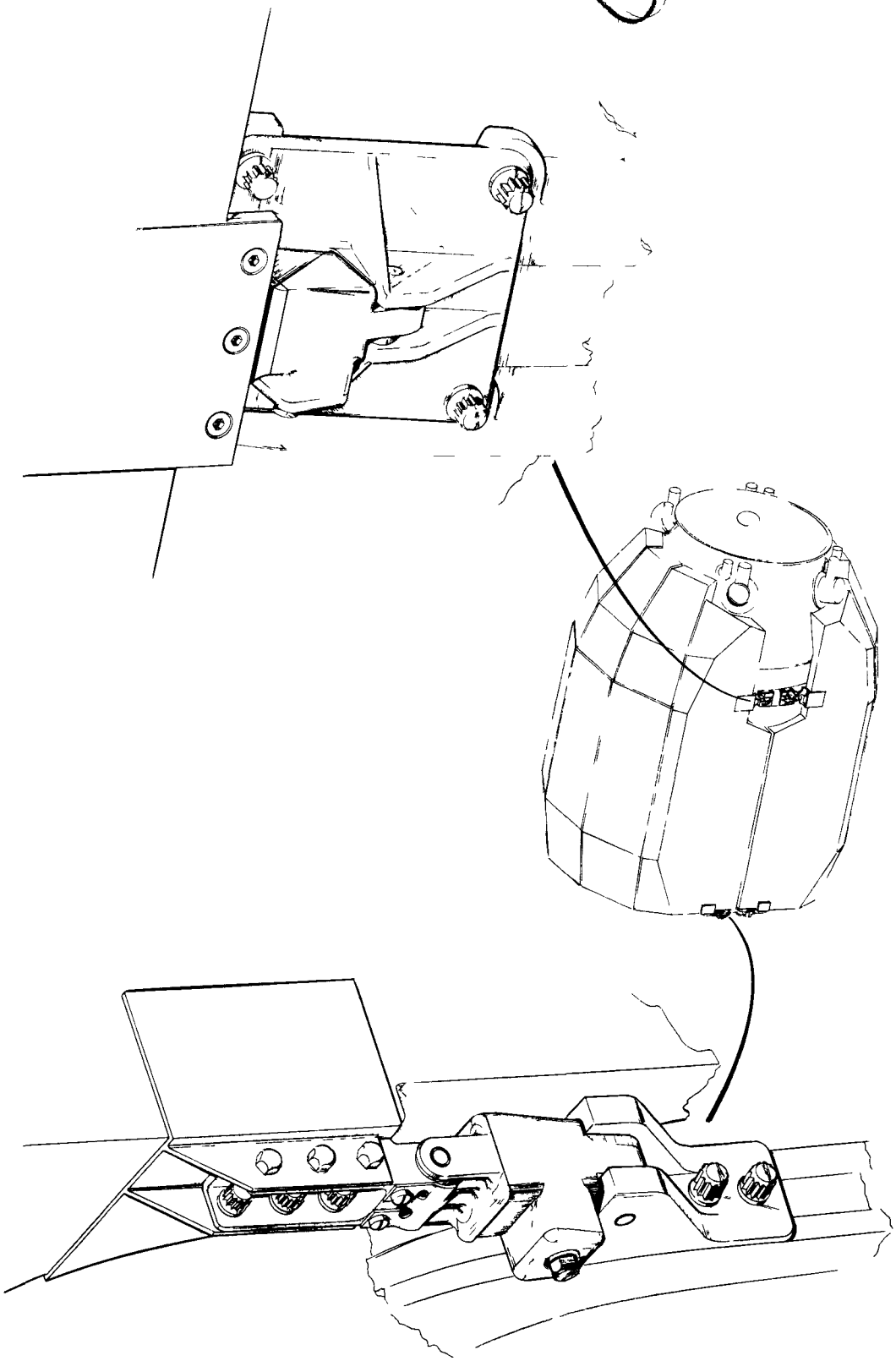

Fig. 5.67 – Attachment points of XNJ140E-1 side shield upper and lower halves

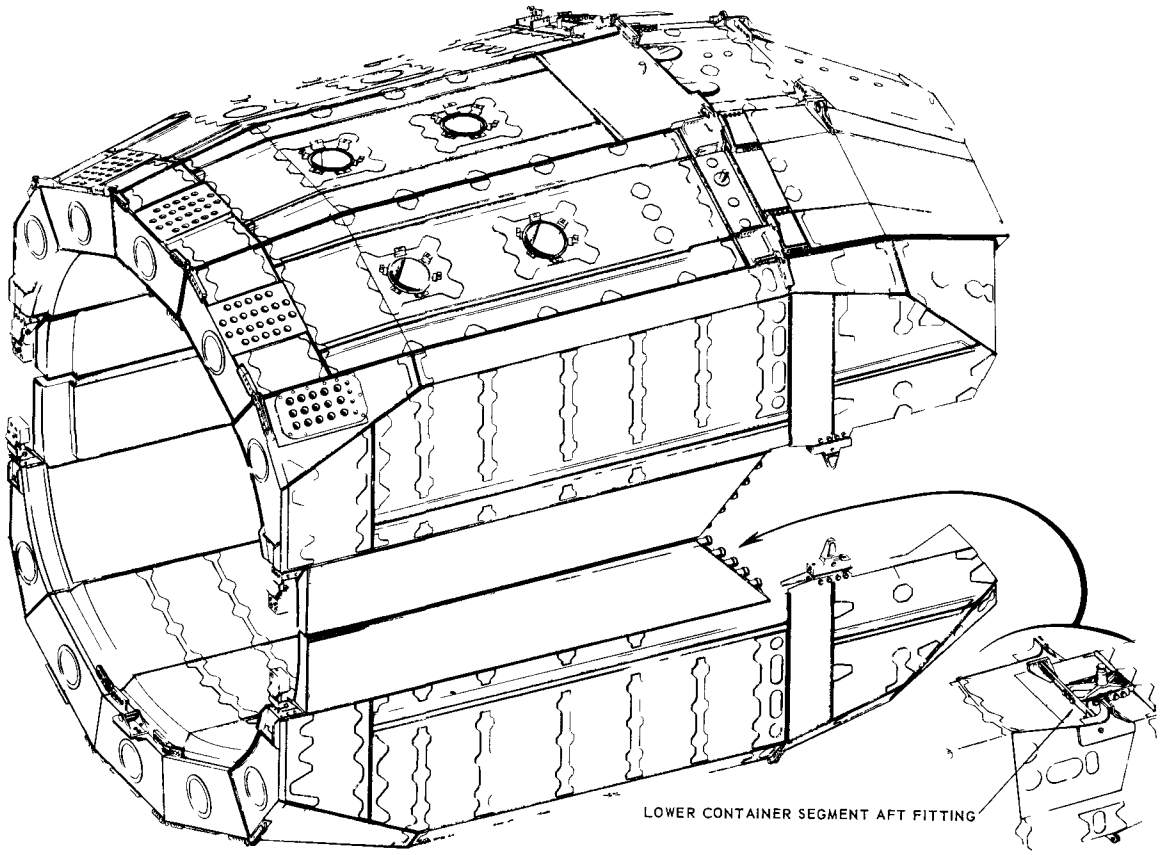

Fig. 5.68 – Interconnection of side shield segments (Dwg. DI567)

of the top half were separated from the forward sections. As shown in Figure 5.69, the aft sections then could be slid back from the forward sections for installation or removal of the upper half of the side-shield assembly.

Two sensor wells, shown in Figure 5.68, were located in each of the forward segments of the upper half. These wells contained nuclear sensors for the control system during engine test operations.

The methods of fabricating the segments and assembling them to form the side shield is illustrated by the sequence of drawings shown in Figures 5.70 through 5.74. Figure 5.70 is an exploded view of the various segments comprising the upper half of the side shield. The forward center segment, including the sensor wells, is shown in Figure 5.71. Figure 5.72 shows the aft center segment. The A frame support at the aft end of the engine passed through the grooves shown in the front face of this segment. Fabrication details of the forward center segment, including cooling tubes, are shown in Figure 5.73. Fabrication details of the left upper side segment are shown in Figure 5.74. Fabrication details of a typical segment of the lower half were shown in Figure 5.11.

Although an effort was made to keep symmetrically located segments identical, clearances needed for instrumentation disconnects, fuel lines, and other items required various local cutouts and indentations. The upper-half side segments were designed for all flight maneuver loads. When the upper segments were used as lower-half side segments, as a design expediency, they were not capable of taking flight loads. However, no design modifications were made since the XNJ140E-1 engine was to be used as a ground test engine.

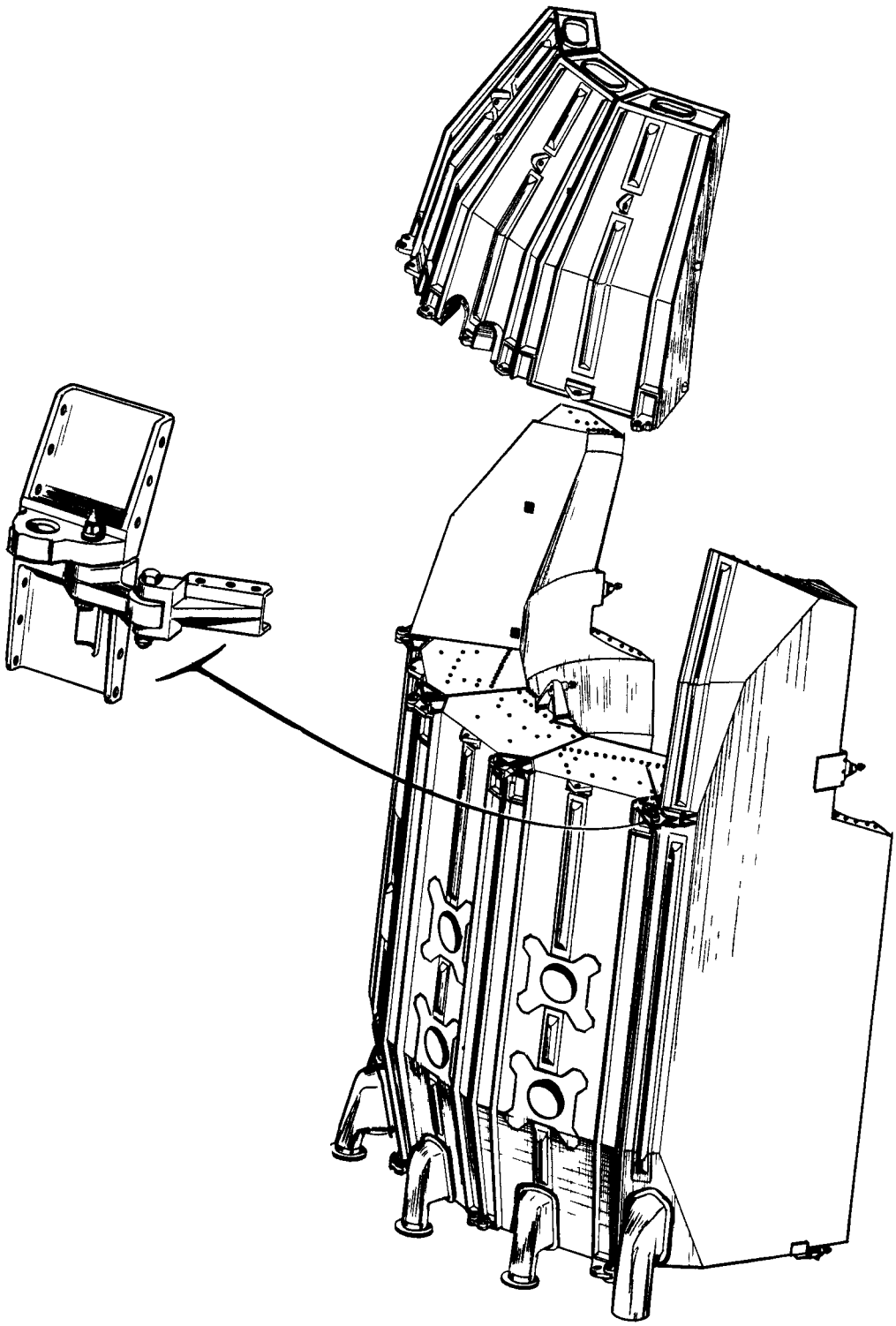

Fig. 5.69 – Hinged attachment of side segments

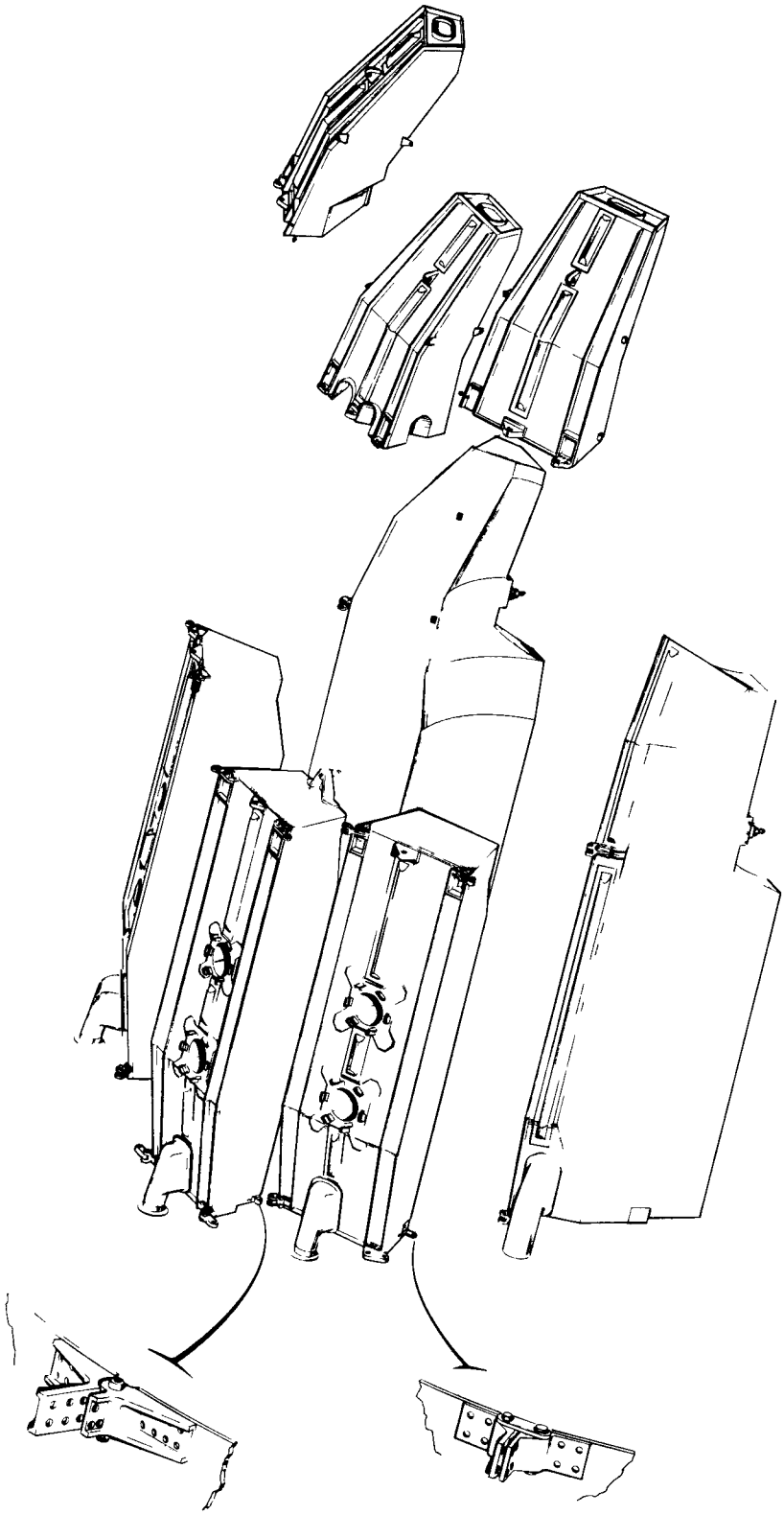

Fig. 5.70 – Upper half of side shield, exploded view (Dwg. DI435)

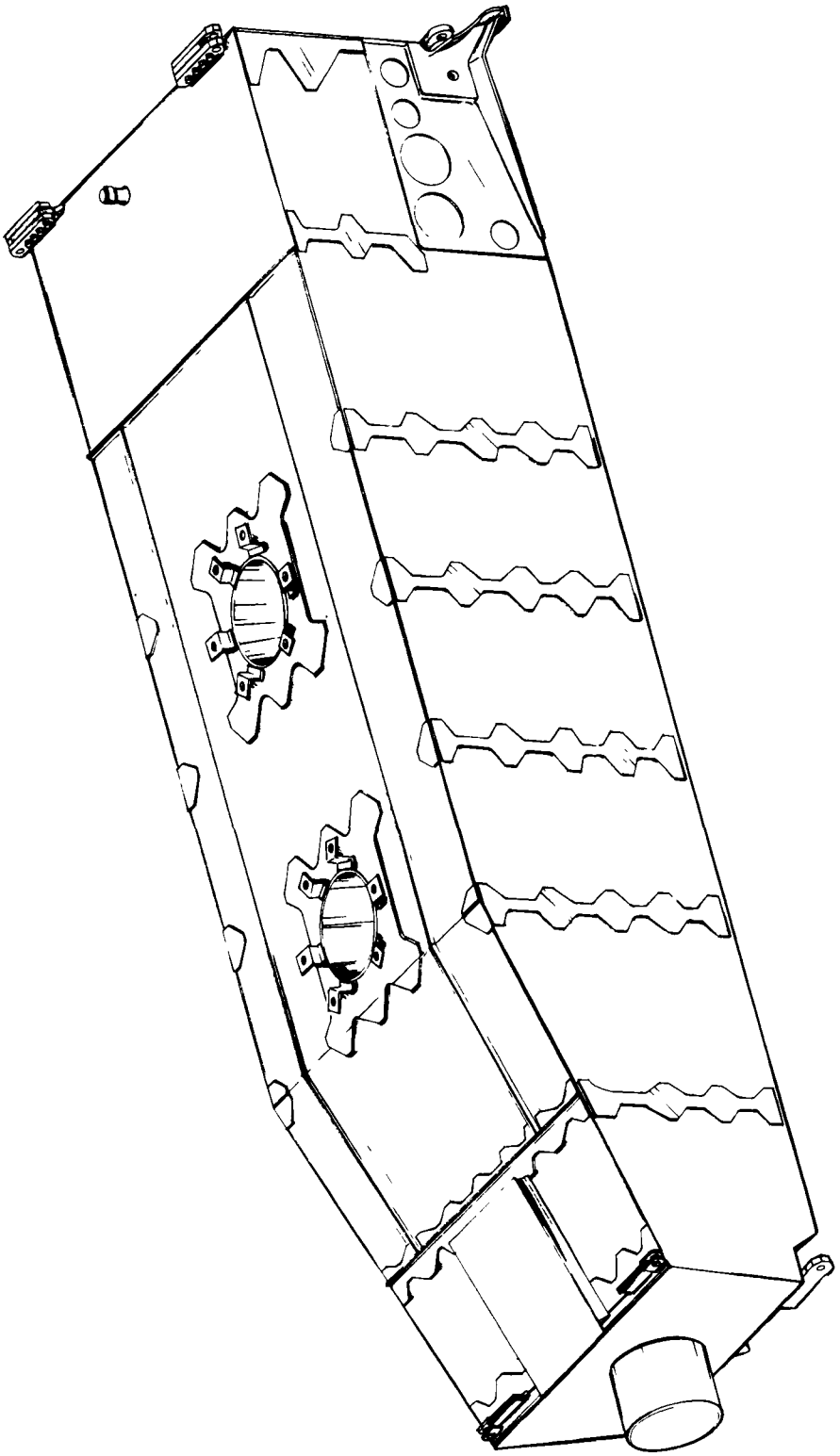

Fig. 5.71 – Forward center segment, upper half (Dwg. DI561)

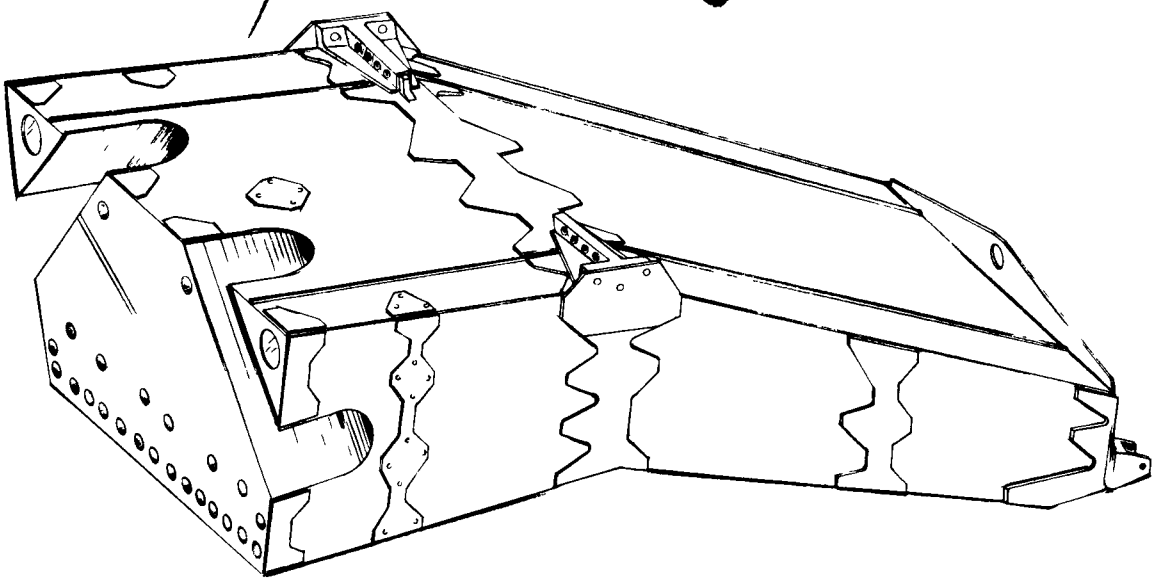

Fig. 5.72 – Aft center segment, upper half (Dwg. DI562)

Semi-monocoque construction was used in the design of all cans. A typical can consisted of a 0.03-inch-thick skin reinforced with stringers and frames. Stringers were spaced approximately 4 inches apart and the frames were spaced approximately 10 inches apart. The stringers were 0.04 inch thick, and the frames were 0.04 inch and 0.05 inch thick. The forward bulkheads of the cans served as the forward support structure of the side shield when the segments were interconnected. The aft support structure for the shield was formed by the aft bulkhead of the top three cans and internal truss frames in the side and lower segments.

The cooling tubes contained fins in areas of high heat generation to insure good heat transfer between the tubes and the shielding material. The can was leak-tight to prevent moisture from getting into contact with the LiH_x. A one-way vent system was provided to relieve internal pressure due to gas generation and changes in the ambient pressure.

The LiH_x was cast into prefabricated cans rather than being used in the form of machined blocks. Past experience (XMA-1A power plant design) showed that severe heat transfer problems existed when using machined blocks, and that costly fabrication control was required. In the casting process, the cooling tubes reduced the heat transfer problem and eliminated the costly machining operations. However, there were limitations relative to the practical size of LiH_x castings. The side shield was divided into segments which reflected these limits.

The method of interconnecting the segments to form the assembly and attaching that assembly to the engine eliminated serious tolerance stack-up problems and allowed for differential thermal expansion between parts by providing gaps between the segments which varied from 0.25 inch to 0.50 inch. Rather than step the cans, and thereby complicate fabrication, it was planned to fill the gaps with insulation serving both as shielding material and as thermal barriers isolating one segment from another.

5.6.1.1 Shield Cheeks

The shield-cheek assembly, shown in Figures 5.75 and 5.76, simulated the shielding required to complete the side-shield outer contour at the flattened horizontal sides. These assemblies were supported from the FET transport vehicle, and simulated flight-type

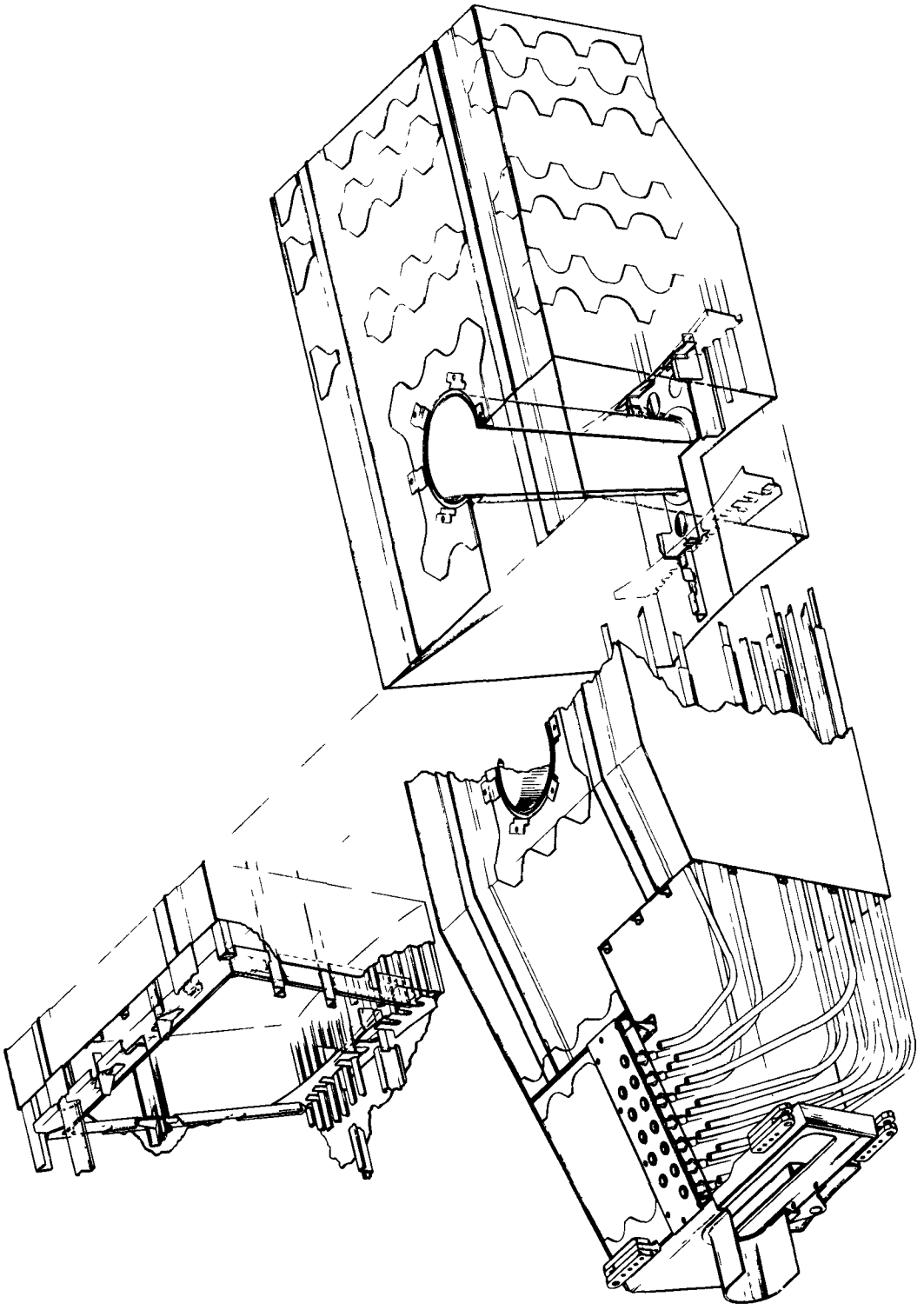

Fig. 5.73 – Fabrication details of forward center segment (Dwg. DI467)

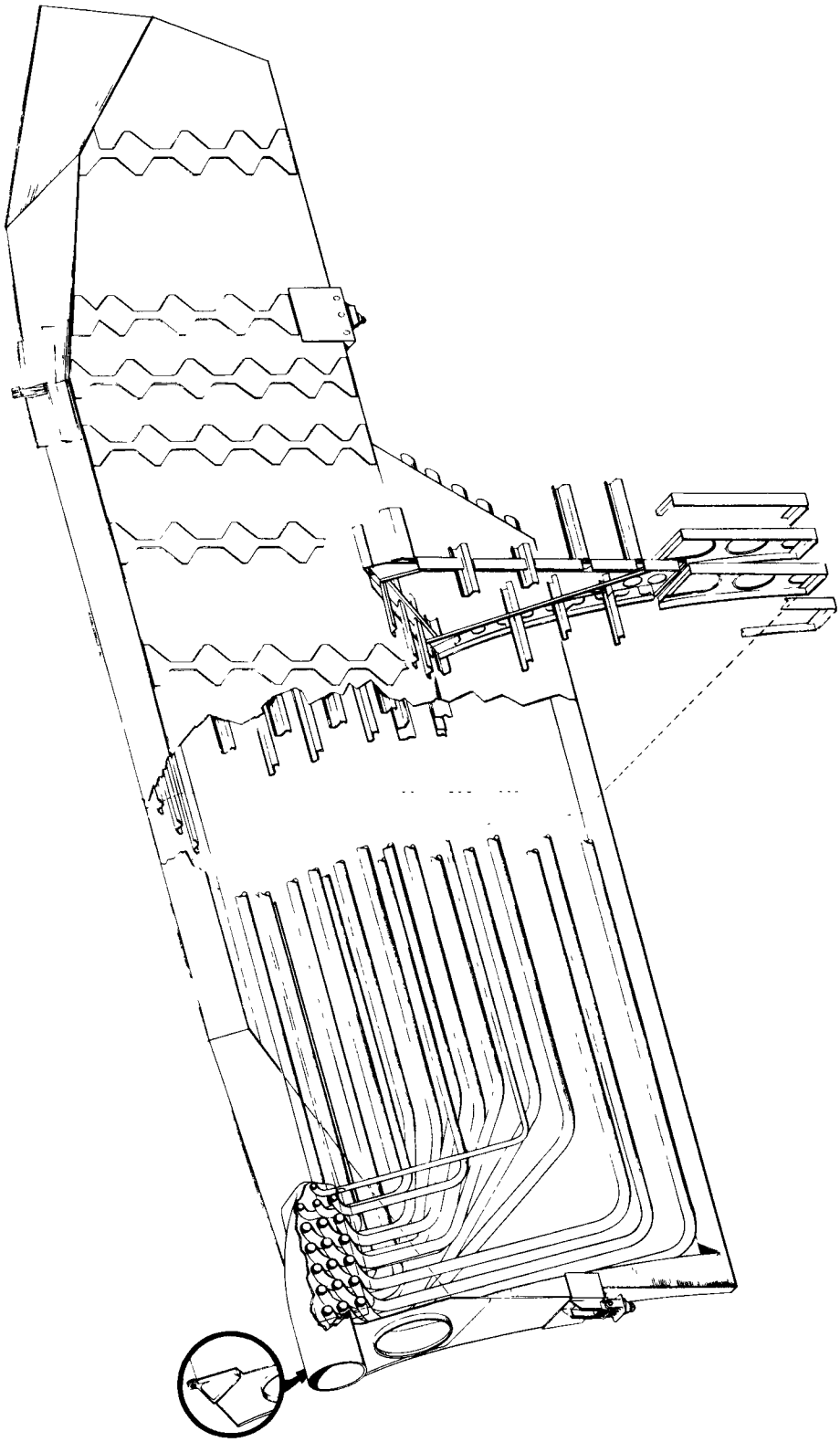

Fig. 5.74 – Fabrication details of left upper side segment (Dwg. DI468)

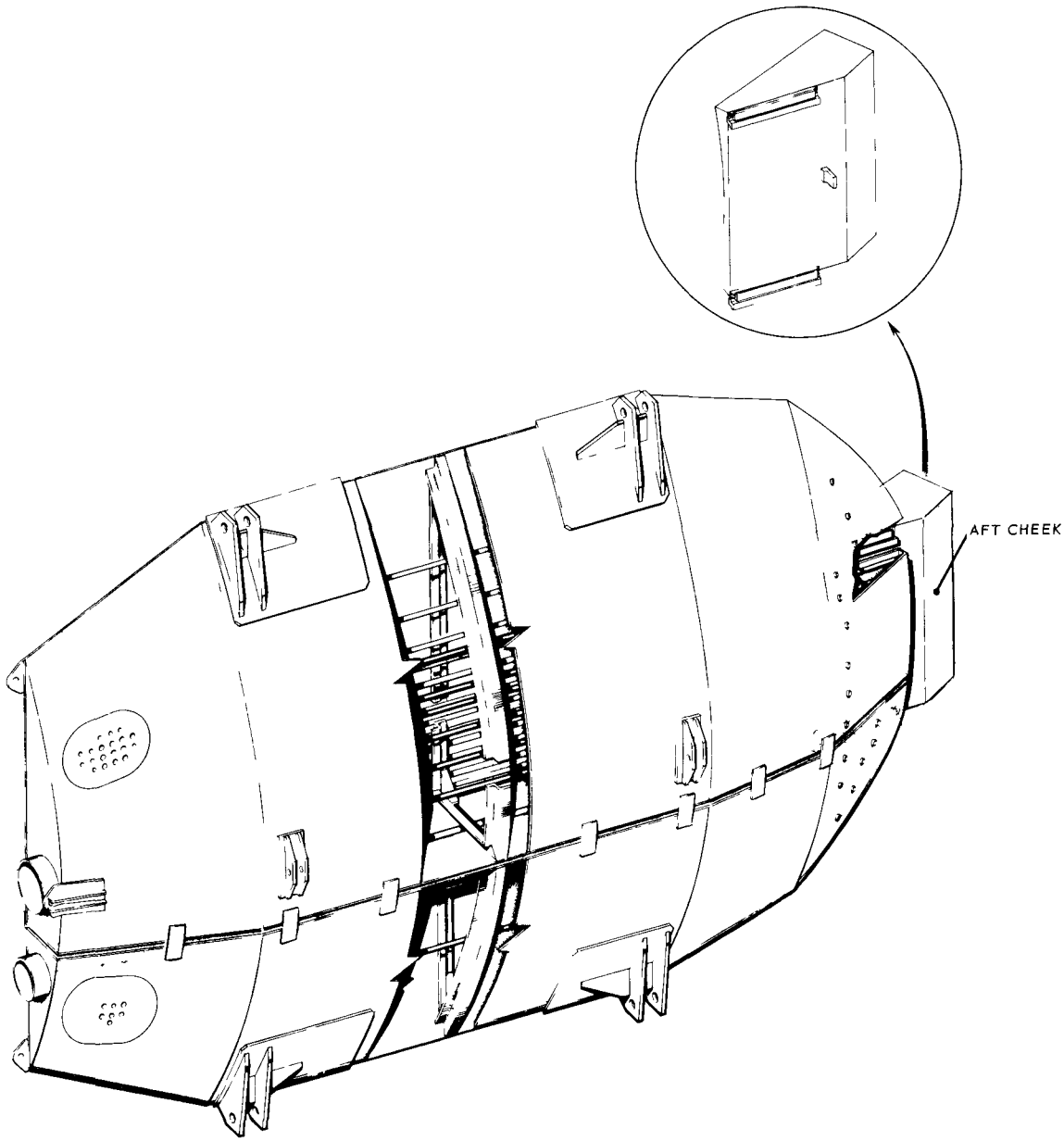

Fig. 5.75 – Schematic view of shield cheek assembly (Dwg. DI472)

CONFIDENTIAL

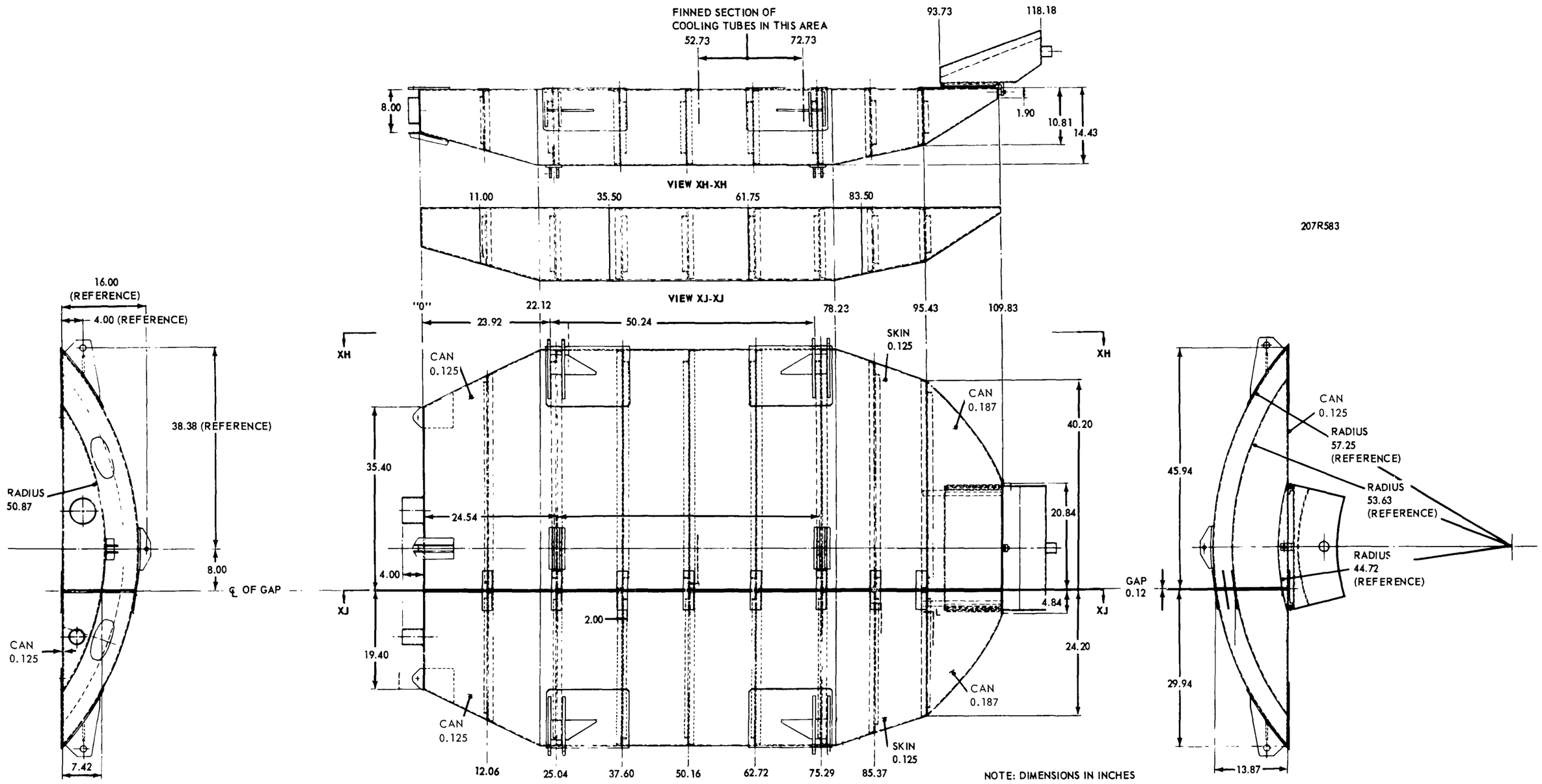

Fig. 5.76 – Shield check assembly for XNJ140E-1 side shield (Dwg. 207R583)

CONFIDENTIAL

assemblies that would be mounted on the airframe structure. For the XNJ140E-1 shield, the cheek assemblies were constructed with relatively thick (0.125 inch and 0.187 inch) walls to eliminate the need for costly casting fixtures. Since these cheeks were strictly test-stand hardware, they were not designed as light-weight flight-type structure.

5.6.1.2 Actuator Shielding Pads

Shielding pads mounted in the forward side-shield area, around the control rod actuators, would have been supported from the airframe structure in flight-type versions of the XNJ140E engine. Simulated shielding pads, shown in Figure 5.77, were suspended from the transport vehicle in the XNJ140E-1 FET arrangement. To facilitate in-place actuator maintenance in the FET, these pads could be rolled forward on tracks built into the transport vehicle, and direct access to the actuators was possible.

Since these pads were designed for use solely in the ACT program, they were not flight-type structure.

5.6.2 AEROTHERMAL

Flight-type side shields were cooled by ram-air during flight. Although the XNJ140E-1 side shield was cooled by facility-supplied air, the aerothermal design was based on flight parameters.

The following terminology was employed to identify specific segments, based on their representative cross sections:

1. 27.5-degree segment
2. Side segment
3. Cheek segment.

Figure 5.78 illustrates the nomenclature and arrangement of segments.

Cooling-tube patterns were based on the cooling requirements at the most aerothermally critical flight point, the emergency power setting: hot day, 5000-feet altitude, Mach = 0.43, Q_{core} = 109 megawatts. Since cooling was accomplished by ram-pumped air, the flight condition having low flight speed, high inlet-air temperature, and high core power was the limiting case for steady-state operation. Operation at the cruise condition: standard day, 35,000-feet altitude, Mach = 0.85, Q_{core} = 50.5 megawatts, was next in importance. Cooling was adequate at all other flight points.

Ram-air was brought on board through ram-air scoops and was ducted to the individual segments. Each segment had a forward plenum to decelerate the flow and divide the flow among the cooling tubes. After passing the length of the segment, the air was collected in a rear plenum and disposed of in a favorable aerodynamic manner. For ACT operation, the XNJ140E-1 aft plenums were omitted and the air was dumped directly from the tubes.

A side shield designed to perform satisfactorily (aerothermally) in accordance with the design data defined by the emergency power setting, would have operated at considerably lower temperatures at other points in the flight profile unless the flow of cooling-air were controlled as a function of ambient conditions. The reasons were (1) increased aircraft speed and greater ram pressure caused increased cooling-air flow, (2) lower ram-air temperature resulted in more efficient cooling, and (3) lower steady-state nuclear power levels resulted in lower secondary heat deposition. The generalized results of "off-design-point" operation are compared to "on-design-point" operation in Table 5.7 for the uncontrolled flow of ram-air.

Cooling-tube patterns for the 27.5-degree segments and the side segments were established neglecting the effects of local cutouts. The cutouts were removals of shield-

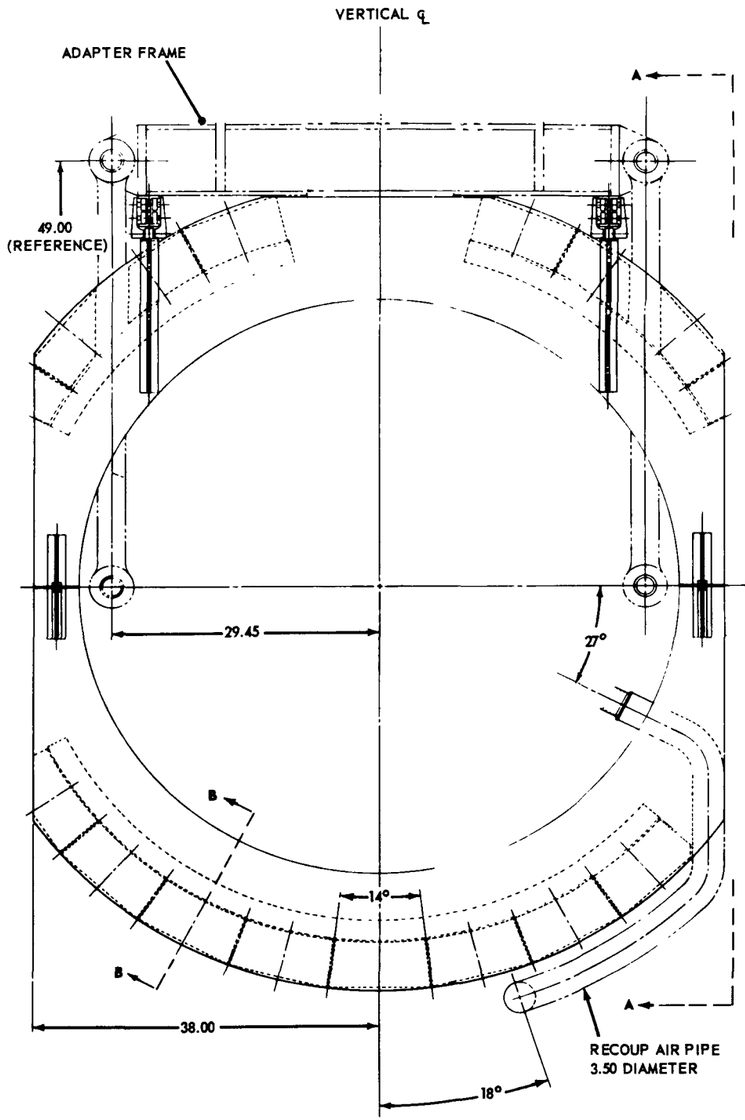

VIEW LOOKING AFT

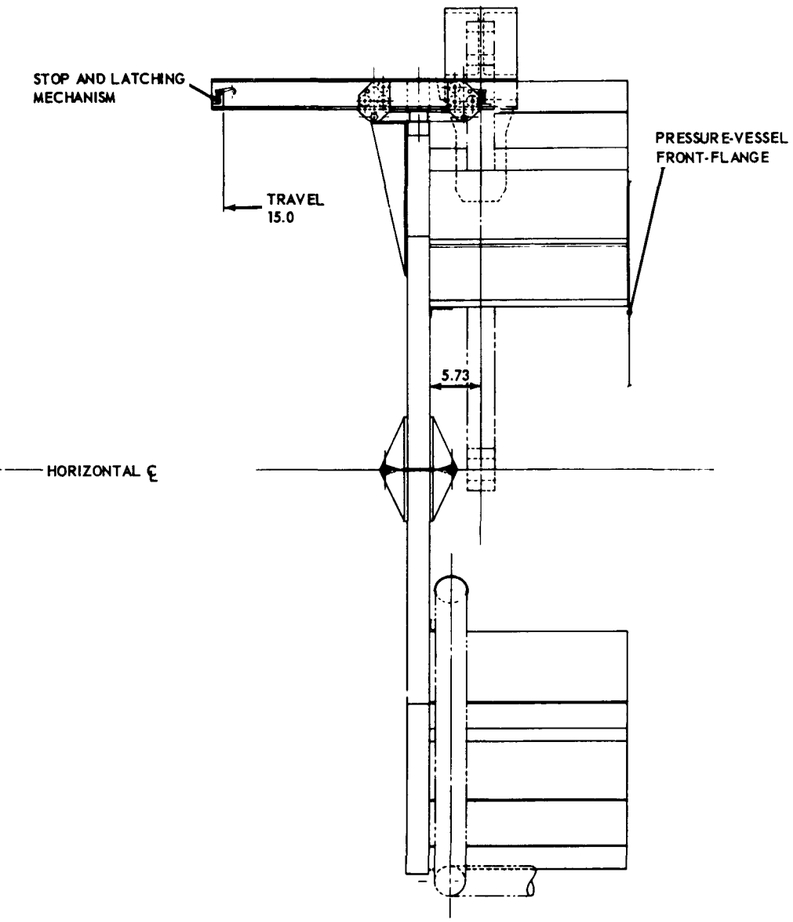

VIEW A-A

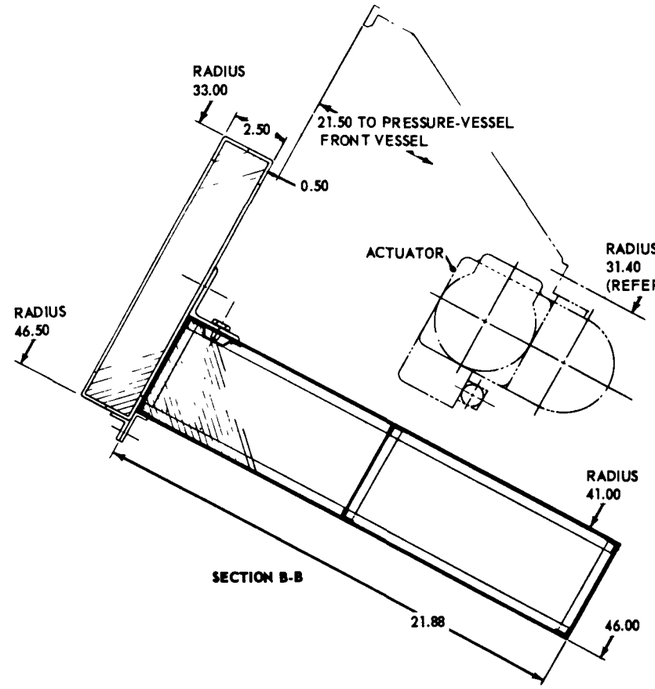

SECTION B-B

NOTE: DIMENSIONS IN INCHES 207R581

Fig. 5.77 – Actuator shield pads, XNJ140E-1 side shield (Dwg. 207R581)

NOTE: Cross section typical at the core midplane

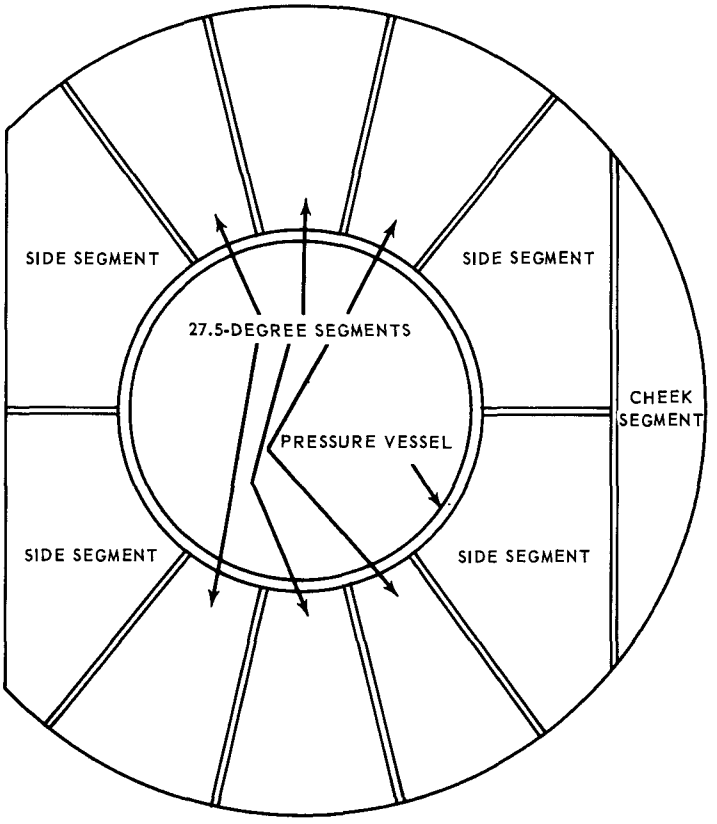

Fig. 5.78 – Side shield segment nomenclature and arrangement

TABLE 5.7

GENERALIZED SIDE SHIELD AEROTHERMAL DESIGN DATA

	Climb To Station	Cruise	Maneuver	Two-Engine Operation	Emergency[a] Power Setting
Altitude, ft	20,000	35,000	35,000	10,000	5,000
Type of day	Std	Std	Std	Std	Hot
Mach No.	0.7	0.8	0.8	0.6	0.43
$\Delta P_t / P_{t_{in}}$[b]	0.161	0.213	0.213	0.122	0.080
$W_{ram\text{-}air}$, lb/sec	1.7	1.05	1.05	2.2	1.72
$T_{t_{in}}$, °F	31	-16	-16	58	103
$T_{t_{out}}$, °F	348	316	335	372	533
$T_{LiH_{x_{max}}}$, °F[c]	621	574	610	650	911
Q_{core}, mw	78.1	50.5	53.6	98.5	109

[a]Design point.
[b]Pressure drop of cooling-air divided by inlet total pressure.
[c]These temperatures are approximate.

ing material to simplify the mechanical arrangement and remote handling procedures. Their effect was more pronounced in local temperature gradients than in over-all heat removal.

5.6.2.1 27.5-Degree Segments

A model of a typical 27.5-degree segment was employed that was representative of all 27.5-degree segments. The lower-center 27.5-degree segment was used as the model.

Steady-State Analysis - The emergency power setting flight condition was the design point. Figure 5.79 shows the cooling-tube pattern at the core midplane and Figure 5.80 defines the nodal network used for the aerothermal analysis. The cooling-tube diameters and cooling-air flow are shown in Table 5.8.

The temperatures of LiH_x, cooling tube walls, and cooling-air at locations near the inner radius of the segment are shown in Figure 5.81. The respective nodal positions are identified on the figure. Comparable data for LiH_x and cooling-air temperatures at nodes near the outer wall are shown in Figure 5.82. The maximum temperature of the LiH_x surrounding cooling tubes occurred at node Nos. 27, 33, and 37 and was $850^{\circ}F$.

The temperature profile through the segment at a plane 42.00 inches aft of the core midplane is shown in Figure 5.83. This plane represented the maximum temperature in the side shield. Temperature profiles through other planes are shown in reference 4. The maximum temperature was $900^{\circ}F$ and was considerably below the $1050^{\circ}F$ allotted in the design requirements. The cooling-tube pattern was established on the basis of initial calculations which neglected the effect of finning on the cooling tube surfaces. Subsequent analytical studies and experimental data[27, 28, 29] showed that the LiH_x thermal conductivity was considerably increased by the use of finned surfaces. Temperature profiles then were recalculated, using the effective thermal conductivity shown in Figure 5.84, and significantly lower temperature levels and gradients resulted.

Stress Within Cans and Structural Members - Metallic structural members were cooled by the same cooling tubes that cooled the LiH_x. Removal of heat from these metallic parts

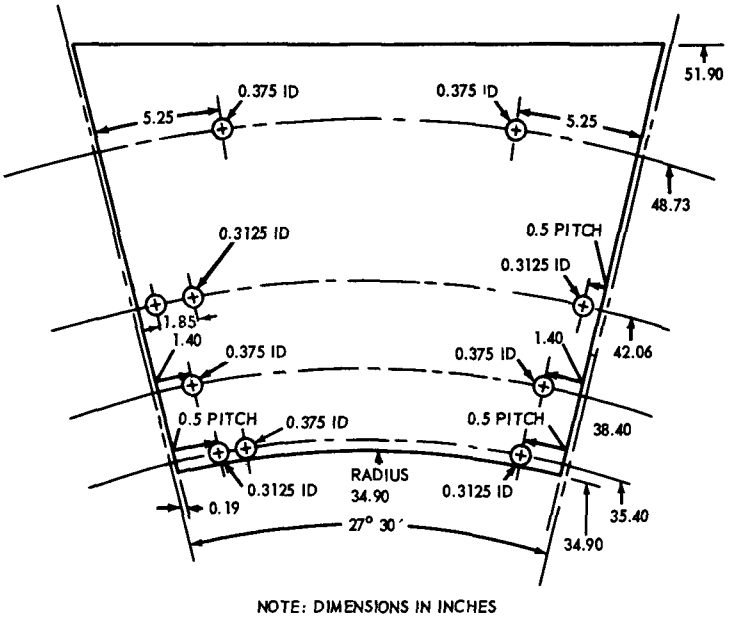

NOTE: DIMENSIONS IN INCHES

Fig. 5.79 – Cooling tube pattern for XNJ140E-1 27.5 degree side-shield segments at the reactor core midplane

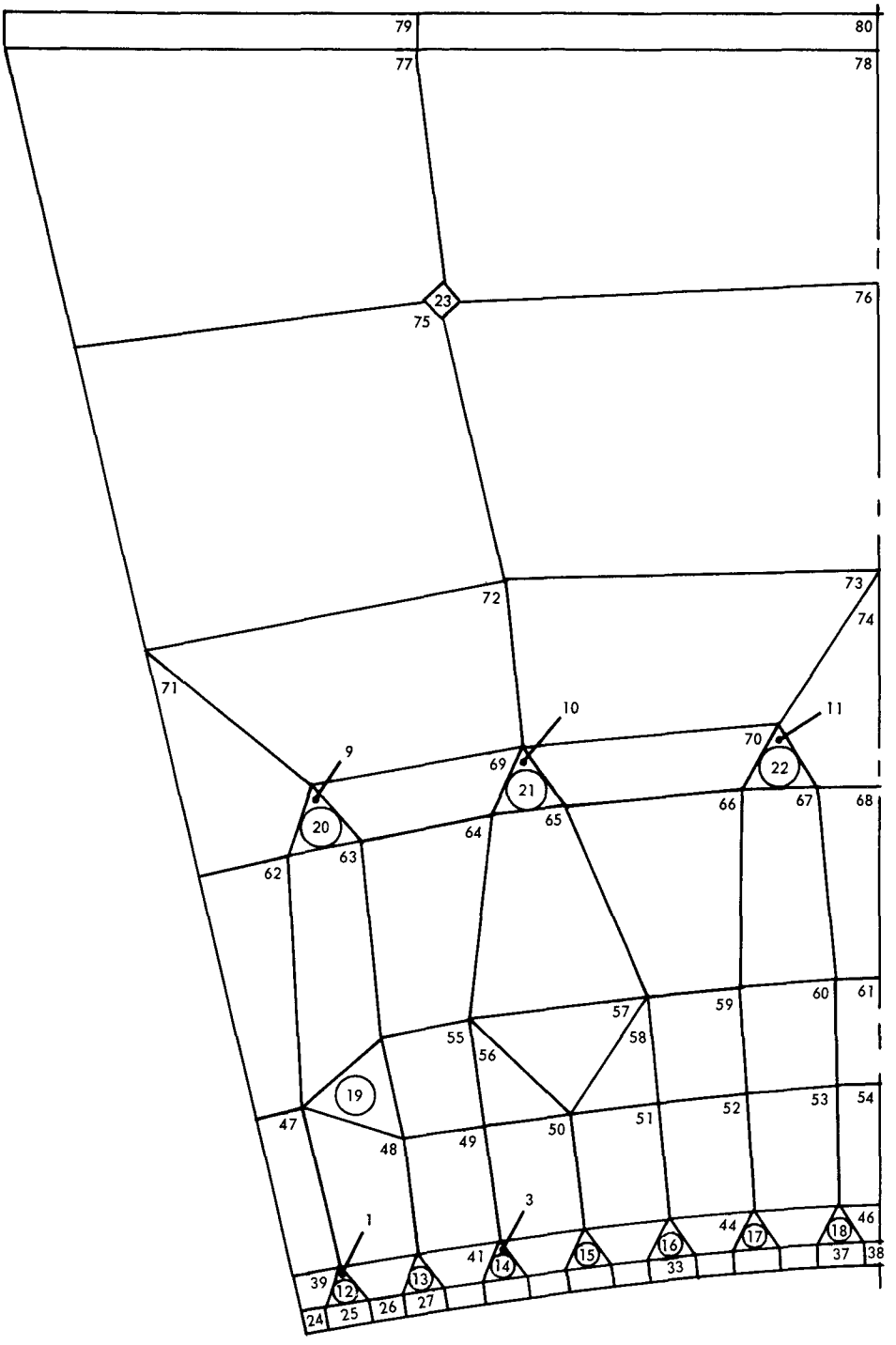

Fig. 5.80 – Nodal network of 27.5-degree segment

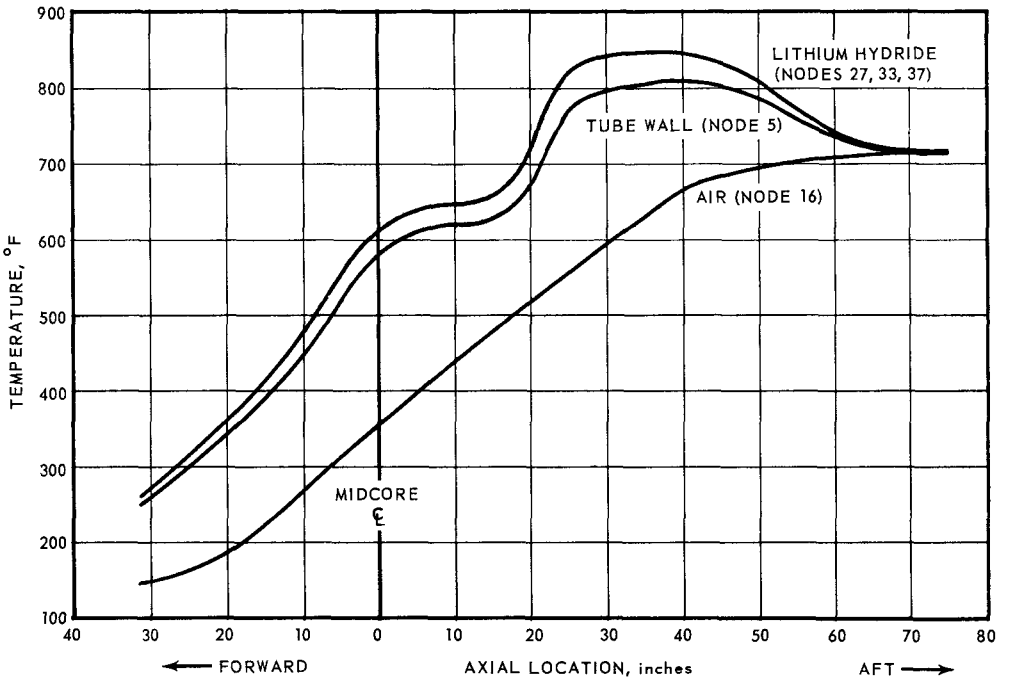

Fig. 5.81 – Temperature of lithium hydride, cooling tube wall, and cooling air at inner radius of 27.5-degree segment

TABLE 5.8

COOLING TUBE DIAMETER AND COOLING-AIR FLOW[a] IN 27.5-DEGREE SEGMENT

Tube At Node No.	Inner Diameter, inch	Coolant Flow Rate,[b] lb/sec
12	0.3125	0.0021
13	0.3750	0.0030
14	0.3750	0.0035
15	0.3750	0.00396
16	0.3750	0.00437
17	0.3750	0.00455
18	0.3750	0.00465
19	0.5625	0.00119
20	0.3125	0.00260
21	0.4375	0.00775
22	0.4375	0.00775
23	0.3750	0.00140

[a]Orificing was required in some of the above tubes for proper flow distribution. Provisions also were made to effect additional orificing to accommodate deviations in heating rate distribution from the design values.

[b]Total coolant flow = 0.09363 lb/sec.

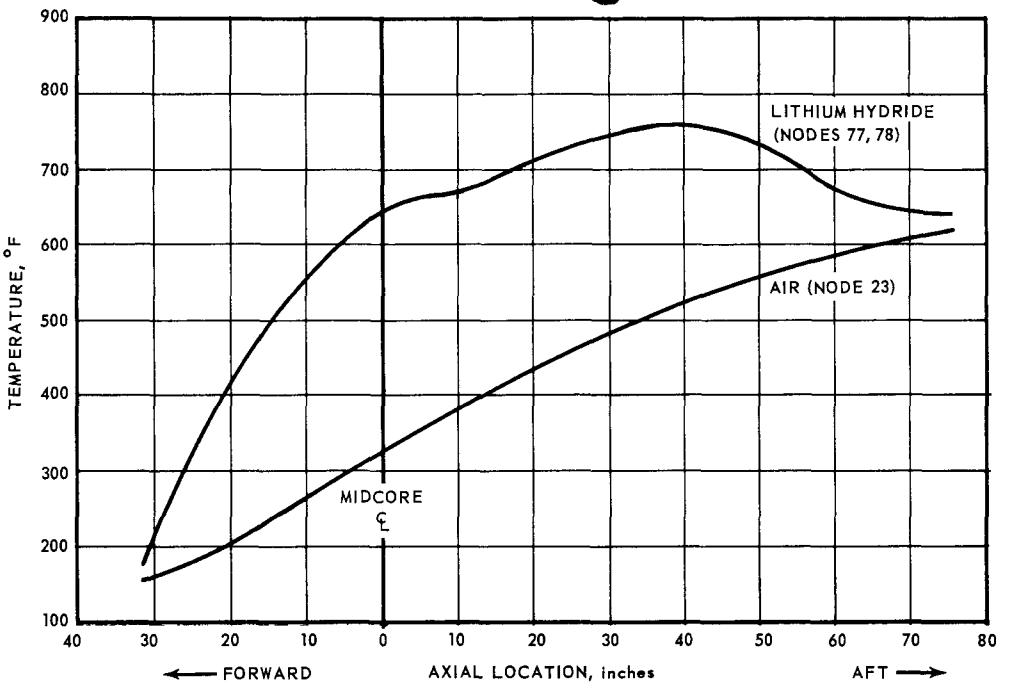

Fig. 5.82 – Temperature of lithium hydride and cooling air at outer radius of 27.5-degree segment

was not a significant aerothermal design constraint; however, the resultant temperature differentials required careful consideration. Minimizing the thermal stresses that resulted from these temperature differentials strongly influenced the placement pattern of the cooling tubes with respect to the can walls and further dictated specific coolant flow distribution among the cooling tubes.

Temperature distribution and temperature differentials existing within the internal metallic structural members of the segments were controlled by the temperature distribution within the LiH_x. This condition resulted from two factors: (1) the total amount of nuclear heat deposited in the structure was low because of its small volume fraction, and (2) the thermal conductivity of the LiH_x was low compared to that of the structural materials. The can skin temperature was assumed to vary the same as the adjacent LiH_x temperature. Since the can was thin (0.030 inch), heat flow along the skin periphery was small compared to heat flow inward to the LiH_x.

Three types of temperature differentials occurred in the segment cans:

1. Peripheral temperature differentials
2. Radial temperature differentials
3. Longitudinal temperature differentials.

The peripheral temperature differential was the differential that was set up along the can because of its proximity to coolant tubes. This temperature differential varied locally along the can periphery and was treated as a local effect. The radial temperature differential was the differential that existed between the inner and outer walls of the segment as a result of the average temperatures in those sections. The longitudinal temperature differential was the result of the longitudinal temperature distribution within the segment. These temperature differentials are further defined in Figure 5.85.

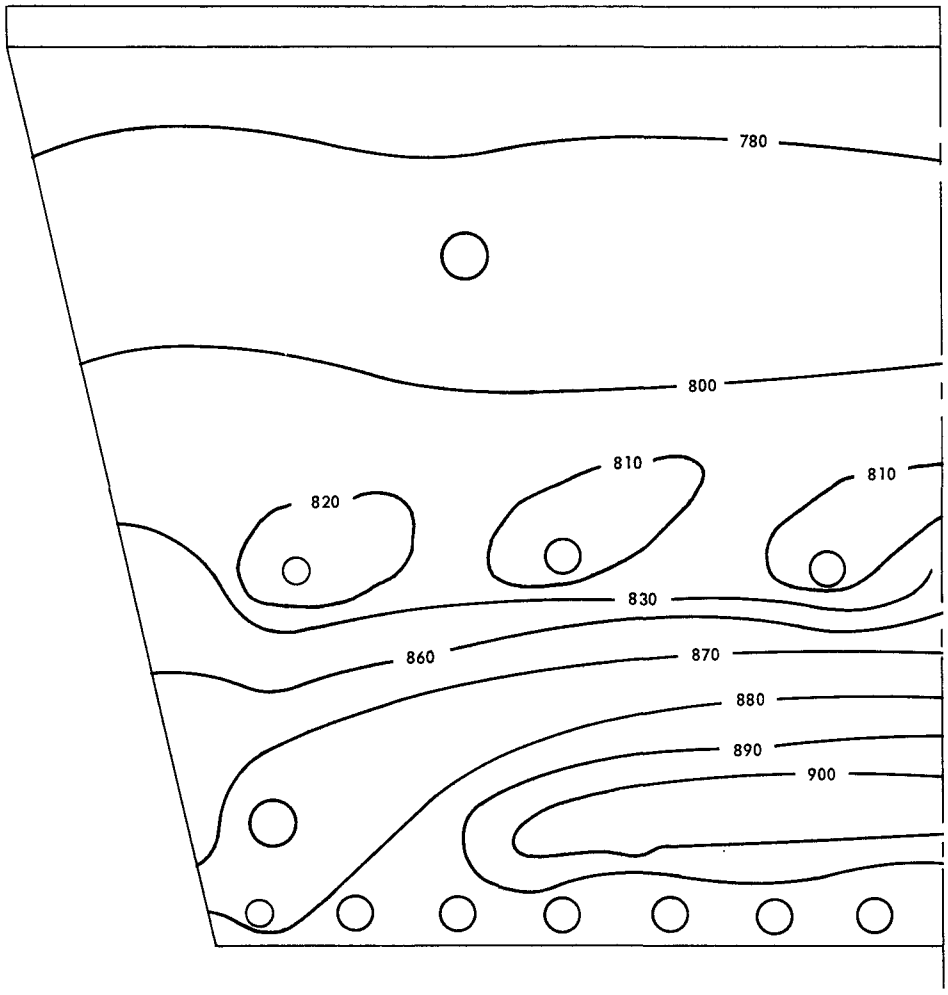

Fig. 5.83 – Temperature profile through 27.5-degree segment at a plane 42.00 inches aft of the core midplane

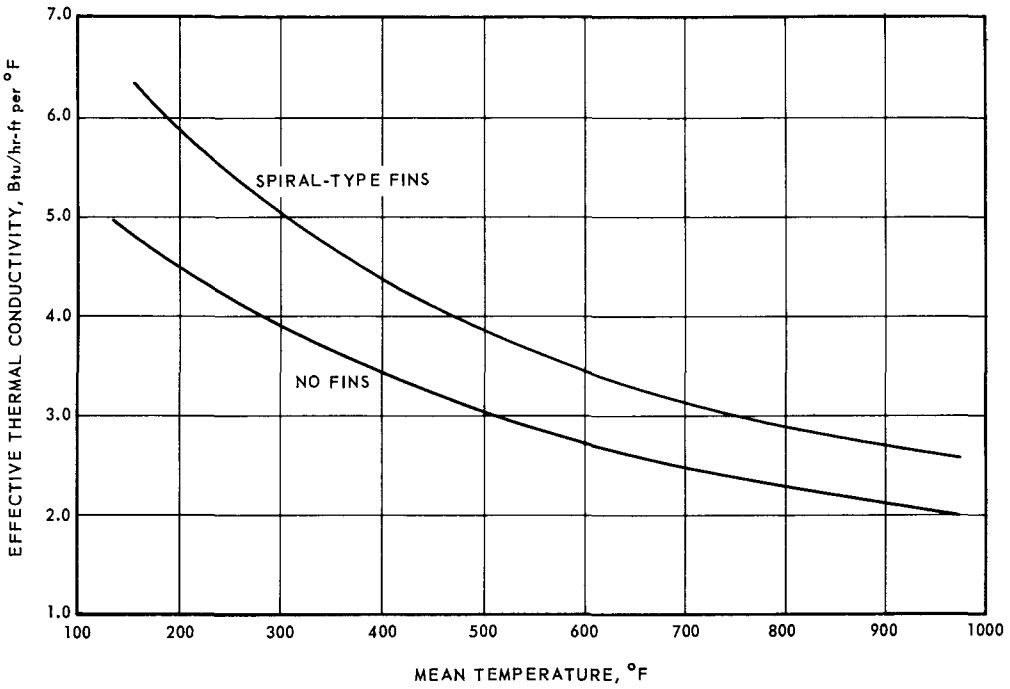

Fig. 5.84 – Effective thermal conductivity of lithium hydride

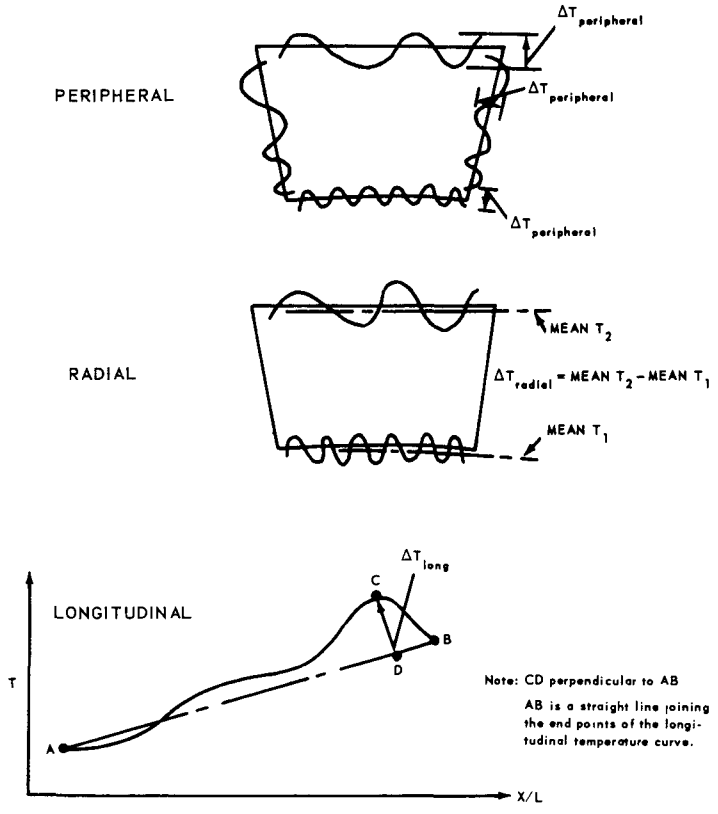

Fig. 5.85 – Side-shield-segment temperature differentials

The peripheral temperature differential accounted for approximately 70 percent of the total thermal stress that occurred in the segment cans. With the effects of local cutouts neglected, the maximum temperature differentials were:

Temperature Differentials	Emergency Flight Condition, ^{o}F	Cruise Flight Condition, ^{o}F
Peripheral	60 ± 10	40 ± 10
Longitudinal	430 ± 50	320 ± 50
Radial	150 ± 50	150 ± 50

Transient Analysis - Transient analysis of the temperature distribution and temperature differentials in the XNJ140E-1 side-shield segments was performed for two cases:

1. Reactor scram during FET operation on an AFHD at emergency power setting (110 megawatts).
2. Stepwise startup from equilibrium shutdown conditions to FET operation on an AFHD at emergency power setting (110 megawatts).

Partial results of transient analysis of the segmental plane through the reactor midpoint are presented below. Other data are contained in reference 4.

The temperature response of node Nos. 59, 78, and 38 are shown in Figures 5.86 and 5.87 for the above cases. These data show that the maximum temperature differentials between the inner and outer radii occurred 5 hours after initiation of the startup transient, and 4 hours after initiation of the scram transient. Temperature profiles through the segment 4 hours after the initiation of the scram transient are shown in Figure 5.88. Figure 5.89 shows the temperature profile 5 hours after the initiation of the startup transient.

The data shown in Figures 5.86 through 5.89 were based on the rates of cooling-air flow shown in Table 5.8. A detailed analysis of the effects of a thermal transient is contained in reference 30. Other data are contained in references 31 and 32.

Due to the large heat capacity of the side shield, it was protected from rapid responses to changes in external aerothermal influences. On the other hand, extensive periods of time were required to cool the system to ambient temperatures following engine operation.

The following generalized comments apply to the scram transient:

1. If the design steady-state cooling-air flow was continuously maintained, 20 to 25 hours were required to cool the 27.5-degree segment to the ambient temperature.
2. Increasing the rate of aftercooling-air flow to decrease the cool-down time produced high radial temperature differentials.
3. A properly scheduled, intermittent, over-cooling sequence could be used to decrease the cool-down time without increasing temperature gradients to stress-failure levels.

The following generalized comments apply to the startup transient:

1. If temperatures in excess of 1050^{o}F within the LiH_x were the only system restraint, it was possible to operate the 27.5-degree segment for periods of 3 to 4 hours with no coolant flow, subsequent to an instantaneous startup.
2. However, long before over-temperaturing occurred, radial temperature differences would have been excessive. These excessive temperature differentials could have been mitigated by starting to cool the system at a lower rate between 1/2 and 1 hour after startup.
3. Properly scheduled, intermittent cooling probably would have allowed segment operation 8 to 10 hours before the steady-state cooling-air flow was required continuously.

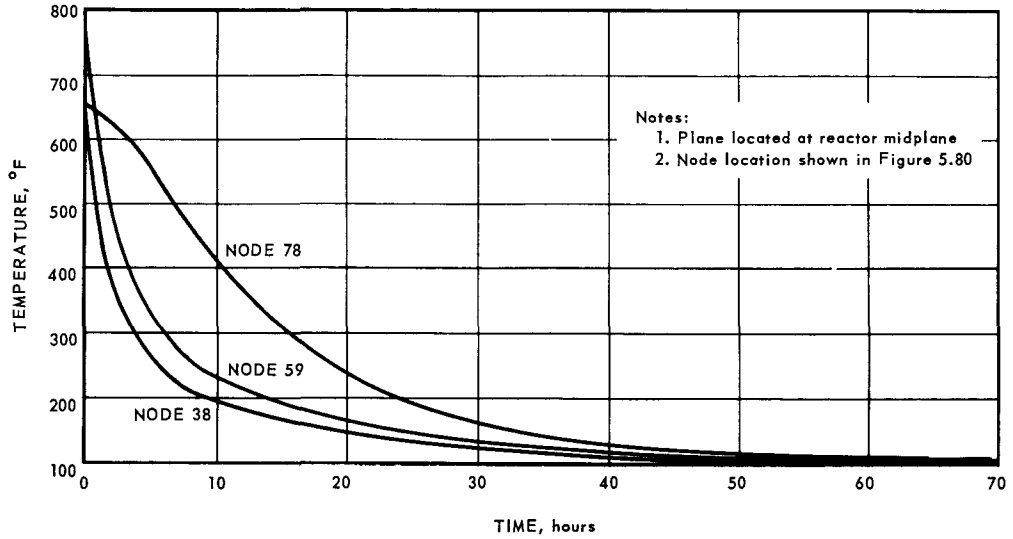

Fig. 5.86 – Temperature response of 27.5-degree segment during case No. 1 transient

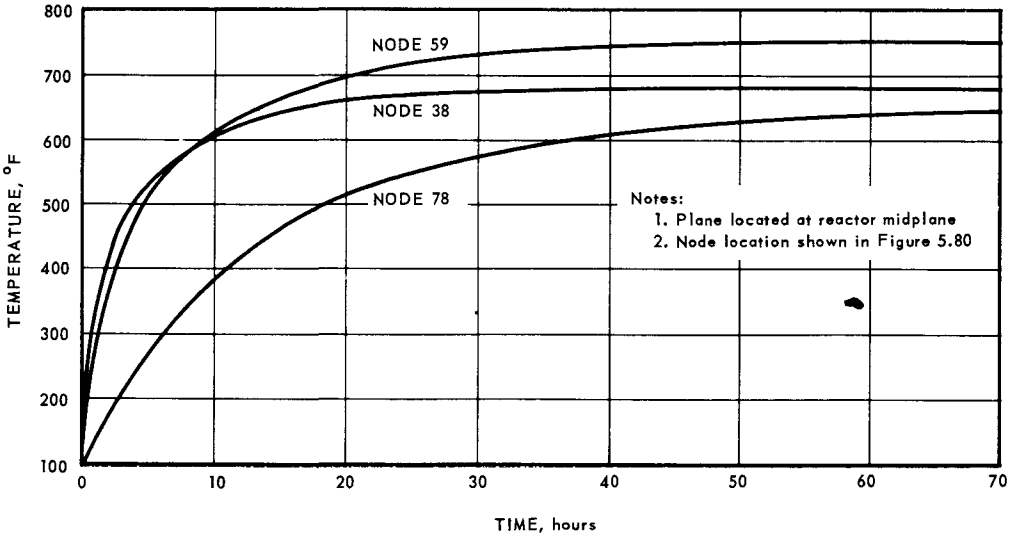

Fig. 5.87 – Temperature response of 27.5-degree segment during case No. 2 transients

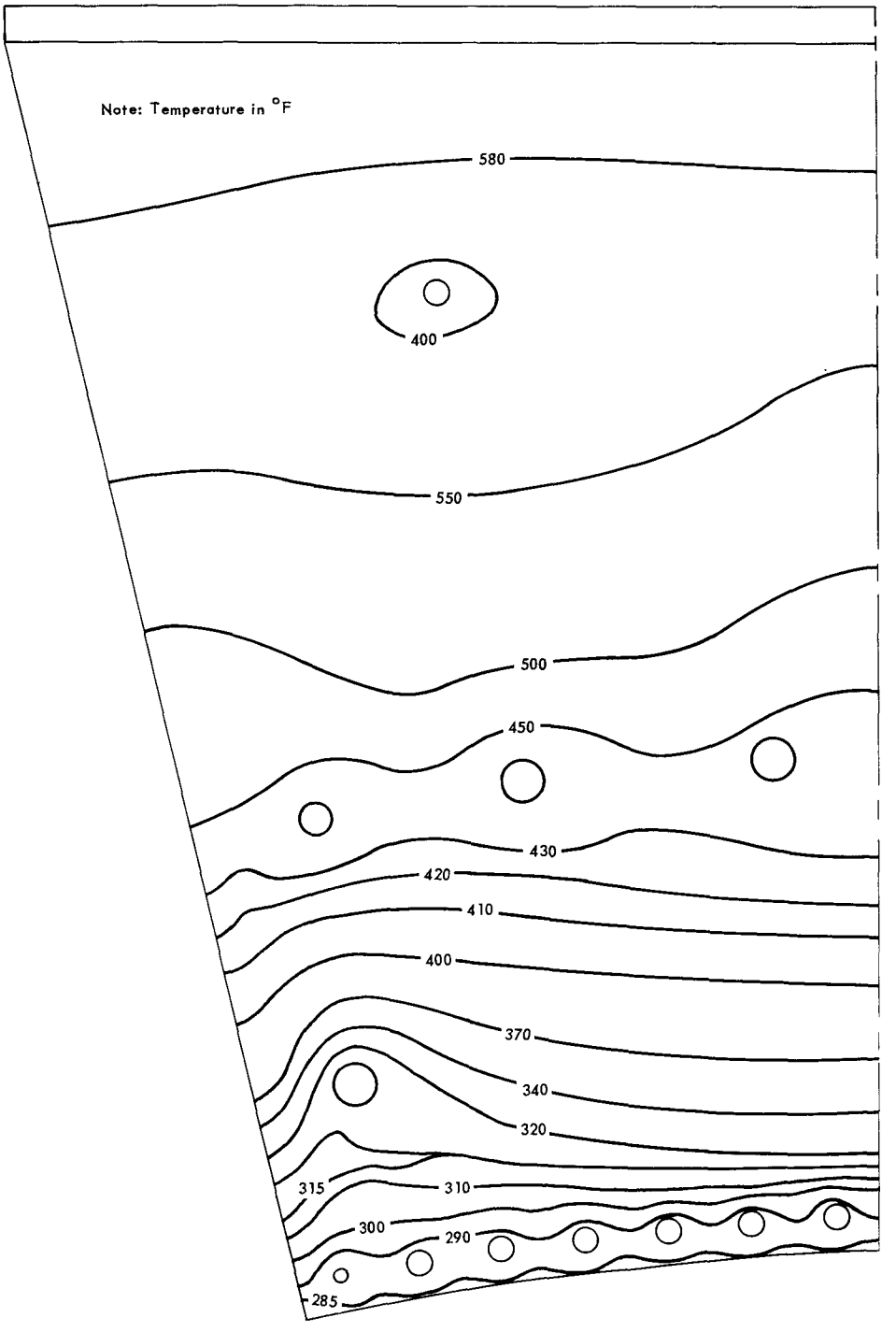

Fig. 5.88 – Temperature profiles through 27.5-degree segment 4 hours after initiation of scram transient

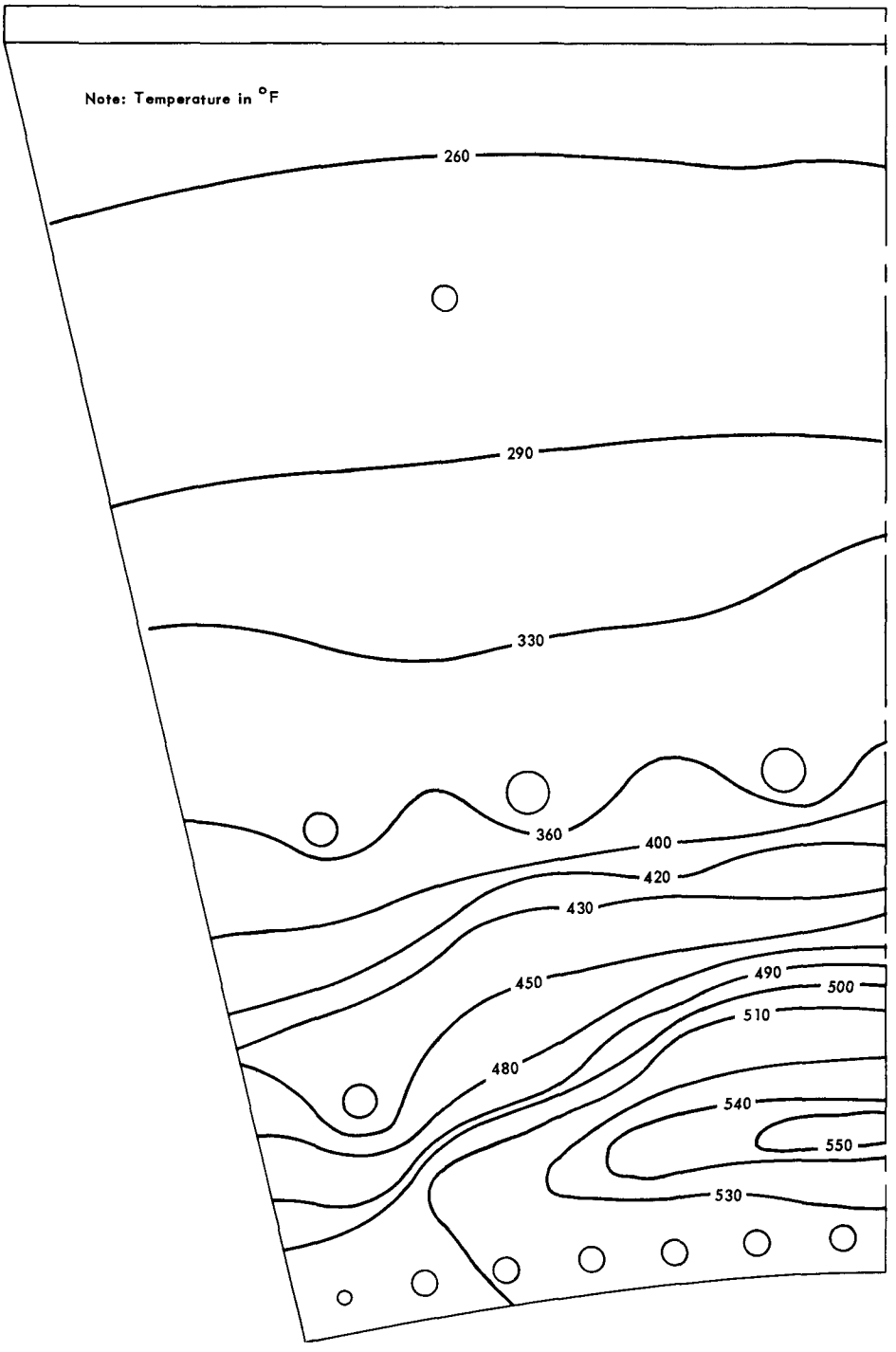

Fig. 5.89 – Temperature profiles through 27.5-degree segment 5 hours after initiation of startup transient

These general observations are supported by the data shown in Figures 5.90 through 5.94. These data are the results of initial calculations in which the thermal conductivity of LiH_X did not include the fin effectiveness. Although the times and temperature levels reported in these data are higher than those which corrected calculations would yield, the trends are valid and the results are pessimistic.

The longitudinal temperature profiles through the segment for the Case No. 1 transient are shown in Figure 5.90. Uninterrupted cooling-air flow at design rates was assumed. The normal steady-state temperature distribution also is shown for comparison. The discrepancy between the steady-state temperature 30 inches aft of the core midplane, as shown in Figure 5.90, (1010°F) and the comparable temperature, shown in Figure 5.83, (approximately 900°F) is due to the later and more refined calculations used to generate the data shown in Figure 5.83. Extended periods of time (20 to 30 hours) were required to cool the side shield to internal temperatures approaching ambient.

The transient temperature response of the inner and outer walls of a 27.5-degree side-shield segment are shown in Figures 5.91 and 5.92, respectively, for the transient condition of reactor scram. Both curves depict the temperature at a plane 30 inches aft of the reactor midplane and were plotted for design cooling-air flow, 50 percent of design airflow, and 200 percent of design airflow. The ambient temperature was 103°F. These curves also show that increasing the airflow significantly increased the temperature gradients, and that it was desirable to reduce the airflow.

The Case No. 2 transient was studied for the two conditions: (1) design cooling-air flow, and (2) no cooling-air. These results are shown in Figures 5.93 and 5.94, respectively, for a plane through the reactor midpoint.

These data indicate that the side shield could remain uncooled for several hours after startup if only LiH_X temperature limits were considered. However, the temperature gradients became severe and limited the length of time the side shield could remain uncooled.

5.6.2.2 Side Segment

As was the case for the 27.5-degree segment, a model side segment was employed for the aerothermal analysis. There were two possible modes of operation:

1. Inboard operation, the side segments being situated between two engines
2. Outboard operation, the side segments being situated adjacent to the shield cheek.

The first of these operating modes posed the problem of additional secondary heat deposition from the adjacent reactor and an increased heating rate, especially in the toe region. Aerothermal analysis, however, was based upon the outboard mode since the XNJ140E-1 side segments would have been used in the outboard mode. Larger tube sizes than required were used, and were orificed to provide the desired cooling-air flow. This approach resulted in a thermodynamically less efficient system. However, the system had the capacity of handling inboard operation without resizing the coolant tubes. All data presented below were based on outboard, or single engine, operation.

Steady-State Analysis - The cooling-tube pattern and the nodal analysis network are shown in Figures 5.95 and 5.96, respectively, for the reactor midplane location. Coolant tube sizes and cooling-air flows are listed in Table 5.9.

The steady-state LiH_X temperature profile at the reactor midplane is shown in Figure 5.97 for the design condition, emergency power setting. The maximum temperature shown, 820°F, was approximately the maximum temperature that occurred in the side segments.

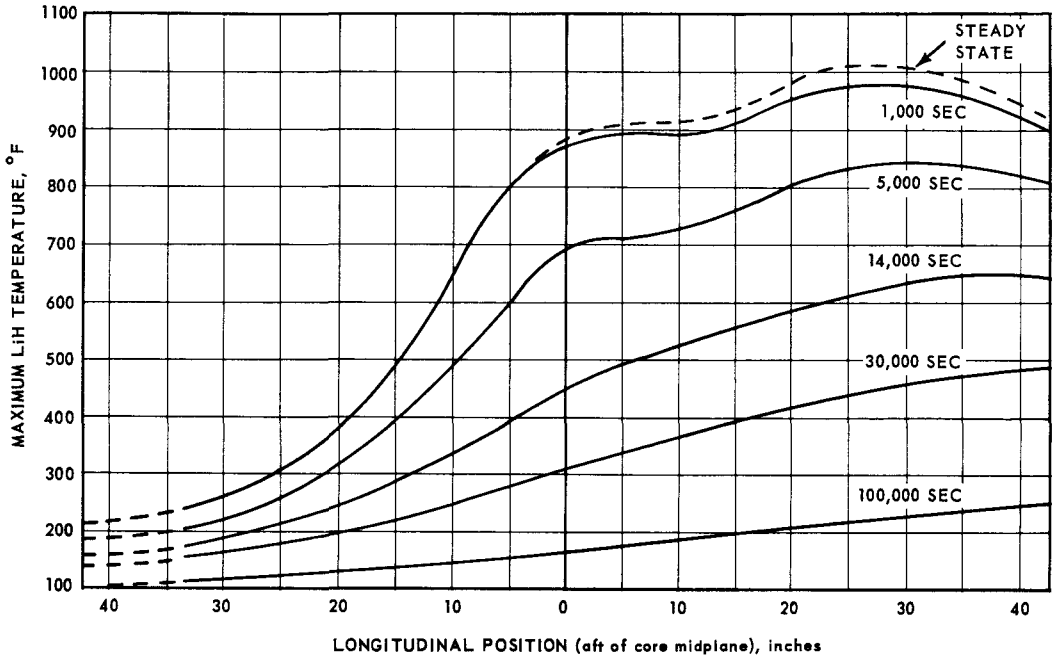

Fig. 5.90 – Temperature distribution in XNJ 140E-1 27.5-degree side-shield segment following reactor scram

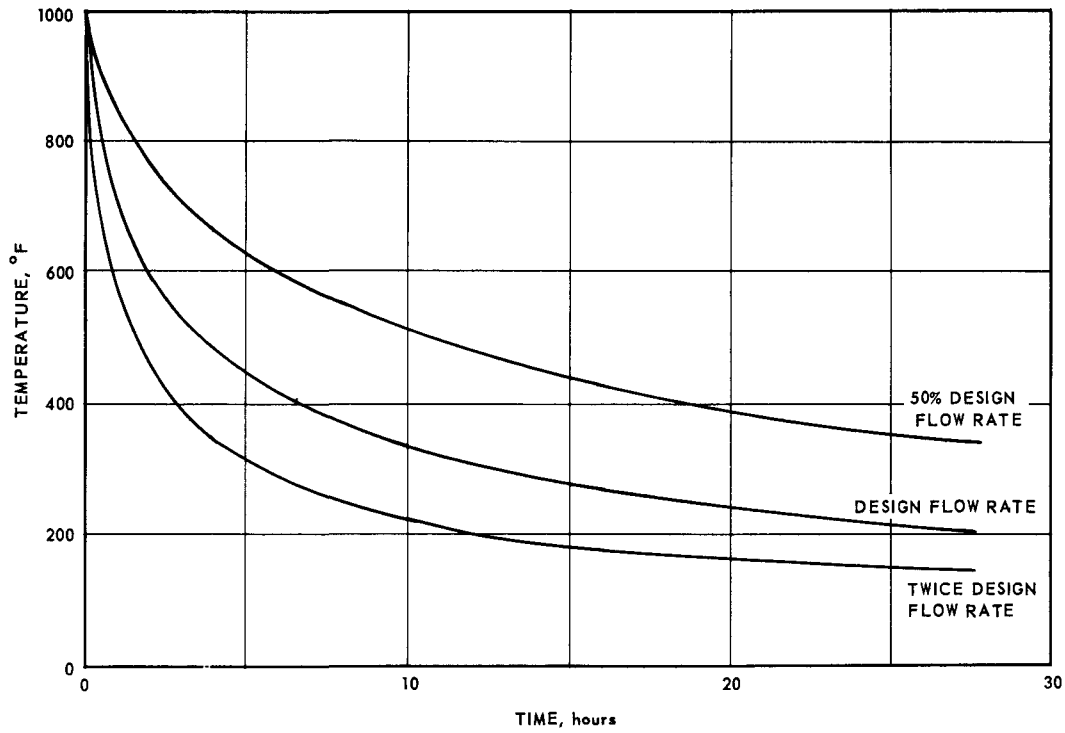

Fig. 5.91 – Transient temperature in inner wall of 27.5-degree side-shield segment following scram, XNJ140E-1

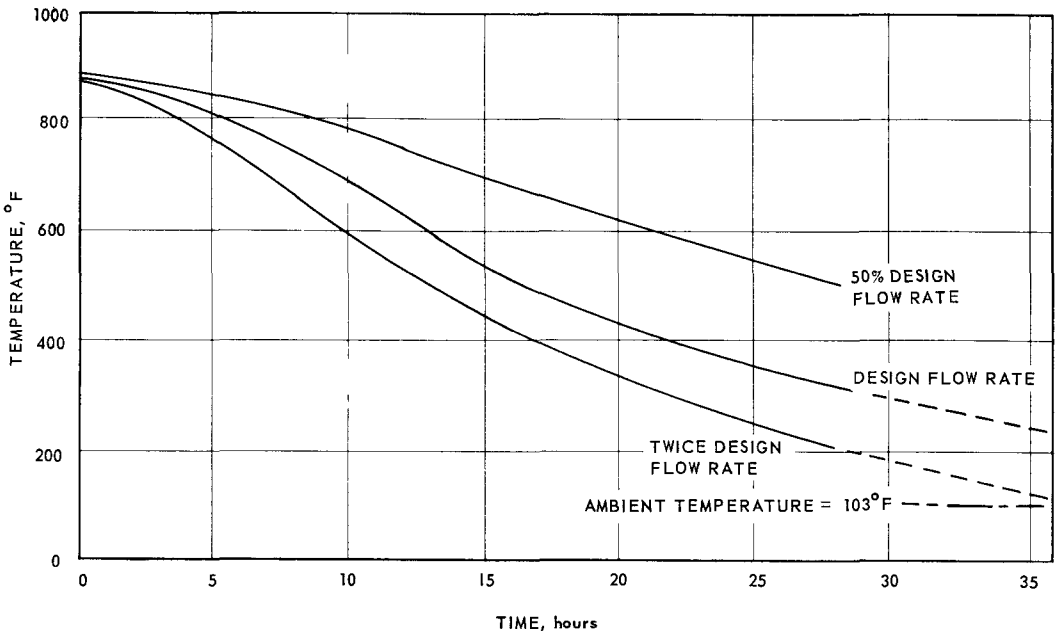

Fig. 5.92 – Transient temperature in outer wall of 27.5-degree side-shield segment following reactor scram, XNJ140E-1

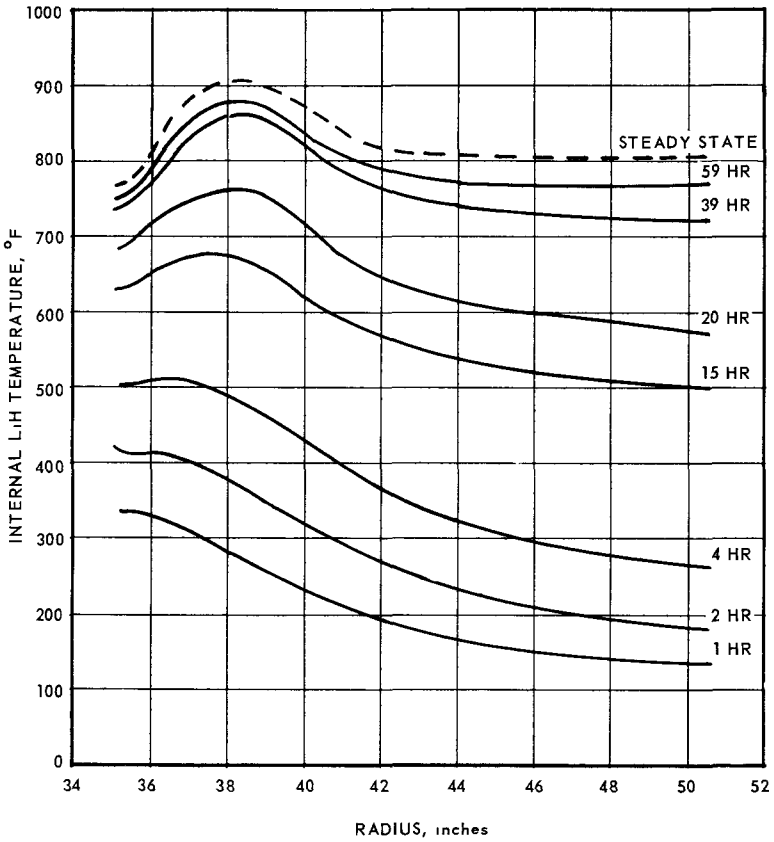

Fig. 5.93 – Temperature distribution in 27.5-degree side-shield segment following reactor startup with cooling air at design flow rate, XNJ-140E-1

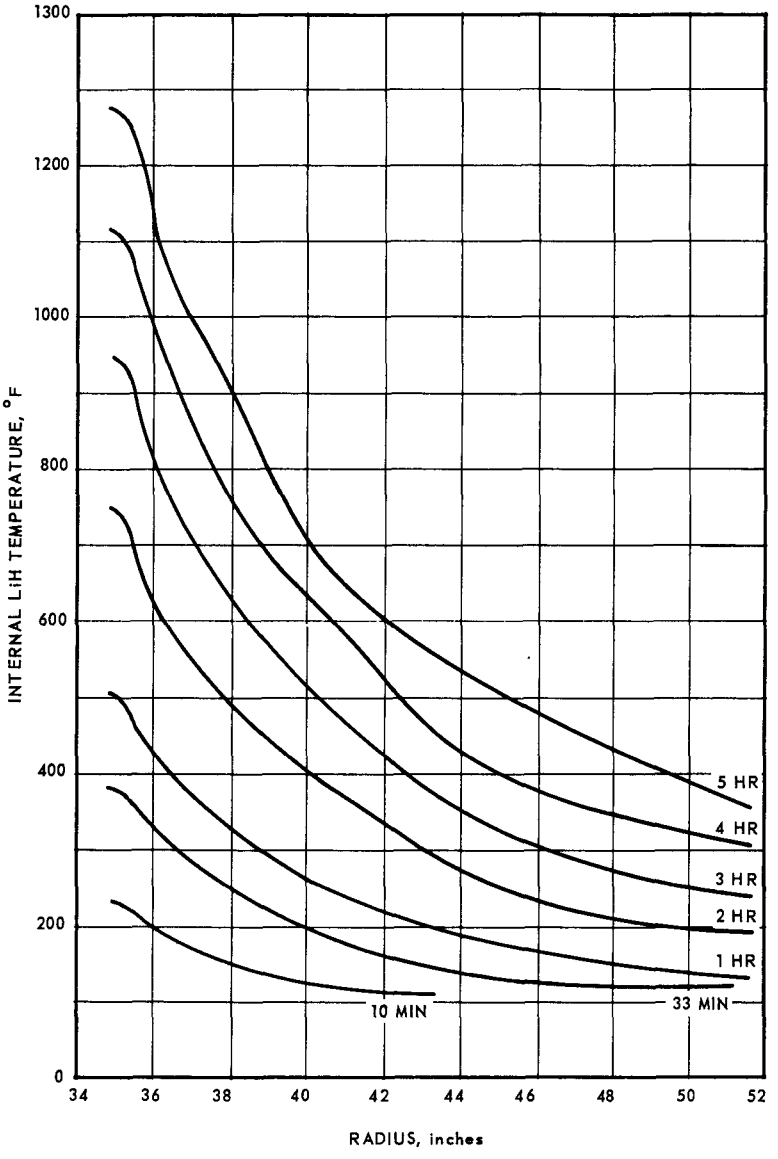

Fig. 5.94 – Temperature distribution in 27.5-degree side-shield segment following reactor startup with no cooling airflow, XNJ140E-1

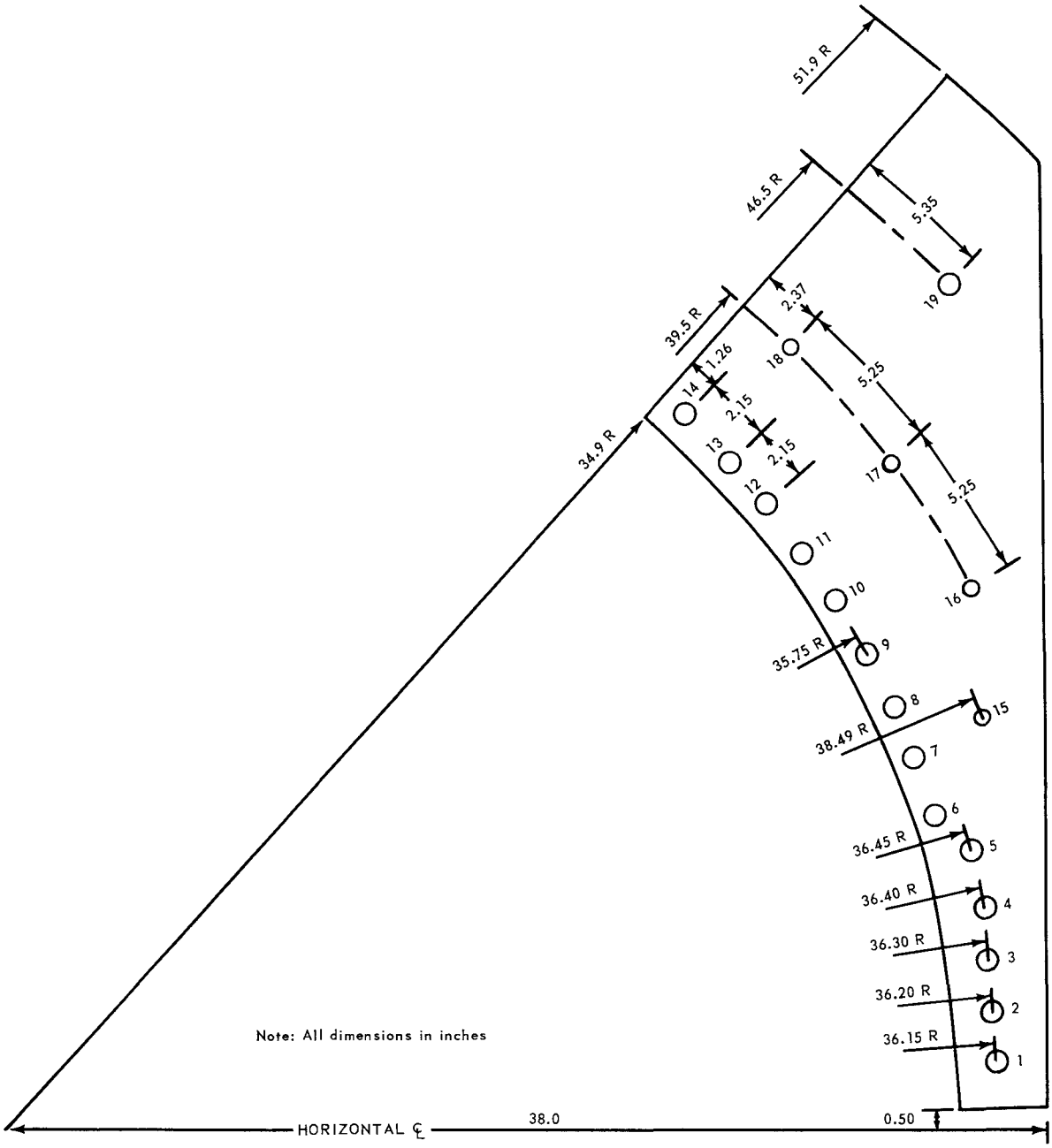

Fig. 5.95 – Side segment cooling tube pattern at reactor midplane

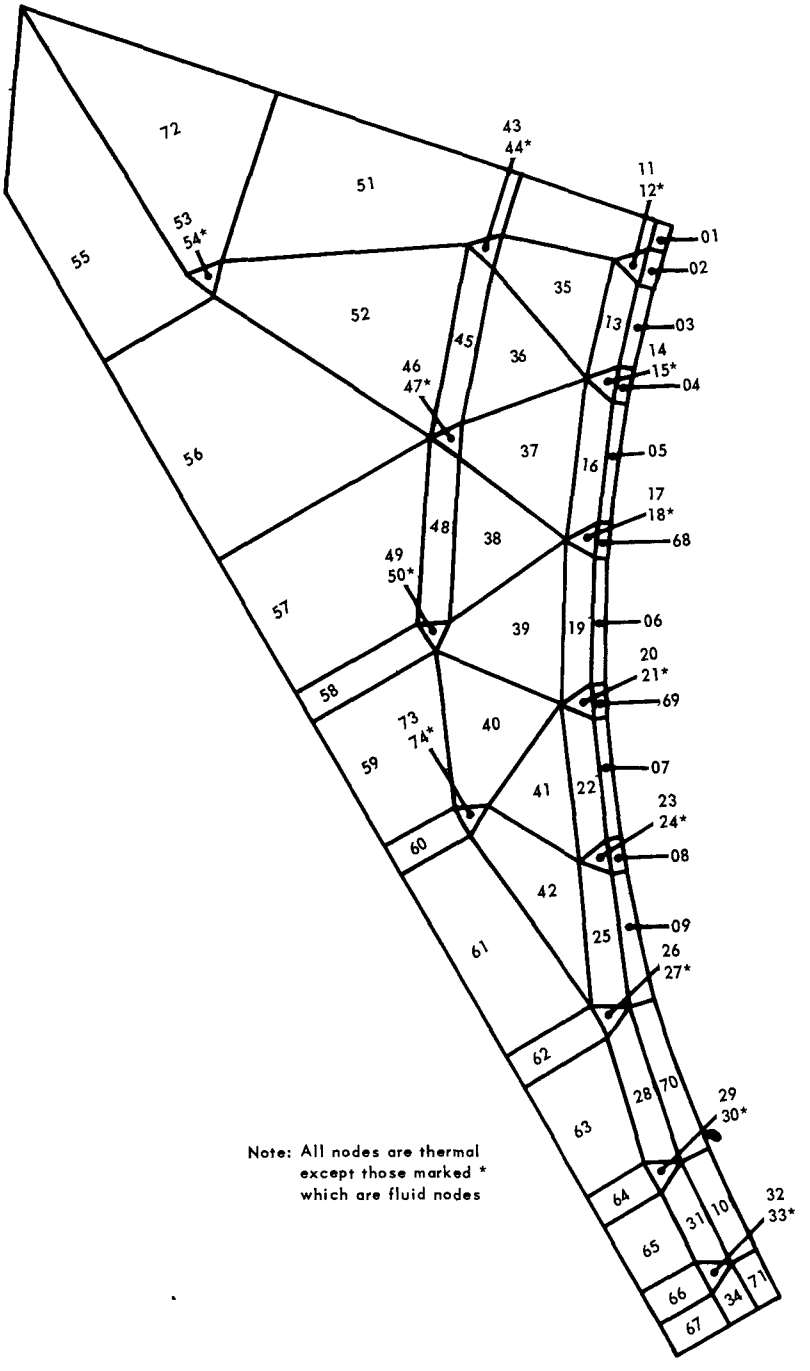

Fig. 5.96 – Side segment nodal analysis network

TABLE 5.9

SIDE SEGMENT COOLANT TUBE DIAMETER AND COOLING-AIR FLOW

Tube Number[a]	Inner Diameter, inch	Coolant Flow Rate, lb/sec	Node Number[b]
1	0.750	0.0170	33
2	0.750	0.0146	30
3	0.750	0.0146	
4	0.750	0.0150	27
5	0.750	0.0255	
6	0.750	0.0166	24
7	0.750	0.0166	
8	0.750	0.0166	21
9	0.750	0.0166	
10	0.750	0.0166	18
11	0.750	0.0166	
12	0.750	0.0166	15
13	0.750	0.0166	
14	0.750	0.0166	12
15	0.500	0.005	74
16	0.5625	0.0105	50
17	0.5625	0.0140	47
18	0.500	0.0085	44
19	0.750	0.0155	54
Total		0.2880	

[a]Tube numbering convention shown in Figure 5.95.
[b]Node numbering convention shown in Figure 5.96.

Due to the limited nodal capacity of the thermodynamic analysis program with respect to the three-dimensional geometry considered, the temperature distribution was not as detailed as that of the 27.5-degree segment. Nevertheless, the temperatures shown probably agreed within ± 20°F of those that would have been obtained in a more detailed analysis. The definition of the skin temperature distribution was inadequate for wall stress calculations.

Transient Analysis - Figures 5.98 and 5.99 show the transient temperatures in the side segment during the Case No. 1 and Case No. 2 transients, respectively, for a plane passing through the core midpoint. These figures show that the maximum temperature differences between inner and outer surfaces occurred approximately 2.5 and 5.5 hours after initiation of the startup and scram transients, respectively. Figure 5.100 shows the internal LiH_x temperature profiles for Case No. 1 maximum temperature differential condition with steady-state cooling-air flowrate maintained throughout the transient. The corresponding temperature profiles for Case No. 2 are shown in Figure 5.101. As shown in Figures 5.99 and 5.101, the temperature level at the time of maximum temperature differentials was considerably below the steady-state temperature level.

These aerothermal analyses did not take into account the effect of finning the coolant tubes in critical heating regions. At the time of project cancellation, a new nodal network, more detailed at the inner radial surface, was being formulated to account for the increased effective thermal conductivity.

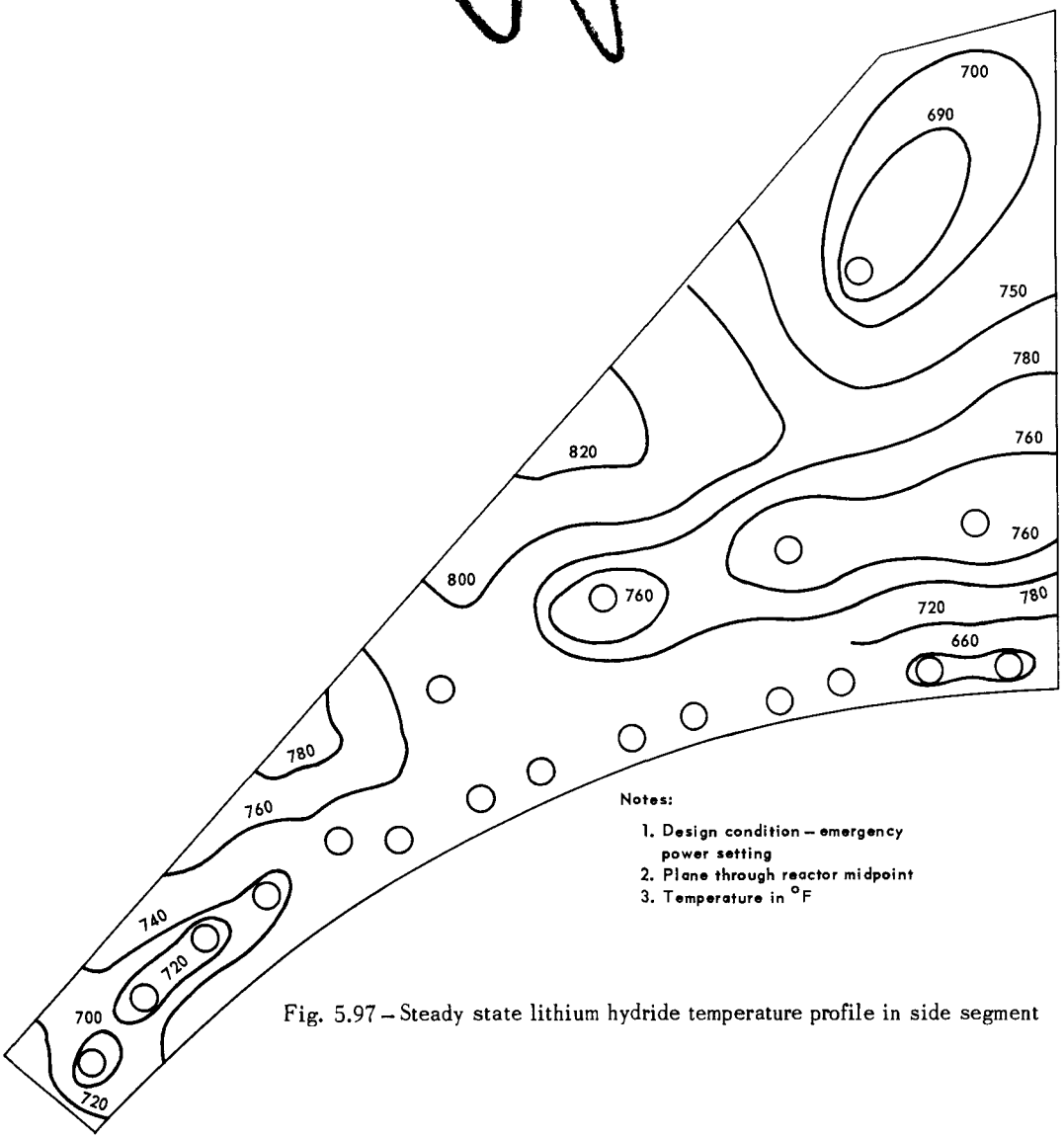

Fig. 5.97 – Steady state lithium hydride temperature profile in side segment

5.6.2.3 Shield Cheeks

Aerothermal analysis for these components was very limited in detail, and confined to a single analysis of steady-state conditions during operation at the emergency power setting. The analysis resulted in temperature profiles through the side cheek. Figure 5.102 shows a typical profile, the plane of which was located 37 inches aft of the reactor midplane.

5.6.3 NUCLEAR DESIGN

Secondary heating rates were calculated using the methods discussed in section 5.9. Detailed longitudinal and radial secondary-heating-rate traverses are contained in reference 4.

5.6.4 STRESS AND WEIGHT

5.6.4.1 Structural Considerations

The individual segments were designed in accordance with semi-monocoque structural practices. A typical cross section of a 27.5-degree segment, shown in Figure 5.103, contained stringers, frame, can (skin), and attachments. The LiH_x was considered nonstructural and the enveloping can absorbed all loads. Because of its strength and ability

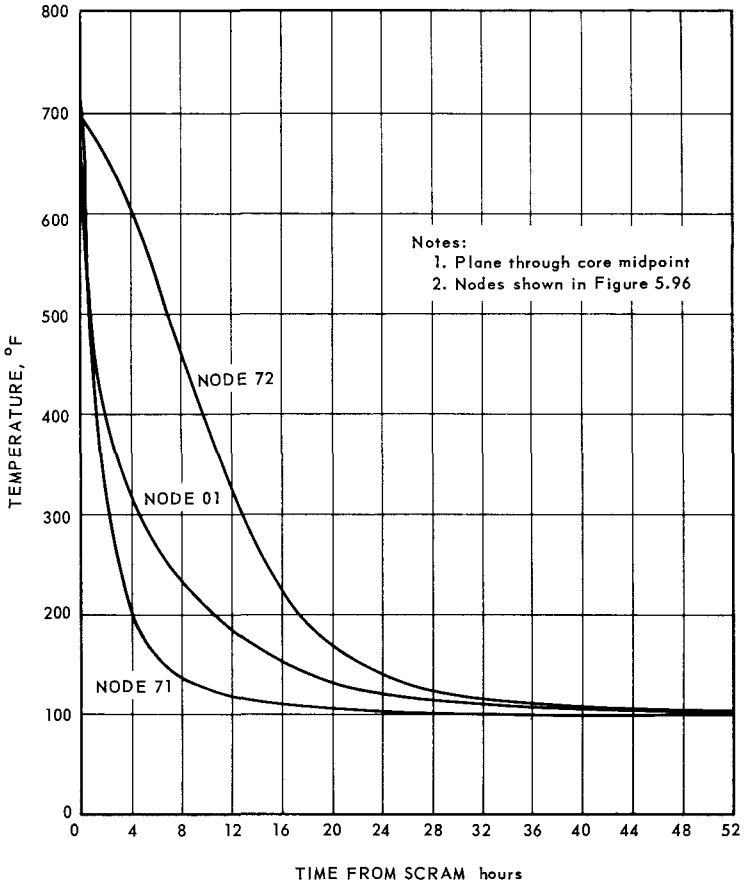

Fig. 5.98 – Temperature response of side segment during case No. 1 transient

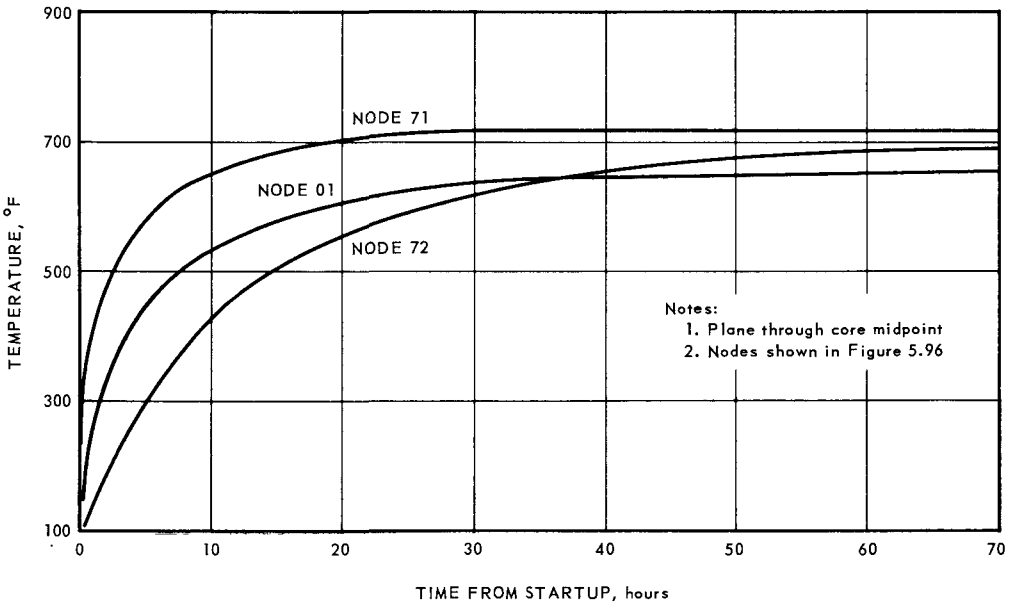

Fig. 5.99 – Temperature response of side segment during case No. 2 transient

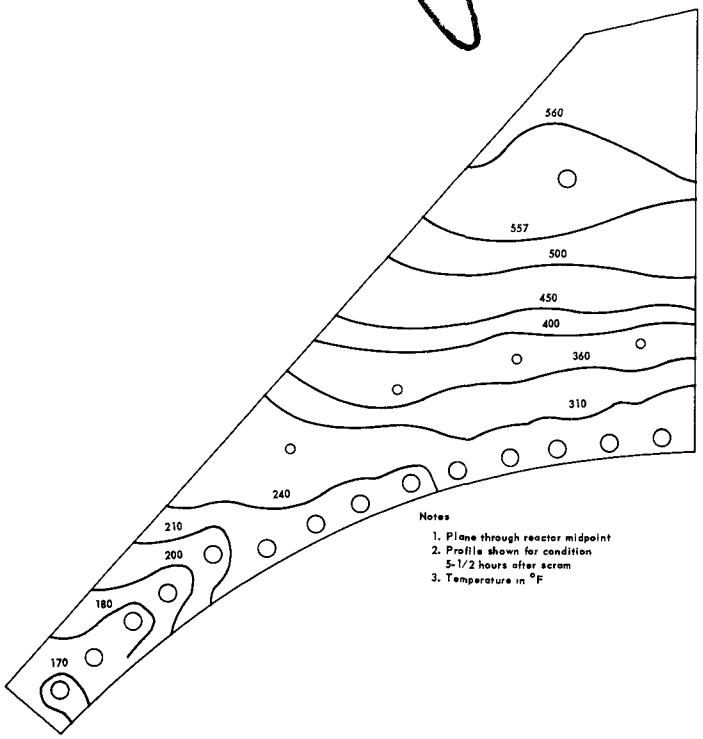

Fig. 5.100 – Temperature profiles through side segment during Case No. 1 transient

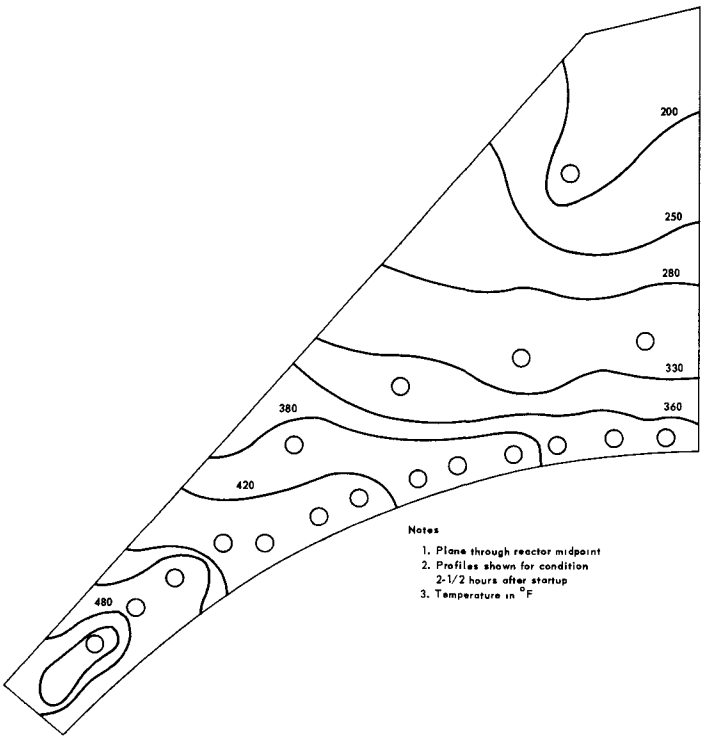

Fig. 5.101 – Temperature profiles through side segment during Case No. 2 transient

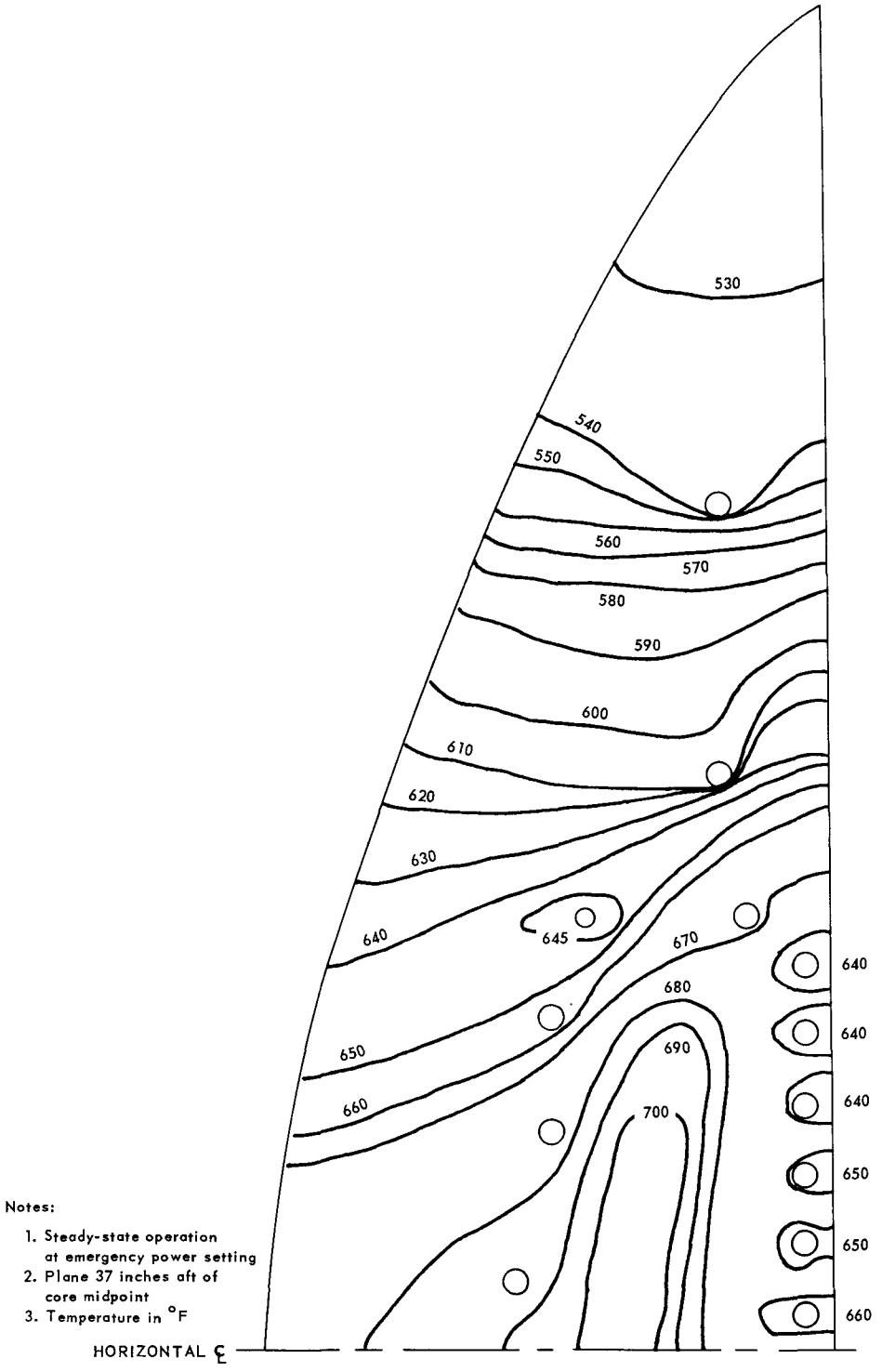

Fig. 5.102 – Temperature profile through shield cheek

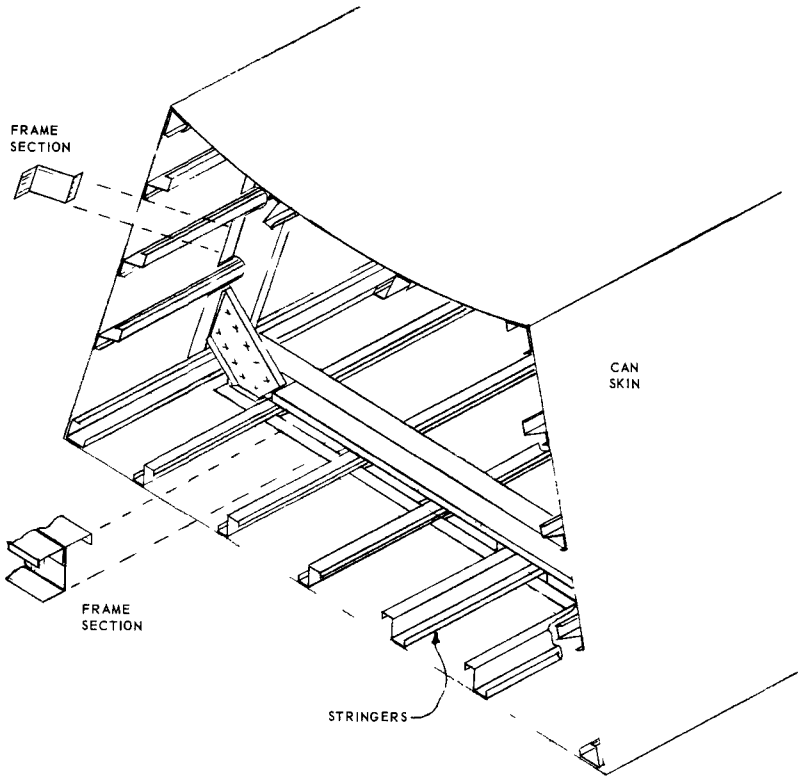

Fig. 5.103 – Structural cross section of 27.5-degree segment

to resist the corrosive action of molten LiH_X, 19-9DL stainless steel was selected as the structural material.

During vertical and side inertial accelerations, the LiH_X was assumed to exert a hydrostatic pressure on the can. The can, in turn, loaded the stringers and frames. The load on the stringers was transmitted to the frames which, in turn, redistributed this load to the can which acted as a simply supported beam. However, during axial inertial accelerations, the LiH_X was assumed to exert hydrostatic pressure only on the ends of the cans, and the stringers and frames were assumed to transmit 80 percent of this hydrostatic pressure to the sides of the can.

The segments acted as simply supported beams. A sketch of the support arrangement for the lower half is shown in Figure 5.104. The upper half was similarly supported, but with modifications for the aft segments as indicated in Figure 5.105.

The support structure at the forward end of the segments was placed at the ends of the segments. Continuity of the structure was maintained by external connections between segments. The connection between the center 27.5-degree segment and the canted 27.5-degree segment was a link on the outer radius which transmitted tangential loads only, and a pin-joint arrangement on the inner radius which transmitted radial and tangential loads. The connection between the canted 27.5-degree segment and the side segment was a pin joint on the outer radius which transmitted radial and tangential loads. The connection between the side segment and the pressure vessel was a pin joint. These connections also contained provisions for forward and aft lateral motion of the ends of the segments to accommodate thermal expansions.

The support structure at the aft end was an open-truss structure for all lower-half segments and the two side segments of the upper half. The aft ends of the three aft seg-

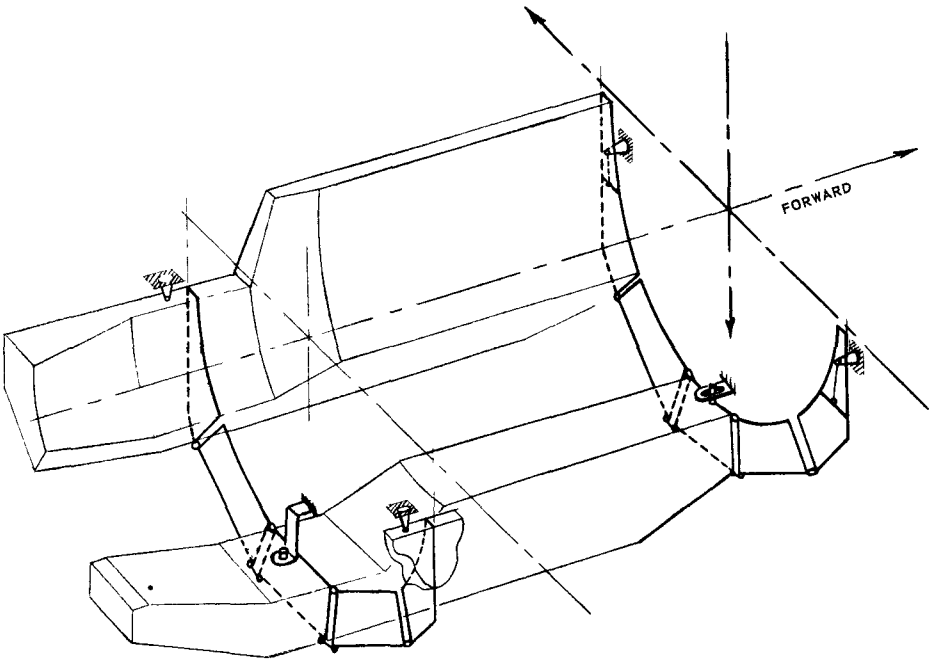

Fig. 5.104 – Support arrangement for lower half of side shield

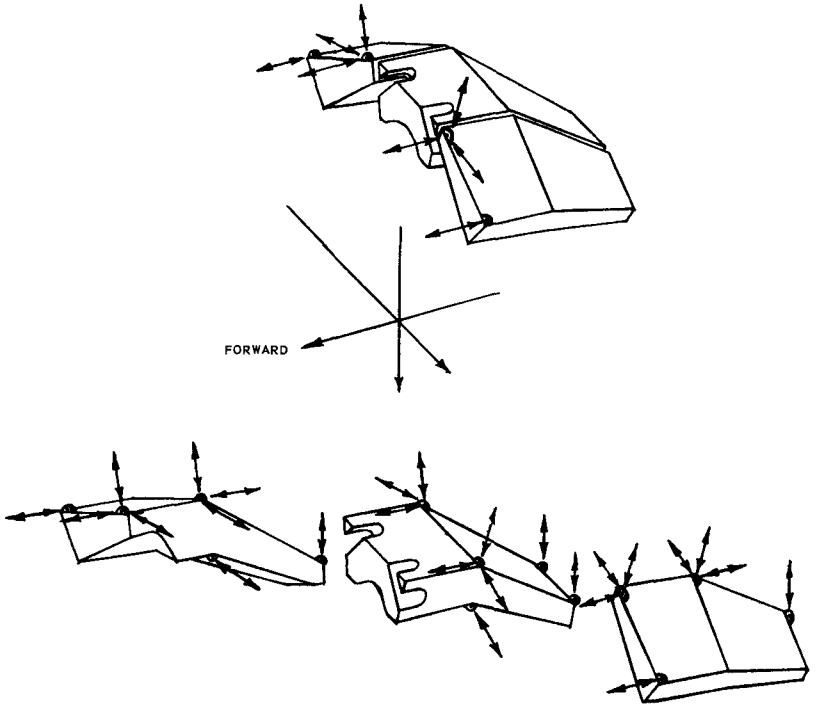

Fig. 5.105 – Support arrangement for aft segments of upper half of side shield

ments were joined to form their own support structure. Continuity was maintained the same as at the forward end by externally connecting the segments. At the aft support structure, 2-G axial inertial loads were absorbed by pin connections tieing the center 27.5-degree segment and the side segments of the upper and lower assemblies to the aft trunnion ring of the pressure vessel. Axial loads during 8-G crash loading were absorbed by pads on the 27.5-degree canted segments that engaged the pressure-vessel aft flange and prevented separation of the side shield from the rest of the engine.

Support of the upper aft assembly was accomplished by connecting the 27.5-degree center segment to the two 27.5-degree canted segments and then connecting this assembly to the upper-forward segment assembly. Connections at the inner radius transmitted tangential loads. Connections at the outer radius transmitted radial, tangential, and axial loads. The aft end connection between segments transmitted vertical loads only. The forward connection at corners nearest the centerline transmitted radial, tangential, and axial loads, and the connection at the corners farthest from the centerline transmitted axial loads only.

This method of connecting the segments met the following design objectives:

1. Meet all mechanical and structural requirements using structure and not a mechanism
2. Design for reasonable stress levels resulting from all inertial loads
3. Minimize effects of thermal gradients by proper design of connections
4. Minimize effects resulting from different coefficients of expansion
5. Meet all deflection requirements.

5.6.4.2 Loading Considerations

Loadings on the side shield were treated in four categories:

1. LiH_X pressure loads
2. Shear and moment loads from inertia
3. Support frame loads
   a. Loads from mechanical effects including friction
   b. Loads from thermal effects
4. Thermal loads.

The density of LiH_X was taken as 0.0262 pounds per cubic inch. The locations of the various centers of gravity and the distribution of running loads used in shear and moment analysis were based on component weights calculated from drawings.

Unit LiH_X Pressures - LiH_X was considered to exert a uniform pressure on the cans during vertical, horizontal, and axial inertial accelerations. These loads were resolved for all segments, as unit LiH_X pressures. The unit pressures then were multiplied by appropriate G-loading factors, and were combined to form resultant horizontal and vertical loads. This procedure was followed for each design loading condition. The detailed results are contained in reference 4.

LiH_X pressure loads resulting from roll, pitch, and yaw acceleration loadings for the individual segments were not itemized, but they were accounted for in the stress analysis by utilizing resultant shear diagrams for each individual acceleration. Pressures were resolved in terms of G loading, rather than pounds per square inch, and combinations of design loading conditions were determined for vertical, horizontal, and axial loads using the factors shown in Table 5.10.

Shear and Moment Loads - Shear and moment loads were determined by usual engineering methods with respect to vertical and horizontal inertial loads of 1 G_Z (vertical), 1 G_Y (side), and 1 G_X(axial). Shear and moment loads also were determined for roll, pitch,

TABLE 5.10

FACTORS USED IN CALCULATING STRESSES[a] DUE TO UNIT LiH_X PRESSURE

	Distance Aft From Front Support Structure,[c] inches					
Condition[b]	22	33.32	63.5	73.2	77.5	94.7
A_1 (M_y)	4.78	4.98	16.67	7.85	6.33	6.05
$\pm B_1$ (M_y)	2.94	3.21	18.62	6.95	4.77	3.20
$\pm C_1$ (M_y)	2.94	3.21	18.62	6.95	4.77	3.20
D_1 ($M_{y\ ult.}$)	3.74	5.10	66.50	20.25	12.10	4.76
A_2 (M_z)	1.23	1.23	1.97	1.35	1.28	1.29
$\pm B_2$ (M_z)	1.00	1.00	1.00	1.00	1.00	1.00
$\pm C_2$ (M_z)	2.00	2.00	2.00	2.00	2.00	2.00

[a]Stresses due to 1 G vertical and 1 G side unit LiH_X pressures were multiplied by the tabulated factors.

[b]Condition A_1 - Flight maneuver (vertical load)
A_2 - Flight maneuver (side load)
Condition B_1 - Ground checkout (vertical load)
B_2 - Ground checkout (side load)
Condition C_1 - Ground handling (vertical load)
C_2 - Ground handling (side load)
Condition D_1 - 8 G crash

[c]Plane 42.73 inches forward of core midpoint.

and yaw unit accelerations of 1 rad/sec^2. From these unit conditions expressed in terms of G-factors, combinations of loads were determined for direct vertical, horizontal, and axial loads with the roll, pitch, and yaw acceleration factors added. Detailed analytical methods and data are contained in references 4 and 33.

Support Frame Loads - Loading of all support frames were calculated for the following conditions:

1. Direct inertial loads of 1-G vertical, 1-G side, and 1-G axial
2. Inertial acceleration loads of yaw, pitch, and roll for unit acceleration (1 radian per second per second)
3. Frictional effects resulting from a unit vertical load combined with all side loads.

Loads on the lower aft-support-frame were calculated for the condition of a 100°F temperature difference between the inner and outer surfaces of the segments. These loads then were applied to the upper and lower forward-support-frames, and the upper aft-support-frame. Loads on the frames due to inertial effects were determined by solution of static equations. Frictional and temperature differential loads were determined by the ASIST Program.[34] Results of the analyses are contained in reference 4.

Thermal Loads - The methods of analysis were established by grouping elements of the structure requiring common analysis. The groupings used during the analysis were (1) skin, (2) stringers, (3) frames, and (4) support frames. Each group is discussed below.

1. Skin - The structural concept of the segments was stringer-frame. The spacing of the stringers was established by (1) the ability of 0.030-inch-thick skin to absorb the hydrostatic pressure of the LiH_X resulting from vertical and side loads, and (2) the

allowable stress of 26,500 psi which was equal to the 0.2 percent yield strength at 950°F with a further 6 percent reduction to allow for corrosion by the LiH_x.

The method of calculating skin stresses was to determine equivalent flat plate stresses, including membrane effects, in a uniformly loaded flat plate with fixed boundaries. This analysis utilized the graphs presented in reference 35, and the resultant stresses are contained in reference 36.

2. Stringers - Stresses were determined for several typical stringers in various segments for several loading conditions. For each loading condition, direct, roll, pitch, and yaw accelerations were considered when calculating over-all moments and unit LiH_x pressures. For over-all bending, each segment was taken as a simply supported beam, and the stringer stresses were determined for 1 G_z (vertical) and 1 G_y (horizontal) loads by the equation $S = \frac{Mc}{I}$.

   The method used in resolving the radial and peripheral gradients is described in reference 37. Thermal stresses were determined by the equation

$$\sigma_T = -E\alpha T(y) + \frac{1}{A}\int T(y)dA + \frac{y}{I}\int T(y)\ ydA.$$

   This equation was programmed for the 704 IBM computer.

   The method used in resolving the axial thermal gradients is presented in reference 38. Gradients on a plate were replaced by an equivalent pressure on a clamped plate and the moments on the plate due to pressure were analagous to the stresses of the plate due to thermal gradients.

   Detailed results of these calculations are contained in references 4 and 39.

3. Frames - Typical frames were checked for a series of loading conditions. Load distribution and stresses were determined by using the ASIST Program. Detailed results of this stress analysis are contained in reference 4.

4. Support Frames - Preliminary structural analysis of the forward-upper-left side frame, the aft-upper-left-side frame, and the aft-lower 27.5-degree canted frame is contained in reference 4.

   The ASIST Program could not analyze frames containing webs. For calculation purposes, the forward and aft upper-support-frames were modified by replacing the webs with equivalent trusses of two diagonal members. The cross sectional area of the diagonal members were determined by the formula

$$A = \frac{t\left\{(a^2+b^2)^{3/2}\right\}}{4ab}$$

   where

   A = Area of diagonal
   a = Side of web
   b = Side of web
   t = Thickness of web.

   For square web, the formula reduced to

$$A = \frac{ta}{\sqrt{2}}.$$

   Reference 33 itemizes the distribution of axial, shear, and bending loads; the resultant stresses; and the deflections at various points in each frame.

TABLE 5.11

SIDE SHIELD WEIGHTS

Component	Weight, lb	Moment Arms, inch			Centroidal Moments Of Inertia, lb-inch^2		
		x	y	z	I_{ox-x}	I_{oy-y}	I_{oz-z}
Upper half	5,528	52.90	0	34.00	3,385,000	5,686,000	8,322,000
Lower half	5,443	52.26	-0.16	-33.91	3,346,000	5,551,000	8,150,000
Actuator pads[a]	1,724	-15.16	1.09	- 2.28	2,543,000	1,188,000	1,441,000
Shield cheek[a]	6,041	53.23	0.74	0	12,149,000	5,205,000	17,354,000
A frame	130	82.21	0	50.00	27,000	9,000	19,000
Fittings	69	41.00	0	0	92,000	148,000	176,000
Total	18,935	46.76	0.29	0.31	34,452,000	38,097,000	42,831,000

[a]Non-flight-type component.

5.6.4.3 Weights

Weights of the major components of the side shield are presented in Table 5.11. Figure 5.106 defines the reference lines used in deriving the data shown in Table 5.11. A detailed weight breakdown of the major subassemblies is contained in reference 4.

5.7 MISCELLANEOUS COMPONENT DESIGN DATA

5.7.1 COUPLING SHAFT INSERTS

These inserts were shown in Figure 5.12. They prevented excessive radiation streaming axially through the hollow shaft. Be was selected as the insert material because of its neutron-shielding properties as well as its thermal and mechanical properties. Those portions of the inserts adjacent to the reactor end reflectors were made of unborated Be. The remainder was borated (1 weight percent natural boron) to reduce gradients in the secondary heating rates of adjacent regions in the front and rear shields. If the shaft inserts had been unborated, a large buildup of thermal neutron flux would have resulted, causing a high $(n-\alpha)$ heating rate in adjacent borated regions. The boron additive also served to lower the $(n-\gamma)$ reactions in the shaft and surrounding structural materials, thereby reducing secondary gamma-ray radiation levels and heating rates.

Secondary heating rates in the inserts were calculated using the methods described in section 5.9. Detailed plots of the calculated heating rates are contained in references 4 and 40. They were cooled by ninth-stage compressor bleed-air passing through axial holes machined into the inserts. Since Be has a lower coefficient of expansion than the shaft material (A-286), the inserts could not be attached mechanically to the coupling shaft. Instead, they were mounted on torsional springs designed so that the natural frequencies of the parts were above operating frequencies.

5.7.2 PRESSURE VESSEL ASSEMBLY

5.7.2.1 Mechanical

The pressure-vessel assembly, consisting of the pressure vessel, the triple-flange assembly, and the front-shield cone, formed the backbone of the reactor-shield assembly.

Figure 5.13 showed the pressure vessel. It was a cylindrical shell flanged at each end and approximately 68 inches in diameter. The over-all length was approximately 76 inches.

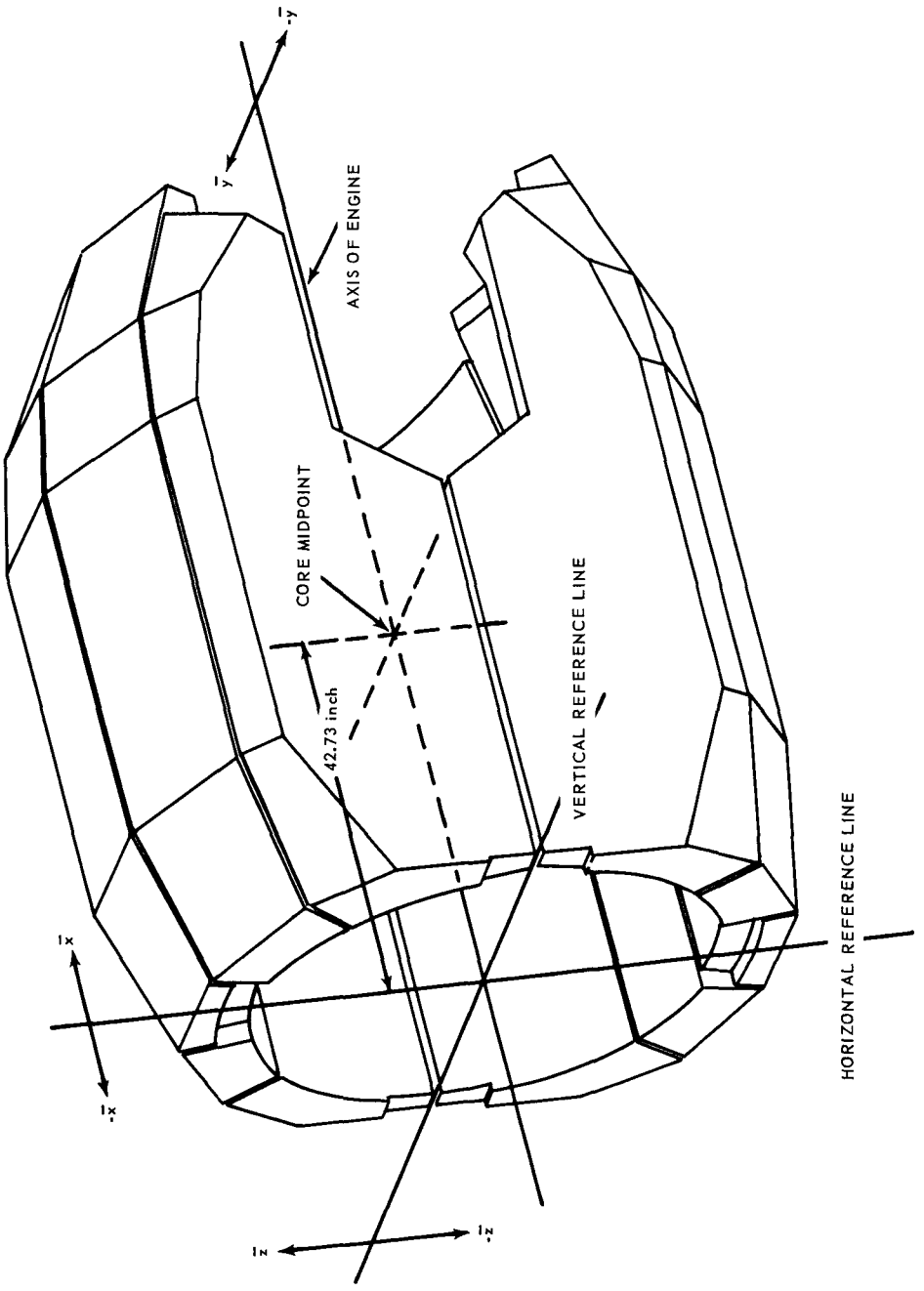

Fig. 5.106 — Reference lines for side shield weight analysis

External support lugs were located around the periphery near the forward flange; these lugs were intended for support during remote handling procedures. Internal mounting devices near the front end supported the forward ring of shielding material in the front shield outer section.

The pressure vessel was designed to meet the restraints of its most critical operating condition, i.e., flight condition No. 2, maximum acceleration to "q" limit, maximum power limit, cold day. During this flight condition, the compressor discharge pressure was 220 psia. Inconel X was used for the shell and the flanges.

The aft flange was conventionally designed but the forward flange, which formed the main triple-flange assembly of the reactor-shield assembly, was a different concept, utilizing barrel-nut connections. Details of this flange are shown in Figure 5.107.

5.7.2.2 Aerothermal

During operation the vessel was cooled on its inside surface by bleed-speed air. The maximum temperature level was 838°F and the maximum longitudinal temperature differential was 38°F.

Transient analysis studied the locked rotor condition, followed by reactor scram with aftercooling-air flow of 25 pounds per second instantaneously initiated. This analysis indicated that transient temperatures of the pressure vessel never exceeded steady-state temperatures. The radial differential temperatures were 113°F in the forward flange and 202°F in the aft flange.

5.7.2.3 Stress and Weight

Stresses calculated for operation at the "worst" condition included inertial, vibratory, pressure, and thermal. Combined stresses, together with the margins of safety, are contained in reference 4. Weights are listed in Table 5.12.

5.7.3 STATIC AIR SEALS

Static air seals were used to maintain the required pressure in the system, and were used at locations inaccessible for normal flanged fasteners. They permitted adjacent components to deflect, allowed for manufacturing tolerance stackup, and reduced mechanical and thermal loads. The nine seals listed in Table 5.13 are described.

5.7.3.1 Front-Shield Seals

Seal Nos. 1 and 10, listed in Table 5.13, were located in the front shield.

Front-Shield Central Island - Reactor Liner Seal - This seal, No. 1 in Table 5.13, was located between the aft end of the front-shield central island and the forward portion of the core liner near the tunnel. The purpose of the seal was to separate primary-air in the front-shield annulus from the front-shield central-island cooling air being channelled to the rear-shield forward central island. Details of this seal are shown in Figure 5.108.

This seal consisted of a piston, piston ring, and cylinder assembly. The cylinder housing was attached in four places to the central island. The piston-ring retainer was a part of, and attached to, the forward end of the reactor core liner. Over-all, the seal was 16 inches in diameter and 2 inches long. The cylinder was made of Inconel with a proprietary chromalizing diffusion surface treatment to provide a hard-wearing surface. The ring retainer was Inconel with the same surface treatment as that given the cylinder. The piston ring was L605 (Haynes No. 25 alloy). The maximum operating temperature was 878°F with a thermal gradient of 100°F. When exposed to engine vibration frequency, the seal vibration amplitude was 0.004 inch.

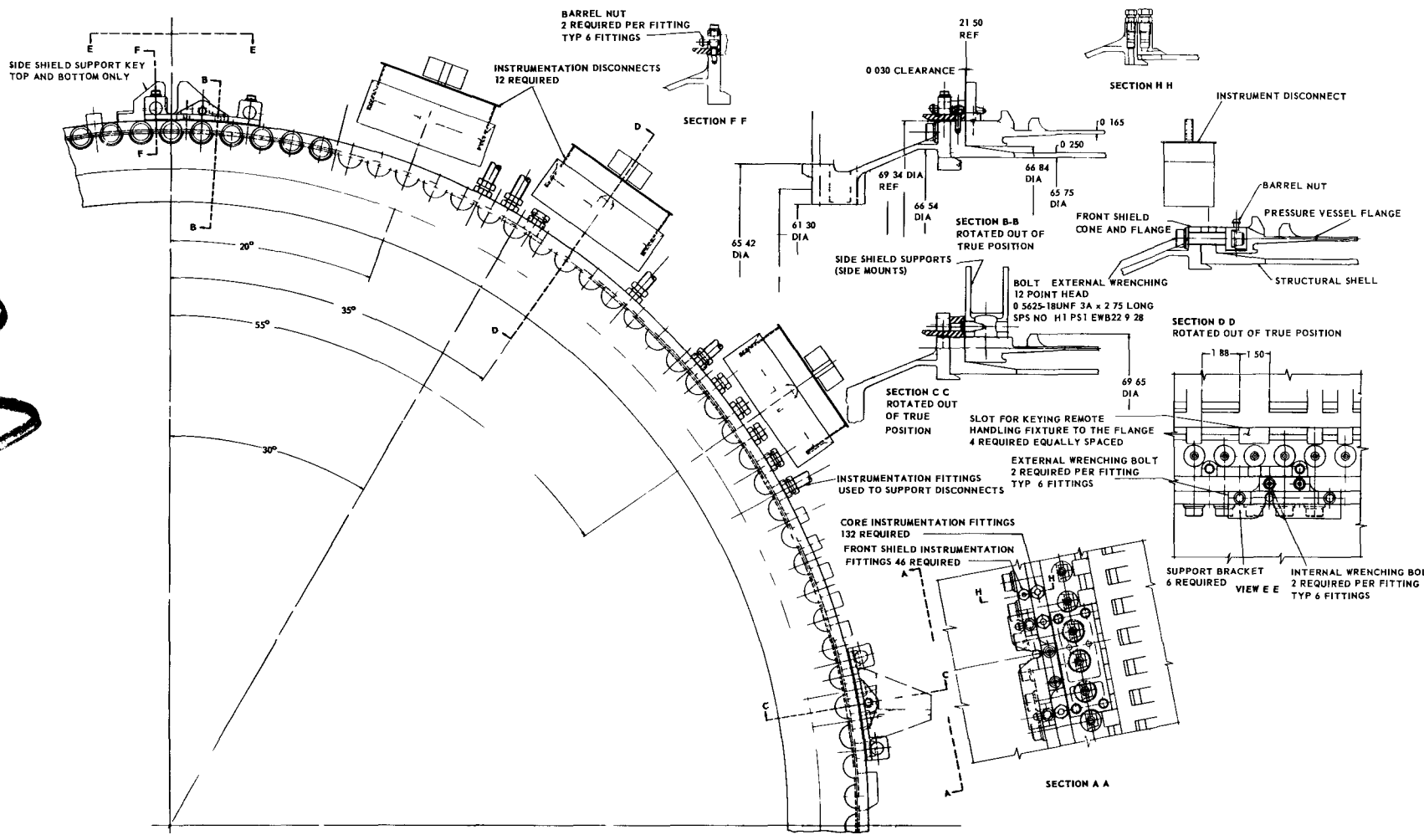

Fig. 5.107 – Triple-flange assembly (Dwg. 207R831)

TABLE 5.12

PRESSURE VESSEL WEIGHTS

Component	Weight, lb
Cylindrical shell	760
Forward flange	189
Aft flange	134
Brackets	1
Weldments	12
Total	1096

TABLE 5.13

XNJ140E-1 STATIC AIR SEALS

Number	Location And Name	Purpose
1	Front-shield central island - Reactor liner seal (Figure 5.108)	Separate primary air from shield cooling air (front shield to rear shield)
3	Rear-shield outer section - Turbine front-frame seal (Figure 5.110)	Separate primary air from bleed-speed air
4	Reactor liner - Rear-shield forward central-island seal (Figure 5.110)	Separate primary airflow from shield cooling air (front shield to rear shield)
5	Shaft tunnel - Rear-shield forward central-island seal (Figure 5.110)	Separate shield cooling air (front shield to rear shield) from tunnel-purge and strut-segment air
6	Rear-shield forward central island - Turbine front-frame duct-wall seal (Figure 5.110)	Separate shield cooling air (front shield to rear shield) from tunnel-purge and strut-segment air
7	Rear-shield forward central-island duct wall - Forward central-island shield-material seal (Figure 5.110)	Route shield cooling air (front shield to rear shield) through forward central island of rear shield
8	Rear-shield forward central island - Turbine front-frame seal (Figure 5.110)	Route tunnel-purge and strut-segment cooling air through strut segments
9	Rear-shield aft central island - Combustor inner-liner seal (Figure 5.110)	Route turbine-front-frame-strut and aft-central-island cooling air through aft central-island shield
10	Compressor rear frame - Front-shield central-island seal (Figure 5.109)	Separate tunnel-purge and strut-segment cooling air from compressor rear-frame cavity

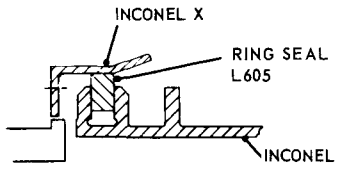

Fig. 5.108 – Air seal No. 1

Compressor Rear Frame - Front-Shield Central-Island Seal - This seal, No. 10 in Table 5.13, is shown in Figure 5.109. It contained a diaphragm that consisted of a thin, sheet-metal circular section with circumferential corrugations. The outer edge was bolted to the forward face of the front shield. The inner edge was deflection-loaded against a wear plate. The wear plate was bolted to the flange of the No. 2 sump aft labyrinth-air-seal. The diaphragm was made from age-hardened Inconel X. The wear plate was made from Inconel. A hard-wearing surface was provided on both parts by utilizing a proprietary chromalizing diffusion surface treatment. The maximum operating temperature was 788°F with a thermal gradient of 10°F. When exposed to engine vibration frequencies, the amplitude of the seal vibration was 0.005 inch.

5.7.3.2 Rear-Shield Seals

Seven static air seals, Nos. 3 through 9 in Table 5.13, were located in the rear-shield area. Typical seals, Nos. 3 and 8, are shown in Figure 5.110. Figure 5.111 shows the locations of these seals.

5.8 COMPONENT TESTING

5.8.1 FRONT SHIELD

5.8.1.1 Mechanical

The major portion of structural testing for the front shield was directed toward determining the ability of Be to double as a structural component, principally in furnishing its own support and resisting thermal loads caused by temperature gradients. Previous structural uses of this material were very limited.

Be Circular Disc with Radial Thermal Gradient - A series of tests was conducted on pierced Be discs with an imposed radial temperature gradient to determine the ability of Be shapes to sustain thermal stress, thermal shock, and low-cycle thermal fatigue. The results of these tests are contained in reference 41.

Figure 5.112 shows a photograph of the test setup with a Be test piece in position for thermal cycling. Heat was produced in the outer circumference of the disc by the magnetic field of the four-turn induction coil. A 1-inch-diameter hole through which cooling water was circulated was located in the center. The cooling water was in intimate contact with the inner circumference and flowed continuously during the cycling tests. Heat was applied at a uniform rate until a specified radial temperature gradient was reached. The heat then was turned off and the temperature dropped until a specified temperature level was reached. At this time, heat again was applied, and cycling was continued.

The test philosophy required that each successive specimen tested have its thermal gradient either increased or decreased a definite amount, depending on whether or not the previous specimen survived a definite number of cycles (of thermally induced stress).

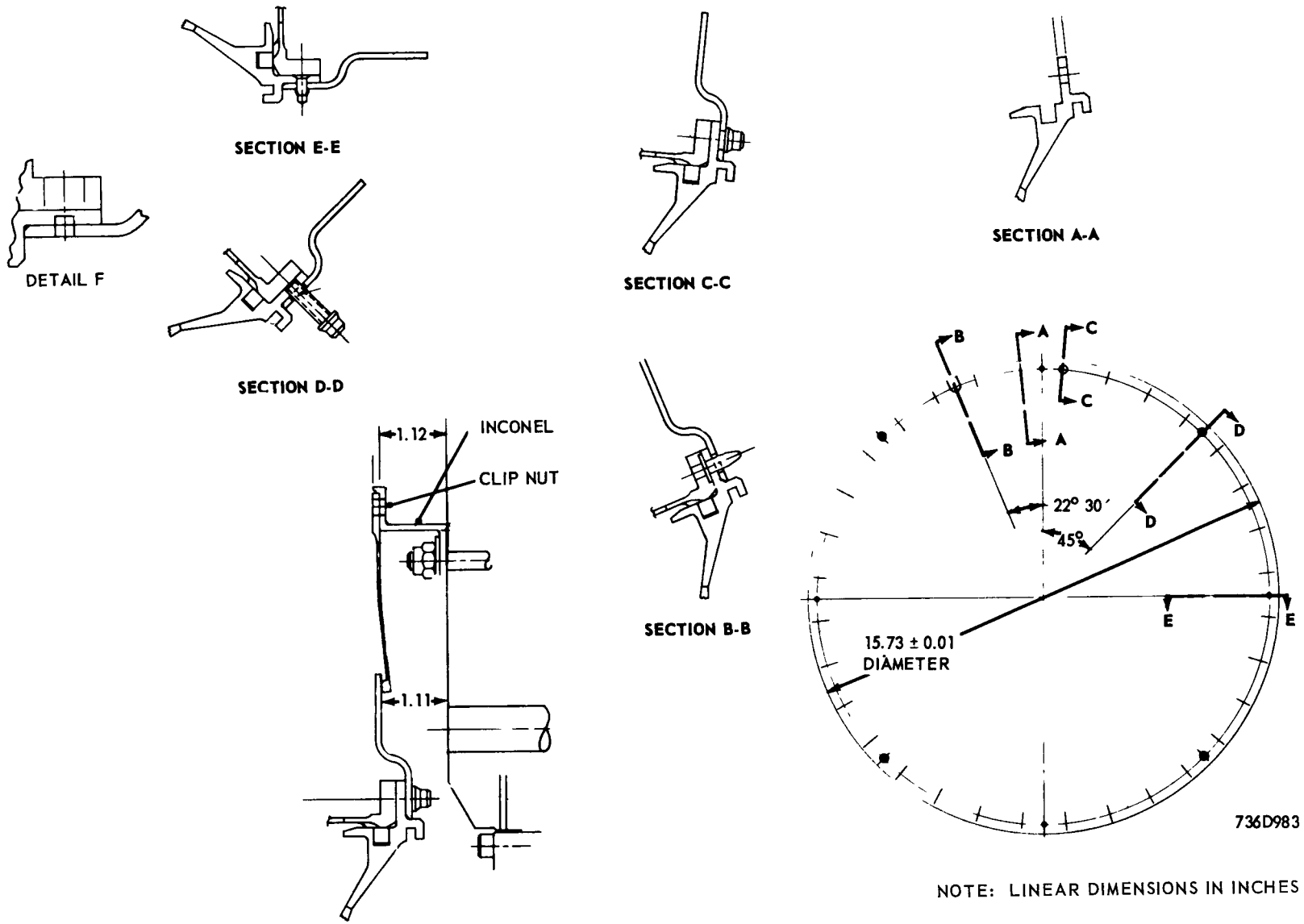

NOTE: LINEAR DIMENSIONS IN INCHES

Fig. 5.109 – Air seal No. 10 (Dwg. 736D983)

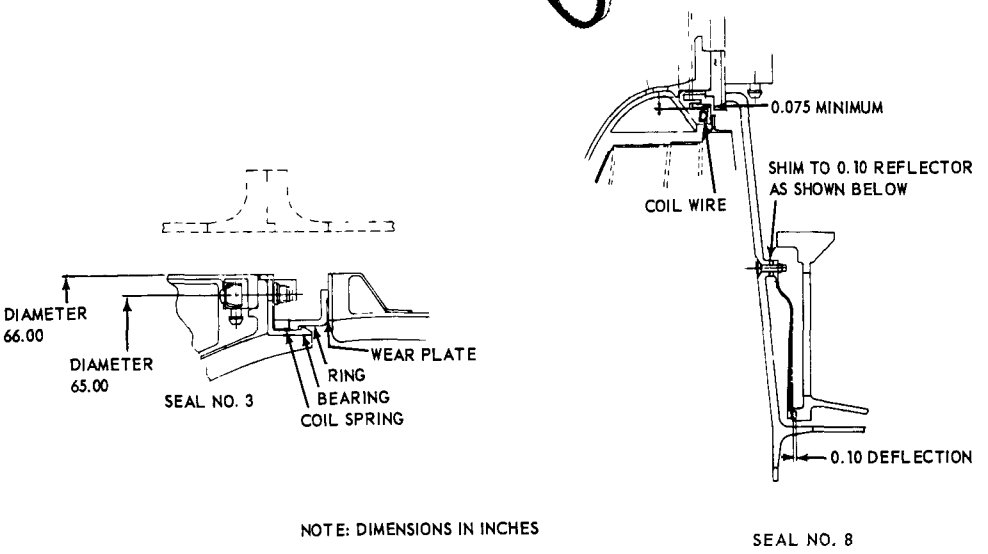

Fig. 5.110 – Typical rear shield air seals

The increment (or decrement) used in this investigation was 50°F; the number of cycles was 500. Reference 42 describes the theory of this test procedure.

Be Mechanical Fasteners - A test program was initiated to investigate the ability of tapped holes in Be, with and without inserts, to resist loads introduced by an inserted stud. The program was completed studying tapped holes without inserts, but the test program was cancelled before work was started on the insert study. Although the study of mechanical fasteners was not carried to a point where definite conclusions were possible, the results obtained were encouraging. The use of threaded inserts was successfully demonstrated. The results of this test are contained in reference 43.

5.8.1.2 Aerothermal

Aerothermal developmental testing was performed to satisfy the following objectives:

1. Determine the optimum shape of the core inlet header
2. Establish the stability of the cooling flow circuitry and determine the discrete flow variation through the radial cooling passages
3. Determine the pressure drop in the bleed-speed annulus as a function of rate of airflow
4. Determine the dynamic flow characteristics of the aftercooling-air entry system wherein airflow direction was reversed through the bleed-speed annulus.

The following three significant tests are discussed:

Test	Mockup Used	Facility Used
1. Scaled primary-air duct	Plastic cold-flow model of primary flow system	Gas Dynamic Facility - II
2. 60-degree sector of front duct	Full-scale 60-degree plastic model of third iteration cooling circuitry	Gas Dynamic Facility - I
3. 90-degree sector of bleed-speed annulus	Full-scale 90-degree plastic model	Gas Dynamic Facility - I

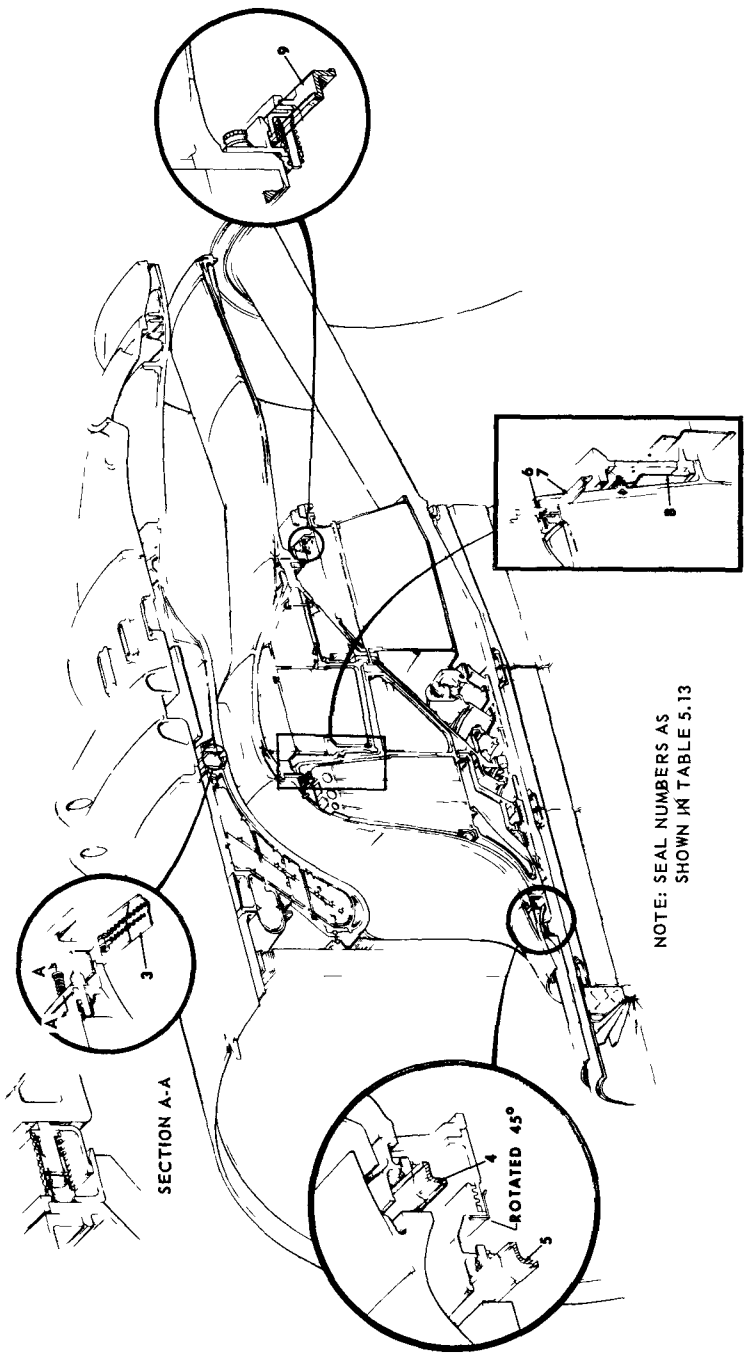

Fig. 5.111 – Location of rear shield air seals (Dwg. DI576)

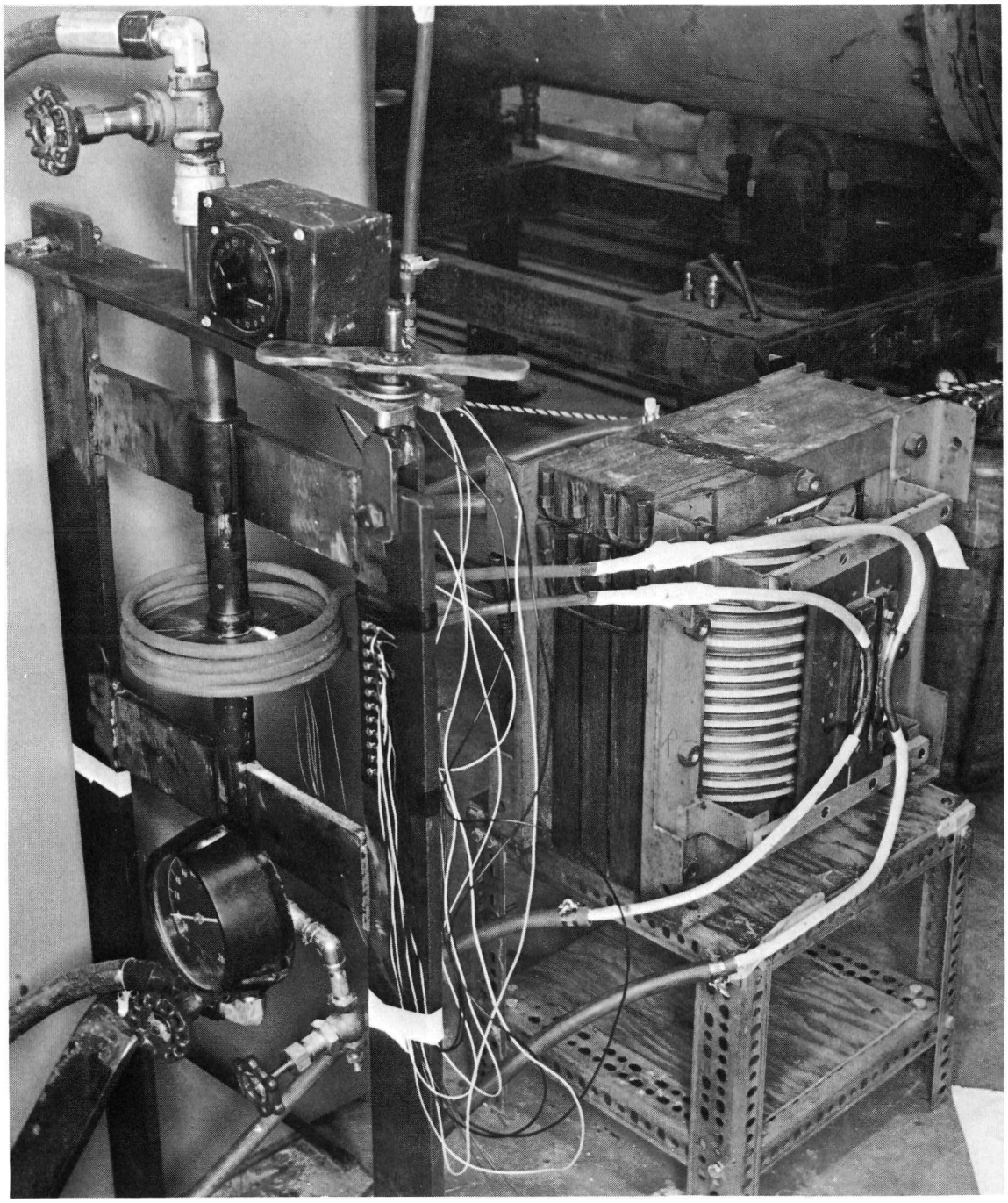

Fig. 5.112 – Beryllium disc testing using radial thermal gradients (Neg. U38893C)

Scaled Primary-Air Duct - The objectives of this test were to establish header and collector profiles which led to an acceptably uniform flow distribution within the reactor, in both radial and circumferential directions, while yielding the lowest practical pressure loss for the primary-air duct system. In order to integrate the requirements of nuclear shielding, structural design, control rod location, component cooling, and primary-cycle aerodynamic requirements, the annular ducts followed a devious flow path within the pressure vessel and required careful design. Figure 5.113 gives a schematic diagram of the test model. Station 1 corresponded to engine station 3.0, station 3 corresponded to station 3.5; station 7 corresponded to station 3.7, and station 8 corresponded to station 4.0. Other stations did not have correspondence with engine stations. Results of this test program are reported in references 4 and 44.

60-degree Sector of Front Duct - A 60-degree full-size model of (1) the primary-air duct through the front shield, and (2) the central-island cooling passages was used in this test program. The objectives of the program were as follows:

1. Determine static pressure distributions along the surfaces of the primary-air duct
2. Establish the stability (or direction) of flow through the central-island cooling channels as a function of rate of flow
3. Determine the percent of primary air which could be extracted within the limits of the 0.94 pressure ratio
4. Determine airflow in each of the radial cooling slots as a function of their width.

Results of this test program are contained in references 4, 45, 46, 47, and 48.

90-Degree Sector of the Bleed-Speed Annulus - A model of a 90-degree sector of the front primary-air duct and the bleed-speed annulus was designed, and fabrication was partially completed at the time of contract termination. A data reduction computer program also was partially completed.

The objectives of this test were as follows:

1. Determine the pressure-loss characteristics of the bleed-speed annulus during normal engine operation, and during those modes of aftercooling wherein aftercooling air would be flowing forward to the front primary-air duct and then to the reactor and rear shield.

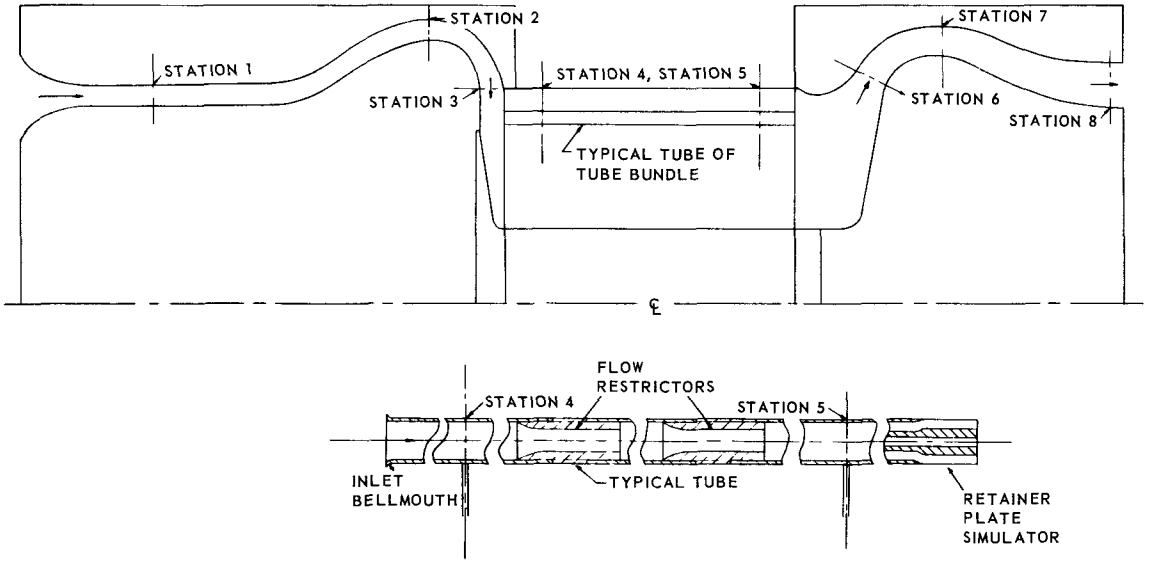

Fig. 5.113 – Model used in scaled primary-air duct test

2. Determine flow distribution across the forward face of the reactor during both normal airflow and afterheat-removal-system airflow.

The details of this test program are discussed in reference 4.

5.8.2 REAR SHIELD

5.8.2.1 Mechanical

Structural testing supporting the rear shield design was directed toward experimental verification of stress analysis of structural components, and proof-testing of the insulation pads and inner duct wall.

Inner Duct Wall - Stresses and deflection of the inner duct wall under thermal and mechanical loading, and the allowable buckling load for this element were studied. Experimental stresses were in good agreement with analytical values. The test for buckling load had not been completed at the time of contract termination. The test mockup is shown in Figure 5.114. Test results are contained in reference 49, and, in general, showed that the design was adequate.

Insulation Pads - The stresses due to mechanical loads applied to a typical insulation pad were analyzed experimentally, and are reported in reference 50. A proof-test using cyclic thermal loading due to a fluctuating temperature gradient had not been completed at the time of contract termination.

5.8.2.2 Aerothermal

The objectives of aerothermal testing were as follows:

1. Determine temperature profiles on insulation surfaces
2. Determine penetration of hot streaks at various radial locations, velocity distributions in the rear duct, and static pressure distributions on the annular duct surfaces
3. Determine the optimum core-exit header shape
4. Determine the adequacy of the rear shield cooling-channel design.

The following significant tests were performed in support of the rear shield aerothermal design:

Test	Mockup Used	Facility Used
Full-scale rear duct	Full-scale plastic model with simulated inlet grid	FPLD
Scaled primary duct	Plastic cold-flow model of primary flow system	GDF-II
60-degree sector of rear shield	Full-scale plastic model	GDF-I

Full-Scale Rear Duct - This test produced experimental data relative to static pressure distribution on the annular surfaces, as well as some total pressure data and some film cooling data. Figure 5.115 shows the test mockup installed in the test stand. Details of the test program and test data are contained in references 4 and 51.

Scaled Primary Duct - The details of this program were discussed in section 5.8.1.2.

Sixty-degree Sector of Rear Shield - The purpose of this test was to determine pressure and flow distribution characteristics of the internal cooling passages for various rates of airflow and various amounts of cooling air bled off for insulation cooling. The results of this test program were limited, and are contained in reference 52.

TOP VIEW U-38892C

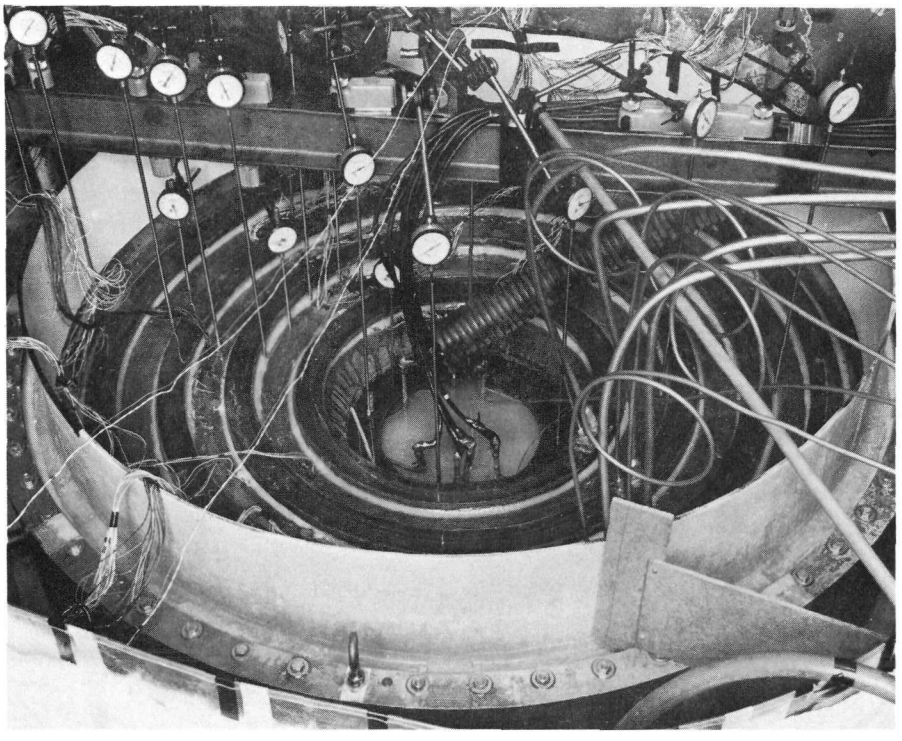

SIDE VIEW U-38938B

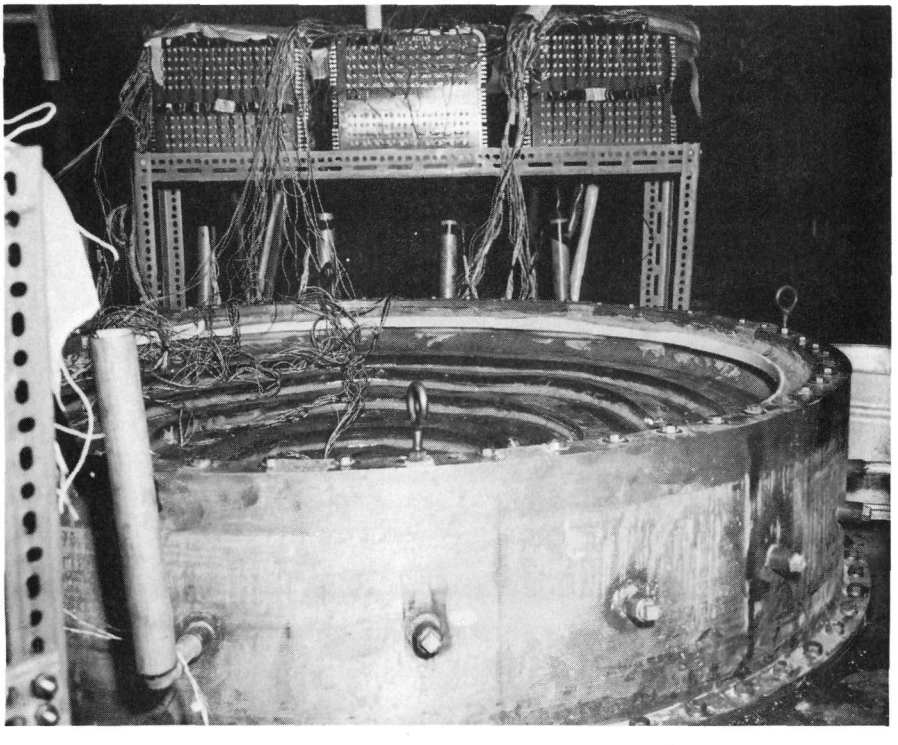

Fig. 5.114 – Test mockup for rear shield inner duct wall test program (Neg. U38892C and U38938B)

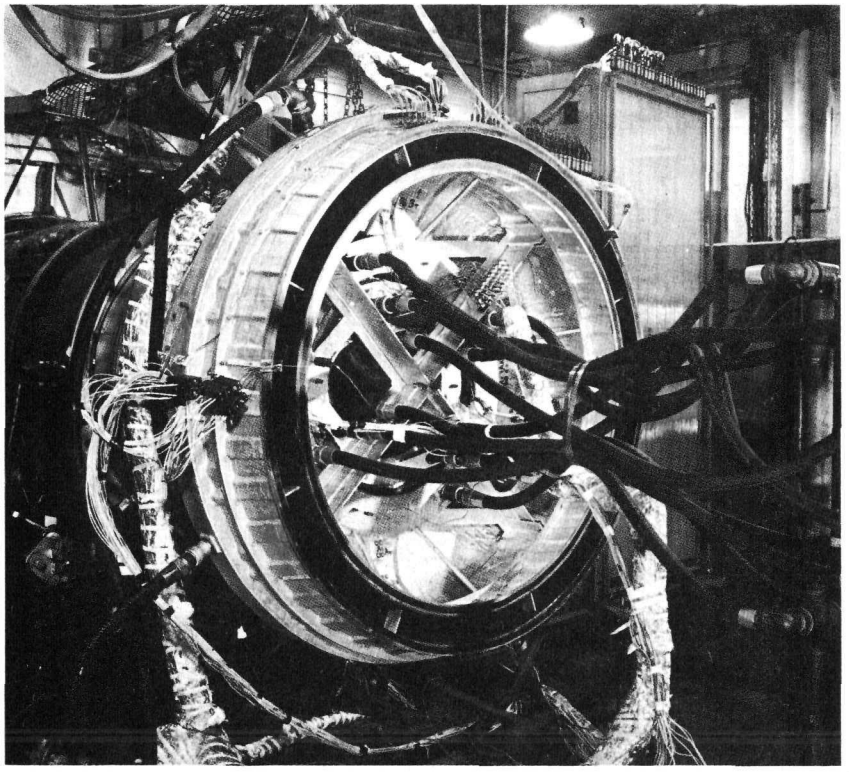

Fig. 5.115 – Full scale rear duct test mockup

5.8.3 SIDE SHIELD

5.8.3.1 Mechanical

Structural testing of components in the side shield was directed towards (1) verification of the stress analysis of the cans, and (2) proof-testing specimens under simulated operating conditions. Welding techniques for 19-9DL stainless steel, particularly spot-welding of sheet material, were studied. To supplement this study, additional tests investigated the effect of molten LiH_X corrosion on the strength of the welds. The status of these programs is discussed in reference 53.

5.8.3.2 Aerothermal

Aerothermal testing was concentrated on studying the thermal conductivity of LiH_X and various methods of improving heat transfer from the bulk LiH_X to the surface of the cooling tubes. Specific tests are identified below.

Heat Transfer Tests on Small Cylindrical Cans Containing LiH_X - The purpose of these tests was to determine the effective thermal conductivity of cast LiH_X as it existed in the nonhomogeneous (cracked) condition, and to evaluate the influence of:

1. Temperature level
2. Various inert gases filling the cracks and LiH_X - metal interfaces
3. Thermal cycling
4. Finning the coolant tube.

These tests, described in references 54, 55, and 56, showed that the thermal conductivity of LiH_X decreased with increasing temperature. The thermal conductivity of a LiH_X matrix was dependent upon a gas filling the cracks and voids. Introduction of an inert gas

(as contrasted to a vacuum) within the interstitial cracks in the LiH_x matrix, and in the LiH_x - metal interface tended to raise the heat transfer by a factor of 1.3, and the over-all effective conductivity (including metal container, cooling tube, and contact resistances) by a factor of 2.7. Continued thermal cycling tended to change the crack pattern from one of reasonable uniformity to one of fracturing at discrete longitudinal locations, but did not appreciably affect the over-all thermal properties of a gas-filled test specimen.

Extending metallic spirally-finned heat transfer surfaces into the LiH_x improved the over-all effective thermal conductivity by a factor of 2.3. Adding an inert gas and finned surfaces increased the over-all effective thermal conductivity by a factor of 3.4.

Heat Transfer Tests of Small Hexagonal Cans Containing LiH_x - The purpose of these tests was to determine the effects of nonsymmetry in the shape of the casting and in the spacing of cooling tubes as measured by changes in the effective thermal conductivity. The tests, described in references 29 and 54 through 56, showed that changing the shape of the test specimen from a cylinder to a hexagon and adding more coolant tubes did not alter the thermal conductivity of the specimen on an over-all basis. Local values of thermal conductivity (i.e., between coolant tubes) were not measured due to limitations of the closely packed instrumentation.

Full Size Segment Irradiation Test - The purpose of this test was to obtain operating experience on a prototype segment prior to full-power engine testing. A search for possible trouble areas was planned. System response to, and synergistic effects of, combined aerothermal, nuclear, and mechanical loadings were to be studied. The test site selected was the Georgia Nuclear Laboratories, Dawsonville, Georgia, under the supervision of Lockheed Aircraft Corporation. The Radiation Effects Reactor (RER) was to be utilized as the nuclear source.

Detailed planning for this test is described in references 57 through 61. Testing had not been started.

5.9 NUCLEAR ANALYSIS

5.9.1 METHODS OF COMPUTING DIRECT-BEAM DOSE RATES

Shielding computer program 14-0[14] was used for computing direct-beam neutron and gamma-ray dose rates. This program performed radiation penetration calculations along line-of-sight paths from each of numerous source point locations to a specified receiver or detector point location. It then integrated the line-of-sight calculations over the reactor volume to get the total effect of the entire source.

Reactor and shield geometries were described by combinations of regions formed by rotating rectangles and trapezoids about the reactor-shield assembly axis. The description obtained was referred to as the nuclear model. Program 14-0 could treat regions partially or fully rotated about axes parallel to the model axis, but only cylindrically symmetric zones about the axis were used to describe the XNJ140E-1 reactor-shield assembly.

To compute attenuation along a line-of-sight path from source to receiver point, the program stepped through the various regions of the model, determined the types and thicknesses of materials encountered, and used this information in functional form. The nature of the function was dependent upon the type of radiation and the nuclear reaction being considered. The resultant effect of all paths to a single receiver point was determined by a trapezoidal integration, at that point, over the source volume taking source intensity and relative distribution into account.

5.9.1.1 Neutron Dose Rates

Program 14-0 computation of neutron dose rates was performed by an equation that was not energy dependent. The calculated neutron dose rate was that due to fission neutrons of all energies.

The equation used in Program 14-0 was as follows:

$$D_n = C \int_{Z_{si}}^{Z_{su}} S(z)\,dz \int_{r_{si}}^{r_{su}} r\,S(r)\,dr \int_{\phi_{si}}^{\phi_{su}} \frac{\Psi_n(\Sigma_m, \rho_m)}{4\pi\rho^2}\,d\phi \qquad (1)$$

where

D_n = fast neutron dose rate, rads (ethylene)/hr-mw
$S(r), S(z)$ = functions describing the radial and longitudinal variation in source strength (generally reactor power profile)
C = multiplying factor, generally included power density per megawatt of reactor power, watt/cm^3-mw
$\Psi_n(\Sigma_m, \rho_m)$ = material attenuation function including the fission source-to-dose conversion, rads (ethylene)-cm^2/hr-watt
$1/4\pi\rho^2$ = geometric attenuation for a distance ρ from source point to receiver point, 1/cm^2

Integration over the source volume was performed from lower to upper limits of the source region space coordinates ϕ, r, and z, taking into account the source variation over the core. Section 5.9.4 contains the S(z) and S(r) values used in the detailed calculations.

The material attenuation function, $\Psi_n(\Sigma_m, \rho_m)$, was a function of material nuclear properties and thicknesses, and therefore varied over ϕ, r, and z with further differences in source-receiver path length and materials encountered along the line-of-sight. Two forms of this function were used, dependent upon the amount of hydrogeneous material present along a given path. The equivalent water thickness, α_6, was 8.262 cm for water and 10.11 cm for LiH_X.

The values used were as follows:

α_6 = equivalent water thickness, cm
ρ_m = path length through material m, cm
$\eta_m = \dfrac{\text{hydrogen density in material m}}{\text{hydrogen density in } H_2O}$
Σ_m = macroscopic fast neutron removal cross section for the non hydrogenous constituents of material m, cm^{-1}
M = total number of materials

The first form, a modified Albert-Welton kernel, was used for thicknesses of hydrogenous materials greater than an equivalent water thickness. For

$$\alpha_6 < \sum_{m=1}^{M} \rho_m \eta_m \qquad (2)$$

$$\Psi_n(\Sigma_m, \rho_m) = \alpha_1 \left[\sum_{m=1}^{M} \rho_m \eta_m\right]^{\alpha_2} \exp\left[-\alpha_3 \left(\sum_{m=1}^{M} \rho_m \eta_m\right)^{\alpha_4}\right] \exp\left[-\sum_{m=1}^{M} \rho_m \Sigma_m\right] \qquad (3)$$

Monte Carlo calculations[62] indicated that fast-neutron dose rates at receiver points distant from surfaces of finite LiH_X spheres surrounding point fission sources differed from fast-neutron dose rates at a corresponding LiH_X thickness in an infinite LiH_X media by a factor of 0.71 (over and above the effects of geometrical attenuation). Therefore, a correction factor was applied when using equation (3) for receiver points within, and external to, the side shield. For external dose rate calculations, the constant α_1 was reduced by 30 percent.

For nuclear analysis involving use of equation (3), the following constants were used:

Internal	External
$\alpha_1 = 2.212 \times 10^6 \frac{\text{rads (ethylene) - cm}^2}{\text{hr-watt}}$	$\alpha_1 = 1.548 \times 10^6 \frac{\text{rads (ethylene) - cm}^2}{\text{hr-watt}}$
$\alpha_2 = 0.34921$	
$\alpha_3 = 0.42231$	
$\alpha_4 = 0.69842$	

The second form of the neutron material attenuation function was used for source-receiver paths which encountered hydrogenous material equal to, or less than, an equivalent water thickness. For

$$\alpha_6 \geq \sum_{m=1}^{M} \rho_m \eta_m \tag{4}$$

$$\Psi_n (\Sigma_m, \rho_m) = \alpha_5 \exp\left[-\alpha_7 \sum_{m=1}^{M} \rho_m \eta_m\right] \exp\left[-\sum_{m=1}^{M} \rho_m \Sigma_m\right]. \tag{5}$$

For nuclear analysis involving use of equation (5) the following constants were used:

Internal	External
$\alpha_5 = 4.46 \times 10^6 \frac{\text{rads (ethylene)-cm}^2}{\text{hr-watt}}$	$\alpha_5 = 2.39 \times 10^6 \frac{\text{rads (ethylene)-cm}^2}{\text{hr-watt}}$
$\alpha_7 = 0.2188$	$\alpha_7 = 0.1863$

For a path containing no hydrogenous material ($\eta_m = 0$), equation (5) reduced to a straight exponential; i. e.,

$$\Psi_n (\Sigma_m, \rho_m) = \alpha_5 \exp\left[-\sum_{m=1}^{M} \rho_m \Sigma_m\right] \tag{6}$$

The use of different internal and external constants was based on the results of analytical studies of neutron penetration from point fission sources in infinite and finite media. This methodology is discussed in APEX-918, "Reactor and Shield Physics."

Because of the combined nuclear and geometric characteristics of the core and end shields, situations were often encountered wherein the thicknesses of hydrogenous material encountered were considerably less than the constant α_6. Accordingly, the constants used in equation (5) were modified to fit attenuation data of Be and BeO. Be and BeO kernel constants were derived from moments-method calculations involving data relative to neutrons from a point fission source penetrating infinite media of Be and BeO.[63] The penetration data followed an exponential fit at thicknesses greater than 10 cm.

Similar to data for LiH_X, Monte Carlo fast-neutron penetration data for finite Be and BeO media were found to be approximately one-half the values for analogous infinite media calculations; therefore, the constant α_5 was modified depending upon whether receiver points were inside the shield or external to it.

The two kernel equations (3) and (5) were equivalent when

$$\sum_{m=1}^{M} \rho_m \eta_m = \alpha_6,$$

and

$$\alpha_7 = \frac{-1}{\sum_{m=1}^{M} \rho_m \eta_m} \left[\ln\left(\frac{\alpha_1}{\alpha_5}\right) + \alpha_2 \ln\left(\sum_{m=1}^{M} \rho_m \eta_m\right) - \alpha_3 \left(\sum_{m=1}^{M} \rho_m \eta_m\right)^{\alpha_4} \right]$$

Fast-neutron removal cross sections for Be and BeO were found to be consistent with the kernel constants for equation (5). If the neutron penetration data were plotted as a function of surface density (material density times the material thickness), the neutron attenuation function (removal cross section divided by the material density) numerically equalled the slope of the exponential fit to the experimental neutron penetration data. Since the neutron penetration data did not exactly fit the exponential, the slopes of the fits were adjusted to close- and distant-portions of the penetration data curves for internal and external calculations, respectively. Internal and external removal cross sections used in the analysis are listed in section 5.9.4.

5.9.1.2 Gamma-Ray Dose Rates

Program 14-0 computation of gamma-ray dose rates was performed by an energy dependent equation that considered j groups of gamma rays, each group having an average energy of E_j. In most cases, 13 energy groups were used for gamma rays emitted during nuclear operation and 7 groups for shutdown gamma rays. The following equation was used:

$$D_\gamma = C \sum_{j=1}^{J} K(E_j)\, \Gamma(E_j) \int_{z_{s_\ell}}^{z_{s_u}} S(z)\, dz \int_{r_{si}}^{r_{su}} r\, S(r)\, dr \int_{\phi_{si}}^{\phi_{su}} \frac{\Psi_\gamma(\mu_m(E_j)\rho_m)}{4\pi\rho^2}\, d\phi \qquad (7)$$

where

$D\gamma$ = gamma-ray dose rate, rads (carbon)/hr-mw
$\Gamma(E_j)$ = gamma-ray source intensity term for energy group j, Mev/watt-sec
$K(E_j)$ = flux-to-dose conversion factor for gamma rays of energy E_j, rads (carbon)/hr, divided by Mev/cm^2-sec
$\Psi\gamma(\mu_m(E_j)\rho_m$ = material attenuation function for gamma rays
C = multiplying factor*

The remaining symbols were previously defined.

The gamma ray attenuation function was computed for each source receiver path, and for each of the j energy groups. Trapezoidal integration was performed over the entire source region and the gamma-ray dose rate for each group was obtained. Summation over all groups resulted in the total gamma-ray dose rate. Values of $\Gamma(E_j)$ and $K(E_j)$ used in this study are given in section 5.9.4. The source intensity term, $\Gamma(E_j)$, included prompt-fission gamma rays, fission-product-decay gamma rays (assuming saturated activity), and core-capture gamma rays.

*The multiplying factor, or symmetry constant, is discussed in APEX-918.

The gamma ray attenuation function was given by the formula

$$\Psi_\gamma(\mu_m(E_j)\rho_m) = B\,(\mu_m(E_j)\rho_m) \cdot \exp\left[-\sum_{m=1}^{M} \rho_m \mu_m(E_j)\right], \qquad (8)$$

wherein B was a dose buildup factor and the other symbols were as previously defined.

The dose buildup factor, B, accounted for the contribution due to scattering. Its magnitude along each source-to-receiver path was dependent on types, arrangement, and thicknesses of materials encountered; and on the initial photon energy. The factor was computed by Shield Program 14-0, using polynominal expressions for which constants were supplied as input data. For this analysis iron and water buildup factors, taken from the reference 64 "heavy followed by light" case, were used. The exponential term computed the uncollided gamma-ray flux by using the linear gamma-ray total absorption coefficients listed in section 5. 9. 4.

5. 9. 2 METHODS OF COMPUTING DUCT SCATTERING

The methods used for calculating the duct-scattered contribution to the total neutron and gamma dose rates are described in APEX-918, "Reactor and Shield Physics."

5. 9. 3 METHODS OF CALCULATING SECONDARY HEATING RATES

Secondary heat was generated in nonfueled portions of the reactor-shield assembly due to (1) absorption of core-originated gamma rays, (2) kinetic energy loss of fast neutrons, and (3) n-α reactions in B^{10} and Li^6. Methods used for calculating secondary heating due to these sources are described below. Other sources of secondary heating, e. g., n-γ reactions, were minor and were neglected in this analysis.

5. 9. 3. 1 Absorption of Core-Originated Gamma Rays

These heating rates were calculated using Shielding Program 14-0. The method was similar to the gamma-ray dose rate method described in section 5. 9. 1. 2; computations involved equations (7) and (8) with different input data for some terms.

The gamma ray source data used were the same as those used in dose rate computations. Since the only gamma ray sources considered were within the active core, the gamma-ray heating rates were designated as due to core-originated gamma rays. For the material attenuation function, $\Psi\gamma$, the total gamma-ray absorption coefficients used were similar to those used in dose rate calculations, but energy absorption buildup factors replaced dose rate buildup factors. Mass gamma-ray absorption coefficients were used in place of the flux-to-dose conversion factor, $K(E_j)$, used for dose rate calculations. These mass gamma-ray absorption coefficients are given in reference 65.

Gamma ray energy fluxes were determined for 13 energy groups based on total gamma-ray absorption coefficients and energy absorption buildup. The gamma-ray energy flux for each group was multiplied by the mass gamma ray energy absorption coefficient for the material present at the particular location. Summation over 13 energy groups and multiplication by appropriate conversion factors (included in the multiplying factor, C) gave the total heating rate in units of watts of energy deposited per gram of material per watt (or megawatt) of reactor power.

5. 9. 3. 2 Kinetic Energy Loss of Fast Neutrons

Detailed knowledge of the spatial and spectral distribution of fast neutron flux throughout the shield was required to calculate secondary heating due to loss of kinetic energy, or moderation, of fast neutrons. The method used to generate this information was based on the combined use of Shielding Program 14-0 and Diffusion Program G-2.[15] It was assumed that Program G-2 predicted the correct neutron spectral distribution (relative neutron

flux as a function of energy), but not necessarily the correct magnitude or spatial distribution in the shield. This assumption also applied to Program G-2 FND (fast neutron dose rate) which included integration of the product of Program G-2 neutron flux and the Hurst response (cf., section 5.9.5). However, Program 14-0 computations of Program G-2 FND at all locations in the shield were assumed to be correct. Therefore, Program G-2 spectral results were corrected by the quotient of Program 14-0 FND divided by Program G-2 FND to obtain absolute neutron flux. This quotient varied throughout the shield, and was identified as the normalization factor.

Using the corrected Program G-2 spectral results, heating rates resulting from kinetic energy loss of fast neutrons were computed in accordance with equation (11). The product of the neutron flux and the neutron energy deposition response was integrated over lethargy as shown below:

$$HR(r)_m = N \sum_u \phi(u,r)_{rel}\, Q(u)_m\, \Delta u \tag{11}$$

where:

$HR(r)_m$ = heating rate at location r in material m, watt/gm-mw

$N = \dfrac{\text{absolute Program 14-0 FND/mw of reactor power}}{\text{relative Program G-2 FND}}, \dfrac{1}{\text{mw}}$ (normalization factor)

$u = \ln(E_o/E)$ (lethargy, $E_o = 10^7$ electron volts)

$\phi(u,r)_{rel}$ = relative neutron flux at location r as a function of lethargy, neutrons/cm^2-sec-unit lethargy

$Q(u)_m$ = energy deposition per gram of material m per unit neutron flux as a function of lethargy, $\dfrac{\text{watts}}{\text{gm of material m}} \div \dfrac{\text{n}}{\text{cm}^2\text{-sec}}$

The energy deposition response, $Q(u)_m$ for kinetic energy loss of fast neutrons was given by the following equation:

$$Q(u)_m = K \frac{\Sigma(u)_m}{\rho_m} E(u)\left[\frac{1-\alpha_m}{2}\right] \tag{12}$$

where:

K = conversion factor, $\dfrac{\text{watts}}{\text{Mev/sec}}$

$\dfrac{\Sigma(u)_m}{\rho_m}$ = macroscopic mass neutron scattering cross section of material m, as a function of lethargy, $\dfrac{\text{neutron scatters}}{\text{gm-neutron/cm}^2}$

$E(u)\left[\dfrac{1-\alpha_m}{2}\right]$ = average neutron energy loss per scatter in material m, $\dfrac{\text{Mev}}{\text{neutron scatter}}$ (13)

$\alpha_m = \left[\dfrac{A-1}{A+1}\right]^2$ where A is the atomic mass of the element (for cases when m is an alloy, the value is given in Table 5.14) (14)

Equations (13) and (14) were derived on the basis of elastic scattering.[66] The assumption that all collisions contributing to the neutron-induced heating rate were elastic collisions led to negligibly small errors. For example, $Q(u)_m$ for BeO computed from equation (12) was compared with the same quantity computed by a moments-method calculation in which nonelastic, as well as elastic, processes were considered;[67] the agreement was very close.

TABLE 5.14

HEATING RATE RESPONSE USED IN CALCULATIONS OF FAST NEUTRON KINETIC ENERGY LOSS

Lethargy Level	Energy, Mev	Be		BeO		LiH_x		Hastelloy X		Inconel X		304 Stainless Steel	
		$\frac{1-\alpha_m}{2}$	$Q(u)_m$[a]	$\frac{1-\alpha_m}{2}$	$Q(u)_m$	$\frac{1-\alpha_m}{2}$	$Q(u)_m$	$\frac{1-\alpha_m}{2}$	$Q(u)_m$	$1-e^{\xi m}$	$Q(u)_m$	$1-e^{\xi m}$	$Q(u)_m$
1	6.065	0.180	2.13/-14[b]	0.154	1.04/-14	0.328	8.48/-14	0.037	9.23/-16	0.0341	9.54/-16	0.0354	9.38/-16
2	3.679	0.180	1.43/-14	0.143	8.68/-15	0.353	6.79/-14	0.0405	6.70/-16	0.0343	6.18/-16	0.0356	6.29/-16
3	2.231	0.180	9.54/-15	0.157	4.49/-15	0.392	4.84/-14	0.0335	3.46/-16	0.0342	3.80/-16	0.0353	3.89/-16
4	1.353	0.180	6.33/-15	0.143	3.81/-15	0.415	3.71/-14	0.0360	2.18/-16	0.0315	2.18/-16	0.0358	2.04/-16
5	0.8208	0.180	7.11/-15	0.142	4.44/-15	0.437	2.70/-14	0.0360	1.41/-16	0.0343	1.48/-16	0.0358	1.12/-16
6	0.4979	0.180	3.82/-15	0.145	2.23/-15	0.457	2.02/-14	0.0285	8.06/-17	0.034	9.14/-17	0.0355	9.89/-17
7	0.302	0.180	2.12/-15	0.145	1.25/-15	0.439	1.67/-14	0.0315	6.79/-17	0.0339	7.98/-17	0.034	5.73/-17
8	0.1832	0.180	1.91/-15	0.151	9.79/-16	0.452	1.21/-14	0.0440	6.12/-17	0.0339	5.32/-17	0.0356	4.03/-17
9	2.479/-2	0.180	2.82/-16	0.153	1.41/-16	0.480	2.79/-15	0.0425	1.44/-17	0.0346	1.55/-17	0.0354	7.99/-18
10	3.354/-3	0.180	3.88/-17	0.153	1.93/-17	0.485	4.09/-16	0.1880	2.03/-17	0.034	3.18/-18	0.0358	1.76/-18
11	4.54/-4	0.180	5.25/-18	0.153	2.61/-18	0.485	5.65/-17	0.0835	9.11/-19	0.0339	4.05/-19	0.0352	2.68/-19
12	6.144/-5	0.180	7.10/-19	0.153	3.54/-19	0.485	7.64/-18	0.0225	3.03/-20	0.0335	5.38/-19	0.0352	3.95/-20

[a] Units of $Q(u)_m$ are $\frac{\text{watts}}{\text{gm of material m}} \div \frac{\text{n}}{\text{cm}^2\text{-sec}}$.

[b] Read 2.13/-14 as 2.13×10^{-14}.

For single elements, α_m was found easily by means of equation (14). For combinations of elements, α_m was found by the following expressions:

$$\alpha_m = \frac{C_a \alpha_a + C_b \alpha_b + C_c \alpha_c}{C_a + C_b + C_c} \tag{15}$$

where:

$\alpha_m = \alpha$ for combination of elements a, b, and c
$\alpha_a = \alpha$ for element a
C_a = (wt. fraction of a in m) x $\left[\frac{\Sigma^{scat.}}{\rho}\right]_a$
or
C_a = (vol. fraction of a in m) x $\Sigma_a^{scat.}$
or
C_a = (atoms of a per molecule of m) x $\sigma_a^{scat.}$

and α_b and α_c were treated similarly. Since $\Sigma^{scat.}$ or $\sigma^{scat.}$ were energy dependent, α_m also was energy dependent and was determined for each lethargy level of interest.

For mixtures containing high Z elements, an approximation to $\frac{1 - \alpha_m}{2}$ was used:

$$\frac{1 - \alpha_m}{2} \approx 1 - e^{\xi_m} \tag{16}$$

where ξ_m = average logarithmic energy decrement per collision. Values of ξ_m as a function of lethargy are contained in reference 68. Values of $Q(u)_m$, $\frac{1 - \alpha_m}{2}$, and $1 - e^{\xi_m}$ are listed in Table 5.14 for materials of interest. All values in this table are expressed as functions of lethargy level.

For a given material, the ratio of the Program 14-0 fast-neutron dose rate to the fast-neutron heating rate obtained by the method outlined above very nearly was constant regardless of location. At shield locations other than along the midplane or centerline traverses, fast-neutron heating rates were obtained by multiplying the Program 14-0 FND with an adjustment factor dependent only upon the material at that location. Representative adjustment factors are given in Table 5.15.

TABLE 5.15

ADJUSTMENT FACTORS FOR CONVERTING PROGRAM 14-0 FND TO HEATING RATES

Material	Adjustment Factor, watts/gm-mw rads (ethylene)/hr-mw
LiH	4.2/-9[a]
Be	6.7/-10
BeO	4.1/-10
304 SS	2.6/-11
Inconel X	2.57/-11
Hastelloy X	2.45/-11
Hevimet	7.57/-12

[a]Read 4.4/-9 as 4.4×10^{-9}

5.9.3.3 n - α Reaction

This source of secondary heat was energy deposited by capture of alpha particles and recoil nuclei released by neutron captures in B^{10} or Li^6. Spatial and spectral distribution of low-energy neutrons were required for these calculations, and were determined in the same manner that fast-neutron flux was obtained for fast-neutron-induced secondary heating; i.e., by the combined results of Programs 14-0 and G-2.

Activation normalization factors were computed and used to calculate the n-α heating rates. Energy deposition response function was expressed as follows:

$$Q(u)_m = K\left[\frac{\Sigma(u)_{n,\alpha}}{\rho}\right]_c [\zeta_{c \text{ in } m}]\, q_c \qquad (17)$$

where:

$Q(u)_m$ = alpha particle energy deposition per gram of composition m, per unit neutron flux, as a function of lethargy, $\frac{\text{watts - cm}^2\text{ - sec}}{\text{gm}_m\text{ - neutrons}}$

K = conversion factor, $\frac{\text{watts}}{\text{Mev/sec}}$

$\left[\frac{\Sigma(u)_{n,\alpha}}{\rho}\right]_c$ = macroscopic mass n-α cross section of the alpha-emitting element c, as a function of lethargy, $\frac{\text{neutron-captures}}{\text{gm}_c\text{-neutron/cm}^2}$

$\zeta_{c \text{ in } m}$ = weight fraction of the capturing element in composition m, $\frac{\text{gm}_c}{\text{gm}_m}$

q_c = kinetic energy of the alpha particle emitted by the element c, $\frac{\text{Mev}}{\text{neutron capture}}$

The energy deposition (heating) response function was applied to a given absorber and was a function of the weight fraction of that absorber in the total absorbing material. Thus, for a given neutron flux and given weight fraction of absorber, the n-α heating rate was the same on a unit weight basis of any composition or mixture, assuming that the energy of the reaction was dissipated at the point of neutron capture.

The two elements of interest for n-α reactions were boron and lithium. The n-α reaction occurred in the isotopes B^{10} and Li^6. B^{10} was present in either the natural or the enriched boron used as an additive to materials in the end shields. Li^6 was present in LiH_X as a naturally occurring isotope of lithium.

The n-α reaction energies used in the nuclear analysis, expressed as Mev/neutron capture, were 4.78 for lithium and 2.792 for boron. The reaction energy for boron included a 0.478 Mev gamma photon whose energy was assumed to be absorbed at the point of capture. If the gamma photon were treated separately, the boron reaction energy was 2.314 Mev/neutron capture. Heating rate responses are listed in Table 5.16 for lithium (natural) hydride, materials containing 1 weight percent of natural boron, and materials containing 1 weight percent of enriched boron.

5.9.4 OTHER NUCLEAR DATA

Other nuclear data used in shielding nuclear analysis are shown in Tables 5.17 through 5.19 and Figures 5.116 and 5.117.

Material attenuation data for the significant materials used in the reactor-shield assembly are shown in Table 5.17. Table 5.18 lists the linear gamma ray total absorption coefficient for these materials. Iron and water gamma ray dose buildup factors and energy absorption

TABLE 5.16

HEATING RATE RESPONSE FOR n-α REACTIONS

Lethargy Level	Energy, Mev	LiH_x	$Q(u)_m$[a] 1 wt % B natural[b]	$Q(u)_m$[a] 1 wt % B^{10}[b]
1	6.065	2.687/-16[c]	1.213/-17[c]	6.960/-17[c]
2	3.679	3.449/-16	1.557/-17	8.935/-17
3	2.231	4.416/-16	1.994/-17	1.144/-16
4	1.353	5.707/-16	2.577/-17	1.478/-16
5	0.8208	7.290/-16	3.291/-17	1.888/-16
6	0.4979	9.374/-16	4.232/-17	2.428/-16
7	0.3020	1.204/-15	5.435/-17	3.119/-16
8	0.1832	1.546/-15	6.977/-17	4.033/-16
9	2.479/-2	4.208/-15	1.900/-16	1.090/-15
10	3.354/-3	1.141/-14	5.153/-16	2.957/-15
11	4.540/-4	3.108/-14	1.403/-15	8.050/-15
12	6.144/-5	8.457/-14	3.818/-15	2.191/-14
13	8.315/-6	2.295/-13	1.036/-14	5.946/-14
14	1.855/-6	4.320/-13	1.950/-14	1.119/-13
15	6.826/-7	8.295/-13	3.744/-14	2.148/-13
16	2.511/-7	1.250/-12	5.644/-14	3.238/-13
17	9.237/-8	2.178/-12	9.834/-14	5.642/-13
18	3.216/-8	3.695/-12	1.668/-13	9.570/-13
19	3.216/-8	3.695/-12	1.668/-13	9.570/-13

[a] $Q(u)_m$ expressed as $\frac{\text{watts}}{\text{gm of material}} \div \frac{\text{n}}{\text{cm}^2\text{-sec}}$.

[b] Includes a 0.478 Mev gamma photon.

[c] Read 2.687/-16 as 2.687×10^{-16}.

TABLE 5.17

MATERIALS ATTENUATION DATA

Material	Density, gm/cc	Σm,[a] cm^{-1}	Σm(internal), cm^{-1}	Σm(external), cm^{-1}
LiH[b]	0.725	0.0682		
BeO	2.9		0.1305	0.1386
Be	1.84		0.1306	0.1371
Inconel X	8.31	0.1581		
Al_2O_3	3.89	0.1235		
ZrO_2	5.3	0.10882		
304 SS	7.92	0.1678		
A-286	7.94	0.1615		
UO_2	10.74	0.1305		
Y_2O_3	4.93	0.0976		
Rene' 41	8.249	0.1456		
Be + 1 wt % B	1.84	0.1371		
304 SS + 1 wt % B	7.92	0.1669		

[a] Σm, macroscopic fast neutron removal cross-section for the nonhydrogenous constituents of material.

[b] The ratio of hydrogen density in lithium hydride to hydrogen density in water was 0.8205.

TABLE 5.18

LINEAR GAMMA-RAY TOTAL ABSORPTION COEFFICIENT,[a] $\mu_m(E_j)$

Material	Energy Level, Mev												
	0.4	0.7	1.0	1.5	2.0	2.5	2.8	3.5	4.5	5.5	6.5	7.5	8.5
LiH	0.0697	0.0551	0.0464	0.0379	0.0323	0.0286	0.0268	0.0234	0.0201	0.0179	0.0162	0.0149	0.0139
BeO	0.2654	0.2068	0.1769	0.1441	0.1238	0.1099	0.1032	0.0911	0.0795	0.0722	0.0667	0.0621	0.058
Be	0.1558	0.1216	0.104	0.0845	0.0725	0.0642	0.0602	0.0526	0.0454	0.0408	0.0374	0.0344	0.0318
Inconel X	0.7737	0.5917	0.4953	0.4055	0.3557	0.3249	0.3108	0.2875	0.2692	0.2601	0.2551	0.2518	0.2501
Al_2O_3	0.3643	0.289	0.2473	0.2015	0.1731	0.154	0.1451	0.1294	0.1147	0.1041	0.0974	0.0917	0.0879
ZrO_2	0.5532	0.402	0.3351	0.2744	0.2401	0.2205	0.2111	0.1968	0.1855	0.181	0.1786	0.1774	0.1768
304 SS	0.7318	0.5592	0.4728	0.3857	0.3374	0.3105	0.2962	0.2732	0.2558	0.2455	0.24	0.2368	0.2352
A-286	0.7256	0.56	0.467	0.3815	0.3341	0.3068	0.293	0.2706	0.2532	0.2442	0.2387	0.2357	0.2343
UO_2	2.5712	1.1355	0.6831	0.5563	0.5148	0.4877	0.4744	0.4555	0.4513	0.4584	0.4692	0.4794	0.4901
Y_2O_3	0.4733	0.3446	0.2871	0.2352	0.2061	0.1894	0.1816	0.1693	0.1603	0.1566	0.155	0.154	0.1538
Rene' 41	0.7682	0.5828	0.4873	0.3987	0.3503	0.3196	0.3057	0.2834	0.2661	0.2575	0.2528	0.2503	0.2489
Be + 1 wt % B	0.1558	0.1216	0.104	0.0845	0.0725	0.0642	0.0602	0.0526	0.0454	0.0408	0.0374	0.0344	0.0318
304 SS + 1 wt % B	0.7114	0.5522	0.4598	0.3753	0.3283	0.3019	0.2882	0.2657	0.2482	0.2389	0.2331	0.23	0.2281

[a]Units are cm^{-1}.

TABLE 5.19

GAMMA-RAY SOURCE TERMS AND FLUX-TO-DOSE CONVERSION FACTORS

Source Energy, Mev	Source Intensity		Flux-To-Dose Conversion Factor, rads(carbon)/hr / Mev/cm^2-sec
	Mev/fission	Mev/watt-sec[a]	
0.4	1.850	5.893×10^{10}	1.7×10^{-6}
0.7	4.166	13.273×10^{10}	1.67×10^{-6}
1.0	2.957	9.42×10^{10}	1.61×10^{-6}
1.5	2.218	7.068×10^{10}	1.48×10^{-6}
2.0	1.603	5.106×10^{10}	1.37×10^{-6}
2.5	1.227	3.91×10^{10}	1.27×10^{-6}
2.8	0.8515	2.713×10^{10}	1.23×10^{-6}
3.5	1.374	4.377×10^{10}	1.15×10^{-6}
4.5	0.5957	1.898×10^{10}	1.05×10^{-6}
5.5	0.210	6.69×10^{9}	9.5×10^{-7}
6.5	0.107	3.41×10^{9}	9.2×10^{-7}
7.5	0.0228	7.26×10^{8}	8.8×10^{-7}
8.5	0.00593	1.89×10^{8}	8.5×10^{-7}
Shutdown Energy, Mev			
0.4	0.0352	1.12×10^{9}	1.7×10^{-6}
0.7	0.1632	5.2×10^{9}	1.67×10^{-6}
1.0	0.0339	1.08×10^{9}	1.61×10^{-6}
1.5	0.0330	1.05×10^{9}	1.48×10^{-6}
2.0	0.0333	1.06×10^{9}	1.37×10^{-6}
2.5	0.00581	1.85×10^{8}	1.27×10^{-6}
2.8	0.000455	1.45×10^{7}	1.23×10^{-6}

[a]Based on 3.186×10^{10} fissions/watt-sec.

[b]Shutdown source intensities are based on 100 hours reactor operation followed by 10 hours shutdown.

buildup factors for gamma ray heating calculations were taken from reference 64. Mass gamma ray energy absorption coefficients were taken from reference 65. Gamma ray source terms and flux-to-dose conversion factors for 13 energy groups during reactor operation and for seven energy groups after shutdown (10 hours shutdown following 100 hours reactor operation) are listed in Table 5.19. The 13 during-operation groups included prompt-U^{235} fission gamma rays, fission-product-decay gamma rays (saturated activity), and capture gamma rays resulting from neutron capture in the active core. The seven after-shutdown groups included only fission-product-decay gamma rays.

The relative radial and longitudinal power distributions used in shielding calculations are shown in Figures 5.116 and 5.117, respectively. Cosine and exponential functions were fitted to these curves for use in Program 14-0.

5.9.5 PROGRAM G-2

Program G-2, references 15 and 69, is a one-dimensional multiregion, multienergy IBM-704 program based on diffusion theory. It computes spatial and spectral distribution of neutron flux along a radial traverse at the core midplane and along an axial

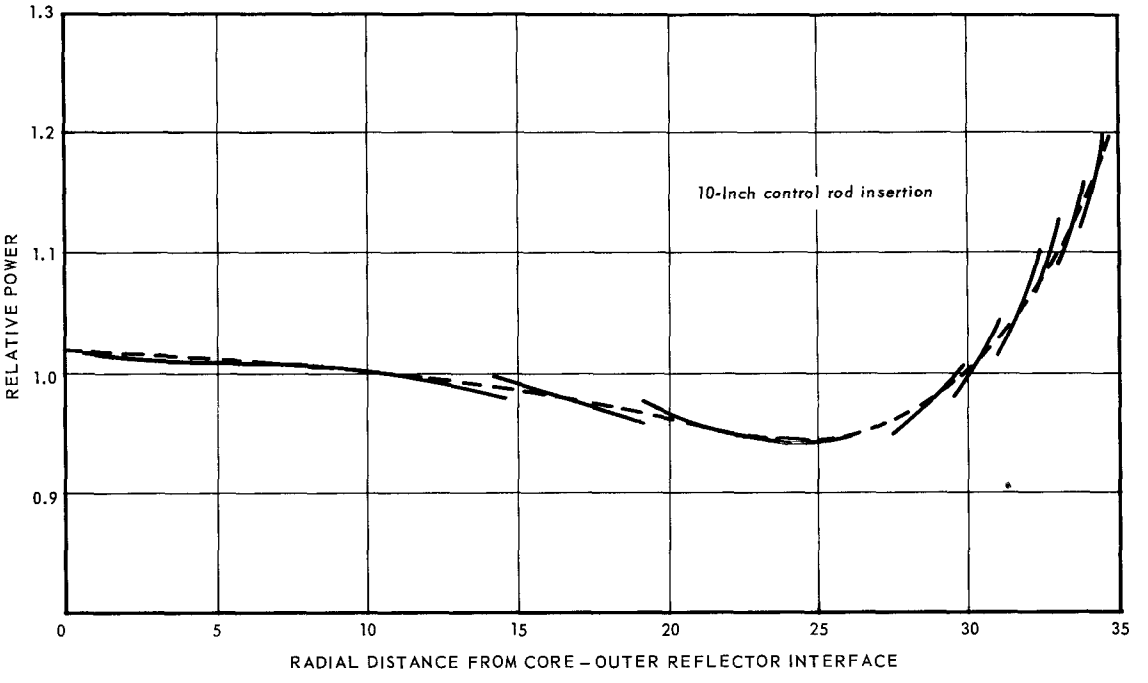

Fig. 5.116 – Reactor radial power distribution used in shield calculations

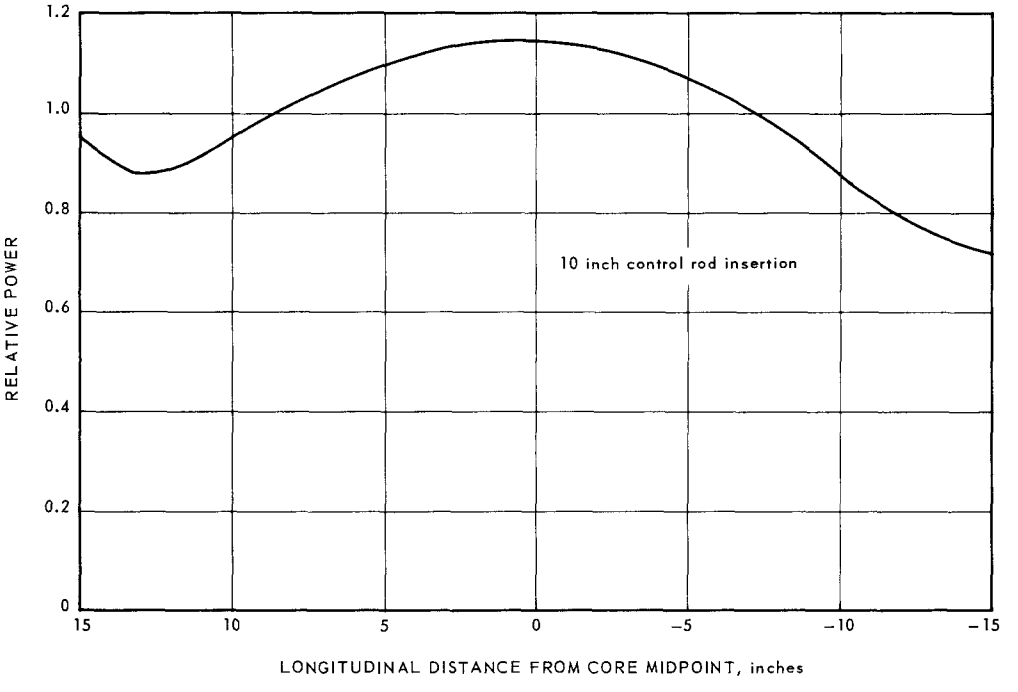

Fig. 5.117 – Reactor longitudinal power distribution used in shield calculations

traverse at the core centerline, but does not treat other locations. The midplane traverse and the axial traverse are treated as separate one-dimensional problems.

Input data for Program G-2 computations include (1) a one-dimensional regional description of the reactor with side and/or end shields, (2) material volume fractions in each region, and (3) certain nuclear data. The nuclear data, primarily neutron cross sections, are supplied to the computer by a data tape.[68] Program output of primary concern to shield nuclear analysis is the relative neutron flux as a function of lethargy. This flux is given for 18 different lethargy (energy) levels from 10 Mev to thermal energy, plus a nineteenth thermal group having a Maxwellian distribution. The lethargy (and energy) levels at which these fluxes are computed, together with the lethargy interval corresponding to each level, are listed in Table 5.20.

In addition to computations of neutron flux, an activation modification was used to obtain a flux response by integrating, over lethargy, the product of flux multiplied by a specified response function. The flux response was obtained at any specified location along the midplane or centerline traverses. The modification further performed the conversion from relative to absolute response at each location by use of a normalizing factor. The normalizing factor used was based on the ratio of Program 14-0 FND to Program G-2 FND. The Program 14-0 FND was supplied as input data and the Program G-2 FND was computed by integration over a Hurst response function. Table 5.21 lists the fast-neutron dose response, and the responses used to get subcadmium, epicadmium, and fast neutron fluxes.

All shielding calculations involving the computations of Program G-2 were based on a uniform temperature of 68°F through the reactor-shield assembly. The modified-age slowing-down model was used for all regions.

TABLE 5.20

PROGRAM G-2 LETHARGY AND ENERGY LEVELS AT 68°F

Group	Lethargy, $\ln (E_0/E)$	Energy (E_0), ev	Lethargy Increment, Δu
0	0	10^7	
1	0.5	6.065×10^6	0.5
2	1.0	3.679×10^6	0.5
3	1.5	2.231×10^6	0.5
4	2.0	1.353×10^6	0.5
5	2.5	8.208×10^5	0.5
6	3.0	4.979×10^5	0.5
7	3.5	3.020×10^5	0.5
8	4.0	1.832×10^5	1.25
9	6.0	2.479×10^4	2.0
10	8.0	3.354×10^3	2.0
11	10.0	4.540×10^2	2.0
12	12.0	6.144×10^1	2.0
13	14.0	8.315×10^0	1.75
14	15.5	1.855×10^0	1.25
15	16.5	6.826×10^{-1}	1.0
16	17.5	2.511×10^{-1}	1.0
17	18.5	9.237×10^{-2}	1.0275
18	19.555	3.232×10^{-2}	0.5275
19	19.555	3.232×10^{-2}	1.0

TABLE 5.21

RESPONSES FOR FAST NEUTRON DOSE RATE AND SUBCADMIUM, EPICADMIUM, AND FAST NEUTRON FLUXES

Level	Energy, ev	FND Response rads (ethylene)/hr n/cm^2-sec	Subcadmium Flux 0 to 0.4 ev	Epicadmium Flux 0.4 ev to 0.235 Mev	Fast Flux 0.235 to 10 Mev
1	6.065/6[a]	2.30/-5			1
2	3.679/6	2.10/-5			1
3	2.231/6	1.60/-5			1
4	1.353/6	1.30/-5			1
5	8.208/5	1.00/-5			1
6	4.979/5	8.30/-6			1
7	3.020/5	5.70/-6			1
8	1.832/5	4.90/-6		1	
9	2.479/4	1.10/-6		1	
10	3.354/3			1	
11	4.54/2			1	
12	6.144/1			1	
13	8.315			1	
14	1.855			1	
15	6.826/-1		1.7/-1	8.3/-1	
16	2.511/-1		1		
17	9.237/-2		1		
18	2.530/-2		1		
Thermal Group			1		

[a]*Read 6.065/6 as 6.065 x 10^6.*

5.9.6 NUCLEAR TEST PROGRAM

5.9.6.1 Critical Experiment Facilities

The primary objective of the shield nuclear test program was to provide data correlating and verifying methods used in design analysis. Secondary objectives were to provide data directly related to over-all engine design aspects and other data verifying the measurement techniques which were to have been used during the Advanced Core Test program. Two critical experiment facilities were used to provide this data, the SSR-VI-B and the KEYCE.

SSR-VI-B - The SSR-VI-B[69] was a modification of a critical experiment mockup previously used in the XMA-1 program. It was fueled with metallic fuel elements and moderated with zirconium hydride. Shielding consisted of two 1-inch-thick borated (1 percent natural boron by weight) radial stainless steel gamma ray shield plates, a LiH_x neutron side shield, and a simulated rear reflector-shield of 4-inch-thick Be.

The side shield contained three instrument wells located at longitudinal positions, relative to the core midplane, as follows: (1) front instrument well, 22.6 centimeters; (2) center instrument well, -1.0 centimeter; and (3) rear instrument well, -23.9 centimeters. Borated stainless steel and LiH_x discs were inserted in the wells ahead of the sensors when measuring sensor responses as a function of side shield thickness.

The side shield plates were located approximately 3/4 inch from the dummy pressure vessel. The LiH_x was separated from the borated stainless steel by approximately 1-3/8 inches. The Be slab used to simulate the rear reflector and shield was located approximately 4 inches aft of the rear tube sheet.

Although the core was entirely different from the XNJ140E-1 core, the geometric configuration, neutron spectrum, and shielding materials were similar enough to provide preliminary data for methods verification. This program was terminated when the KEYCE was built.

KEYCE - The KEYCE assembly contained a ceramic core mockup consisting of BeO fuel elements and Be reflectors. In addition to the core mockup, the shield assembly was mocked up by Be front and rear shields and an epoxy resin-LiH_x side shield. Further, core and shield materials were inserted into a matrix of aluminum hexagonal tubes to provide a detailed geometric simulation of the actual shield.

Establishing limits of uncertainty to be applied to secondary heat generation calculations was of primary importance. Gamma-ray heating rates were measured directly with Bragg-Gray-type ionization chambers; neutron heating rates, on the other hand, could not be measured directly. Verification of neutron heating rate analytical methods was accomplished by correlating data from neutron-induced foil activity, an analogous but measurable phenomenon. Neutron activation foils used in the critical experiments program included bare and cadmium-covered copper foils ($Cu^{63}(n,\gamma)Cu^{64}$), bare and cadmium-covered indium foils ($In^{115}(n,\gamma)In^{116}$), sodium chloride pellets ($Na^{23}(n,\gamma)Na^{24}$), aluminum-uranium catcher foils ($U^{235}(n,f)$F. P.), and sulfur foils ($S^{32}(n,p)P^{32}$).

5.9.6.2 Foil Activation Analysis

Absolute disintegration rates were calculated from neutron activation data using Program G-2. Foil responses were determined by multiplying the lethargy-dependent microscopic reaction cross section (in barns) by a factor, R, given by the equation:

$$R = \frac{N_0 \, a \, c \times 10^{-24}}{A} \qquad \frac{\text{atoms of target isotope - cm}^2}{\text{gram of foil - barn}}$$

where

N_0 = Avogadro's Number, 6.025×10^{23} atoms per gram atomic weight of parent element
a = fractional abundance of target isotope in parent element
c = fractional abundance of parent element in foil
A = atomic weight of parent element
10^{-24} = conversion from barns to cm^2.

Reaction cross sections used in this analysis are contained in references 68, 70, and 71. The resulting foil responses were as follows:

Foil	a	c	R
Copper	0.69	1.0	6.54×10^{-3}
Indium	0.958	0.1	5.04×10^{-4}
NaCl	1.0	0.393	1.03×10^{-2}
Sulfur	0.95	1.0	1.79×10^{-2}
Catcher	1.0	1.0	5.42×10^{-2}

Using these foil responses, the analytical disintegration rate was given in units of disintegrations per second per gram of foil, and was equal to

$$A = \int R \, \sigma(u) \, \phi(u) \, du$$

where

$\phi(u)$ = lethargy-dependent neutron spectrum.

$\sigma(u)$ = lethargy-dependent microscopic reaction cross section.

Two methods were used to normalize the disintegration rate to unit reactor power. The first method was point-to-point normalization. The calculated responses were normalized to the fast-neutron dose rate obtained from a point-kernel program (Program 14-0), and included the fast-neutron dose rate responses calculated by Program G-2. The power-normalized disintegration rate was

$$A_n = \frac{F \int R\ \sigma(u)\ \phi(u)du}{\int H(u)\ \phi(u)du}$$

where

F = fast-neutron dose rate per unit power from point-kernel calculation.
H(u) = lethargy-dependent fast-neutron dose rate response.

A_n was in units of disintegrations per second per gram of foil per unit power level. The second method, core power normalization, was given by the equation

$$A_n = K \int R\ \sigma(u)\ \phi(u)du$$

where

K = the fission rate per unit power divided by the calculated fission rate in the core (Program G-2) and other terms as previously defined.

Data also were calculated for two slowing-down models: (1) modified-age slowing-down, the model most frequently used in shield nuclear analysis; and (2) Coveyou-McCauley slowing down. The first normalization method used the modified-age model for all compositions; in the second method the Coveyou-McCauley slowing-down model was used for the Be regions and the modified-age model was used for all other regions. Use of the Coveyou-McCauley slowing-down model in Be regions was due to the fact that this model was better applicable to low atomic number, nonabsorbing materials.

Use of the above methods of normalization and slowing-down models led to the following four methods of calculating analytical foil response data:

1. Modified-age slowing-down and point-to-point power normalization.
2. Coveyou-McCauley slowing-down and point-to-point power normalization.
3. Modified-age slowing-down and core power normalization.
4. Coveyou-McCauley slowing-down and core power normalization.

5.9.6.3 SSR-VI-B Experimental Data

Gamma-ray heating rate measurements were made in both borated stainless steel and LiH_x. The experimental uncertainty of the data in the borated stainless steel and LiH_x regions was ± 20 percent and ± 40 percent, respectively; these uncertainties did not include the reactor power uncertainty of ± 20 percent.[72] The root-mean-square uncertainties were ± 28 percent and ± 45 percent, respectively. Gamma-ray heating rate measurements were taken behind the following thicknesses of borated stainless steel: 0, 1/2, 1, and 1-1/2 inches; measurements also were taken behind the following thicknesses of LiH_x: 5/16, 1-9/6, 2-9/16, 4-7/8 and 9-1/16 inches. These data were reported in units of watts per gram of shield material per watt of reactor power.

Exposures of bare and cadmium-covered copper, bare and cadmium-covered indium, sodium chloride, sulfur, and uranium-aluminum catcher foils were made behind 1/2, 1,

1-1/2, and 2 inches of borated stainless steel and behind 1-1/4, 2-1/2, 4-3/4, 7, and 11-3/4 inches of LiH_x. The experimental foil data were corrected to saturated activity expressed in units of disintegrations per second per gram of foil per watt, and were time-extrapolated back to reactor shutdown.

Assuming that (1) the foil counting statistics were better than ± 10 percent, (2) the uncertainty in the power level was ± 20 percent, and (3) the absolute counter calibration was within ± 12 percent, the root-mean-square uncertainty of the foil data was about ± 25 percent. This uncertainty did not apply to subcadmium foil data since differences of two experimental activities, as required for subcadmium foil data, could result in uncertainties up to 50 percent depending upon the relative magnitudes of the two quantities.

Experimental data are reported in references 69, 73, 74, and 75. A summation of the average factors of difference between the experimental data and the analytical data (modified-age slowing-down and point-to-point normalization for the foil responses) is given in Table 5.22. This table shows the maximum, minimum, and average factors of difference for each of the three instrument wells as well as the average factor for all three wells. Table 5.23 compares the average factors-of-difference between experimental and analytical data for the four analytical methods of calculating foil response data. These data represent average factors for all three instrument wells.

5.9.6.4 KEYCE Experimental Data

At the time of contract termination, KEYCE data that had been accumulated and correlated were insufficient to provide complete evaluation of the analytical methods. However, when combined with data from the SSR-VI-B program, the experimental data indicated that the analytical data, in general, were within a factor of 2 for neutron-induced reactions, and within a factor of 1.5 for gamma-ray heating rates.

TABLE 5.22

FACTORS OF DIFFERENCE BETWEEN ANALYTICAL DATA[a] AND EXPERIMENTAL DATA IN THE SSR-VI-B[b]

Location	Gamma-Ray Heating Rate	Fast-Neutron Dose Rate	Foil								
			U^{235}	Bare Copper	Cd Covered Copper	Subcd. Copper	Bare Indium	Cd Covered Indium	Subcd. Indium	Sodium	Sulfur
Front Well											
Average	±1.2		-2.0	+2.6	+3.4	-1.8	+1.5	+1.5	-3.3	-1.4	-2.6
Maximum	-1.6		-2.6	+2.7	+4.0	-13	+2.3	+2.5	-5.8	-1.8	-3.0
Minimum	1.0		-1.5	+2.0	+2.6	1.0	1.0	+1.2	1.0	1.0	-1.7
Center Well											
Average	±1.2	+2.3	-1.8	+3.4	+4.2	-3.5	+2.0	+1.8	-3.8	-1.2	-2.0
Maximum	+1.6	+2.6	-3.0	+4.6	+5.0	-10	+2.7	+3.1	-4.9	-1.4	-2.3
Minimum	1.0	+2.0	-1.3	+2.2	+3.6	-1.2	+1.2	+1.3	-2.3	1.0	-1.6
Rear Well											
Average	±1.5		-1.5	+4.3	+5.1	-3.0	+1.9	+2.0	-2.6	-1.1	-1.8
Maximum	+2.4		-2.0	+5.0	+5.4	-8	+2.5	+3.1	-3.5	+1.2	-2.2
Minimum	1.0		-1.2	+2.9	+2.6	1.0	+1.3	+1.7	1.0	1.0	-1.1
Average	±1.3	+2.3	-1.8	+3.4	+4.2	-2.8	+1.8	+1.8	-3.3	-1.2	-2.1

[a] Analytical data based on modified-age, point-to-point normalization for foil responses.
[b] -1.6 indicates an underprediction by a factor of 1.6, +1.6 indicates an overprediction by a factor of 1.6.

TABLE 5.23

AVERAGE FACTORS-OF-DIFFERENCE[a] BETWEEN EXPERIMENTAL FOIL RESPONSE DATA AND ANALYTICAL DATA CALCULATED BY DIFFERENT METHODS

	Foil								
Analytical Method	U^{235}	Bare Copper	Cd Covered Copper	Subcd. Copper	Bare Indium	Cd Covered Indium	Subcd. Indium	Sodium	Sulfur
Modified-Age Point-to-point	-1.8	+3.4	+ 4.2	-2.8	+1.8	+1.8	-3.3	-1.2	-2.1
Coveyou-McCauley, Point-to-point	-1.6	+4.0	+ 4.9	-2.8	+2.0	+2.0	-3.3	-1.3	-2.5
Modified-Age Core Power	+1.4	+8.0	+11.8	+2.6	+3.7	+4.0	-1.6	+1.8	+1.2
Coveyou-McCauley, Core Power	+1.4	+8.1	+ 9.9	+2.6	+3.6	+4.0	-1.5	+2.0	-1.3

[a] -1.8 indicates an underprediction by a factor of 1.8; +1.8 indicates an overprediction by a factor of 1.8.

5.10 PRODUCT HANDBOOK

The Shield Handbook for 140E[4] was identified in section 1.6. Material contained in this handbook is illustrated by the following Table of Contents:

TABLE OF CONTENTS

TABLE OF CONTENTS (Continued)

TABLE OF CONTENTS (Continued)

5.11 REFERENCES

1. Boudreaux, R. A., "Advanced Configuration Study Shield Aerothermodynamic Ground Rules," GE-ANPD, DC 59-10-81, October 1959.
2. Hobbs, J. L., "Bleed Requirements, Configuration Study Power Plant," GE-ANPD, XDCL 59-12-191, December 1959.
3. Layman, D. C., "Handbook of Instructions for 140E1," GE-ANPD, DC 60-7-1, July 1960.
4. Aschenbrenner, F. A., "Shield Handbook for 140E1," GE-ANPD, DC 60-9-22, September 1960.
5. Klabosh, C., "Cycle Conditions Used as a Basis of Aerothermal Design as Defined by DC 60-7-1," GE-ANPD, DC 61-3-139, March 1961.
6. Boudreaux, R. A., "Advanced Configuration Study, 1st Iteration, Shield Aerothermal Design Evaluation," GE-ANPD, DC 59-11-182, November 1959.
7. Hobbs, J. L., "Bleed and Cooling Flow Paths for Use In Configuration Study," GE-ANPD, DC 59-11-1, November 1959.
8. Hobbs, J. L., "Bleed and Cooling Flow Paths for Configuration Study, 2nd Issue," GE-ANPD, DC 59-12-102, December 1959.
9. Boudreaux, R. A., "Advanced Configuration Study, Final Shield Aerothermal Design Evaluation," GE-ANPD, DC 60-7-48, July 1960.
10. Hobbs, J. L., et al, "D140E1 Static and Total Pressures," GE-ANPD, DC 60-8-114, August 1960.
11. Granger, H. E., et al, "Advanced Configuration Study - Shield Nuclear Design and Analysis," GE-ANPD, DC 60-10-102, October 1960.
12. Moteff, J., "General Electric - Convair Shield Optimization Studies," GE-ANPD, DC 60-3-161, March 1960.
13. "ANPD Engineering Progress Report No. 34," October-December, 1959, Section 6.23, GE-ANPD, APEX-34, December 1959.
14. Edwards, W. E., et al, "Shielding Computer Programs 14-0 and 14-1, Reactor Shield Analysis," GE-ANPD, XDC 59-2-16, February 1959.
15. Campbell, D., "Program G-2," GE-ANPD, XDC 58-4-63, April 1958.
16. Haffner, J. W., "Use of Program G-2 for Shielding Calculations," GE-ANPD, DC 59-7-176, July 1959.
17. Culp, A. W., "Activation and Residual Dose from an Irradiated J-79 Engine," ASTRA, Inc., Medford, Conn., ASTRA 301-P-13.4, June 10, 1958.
18. Culp, A. W., and Page, E. M., "Calculational Method for Predicting the Residual Dose Rates from Activated Aircraft Turbo-Rotating Machinery," ASTRA, Inc., Medford, Conn., ASTRA 301-P-13.5, July 10, 1958.
19. Duffy, P. E., "Loads Report, D140E1 Power Plant, Rough Draft," GE-ANPD, PREDC-918, March 17, 1961.
20. Layman, D. C., "Stress and Weight Summary of the XNJ140E-1 Shield," GE-ANPD, DC 62-1-3, January 1962.
21. Phelps, E., "Power Plant Weight Status 140E1 (ACT)," GE-ANPD, DCL 61-3-125, March 23, 1961.
22. Layman, D. C., "Stress Analysis of the XNJ140E-1 Front Shield," GE-ANPD, DC 62-1-4, January 1962.
23. Tajirian, G., "Front Island Shield Thermal Displacements," Allstates Design and Development Co., Inc., Trenton, N. J., PREAS 4041-R4, March 16, 1961.
24. Ali, S. A., "Temperature and Pressure Data on D140E1 Front Shield Island Shielding Slabs," GE-ANPD, XDCL 60-11-145, November 1960.
25. Phelps, E., "Front Shield Weight and C. G.," GE-ANPD, DCL 61-2-82, February 16, 1961.

26. Layman, D. C., "Stress and Weight of the XNJ140E1 Rear Shield," GE-ANPD, DC 62-1-8, January 12, 1962.
27. McKee, D. J., "Investigation of the Effective Thermal Conductivities for a Finned Coolant Tube Lithium Hydride Specimen," GE-ANPD, DC 61-1-22, January 1961.
28. Welch, R. A., "Lithium Hydride Properties," GE-ANPD, DC 61-3-73, March 1961.
29. McKee, D. J., "Investigation of the Effective Thermal Conductivity of Cast Lithium Hydride," GE-ANPD, XDC 61-5-68, May 1961.
30. Serkiz, A. W., "An Analysis of the Temperature-Time Characteristics of a D140E1 Radial Shield 27-1/2° LiH Container," GE-ANPD, DC 61-4-24, April 1961.
31. Ollendorf, S., "Cast Salt Specimens, Transient Heat Transfer Analysis," GE-ANPD, DC 60-6-64, June 1960.
32. "Report on Reactor Side Shield Cooling System Designs," Kinetics Corporation, Cincinnati, Ohio, XDC 60-8-104, April 30, 1960.
33. Eelman, A. R., Podoliuk, B. A., et al, "Support Frame Stresses and Deflections from $1G_Z$ and $1G_Y$ Inertia Loads," GE-ANPD, DC 61-8-13, August 1961.
34. Beitch, L., "ASIST - A Digital Computer Program for Solution of Loads and Deflections in Frame Structures," GE-FPD, R59AGT59, January 26, 1959.
35. "Royal Aeronautical Society Data Sheets," Royal Aeronautical Society, Volume I and II, 1948.
36. "Stress Analysis Side Shield," Allstates Design and Development Co., Trenton, N. J., PREAS 4037-R9, April 3, 1961.
37. Gatewood, B. E., "Thermal Stresses," McGraw-Hill Publishing Co., 1957.
38. Ross, A. L., "Thermal Stress Analysis of Finite Sections," GE-ANPD, APEX-480, January 20, 1959.
39. Patschke, F. J., "D140E1 Side Shield Thermal Stresses from Peripheral Gradient - 27-1/2° Can and 48° Can, GE-ANPD, DC 61-7-50, July 1961.
40. Layman, D. C., "Heating Rates in XNJ140E1 Shaft Inserts," GE-ANPD, DC 62-1-9, January 1962.
41. Kurtz, H. J., "Thermal Cycling of Beryllium Discs," GE-ANPD, DC 61-7-2, July 1961.
42. Felgar, R. P., "Statistics of Fatigue Testing," GE-General Engineering Laboratory, R57-GL-56, February 21, 1957.
43. Feith, A. D., "Tapped Holes in Beryllium," GE-ANPD, APEX-649, July 10, 1961.
44. Asher, A. J., et al, "Cold Flow Air Tests Using a 0.27 Scale Model," GE-ANPD, DC 61-5-8, May 1961.
45. Yarosh, J. G., "Pre-Sector Flow Test," GE-ANPD, DC 61-4-64, April 1961.
46. Casagrande, R. D., "Results of the Cold Flow Testing of a 60° Sector Model of the D140E Rear Plug Internal Cooling Flow Network," GE-ANPD, DC 61-5-9, May 1961.
47. Bell, R. W., "Air Flow Tests of a Narrow Collector Passage with Eight Transverse Feeder Slots," GE-ANPD, APEX-650, February 21, 1961.
48. Bell, R. W., "Report on Flow Tests in the 1.5 Scale Model of a Typical Radial Cooling Slot in the Front Plug of the D140E1 Phase I," Naval Postgraduate School, Monterey, Calif., GV 765, February 24, 1961.
49. Brown, A. T., and Wells, T. E., "Structural Tests Duct Wall Forward Island Rear Shield," GE-ANPD, DC 61-8-10, August 1961.
50. Mohring, D. H., "Static Test Experimental Stress Analysis on Insulation Panel - GE682E-156," Kinetics Corporation, Cincinnati, Ohio, GE1272, November 11, 1960.
51. Asher, A. J., et al, "Experimental and Analytical Values for the Static Pressure Distribution Obtained for a Rear Shield Primary Duct Configuration," GE-ANPD, DC 60-12-109, December 1960.
52. Cook, R. F., "Heat Transfer Tests of D140 Rear Plug Insulation Panel," GE-ANPD, DC 61-6-14, June 1961.

53. Layman, D. C., "Side Shield Development Testing XNJ140E1," GE-ANPD, DC 62-1-10, January 1962.
54. Davis, D., "Thermodynamic Property Tests of Lithium Hydride, Phase I," GE-ANPD, DC 60-6-71, June 1960.
55. Ollendorf, S., "Thermodynamic Property Tests of Lithium Hydride, Phase II," GE-ANPD, DC 60-12-132, December 1960.
56. McKee, D. J., "Investigation of the Effective Thermal Conductivities for a Finned Coolant Tube Lithium Hydride Specimen," GE-ANPD, DC 61-1-22, January 1961.
57. Pugh, R. A., "Shield Tests - Georgia Nuclear Aircraft Laboratory, Marietta, Georgia," GE-ANPD, DCL 60-5-58, May 1960.
58. Pugh, R. A., "Test of General Electric Shield Segment, Statement of Work," GE-ANPD, XDC 60-12-48, December 1960.
59. Serkiz, A. W., et al, "Shield Segment Test, Test Procedures and Specifications for the G.E. Shield Segment Test," GE-ANPD, PREDC-695, June 28, 1960.
60. Serkiz, A. W., "Termination Report on the Irradiation Test of a D140E1 Prototype Side Shield Segment," GE-ANPD, APEX-655, July 7, 1961.
61. Boudreaux, R. A., et al, "Test of General Electric Shield Segment," GE-ANPD, XDC 60-7-134, July 1960.
62. Fleishan, M. R., "A Monte Carlo Study of the Leakage from Finite Hydrogeneous Regions of the Neutrons from a Point Fission Source," Nuclear Development Corporation of America, NDA 2092-6, June 2, 1956.
63. Goldstein, H., and Krumbein, A. D., "Moments Method Calculations of the Penetration of Neutrons from a Point Fission Source Through Be,and BeO," Nuclear Development Corporation of America, NDA Memo 2124-1, May 27, 1960.
64. Capo, M. A., "Polynominal Approximation of NDA Gamma Ray Buildup Factors for a Point Isotropic Source," GE-ANPD, XDC 58-11-209, November 1958.
65. Edwards, W. E., and Capo, M. A., "Nuclear Data," GE-ANPD, XDC 57-1-8, January 1957.
66. Glasstone, S., "Principles of Nuclear Reactor Engineering," D. Van Nostrand Company, Inc., Sections 3.45 to 3.61, 1955.
67. Goldstein, H., and Mechanic, H., "Penetration of Neutrons from a Point Fission Source through Beryllium and Beryllium Oxide," Nuclear Development Corporation of America, NDA 2092-9, June 23, 1958.
68. Henderson, W. B., and Stanley, M. J., "Cross-Sections for Reactor Analysis," GE-ANPD, APEX-515, May 1957.
69. Brooks, E. H., and Milburn, E. L., "Shielding Measurements about the SSR," GE-ANPD, DC 61-2-3, February 1961.
70. Henderson, W. B., and Stanley, M. J., "Supplement I to APEX-515," GE-ANPD, XDC 59-11-72, November 1959.
71. Roberts, T. D., "Photon Producing and Neutron Activation Cross Section," GE-ANPD, XDC 60-8-81, August 1960.
72. Bermanis, H. L., "Absolute Power Calibration of the SSR-VI-B Reactor," GE-ANPD, DC 60-8-6, August 1960.
73. Zoller, L. K., "Correlation of Experimental and Analytical Shield Nuclear Data from the Shield Source Reactor," GE-ANPD, DC 61-7-19, July 1961.
74. McVey, C. I., "Shield Gamma Heating Measurements in the SSR-4B Reactor," GE-ANPD, DC 61-2-59, February 1961.
75. Vieli, N., "Prediction of Foil Activation Inside the Nuclear Side Shield of the SSR-II-3 Critical Assembly," GE-ANPD, DC 60-12-38, December 1960.

6. TURBOMACHINERY

6.1 INTRODUCTION

The XNJ140E-1 turbojet engine incorporated a single set of X211-E1 turbomachinery. Wherever possible, the components used were identical to the X211 turbomachinery components developed for the XMA-1 nuclear turbojet engine. The modifications required were directed toward the flight version of the XNJ140E engine; those made were influenced by the practical considerations of technology, cost, and time.

Since the XNJ140E-1 engine was intended for operation in the Advanced Core Test Program, the turbomachinery functioned primarily as an air supply for the reactor. Development of advanced turbomachinery components for operational engines was a secondary consideration. Turbomachinery proposed for XNJ140E-1 is identified as Model X211-E1 and utilized, wherever possible, Block II or Block III components originally developed for the XMA-1 Program. These components were redesignated Block IV.

Major components of the turbomachinery were: (1) the compressor section, consisting of the compressor stator and the compressor rotor; (2) the turbine section, consisting of the turbine stator, turbine rotor, and the chemical interburner system; (3) the bleed-speed manifold mounted aft of the turbine rear frame; (4) the exhaust section, consisting of the exhaust duct and the exhaust nozzle; and (5) the accessory drive system.

6.2 DESIGN REQUIREMENTS

6.2.1 STRUCTURAL DESIGN

The X211-E1 turbomachinery was designed to meet the following structural requirements:

1. Compressor shutoff-doors were to be provided.
2. The structural components of the chemical interburner were to be an integral part of the system.
3. Air bled from the trailing edge of the turbine nozzles was to be used to control the T_4 profile.
4. Chemical afterburning was not required.
5. A primary exhaust nozzle with simplified linkage was to be provided. Secondary pumping capacity (secondary nozzle) was not required.
6. Provisions for anti-icing were not required.
7. The engine starter was to be bullet-nose-mounted at the compressor inlet. Starter exhaust air was to be ingested by the compressor.
8. All components were to be capable of surviving, without damage, not less than 50 compressor stalls at 85 percent speed or above, and not less than 200 compressor stalls at approximately 50 percent speed. These compressor stalls could occur in any order.

Detail design requirements are contained in reference 1. The Preliminary Model Specification is contained in reference 2. The Preliminary Mechanical Reliability Evaluation Specification is given in reference 3. The Preliminary Acceptance Test Specification is contained in reference 4.

6.2.2 TEST OPERATIONS

The X211-E1 turbomachinery was designed to meet the following operational requirements.

Ground Usage

1. Ground test at GE-Evendale using Engineering Test Burner (ETB).
2. Ground test at FET (ITS) using both chemical heat only and nuclear heat only.
3. Ground ambient atmosphere containing dust/sand content varying from 0.04 to 0.15 mg/cubic meter, average 0.0726 mg/cubic meter.
4. Ground atmospheric pressure to vary between 25 to 26 inches Hg (4790 feet alitude).
5. Ground atmospheric temperature to vary between -30° to 120°F.

Initial Flight Demonstration

1. Capable of initial flight demonstration during which the engine was not required to contribute to the support of the aircraft.
2. Initial flight demonstration, nuclear heat only (typical flight).

Altitude, ft	M_N	Power Setting	T_4, °F	Time, hr
35,000	0.8	N.C.	1695	60
35,000	0.8	Mil	1760	2
20,000	0.7	N.C.	1695	35
20,000	0.7	Mil	1760	2
5,000	0.6	Emergency	1795	1

6.2.3 TEMPERATURE LIMITATIONS

6.2.3.1 Surface Temperatures

The aerodynamic design of the turbomachinery met the following maximum temperatures on the outer surfaces of the turbomachinery components.

Surface	Temperature, °F
Compressor casing 3rd stage	250
Compressor casing 4th stage	280
Compressor casing 5th stage	330
Compressor casing 6th stage	370
Compressor casing 7th stage	420
Compressor casing 8th stage	460
Compressor casing 9th stage	510
Compressor casing 10th stage	550
Compressor casing 11th stage	600
Compressor casing 12th stage	650
Compressor casing 13th stage	690
Compressor casing 14th stage	730
Compressor casing 15th stage	780
Compressor 16th stage	810
Compressor rear frame	900

Surface	Temperature, °F
Turbine front frame	950
Turbine casing front circumferential flange	1100
Turbine casing ring	1100
Turbine casing 1st stage	1100
Turbine casing 2nd stage	1050
Turbine casing 3rd stage	950
Turbine casing rear circumferential flange	900
Turbine casing horizontal flange 1st stage	1100
Turbine casing horizontal flange 2nd stage	1050
Turbine casing horizontal flange 3rd stage	940
Turbine rear frame	1100
Exhaust duct	1000
Nozzle flaps	1000
Nozzle, other parts	1000
Accessory drive gearboxes	300

6.2.3.2 Ambient Temperatures

Turbomachinery control system components and subcomponents were designed to operate satisfactorily in the following ambient temperatures.

Component	Temperature, °F
Engine-mounted control components forward of turbine	225
Engine-mounted control components aft of turbine	300
Off-engine-mounted controls	120
Nozzle area transducers	300

6.3 DESCRIPTION OF COMPONENTS

6.3.1 COMPRESSOR SECTION

An isometric cutaway drawing of the compressor section is shown in Figure 6.1.

6.3.1.1 Front Frame Assembly

The front frame assembly is shown in Figure 6.2. It was designed to provide a smooth aerodynamic air passage into the compressor with a minimum effect on compressor-inlet flow distribution, and to limit distortion of the stator casing. It supported and provided services for the No. 1 bearing sump, supported the inlet guide vanes, and also supported the inlet-air-duct extension. The design differed from the Block II frames only because of those changes necessary to utilize the Block III gearbox, to provide admittance into the bulletnose area of starter controls and service equipment, and to expedite remote assembly and disassembly of the compressor section. It was a fabricated Chromoloy* sheet metal structure with eight evenly spaced radial struts.

The structure consisted of an outer cylindrical shell which supported the variable angle inlet guide vanes and provided an outer support for the struts and the transfer gearbox, together with various engine accessories. The struts were used to carry oil to and from the forward (No. 1) main engine bearing, and to supply air for pressurizing the sump. The struts also supported an inner box-member containing the No. 1 bearing and an aft

*General Electric Company, Material Specification.

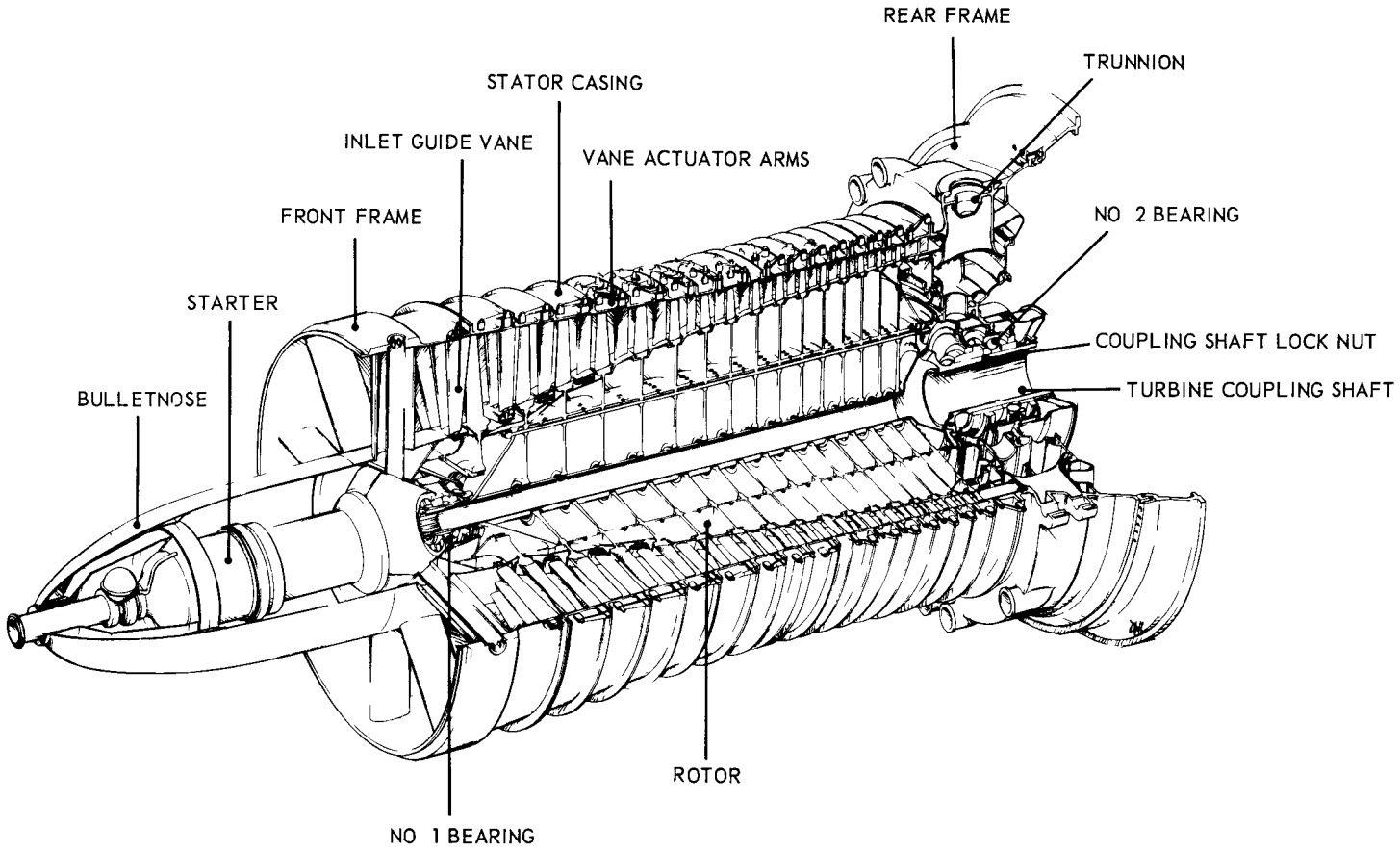

Fig 6 1 – Compressor section

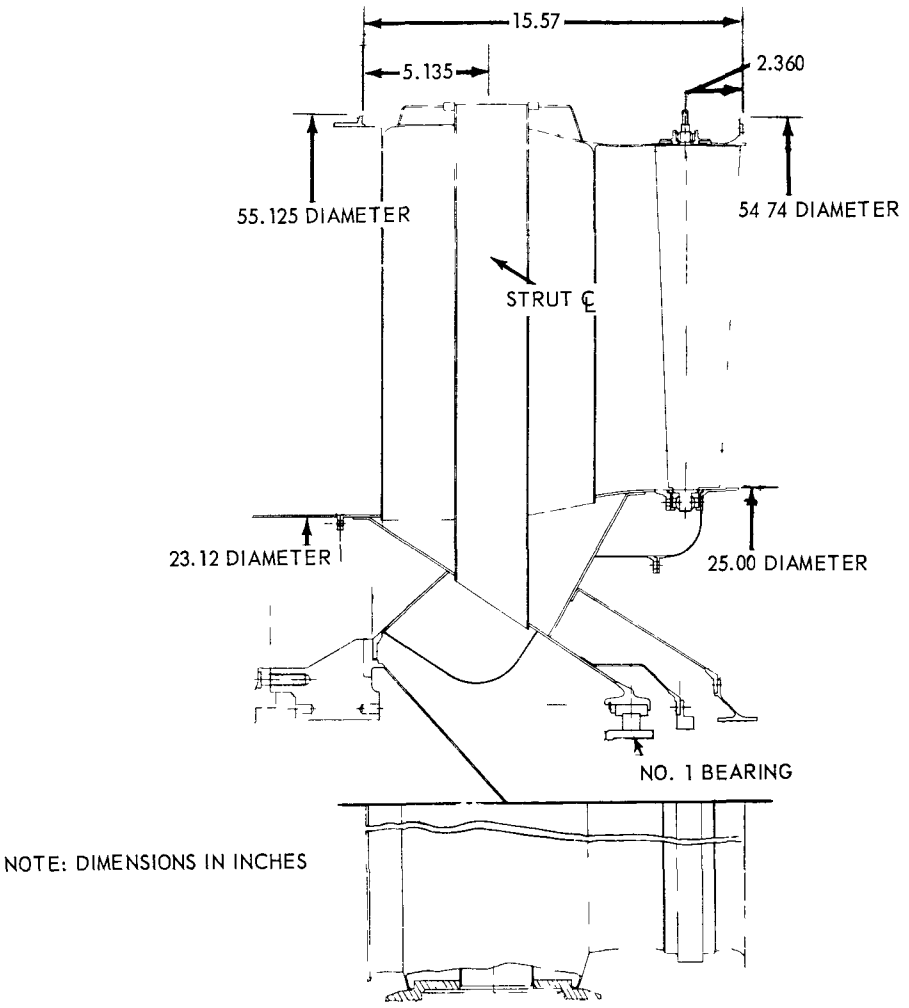

Fig. 6.2 – Compressor front frame assembly

carbon seal. The inner box-member supported the inlet gearbox, the air starter, and the variable inlet guide vanes.

The outer casing had a quick-disconnect front-flange and a bolted rear-flange. The inlet duct extension was connected to the front flange by a quick-disconnect clamp and did not introduce loads on the exceeding 822 pounds shear, 2736 pounds axial, and 17, 280 inch-pounds overhung moment. Pads for ground handling capable of a maximum loading moment of 12, 500 inch-pounds were located at the 3- and 9-o'clock positions.

Strut-end castings were utilized to connect the casing to the struts (1) to decrease fabrication problems and (2) to minimize the possibility of fatigue failures. The struts provided support for the bearing housing and were designed to minimize the deflection of the bearing with respect to the outer casing. The two vertical struts had different thickness-to-chord ratios than the other six. The larger struts had a 24 percent maximum thickness-to-chord ratio while the smaller struts had a 15 percent ratio. The bottom vertical strut (strut No. 5) contained a radial drive shaft for the transfer gearbox. This shaft established the thickness of the strut. The top vertical strut was of the same thickness-

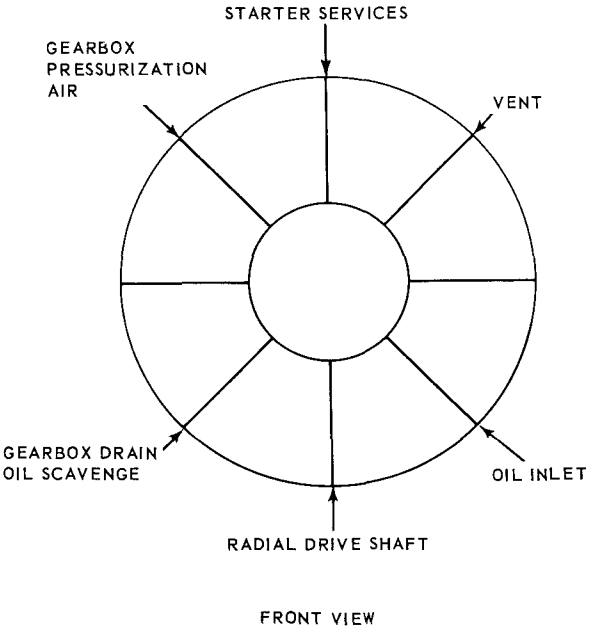

Fig. 6.3 – Compressor front frame strut usage

to-chord ratio in order to maintain aerodynamic symmetry. Figure 6.3 shows the arrangement of the struts and indicates strut usage.

The variable inlet guide vanes consisted of wrap-around, hollow 17-7 PH sheet metal airfoils brazed to internal corrugated stiffeners. There were 48 vanes located aft of the struts, supported on the outer end by the outer cylindrical casing and supported on the inner end by the diffuser inlet wall. Spherical bearings supported each end of the vanes. The vanes were actuated by a linkage system connected to, and similar to the variable stator mechanisms. The force applied to the actuator ring to position the inlet guide vanes was approximately 350 pounds. The inlet guide vanes were not designed for either anti-icing or hailstone ingestion.

The No. 1 bearing was a single-row roller bearing. The rollers and races were M50 tool steel with a silver plated iron-silicon-bronze cage. The bearing had a B_{10}* life of 25,950 hours at 5,000 rpm and at its equivalent design radial load of 2,730 pounds.

The oil seal located aft of the bearing was a single-element carbon circumferential-bore rubbing seal. The No. 1 sump air seal was located aft of the carbon seal and provided a barrier to maintain adequate sealing pressures for the carbon oil seal and thereby prevent oil leakage into the compressor primary-air flow path.

6.3.1.2 Rotor Assembly

The rotor assembly was a 16-stage axial flow unit as shown in Figures 6.4 and 6.5. At sea-level-static pressure and at a rotational speed of 5000 rpm, the compressor operated at a pressure ratio of 12.5 to 1, and delivered an airflow of 425 pounds per second.

The rotor assembly was the same as the Block II design except for minor modifications necessary to adapt it for XNJ140E-1 engine usage. The rotor blades in stages 1 through 4

*B_{10} life: A combination of speed and load that will lead to a statistical 90 percent survival (10% failure) at the stated life.

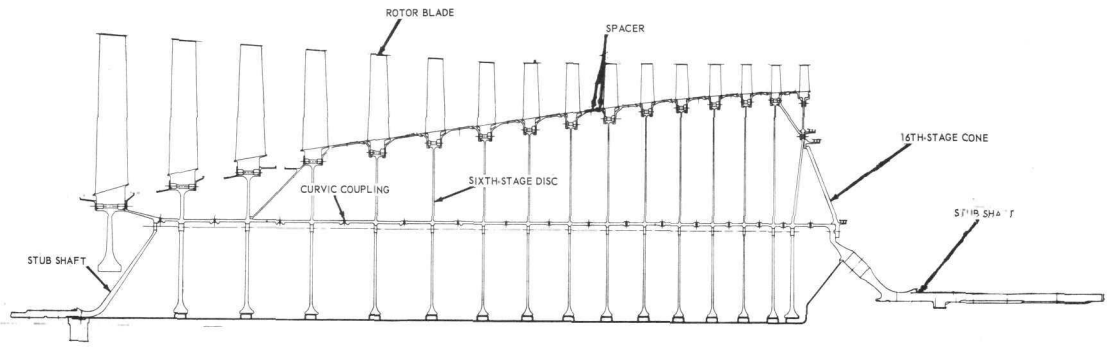

Fig. 6.4 – Compressor rotor assembly

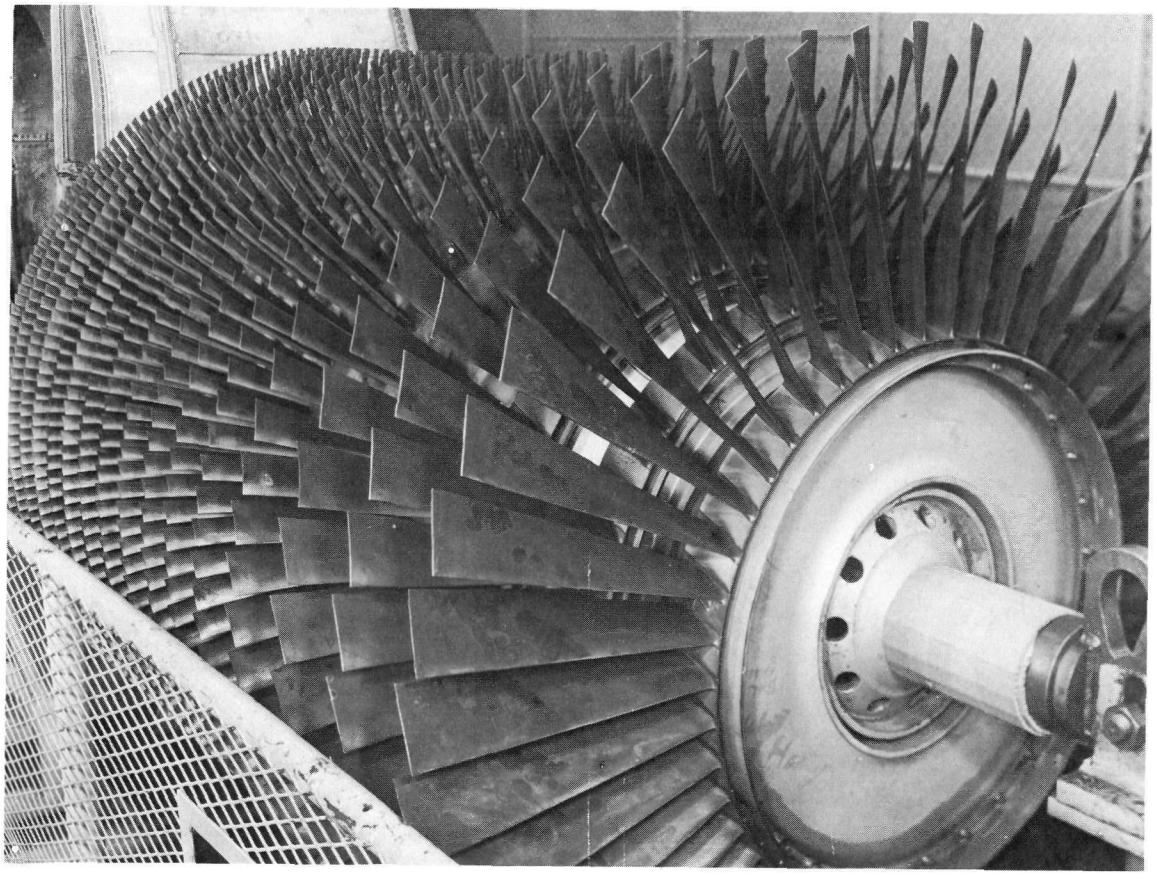

Fig. 6.5 – Compressor rotor assembly

were manufactured from forged, vacuum melted A286 material. Calculated steady-state and vibratory blade stresses were within the limits of the Goodman diagram. A summary of the compressor blade data is given in Table 6.1. Although the compressor was subsonic, the airfoils were transonic in stages 1 and 2 and subsonic NACA series 65 in stages 3 through 16. The blades contained squealer tips to allow operation with close clearances. During operation these squealer tips were rubbed off by an abrasive material (sprayed on the compressor stator casing above the blade tip) without damage to either the stator or the rotor blade.

All stages of compressor discs were forged and machined B5F5[†] (chromium-molybdenum-vanadium alloy steel). Stages 2 through 16 had extensions on either side of the web with ground curvic-coupling-teeth grouped in such a fashion that accurate axial dimensions were maintained. When adjacent discs were mated there was no radial movement. The cylinder that was formed when the discs were assembled acted as the main structural member to resist bending, to transmit torque, and to position the discs radially and axially. The entire disc structure was held together by 24 half-inch-diameter tie-bolts. All discs were designed to either 0.02 percent yield strength or 0.2 percent plastic creep strength except near the bore where stresses were as high as 0.2 percent yield strength.

An axial force which tended to restrict axial deflection at the disc rims was transmitted forward through the rim of the fifteenth-stage disc by a cone located aft of the fifteenth-stage disc. This force was then transmitted through spacers and rims to the third-stage forward spacer which, in turn, transmitted the force to the second-stage curvic-coupling area and finally to the front stub-shaft. The sixteenth-stage disc airseal was radially positioned such that the differential rotor thrust absorbed by the No. 2 thrust bearing located in the compressor rear frame was properly balanced and minimized.

Spacer rings located between the discs were split circumferentially with the aft spacer of each stage mating with the forward spacer of the next stage. The design permitted separately assembling an entire stage. Thus, the rotor could be assembled and disassembled without removing spacers from disc. These rings were made of forged and machined B5F5 material, and were stressed below the 0.02 percent yield strength.

The front and rear stub-shafts also were made from forged and machined B5F5 material. The front stub-shaft was supported radially by the No. 1 bearing and was free to move axially. The shaft had an internal diameter large enough to allow passage of remote handling tooling which locked and unlocked the internal turbine coupling-shaft locking device. Since the front stub-shaft was supported in the compressor front frame by means of a roller bearing, no axial forces were transmitted to the front frame and the shaft was required to support only those loads caused by rotational hoop and bending forces.

Holes in the cone section of the aft stub-shaft allowed ninth-stage compressor bleed air to flow through the inside of the turbine coupling shaft for shaft cooling. The aft stub-shaft was supported by the No. 2 (combined thrust and radial) bearing and was designed to withstand the rotational stresses induced by transmitting the entire turbine coupling shaft torque. It also reacted any axial forces developing from rotor thrust unbalance and pressure differential across the rotor.

6.3.1.3 Stator Assembly

The stator assembly (1) converted to pressure the kinetic energy imparted to the air by the rotor, (2) supported the rear gearbox, (3) acted as a structural member connecting the compressor front and rear frame, and (4) contained the air-bleed ports for turbine cooling-air and seal pressurization-air. The assembly, shown in Figures 6.6 and 6.7,

[†]General Electric Company, Standard Material Specification.

TABLE 6.1

SUMMARY OF COMPRESSOR BLADE DATA

Stage	Number of Blades	Aspect Ratio	TM/C Root	TM/C Tip	Flexural and Torsional Natural Frequencies				Blade Dovetail Stresses		Airfoil Root Stresses[a] at 100% N (Mach 0.9) at SL	
					f_1	f_2	f_3	f_{1t}	Allowable Stress, psi	Design Stress, psi	σ_{eff}	σ_{vib}
1	40	4.29	0.0825	0.040	122	382	913	411	8,500	6,904	58,663	36,700
2	44	4.29	0.100	0.050	142	433	1,178	446	9,500	9,412	54,292	36,457
3	50	3.44	0.105	0.040	200	555	1,190	831	26,000	22,370	39,900	42,600
4	57	3.43	0.110	0.040	214	628	1,312	790	22,000	19,837	34,200	28,900
5	66	3.42	0.110	0.040	230	658	1,392	748	30,000	17,138	31,850	21,100
6	78	3.34	0.115	0.040	267	790	1,675	870	30,000	26,921	25,900	16,230
7	88	3.10	0.110	0.040	308	934	2,064	1,010	32,500	23,874	28,600	15,600
8	94	2.95	0.115	0.050	345	1,297	2,378	1,112	33,500	21,113	30,000	15,200
9	102	2.87	0.115	0.050	387	1,363	3,303	1,449	34,700	20,696	32,800	19,700
10	103	2.55	0.115	0.524	471	1,873	3,396	1,606	36,700	18,314	31,100	16,800
11	109	2.41	0.110	0.050	517	2,114	3,760	1,563	37,200	28,325	31,600	20,150
12	109	2.15	0.110	0.0522	626	2,628	4,625	1,938	35,700	27,967	30,700	16,350
13	116	2.09	0.110	0.050	687	2,896	4,627	1,911	37,700	25,239	27,000	17,050
14	124	2.07	0.110	0.050	748	3,075	5,010	2,080	39,200	21,251	29,800	17,450
15	131	2.07	0.115	0.050	755	3,175	5,358	2,210	41,000	17,532	29,400	17,520
16	126	1.91	0.115	0.050	833	3,522	5,610	2,335	43,300	15,639	28,200	15,450

[a] σ_{vib} is allowable vibratory stress from the Goodman diagram; σ_{eff} is effective steady-state stress.

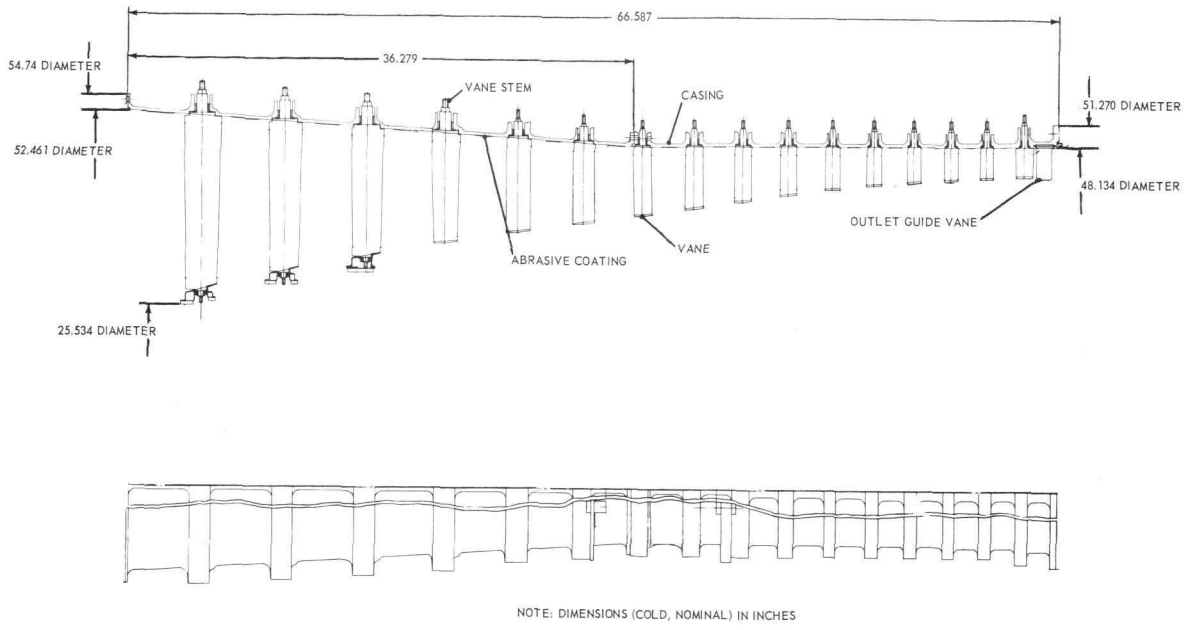

Fig. 6.6 – Compressor stator assembly

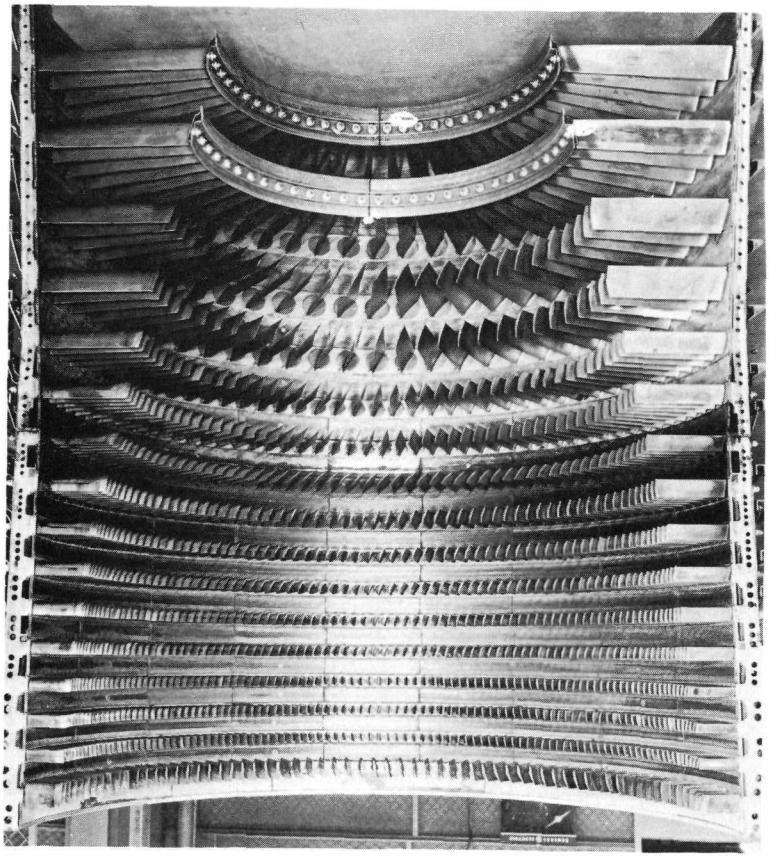

Fig. 6.7 – Compressor stator assembly (Neg. 254544)

was similar to the Block II design except for changes necessary to adapt it to the XNJ140E-1 configuration.

The stator assembly consisted of front and rear sections. The front section was conical and the rear section was cylindrical. Both sections were made of forged and machined Chromoloy and were of horizontally split, single wall construction. Bleed air was extracted at the ninth-stage for turbine cooling and seal pressurization. This bleed air, discharged from the ninth-stage manifold, was approximately 430°F total temperature and 56 psia at 100 percent corrected speed, sea-level-static, standard-day conditions.

The front section housed vane stages 1 through 6 and the rear section housed stages 7 through 16, together with the outlet guide vanes. The inner diameters were sprayed with an abrasive coating to rub off the rotor blade squealer tips. The compressor was designed to operate with close tip tolerances and the abrasive coating rubbed off the blade squealer tips without damage to either the stator or the rotor blades. Axial spacing of the vane stages was established so as to keep the vanes from deflecting into the rotor blades in the event of a compressor stall.

All vane stages were designed to be variable. The outer end of each vane formed a stem to which a vane lever was attached. The vane lever, in turn, was attached to an actuating ring which varied the angular positions of all stages in unison during engine operation. As the ring was rotated about the outside diameter of the compressor, the levers positioned the vanes as required for efficient engine operation.

The levers used to actuate the vanes were of lightweight, low cost design, and were made of 410 stainless steel. The actuation rings were also lightweight, low cost design, and were made of AMS4150 aluminum, extruded into box-sections, shaped into half-rings. There were two half-rings per stage joined at the horizontal joint to provide a complete ring.

Although all stages were initially designed to be variable, full scale compressor testing showed that only the inlet guide vanes and the first six stages of vanes needed to be variable. Stages 7 through 16, therefore, were fixed in position.

Stage 16 vanes, rings, and levers were designed to permit closing the vanes until the airfoils overlapped in venetian-blind fashion and provided compressor isolation capability by acting as shutoff doors. Two actuators were used to position the inlet guide vanes and the first six stages of the stator vanes. A bell crank mechanism ganged all variable stages together.

The number of vanes per stage varied between 44 and 142. Stator vanes in stages 1 through 10 were made of 403 stainless steel and vanes in stages 11 through 16 were made of A286. The vanes in stages 1, 2, and 3 were shrouded to limit deflection in the event of a compressor stall. Each vane was mounted in a bushing in the compressor casing. These bushings were made of 416 stainless steel with 56HT carbon inserts. Carbon inserts were selected because this material was resistant to radiation damage.

Air seals were mounted on the inner shrouds of the stator vanes in stages 1, 2, and 3 and were required because of the shrouded design of these stages. Inter-stage sealing was provided on the other stages by limited clearance between the stator-vane-tip and rotor-spacer. A summary of the compressor vane data is given in Table 6.2.

6.3.1.4 Rear Frame Assembly

The rear frame assembly was similar to that shown in Figures 6.8 and 6.9. It was designed to (1) provide the compressor-discharge airflow path, (2) support the thrust (No.

TABLE 6.2

SUMMARY OF COMPRESSOR VANE DATA

Stage	Number of Blades	Aspect Ratio	TM/C Root	TM/C Tip	Flexural and Torsional Natural Frequencies			
					f_1	f_2	f_3	f_{1t}
1	44	4.44	0.12	0.04	109	428	1,059	885
2	48	4.12	0.12	0.04	134	535	1,325	977
3	52	3.78	0.12	0.04	167	683	1,694	1,104
4	58	3.62	0.12	0.04	191	809	2,028	1,183
5	68	3.56	0.12	0.04	208	929	2,348	1,248
6	80	3.42	0.12	0.04	244	1,106	2,795	1,388
7	100	3.32	0.13	0.05	285	1,350	3,500	1,695
8	108	3.13	0.13	0.05	345	1,642	4,157	1,887
9	112	2.89	0.13	0.06	412	2,032	5,395	2,140
10	118	2.78	0.13	0.06	483	2,415	6,337	2,365
11	124	2.61	0.13	0.06	539	2,687	7,095	2,473
12	128	2.35	0.13	0.0702	643	3,307	8,800	2,783
13	132	2.33	0.13	0.06	726	3,621	9,550	2,952
14	138	2.19	0.13	0.066	802	4,075	10,800	3,150
15	142	2.20	0.13	0.06	856	4,270	11,250	3,262
16	130	1.63	0.13	0.11	1,082	6,030		3,698
OGV	130	2.0	0.10	0.10	611	3,832	10,734	2,705

2) bearing and engine mounts, (3) provide uncontaminated customer bleed air, and (4) provide a passage for cooling-air to the turbine coupling-shaft and turbine. Furthermore, it limited distortion of the compressor casing. It supported and provided services for the No. 2 oil sump, and provided an outer structural support for the compressor section and the reactor pressure vessel. In addition to the above functions, the compressor rear frame was sufficiently rigid to permit close compressor clearances and to support the stationary portions of the compressor-discharge airseal.

The compressor rear frame was a fabricated Inconel W structure containing eight cast Inconel 718 radial struts welded into an outer cylindrical casing and into an inner box-structure. The entire assembly except the sump was bathed in compressor-discharge air to minimize thermal stresses.

The outer box-structure contained a forward flange supporting the compressor rear stator casing, and an aft flange which bolted to the forward flange of the reactor pressure vessel. The frame also contained three engine mounts to absorb the horizontal, vertical, and side engine loads. These mounts were located at the 9-, 12-, and 3-o'clock positions, and were designed to accept axial loads of 118,000 pounds maximum, side loads of 40,000 pounds maximum, and vertical loads of 137,000 pounds maximum. The frame also had two ground handling pads located at the 3- and 9-o'clock positions.

The struts carried oil to, and from the No. 2 sump and provided passage for cooling-air extracted from the ninth-stage manifold. The No. 2 sump was vented through the struts. The sump and oil lines were isolated from the compressor discharge-air by service passages through the struts. Strut usage is shown in Figure 6.10.

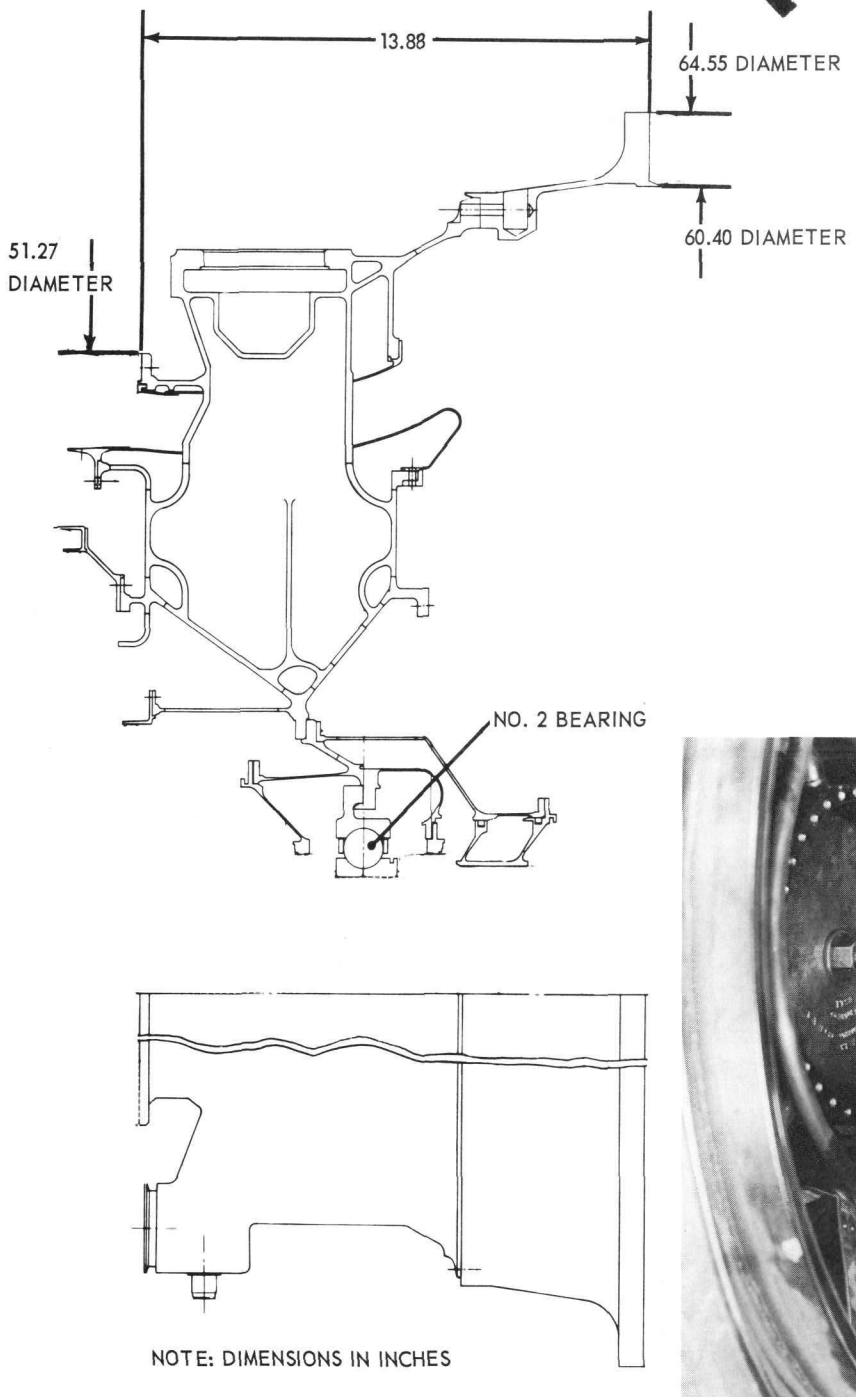

Fig. 6.8 – Compressor rear frame assembly

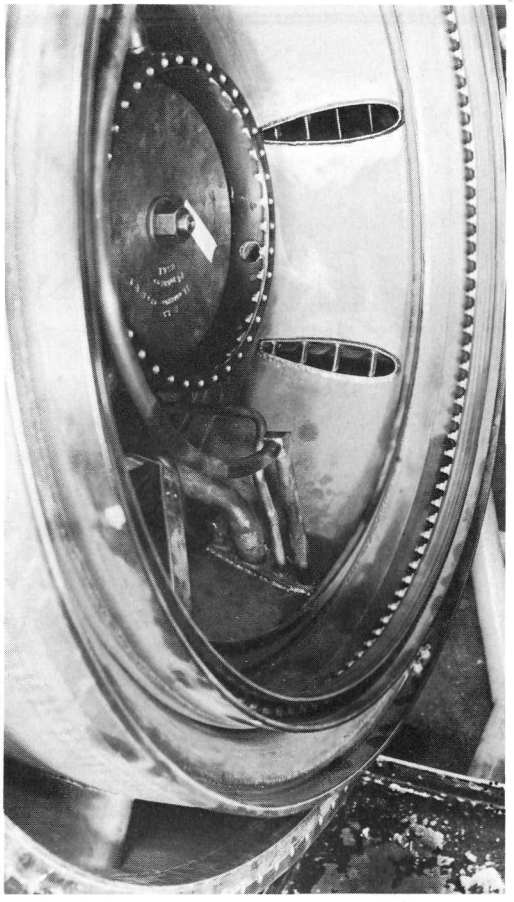

Fig. 6.9 – Compressor rear frame assembly (Neg. 247086)

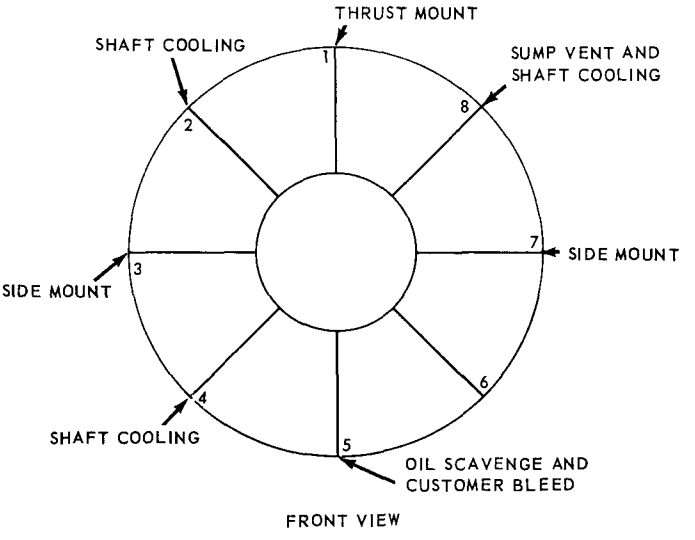

Fig. 6.10 – Compressor rear frame strut usage

The inner box-structure supported the No. 2 bearing sump and incorporated an inner-ring strut-support in order to transmit the axial inner-hub pressure, the axial rotor thrust, and the radial bearing load to the outer casing with minimum bearing deflection. Thermal expansion resulting from the struts being bathed in compressor discharge-air produced a maximum radial load of 19,000 pounds per strut. Since this load resulted in a negligible stress increase in the inner support rings, a heat shield was not required to reduce strut heating.

The No. 2 sump was separable to reduce manufacturing problems. The No. 2 bearing was a single-row ball-bearing, and carried both thrust and radial loads. The frame was designed for a maximum radial load of 25,000 pounds and a maximum thrust load of 30,000 pounds. The axial clearance was 0.064 inch.

6.3.2 TURBINE SECTION

An isometric cutaway view of the turbine section is shown in Figure 6.11. Figure 6.12 shows a view of the turbine section instrumented and on test.

6.3.2.1 Front Frame Assembly

The front frame assembly, Figures 6.13 and 6.14, provided a smooth, uninterrupted aerodynamic flow path from the reactor discharge to the combustor. It supported the rear trunnion of the engine (side and vertical loads only) and provided support and service passages for the No. 3 bearing and sump. Part of the front frame served to retain a portion of the rear shield. It provided air ducting into, and all mounting provisions for the combustor, and also provided flow passages for bleed-speed air, aftercooling air, and turbine-cooling air.

The front frame assembly was an Inconel W structure. It consisted of a flanged outer cylindrical casing, ten equally spaced radial struts, and an inner ring-shaped box-type structure. It was reinforced with two external hat-shaped sections which carried the rear engine mount loads, and also distributed radial and axial strut loads. The hat-sections also transferred engine mount loads into the outer casing. They provided a manifold which distributed balance-piston air from its external piping to the strut passages, and acted as a manifold to conduct seal-leakage air to external vents.

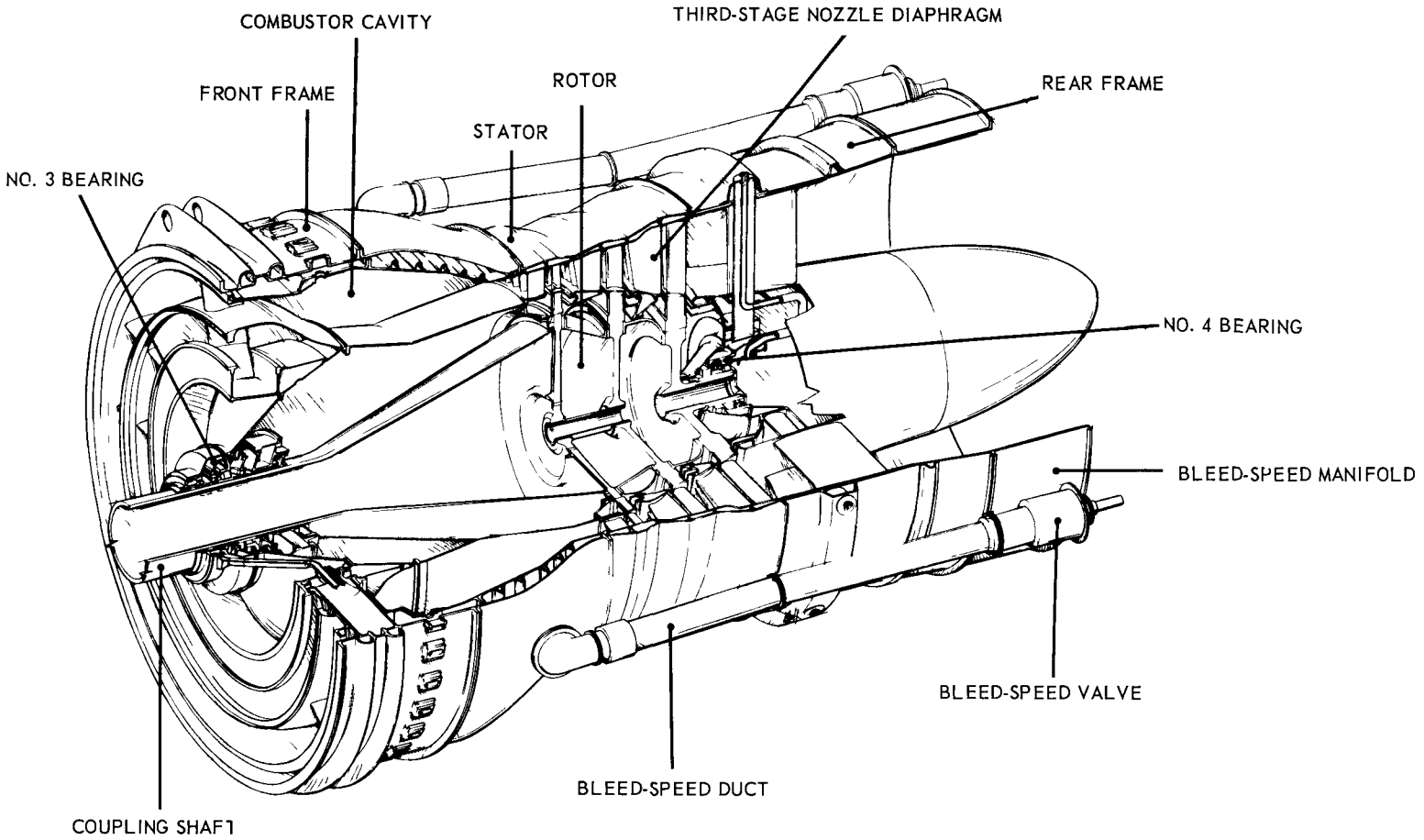

Fig. 6.11 – Turbine section

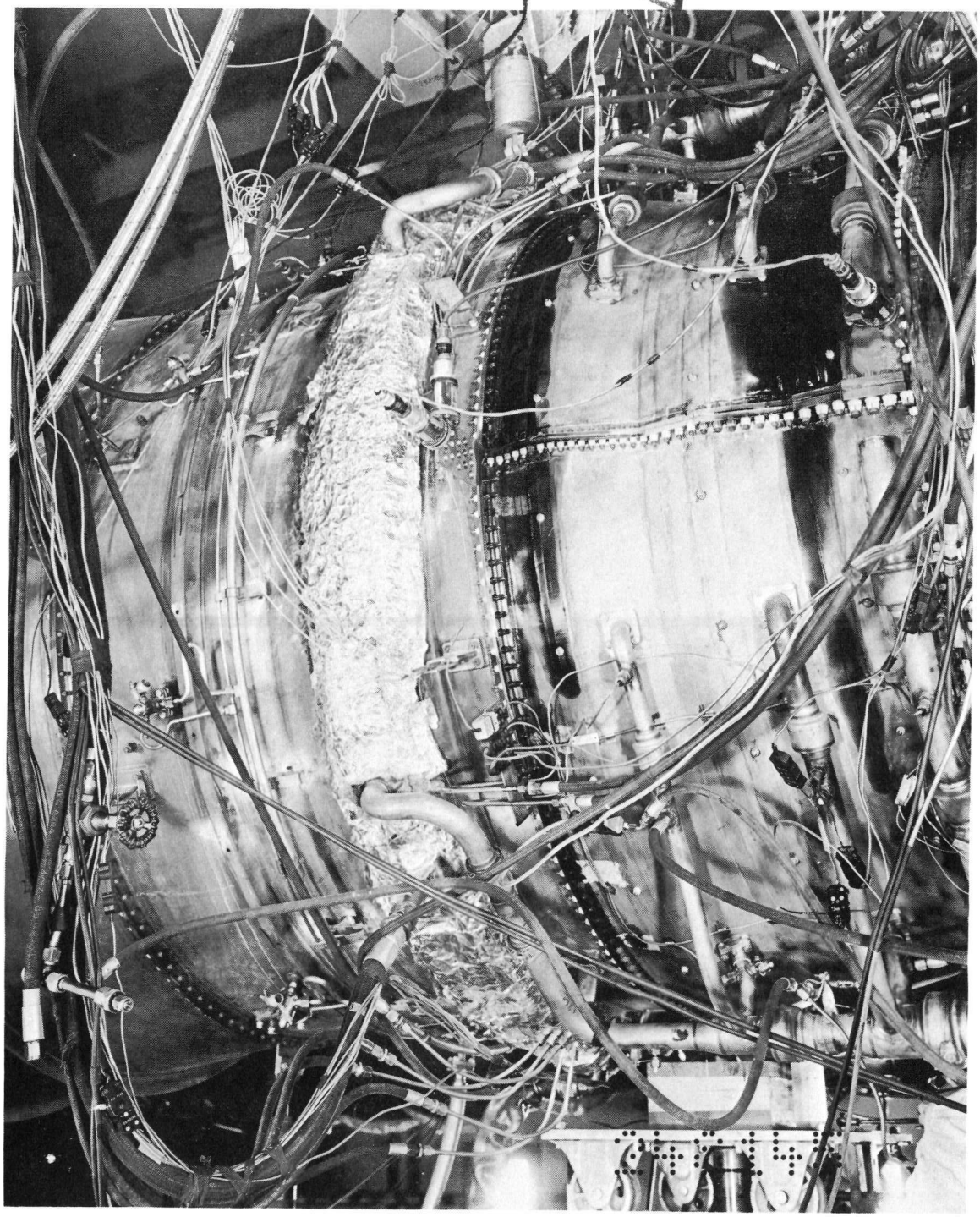

Fig. 6.12 – Turbine section (Neg. 246145)

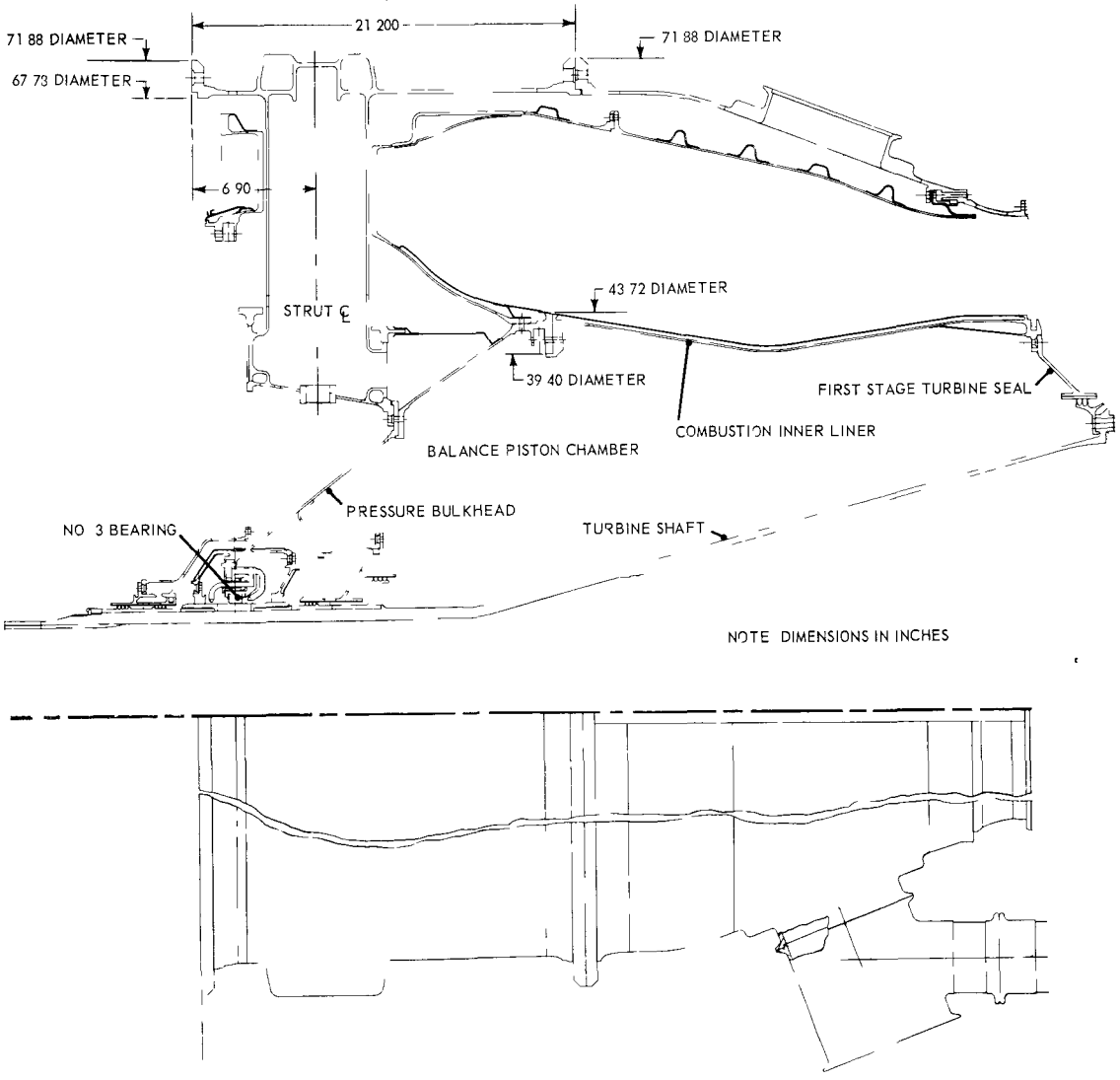

Fig. 6.13 – Turbine front frame assembly

The radial struts connected the outer casing with the inner-ring box-structure comprised of two radial rings connected by the strut end-castings. These struts carried the radial loads of the No. 3 roller bearings, served as passages for balance-piston air from the outer hat-sections, and provided passages for all sump services and vents. They were designed to withstand deflection bending stresses of 27,500 psi. Figure 6.15 shows strut usage.

Air-cooled insulation panels were used to limit the temperature of the front frame air passage and structural wall, and to prevent excessive heat transmission into the inner cavity and the outer airflow channel. This insulation panel contained an insulation blanket, a Hastelloy X liner, and a convoluted Hastelloy X sheet seam-welded to the underside of the liner. Cooling-air passages in the blanket directed compressor discharge-air axially along the liner and exhausted the air over the leading edge of the next panel. Air was metered into the panel through fittings at the forward end and through an orifice in the entrance of each convolution. A typical insulation panel is shown in Figure 6.16.

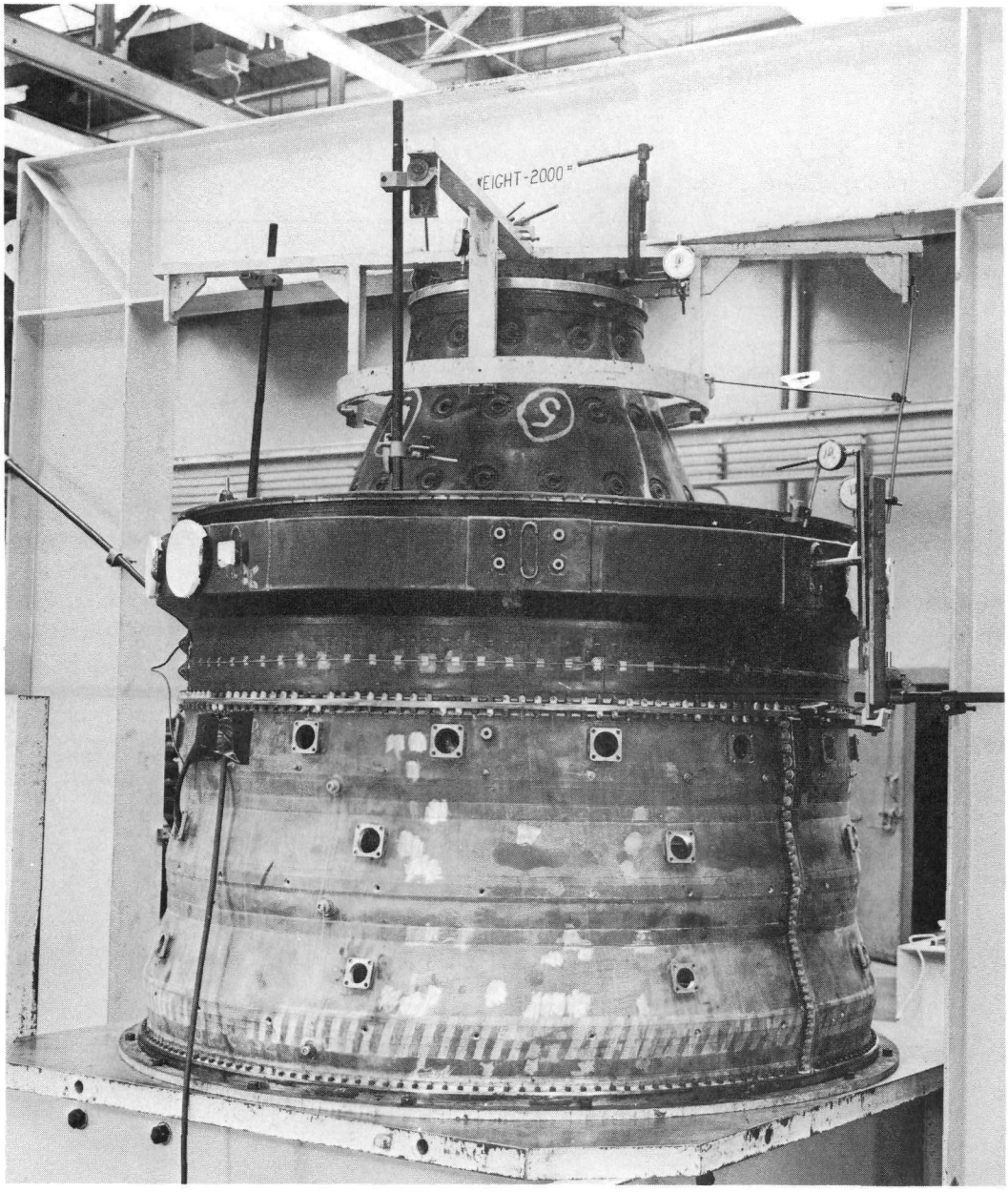

Fig. 6.14 – Turbine front frame assembly

The aft engine-mounting-trunnions were located on the front frame. Two trunnions were positioned 33 degrees on either side of the top vertical centerline of the frame and were capable of absorbing vertical loads of ± 111, 200 pounds and side loads of ± 58, 800 pounds. These mounts did not have axial-load carrying capability. Ground-handling pads located at the 3- and 9-o'clock positions on the outer casing were capable of withstanding a radial load of 23, 800 pounds each.

A balance-piston chamber, shown in Figure 6.13, served to reduce the axial bearing-load. Compressor discharge-air was bled from the bleed-speed cavity through the struts and rear shield into the balance-piston chamber. This cavity provided a pressure-load directed forward by confining compressor-discharge-pressure air between the turbine

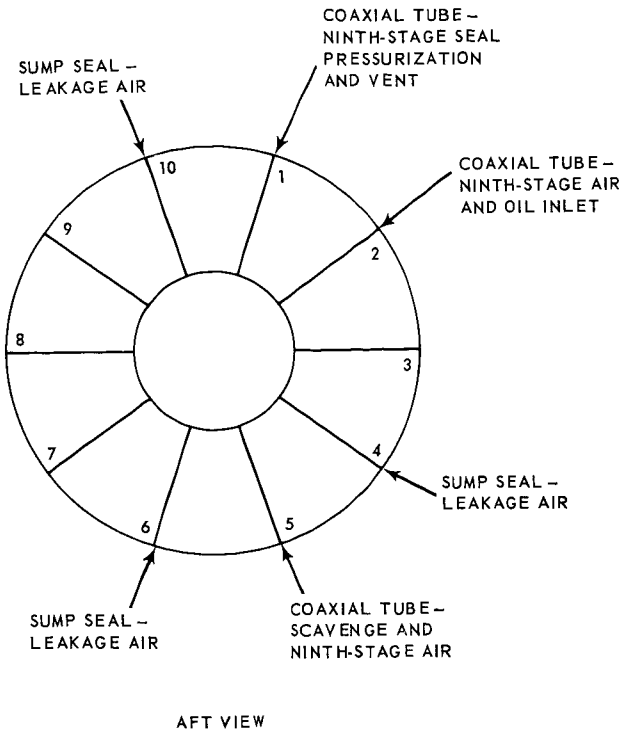

Fig. 6 15 – Turbine front frame strut usage

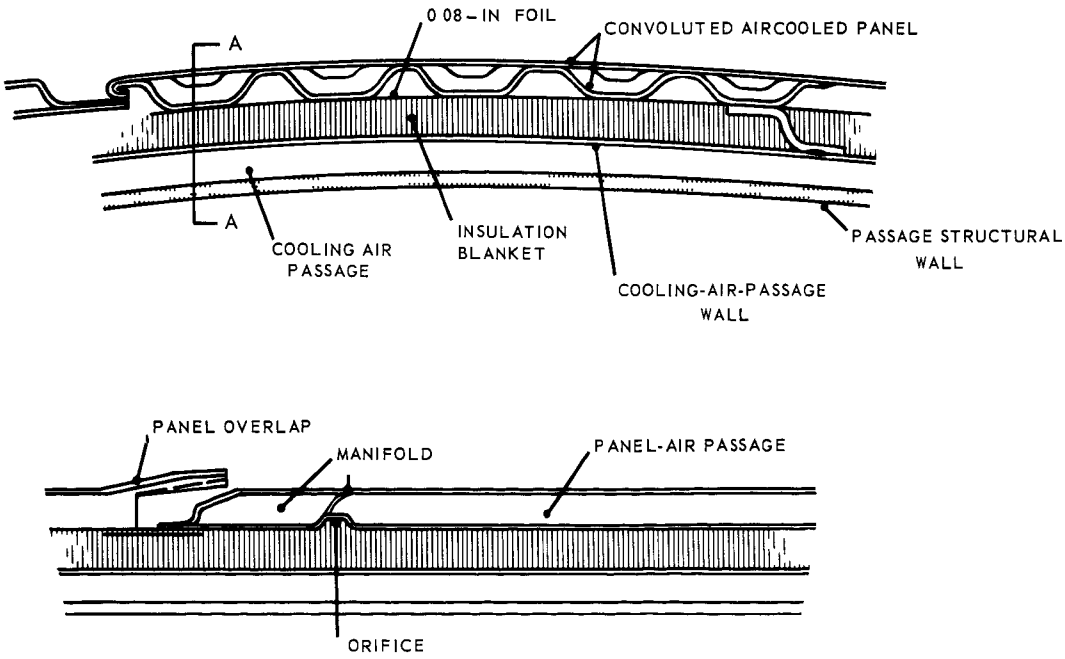

Fig. 6 16 – Turbine front frame insulation panels

shaft and a bulkhead provided by the front frame structural cones. The net unbalanced thrust load between the compressor rotor and turbine rotor was thereby reduced and the No. 2 (thrust) bearing absorbed a lower, and less fluctuating axial load.

The No. 3 sump supported, and provided lubrication passages for the No. 3 roller bearing. This bearing was designed for a B_{10} life of 29,900 hours at 5000 rpm based on an equivalent design load of 4500 pounds. In addition to the bearing, the No. 3 sump included two pressurized carbon circumferential seals and four labyrinth air seals. The two pressurized carbon circumferential seals prevented oil leakage from the bearing-sump cavity by means of a pressurization system, while the outer set of labyrinth seals kept hot pressurized air away from the oil seals. All air seal leakage was bled overboard. The entire No. 3 sump was capable of being remotely assembled and disassembled.

6.3.2.2 Rotor Assembly

The rotor assembly extracted power from the kinetic energy of the heated primary-air flowing through it, and transmitted the extracted power through the coupling shaft to the compressor and accessories. Figures 6.17 and 6.18 show the turbine rotor. It was supported by two roller bearings, one on the front stub-shaft forward of the first-stage turbine disc and the other on the aft stub-shaft which was an integral part of the aft side of the third-stage disc.

Special criteria used in bucket design were as follows:

1. Bucket torsional frequency to be within stability criteria.
2. Flexural and torsional natural frequencies to avoid, whenever possible, excitation by frequencies of 1, 2, 3, and 4 per revolution, and the passing frequencies of nozzle diaphragm partitions.
3. Stresses to fall within the Goodman diagram limits.
4. Bucket creep to be such that radial growth in the bucket would not exceed 0.5 percent of the total bucket height during the severest conditions.
5. Bucket damping to be effected at the platform by bucket-to-bucket contact.

The turbine buckets were uncooled. Udimet 700 forged alloy was used in the first stage to allow operation at the high air temperatures involved. Waspalloy was used in the second and third stages. Baffles made of A-286 alloy were located on both the forward and aft sides of the bucket shanks. These baffles, assisted by cooling air, were used to keep the bucket shanks operating within permissible temperature limits.

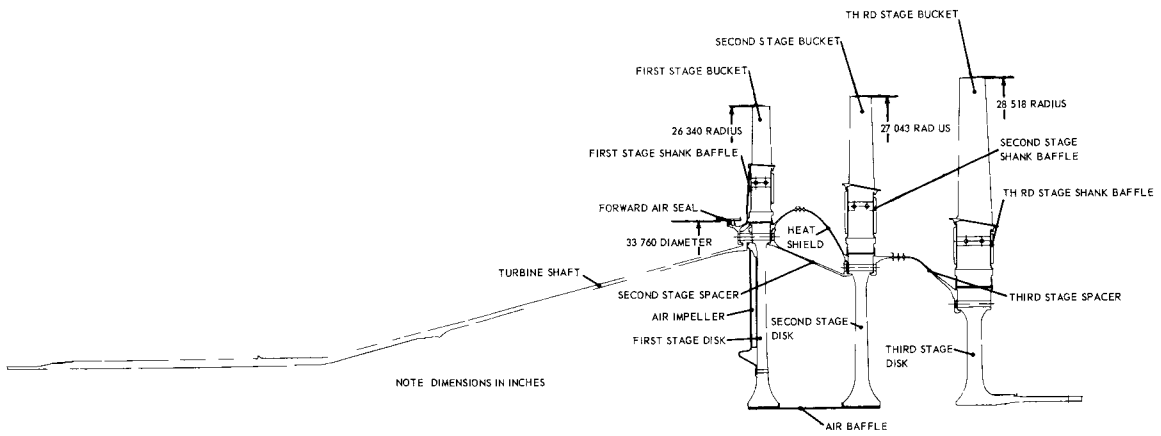

Fig. 6.17 – Turbine rotor assembly

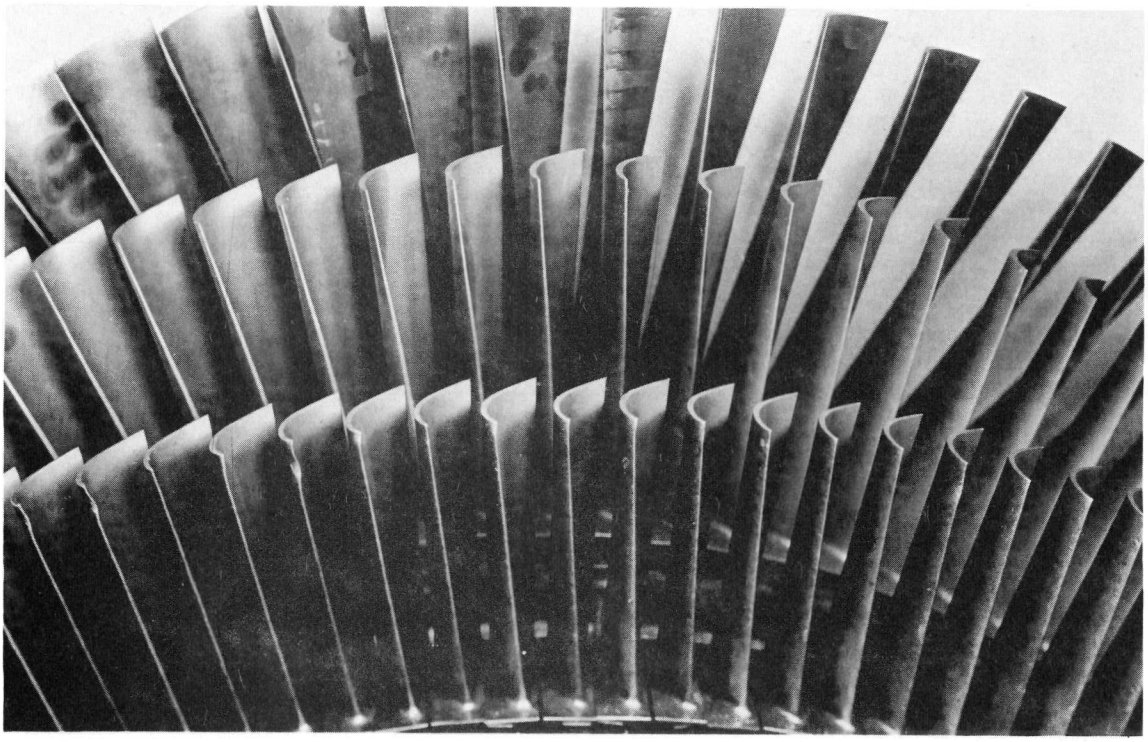

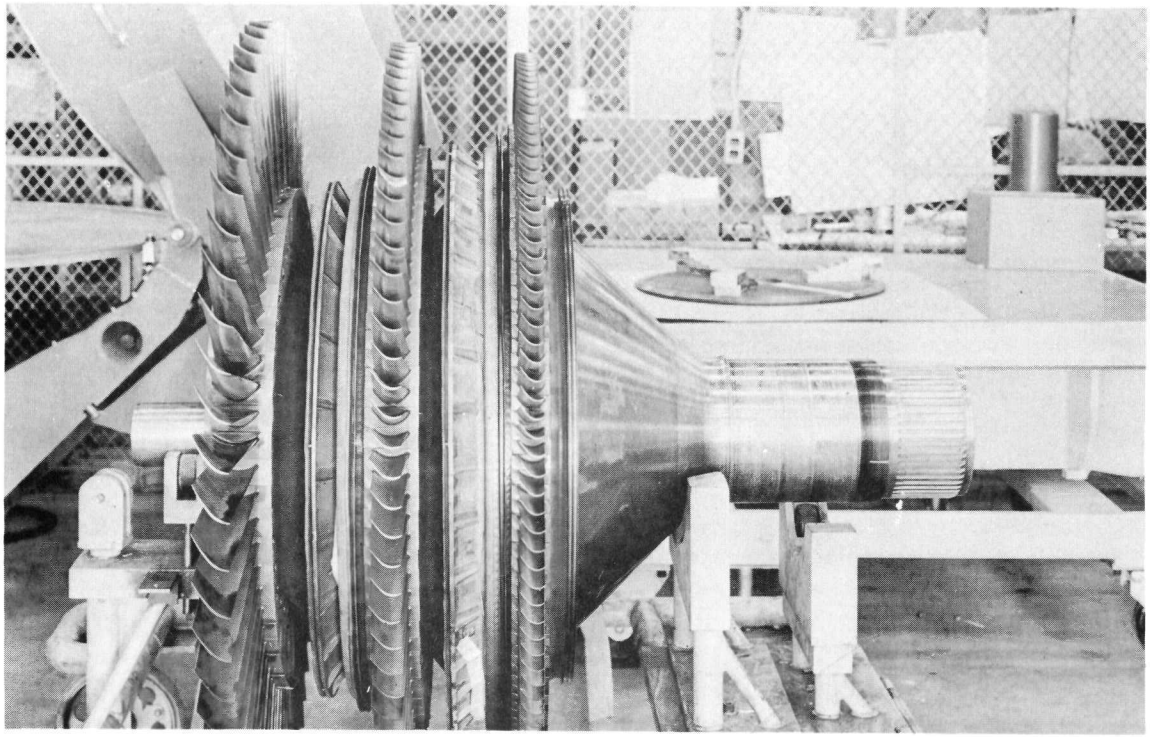

Fig. 6.18 – Turbine rotor assembly (Neg. 256591)

The turbine discs (wheels) were manufactured from A-286 vacuum-melted alloy. Some special criteria used in disc design were as follows:

1. The equivalent stress due to the combination of centrifugal force and the most severe thermal gradient not to exceed the 0.2 percent yield limit at a point not more than 0.5 inch from the inside diameter. The equivalent stress at 0.010 inch from the inside diameter not to exceed 1.2 times the 0.2 percent yield limit.
2. Disc creep to be such that the total growth of the rim would not exceed 11 percent of the rim radius under the most severe conditions.

An impeller attached to the forward side of the first-stage disc served to reduce the internal cooling-system pressure loss by acting as a recoup pump.

Spacers between the turbine discs performed three functions: (1) transmit stage torques to the turbine shaft, (2) provide separation and support between the discs, and (3) serve as interstage air seals. The catenary seal, a catenary-shaped outer seal ring, served as the primary interstage seal between the first and second stages, and also as the heat shield for the spacer between the first and second stages. The heat shield and spacers were manufactured from A-286 alloy.

6.3.2.3 Stator Assembly

The stator assembly, Figures 6.19 and 6.20, consisted of the casing, nozzle diaphragms, nozzle diaphragm air seals, bucket shrouds, and all hardware necessary for mounting. It served the function of converting the pressure energy of the reactor discharge-air and combustion-gases into kinetic energy, and also acted as the structural member supporting the front and rear frames.

The stator casing was a fabricated structure manufactured from A-286 alloy. It contained three nozzle diaphragms and turbine shrouds, and absorbed the tangential air loads of the nozzle diaphragms. Axial alignment of the first-stage nozzle diaphragm was maintained by anchoring its band to the combustor inner liner in such a manner that it could not move except to accommodate differential thermal movements occurring in (1) the stator casing, (2) the nozzle diaphragm, or (3) the turbine front frame and combustor inner liner. The second- and third-stage nozzle diaphragms were cantilevered from a fabricated band which, in turn, was mounted to the stator casing. Cooling-air for all nozzles was piped in through external manifolding.

Figure 6.21 shows the designs of the vane inserts and cooling-air passages in the first-stage nozzle diaphragm. Vane inserts in the second and third stages were similar to those in the first stage. The stationary portion of the labyrinth airseal mounted to the nozzle diaphragm was of lightweight, open honeycomb construction. The honeycomb was brazed to a cone on the first-stage nozzle diaphragm and was rigidly attached to the combustor inner liner.

Second- and third-stage seals were brazed to machined rings which were attached to the nozzles. These seals could tolerate diaphragm growth and were self-centering. The labyrinth design of the interstage seals regulated leakage to maintain desired temperature levels of the turbine spool parts (discs, spacers, etc.). All nozzle diaphragm seals were of one-piece construction. Bucket tip seals were mounted in slots in the nozzle diaphragm outer-shrouds.

6.3.2.4 Rear Frame Assembly

The rear frame assembly is shown in Figures 6.22 and 6.23. The frame served to (1) provide a smooth diffusing passage for the turbine discharge gases, (2) support the diffuser and exhaust duct, and (3) keep the turbine stator assembly round, and (4) pro-

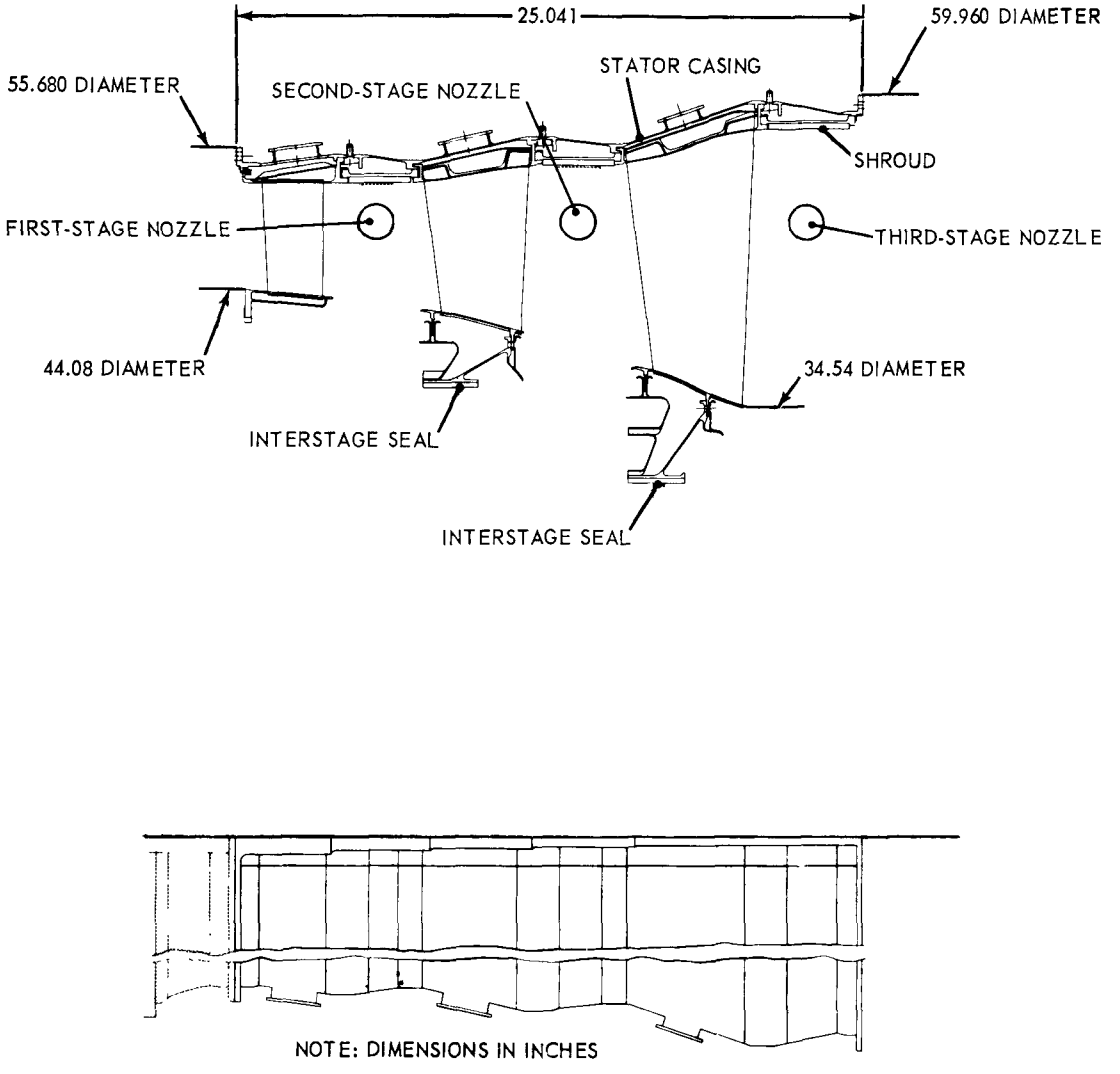

Fig. 6.19 – Turbine stator assembly

vide support and services for the No. 4 bearing and sump. It was fabricated of A-286 alloy and, except for minor modifications, was the same as the Block II design.

The assembly consisted of a conical outer shell supporting both an inner box-structure and a fabricated Hastelloy X aerodynamic diffusing-passage. A forward flange welded to the outer shell supported the turbine stator casing, and an aft flange welded to the outer shell supported the bleed-speed manifold. Ground handling-pads located at the 3- and 9-o'clock positions were capable of absorbing a load of 12,000 pounds applied at a maximum moment arm of 1-1/2 inch. These pads, however, could not be used to lift the entire turbine assembly and associated parts. Separate handling pads were provided for that purpose.

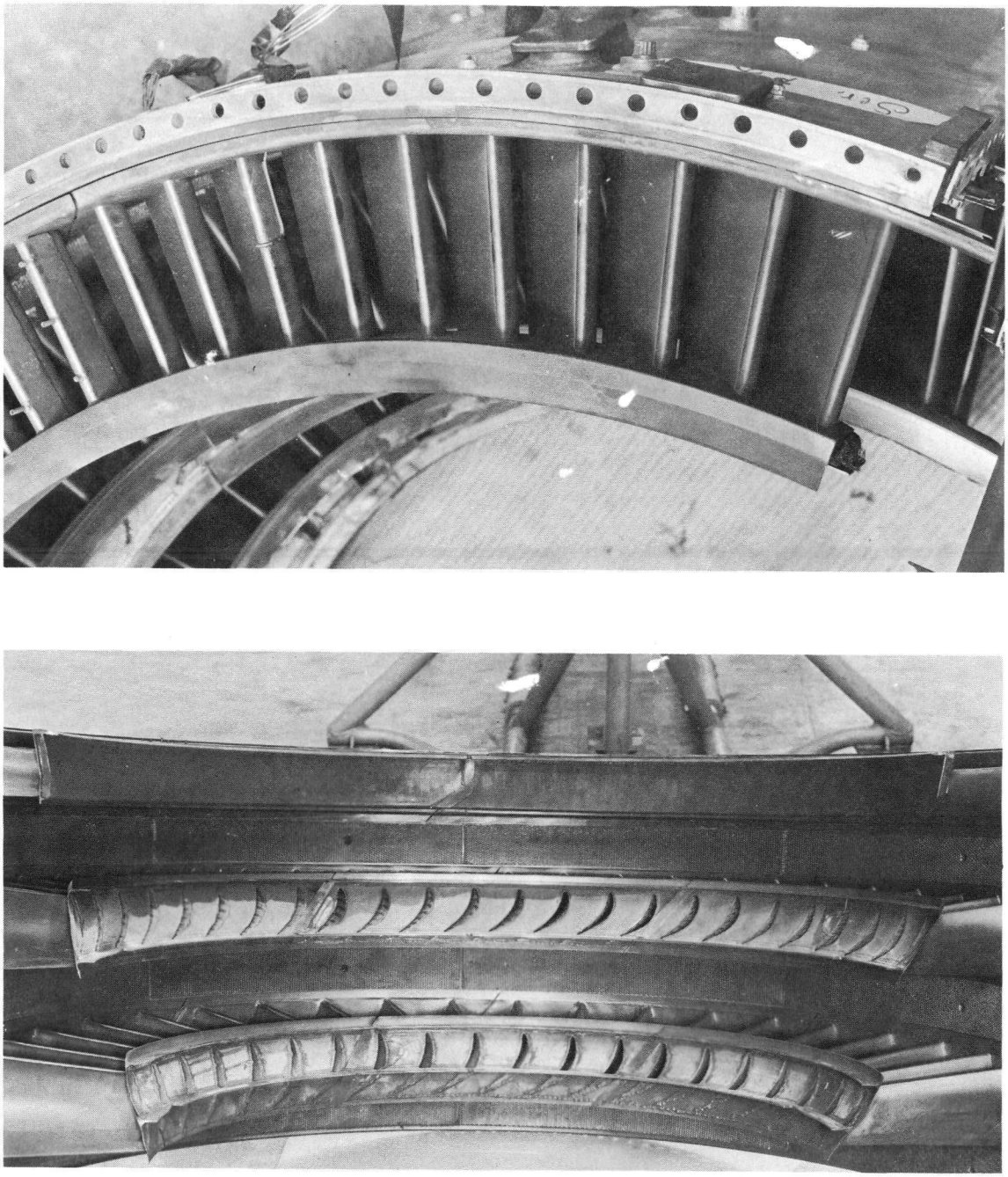

Fig. 6.20 – Turbine stator assembly (Neg. 258593)

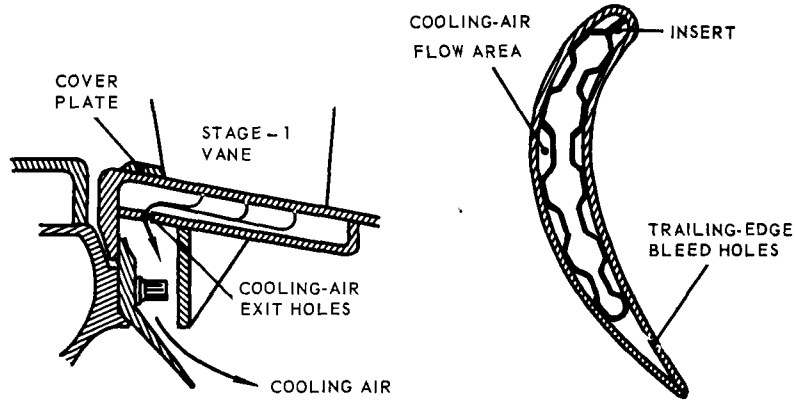

Fig. 6.21 – Vane insert and cooling-air passage in first-stage nozzle diaphragm

Eight struts served as support for the inner box-structure and the No. 4 bearing. They also provided a passageway for supply oil, scavenge oil, sump pressurization air, and sump vent air. Strut usage is shown in Figure 6.24.

Ninth-stage compressor-bleed air was used to cool and pressurize the No. 4 bearing sump cavity. The bearing was a single-row, roller bearing with inner and outer races of M50 tool steel and a silver-plated silicon-iron-bronze cage. The bearing had a B_{10} life of 5,500 hours at 5,000 rpm based on its equivalent design load of 3,500 pounds. A carbon-bore rubbing seal prevented oil leakage by virtue of seal pressurization air.

6.3.3 COMBUSTOR ASSEMBLY

The combustor assembly, shown in Figure 6.25, consisted of a combustor casing, an outer liner, an inner liner, and a fuel-injection flame-holder containing fuel nozzles. The casing and inner liner were bolted to the turbine front frame assembly, and provided capability for chemical checkout of the engines prior to nuclear operation, chemical start-up, chemical take-off and landing, and power transfer. It was an annular design.

The combustor section was designed to provide the optimum temperature profile to the turbine with minimum pressure loss. Since it was located in series between the reactor and the turbine inlet, parts of the system were exposed to the high temperature reactor discharge-air during nuclear operation of the engine. As a result of these long soaking periods at high temperature, the combustor section was exposed to conditions more severe in many respects than those experienced by afterburners.

The combustor casing was made of Inconel W sheet metal. It was attached to the turbine front frame rear outer flange and to the turbine stator casing forward flange, and provided passage for turbine nozzle cooling-air and bleed-speed air.

The outer liner was made of Hastelloy X reinforced on the outside diameter by hat-section stiffener rings. The inner surface was blanketed with insulation panels similar to those used in the turbine front frame. The aft end was free to expand both radially and axially. To maintain concentricity while in operation, the aft end of the outer liner was supported by a cone attached to the combustor casing.

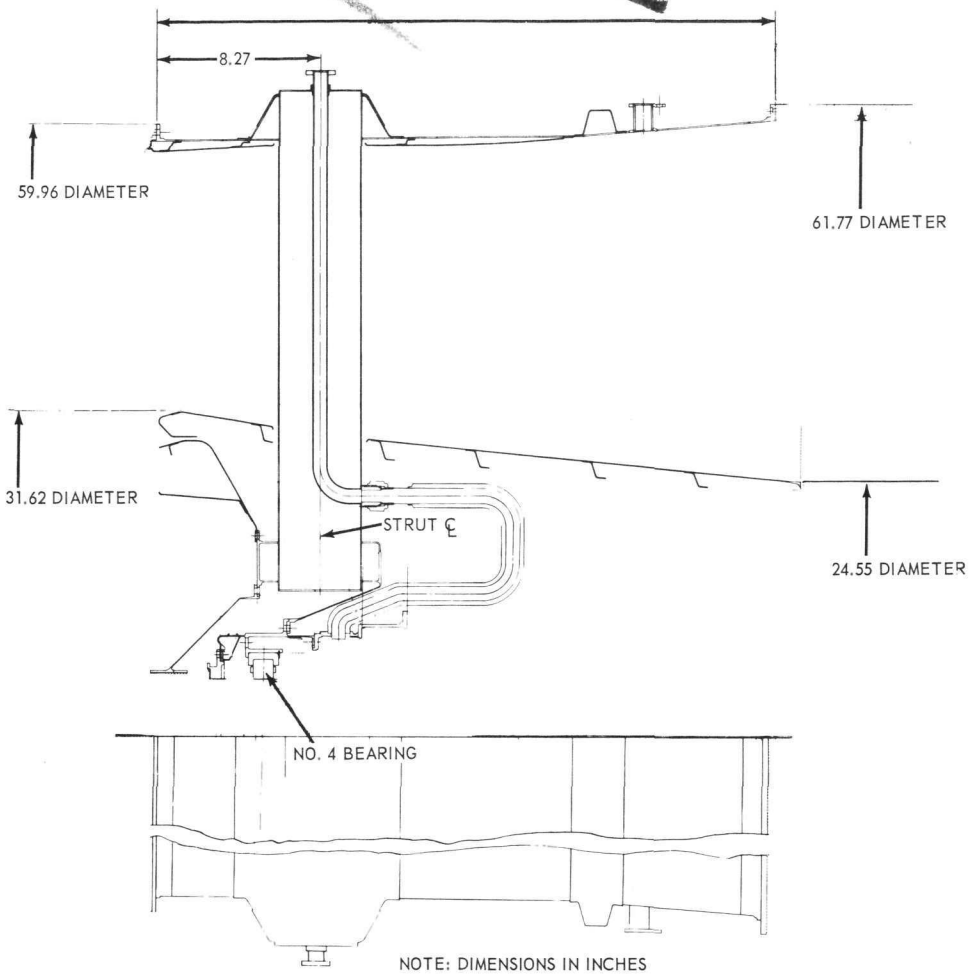

Fig. 6.22 – Turbine rear frame assembly

Fig. 6.23 – Turbine rear frame assembly (Neg. 245558)

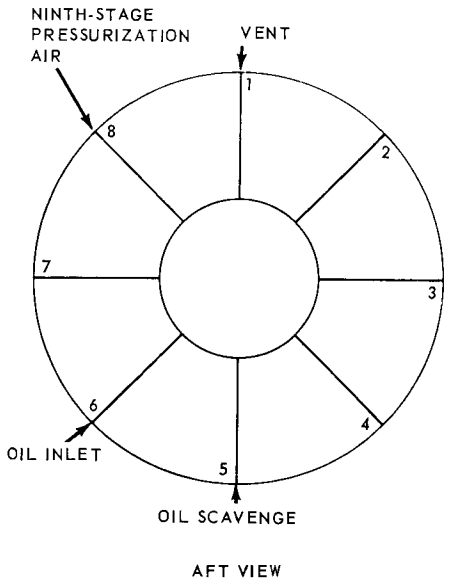

Fig. 6.24 – Turbine rear frame strut usage

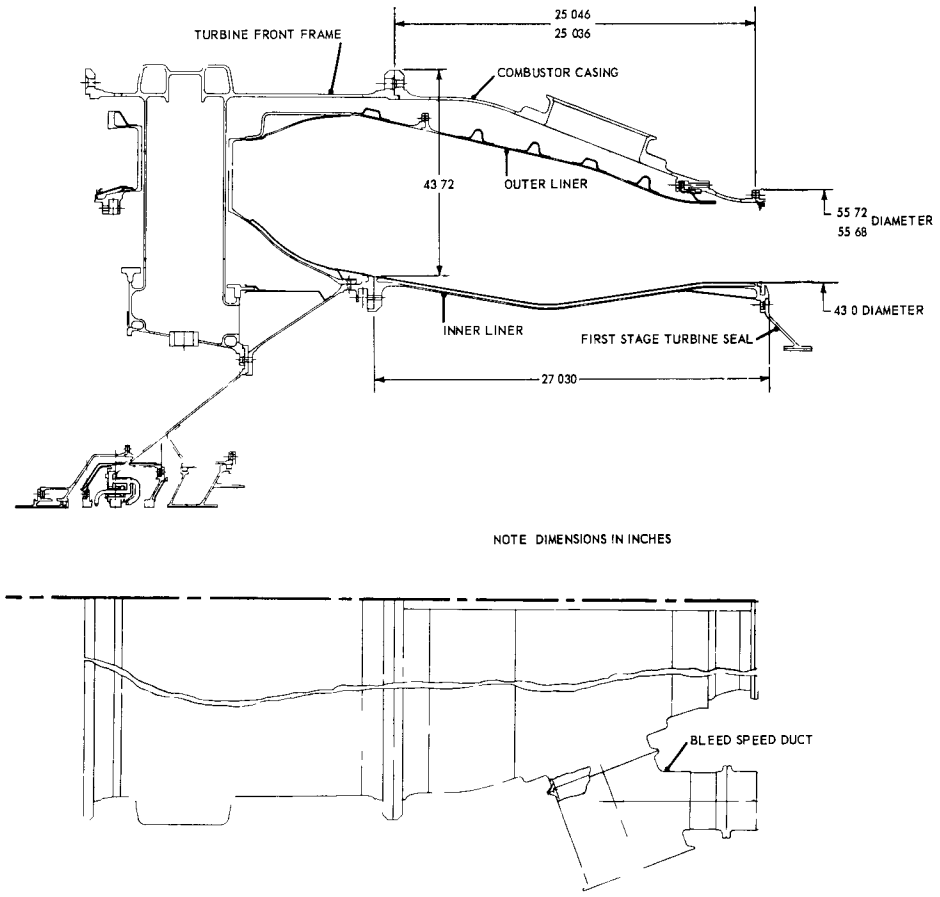

Fig. 6.25 – Combustor section

The inner liner also was made of Hastelloy X, and had its outside surface blanketed with insulation panels. The forward end of the inner liner was bolted to the turbine nozzle diaphragm. It served as the outer pressure wall of the balance-piston chamber.

The fuel injection flameholder was composed of 20 sections located immediately aft of the struts and supported by the front frame assembly. The flameholder had a passage blockage area of approximately 60 percent, and contained 50 spill-type fuel nozzles to insure uniform fuel injection. The nozzles were internally manifolded in alternate groups of two and three. This manifolding resulted in 40 external fuel connections.

6.3.4 COUPLING SHAFT

The coupling shaft, Figure 6.26, passed through the center of the reactor and coupled the turbine rotor with the compressor rotor. No support was required within the reactor zone since the aft end of the shaft (forward of the turbine first-stage disc) was supported by the No. 3 main bearing (turbine front frame) and the forward end of the shaft was attached by a spline-and-nut connection to the compressor rotor rear stub-shaft. It was machined from forged A-286 steel.

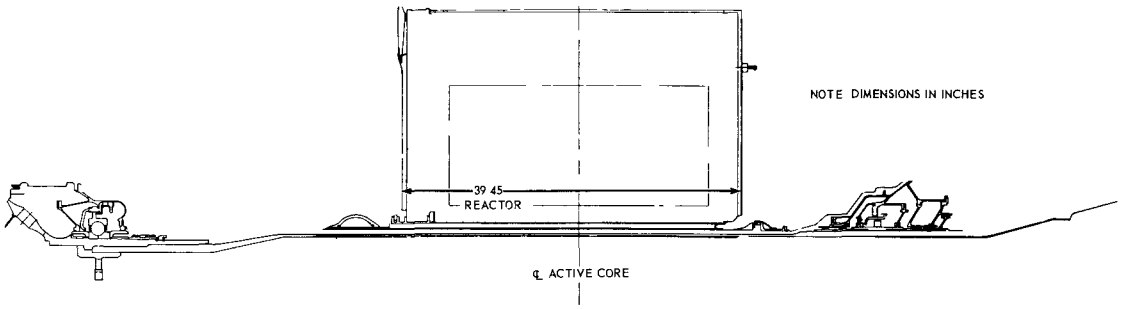

Fig. 6.26 – Coupling shaft

Because the coupling shaft passed through the center of the reactor, it was located in a region of very high radiation flux, and, consequently, very high secondary heat deposition. Cooling-air from the compressor ninth-stage bleed ports was passed through the hollow bore to maintain the shaft operating temperature within allowable limits. Internal helical fins were machined into the bore to improve heat transfer to the cooling-air. These cooling-air fins were machined at a 45 degree helical angle and served the dual purpose of improving heat transfer efficiency as well as increasing shaft load-carrying capacity. The shaft was designed with a large cone on the aft end to provide maximum stiffness with minimum weight. The design also maintained the turbine rotor critical speed above engine operating speed. The aft end of the coupling shaft was bolted to the front side of the first-stage turbine rotor disc and supported the cooling-air impeller mounted on the front side of the first-stage disc.

Five borated and unborated beryllium inserts were located in the bore of the shaft and functioned as a part of the reactor end-shields by preventing the escape of direct-line radiation.

6.3.5 EXHAUST DUCT

The exhaust duct, shown in Figure 6.27, provided passage of exhaust gases to the jet nozzle, and supported the jet nozzle. The forward section acted as an aerodynamic diffuser. It consisted of two A-286 alloy cylindrical sections joined together by bolted flanges. Both sections were stiffened externally for rigidity, and were designed to with-

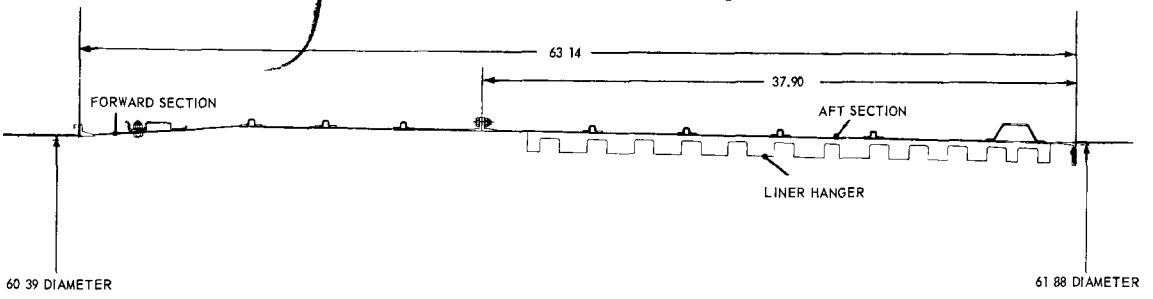

NOTE: DIMENSIONS IN INCHES

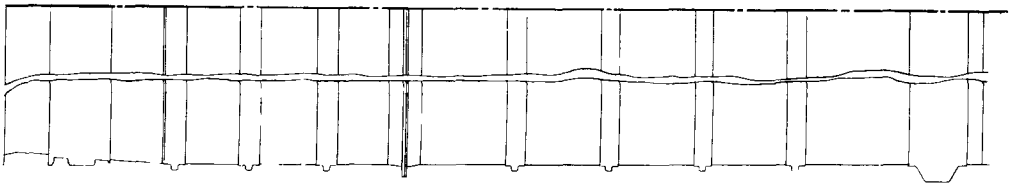

Fig. 6.27 – Exhaust duct

stand a maximum steady-state differential crushing pressure of 3 psi. The maximum steady-state differential bursting pressure was 30 psi. Six exhaust nozzle actuator mounting brackets were located on the aft section of the exhaust duct and were equally spaced around the circumference of the duct.

The duct was suitable for use in the XNJ140E engine (afterburning) with the addition of an already-designed liner. Although the total length of the exhaust duct was not required for XNJ140E-1 usage, it was being used "as is" to eliminate procurement of a special duct.

6.3.6 EXHAUST NOZZLE

The function of the exhaust nozzle was to control both engine speed and thrust. It was a variable-area, finger-type convergent nozzle formed by 24 Rene' 41 flaps similar to the flap shown in Figure 6.28. The variable area was obtained by positioning the flaps. Overlapping Rene' 41 seals minimized gas leakage between adjacent flaps. Hinges mounted on a support ring attached to the exhaust duct supported the flaps. The nozzle area was 950 square inches fully closed, and 1800 square inches fully opened.

All flaps were actuated in unison through the desired range of operating area by an arrangement of a unison-ring and linkage to each flap. The ring was driven by six hydraulic actuators having an over-all stroke of 7.8 inches. Actuation was accomplished by the unison-ring driving a Y-shaped link attached to each flap. The actuation ring was constructed of Inconel W sheet metal with Inco 718 castings inserted to provide bearings for the link pins. The links were fabricated from Rene' 41 sheet metal stampings and Rene' 41 end-castings. Maximum actuator loads were 55,000 pounds during closing and 12,000 pounds during opening.

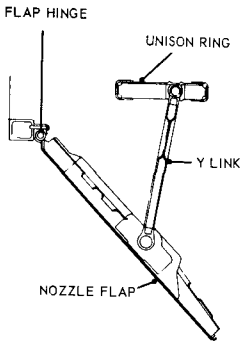

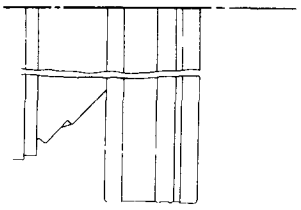

Fig. 6.28 – Exhaust nozzle flap
(shown in closed position)

6.3.7 BLEED-SPEED MANIFOLD

A manifold was required to return bleed-speed control-air to the primary-air stream at a point just aft of the turbine rear frame. This manifold assembly, Figure 6.29, was mounted aft of the turbine rear frame and supported the exhaust duct. It had a cross-sectional bleed-speed-air re-entry area of 12 square inches consisting of 40 two-inch-diameter holes. The manifold was approximately 16.25 inches long, with flanges on either end. These flanges were bolted to the turbine rear frame and to the exhaust duct. It was made of A-286 alloy.

A reduction in over-all engine length could be effected by redesigning the bleed-speed manifold as an integral part of the turbine rear frame assembly. Smoother peripheral re-entry of the bleed-speed bypass-air into the primary-air stream also would have been integrated into this redesign.

6.3.8 ACCESSORY DRIVE SYSTEM

The purpose of the accessory drive system was to transmit power from the main engine rotor shaft to engine and customer accessories. It also provided mounting for all accessories except the 120 KVA alternator. The system consisted of three basic gearboxes: (1) inlet gearbox located in the compressor front frame hub, (2) transfer gearbox located at the bottom of the front frame, and (3) rear gearbox located on the bottom of the compressor stator casing.

Significant requirements imposed on the design of the gearboxes were as follows: (1) resistant to radiation damage, (2) capable of operating with a 200°F oil supply, (3)

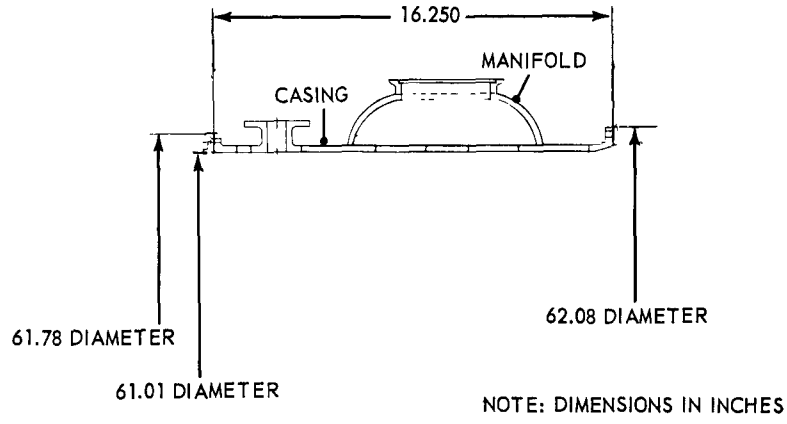

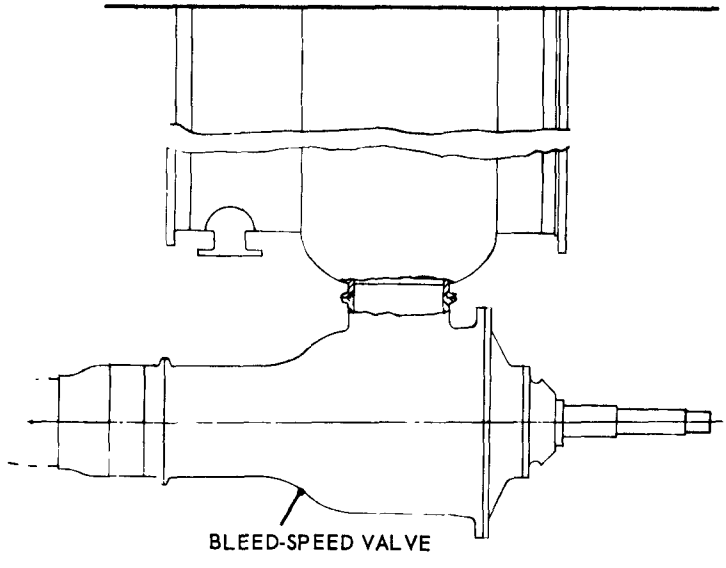

Fig. 6.29 – Bleed-speed manifold

minimum frontal area, (4) adequate capacity for satisfying all customer requirements, and (5) provide customer mounting pads easily accessible for maintenance.

The gearbox casings were cast from Dow C magnesium and were protected from corrosion with HAE ceramic coating and an aluminum-silicone paint.

Power was transmitted from the compressor front frame hub to the inlet gearbox through a radial drive shaft driven through a set of spiral bevel gears. The transfer gearbox was mounted on the accessory tray at the 6-o'clock position of the compressor front frame and received power from the inlet gearbox through the radial drive shaft. The transfer gearbox transmitted power to the rear gearbox through a horizontal drive shaft and also drove the various accessories which it supported. The rear gearbox was supported on the accessory tray at the aft portion of the stator casing. It transmitted power through spur gears to the various accessories which it supported.

A scavenge pump was mounted on the transfer gearbox to scavenge oil draining from both (1) the inlet gearbox through the front frame vertical strut and around the radial drive shaft, and (2) the transfer gearbox.

Gears used in the gearboxes were both spiral bevel and spur design. Spiral bevel gears were used because they have more teeth in contact simultaneously than straight bevel gears and, therefore, have greater load carrying capacity. They are also smoother in operation and are more easily adjusted. Spur gears were chosen in place of helical gears to reduce bearing sizes and eliminate end thrust.

Bearings used in the gearboxes were both ball- and roller-types. Where capacity permitted, the spur gears were mounted on one ball-bearing and one roller-bearing to allow for thermal expansion and tolerance stackup. This method of mounting also assured gear-tooth alignment and proper radial play. In general, bearing sizes were dictated more by the required spline size than by loading. All bearings were made of vacuum melted M50 material and were heat treated for operation as high as 400°F. The gearbox shaft seals were metal-bellow-type with a carbon rubbing seal.

6.3.9 ENGINE STARTER

The engine starter[5] (Model AW-10) is shown in Figure 6.30. It consisted of a two-stage air turbine, a set of reduction gears, a speed cut-out device, a sprag clutch, a reverse-torque release mechanism, and a drive spline incorporating a shear section. The turbine casing was designed with provisions to contain the turbine buckets in the event of bucket

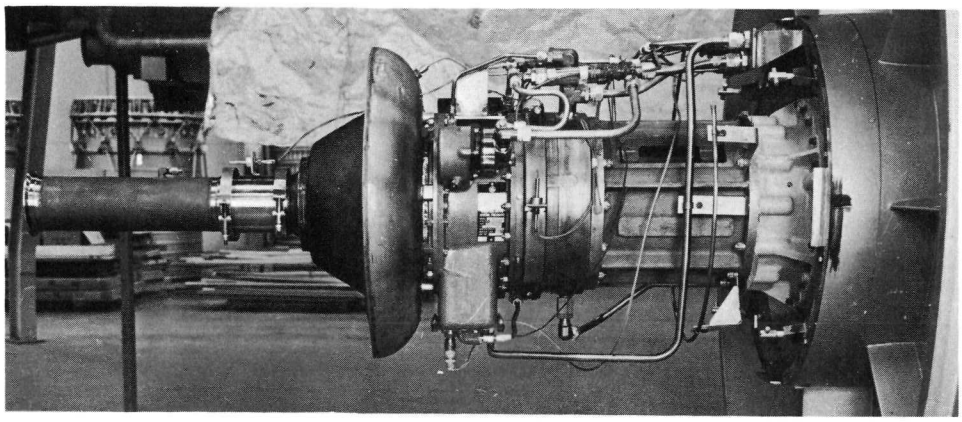

Fig. 6.30 – Engine starter (Neg. U39146C)

failure. The buckets of the second stage were fitted with 0.055-inch-diameter wires to tie the bucket tips together. A heat insulation shield was installed between the turbine-air-passage and the reduction-gearcase to retard heat flow into the gearcase. The turbine exhaust duct contained an annular venturi for aerodynamically limiting turbine speed at high altitude conditions in the event of inlet control valve failure.

The reduction gear ratio from turbine to output spline was 11.5 to 1. The reduction gears were lubricated by a self-contained lubrication system. Oil was contained in the sump at the bottom of the gearcase, and an oil pump, driven from the reduction gears, was mounted within the sump. This pump was a single-element positive displacement type incorporating a relief valve. Oil passed from the pump, through one side of a starter-mounted wrap-around heat exchanger, and then to the various bearings and gears. The capacity of the oil reservoir was 120 cubic inches.

The starter assembly was designed for remote removal or replacement. A mounting adapter, provided as a part of the starter, was bolted to the engine front gearbox. The starter was attached to this mounting adapter by a V-band clamp. A centering guide and an index alignment pin were provided on the starter to insure proper mating with the mounting adapter. A lead-in angle was provided on the spline teeth. The V-band clamp was designed such that it could be cut at the bottom in the event the loosening screw was bent or damaged so severely that the starter could not be removed in the normal fashion. The weight of the starter was approximately 150 pounds and the center of gravity was 8.15 inches from the mounting face.

Figure 6.31 displays the time-temperature starting requirement imposed on the starter.

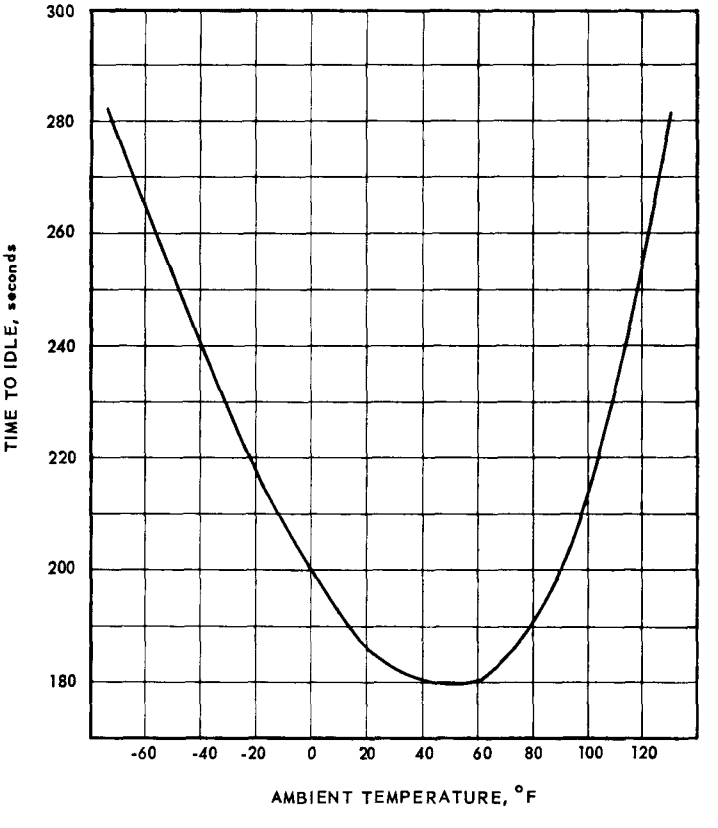

Fig. 6.31 – Time - temperature relationship for engine starting

6.4 MAINTENANCE AND REMOTE HANDLING

6.4.1 RADIATION ENVIRONMENT

Fast neutron and gamma isodose patterns through and surrounding the turbomachinery are shown in Figures 6.32 and 6.33, respectively. The isodose patterns shown lay in the horizontal midplane through the engine, and are shown as a function of the azimuthal angle and radii around the reactor midpoint. The values are normalized to one megawatt reactor power; values for other power levels are directly proportional.

The fast neutron dosage in the turbine front frame area was as high as 1×10^6 rads (ethylene) per hour during nuclear operation. The fast neutron dosage in the No. 3 bearing sump varied from 5×10^5 rads (ethylene) per hour to 5×10^4 rads (ethylene) per hour depending upon location. The fast neutron dose rate in the compressor rear frame was as high as 1×10^5 rads (ethylene) per hour.

Radiation damage to organic and structural materials is discussed in APEX-917. When working under the combined thermal and radiation environment of the No. 3 bearing and sump, lubricating oil was expected to perform satisfactorily if changed every 120 to 150 hours.

6.4.2 PROVISIONS FOR REMOTE HANDLING

6.4.2.1 Design Requirements

Because of the high levels of radiation incident on the X211-E1 turbomachinery components during nuclear operation, full cognizance of the need for subsequent remote handling and maintenance procedures was retained in all turbomachinery designs.

The following general requirements were imposed on the design of the X211-E1 turbomachinery for maintenance purposes:

1. High reliability of remote handling features
2. Compatibility with existing remote handling equipment
3. Provision for direct viewing wherever practical
4. Minimum assembly and disassembly time
5. Minimum cost
6. Minimum weight.

The following items were designed for remote assembly/disassembly procedures:

1. Accessory tray
2. Transfer-gearbox and rear-gearbox mounts
3. Starter and bulletnose
4. Compressor rear frame outer rear flange
5. Compressor aft stub-shaft to turbine coupling shaft (internal coupling)
6. Bleed-speed valves
7. Turbine front frame outer flange to pressure vessel
8. Turbine front frame outer flange to combustor casing
9. No. 3 bearing sump
10. Turbine rear frame outer flange to exhaust duct
11. Turbine rear frame to turbine casing
12. Turbine stator and combustor horizontal flanges
13. Inner exhaust duct cone to turbine rear frame
14. Filters
15. Air ducting, fluid and electrical lines (as required).

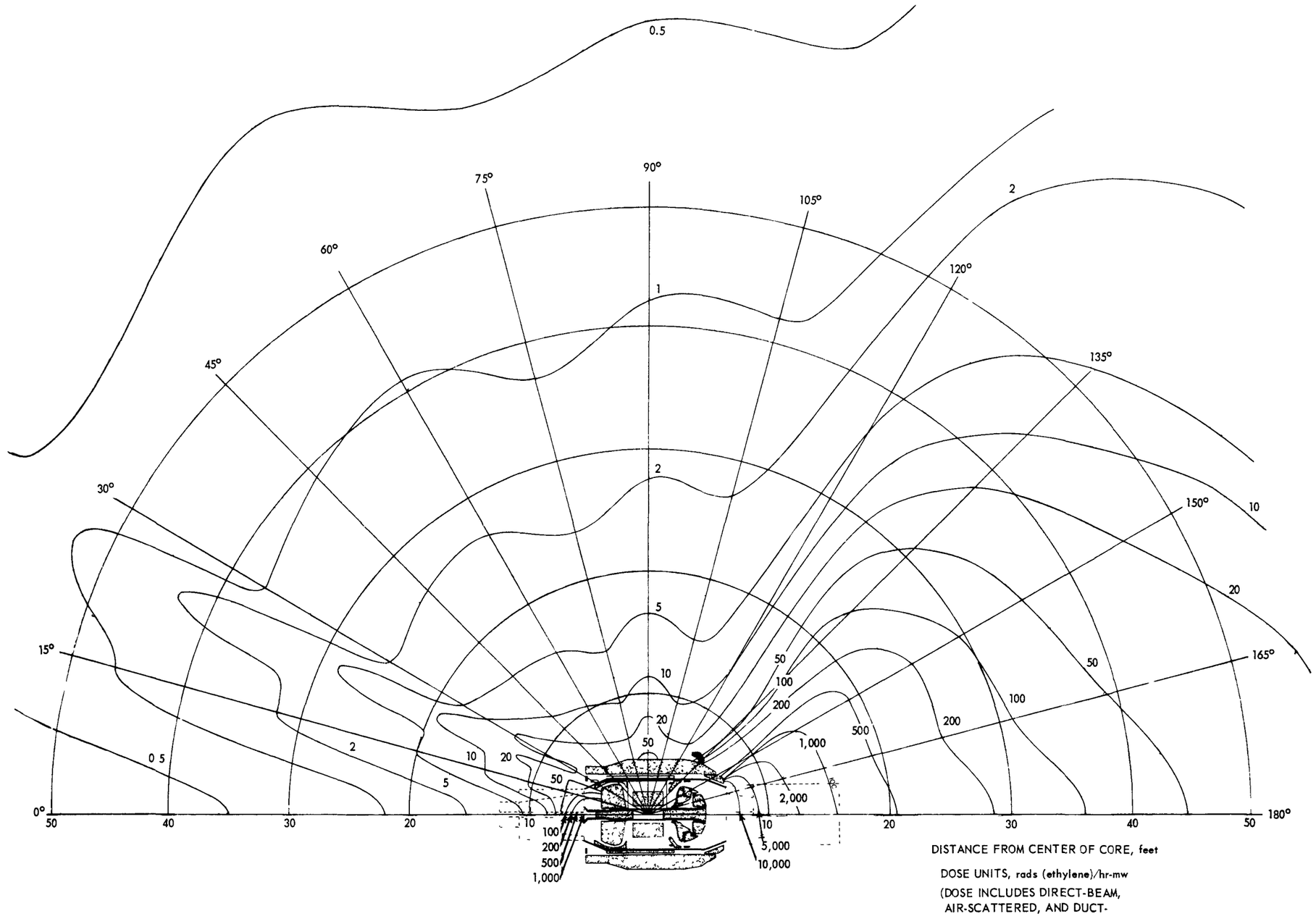

Fig. 6.32 – External fast neutron isodose pattern during nuclear operation, XNJ140E-1 engine

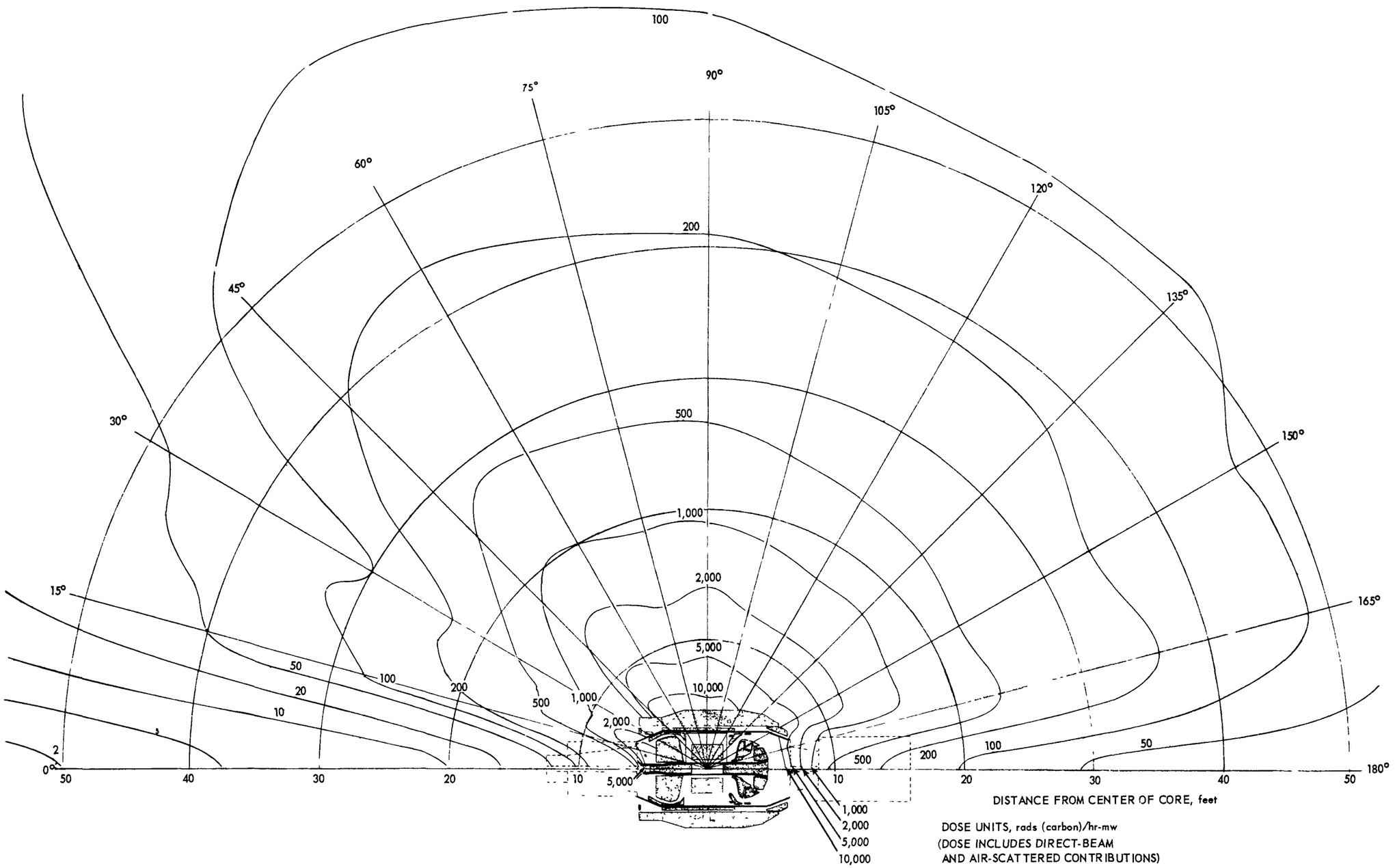

Fig. 6.33 – External gamma isodose pattern during nuclear operation, XNJ140E-1 engine

The following items were designed for semi-remote maintenance procedures:

1. Combustor
2. Turbine front frame
3. Turbine casing
4. Turbine
5. Turbine rear frame.

6.4.2.2 Special Remote Handling Devices

Captive bolts and nuts, developed specifically for the X211-E1 application, were used in all main flanges designed for remote handling. A typical nut and bolt of this type is shown in Figure 6.34. Both the bolts and nuts were remotely replaceable so that one bolt or nut could be replaced without separating the mating flanges. Bolts were held captive by a C-ring which snapped into a counterbore in the face of the flange; the bolt threads were truncated except for the three at the end. These truncated threads could pass through the inner diameter of the C-ring while the full threads at the end could not. The nuts were retained by shank fingers with beaded ends. When the nut was pushed into the flange, these beads fitted into a counterbore on the inner-face of the flange. The nut could not be pushed out by the bolt and was self wrenching. This design represented a simple modification of existing parts and had a high degree of reliability. Bolts and nuts of this type were tested successfully on two full-scale mockups in the hot shop at the Idaho Test Station.

Remote disconnects were developed for use in fluid lines. The disconnects consisted of two end plates handling up to six lines. The two halves of the disconnect were clamped together by one captive bolt. Sealing was accomplished by metallic or organic O-rings clamped between the flat surfaces of the two plates. The O-rings were carried by a wafer plate which was captive to one of the plates. Disconnects of this type, using metallic O-rings, were successfully tested using both air and fluids. Air at a pressure of 250 psig and a temperature of 1200°F were sealed. One of these disconnects was used without difficulty in the lube system of an X211 assembly during tests.

A remote electrical disconnect having twelve pins and held together by one captive bolt was developed and tested. It was designed so that the two halves could be mated without damaging the pins. Splines of different widths made it impossible to assemble the connector unless the pins were properly oriented.

6.5 X211-E3 TURBOMACHINERY

The X211-E3 turbomachinery is briefly compared with the X211-E1 turbomachinery. The X211-E3 is an advanced version of the X211 and was intended for use in flight versions of the XNJ140E engine.[6]

6.5.1 ADVANTAGES OF THE X211-E3 TURBOMACHINERY

The X211-E3 turbomachinery, used in the S-23A cycle, was originated as a means of obtaining increased engine thrust and a more favorable thrust/weight ratio. This was accomplished by redesigning the compressor to provide 500 pounds per second inlet-airflow and incorporating a two-stage air-cooled turbine. The turbine inlet-air temperature was increased to 1750°F at normal continuous power setting, and 1810°F at military power setting during nuclear operation. Engine speed equivalent to 100 percent N was increased to 5150 rpm. The reason for selecting the 500 pounds per second inlet-airflow compressor was to increase the mass flow through the engine. The two-stage turbine was chosen because it yielded lower metal operating temperatures, thereby increasing reliability and

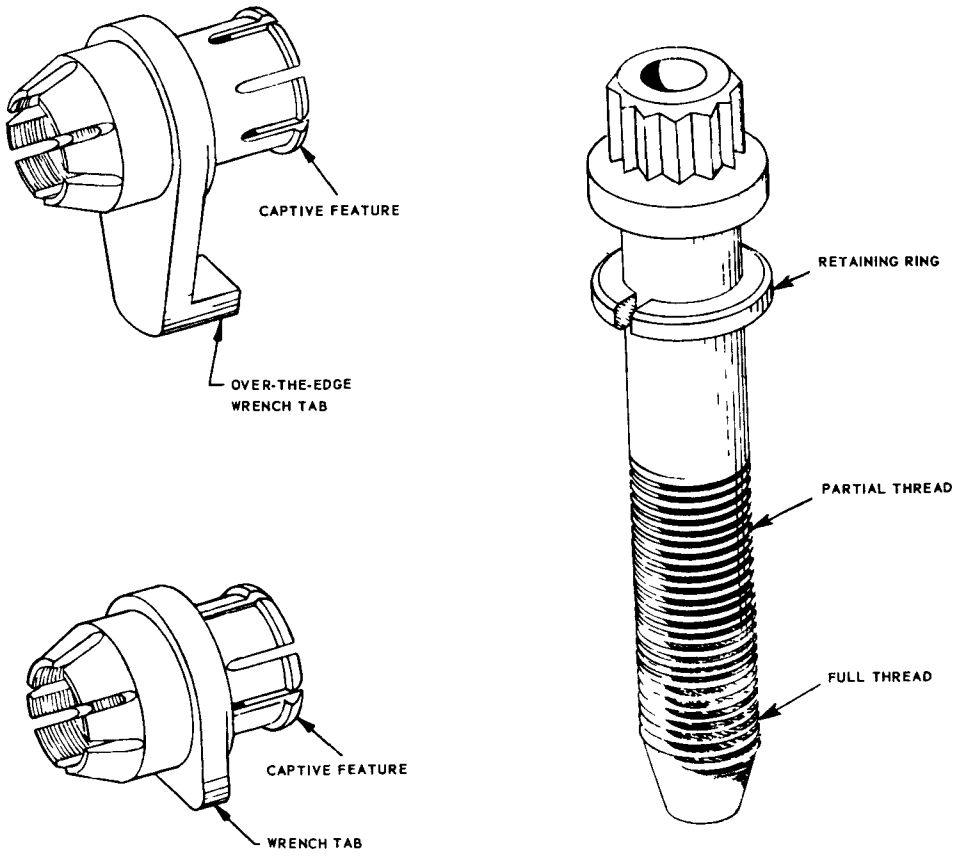

Fig. 6 34 – Captive nuts and bolt

lifetime as a result of the larger enthalpy drop per stage. The effects of the larger enthalpy drop more than compensated for the slightly increased turbine-inlet-air temperature.

Using the S-23A cycle engine, the cruising altitude of the Convair NX2 aircraft increased from 33,000 feet to 35,000 feet. During two-engine operation on a hot day, the emergency-return altitude increased from 8,500 feet to 12,700 feet. The integrated nuclear power generated during the 1000-hour lifetime profile defined in section 3.2 was less for the S-23A cycle than it was for the S-18B cycle. This reduction in integrated power was due to increased cruising altitude and increased rate-of-climb.

Only those components of the X211-E3 turbomachinery which significantly differed from the X211-E1 turbomachinery are described below.

6.5.2 COMPRESSOR

The only aerodynamic changes were those which improved performance and added a zero stage to the front end of the compressor. Minor changes were made to the fifteenth-stage stator and new outlet guide vanes were provided. The X211-E3 compressor was developed from the X211-E1 compressor by (1) adding a new front stage, (2) modifying the design of the existing first stage and rotor stages No. 2 and No. 3, and (3) removing the last stage. The weight-flow per unit annulus-area was increased to a value midway between that of the X211-E1 and the J79 compressors.

Table 6.3 is a comparison of design characteristics of the X211-E1 and X211-E3 compressors.

TABLE 6.3

COMPARISON OF X211-E1 AND X211-E3 COMPRESSORS

	X211-E1	X211-E3
Airflow (lb/sec)	425	500
Design Pressure Ratio	14.0	15.25
Inlet Hub-to-Tip Radius Ratio	0.48	0.40
Flow/Annulus Area (lb/sec-ft^2)	36.788	38.214
100% Rotative Speed (RPM)	5000	5153
Discharge Velocity (ft/sec)	450	480
Number of Stages	16	16
Number of Variable Stages	IGV + 6	IGV + 7
Percent Speed Increase	-	3
Percent Flow Increase	-	17.6

The compressor front frame was the same as the X211-E1 in basic design with the difference between frames being limited to physical size. The outer-annulus diameter of the X211-E3 front frame was about one inch larger and the inner-annulus diameter was about two inches smaller. The only difference between the rear frames was a minor reduction in the inner-flow-path wall diameter, approximately 0.090 inch. The inner-flow-path wall was sheet metal and this change represented a minor modification of existing design.

6.5.3 TURBINE

The aerodynamic design concepts of the X211-E3 turbine were very similar to those of J79 and X211-E1 turbines, with the principal difference being the increased enthalpy

drop per stage. The maximum diameter was increased by 5.9 inches to provide increased wheel diameter for increasing the energy extracted per stage. The conventional free-vortex tangential-velocity distribution was modified slightly to provide more favorable hub conditions along the sloping inner wall and to provide a constant section, untwisted, stage-1 nozzle partition.

The principal aerodynamic reasons for selecting the two-stage turbine were as follows:

1. Lower first-stage bucket temperature. For a turbine inlet-air temperature of 1800°F, the two-stage turbine first-stage bucket inlet-air temperature was 60°F lower than in an equivalent three-stage design for the same total enthalpy drop.
2. More flexibility in attaining increased flow requirements for future designs. A 25 percent increase in turbine flow function, $(W\sqrt{T}/P)_4$, was obtained by nozzle-vane reorientation and first-stage bucket redesign. A three-stage turbine would require reorientation of the two first stages of vanes (and possibly the third as well), and the redesign of the first two stages of buckets to produce the same effect. In addition, the interstage losses were a larger portion of the extracted energy-per-stage in a three-stage turbine (when redesigned for higher flow functions) than that of a two-stage turbine.
3. Since the 5.9-inch increase in diameter was not detrimental from an over-all engine-envelope viewpoint, the usual incentive for the more complex three-stage turbine was lacking.

The assumed turbine efficiency was based upon performance experience of the J79 and the testing experience of the X211-E1 turbines. It was 1 percent below the "experience line" to account for the thicker bucket trailing edges. However, the reduced cooling-airflow requirement more than compensated for this 1 percent conservatism, and cycle performance remained the same.

The principal mechanical design reasons favoring the X211-E3 turbine were as follows:

1. Mechanical design was simpler because of the simplified cooling-airflow path and the fewer parts involved.
2. The first-stage turbine bucket metal-temperature for a given turbine-inlet-air temperature was approximately 60°F less than in the X211-E1 turbine. This 60°F decrease in metal temperature corresponded to a five-fold increase in operating lifetime for a given turbine-inlet-air temperature (at the operating temperature levels involved).
3. The first-stage nozzle diaphragm partitions were redesigned for a constant-chord constant-section. This redesign resulted in a lower unit price and tooling costs.
4. The two-stage turbine required a lesser number of buckets than did the three-stage turbine. Although the buckets were of a larger size, the total cost-per-set was less.
5. The turbine redesign was such that, by reorienting the first- and second-stage partitions and replacing first-stage buckets, the sonic flow function could be increased to supersonic flight requirements without further modifications.

6.5.4 EXHAUST DUCT AND AFTERBURNER

The X211-E3 afterburners had not been designed at the time of contract cancellation. The design, however, would have provided for aircraft Mach 0.9 capability on-the-deck. In order to provide growth for other missions, which were made possible with the increased turbine-inlet-air temperatures, the mechanical design of the afterburner would have allowed for full modulation.

The exhaust duct of the X211-E1 and the X211-E3 were of the same basic design; however, there was a difference in physical size, the X211-E3 being about 3 inches larger in diameter.

6.5.5 SUPPLEMENTARY REFERENCES

The Preliminary Model Specification is given in reference 7. The preliminary Installation Bulletin is given in reference 8. A discussion of reliability and maintainability plans is given in reference 9.

6.6 ENGINEERING DRAWING LIST

A drawing list for the X211-E1 turbomachinery is contained in reference 10.

6.7 PRODUCT HANDBOOK

The "Turbomachinery Handbook for 140E1" is identified in section 1.6. Material contained in this handbook is illustrated by the following Table of Contents:

Section	Title
A	Table of Contents
B	Distribution
C	Responsibility
D	Introduction
E	Turbomachinery Product Breakdown Numbers
1-4000-0.0	Design
1-4000-1	Turbomachinery Description and Requirements for the 140E1
1-4000-8.0	Drawing Planning List
1-4902-9.0	FET Facilities
1-4931-9.0	Manual Fuel System
1-4933-9.0	Auxiliary Lubrication System (Facility)
1-4935-9.0	Secondary Cooling System
1-4963-9.0	Tunnel Cooling Air
1-4968-9.0	Nitrogen Fire Extinguisher
1-4980-9.0	Control Room Equipment
1-4983-9.0	Control System Equipment Racks
2-4000-0.0	Materials Development
3-4000-0.0	Manufacture, Assembly, Shipment
4-4000-0.0	Component Testing
5-4000-0.0	Operations
6-4000-0.0	Schedules

6.8 REFERENCES

1. Layman, D. C., "Ref. 6-1, X211-E3 Design Requirements," GE-ANPD, DC 61-8-22, August, 1961.
2. Layman, D. C., "Ref. 6-2, General Electric Company Specification Number E-2008 (X211-E1 Model Specification)," GE-ANPD, DC 61-8-18, August, 1961.
3. Layman, D. C., "Ref. 6-3, General Electric Company Specification Number M50T J7011 (51) (X211-E1 Mechanical Reliability Specification)," GE-ANPD, DC 61-8-19, August, 1961.
4. Layman, D. C., "Ref. 6-4, General Electric Company Number M50T J7007 (51) (X211-E1 Preliminary Acceptance Test Specification)," GE-ANPD, DC 61-8-20, August, 1961.
5. McCulloch, J. C., "AW-10 Starter Design Report," GE-ANPD.
6. Layman, D. C., "Reference B13-X211-E3 Design Requirements," GE-ANPD, DC 61-9-2, September, 1961.
7. "Preliminary Model Specification - Engine, Aircraft, Turbojet: J87-GE-1," Specification No. E-747A, Revised 9-14-60, GE-LJED, E747A, April 21, 1959.
8. "Reference B.15 - Installation Bulletin XNJ140E(S-23A)," GE-ANPD, DC 61-9-1, September, 1961.
9. Adler, A. R., "XNJ140E Reliability and Maintainability Plans," GE-ANPD, DC 61-11-11, June 26, 1961.
10. Layman, D. C., "General Electric Company (X211-E1 Engineering Release List)," GE-ANPD, DC 61-8-21, August, 1961.
11. Linn, F. C., "Turbomachinery Handbook for 140E1," GE-ANPD, DC 60-9-23, September 16, 1960.

7. CONTROL SYSTEM

7.1 INTRODUCTION

The proposed XNJ140E-1 engine was to be controlled by a system of closed-loop servomechanisms that regulated various engine parameters. The essential closed-loop servosystems were as follows.

Temperature Control - This loop controlled the turbine discharge-air temperature, $T_{5.1}$. It adjusted the supply rate of chemical fuel, W_f, during CHO operation, or the level of reactor neutron flux, ϕ, during NHO operation to hold the demanded $T_{5.1}$ level.

Engine Speed Control - This loop controlled the engine speed, N, by controlling the port area, A_B, of the bleed-speed bypass system and/or the area, A_8, of the primary jet nozzle.

Compressor Stator Position - This loop controlled the angular position, β, of the compressor stators in accordance with a preset schedule.

Reactor Startup - This loop was a subsystem within the reactor control system. It accomplished period-controlled reactor startup from subcritical to 1.5 percent of full power.

Safety System - These components performed a supervisory function of monitoring engine parameters and prevented engine operation in unsafe modes. The system was composed of computing channels, interlocks, and trip circuitry.

The engine control system was divided into two related smaller systems; the reactor control system, and the turbomachinery control system. During operation, the two subsystems were integrated by a single demand (throttle). Since the reactor was the primary heat source for the engine, the turbomachinery control system computed the required energy and placed this demand upon the reactor control system. The engine control system was capable of controlling the engine through all phases of the engineering test program. Specific modes of planned operation included the following:

1. Manual and automatic reactor startups
2. Manual and automatic control of reactor power level from a few watts to full power
3. Control of turbine discharge-air temperature either by automatic modulation of nuclear power, by manual programming of chemical fuel flow, or by modulation of nuclear and chemical power in combination
4. Regulation of engine speed from idle to 5000 rpm
5. Transfer of power between nuclear and chemical heat sources
6. Manual positioning of the compressor stator as a function of engine speed and compressor inlet temperature
7. Automatic positioning of the compressor stators as a function of engine speed and compressor inlet-air temperature
8. Manual engine starts on either chemical or nuclear power.

An engine-driven constant-speed-drive electrical power system provided control system electrical power for engine speeds at or above idle. It contained paralleling controls to enable automatic paralleling with electrical supplies of other engines or ground supplies.

Wherever possible, all XNJ140E-1 systems were being designed to meet flight requirements so that the ACT program would be instrumental in the development of flight-type systems. Power plants with operational flight capability would have contained a throttle-controlled nonmodulated chemical afterburner system. The XNJ140E-1 manual chemical fuel control system would have been replaced with a comparable automatic control loop.

7.2 ENGINE CONTROL SYSTEM

7.2.1 OVER-ALL REQUIREMENTS

A detailed presentation of the over-all engine control system requirements is given in reference 1.

7.2.1.1 Functional

In addition to automatically controlling the engine during all modes of normal steady-state operation, the system was capable of controlling the engine during the following modes of transient and shutdown operation:

1. Nuclear starts from 0 percent speed to idle
2. Chemical starts from 0 percent speed to idle
3. Power transfer from nuclear to chemical or chemical to nuclear
4. Shutdown, both normal and emergency, from either nuclear or chemical operation
5. Nuclear operation with aftercooling air provided by the AHR system blowers
6. Nuclear operation with the engine motorized by the starter.

The engine control system was composed of two integrated systems, the turbomachinery control system, and the reactor control system. The main functional units of these systems were as follows:

1. Engine speed control, using the bleed-speed valve area loop and the jet nozzle area loop
2. Compressor stator control
3. Manual fuel control
4. Reactor startup control
5. Reactor power range control, using either flux or temperature
6. Hydraulic systems for stator, nozzle area, and bleed-speed valve area control
7. Hydraulic system for electrical power supply (constant speed drive) and starter lube oil cooling
8. Lube system
9. Ignition system
10. Starter
11. Electrical power supply
12. Control-rod power supply
13. Control console
14. Aftercooling system, including air supply, engine rotor lock, and compressor shut-off doors.

7.2.1.2 Performance

The performance requirements corresponded generally to those contained in MIL-E-5007B. These requirements were modified or supplemented by additional requirements uniquely dictated by the application of nuclear power to aircraft propulsion. Significant requirements were as follows:

Idle - When the throttle was set at Idle, the thrust did not exceed 6 percent of the military thrust available at standard-day conditions at altitudes up to 6000 feet.

Thrust Transient - During throttle movements in any sequence and at any rate, freedom from objectionable overspeed, overtemperature, combustion instability, and compressor instability was maintained. Following throttle movement at its maximum rate, the time required to accomplish 95 percent of the thrust change safely did not exceed the values specified below for standard-day conditions. The total time required to accomplish each specified transient and reach stable operation did not exceed the time specified for 95 percent of the change in thrust plus 10 seconds for chemical, or 30 seconds for nuclear-powered operation.

1. Accelerations (to 95 percent thrust level), NHO
   a. Idle to military thrust in 15 seconds at an indicated air speed of 150 knots or less, and 12 seconds for indicated air speeds above 150 knots, at all altitudes between sea level and 6000 feet
   b. 30 percent military to military thrust in 9 seconds for indicated air speeds of 150 knots or less, at all altitudes between sea level and 6000 feet
   c. Idle to military thrust in 50 seconds at 150 knots or more, at all altitudes above 6000 feet
   d. Military thrust to maximum thrust in 5 seconds under all operating conditions.
2. Decelerations (to 95 percent thrust level), NHO
   a. Maximum thrust to military thrust in 25 seconds under all operating conditions.
   b. Military thrust to idle thrust in 40 seconds at a minimum indicated air speed of 150 knots, at all altitudes between sea level and 6000 feet.

Stability - Under steady-state operating conditions and within the operating limits defined above, engine thrust oscillation between idle and normal continuous did not exceed $\pm$ 1.0 percent of normal continuous thrust, or $\pm$ 5.0 percent of the thrust available as established by the throttle position and flight condition; whichever was less. During operation at throttle settings above normal continuous, thrust oscillation did not exceed $\pm$ 1.0 percent of the thrust available at that condition.

Stopping - Normal stopping of the engine (either CHO or NHO) was accomplished by single, rapid, pilot-controlled actuation of the throttle during any operating condition.

Starting - The engine was required to make satisfactory ground and air starts. Both nuclear and chemical ground starts from zero to idle rpm were to be accomplished in three minutes at standard-day conditions and at all altitudes between sea level and 5000 feet. Starting time for a nuclear start was considered to begin after the reactor had been stabilized at 1.5 percent of full power. Repetitive starts were required. The normal starting procedure did not require critical timing. With the throttle in the idle position, initiation of the starting sequence provided for ground or inflight starting, and acceleration to stable idle operating conditions.

Throttle - A single lever modulated thrust from idle to maximum rating, and also initiated engine startup and shutdown. The torque required to operate the thrust lever through its range of travel from idle to maximum did not exceed 15 pound-inches.

Adjustments - Pre-operational checkouts of control amplifiers, measuring circuits, nuclear instrumentation, flow indicators, and temperature indicators were to be performed wherever desirable and feasibly possible. Where daily checkout and/or calibration was not expected to be adequate or feasible, due to complexity or other factors, a test or checkout package or cart was to be provided which allowed complete pre-operational setup and adjustment of the system. Complete operating, assembly, maintenance, and trouble-shooting instructions were to be provided with the equipment.

Reliability - The over-all control system and component parts were designed for inherent reliability in all modes of operation.

7.2.1.3 Environmental

All components of the control system were to operate satisfactorily when exposed to the environmental conditions specified in Table 7.1. The radiation environment is defined in reference 2 and discussed in section 6.4.1.

TABLE 7.1

ENVIRONMENTAL CONDITIONS

Parameter	XNJ140E-1		XNJ140E (Flight Type)		
	Control Room	Engine Mounted	Crew Compartment	Equipment Compartment	Engine Mounted
Ambient temperature	-30° to +120°F (non-operating) +50° to 100°F (operating)	-30°F to temperature shown in section 6.2.3.2	-65° to +160°F	-65° to +160°F	-65°F to temperature shown in section 6 2 3 2
Vibration	None	5-500 cps[a]	5-500 cps[b]	5-500 cps[b]	5-500 cps[a]
Shock	None	30G[a]	15G[b]	15G[b]	30G[a]
Altitude	5,000 ft	5,000 ft	0-35,000 ft	0-35,000 ft	0-35,000 ft
Humidity	5% - 95%	To 100%[a]	To 100%[b]	To 100%[b]	To 100%[a]
Explosion proof	No	Yes[a]	Yes[b]	Yes[b]	Yes[a]
Salt spray	None	None	Yes[b]	Yes[b]	
Fungus	None	None	Yes[b]	Yes[b]	Yes[a]
Sand and dust	None	Yes[a]	No	Yes[b]	Yes[a]
Radiofrequency interference	MIL-I-6181	MIL-E-5009B	MIL-I-6181	MIL-I-6181	MIL-E-5009B

[a]Test procedure given in Military Specification MIL-E-5009B.
[b]Test procedure given in Military Specification MIL-E-5422E.

7.2.2 TURBOMACHINERY CONTROL SYSTEM

The turbomachinery control system included the complete engine control system except that portion associated with the nuclear reactor. It automatically controlled engine speed, compressor stator position, air temperatures, engine acceleration and deceleration, and engine starting and stopping. Manual selection of jet nozzle area was permitted with proper switching. It regulated the flow of chemical fuel to the combustors, and furnished a temperature-demand signal to the reactor control system. Automatic transfer either way between chemical and nuclear power was effected without shutting down the engine. No emergency or backup systems were provided; instead, reliable operation was obtained by redundancy, split systems, mechanical stops, and/or limited authority systems.

The turbomachinery control system and its operation, as described herein, was applicable to flight-type (XNJ140E) power plants. The XNJ140E-1 control system contained additional servo loops that permitted other manual operations and/or biases. These exceptions are specifically defined.

Operator (aircraft pilot) action was relayed to the control system through throttle motion input into the thrust selector. The thrust selector provided engine speed, bleed-speed valve area, energy, and turbine discharge-air temperature demands to the separate loops as a function of the throttle setting and the compressor inlet-air temperature. At idle power setting, the jet nozzle pressure ratio was too small to have a significant effect on engine speed. A large percentage of bleed-speed air was scheduled, and automatic speed control was achieved by the variation of bleed-speed air. At higher power settings, the jet nozzle was capable of satisfactorily controlling the engine speed. Bleed-speed air was minimized to optimize performance, and to make the full bleed-speed air capacity available for overspeed control in case of a jet nozzle failure.

For all power settings, energy input was scheduled to provide a temperature demand. An energy/compressor-discharge-pressure signal from the thrust selector was multiplied

by the system pressure to provide an energy demand proportional to engine airflow. Vernier control was obtained by comparing the actual $T_{5.1}$ to the demanded $T_{5.1}$, and computing a corrected energy demand signal proportional to the temperature error. This vernier was considered a limited authority system, and its failure had a minor effect on system performance.

The throttle also initiated afterburning. Afterburner fuel flow was automatically regulated as a function of system pressure, and was not modulated.

The turbomachinery control system contained the following subsystems:

1. Engine speed control, containing the bleed-speed valve area control, and the automatic and manual jet nozzle area controls
2. Compressor stator position control
3. Hydraulic fluid supply
4. Manual fuel control
5. Nozzle bound control
6. Thrust selector.

In addition to these major subsystems, the turbomachinery control system contained an electrical ignition system for the combustors, and required the following input services:

1. Various electrical power supplies
2. Input and feedback signals from the reactor control system
3. Chemical fuel supply from the facility installed fuel supply system
4. Hydraulic coolant fluid
5. Lube oil from the facility installed lube oil system

Flight-type systems would substitute automatic control in the fuel control system, and would add an afterburner fuel control system.

These subsystems, and their auxiliary sensing elements, performed the following functions:

1. Jet nozzle area bounding
2. Engine speed biasing
3. Bleed-speed airflow biasing
4. Turbine discharge-air temperature biasing
5. Overtemperature limiting (for nuclear operation)
6. Overspeed and overtemperature limiting (for chemical operation)
7. Combustor purging.

7.2.3 REACTOR CONTROL SYSTEM

This system regulated the neutron fission flux in the reactor core to maintain the desired rate of heat generation. Closed-loop servosystems positioned the control rods in accordance with neutron flux or turbine exit-air demands. The controlled parameter was neutron flux and the resultant power level was reflected in the turbine exit-air temperature. The control system consisted of the following equipment assemblies:

1. The operator's console, containing the meters and switches necessary to control and monitor operation of the reactor and engine
2. Electrical and electronic control components for computing the servosystem error signals and driving the control rod actuating system
3. Control rod actuators
4. Position, flux, and temperature sensors supplying feedback signals to the servosystems, and mounted on the engine
5. Redundant computing channels, interlocks, and parameter trip circuitry to perform the monitoring function.

The system was capable of performing a period controlled automatic reactor startup from subcritical to 1.5 percent of full power and regulated neutron flux or temperature from 1.5 to 100 percent full power. The following subsystems were required to perform this regulation in a safe manner:

1. Control rod actuation subsystem
2. Startup subsystem
3. Power range flux and temperature subsystem
4. Manual reactor control subsystem
5. Safety subsystem.

Automatic control was initiated by clearing all scram conditions, positioning the actuator mode selector to Servo position, selecting the desired startup period, and positioning the mode selector to Flux position.

Subpower-range flux control could be selected by the operator and provided automatic power leveling from approximately 10^{-8} percent of full power to 1 percent of full power. It was initiated by manually switching (1) the cable of the controlling ion chamber to the micromicroammeter input, and (2) the subpower range switch to On before reactor startup was initiated. Manual reactor startup to the desired power level was required to zero the flux loop error. The mode selector then was positioned to Flux and the actuator mode selector to Servo.

The reactor safety system served the function of protecting the engine against damage in the event of accidents caused by any conceivable control system failure. In addition to protecting against damage, improper operation was forestalled when such operation could cause dangerous conditions.

Since the XNJ140E-1 power plant was intended for ground test operations, safe operation was considered more important than continuous operation. A design objective of the control system was to prevent engine damage due to the failure of control system components. The system was designed to be failsafe, i.e., all failures that occurred resulted in a safety action. Because of this objective, the operational reliability was decreased but the safety reliability was increased.

7.2.4 INTEGRATION OF TURBOMACHINERY AND REACTOR CONTROL SYSTEMS

The turbomachinery control system and reactor control system were integrated into a single engine control system as shown in Figure 7.1.

The resultant regulatory parameters, and modes of control, were as follows:

1. Engine rotor speed, N - controlled by bleed-speed valve area, A_B, and jet nozzle area, A_8
2. Turbine discharge-air temperature, $T_{5.1}$ - controlled by neutron flux, ϕ, and/or combustor fuel flow, W_f
3. Neutron flux, ϕ - controlled either by automatic or manual positioning of control rods
4. Reactor startup period, τ - controlled by automatic positioning of control rods
5. Compressor-stator-blade angle, β - controlled as a function of corrected speed
6. Bleed-speed valve area, A_B - reset by jet nozzle area, A_8
7. Jet nozzle area, A_8 - controlled automatically or manually
8. Engine fuel flow, W_f - controlled manually by fuel valve area.

Engine operation was governed by throttle lever motion input into a single thrust selector that was mounted on the operator's control console. The thrust selector programmed a combination of input demands to the individual servoloops that regulated the control parameters. The position of the throttle determined the orientation of three 2-dimensional cams

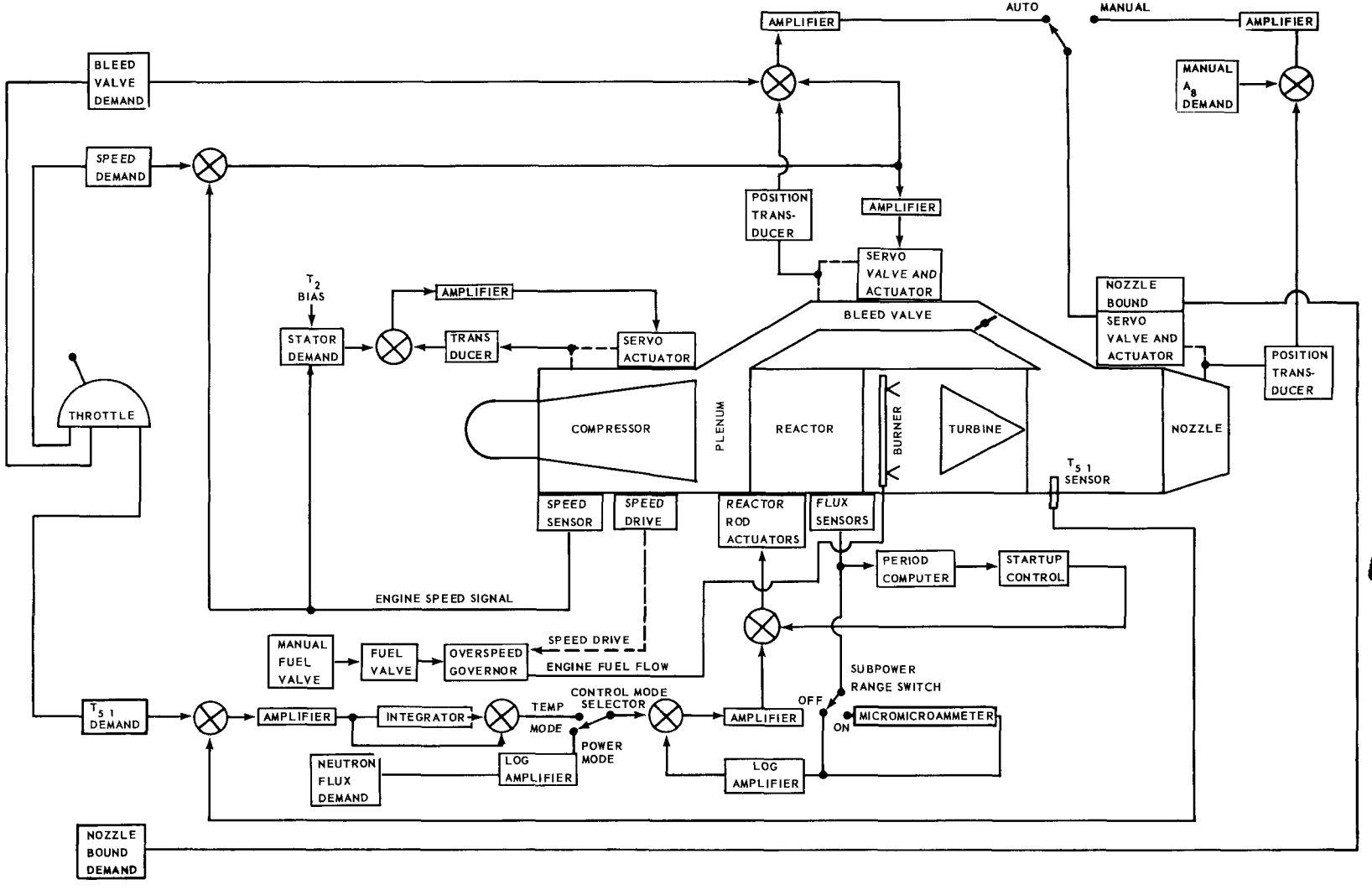

Fig. 7.1 – Engine control system, XNJ140E-1

inside the thrust selector and scheduled the selected engine operating point. Individual throttle biases, adjustable from the operator's console, were incorporated into the speed, turbine discharge-air temperature, and bleed-speed valve area demands. These biases trimmed performance during operation and aided in establishing proper steady-state demand schedules. They also allowed the operator to establish any off-schedule operating modes that were required during engineering testing. The operator insured that any individual bias was not adjusted beyond the limits required for safe operation.

7. 2. 5 LAYOUT OF CONTROL AND DATA ROOMS IN THE FET FACILITY

A plan view of the control and data rooms in the FET facility is shown in Figure 7. 2. Placement of the operator's console and secondary panels within the control room, and the relative location of the data room and the cell window are shown. Also indicated is equipment installed or planned to be installed in the secondary panels.

A view of secondary panels existing at the time of contract termination is shown in Figure 7. 3. Twenty-seven recorders (24 single-point recorders and 3 8-point recorders) were located in the B, C, and D racks. Twenty-four unassigned panel alarms were located on the B racks above the recorders. Facility systems installed in these racks included the weather instruments and communication system, the stack monitor, the rupture detector, the cell TV system, the fuel supply system controls, the cooling water system controls, the cell door and warning light controls, the contaminated waste tank controls, and facility electrical system monitoring.

An operator located at the window had an unobstructed view of the engine installation, and also had a television monitor at his disposal. Controls assigned to this operator included fire-fighting and personnel access doors to the test area.

7. 2. 6 OPERATOR'S CONSOLE AND DATA READOUT

The combined control, data instrumentation, and facility monitoring systems contained approximately 2000 sensors. A complete list of these sensors is contained in reference 3. Output signals from most of these sensors were connected to the data readout system patch panels located in the cable room beneath the FET control room. The data readout system was connected to these patch panels and provided means of monitoring, recording, and reading out any of the input sensor signals. Although many of these parameters were control or supervisory in nature, rather than engineering data, they were patched into the data system. The data system, with its computer, compared these data with predetermined limits and provided additional warnings to supplement operator surveillance.

All control and supervisory parameters were monitored on meters in the control room and were displayed on either the operator's console or the secondary panels. Meters located on the operator's console are shown in Figures 7. 4a and 7. 4b; those located on the secondary panels are discussed later. Most of the control system parameters displayed on the operator's console were also monitored and/or recorded on the secondary panels. Disadvantages in providing this flexibility of readout was that failure of an indicating device could reflect itself in a control system failure, and readout devices could interact with the control system. Wherever possible, separate sensors for the control system and data instrumentation system were provided.

Table 7. 2 lists the number of data points originating in the control system and readout on the operator's console, the secondary panels, or special transient recorders. Further details are discussed in reference 3.

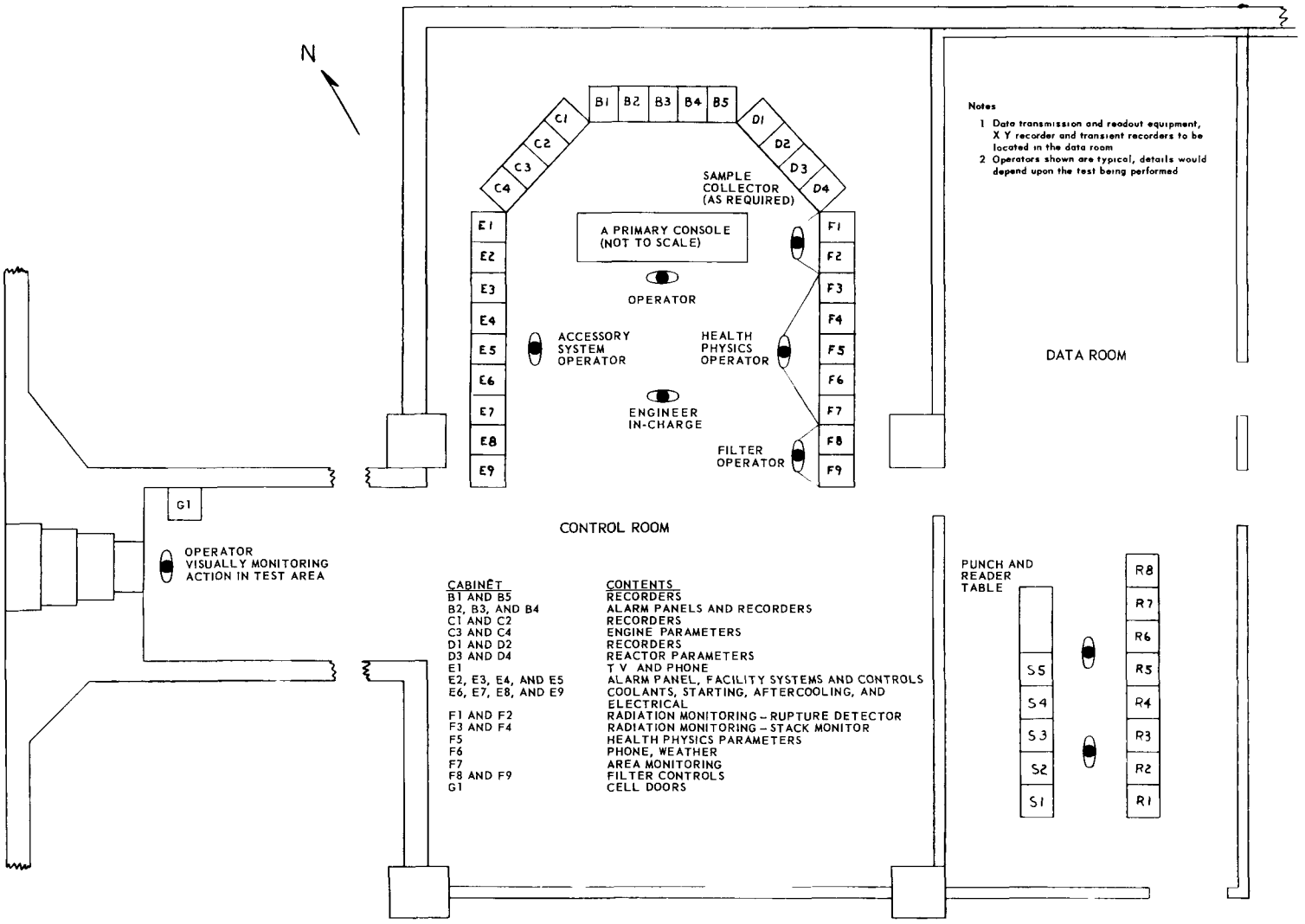

Fig. 7.2 – Control room and data room, FET Dwg. SK 977C214

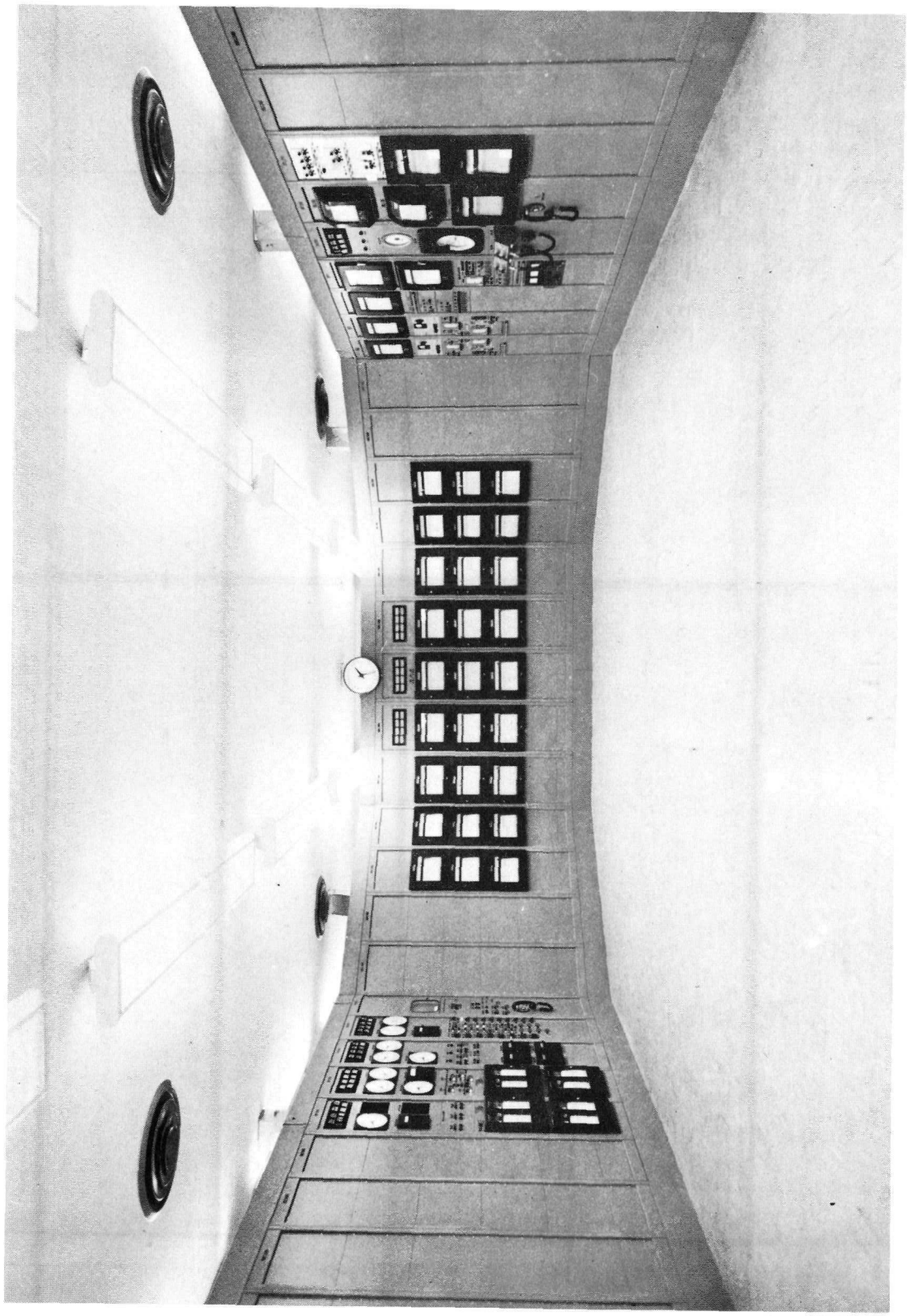

Fig. 7.3 – Secondary panels

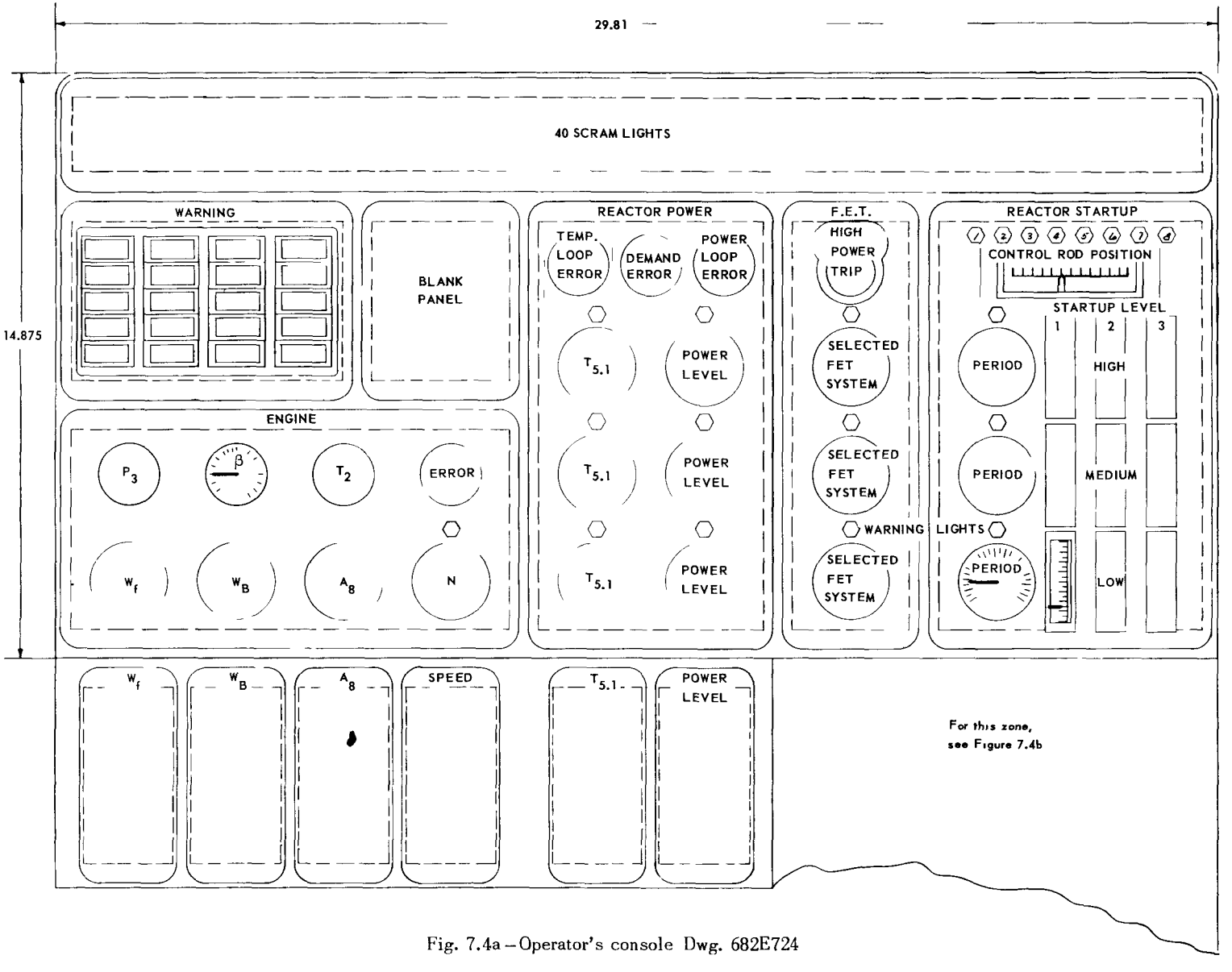

Fig. 7.4a – Operator's console Dwg. 682E724

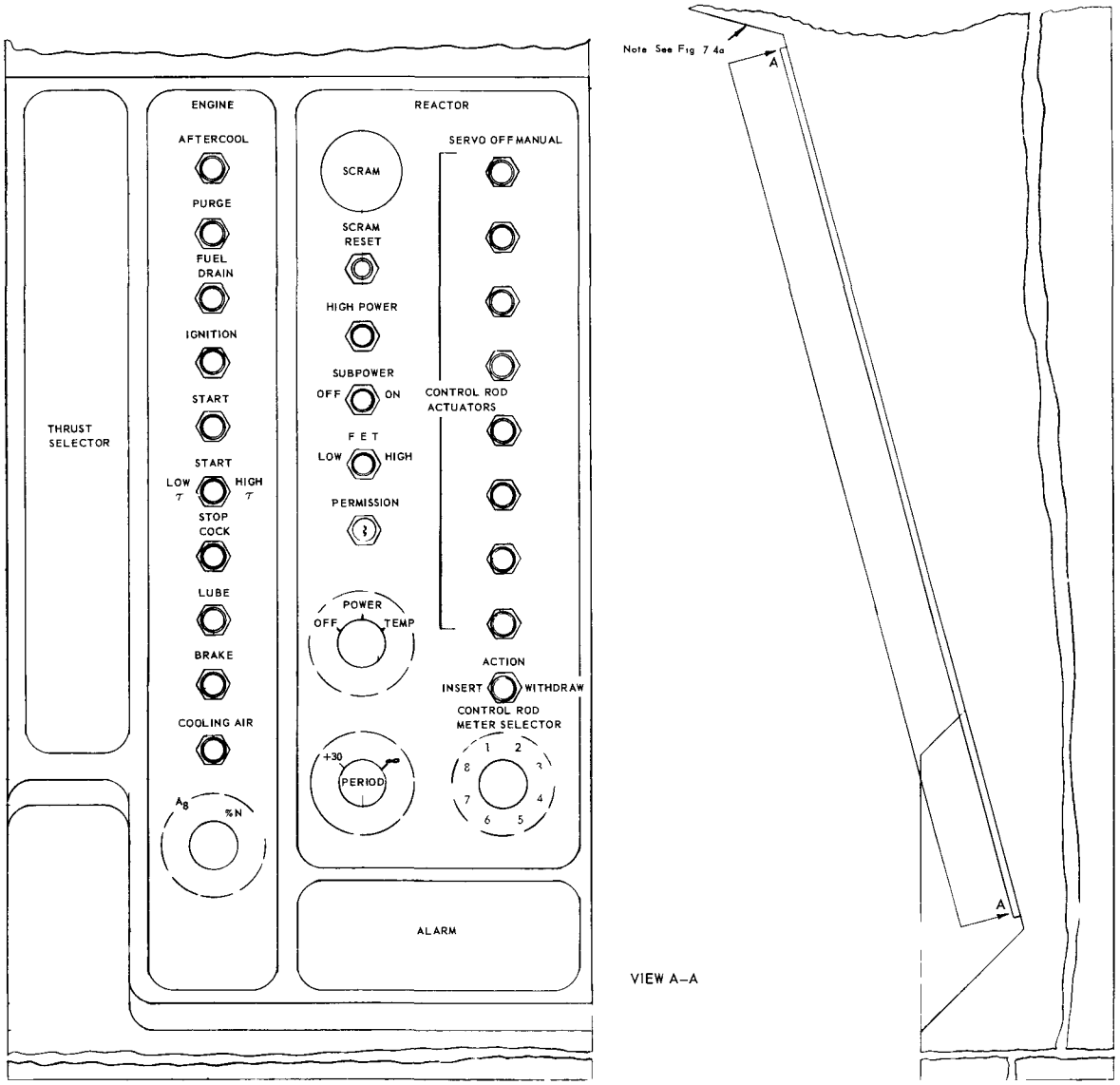

Fig. 7.4b – Operator's console (Dwg. 737D479)

TABLE 7. 2

CONTROL SYSTEM DATA READOUT

Parameter	Operator's Console	Secondary Panel Meter	Secondary Panel Recorder	Transient[a] Recorders
Fuel element surface temperature	3[b]		3	HP
Turbine discharge-air temperature	3		3	HP
Control rod position	1	8	8	LP & HP
Flux level	3		4	HP
Engine speed	1	1	1	HP
Startup power level	9		3	LP
Period	3		3	LP
Micromicroammeter	1		1	LP
Fuel flow	1			HP
Thrust		1		
Flux loop error	1			
Temperature loop error	1			
Demand error	1			
Compressor inlet-air temperature	1			
Compressor discharge-air pressure	1		1	HP
Stator vane position	1		1	HP
Bleed-speed valve area	1		1	HP
Nozzle area	1		1	HP
Nozzle error	1			
Exhaust duct pressure	1			HP

[a]HP - monitored during high power testing.
LP - monitored during low power testing.
[b]Numbers indicate number of parameter datum points read out.

7. 2. 6. 1 Operator's Console

The operator's console contained all control devices and sensor readouts necessary to conduct the test operations planned for the ACT program. It could be adapted to flight test operations with minor modifications, and was so arranged that a single operator could operate an XNJ140E engine using only the single throttle contained in the console. The general layout of the operator's console, shown in Figures 7. 4a and 7. 4b, utilized 2-inch meters. A redesign incorporating larger meters for better visibility was underway.

The most important parameters from a safety and operating standpoint (speed, $T_{5.1}$, selected FET services, and reactor flux) were centrally displayed in the most prominent locations. Alarm lights were located close to their associated meters. Manual demand inputs or biases were located adjacent to their associated meters and the meters were grouped functionally. Components contained in the operator's console are described in reference 3.

7. 2. 6. 2 Secondary Panels

The secondary panels contained readout and alarm devices not required on the operator's console. These panels were assigned to racks in accordance with the data room layout shown in Figure 7. 2. Engine parameters were located in the C-racks, reactor parameters in the D-racks, and accessory controls and parameters in the E-racks. Components located in the secondary panels are discussed further in reference 3.

7. 2. 6. 3 Alarm Indication

Alarm lights were provided for all dangerous conditions developing in either the engine or in the facility-supplied services. Alarm lights on the operator's console were small red lights located adjacent to the meter monitoring the associated parameter. These lights cleared when the violating parameter returned to normal. Alarm lights for (1) the 400-cycle voltage, (2) aftercooling system not functioning, and (3) failure of starter air supply did not have associated meters. The 400-cycle voltage alarm was placed on the operator's console because it anticipated a condition during which the controls became sluggish. A frequency meter for this parameter also was located on the electrical secondary panel. Alarms for the aftercooling (AHR) system and starter air supply were provided so that the operator could anticipate malfunctions leading to the possibility of an engine scram.

Since the alarm lights on the operator's console were small, they were repeated on unassigned panel alarms located on the secondary B-rack. Although the operator's console provided a light for each of the individual alarms, only one common light was used on the B-rack panel alarm. Of the 24 panel alarm points, sixteen were assigned to repeating signals from the operator's console. The remaining eight were arranged so that they could be operated by any of the 24 single-point recorders. These recorders also contained microswitches that could be set to trip if the parameter being monitored exceeded a preset level. Additional alarm lights were located at the top of racks containing monitoring meters for those parameters requiring an alarm light. In general, every parameter having an alarm light had an associated meter. If this were not the case, an alarm light was located adjacent to the equipment group with which it was functionally identifiable. In two instances, an alarm light also served as an indication to the operator to take specific action; these lights were located close to the appropriate control and were repeated in the larger alarm lights at the top of the racks.

Alarm lights on the operator's console remained on until the violating parameter returned within limits. Secondary panel alarm lights also remained on until the violating parameter returned within limits, but contained further provisions for acknowledgement. Following operator acknowledgement, the red light turned off and a white light turned on and remained on until the violating parameter returned within limits.

7.3 TURBOMACHINERY CONTROL SYSTEM

7. 3. 1 FUNCTIONAL REQUIREMENTS

The system was designed to meet the following functional requirements:

1. Thrust oscillations did not exceed 1 percent of point at and above normal* power, and 1 percent of normal* thrust or 5 percent of point, whichever was smaller, below normal power.
2. Engine speed was controllable from 2000 to 5500 rpm (40 to 110% N) with an accuracy of ±1. 0 percent N below normal power and ±0. 5 percent N above normal power. Controlled dN/dt did not exceed 1000 rpm per second.
3. Stator position was controllable from 0 to 40 degrees with an accuracy which resulted in holding the engine speed within ±5 percent corrected speed.
4. The bleed-speed valves were capable of bypassing air at 70 percent corrected speed from a maximum of 15 percent W_{a_2} to a minimum of 0 percent W_{a_2} with an accuracy of ±0. 2 percent W_{a_2} above normal power and ±0. 5 percent below normal power.

*Normal power and normal thrust were the values of these engine parameters when the throttle was set at normal continuous.

5. Turbine discharge-air temperature was controllable from 600° to 1150°F with an accuracy of ±2. 0°F above normal power and ±5°F below normal power.
6. The jet nozzle area was regulated from 1100 to 2350 square inches with the accuracy required to maintain speed constant within ±5 percent of the corrected speed.
7. Combustor fuel flow was controllable from 1500 to 37, 000 pounds per hour.
8. Nozzle bounding was held within ±25 square inches accuracy.
9. At the emergency power setting, speed control was within ±0. 25 percent N.
10. Afterburner fuel flow was controllable from 20, 000 to 67, 000 pounds per hour.

Detailed requirements of the turbomachinery control system are contained in references 1, 3, 4, and 5.

7. 3. 2 SYSTEM DESCRIPTION

The turbomachinery control system was functionally similar to that of the XMA-1A power plant described in APEX-907, XMA-1 Nuclear Turbojet. An added loop controlled engine speed, in conjunction with the jet nozzle, by regulating the quantity of bleed-speed air that bled from the compressor discharge, bypassed the turbine, and was reintroduced into the exhaust duct. The addition of this control loop provided: (1) improved transient engine performance during NHO, (2) engine overspeed protection in the event the jet nozzle failed to open during NHO, (3) operational use of the afterburner during NHO, and (4) relaxation or elimination of requirements for other control loops. The system was modified from an electro-pneumatic-hydraulic system (XMA-1A) to an electro-hydraulic-mechanical system for the XNJ140E-1 power plant. The change to the electro-hydraulic-mechanical system increased flexibility and reliability redundancy possibilities, and reduced over-all development costs.

The system automatically controlled engine speed, compressor stator position, cycle temperatures, engine starting and stopping, and acceleration and deceleration. In addition, manual selection of jet nozzle area was possible with proper switching. The system performed all the above-listed functions except cycle temperature control (temperature demand only was furnished) during nuclear operation. It utilized inputs from (1) the throttle, (2) compressor inlet-air and turbine discharge-air temperature sensors, (3) bleed-speed valve and jet nozzle area transducers, and (4) the compressor stator position transducer. It provided the necessary output actuating forces, movements, and demand signals.

The integrated turbomachinery control system is shown in Figure 7. 5.

7. 3. 3 ENGINE SPEED CONTROL SUBSYSTEM

The engine speed control system performed the following functions:

1. The bleed-speed loop and nozzle reset loop controlled engine speeds from maximum to sub-idle.
2. Steady-state high-speed control was effected by changing nozzle area, with fast transients absorbed by the bleed-speed valves. Low-speed control primarily was effected by bleed-speed valves with nozzle area held open.
3. Nozzle-open failures were protected by a nozzle bound which limited nozzle-open area during nuclear, but not during chemical, operation; the limit was adjustable between 1100 and 1500 square inches.
4. The bleed-speed and nozzle reset loops had alternate inputs so that the nozzle and/or bleed-speed valves could be positioned manually and independently for test operations.

The system is shown in Figure 7. 6. It regulated engine speed by simultaneous modulation of two parameters: (1) A_8, jet nozzle area, and (2) A_B, bleed-speed valve area. Both A_8 and A_B areas affected the amount of work delivered to the turbine rotor. The jet noz-

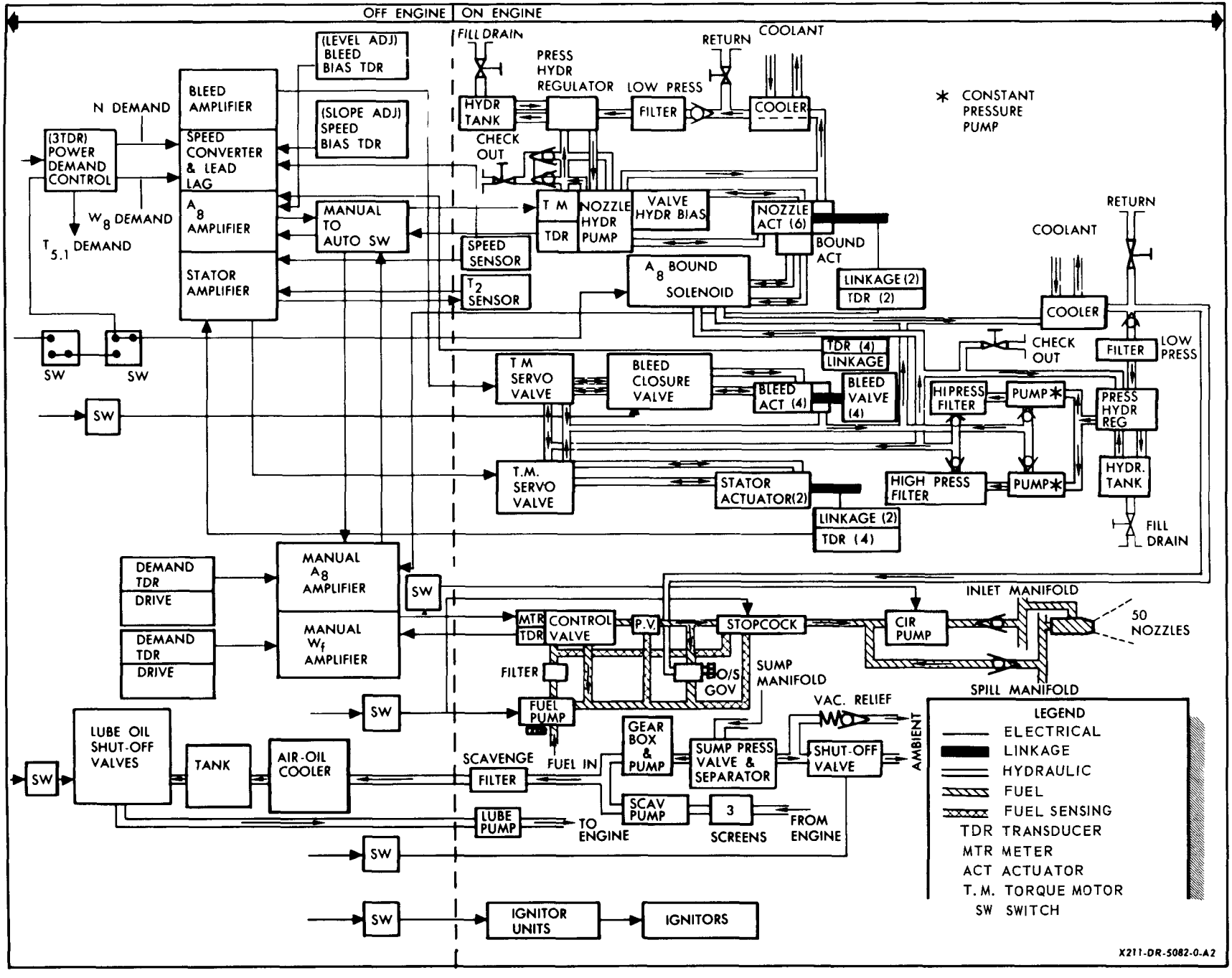

Fig. 7.5 – Turbomachinery control system

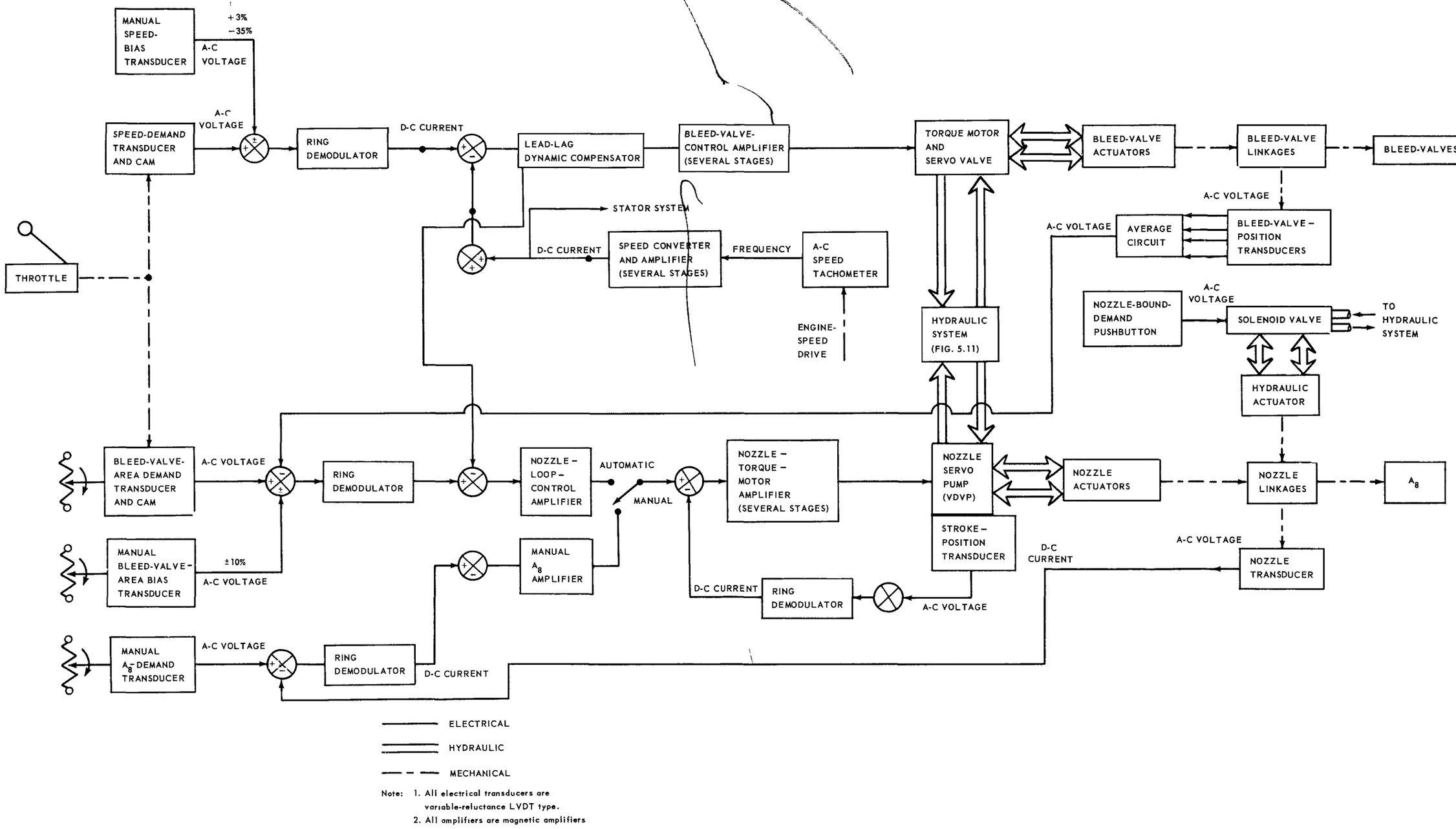

Note: 1. All electrical transducers are variable-reluctance LVDT type.
2. All amplifiers are magnetic amplifiers

Fig. 7.6 – Engine speed control subsystem, including manual control of jet-nozzle area, XNJ140E-1

zle accomplished this by variation of turbine back pressure (P_5), which decreased (increasing turbine work) as A_8 increased. At low airflows, however, A_8 modulation did not produce a significant variation of P_5, and thus the nozzle did not afford effective speed control at low engine speeds. Unlike the jet nozzle, the bleed-speed valves were capable of sharp control of engine speed regardless of the airflow since the percentage of air being bypassed was independent of the rate of airflow. The bypass bleed-speed air varied the amount of turbine work by diverting a portion of the working fluid from the compressor plenum around the turbine and back into the exhaust duct.

The speed control system utilized electro-hydraulic components. Two control loops were required to properly modulate the jet nozzle and bleed-speed valve areas. Engine speed and bleed-speed valve area demand signals were originated in the thrust selector as a function of throttle angle and bias transducer position. The speed demand signal requested a particular engine operating speed, while the bleed-speed valve area demand signal adjusted the engine cycle for peak performance and acceleration potential.

Demand signals programmed by the three 2-dimensional cams in the thrust selector were the speed demand, the temperature demand, and the bleed-speed valve area demand. Each cam positioned the core of a linear variable differential transformer (LVDT) to generate an electrical a-c demand signal proportional to cam-follower position. This signal was electrically summed with another a-c signal from the throttle bias LVDT and fed to a magnetic ring demodulator to produce a d-c signal suitable for additional summation and amplification in subsequent control-loop magnetic amplifiers.

The speed demand signal was fed into both the nozzle and bleed-control loop amplifiers wherein it was electrically compared with a d-c speed feedback signal proportional to actual engine speed. The feedback signal was generated as an a-c frequency, proportional to engine speed, in an engine-mounted permanent-magnet-type tachometer. The signal was then converted to a d-c signal proportional to tachometer frequency, amplified, and introduced to the windings of the nozzle and bleed-speed control magnetic amplifiers.

Speed demand, actual speed, and speed lead-lag compensator signals were compared and amplified in the bleed-speed amplifier to produce a resultant d-c error signal. The error signal displaced a wand in a servo valve torque motor which acted to direct hydraulic fluid to four bleed-speed valve actuators. These actuators moved the bleed-speed valves until either the actuating error signal disappeared or the valves reached their mechanical travel limits. The bleed-speed valves always moved in a direction to force actual engine speed to agree with the engine speed demand from the throttle. Since the bleed-speed valves remained in motion until the difference between the actual speed and a demand speed was zero, a zero-speed-error control was obtained. In addition, four a-c LVDT bleed-speed-valve position signals were demodulated, averaged, and compared with the speed demand, the actual speed, the speed lead-lag compensator, and the bleed-speed-valve position demand signals in the nozzle amplifier. A scheduled bleed-speed-valve area demand signal to the nozzle amplifier was required to maintain the bleed-speed valves at the position of best engine performance. If the bleed-speed valves were off the scheduled position, the nozzle loop adjusted nozzle area to reset the bleed-speed valves to the desired position (the bleed-speed valves moved with changes of jet nozzle area to maintain constant speed).

The output of the nozzle amplifier acted as the demand to a minor pump-stroke position loop regulating the nozzle pump output. Pump-stroke position signals from an LVDT were fed back, demodulated, and compared with the error signal to position the pump stroke and thus regulate pump flow proportional to the error signal. The nozzle pump, a variable displacement – variable pressure type, directed hydraulic fluid to the nozzle actuators, moving them until either the nozzle error signal went to zero or the nozzle reached a travel limit.

Operation of the speed control system during a throttle burst was as follows. The nozzle opened and the bleed-speed valves closed in an attempt to satisfy the increased speed demand. Reactor power level increased to satisfy the $T_{5.1}$ temperature demand. As the desired speed was approached, the bleed-speed valves moved; the jet nozzle area was readjusted until the error between the bleed-speed valve area demand and its actual position was zero.

All components of the speed control system were studied previously and were in an advanced state of development except for the tachometer, the bleed-speed valve actuator, and the bleed-speed servo valve. Many of the components had been tested for 2380 hours, of which 230 hours were during turbomachinery testing and 304 hours were under a radiation environment. The nozzle actuators were tested for 5370 hours, of which 2610 hours were on turbomachinery and 680 hours in a gamma-radiation environment of 10^5 roentgens per hour.

7.3.3.1 Manual Control of Jet Nozzle Area

The manual jet nozzle position control, shown in Figure 7.6, was a part of the engine speed control system and was to be used in tests during which manual nozzle positioning was required. Nozzle position demand and feedback signals were generated by a-c transducers and demodulators similar to those in the speed control system. The nozzle moved to drive the error signal to zero. Transfer from automatic to manual nozzle area control was through a switch on the control console, and was effected at full-open nozzle position to eliminate any chance of a speed transient.

7.3.4 COMPRESSOR STATOR POSITION CONTROL SUBSYSTEM

The control system is shown in Figure 7.7. It could accurately follow stator schedules with slopes as high as 3.2 degrees β, and 0.7 degrees β per percent corrected speed. The ratio of the actual slopes of the maximum schedule and the minimum schedule was less than two.

The system was an electro-hydraulic position control in which the variable stator blades of the compressor were linked together and driven by two stator actuators, and the demanded stator position was scheduled as a function of corrected speed. A speed signal from the tachometer was converted to d-c and combined with a T_2 temperature signal in the magnetic input circuit of the corrected-speed amplifier. The corrected-speed signal was compared with a stator-position feedback signal obtained from a position transducer attached to a stator vane. When an error existed, the signal was amplified in a magnetic amplifier and controlled hydraulic flow from a servo valve into the two stator actuators.

All components of this system were reliable, state-of-the-art items. The stator actuators underwent more than 1000 hours of test. The servo valve was similar to the one used in the jet nozzle control. Amplifiers, the position transducer, and the tachometer were of conventional design.

7.3.5 HYDRAULIC FLUID SUPPLY SUBSYSTEM

The performance characteristics of this subsystem were as follows.

1. The system supplied OS-45,* Type IV, hydraulic fluid to the turbomachinery control system.
2. The delivered flow was equal to (0.165) (%N) $\pm$2 gallons per minute at 2940 psig. The maximum supply pressure did not exceed 3450 psig under any conditions.
3. Under conditions where the pump flow limited over-all control system response, the system delivered available pump flow minus 0.4 gpm to the actuators, in the appropriate direction.

*Monsanto Chemical Company designation.

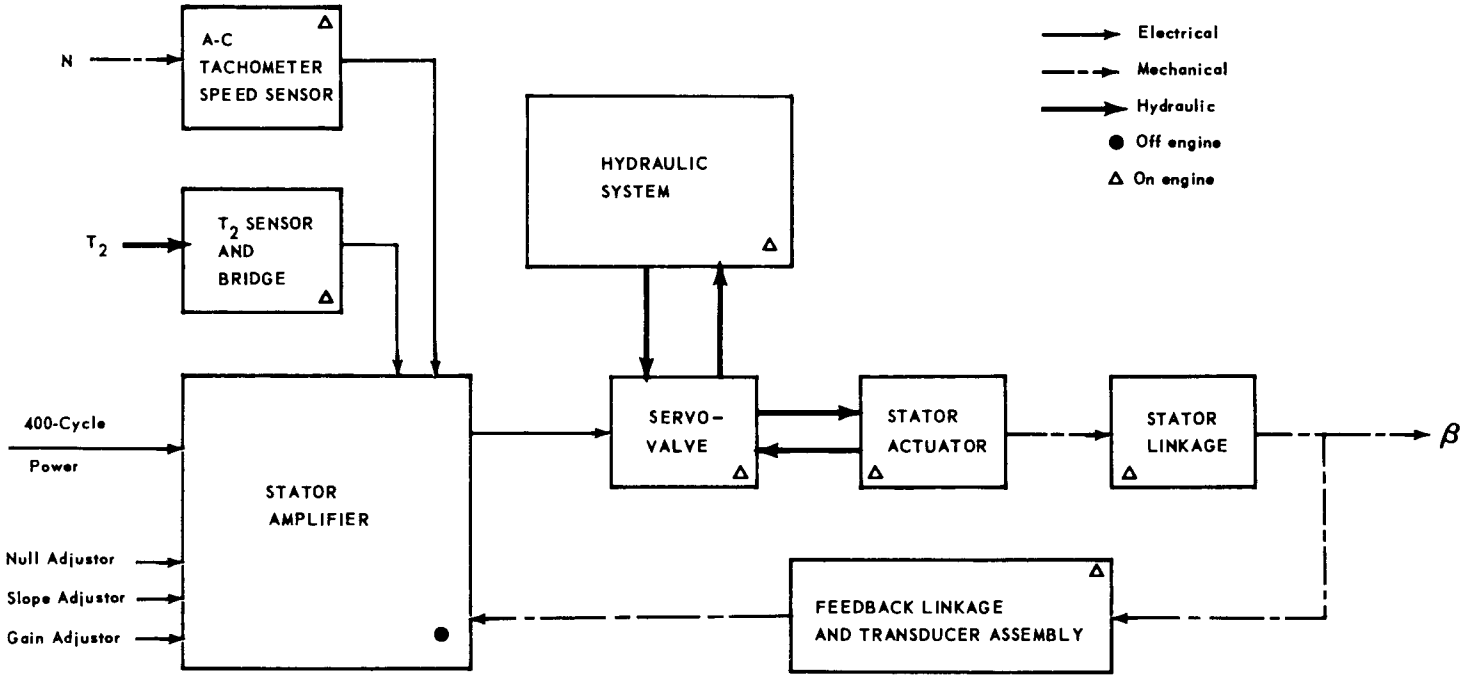

Fig. 7.7 – Compressor stator position control subsystem, XNJ140E-1

4. The return pressure to the reservoir did not exceed 300 psig.
5. The fluid temperature could vary from -65° to 400°F.

This system is shown in Figure 7.8. It furnished hydraulic fluid to the actuators of the variable compressor stator vanes, the jet nozzle, and the bleed-speed valves. Two independent subsystems were provided. One subsystem was provided for the jet nozzle actuators and included (1) a nozzle pump mounted on, and driven from, the rear gearbox and (2) a hydraulic reservoir, heat exchanger, and filter which were mounted on the accessory tray. The second subsystem was used by both the variable stator and the bleed-speed systems, and contained two constant-pressure pumps connected in parallel. These pumps were mounted on, and driven from, the rear gearbox. The associated hydraulic fluid reservoir, heat exchanger, and filters were mounted on the accessory tray.

7.3.6 MANUAL FUEL CONTROL SUBSYSTEM

The facility fuel storage system supplied fuel to the engine combustors by means of the manual fuel control system. This system, shown in Figure 7.9, incorporated spill-type fuel nozzles and a gear-type fuel pump that was engine driven and had an electrically operated clutch in the input drive. Fuel from the pump was filtered and entered the main fuel valve. Fuel flow was controlled by the area of a metering orifice in this valve. The flow area was controlled by a position-servo consisting of a position demand transducer, a main fuel error amplifier, a servo motor, and a position transducer. A pressurization valve, in conjunction with the main fuel regulator, insured a constant pressure drop across the fuel-metering orifice, thus making fuel flow proportional to orifice area. A recirculating spill pump in the metered-flow loop provided the energy necessary to operate the spill nozzles, and, at low metered fuel flows, the spill flow was recirculated by the pump. The system contained an overspeed governor that bypassed fuel from the pressurization valve back to the main fuel pump in the event of engine overspeed during chemical operation. When the engine speed exceeded 101.5 percent N, fuel flow was automatically cut back by a governor, and reduced in a manner that held engine speed at 101.5 percent N.

7.3.7 NOZZLE BOUND CONTROL SUBSYSTEM

This system reduced the amount of bleed-speed air required to limit engine overspeed if the nozzle area control failed. The bound mechanism mechanically limited the area of the jet nozzle to a value less than full open, i.e., 1400 square inches. Nozzle bounding was initiated from a push button mounted on the operator's console, and resulted only if the nozzle was within the bound limits. If it were beyond the limits, no bounding occurred until the nozzle area decreased to a value of less than 1400 square inches. The bound could be released at any time during engine operation if the nozzle failed against the bound limits.

7.3.8 THRUST SELECTOR SUBSYSTEM

The thrust selector was a mechanical subsystem mounted on the operator's console. It programmed a combination of input demands to the turbomachinery control system through three 2-dimensional cams mounted on a common shaft and positioned by the throttle. The position of the throttle determined the orientation of the cams, thereby directly programming the demands controlling operation of the engine.

The throttle was mounted on the input shaft in a manner that assured no slippage between the throttle position and the orientation of the cams. The shaft also carried a pointer indicating by angular rotation, the throttle setting by means of a protractor mounted on the case. An adjustable mechanical stop was provided to allow positive stopping as desired anywhere between 105 degrees and 120 degrees travel. The range and band width of the control modulated thrust from zero to maximum utilizing 120-degree travel. Dwell bands were as follows: Maximum, 117 to 120 degrees; Military, 107 to 110 degrees; Idle, 7 to 10 degrees; Off, below 4 degrees.

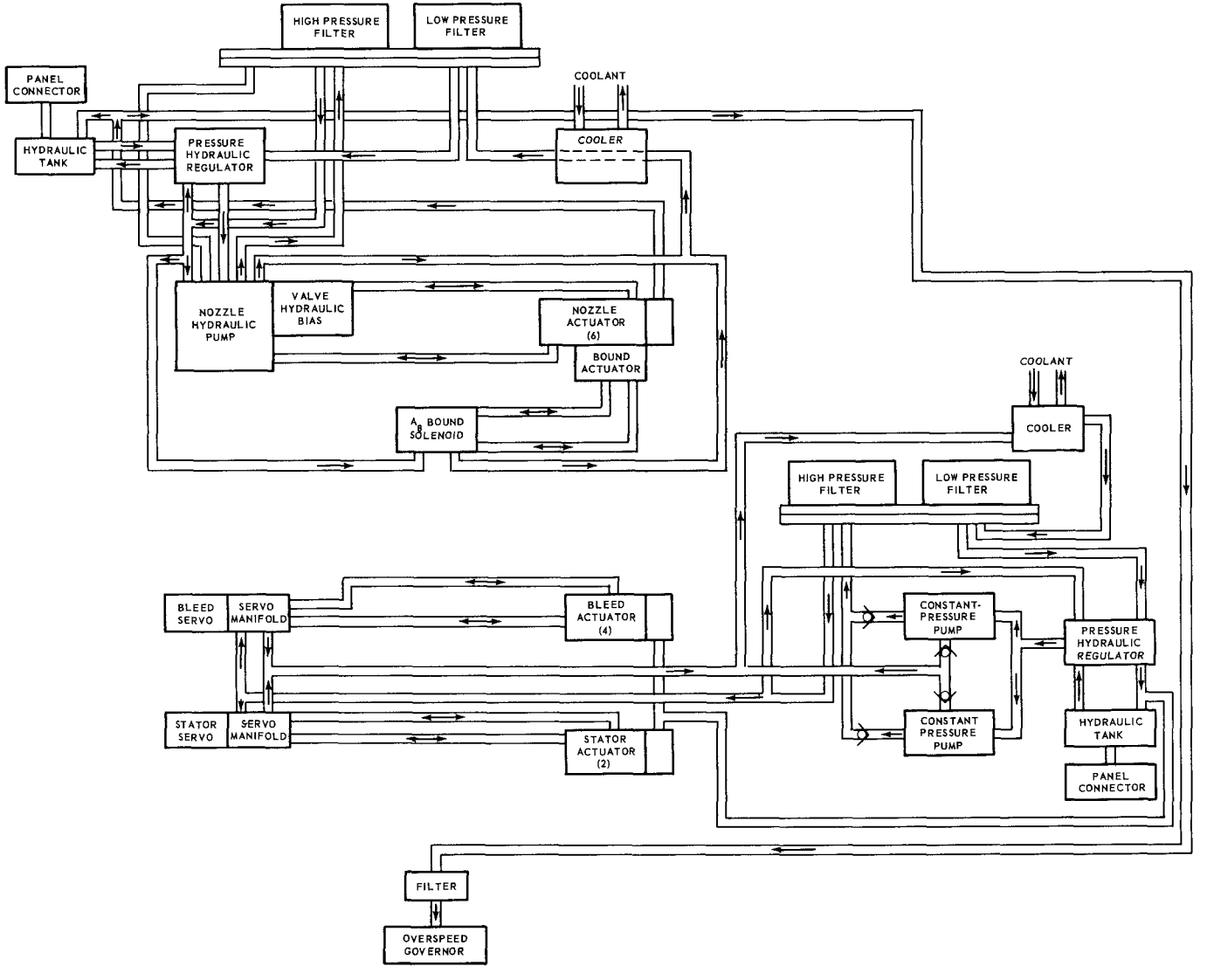

Fig. 7.8 – Hydraulic fluid supply subsystem, XNJ140E-1

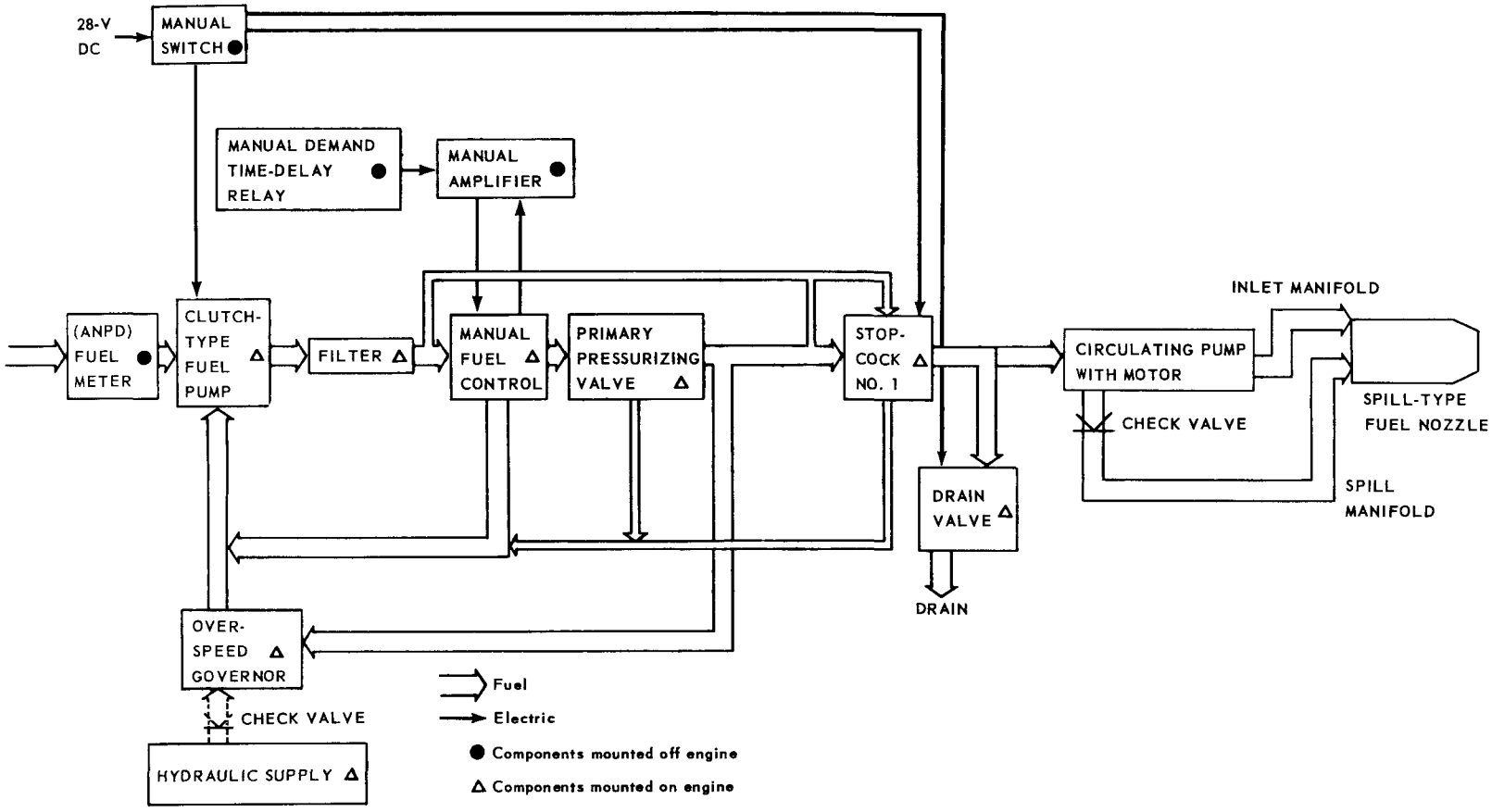

Fig. 7.9 – Manual fuel control subsystem, XNJ140E-1

The three 2-dimensional cams governed the demands to the engine speed control subsystem, the turbine discharge-air temperature loop, and the bleed-speed valve area loop. Individual biases, adjustable from the control console, were incorporated into the engine speed, turbine discharge-air temperature, and bleed-speed-valve area demands. These biases trimmed engine performance during operation and aided in establishing proper steady-state demand schedules. They also allowed the operator to establish off-schedule operating modes required for engine and reactor testing; operator action ensured that any individual bias was not adjusted beyond the limits of safe operation.

7.3.9 MECHANIZATION

7.3.9.1 Engine Speed Control Subsystem

Speed Sensors - Each of the two speed sensors used in this subsystem was an alternator gear-driven from the engine. The frequency of the a-c output was directly proportional to engine speed. A useful signal was produced from 20 to 120 percent speed, and from a speed rate of change from 0 to 1250 rpm per second. The error, when combined with the frequency converter, was ± 0.1 percent at 100 percent rpm and less than ± 0.2 percent at idle speed.

Linear Transducers - The nozzle area (A_8) feedback mechanism mechanically reduced the approximately 7-inch-long actuator stroke to a 0.5-inch cam movement. Feedback to the control loop was provided by a transducer driven by this cam. Four feedback transducers were used in the nozzle reset control loop, and two linear transducers were used in the nozzle area demand loop. These transducers were linear differential transformers.

Nozzle Bound Solenoid and Linkage - The nozzle was bounded by a device that mechanically limited the travel of the nozzle flap actuators. The nozzle bound was released as a function of throttle position by camming a multi-parallel-series switch that sent an electrical signal to a solenoid valve. The valve furnished hydraulic pressure to release the bound. An interlocking signal guaranteed that the afterburner (if used) could not be started if the bound failed to release. The bound limited nozzle travel during loss of either electrical or hydraulic power, and held if 50 percent of the actuator bounds were engaged.

Bleed-Speed Valve Actuators - The bleed-speed valve actuators were flange-mounted and fitted into the body of the bleed-speed valves. The actuator was operated by the 3000-psi constant-pressure hydraulic system in a closed loop servo system. A differential screw reduction mechanism was mounted within the actuator and drove a linear-position transducer mounted on the actuator.

Nozzle Actuators - The jet nozzle area (A_8) was controlled by six synchronized linear hydraulic actuators. The actuators exerted an output force of 9200 pounds for a 2700-psi pressure differential and had a stroke of 8.1 inches. A stroke limiter was provided with each actuator.

7.3.9.2 Compressor Stator Position Control Subsystem

$T_{a2.0}$ Sensors - Two sensors were used, one of which acted as a spare. The sensors were resistance temperature detectors (RTD) located in a resistance bridge network, and were accurate over a temperature range of -65° to $+205^{\circ}$F. Steady-state accuracy was maintained when (1) the rate of change of $T_{a2.0}$ was less than 0.05 degree per second, and (2) the airflow was 7 pounds per square foot of inlet annulus per second or greater.

Position Feedback Mechanism - The position feedback mechanism consisted of a stator vane keyed to a cam which displaced a linear transducer. The nonlinearities of the stator schedule were cut into the cam contour.

Stator Actuators - The variable stators were positioned by two linear, hydraulic actuators. The actuators had a 6.5-inch stroke, and a 2500-pound tension force was produced by the 2000-psi pressure differential across the actuator piston. A two-stage seal in the actuator contained an interstage drain into the hydraulic system tank.

7.3.9.3 Hydraulic Fluid Supply Subsystem

Hydraulic fluid for the bleed-speed valve and compressor stator actuators was supplied by two pumps mounted on the rear gearbox and connected in parallel. They were constant pressure, variable displacement piston pumps delivering 15 gallons per minute at 3000 psi, a pump speed of 5000 rpm, and 400°F fluid temperature.

Hydraulic power for nozzle actuation was provided by a variable-pressure, variable-flow piston pump. This pump was servo controlled; its maximum capacity was 26 gallons per minute at 4000 rpm and 400°F fluid temperature. It was mounted on the rear gearbox near the other hydraulic fluid pumps.

7.3.9.4 Manual Fuel Control Subsystem

Fuel Pump - The facility fuel circulating system supplied fuel directly to a flowmeter and the inlet of this pump. It was an engine-driven, positive-displacement pump delivering at least 45,000 pounds per hour at 1000 psig and 5000 rpm, at a vapor-liquid ratio of 0.1. The fuel required during engine starting was at least 4000 pounds per hour at 150 psig and 800 rpm. A clutch was used to declutch the pump when the system was not in use. The maximum steady-state discharge pressure was limited to 1100 psig above supply-pump pressure by a bypassing relief valve located in the pump.

Fuel Control Valve - This valve scheduled fuel flow as a linear function of an input demand varying from 0 to 140 milliamperes. The valve was a two-stage, 3000-psi, 80-gpm hydraulic servo valve.

Afterburner Fuel Pump - This pump was an engine-driven centrifugal pump capable of delivering 100,000 pounds per hour at 800 psig and 5000-rpm engine speed. The pump contained a clutch that was disengaged when the system was not in use.

Ignition System - This system was capable of providing consistent starts of a cold engine on the ground as well as restarts of a hot or cold engine at altitude. It remained functional after long exposures to reactor discharge-air temperature. It was comprised of a hydrogen storage tank and pressure regulator, igniter exciter box, and a hydrogen torch incorporating an igniter and flow regulator. The pressure drop through the reactor provided the pressure differential for the combustible mixture: the combustion end of the torch was located in the combustion chamber and a variable slot in the stem was located in the cooling-air passage. This passage was connected to the compressor discharge-air. Hydrogen flow was constant and provided a constant energy source.

7.4 REACTOR CONTROL SYSTEM

7.4.1 DESCRIPTION

This system performed the following functions:

1. Provided a means of automatic reactor startup from subcritical to 1.5 percent of full power
2. Provided power regulation and holding from 10^{-8} to 1.5 percent full power
3. Provided reliable control of turbine exit-air temperature within ± 20° from 600° to 1200°F

4. Provided acceleration from idle to military thrust in not more than 60 seconds
5. Provided either automatic or manual control of reactor power level from 1.5 to 125 percent full power.

The primary engine parameter controlled by the system was the turbine exit-air temperature, $T_{5.1}$. A closed logarithmic flux loop and eight parallel closed control rod position loops were supplemented by a temperature control loop. In addition to the temperature control loop, an automatic startup control loop was available, capable of performing a period-controlled reactor startup. Low-level power-holding capability was obtained by inserting a micromicroammeter in the feedback circuit of the flux portion of the temperature control loop.

The system was broadly divided into the reactor startup subsystem, the power-range flux and temperature control subsystem, and the control rod actuation subsystem. The power-range subsystem contained a minor loop that permitted manual control of the reactor power level. Safety circuitry is treated as a separate subsystem, and is discussed in section 7.5.

A single-line block diagram of the power-range control, startup control, and safety circuitry is shown in Figures 7.10a, 7.10b, 7.10c, and 7.10d. Functional code letters for Figure 7.10 are given in Figure 7.11.

Detailed system design and analysis information is contained in references 6, 7, and 8. Requirements for control system mechanization are given in reference 9, and the results of an extensive component evaluation program are contained in references 10 and 11.

7.4.2 REACTOR STARTUP SUBSYSTEM

7.4.2.1 Description

This subsystem contained a period-regulating servo loop which performed an automatic reactor startup. Staggered range fission chambers were used as neutron sensors and provided approximately nine decades of controlled power. The reactor period was computed from a fission chamber feedback signal and compared with a period-demand signal. The error was used as the demand signal to the control rod actuation subsystem for control rod actuation as required to obtain the demanded reactor period. The actual reactor period was within +1 percent and -6 percent of the demanded reactor period.

The neutron flux increased on a selected period to 1.5 percent full power. At this power level, the power-range control subsystem assumed control.

Three primary detector loops were used, each loop containing three fission counters and a power-range ionization chamber. The three fission counters in each loop varied in range and location to produce continuous detection over a ten-decade change in thermal neutron density. Associated with each counter was the electronic circuitry needed to compute log count rate and period. The log count rate was a measure of the reactor power level, and the period was a measure of rate-of-change in power level. A reference demand was compared with the computed period signal and the error was used to position the control rods to obtain the desired period. The circuitry is shown schematically in Figure 7.12.

Each instrumentation loop consisted of three channels; the differences were determined by the sensitivity of the sensors. Each channel covered a four-decade range and, by operating each channel in a sequence of increasing counting rate and allowing for overlap, a span of ten decades was covered by each loop, as shown in Figure 7.13. Counting rate of each channel was computed, displayed, and utilized in a logic circuit. The logic circuit selected the computed period from the channel operating over the pertinent linear range for use by

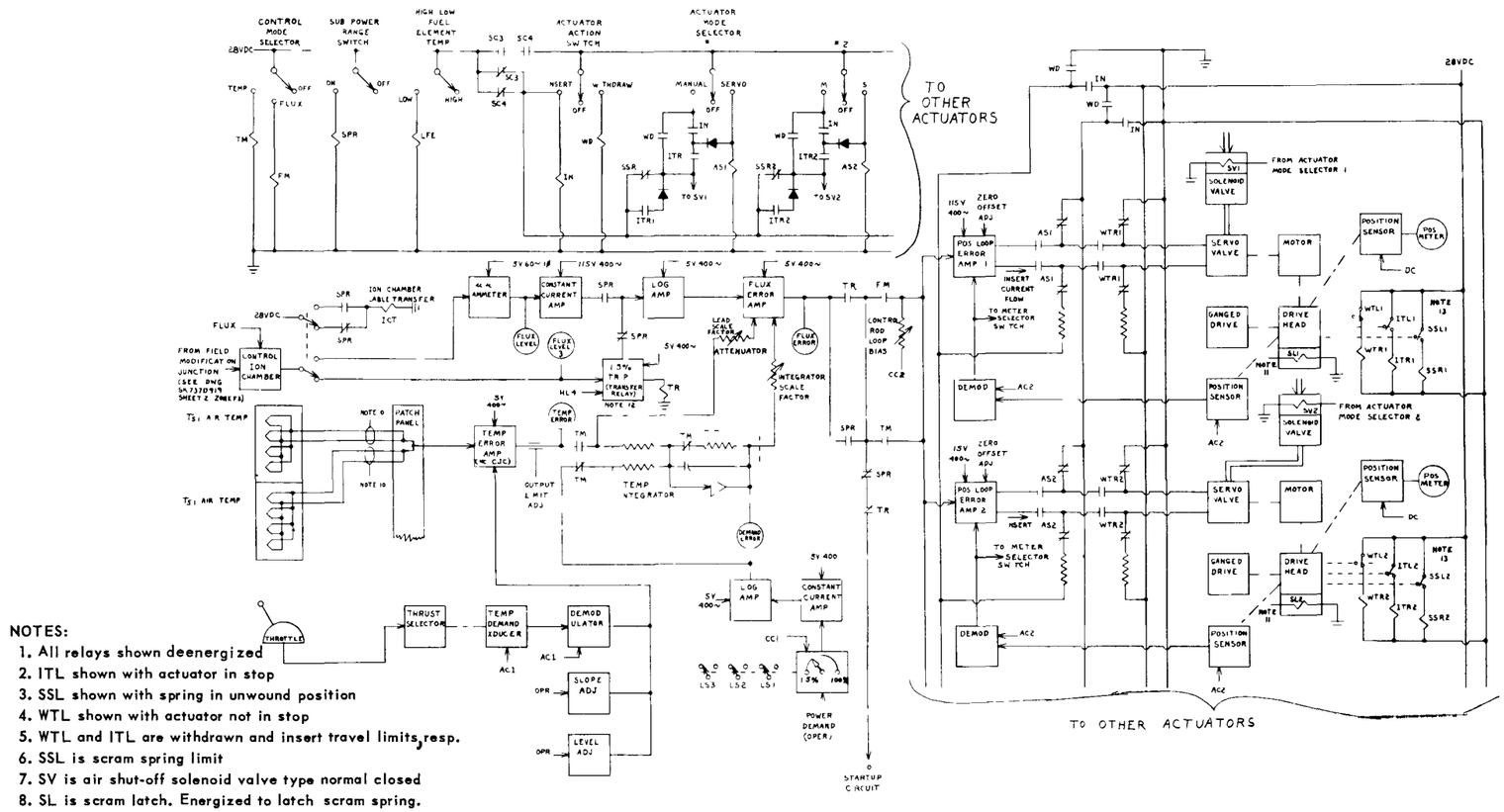

NOTES:

1. All relays shown deenergized
2. ITL shown with actuator in stop
3. SSL shown with spring in unwound position
4. WTL shown with actuator not in stop
5. WTL and ITL are withdrawn and insert travel limits, resp.
6. SSL is scram spring limit
7. SV is air shut-off solenoid valve type normal closed
8. SL is scram latch. Energized to latch scram spring.
9. Each ITR, WTR and SSR operates a console light
10. 4 parallel thermocouples (paralleled in test cell)
11. See SK682E862, Sheet 2, Zone B13
12. TR relay energized for $\phi \geq$ 1.5% full power
13. Located in the secondary rack
14. For functional code letters, see Figure 7.11

Fig. 7.10a – Reactor control system (Dwg. SK737D919, Sh. 1)

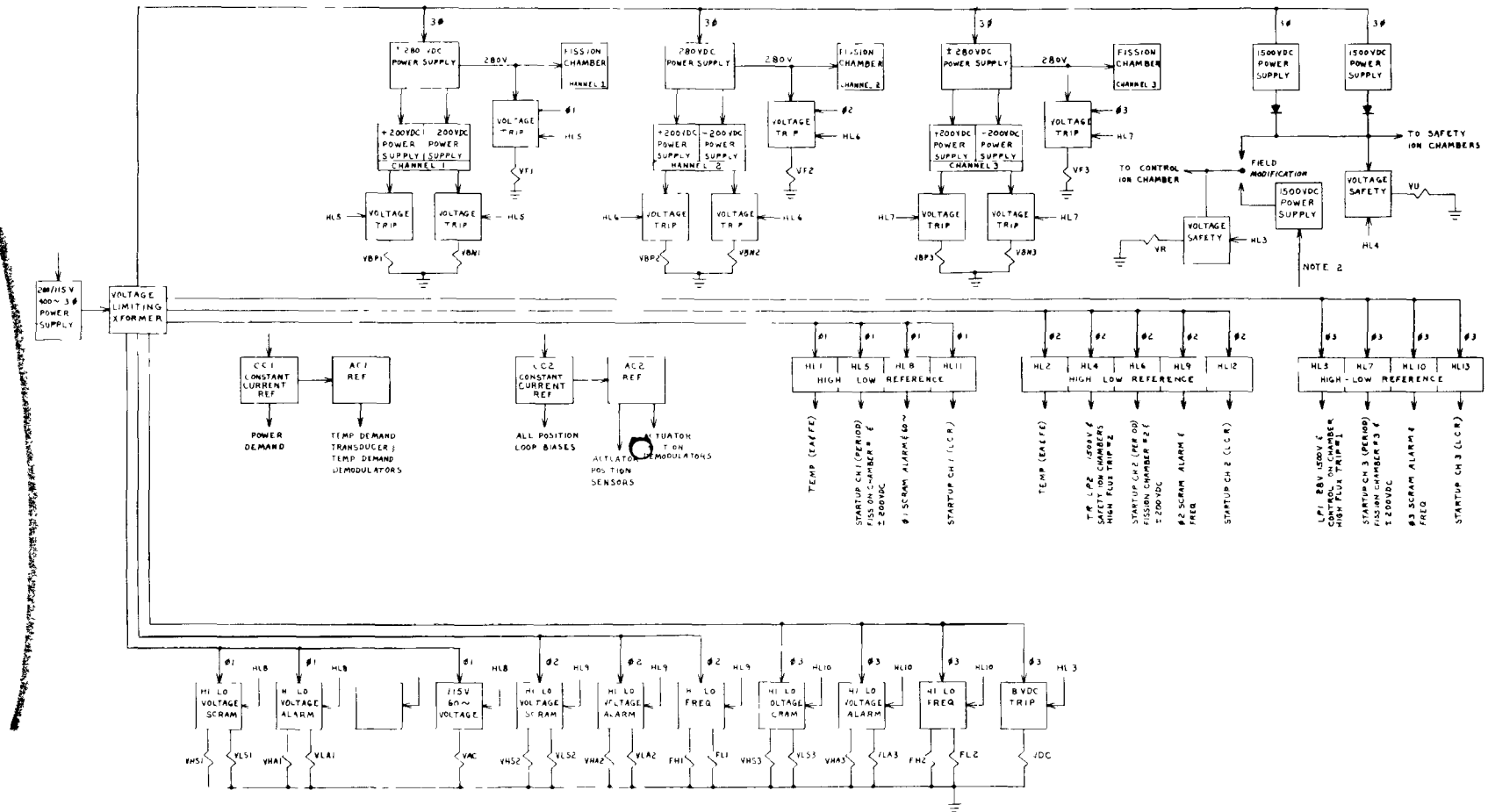

NOTE:
$\phi 1$ is 115V, 400~, first phase
$\phi 2$ is 115V, 400~, second phase
$\phi 3$ is 115V, 400~, third phase

Fig. 7.10b – Reactor control system (Dwg. SK737D919, Sh. 2)

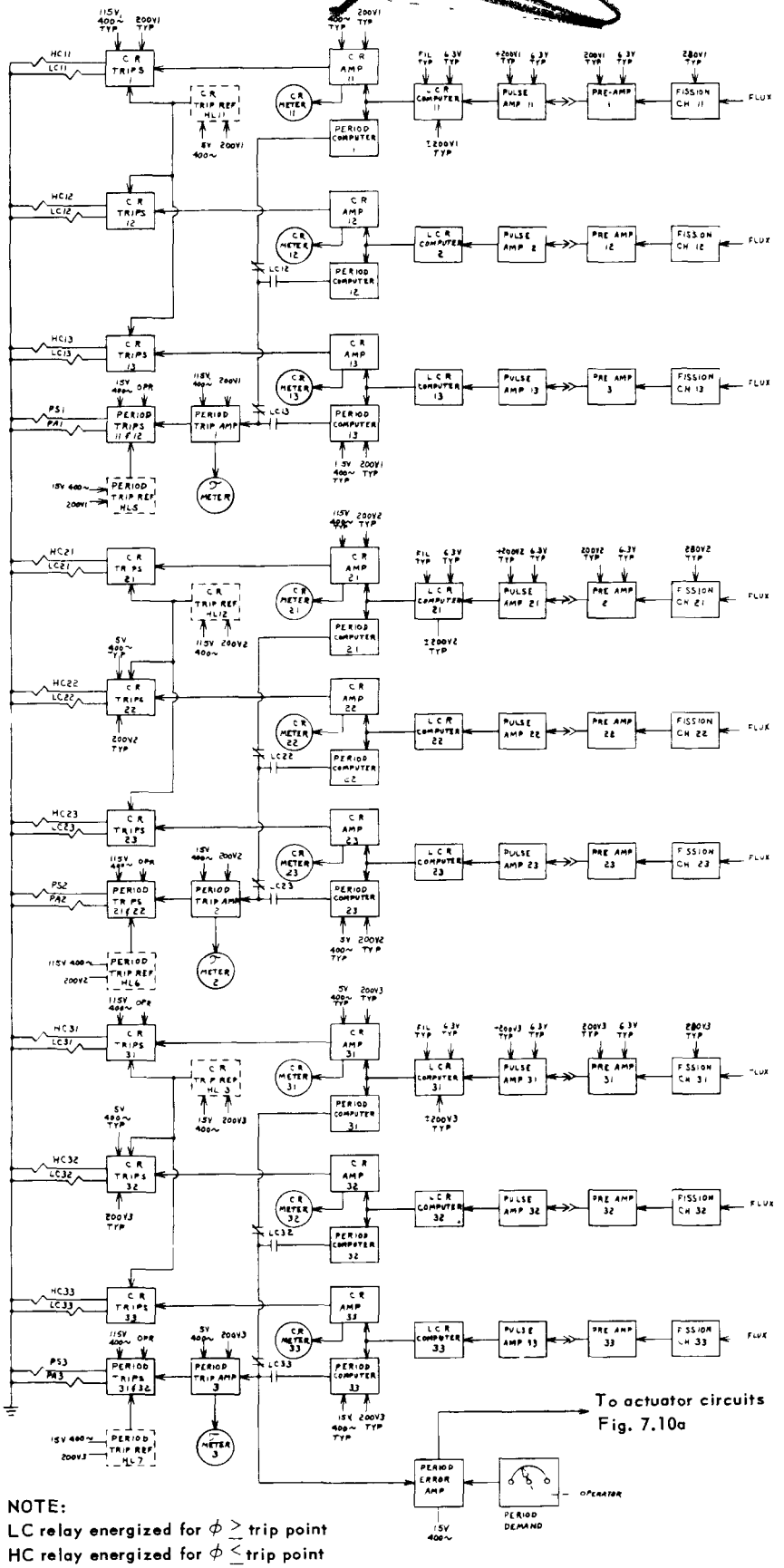

Fig. 7.10c – Reactor control system (Dwg. SK737D919, Sh. 3)

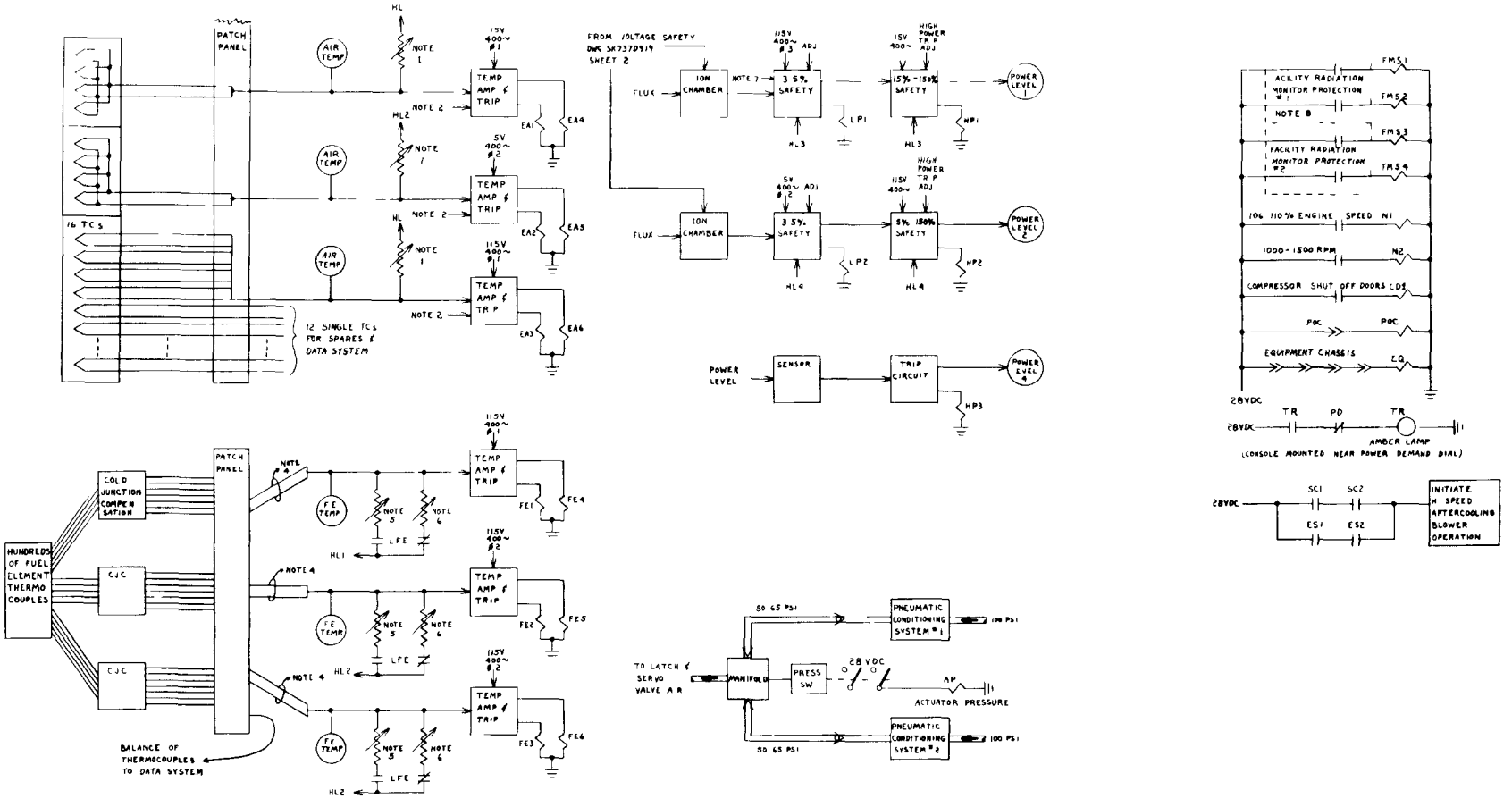

Notes:

1. Trip adj. 700° – 1500° F
2. Includes cold junction compensation
3. Four parallel thermocouples (paralleled in test cell)
4. Five hottest thermocouples
5. Fixed trip 700° F
6. Trip adj. 700° – 2800° F
7. L.P. relay energized for $\phi \leq 3.5\%$
8. Facility monitors provided by FET

Fig. 7.10d – Reactor control system (Dwg. SK737D919, Sh. 4)

FUNCTION CODE	DESCRIPTION
AC1	AC REFERENCE NO. 1
AC2	AC REFERENCE NO. 2
ACB	AFTERCOOLING BLOWER
AP	ACTUATOR PRESSURE
AR	ANNUNCIATOR RESET – INDICATION
AS1	ACTUATOR NO. 1 SERVO
THRU	THRU
AS8	ACTUATOR NO. 8 SERVO
BV	BLEED VALVE CONTROL
CC1	CONSTANT CURRENT NO. 1 – 115 V, 400 CPS
CC2	CONSTANT CURRENT NO. 2 – 115 V, 400 CPS
CD	COMPRESSOR SHUT-OFF DOORS
CJC	COLD JUNCTION COMPENSATION
CR	COUNT RATE
EA	AIR TEMPERATURE
EI	SHUTDOWN INDICATOR LITE RESET RELAY
EQ	EQUIPMENT CONTINUITY
FC	FUEL CONTROL
FE	FUEL ELEMENT
FH	FREQUENCY SAFETY – 400 CPS – HIGH
FL	FREQUENCY SAFETY – 400 CPS – LOW
FM	FLUX MODE
FMS	FACILITY MONITOR SAFETY
FPC	FUEL PUMP CLUTCH
FS	FUEL STOPCOCK
HC11	HIGH COUNT RATE, SUBSYSTEM 1, CHANNEL 1
HC12	HIGH COUNT RATE, SUBSYSTEM 1, CHANNEL 2
HC13	HIGH COUNT RATE, SUBSYSTEM 1, CHANNEL 3
HC21	HIGH COUNT RATE, SUBSYSTEM 2, CHANNEL 1
HC22	HIGH COUNT RATE, SUBSYSTEM 2, CHANNEL 2
HC23	HIGH COUNT RATE, SUBSYSTEM 2, CHANNEL 3
HC31	HIGH COUNT RATE, SUBSYSTEM 3, CHANNEL 1
HC32	HIGH COUNT RATE, SUBSYSTEM 3, CHANNEL 2
HC33	HIGH COUNT RATE, SUBSYSTEM 3, CHANNEL 3
HL	HIGH-LOW REFERENCE
HP1	HIGH POWER 1
HP2	HIGH POWER 2
HP3	HIGH POWER 3
ICT	ION CHAMBER CABLE TRANSFER
IN	INSERT

FUNCTION CODE	DESCRIPTION
ITL1	INSERT TRAVEL LIMIT 1
THRU	THRU
ITL8	INSERT TRAVEL LIMIT 8
ITR1	INSERT TRAVEL LIMIT RELAY 1
THRU	THRU
ITR8	INSERT TRAVEL LIMIT RELAY 8
LC11	LOW COUNT RATE, SUBSYSTEM 1, CHANNEL 1
LC12	LOW COUNT RATE, SUBSYSTEM 1, CHANNEL 2
LC13	LOW COUNT RATE, SUBSYSTEM 1, CHANNEL 3
LC21	LOW COUNT RATE, SUBSYSTEM 2, CHANNEL 1
LC22	LOW COUNT RATE, SUBSYSTEM 2, CHANNEL 2
LC23	LOW COUNT RATE, SUBSYSTEM 2, CHANNEL 3
LC31	LOW COUNT RATE, SUBSYSTEM 3, CHANNEL 1
LC32	LOW COUNT RATE, SUBSYSTEM 3, CHANNEL 2
LC33	LOW COUNT RATE, SUBSYSTEM 3, CHANNEL 3
LCR	LOW COUNT RATE
LFE	LOW FUEL ELEMENT TEMPERATURE
LP1	LOW POWER RELAY NO. 1
LP2	LOW POWER RELAY NO. 2
N1	ENGINE SPEED 106–110 PERCENT
N2	ENGINE SPEED 1000 RPM
N3	ENGINE SPEED 1500 RPM
N4	ENGINE SPEED 500 RPM
PA1	PERIOD ALARM, SUBSYSTEM 1
PA2	PERIOD ALARM, SUBSYSTEM 2
PA3	PERIOD ALARM, SUBSYSTEM 3
PD	POWER DEMAND
POC	PRE-OPERATIONAL CHECKER
PS1	PERIOD SCRAM, SUBSYSTEM 1
PS2	PERIOD SCRAM, SUBSYSTEM 2
PS3	PERIOD SCRAM, SUBSYSTEM 3
SA	STARTER AIR SUPPLY
SC	SCRAM RELAY
SD	SHUT DOWN
SI	SCRAM INDICATOR LITE RESET RELAY
SL1	SCRAM LATCH NO. 1
THRU	THRU
SL8	SCRAM LATCH NO. 8
SM	SWITCHING MONITOR
SSR1	SCRAM SPRING RELAY NO. 1

FUNCTION CODE	DESCRIPTION
THRU	THRU
SSR8	SCRAM SPRING RELAY NO. 8
SV1	SOLENOID VALVE NO. 1
THRU	THRU
SV8	SOLENOID VALVE NO. 8
SPR	SUB POWER RANGE
TL	ANNUNCIATOR TEST
TR	TRANSFER RELAY
TM	TEMPERATURE MODE
VAC	VOLTAGE, 115 VAC, 60 CPS – LOW SCRAM
VBN1	VOLTAGE, B NEGATIVE, SUBSYSTEM 1 – LOW SCRAM
VBN2	VOLTAGE, B NEGATIVE, SUBSYSTEM 2 – LOW SCRAM
VBN3	VOLTAGE, B NEGATIVE, SUBSYSTEM 3 – LOW SCRAM
VBP1	VOLTAGE, B POSITIVE, SUBSYSTEM 1 – LOW SCRAM
VBP2	VOLTAGE, B POSITIVE, SUBSYSTEM 2 – LOW SCRAM
VBP3	VOLTAGE, B POSITIVE, SUBSYSTEM 3 – LOW SCRAM
VDC	VOLTAGE, 28 VDC, LOW SCRAM
VF1	VOLTAGE, FISSION CHAMBER, SUBSYSTEM 1, LOW SCRAM
VF2	VOLTAGE, FISSION CHAMBER, SUBSYSTEM 2, LOW SCRAM
VF3	VOLTAGE, FISSION CHAMBER, SUBSYSTEM 3, LOW SCRAM
VHA1	VOLTAGE, 115 VAC, 400 CPS, PHASE 1, HIGH ALARM
VHA2	VOLTAGE, 115 VAC, 400 CPS, PHASE 2, HIGH ALARM
VHA3	VOLTAGE, 115 VAC, 400 CPS, PHASE 3, HIGH ALARM
VHS1	VOLTAGE, 115 VAC, 400 CPS, PHASE 1, HIGH SCRAM
VHS2	VOLTAGE, 115 VAC, 400 CPS, PHASE 2, HIGH SCRAM
VHS3	VOLTAGE, 115 VAC, 400 CPS, PHASE 3, HIGH SCRAM
VLA1	VOLTAGE, 115 VAC, 400 CPS, PHASE 1, LOW ALARM
VLA2	VOLTAGE, 115 VAC, 400 CPS, PHASE 2, LOW ALARM
VLA3	VOLTAGE, 115 VAC, 400 CPS, PHASE 3, LOW ALARM
VLS1	VOLTAGE, 115 VAC, 400 CPS, PHASE 1, LOW SCRAM
VLS2	VOLTAGE, 115 VAC, 400 CPS, PHASE 2, LOW SCRAM
VLS3	VOLTAGE, 115 VAC, 400 CPS, PHASE 3, LOW SCRAM
VR	VOLTAGE, 1500 VDC, REG. – LOW SCRAM
VU	VOLTAGE, 1500 VDC, UNREG. – LOW SCRAM
WD	WITHDRAW
WTL1	WITHDRAW TRAVEL LIMIT NO. 1
THRU	THRU
WTL8	WITHDRAW TRAVEL LIMIT NO. 8
WTR1	WITHDRAW TRAVEL LIMIT RELAY NO. 1
THRU	THRU
WTR8	WITHDRAW TRAVEL LIMIT RELAY NO. 8

Fig. 7.11 – Functional code letters used in Figure 7.10

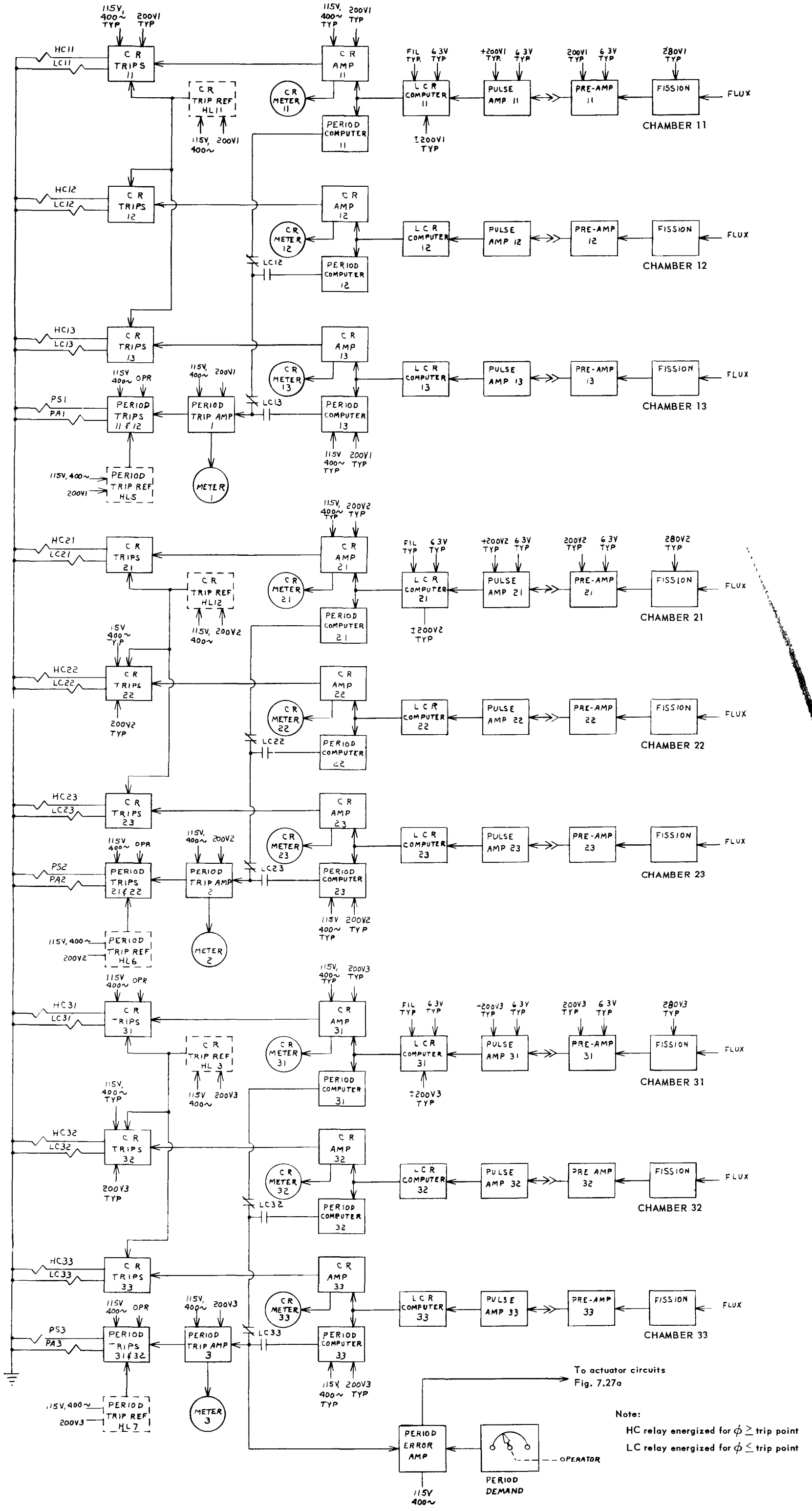

Fig. 7.12—Reactor startup subsystem, showing three loops of instrumentation (Dwg. SK737D919, Sh. 3)

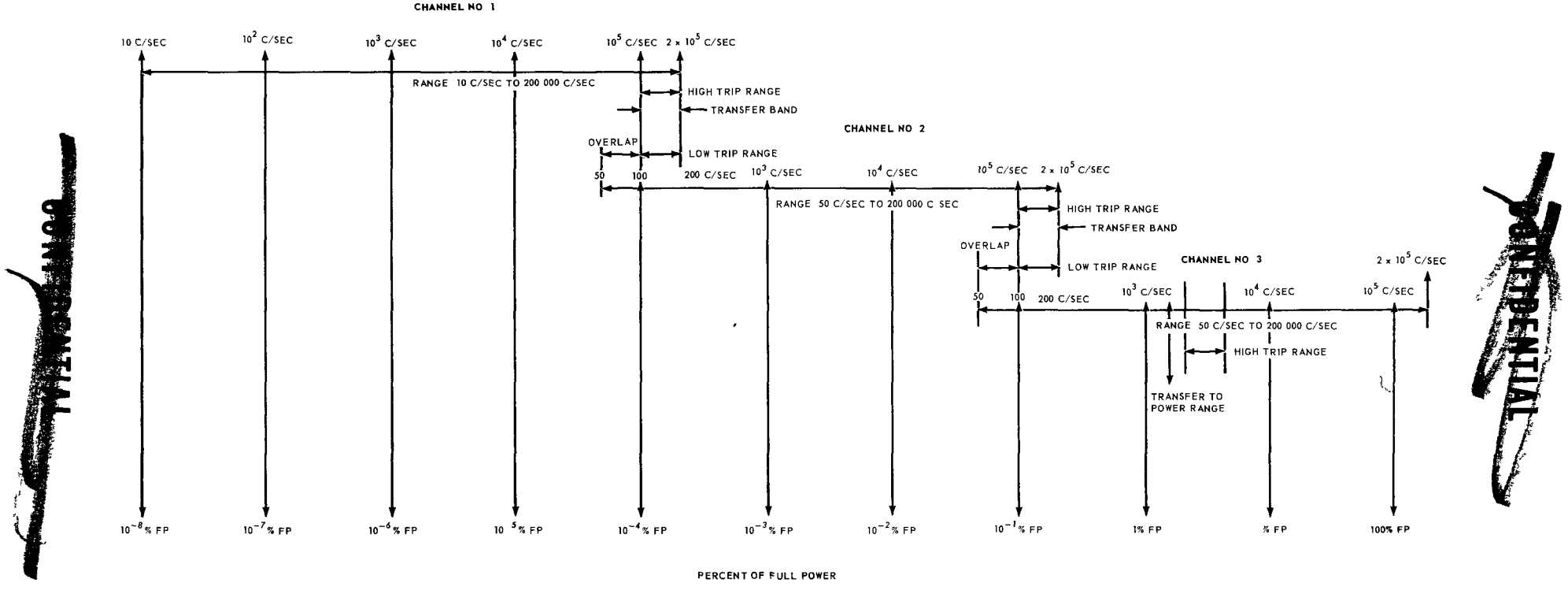

Fig. 7.13 – Typical instrumentation loop in the reactor startup subsystem

the period control servo and the safety system. A minimum output of 10 counts per second in the most sensitive channel of each subsystem was required to clear the scram bus prior to operation. A counting rate output on channel No. 1 in excess of its high-count trip (1. 8 x 10^5 counts per second) caused reactor scram if the channel No. 2 low-count trip (150 counts per second) had not functioned. Similarly, an excessive counting rate on channel No. 2 caused scram if the low-count trip of channel No. 3 had not functioned. The high-count trip on channel No. 3 (3 x 10^3 counts per second) initiated scram if the two-megawatt transfer relay had not functioned to transfer control to the power range system. The two-megawatt transfer relay normally was energized at a counting rate of 1. 5 x 10^3 counts per second, equivalent to 1. 5 percent of full power.

The method described above provided continuous log count rate and period information throughout the ten-decade operating range. Period output from one instrument system was compared with a reference period and the error was used to position the control rods, reducing the period error to zero while driving the actual reactor period to correspond with the reference period.

The subsystem provided reactor period indication to the operator, and could be used for operator surveillance during a manual reactor startup. The switching monitor between sensors insured safe, positive signal switching between channels within instrumentation loops. The range of startup instrumentation completely overlapped the power range, and transfer from startup to power-range control was accomplished automatically. Figure 7.14 shows the results of an analog simulator study of an automatically controlled reactor startup. The period demand was set at 15 seconds, and the system was set to level the reactor power at 3 megawatts.

Logarithmic diagrams of relationship between the attenuation and phase angle of an open loop transfer function are called Bode diagrams. A straight line attenuation-frequency diagram of the reactor startup control subsystem is shown in Figure 7. 15. Two curves are used to show the effect of the variable time response of the logarithmic count rate circuit. The solid lines show the case in which variable time response has negligible effect upon the loop; this condition occurred at high counting rates. The dashed line includes the effect of time response at minimum count rate (100 counts per second). The attenuation curves were drawn in a normalized fashion with crossover points indicated for one-quarter, one-half, and full gain. The adverse effect of time response at the low counting rates is shown, as well as the need for a small lead time-constant at the higher gains. The gains shown in Figure 7. 15 were based on period accuracy depending upon the relative position of the rods and the electrical neutral point. The full-gain case yielded a 10-percent period error for a demanded 30-second period when the relative position was at a maximu. The desired period could be obtained either by increasing the period demand potentiometer setting, or by changing the position of the electrical neutral point of the actuator loops by means of a bias potentiometer.

7. 4. 2. 2 Circuitry and Mechanization

The various components in this subsystem included the neutron source, fission counters, preamplifiers, pulse amplifiers, log count rate computers, count rate amplifiers, count rate trips, count rate meters, period computers, period meters, period trip amplifiers, period trips, period demand potentiometer, period error amplifier, trip references, power supplies, and low voltage trips. The period trip units are described in the section devoted to the safety system.

A functional schematic of the startup subsystem is shown in Figure 7. 16. This figure shows loop No. 3; loops No. 1 and No. 2 were almost identical, and are not shown separately. Three logarithmic channels were used per loop to compress approximately ten decades of

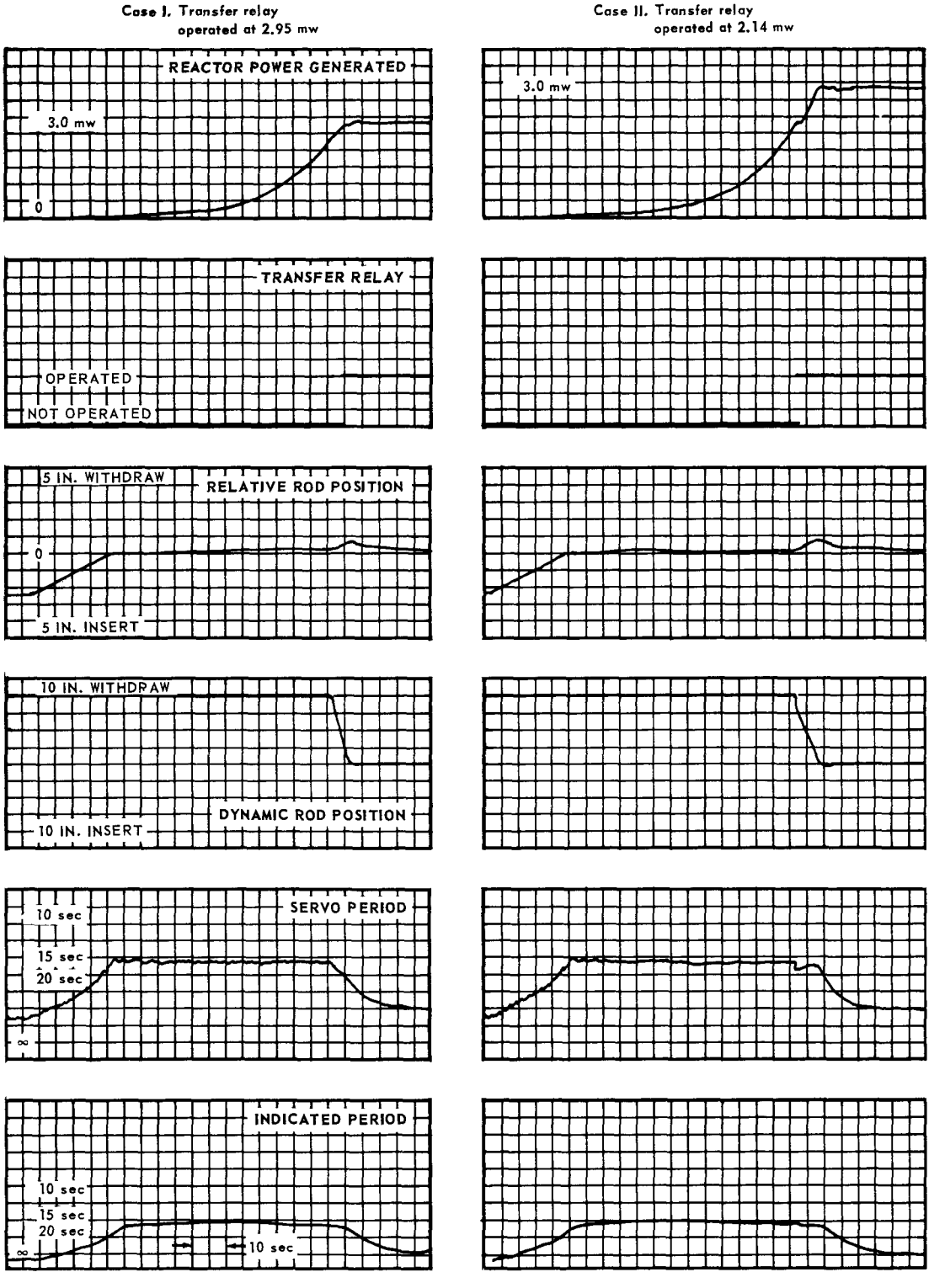

Fig. 7.14 – Analog simulator study of automatic reactor startup

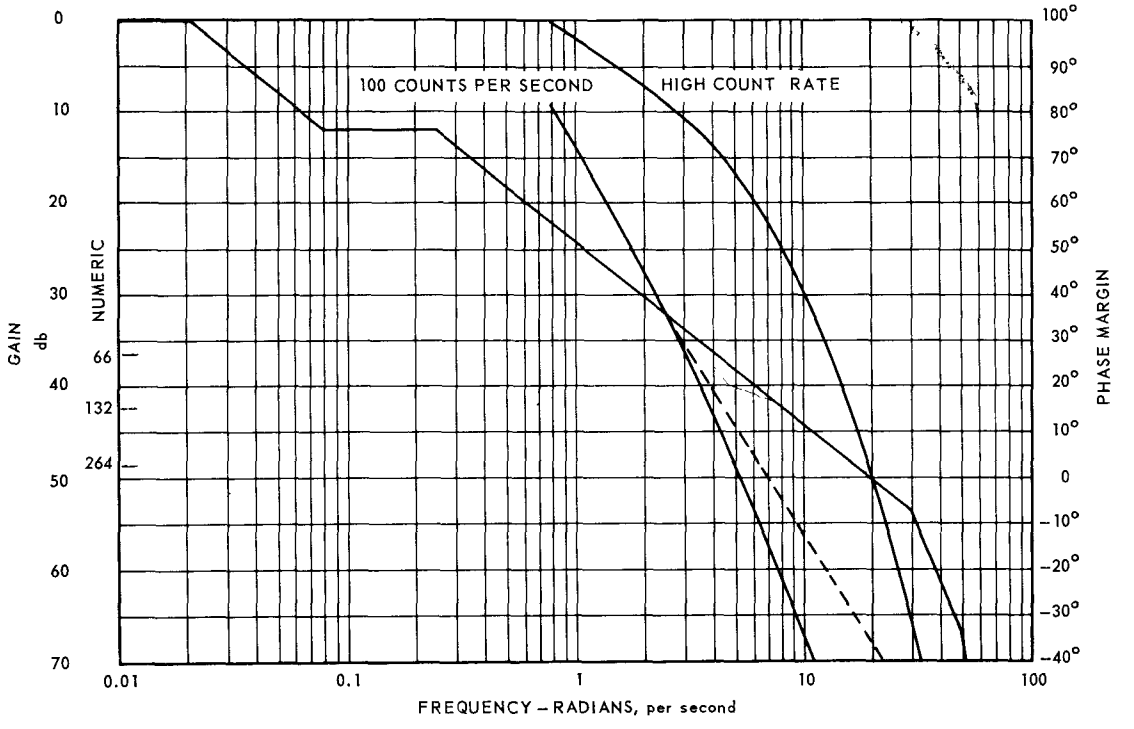

Fig. 7.15 – Bode plot of reactor startup instrumentation

reactor operation for display on three count rate meter scales. The nine nearly identical channels constituted the bulk of the startup equipment. Identical components per channel were: (1) pulse transmission cables, (2) pulse preamplifiers, (3) pulse amplifiers, (4) discriminator, (5) binary log pump circuit, (6) count rate computer, and (7) period computer. Three channels were used to permit smooth automatic control, to obviate the need for switching before the period computer, and to provide reliability. Switching before the period computer was an important consideration because this unit differentiated and amplified the input signal.

The sensitivity per channel was determined by the sensitivity of the fission counter, and a breakdown of the sensitivity for the three-channel tandem operation was shown in Figure 7. 13. The pulse preamplifier and pulse amplifier increased the signal voltage from 100 - 1,000 microvolts to 1 - 10 volts; a gain of 10, 000. The pulse amplifier was followed by a discriminator which electronically rejected all background below its adjustable setting. The larger pulses that passed through the discriminator were shaped and drove a binary flip-flop circuit. The binary output was fed into a passive network, called a pump circuit, that developed an output voltage proportional to the logarithm of the counting rate from the fission counter.

Special features of this equipment were:

1. The amplifiers were broadband in order to handle the 0. 2-microsecond pulse rise-time from the fission counter.
2. The pump circuit time constant varied inversely proportional to the counting rate. It had a 4-second RC time constant for ten counts per second, and 5×10^{-4} seconds for 2×10^{5} counts per second. The voltage sensitivity was 9 volts per decade change of counting rate.

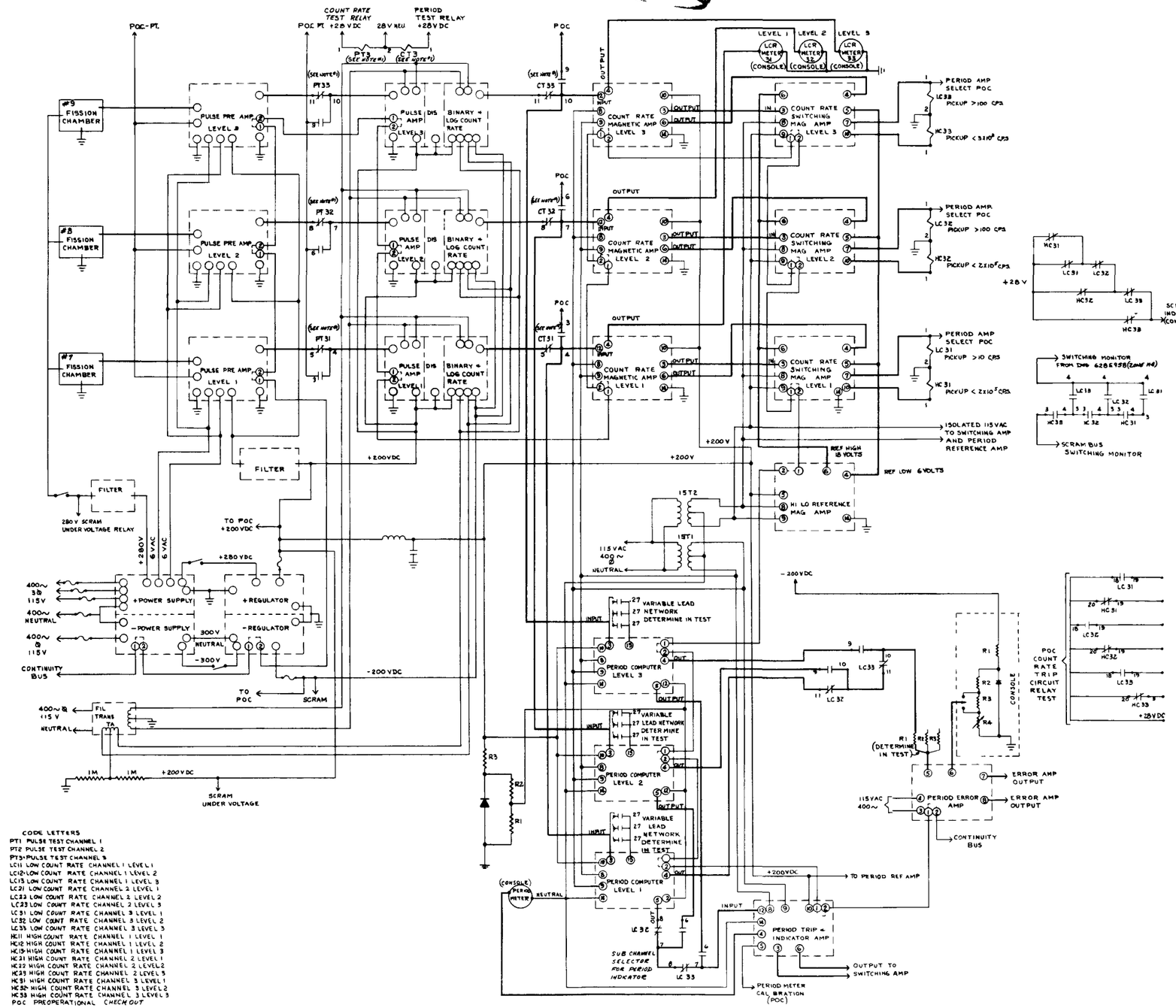

CODE LETTERS
PT1 PULSE TEST CHANNEL 1
PT2 PULSE TEST CHANNEL 2
PT3 PULSE TEST CHANNEL 3
LC11 LOW COUNT RATE CHANNEL 1 LEVEL 1
LC12 LOW COUNT RATE CHANNEL 1 LEVEL 2
LC13 LOW COUNT RATE CHANNEL 1 LEVEL 3
LC21 LOW COUNT RATE CHANNEL 2 LEVEL 1
LC22 LOW COUNT RATE CHANNEL 2 LEVEL 2
LC23 LOW COUNT RATE CHANNEL 2 LEVEL 3
LC31 LOW COUNT RATE CHANNEL 3 LEVEL 1
LC32 LOW COUNT RATE CHANNEL 3 LEVEL 2
LC33 LOW COUNT RATE CHANNEL 3 LEVEL 3
HC11 HIGH COUNT RATE CHANNEL 1 LEVEL 1
HC12 HIGH COUNT RATE CHANNEL 1 LEVEL 2
HC13 HIGH COUNT RATE CHANNEL 1 LEVEL 3
HC21 HIGH COUNT RATE CHANNEL 2 LEVEL 1
HC22 HIGH COUNT RATE CHANNEL 2 LEVEL 2
HC23 HIGH COUNT RATE CHANNEL 2 LEVEL 3
HC31 HIGH COUNT RATE CHANNEL 3 LEVEL 1
HC32 HIGH COUNT RATE CHANNEL 3 LEVEL 2
HC33 HIGH COUNT RATE CHANNEL 3 LEVEL 3
POC PREOPERATIONAL CHECKOUT

Fig. 7.16 – Functional schematic of reactor startup control subsystem, loop No. 3

The functional schematic, Figure 7.16, shows that the output from the pump circuit went to both the count rate magnetic amplifier and the period computer. The amplifier conditioned the signal so that there was a suitable impedance match working into the switching amplifier. The switching amplifier monitored the signal and indicated low and high counting rates through a pair of output relays associated with each amplifier. Three logic circuits were associated with the relay contacts from the three channels. The first circuit was the "scram indication light" circuit which denied power to the scram light as long as the relays energized in the proper sequence. The second circuit was the "switching monitor circuit" which opened a scram bus if the relays did not energize in the proper sequence. The third logic circuit selected the proper period amplifier for the corresponding power level. The selected signal went to an error amplifier that compared the period demand and the period feedback for automatic control. This channel appeared in loop No. 3 only.

The operation of the logic circuits was directly related to the sensitivity of the channels shown in Figure 7.13. Ten counts per second on channel No. 1 caused LC-31 (area 5-J of Figure 7.16) to pick up. This action kept the scram light turned off and maintained continuity in the scram bus. All HC relays were energized below the high level of counting rate, opening the normally closed contacts and preventing the 28 volts dc being applied to the console light. The HC relay contacts in the scram bus were located across the bottom of the circuit and all were closed when the relays were energized. Thus, when LC-31 closed in series with the HC contacts, the scram bus could not cause scramming. For reactor startup, it was necessary that LC-31 be energized. Figure 7.13 also showed the range of trip point adjustment necessary to secure a reliable sequence of operation.

Breadboard tests demonstrated that a separate period error amplifier was not needed; this function was performed by the power-range flux error amplifier.

7.4.2.3 Pulse Components

Each log count rate channel consisted of a pulse transformer, a ceramic tube preamplifier, a main amplifier, and a binary circuit. The total subsystem required three tandem channels as shown in Figure 7.12.

Preamplifier - Figure 7.17 shows the wiring schematic of a ceramic tube pulse preamplifier, and Figure 7.18 is a photograph of a typical component. It amplified high repetition rate, random fission-counter pulses and maintained voltage gain stability under power supply and temperature variations. It prevented spurious addition or loss of pulses, and maintained a high signal-to-noise ratio. The pulse transformer electrically matched 70 feet of triaxial cable between the fission counter and the preamplifier, and made it possible to place the preamplifier in a location remote from the engine.

The preamplifier had three stages of amplification and a cathode-follower output stage for impedance matching. Figure 7.19 shows the measured gain of six test units. The linear gain portion of the average gain curve started at 50 microvolts rms and the saturation point was 16 millivolts rms. The average measured gain of these six units was 41 decibels with an average band width of 5 kilocycles to 1.4 megacycles. There was less than 1 decibel change in gain during a ± 10 percent B^+ variation test, a 16-percent filament voltage variation test, and a 2.84×10^{17} integrated neutron flux irradiation.

Pulse Amplifier and Log Count Rate Computer - This channel received the output of the ceramic tube pulse preamplifier, amplified the signal, discriminated, and then computed the log count rate. The wiring schematic of this channel is shown in Figure 7.20.

The amplifier contained three stages of amplification and a cathode-follower output stage. Figure 7.21 shows the frequency response of the amplifier. Its gain at midband was 62.5 decibels and its half-power frequencies were 140 kilocycles and 1.8 megacycles, respectively. The rise time was 0.16 microsecond and noise level, referred to the input,

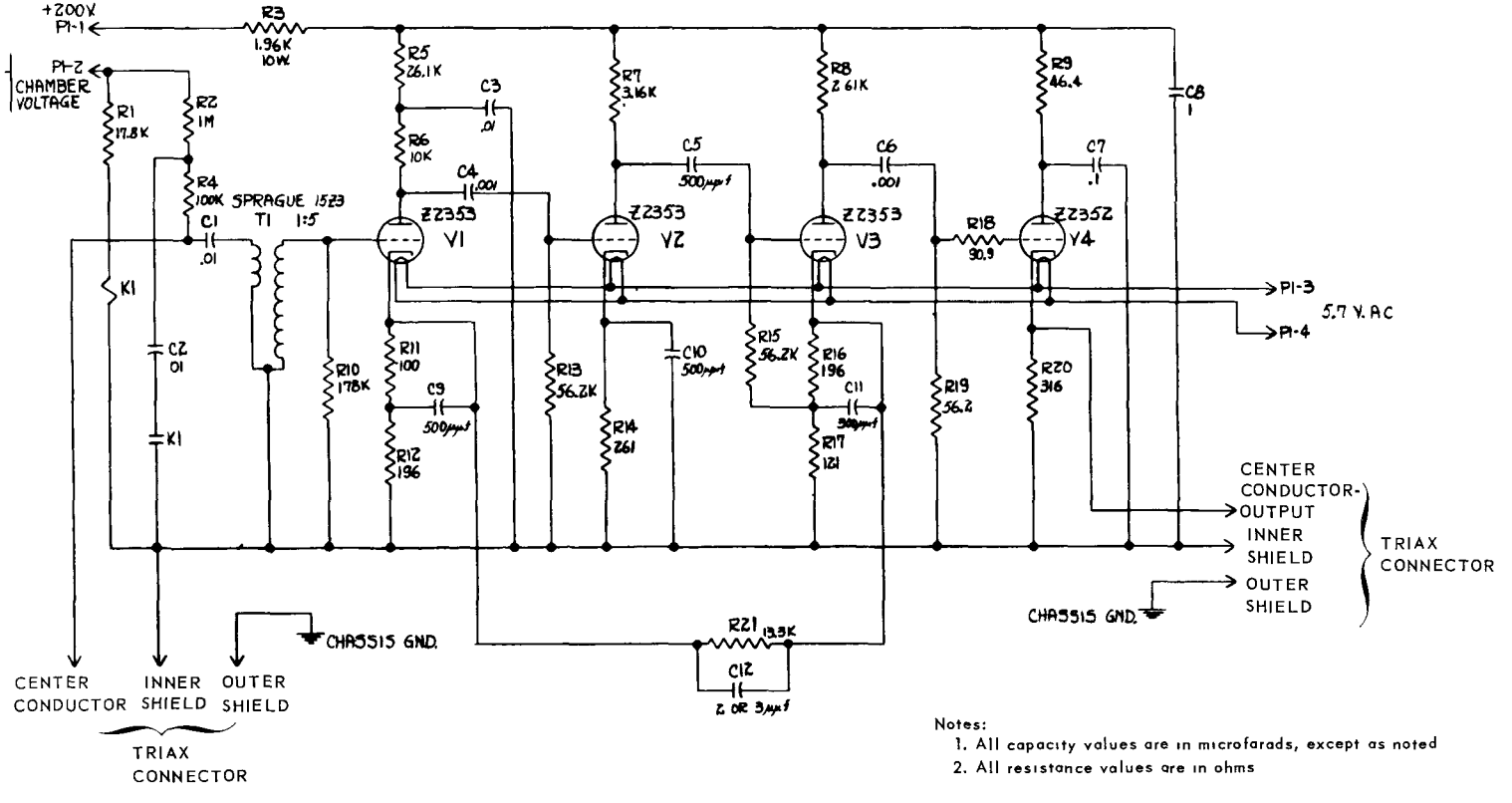

Fig. 7.17 – Schematic of ceramic tube pulse preamplifier Dwg. 977C763

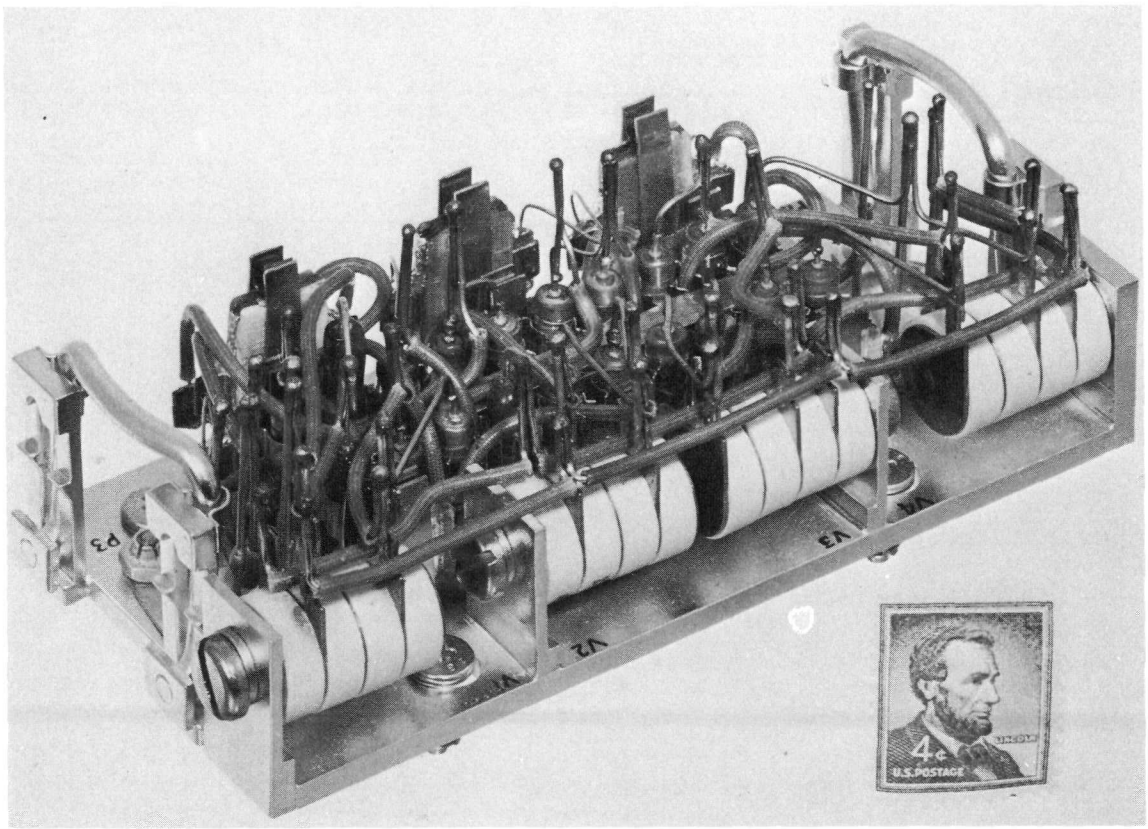

Fig. 7.18 – Ceramic tube pulse preamplifier

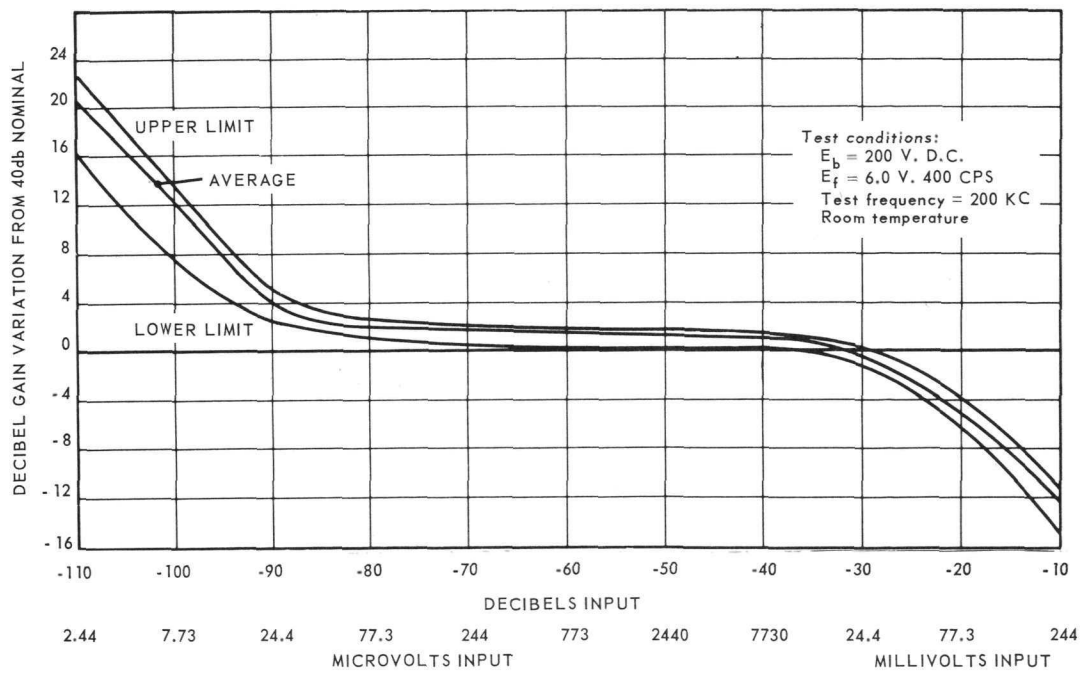

Fig. 7.19 – Measured gain of 6 ceramic tube pulse preamplifiers

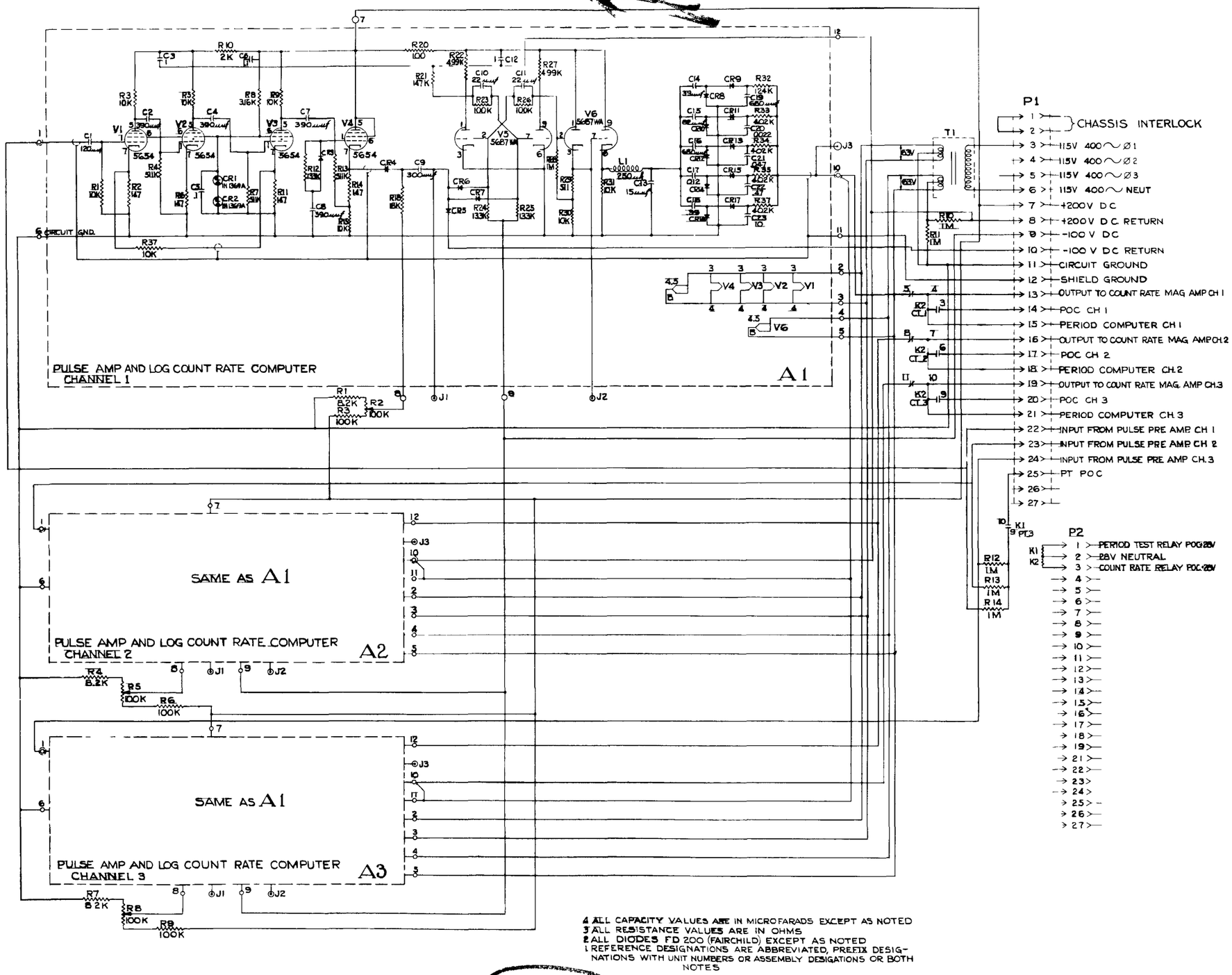

4 ALL CAPACITY VALUES ARE IN MICROFARADS EXCEPT AS NOTED
3 ALL RESISTANCE VALUES ARE IN OHMS
2 ALL DIODES FD 200 (FAIRCHILD) EXCEPT AS NOTED
1 REFERENCE DESIGNATIONS ARE ABBREVIATED, PREFIX DESIGNATIONS WITH UNIT NUMBERS OR ASSEMBLY DESIGNATIONS OR BOTH NOTES

Fig. 7.20—Wiring schematic of log count rate channel

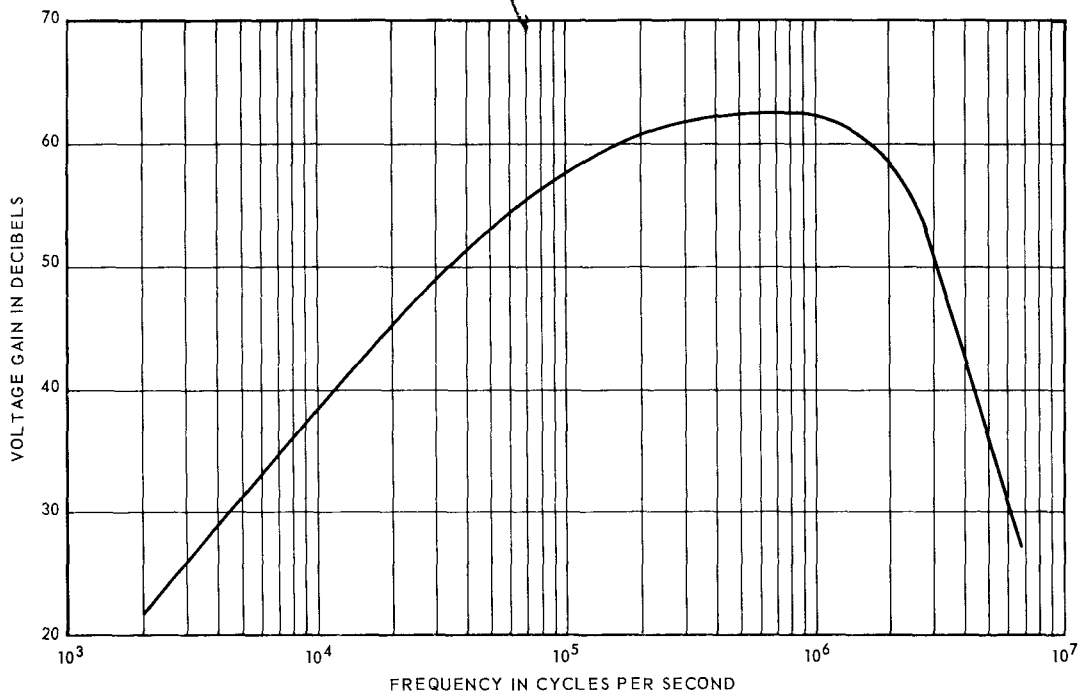

Fig. 7.21 – Pulse amplifier frequency response

was 2 millivolts. The noise level was 20 microvolts when referred to the preamplifier output (amplifier input). The saturation point was 64 volts peak-to-peak. For a B^+ variation of 150 to 210 volts, the gain of the amplifier changed 0.3 decibel. For 5- to 7-volt filament variation, the gain varied 0.2 decibel. A temperature change from -67 to +257°F resulted in a gain increase of 1.1 decibels.

The discriminator was a typical amplitude-clamping circuit. The discriminator data curve shown in Figure 7.22 was obtained by maintaining the discriminator output voltage constant at a level which just triggered the binary circuit. The pulse amplifier input voltage was then measured for different discriminator bias settings. The nonlinearity of this curve at the high discriminator settings indicated that the amplifier was being saturated.

The log-count-rate circuit converted the number of pulses received per unit time to an analog indication of the reactor power level. The discriminator circuit coupled the pulse amplifier to the log-count-rate computer, passing pulses above a predetermined level and ignoring those below the selected level. The passed pulses triggered the binary circuit and established a constant-amplitude square-wave output. The pulse widths of repetitive pulses were somewhat random, but their average width was inversely proportional to the average counting rate. The pulse currents were passed through a parallel arrangement of Cooke-Yarborough diode pump networks to a common load resistance. The entire circuit, including the binary, was designed in accordance with the theory outlined in reference 12. Test results of breadboard and prototype hardware correlated very well with theory. The advantage of this circuit over other diode-switched RC network count-rate computer circuits was that the response time-constant varied inversely with the counting rate. The speed of response varied with the scale reading. At any point on the scale, the speed of response was limited only by the maximum statistical fluctuation that could be tolerated by the circuit.

The binary circuit was composed of two double triodes (tube No. 5687). The first tube served as the flip-flop stage and the second tube as two cathode followers in series. Two

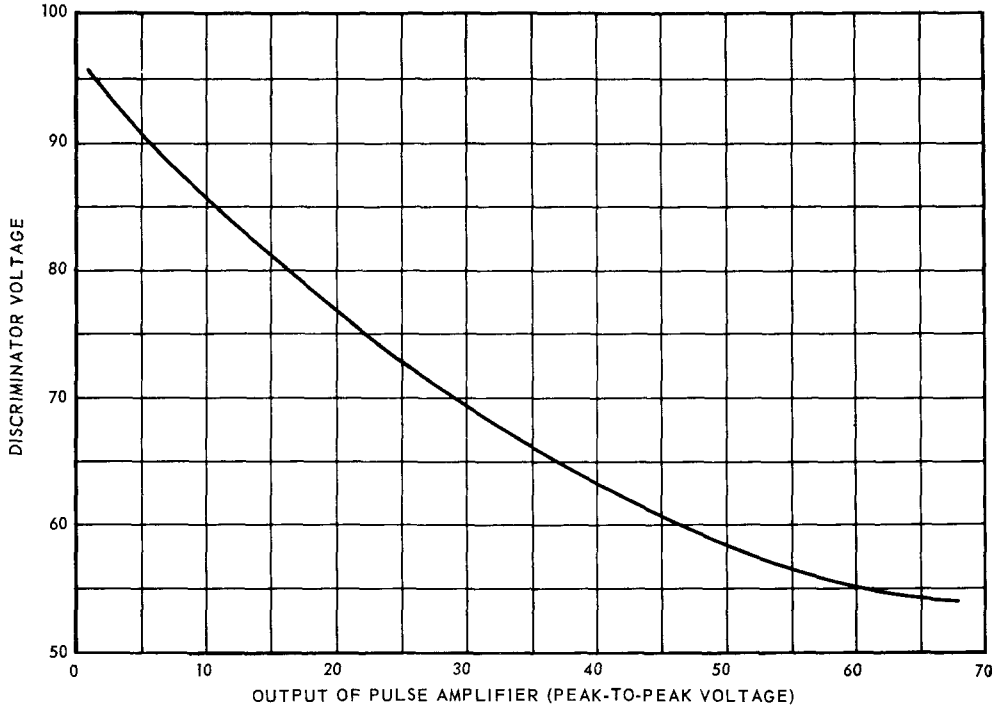

Fig. 7.22 – Discriminator data curve

cathode followers were used because the log-count-rate computer had high capacitive impedance and loaded the cathode-follower stage sufficiently to reflect back to the binary circuit. As a result, the square-wave input to the pump circuit was distorted. With two cathode-follower stages, the brunt of the loading was absorbed by the last cathode follower and the first cathode follower acted as a neutralizer between the binary and the second cathode follower. The binary circuit was quite critical; the resolution was dependent upon circuit layout and the characteristics of the double triode. Matched tubes were required.

The binary circuit triggered at input pulses approximately 2.5 volts peak-to-peak. It had an output of 110 volts peak-to-peak. For frequencies higher than 10^5 cycles per second, the strength of input signal had to be increased. At 10^6 cycles, the minimum triggering signal was found to be 5 volts peak-to-peak. When referenced to the input of the preamplifier, a signal strength of 100 microvolts was required, assuming an amplitude loss of 50 percent in the discriminator. This sensitivity was adequate since pulses from the fission counters were 200 microvolts or greater.

The stability of the binary circuit with its pump circuit connected was determined. Variations in the binary circuit output voltages were reflected at the output of the log-count-rate computer; this point in the circuit was where the effects of any variation reflected into the operation of the startup control. Figure 7.23 shows the output voltage of the log-count-rate computer as a function of frequency. Linearity was obtained for pulse frequencies up to 5×10^4 counts per second. Fast-switching and high-conductance diodes increased the high-count-rate linear range of the pump circuit from 5×10^4 to 2×10^5 counts per second. For a ±5 percent B^+ change, the counting rate varied -5 percent; for ±5 percent B^- change, the counting rate varied less than 1 percent; for 40 percent filament variation, the over-all change of counting rate was 4 percent.

The range of linearity was dependent upon the resolution and accuracy of the binary circuit and a constant binary output amplitude was required over the desired frequency range.

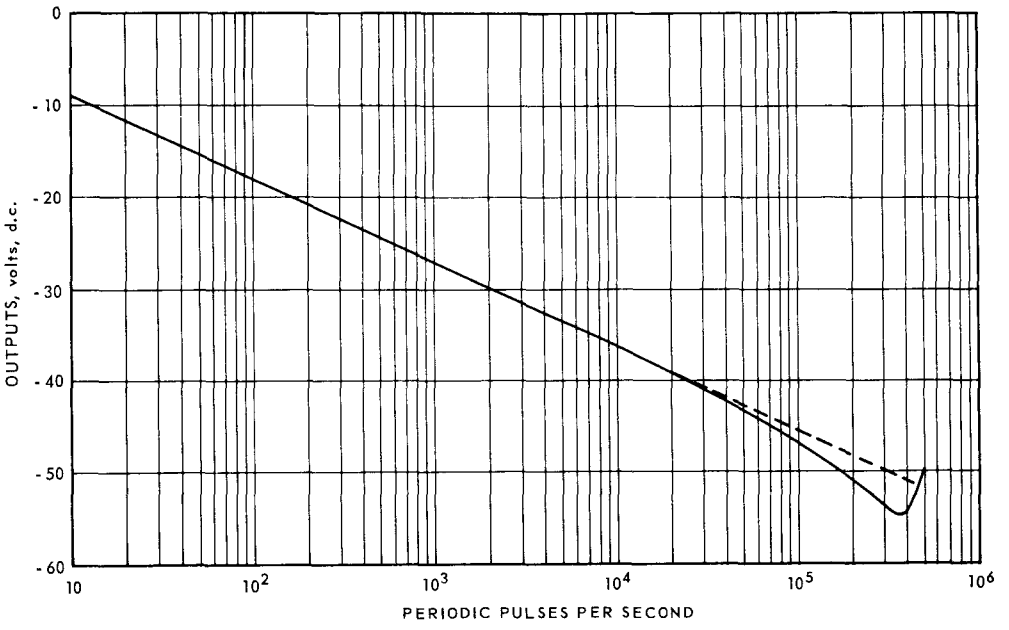

Fig. 7.23 – Linearity of log-count-rate computer

This was accomplished by dropping the output voltage to achieve higher resolution. Testing of prototype circuit showed a resolution of one microsecond when the output voltage was at the limit of the tubes used in the circuit.

The over-all dimensions of the log-count-rate channel were approximately 13 inches by 2.5 inches by 4 inches. The power consumption of the over-all pulse circuitry was 30 watts dc and 17 watts ac.

7.4.2.4 Operational Amplifiers

The count rate amplifier, the period computer amplifier, and the period trip and indicator amplifiers were versions of a basic operational amplifier, and all used the same circuitry. The differences between the amplifiers were in the computing elements; i.e., resistors and capacitators were used in different combinations. The count-rate switching amplifiers and reference voltage amplifiers were derived from types of basic building blocks, and are described in reference 13.

Basic Operational Amplifier - This amplifier is described in references 14 and 15. The circuit schematic is shown in Figure 7.24. Bias and control windings used in the operational amplifiers are not shown.

Blocking potentials were used in a push-pull magnetic amplifying circuit. The blocking potentials were supplied by two pairs of diodes at opposite ends of the circuit; the left pair supplied a positive blocking potential and the right pair supplied a negative blocking potential. The left-hand full-wave magnetic amplifier was coupled with the right-hand full-wave magnetic amplifier to give a full-wave push-pull magnetic amplifier. This provided an open loop device with no external feedback. The current gain was 7000. The output was linear to 50 milliamperes (7.1 microampere input), and the pump circuit saturated at approximately 90 milliamperes.

Count-Rate Amplifier - A schematic of the count-rate amplifier version of the basic operational amplifier is shown in Figure 7.25.

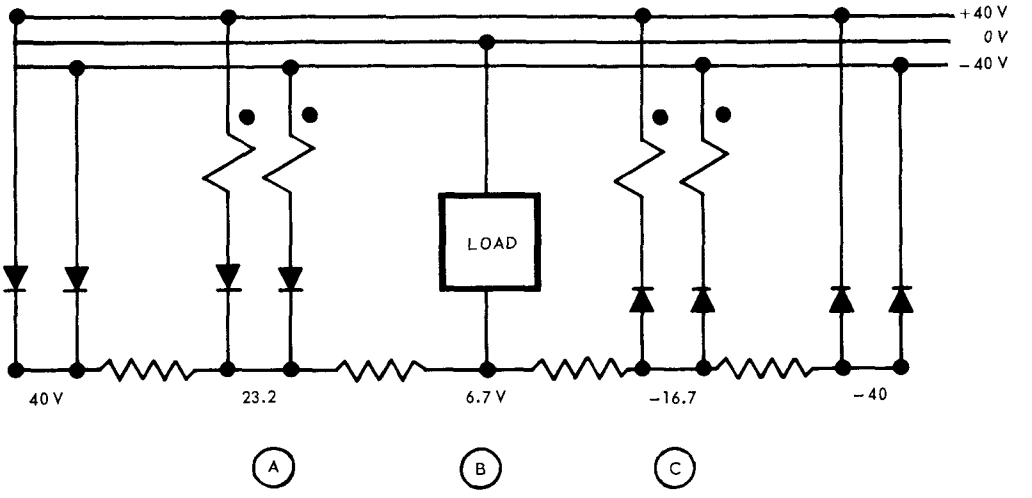

Fig. 7.24 – Circuit schematic of basic operational amplifier

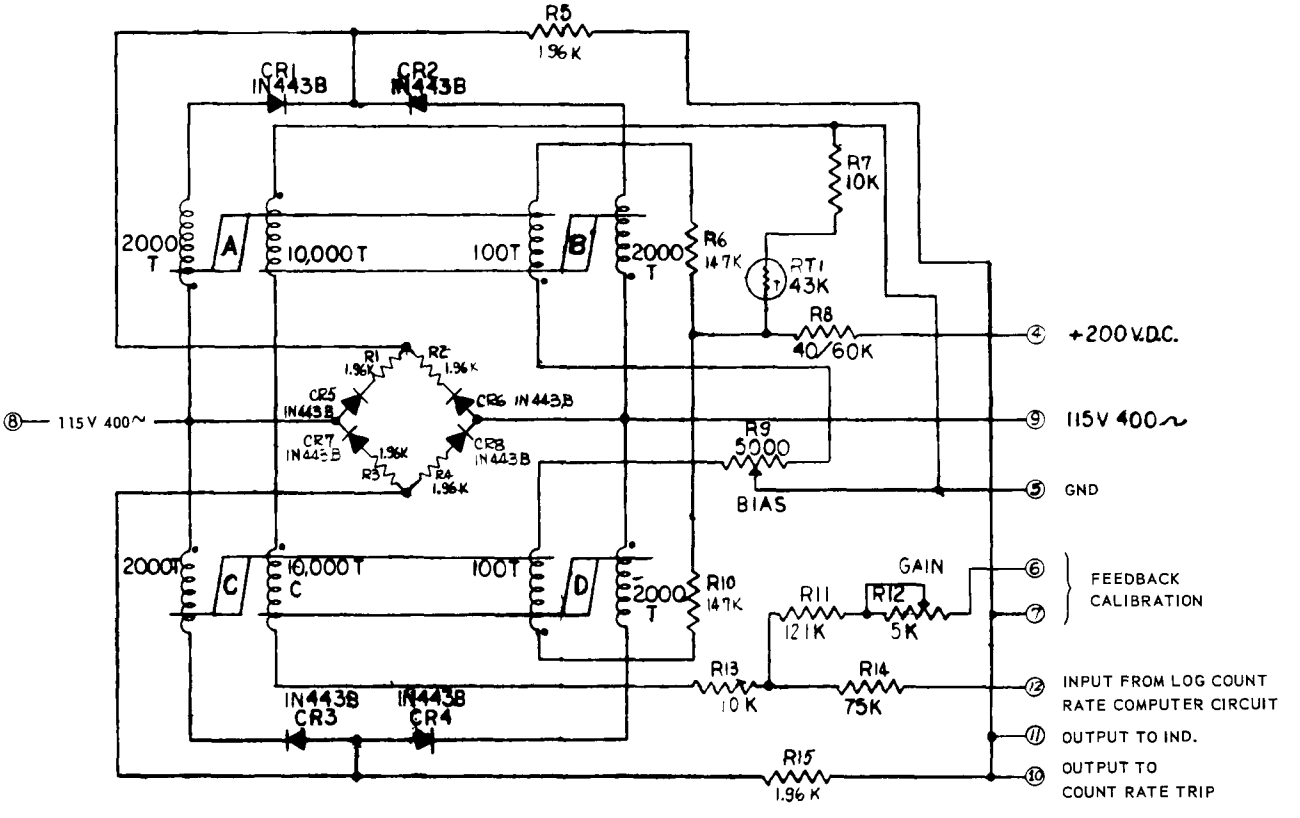

Notes:
1. All resistance values are in ohms
2. All capacitance values are in microfarads
3. Items A, B, C, and D are iron core transformers. The number of turns and interconnections are as shown.

Fig. 7.25 – Schematic of count-rate amplifier Dwg. 977C281

When used as a count-rate amplifier, the operational amplifier had a voltage gain of 1/5 volt per volt determined by the ratio of R10 divided by the sum of R11 and R12 (Figure 7.25). The input signal was the output of the log-count-rate computer circuit. The output signal operated the low-count trip, the high-count trip, and the count-rate indicator. The output of the log-count-rate computer circuit was approximately 9.0 volts per decade, with a gain variation between different circuits of approximately 2.5 percent. Compensation for this variation in gain was by the gain adjustment of the count-rate amplifier.

Power resistors were mounted in clips to help dissipate the heat, and the hottest components were attached to the bottom of the packaged unit. Chassis cooling-air made the chassis a "cold plate." The power dissipated was approximately 86 watts. Amplifier errors as a function of allowable variations in voltage, frequency, and temperature (-55° to +100°C) were less than 2 percent.

The measured transfer function of the count-rate amplifier was:

$$\frac{E_o}{E_{in}} = -\frac{0.208}{\left(1 + \frac{s}{60}\right)}$$

where

s = conventional Laplacian transform.

Period-Computer Amplifier - The period-computer amplifier obtained its signal from the output of the log-count-rate computer circuit. The period-computer amplifier and the count-rate amplifier were connected parallel to prevent the time constant of the count-rate amplifier reflecting into the period indication and trip circuits. This amplifier had two isolated outputs; one output drove the period trip and indicator amplifier, and the second output was compared with the period demand in the period servo loop. The outputs were isolated to prevent the period-error amplifier from loading the period-computer amplifier. If the period-computer amplifier had been loaded, the period meter would have read incorrectly. With isolated outputs, however, the meter was accurate at all times. The period-error amplifier loaded its output circuit of the period-computer amplifier and resulted in reduced gain for large period errors. However, the high gain needed for control purposes was retained when the period error was small, and the loading approached zero as the loop error approached the null point.

The transfer function of the period computer was:

$$\frac{E_o}{E_{in}} = \frac{2.04s\left(1 + \frac{s}{53.8}\right)}{\left(1 + \frac{s}{0.25}\right)\left(1 + \frac{s}{60}\right)\left(1 + \frac{s}{140}\right)}$$

Period-Trip and Indicator Amplifier - This amplifier received a signal from the period-computer amplifier and provided input signals for the scram and alarm trip circuits, and the period indicator. Its time constant was 4 seconds, and provide good filtering against extraneous noise due to the random output of the fission chambers. Erroneous alarms and scrams were prevented by this filtering action.

The amplifier output to the period indicator was equal to

$$E_o = 8.4 - \frac{37.8}{T}$$

where

T = period, sec.

The period indicator was calibrated to indicate a 4.5-second period at 0 volts, and an infinite period at 4.25 volts.

The transfer function of this amplifier was equal to

$$\frac{E_o}{E_{in}} = - \frac{5.63}{\left(1+\frac{s}{0.25}\right)}$$

The combined transfer function of the period-computer amplifier and the period-trip and indicator amplifier was equal to

$$\frac{E_o}{E_{in}} = \frac{11s\left(1+\frac{s}{53.8}\right)}{\left(1+\frac{s}{0.25}\right)^2\left(1+\frac{s}{60}\right)\left(1+\frac{s}{140}\right)}$$

Packaging - Typical packaging of amplifiers in the startup system is shown in Figure 7.26. All components were potted with the exception of the wire-wound potentiometers. Test points were brought outside the potted assembly in order that the amplifier bias, indicator bias, and amplifier gain could be adjusted and calibrated.

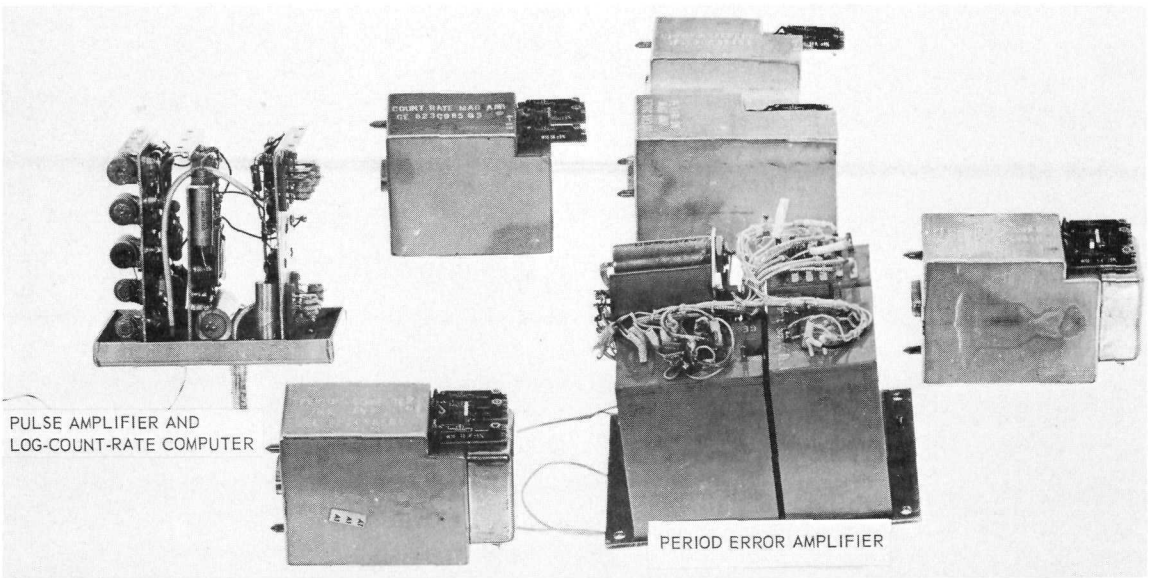

Fig. 7.26 – Packaging of amplifiers used in the reactor startup control subsystem (U39139A)

Frequency Response - The frequency response of all magnetic amplifiers was measured using a Solartron Low Frequency Oscillator and a Solartron Resolved Component Indicator.[16] Since the Solartron equipment would not operate below 2 radians per second, a two-channel high-speed recorder was used for lower frequencies. Filtering was necessary since the output wave form of magnetic amplifiers contained several harmonics in addition to the signal component. Testing indicated that a computer amplifier connected with a 1:1 gain and a 100-radian break gave good results in filtering the distorted wave forms. The effect of the 100-radian break was removed from the various transfer functions before the data were plotted.

7.4.3 POWER RANGE TEMPERATURE AND FLUX CONTROL SUBSYSTEM

7.4.3.1 Description

This subsystem controlled the reactor power level by controlling, through the control rod actuation subsystem, the position of the reactor control rods. The reactor power

level, in turn, controlled the turbine discharge-air temperature at a demanded level. It consisted of the neutron flux and temperature (regulating $T_{5.1}$) automatic control loops, the associated reference input elements, the control mode selector, and various test and calibration controls.

This subsystem was capable of controlling the reactor flux over a 2-decade range (approximately 1.5% to 150% full power). An additional subpower range flux subloop extended the range of control by an additional 8 decades, i.e., down to approximately 10^{-8} percent full power. This subloop permitted system checkout at low power, and provided low level flux regulation. A manual reactor control subloop permitted manual reactor startup and power levelling at any value between approximately 10^{-8} to 150 percent full power.

A schematic of the over-all reactor control system was shown in Figures 7.10a through 7.10d. The power range temperature and flux control subsystem is shown in Figures 7.27a, 7.27b, and 7.27c.

Temperature Loop - This loop was the primary loop of the subsystem. It regulated turbine discharge-air temperature from 600° to 1200°F and held the temperature within ±20°F of demanded temperature. It controlled the temperature by comparing the turbine discharge-air temperature ($T_{5.1}$) signal with the demand signal from the thrust selector and/or a manual bias, and utilized the flux loop as a forward element by replacing the power demand with a combined signal composed of the temperature loop error plus the integral of the error. The flux loop then regulated the control rods to obtain power as required to satisfy the temperature demand with minimum temperature error.

The flux-loop demand signal was composed of the temperature-loop error summed with the integral of the error to obtain minimum steady-state error. The temperature reference was compared with the sensed value from the turbine discharge-air thermocouples. The difference was operated on by proportional plus integral stabilizing action and the result constituted the reactor power demand. Any discrepancy between the demand value and the actual value repositioned the control rods to reduce the power error to zero and provide an actual turbine discharge-air temperature corresponding to the temperature reference.

Further details of this loop are contained in reference 11.

Flux Loop - This loop sensed the neutron flux level with an uncompensated ion chamber and compared the flux level with the power demand to provide a flux loop error signal. The ion chamber signal was converted to a signal proportional to its logarithm and provided automatic gain compensation in the flux loop. This converted signal then formed the demand signal to the control rod actuation subsystem. The subpower range loop utilized the components of the normal power range loop and a sensitive amplifier (micromicroammeter) that accepted the ion chamber output.

The loop provided (1) low-level power holding during automatic transfer from startup to power range, (2) power range operation at low airflows where temperature control was ineffective, and (3) backup for the temperature loop. Control in the power range was initiated by operation of a relay in the ion chamber circuit at about 1.5 percent full power. The power range flux loop regulated neutron flux from 1.5 percent full power to 100 percent full power and held the flux level within ±0.5 percent during steady-state operation. The subpower range loop regulated neutron flux from 10^{-8} percent full power to 1.5 percent full power and held the flux level within ±0.5 percent of the steady-state value.

Automatic temperature control could be initiated only from the automatic flux operating mode. Transfer was accomplished by zeroing the temperature error with the flux control loop and changing the mode selector switch from Flux to Temperature.

Further details of the temperature control loop are contained in reference 11

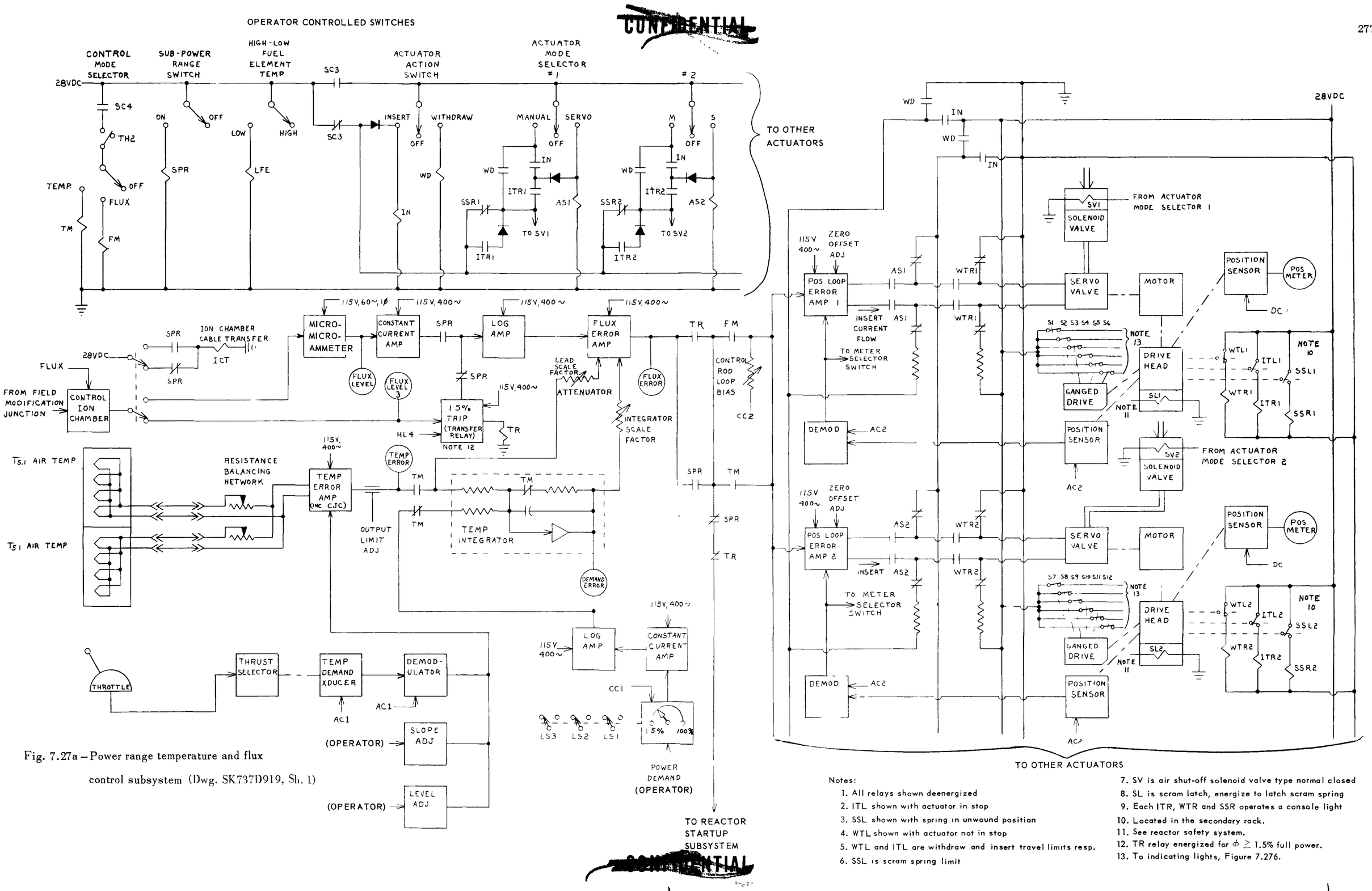

Fig. 7.27a – Power range temperature and flux control subsystem (Dwg. SK737D919, Sh. 1)

Notes:

1. All relays shown deenergized
2. ITL shown with actuator in stop
3. SSL shown with spring in unwound position
4. WTL shown with actuator not in stop
5. WTL and ITL are withdraw and insert travel limits resp.
6. SSL is scram spring limit
7. SV is air shut-off solenoid valve type normal closed
8. SL is scram latch, energize to latch scram spring
9. Each ITR, WTR and SSR operates a console light
10. Located in the secondary rack.
11. See reactor safety system.
12. TR relay energized for $\phi \geq 1.5\%$ full power.
13. To indicating lights, Figure 7.276.

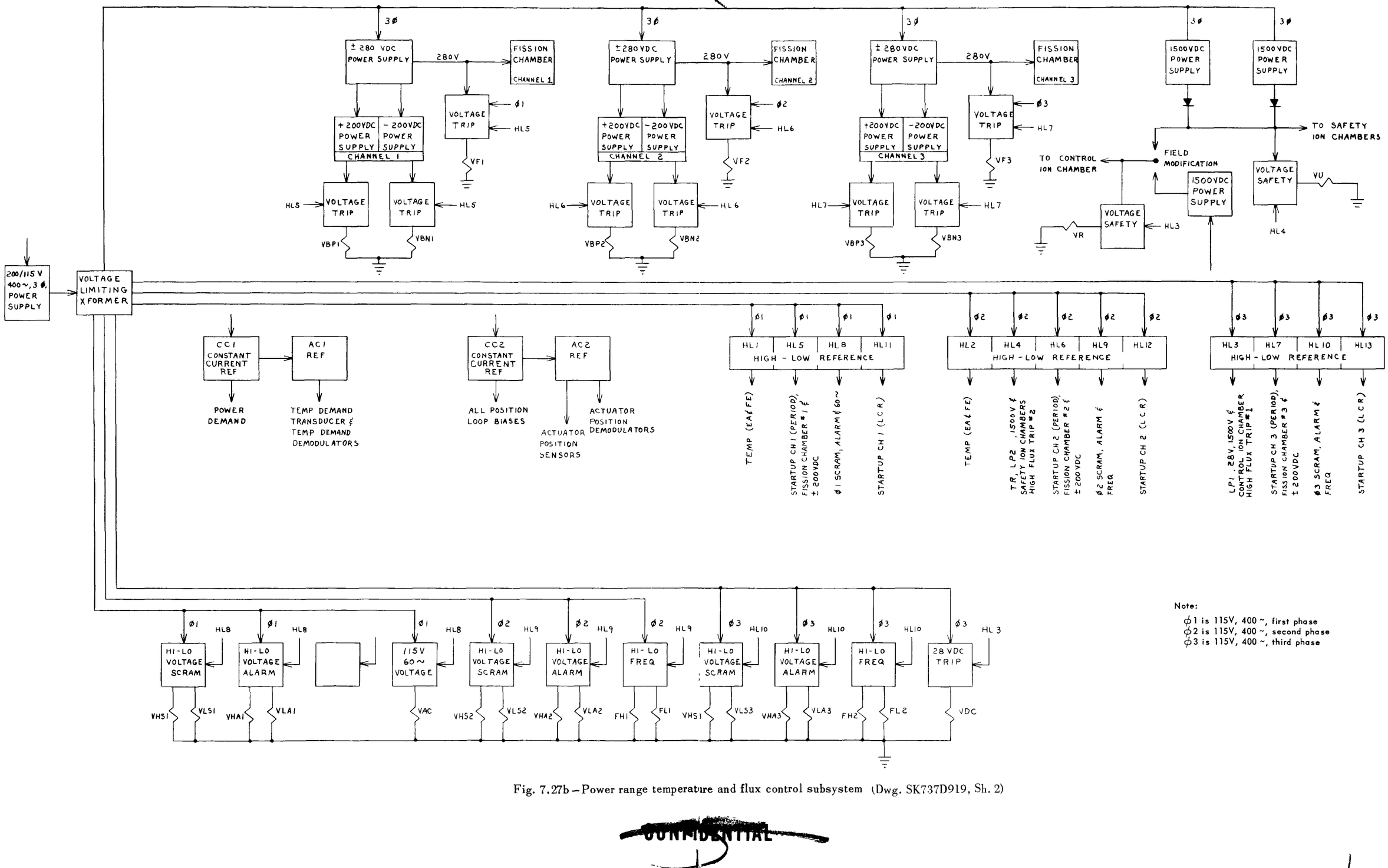

Note:
ϕ1 is 115V, 400 ~, first phase
ϕ2 is 115V, 400 ~, second phase
ϕ3 is 115V, 400 ~, third phase

Fig. 7.27b – Power range temperature and flux control subsystem (Dwg. SK737D919, Sh. 2)

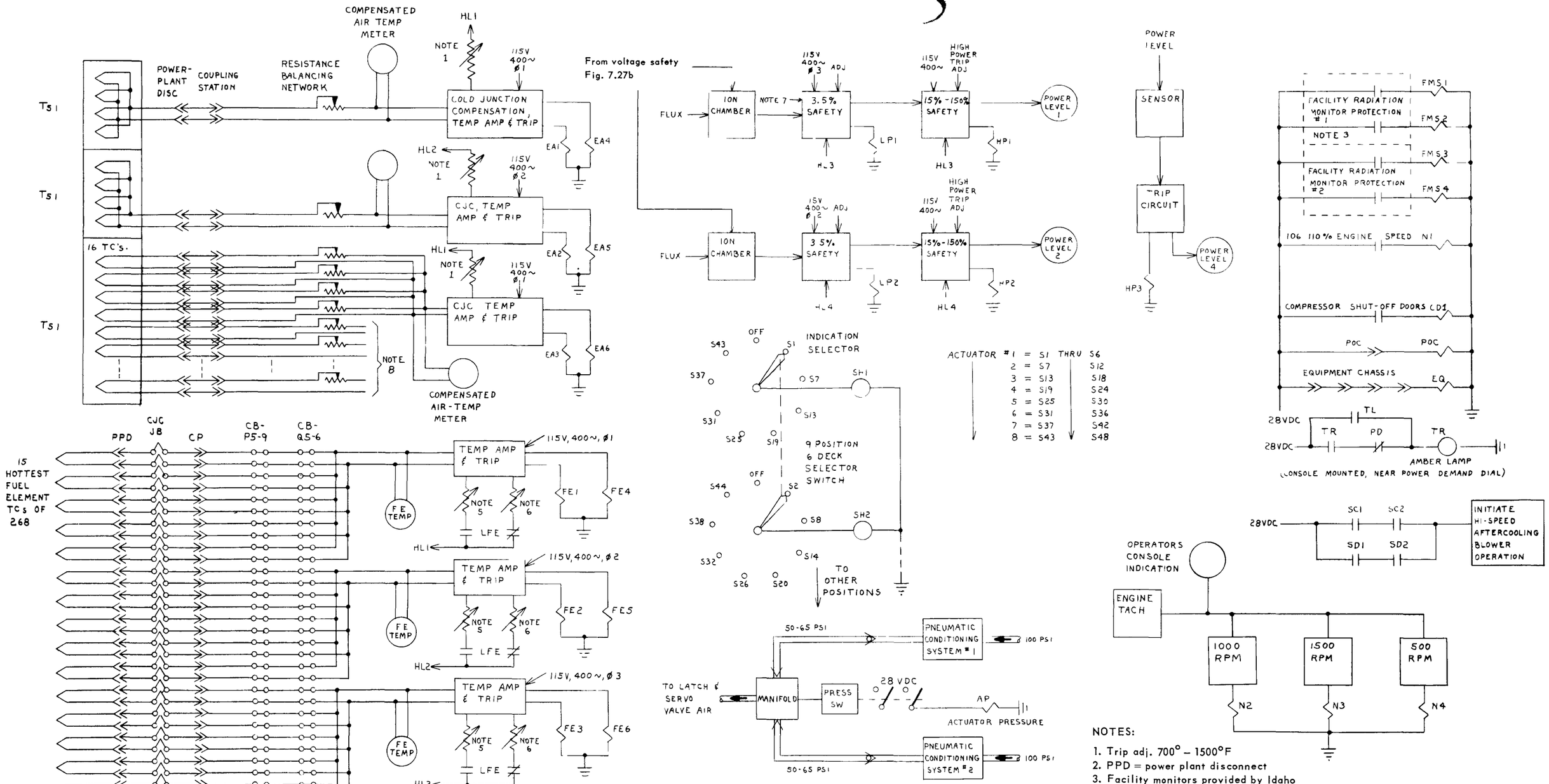

Fig. 7.27c – Power range temperature and flux control subsystem (Dwg. SK737D919, Sh. 4)

NOTES:

1. Trip adj. 700° – 1500°F
2. PPD = power plant disconnect
3. Facility monitors provided by Idaho
4. CP = coupling plug
5. Fixed trip 700°F
6. Trip adj. 700° – 2800°F
7. LP relay energized for $\varphi \leqq 3.5\%$
8. Twelve thermocouples for data systems and spares.

Manual Reactor Control Loop - Manually controlled reactor startup and power leveling was effected by manually initiated signals to the control rod actuators. The actuators to be energized were selected by the operator through the actuator mode selectors. To obtain power levels above 1.5 percent in the manual mode, it was necessary to level the power between 1.5 and 3.5 percent full power and position the flux demand slightly above its lower limit. Higher power levels then could be manually controlled.

7.4.3.2 Temperature Loop Circuitry

Control elements in the loop were the temperature-error amplifier, integrator, and temperature sensors. In addition, a proportional signal in parallel with the integrator provided the loop with the proper lead stabilization. The range of control was from 600°F to 1200°F at station $T_{5.1}$. The temperature-loop demand was generated from the throttle (and a manual bias) and was a function of the engine cycle. A control-mode selector switch was used to select the Flux or Temperature servo mode and permitted the operator to change servo modes. The selector also had an Off position which prevents the flux and temperature servos from controlling the rod-position loops when desired.

The control mode selector switch selected the control actuation system input demand from either the temperature or flux loop, and also prevented inadvertent reactor start-ups. When the control system was in operation and the actuators were in the Servo mode, an automatic start was prevented by placing the control-mode selector in the Off position. This position supplied a signal to all position loops that required all actuators in Servo mode to withdraw 1 inch from the fully inserted position. The control-mode selector was placed in the Off position when the rod-position loops were being tested. One 3-position switch was used with positions labeled Flux, Temperature, and Off; the Flux position was between the Off and Temperature positions.

When the selector was set on Flux, the temperature-loop integrator acted as an amplifier, and presented the flux loop with the logarithmic flux demand from the flux-loop reference elements. Also, the temperature-loop error signal was blocked from the integrator and flux-error amplifier. The flux-error amplifier controlled those rod-position loops having actuators in the Servo mode.

When the selector was set on Temperature, the temperature-loop integrator and flux-error amplifier received the temperature-error signal, and the flux-reference input elements were removed from the circuit. The flux-error amplifier then controlled those rod-position loops having actuators in the Servo mode.

When the selector was set at Off, the output of the flux-error amplifier was blocked from the rod-position loops, and the rod-position loop bias became the rod-position loop demand. The temperature-loop error signal was blocked from the integrator and the flux-error amplifier.

Other significant components in the temperature loop were the 2-megawatt transfer relay, the subpower range switch, the reference input elements, and the rod-position-error amplifier.

Temperature-Error Amplifier - This unit amplified the thermocouple signals several thousandfold without electrically loading the thermocouples. It had a time constant at least one-tenth that of the thermocouple sensors, and was a two-stage magnetic amplifier. The first stage, or preamplifier, was a balanced second harmonic amplifier with a d-c output that was about 1000 times the d-c input. This signal was further amplified about 200-fold by a second-stage full-wave push-pull magnetic amplifier. The output of the second stage drove a high-resistance voltage divider. A small part of this voltage was sampled and compared to the input. All differences were amplified by both stages to correct the

level of the two stages until the output was an exact multiple of the input signal. The basic specifications for this amplifier were:

d-c Amplifier	Gain 15,000 volts per volt maximum
Line supply	115 volts, 400 cycles per second
Output voltage	6 volts dc maximum
Output current	20 milliamperes maximum
Minimum load	300 ohms
Sensitivity	1 microvolt
Driving generator resistance	200 ohms maximum
45-Degree phase lag frequency	50 radians or more

The gain was adjustable from 800 to 2000 volts per volt. The transfer function showed less than 45 degrees phase shift and almost flat attenuation characteristics to 20 radians per second. The output was adjustable from 0.5 to 4.0 volts. Leadwire stabilization was incorporated as a time constant adjustable from 10 to 80 seconds. The output of several Chromel-Alumel thermocouples in parallel provided one of the inputs. The thermocouple voltage was of the following form:

$$V\ (volts) = 2.3 \times 10^{-5}\ T\ (^{o}F) + constant$$

where the constant depended upon the selected cold junction temperature. Another input was provided by the demand circuitry. The amplifier included built-in cold junction compensation for the temperature sensors, and the error caused by this cold junction compensation did not exceed $\pm 1^{o}F$.

Special effort was made to design this amplifier to operate from low level - low impedance d-c signal generators with a minimum of noise. This amplifier is discussed in more detail in references 15 and 17.

Integrator - This unit was a two-stage full-wave push-pull amplifier; the first stage was the forward amplifier with large negative feedback. The second stage was the feedback amplifier with large negative feedback and was used to dictate the integration rate and furnish positive feedback to make the total internal integrator gain unity. A discussion of the theory of operation and specific application is given in reference 3.

The basic specifications were as follows:

d-c Gain	0.1 to 0.005 volt per volt
Line supply	115 volts, 400 cycles per second
Output voltage	4 volts dc maximum
Output current	10 milliamperes maximum
Minimum load	500 ohms
Sensitivity	0.005 volt (error)
135-Degree phase lag frequency	30 radians or more.

The operating gain was 6×10^{-3} volts per second per volt input. The transfer function showed less than 135 degrees lag and essentially 20 decibels per decade attenuation characteristics to 20 radians per second. The maximum output did not exceed 3.7 volts. The minimum detectable signal did not exceed 0.03 volt, and the temperature error required to prevent integration was no greater than 0.05 volt.

Temperature Sensors - These sensors were located in the turbine discharge-air at station 5.1, and included a total of 32 Chromel-Alumel thermocouples. Of the 32 thermocouples, 16 were paralleled in the engine wiring harness into four groups of four each. The Chromel-Alumel wire was connected to compensated lead wire (copper - constantan) at a junction where the ambient temperature did not exceed $200^{o}F$. Accordingly, 20 pairs

of wire (16 pairs corresponding to 16 single thermocouples and four pairs corresponding to the four paralleled combinations of four thermocouples) were brought from the Chromel-Alumel and copper-constantan junction to a control rack in the FET equipment area. The 20 pairs were divided into three separate groups in the wiring harness so that, in the event of a connector or wire tray failure, all $T_{5.1}$ instrumentation would not be lost. These thermocouple leads were not routed through any cold junction compensation devices since compensation was provided by the temperature-error amplifier.

Two pairs of wires, corresponding to two paralleled combinations of four thermocouples, were paralleled at the control rack and the resulting combination of eight paralleled thermocouples drove the temperature-error amplifier. The two remaining pairs, corresponding to the remaining two groups of four paralleled thermocouples, were used by two temperature safety trip circuits, reference 18. An additional group of four pairs corresponding to four single thermocouples was paralleled at the control rack for a third-temperature safety trip circuit, used as a spare.

The remaining 12 pairs were single thermocouples and were available for the data instrumentation system or other readout devices.

The error caused by the junction of the Chromel-Alumel and compensated lead wires did not exceed 5.5°F. The range of the sensors was 0° to 1200°F steady state, with 1500°F transients. The sensor outputs were reproducible within ± 5°F at 1200°F. The time constant was less than 3 seconds. In terms of sinusoidal temperature input, this time constant implied that the phase lag at a frequency of 0.333 radian per second did not exceed 45 degrees for normal conditions of cycle temperature and airflow. The tail-in time (time to go from 90% of a step input to within 1% of the final value) did not exceed 20 seconds.

Two-Megawatt Transfer Relay - This relay was energized at approximately 1.5 percent full power (2 megawatts) and performed the following functions:

1. Transferred the control-rod-position loops from the startup subsystem to the power-range subsystem
2. Operated in the safety circuit
3. Operated an amber light on the operator's console in conjunction with the limit switch on the power demand.

The relay operated within 200 milliseconds after the input signal exceeded the trip point by 30 percent of the trip point.

Subpower Range Switch - This switch was used in conjunction with a manually operated coaxial cable transfer switch located at the equipment racks and transferred the micro-microammeter and constant-current amplifier to the feedback of the flux loop. It was a two-position switch with positions labeled On and Off and operated a relay when in the On position. When the switch was set to the On position, the relay transferred the logarithmic amplifier input from the 2-megawatt trip circuit to the constant-current amplifier driven by the micromicroammeter. When the switch was set to the Off position, the relay was open and the logarithmic amplifier was connected to the 2-megawatt trip circuit.

The coaxial cable transfer switch was used in conjunction with the subpower range switch to place the micromicroammeter and constant-current amplifier into the feedback of the flux loop for low-flux operation. It was a two-position switch with positions labeled Power Range Operation and Subpower Range Operation. In the Power Range Operation position the coaxial cable containing the signal from the ionization chamber was connected to the 2-megawatt trip circuit. In the Subpower Range Operation position the coaxial cable was connected to the micromicroammeter input.

Reference Input Elements to the Temperature Loop - The reference input elements to the temperature loop consisted of an a-c transducer mounted on the thrust selector, a demodulator, and level- and slope-biasing devices.

The voltage span of the thrust-selector-manipulated transducer corresponded to a range of 600° to 1200°F at station $T_{5.1}$; zero voltage corresponded to 840°F ± 100°F. The level bias ranged from +50° to -400°F. The slope bias was +200° to -400°F at idle throttle setting, and was pivoted about 1150°F ($T_{5.1}$ for military power setting).

Rod-Position-Error Amplifier - This amplifier was composed of three units; a slightly modified basic magnetic amplifier, a lead network and a ring-type demodulator circuit.

Power requirements for the magnetic amplifier were 115 volts ac, 400 cycles per second, 4.2 watts. Power requirements and operating specifications were as follows:

Voltage	37 volts, ac, 400 cycles per second
Polarity of input voltage	Positive or negative
Polarity of output voltage	Positive or negative
Gain of amplifier	Adjustable from 12 to 50 milliamperes per milliampere by 100,000-ohm potentiometer in load feedback
Linearity	± 1 percent up to 10 milliamperes output into a 600-ohm load at a gain of 25 milliamperes per milliampere
Maximum output	15 milliamperes into a 600-ohm load
Transfer function characteristics	45-degree lag at 80 radians with nominal gain equaled approximately 25 decibels; curve essentially flat to 80 radians
Input resistance	Approximately 160 ohms on 800-turn input winding
Drift	At zero input, 825 microvolts in 24-hour period
Regulation	(1) When a-c line voltage was varied ± 10 percent, the amplifier output voltage varied by ± 0.25 percent at a gain setting of 16 milliamperes per milliampere and output of 4.0 volts. (2) When a-c line frequency was varied ± 10 percent, the output varied by ± 0.5 percent at a gain setting of 16 milliamperes per milliampere and output of 4.0 volts.
Effective demodulator gain	0.01 and 0.04 d-c volt per a-c volt; adjustable with 100,000-ohm potentiometer at input of amplifier
Extra control windings	Two 400-turn windings and one 1600-turn winding

7.4.3.3 Flux Loop Circuitry

This system contained the neutron-flux automatic control loop, the associated reference input elements, the control mode selector, and various test and calibration controls. The subpower range switch connected the micromicroammeter into the feedback of the power range (flux) loop. A decade selector switch was provided to change the sensitivity of the micromicroammeter by factors of ten. Components in this loop were the flux error amplifier, control-rod-actuator-position loops, ionization chamber, and logarithmic amplifier. Subpower range operation required the addition of a constant-current amplifier.

Reference input elements to the flux loop consisted of a ten-turn potentiometer located on the operator's console, a constant-current amplifier, and a logarithmic amplifier. These components were in tandem from the standpoint of signal flow. The output of the logarithmic amplifier provided an input to the temperature loop integrator and the temperature loop integrator then acted as an amplifier.

The demand potentiometer was manually controlled by the operator and had a range of 1.5 to 99.9 percent of full power, where 100 percent of full power was 130 megawatts. It could be set in increments of 0.1 percent of full power. Loop inaccuracy from the visual meter indication to the output of the demand did not exceed (1) ten percent of the point from 1.5 percent to 10 percent of full power, and (2) three percent of the point from 10 percent to 100 percent of full power.

The output was repeatable within ± 0.1 percent of full power. A limit switch was provided to indicate when the demand was at 1.5 percent of full power, and was used as a safety action.

Flux-Error Amplifier - This unit was used as a mixer stage which added three signals electrically and two signals magnetically. The three electrically mixed signals had a common return and the two magnetically mixed signals had independent isolated inputs. The net summation of these five signals was further amplified by a harmonic amplifier and a full-wave push-pull amplifier with negative feedback around both stages. The signal then was amplified and computed by a last-stage full-wave magnetic amplifier with a gain of one. This last stage was used only for differentiation action at a specific frequency.

Individual adjustable gains were provided for each input signal: 20 to 80 volts per volt for the input from the logarithmic amplifier, 30 to 120 volts per volt from the temperature loop integrator, and 3.6 to 28.8 volts per volt from the temperature amplifier. A spare input to the flux-error amplifier was brought out to a convenient location on the chassis and had the same characteristics as that of the logarithmic amplifier input. The maximum output was 4 volts into a 250 ohm impedance. The resistance of each position-error amplifier input was adjusted to 2000 ohms by adding the required series resistance. The over-all resistance of the eight paralleled position-error amplifier inputs then was 250 ohms.

The transfer function was

$$\frac{K\,(1 + 0.05s)}{(1 + T_3 s)} \quad \text{volts per volt}$$

where T_3 was 0.0143 second and contributed less than 45 degrees phase lag at 70 radians per second.

References 15 and 27 contain further details of this amplifier.

Logarithmic Amplifier - The output voltage of this amplifier was a function of the logarithm of the input current (i.e., $E_o = K_1 \ln i + K_2$) and was accurate within 10 percent over three decades of input current.

A Thyrite* was used as the computing element. When current was passed through the Thyrite, a voltage developed across its terminals. Part of this voltage was sampled by a voltage divider and applied to the input of a high-gain full-wave push-pull amplifier. The output voltage developed by this amplifier was compared to the input voltage and, by servo action, was made equal to the input voltage. This equalization allowed power to be taken from the amplifier without affecting the Thyrite computation. Thyrite elements are very stable devices when subjected to irradiation or fluctuations of ambient temperature. Further information on this amplifier is contained in references 3 and 15.

Constant-Current Amplifier - This amplifier was a full-wave push-pull magnetic amplifier similar to the basic operational amplifiers. It acted as a high-voltage, current doubler with a gain that was almost independent of its load up to the 80-volts output limit. It

*General Electric Co. Trade name.

amplified the low-level linear signal from the micromicroammeter. Its load, the Thyrite of the logarithmic amplifier, was in series with its negative feedback loop.

The transfer function was less than 45 degrees phase shift with almost flat attenuation characteristics to 50 radians per second. The range of input voltage was from 1 to 10 volts, and the range of output currents was from 0.13 to 1.3 milliamperes. Linearity was equal to, or better than, 1 percent of full output and insured linear response up to 110 percent of reactor full power. Saturation did not occur before 150 percent of reactor full power.

7.4.4 CONTROL ROD ACTUATION SUBSYSTEM

7.4.4.1 Description

This subsystem was a servo loop common to the reactor startup and power range control subsystems. It positioned the control rods as required to satisfy the reactor power level demand. The subsystem consisted of eight separate position loops operated in parallel with a common position demand. Each loop compared its rod-position feedback signal with the demand. The resulting error regulated a control-rod-actuator servo valve and air motor and positioned the actuators. All actuator positions were properly synchronized when the actuators were on automatic control, and were within 0.6 inch of the demanded position.

A mode selector switch for each actuator allowed an actuator to be (1) inoperative (off), (2) controlled by the automatic flux or temperature loops (servo), or (3) manually controlled (manual). Each actuator could be operated either closed loop (servo) or manually. Any number of actuators (1 to 8) could be manually positioned at one time.

Each actuator drove a mechanically ganged group of six rods. Only one type of actuator was used, as contrasted to the three functionally different actuators used in the D141A-1 control system and described in section 2.3.10.1. It performed two functions, shim and scram. The shim mode was accomplished by a gear-type air motor and a servo valve in combination. The scram mode was accomplished by clock-type springs that were wound by the air motor and were automatically recocked and latched by fully inserting each actuator and clearing the scram bus.

The shim rate was proportional to the position-loop error signal with a maximum shim rate of 7.7 inches per minute. During scram the rods traveled the first 5 inches in 300 milliseconds and the remainder at a velocity not less than the maximum shim speed. An additional 40 milliseconds were allotted for release time of the actuator latch.

Each actuator assembly consisted of a power-head assembly, a transfer gear box with six output drive shafts, and six chain-drive assemblies. The 8 power-head and transfer-box assemblies were mounted external to the engine on the compressor rear flange. The 48 chain-drive assemblies were located within the front shield and drove the control rods. The guide-tube in which the control rod moved was an integral part of the chain-drive assembly.

Figure 7.28 is a mechanical schematic of a control rod actuator assembly, and Figure 7.29 is a pictorial representation. Electrical position feedback was provided for both control circuitry and data recording. Limit switches were provided at the ends of travel of the power head. The control rod actuator assembly is discussed in detail in reference 19.

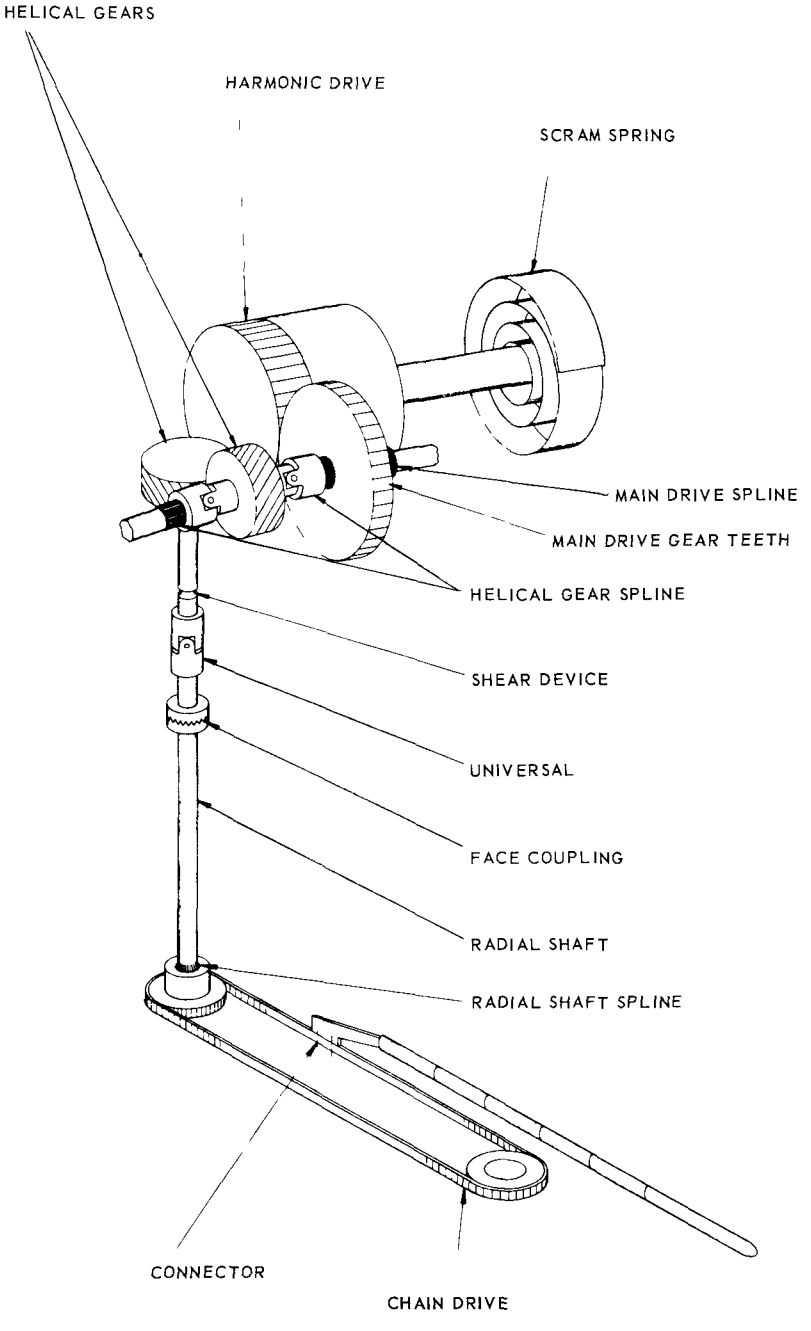

Fig. 7.28 – Mechanical schematic of control rod actuator assembly Dwg. 737D725

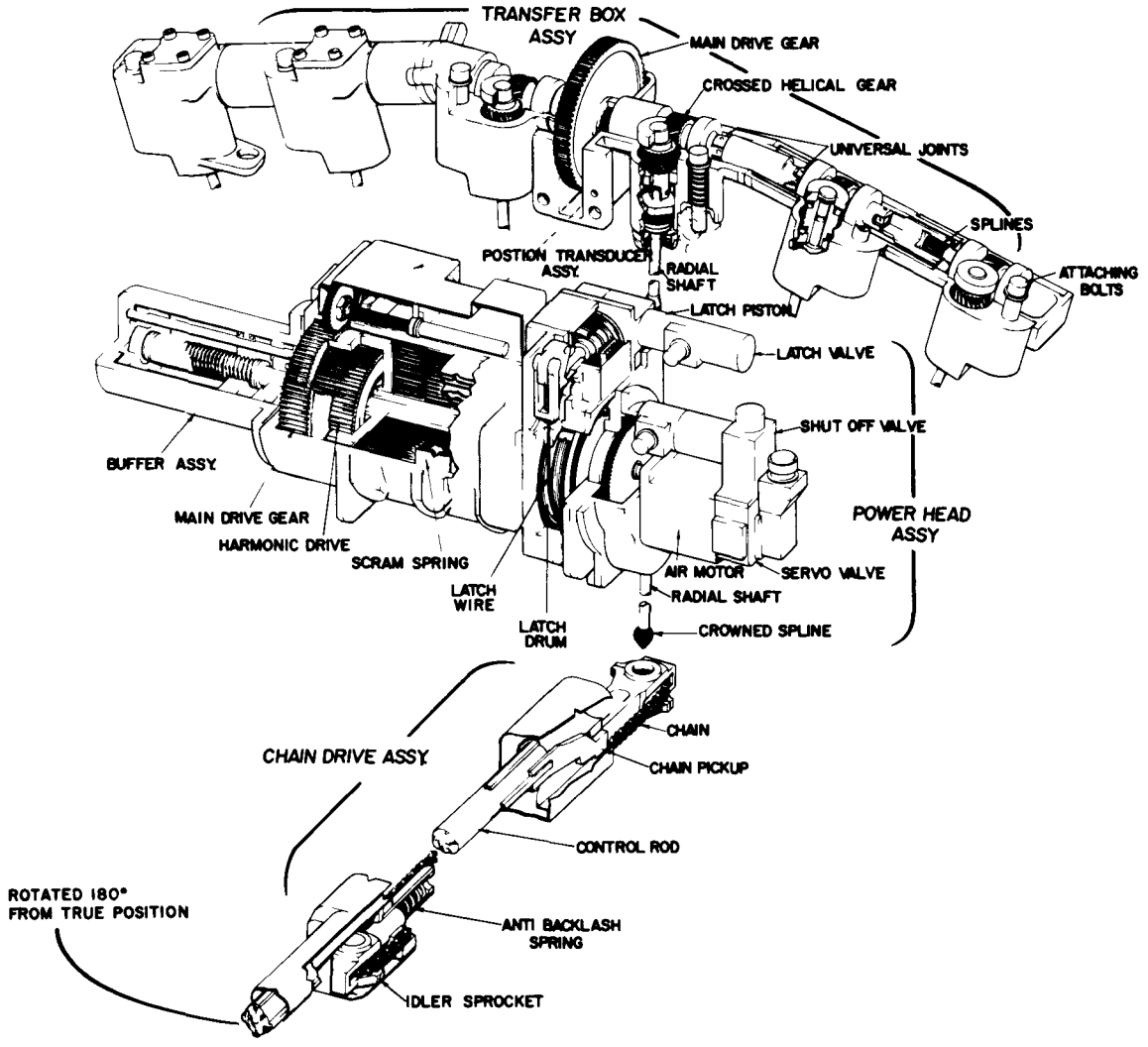

Fig. 7.29 – Control rod actuator assembly Dwg. D.I. 564

7. 4. 4. 2 Circuitry

The circuitry included the following significant components:

1. A position-error amplifier which received demand signals from either the startup range subsystem (period-error amplifier) or the power range subsystem (flux-error amplifier), amplified this signal, and furnished a driving voltage to the servo air valves.
2. A demodulator which received an a-c signal from the control-rod-position transducer, demodulated this a-c voltage, and furnished a proportional d-c signal to the position-error amplifier to null the demand signal.
3. An actuator mode switch to provide selection of either manual or servo mode of rod control.
4. Additional switching to provide for rod withdrawal or insertion when operating in the manual mode.

The over-all circuitry was shown in Figures 7. 10 and 7. 27. Figure 7. 30 is a block diagram of the rod-position loop. This loop kept all control rods in the same longitudinal position during the automatic control mode. The input signal windings of the eight positon-

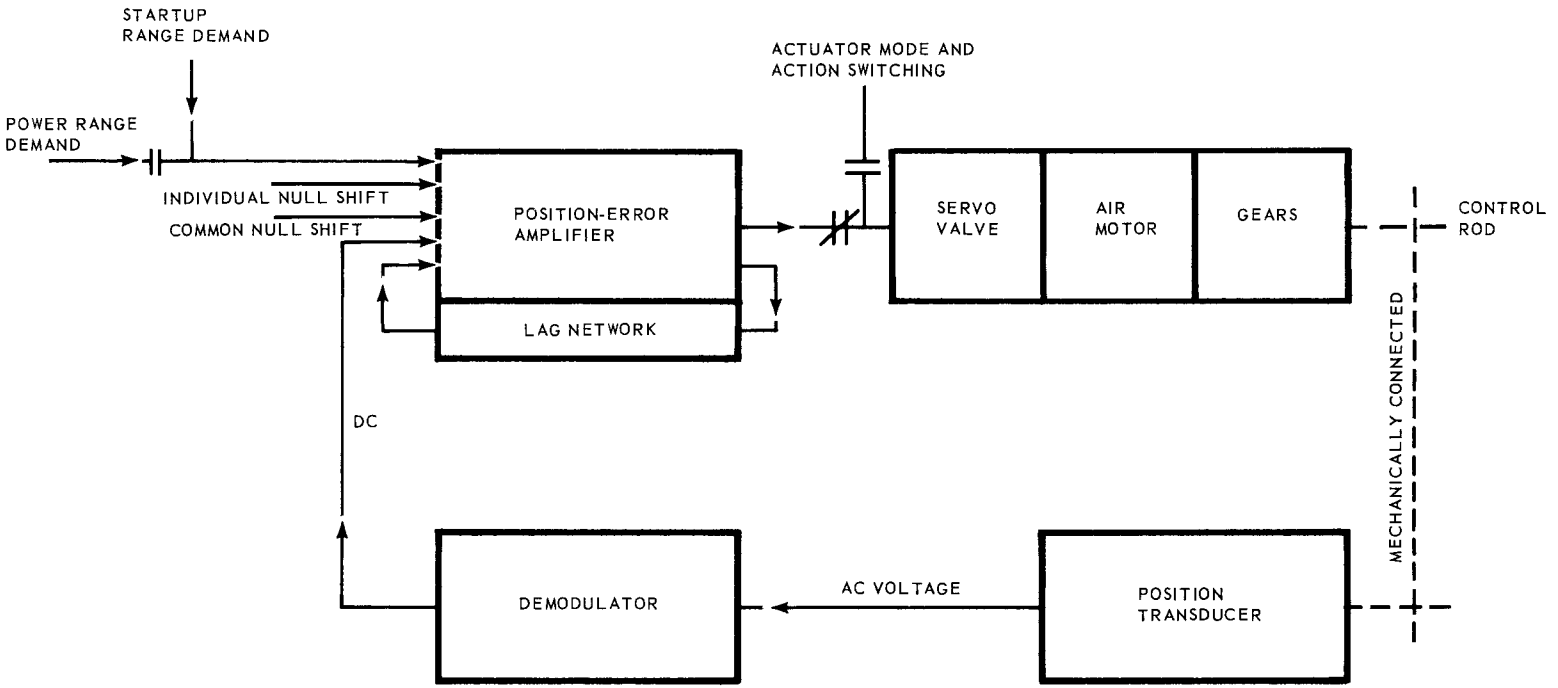

Fig. 7 30 – Rod-position loop schematic

error amplifiers were connected in parallel so that the same demand signal was common to all amplifiers. An adjustable bias arrangement (null shift control) was provided for each amplifier so that the output to the servo valves could be varied ±2. 0 milliamperes. An additional adjustable input of ±4. 8 milliamperes (±0. 6 milliampere per amplifier) was provided and, as was the case of the input signal, was common to all eight position-error amplifiers. In the absence of a signal to the input windings, this common input caused the actuators to withdraw 1 inch from full insertion.

Position Transducer Assembly - The position transducer assembly was mounted on, and driven by the power-head assembly. It contained two identical transducers, the position feedback transducer and the position indication transducer. The transducers provided a null signal at the travel midpoint with a full-voltage (400-cycle ac) signal at both ends of the stroke.

Position-Error Amplifier - This amplifier was a standard full-wave push-pull center-tapped amplifier. It incorporated a lag network in the feedback circuit to provide a response of less than 45 degrees phase shift at 70 radians per second in order to meet loop response requirements.

Demodulator - A ring-type demodulator was employed in the feedback of the position loop. It received an a-c signal from the position transducer, demodulated this signal, and furnished a proportional d-c output signal to the position-error amplifier. An attenuator, electrically located between the demodulator and the position-error amplifier, provided an adjustable a-c gain for the demodulator and the position loop.

7. 4. 4. 3 Power-Head Assembly

This assembly contained a servo valve, shutoff valve, air motor, gear reducer, scram spring latch, scram springs, scram-spring-cocked switch, position transducer, limit switches, and associated air and electrical connectors. The air motor, controlled by the servo valve, ran between 850 and 8500 rpm in either a clockwise or counterclockwise direction. This speed was reduced by a combination of spur gears and a differential-gear unit. The output gear rotated at speeds from 0. 2 to 2. 04 revolutions per minute during operation in the shim mode; in the scram mode the output gear accelerated rapidly. The rotation of the output gear was 6. 37 revolutions for full rod stroke.

The scram springs were cocked by running the air motor in the rod-insert direction with the output gear at its lowest rate of travel. When the scram springs were fully cocked, a switch was activated which stopped the air motor and also energized a solenoid valve that applied air pressure to a latching mechanism. The actuators then could start control rod withdrawal in the shim mode.

The reactor was scrammed by interrupting the holding current to the solenoid valve. Loss of air pressure also initiated a scram. These actions allowed the scram springs to drive through the differential gear box to the output gear. A dashpot controlled the maximum rotational velocity reached during a scram and absorbed energy at the end of travel. Gear reduction for the scram phase of the operation was 1:1. When scram was initiated, the drive-head output gear rotated 480 degrees, or 1-1/3 revolutions, in 300 milliseconds. The rotation started within 40 milliseconds after the scram signal was received by the drive head.

The power-head assembly delivered a torque of 319 pound-inches continuously at 2. 04 output revolutions per minute, and could deliver a torque of 408 pound-inches for one 2-minute interval every 2 hours.

The power-head assembly is discussed further in references 20 and 21.

7.4.4.4 Transfer Gearbox Assembly

This assembly was a 1:1 ratio gearbox which divided and distributed the output of the power-head assembly to six chain-drive assemblies, Figure 7.31. It consisted of a spur gear coupled by shafts, universal joints, and splines to six 45-degree helical gears. Each of the six helical gears was mounted in a separate housing of the structure and meshed with a second 45-degree helical gear to provide an output drive shaft at right angles to the input shaft. Each output shaft drove a universal joint and a multi-jaw coupling which, in turn, drove a second multi-jaw coupling attached to radial shafts. The radial shafts then drove the chain-drive assemblies through a crown-tooth spline. Each gear train contained mechanical shear sections. An electrical indicating device showed when a shear section had failed.

The assembly is discussed further in reference 22.

7.4.4.5 Chain-Drive Assembly

This assembly resembled a bicycle-type chain suspended between two sprockets located in the front shield. Each assembly was connected to a control rod by means of a push rod. Revolving the front sprocket of the chain-drive assembly by means of the radial drive shaft connecting the chain-drive assembly and transfer gearbox assembly resulted in axial movement of the control rod. The total travel was 24 inches, and ranged from the forward face of the active core to a point 24 inches aft.

The equilibrium load was 20 pounds, equivalent to a 20-pound-inch input torque, but the assembly was capable of absorbing an input torque of 300 pound-inches without failure. The maximum speed during shimming was 2.04 revolutions per minute, and drive could accelerate to 1500 revolutions per minute during scramming operation without failure.

The assembly could operate for 1000 hours, without overhaul or adjustment, under the following conditions:

1. Air pressure, 265 psia, maximum
2. Temperature, -65° to 1000°F with a maximum gradient of 300°F over the length of the chain
3. Nuclear radiation, 10^{12} rads total dose
4. Misalignment, 3/16-inch misalignment between the front shield and the core, in any direction.

Figure 7.32 shows an experimental chain-drive assembly used during developmental testing. The final design had not been specified at the time of contract termination. Reference 23 details the design of these assemblies.

7.4.4.6 Power Supplies

Four types of electrical power were required by the reactor control system; (1) 115 volts, 400 cycles, ac; (2) 115 volts, 60 cycles, ac; (3) 28 volts, dc, and (4) 1500 volts, dc.

115-volt, 400-cycle Power - This power was used for excitation in magnetic amplifiers in both the startup and power range subsystems. It was obtained from either the engine-driven alternator or the facility substation; a transfer switch was used to select the source. Voltage-limiting transformers were used immediately downstream of the alternator to limit the voltage within +10 percent in event of malfunctions. The voltage variation did not exceed ±3 percent of the nominal operating voltage for slowly varying deviations; transient variations did not exceed ±5 percent. The frequency variation did not exceed ±2 percent of the nominal operating frequency for slowly varying deviations; transient variations did not exceed ±10 percent.

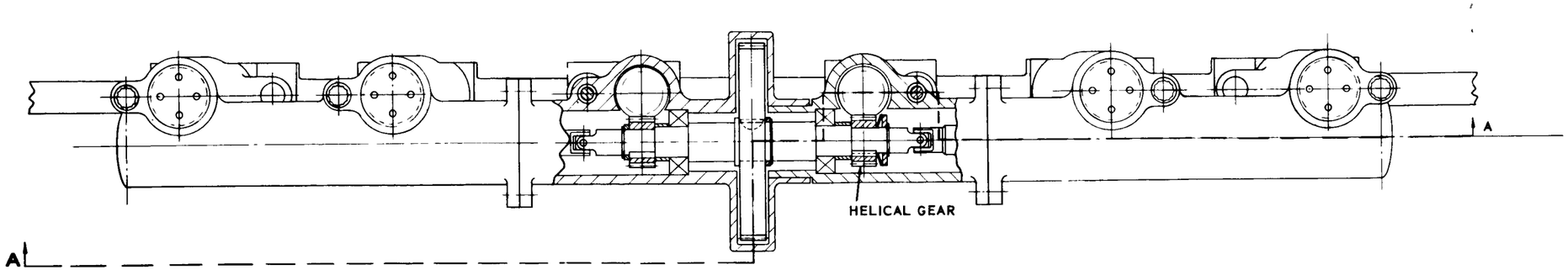

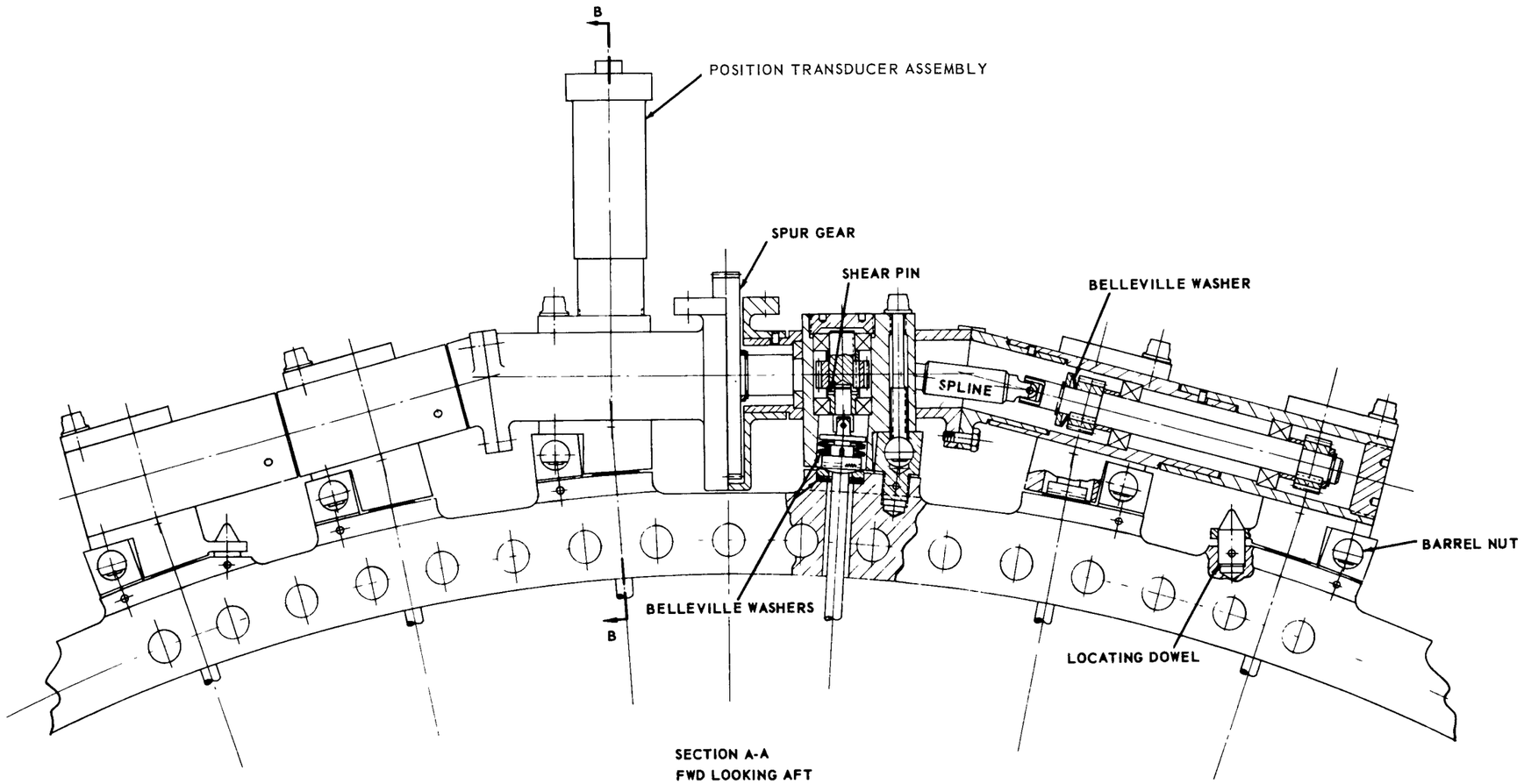

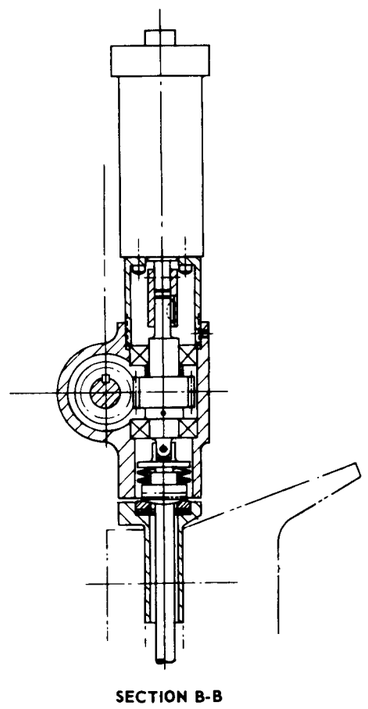

Fig. 7.31 – Transfer gearbox assembly

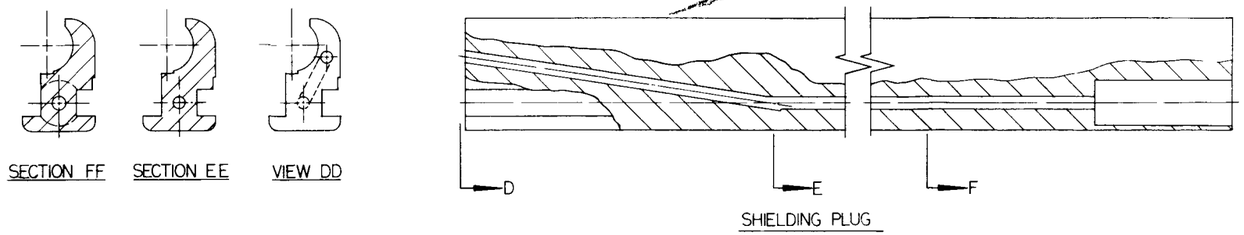

Fig. 7.32 – Experimental chain drive assembly (Dwg. 628E977)

115-volt, 60-cycle Power - This power was used only for excitation of the micromicroammeter, and was supplied from the facility substation.

28-volt d-c Power - This power was used to operate relays, solenoids, and the rod actuator latches. It was supplied from the facility substation, and did not deviate from the nominal operating voltage by more than ±5 volts.

1500-volt d-c Power - This power was obtained from power supplies operating from the 400-cycle-per-second bus bar. There were three supplies: two supplies had voltage regulation adequate for normal control system operation; the third had superior voltage regulation suitable for use with the ionization chambers and the micromicroammeter during subpower range operation. The first two supplies fed a 1500-volt bus through auctioning diodes and operated two safety subsystem ionization chambers. Only the +1500-volt power was used. The power supplies could be continuously operated at 200 percent of the maximum anticipated load without exceeding their ratings. No adjustment was provided which would allow the voltages to be set above the safe operating region of any component using the supply. The voltage did not deviate more than ±275 volts from 1500 volts.

Each power supply consisted of two parallel units. Each unit contained a three-phase stepup transformer and a full-wave bridge rectifier and could deliver 65 milliamperes at an ambient temperature of 100°C with an output ripple of 4.2 percent. The outputs were added through high-voltage blocking diodes so that either unit could fail but the supply would still deliver rated ionization chamber current. A one microfarad capacitor was connected across the combined output as a filter to reduce ripple from 4.2 percent to 0.1 percent. The over-all dimensions of each supply were 4 inches by 6 inches by 9-1/2 inches. Additional data are contained in reference 15.

7.4.4.7 Electrical References

Constant-current d-c and constant-voltage a-c signals were supplied for component calibrations and adjustments.

Constant-Current d-c References - Constant-current d-c references were obtained from power supplies fed from the 400-cycle-per-second bus bar. Each reference was an ultrastable 50-milliampere constant-current generator. The basic specifications were as follows:

Constant current	30 to 150 milliamperes
Line supply	115 volts, ac, 400 cycles per second
Output voltage	90 volts maximum
Output current	150 milliamperes maximum
Load resistance	0 to 1500 ohms
Regulation (room temperature)	0.02 percent
Regulation (-65° to 125°C)	0.09 percent

Changes in line voltage of ±20 percent, line frequency of ±10 percent, load resistance from 0 to 1500 ohms, and temperature from -65° to 125°C did not affect the output by more than 0.08 percent.

The principal components of these references were: (1) saturable reactor, (2) zener diode bridge reference, and (3) high-gain magnetic amplifier. The saturable reactor supplied a current to a load in series with a resistor. The voltage developed across this resistor was compared to the zener diode output voltage. Any difference was amplified by the high-gain amplifier and its output was used to correct the output of the saturable reactor; the saturable reactor established an output level by self bias. Additional information is contained in references 15 and 24.

Constant-Voltage a-c References - The constant-voltage a-c references were obtained from regulators operating from the 400-cycle bus bar. These references were used for rod position transducer excitation, demodulator references, and demand transducer excitation. The basic specifications were as follows:

Voltage output	12, 24, and 37 volts ac at 1.0 amperes, 400 cycles per second
Line supply	115 volts, 400 cycles per second
Load	50 milliamperes dc from d-c reference
Regulation	0.3 percent

The circuit consisted of a gated primary stepdown transformer with gating effected by an amplifier which, in turn, was driven by an error amplifier. The error consisted of the difference between the 50-milliampere d-c reference and a rectified sample of the transformer output. The circuit was a closed-loop wherein the 50-milliampere d-c reference acted as a fixed demand. Additional information is contained in reference 15.

7.5 SAFETY SYSTEM

7.5.1 DESCRIPTION

The over-all safety system protected the engine from damage if failure occurred in any control system component. In addition, it also prevented improper operator action where such action could lead to a dangerous condition. An extensive reactor safety system was required because of the high power levels and rapid response characteristics inherent in nuclear reactors.

Because the engine was intended for ground test operation, safe operation was considered more important than continuous operation. Wherever possible the system was designed so that components "failed-safe," i.e., failed in a manner that resulted in a safety action. As a result of this philosophy, the operational reliability (ability to operate continuously) was decreased while the safety reliability (ability to protect the engine) was increased. Failure of any single component could not lead to reactor damage.

Four distinct safety actions were provided. These were alarm, scram, shutdown, and overspeed limiting during CHO. The alarm action provided indication to the operator that an abnormal condition existed, but no automatic corrective action was taken. Alarm actions were provided when certain parameters exceeded preset levels and when critical power supplies deviated from preset bounds. The scram action was rapid insertion of control rods into the reactor, and resulted in an abrupt reduction of the reactor power level at the fastest possible rate. The shutdown action was abrupt, complete shutdown of the engine; it included (1) scramming the reactor, (2) stopcocking fuel flow (if chemical fuel was being used), and (3) providing aftercooling-air. Shutdown always resulted in scram, and scram resulted in shutdown except when the reactor power level was less than 3.5 percent of full power. The fourth safety action was the reduction of chemical fuel flow by the chemical fuel overspeed governor to limit engine speed.

Several interlocks that insured proper sequencing of events between control and accessory systems were provided. Improper operator action was prevented by the use of interlocks in the compressor stator position control subsystem, in the rotor-lock loop, and in the compressor shutoff-door loop.

Further details of the safety system are contained in references 3, 9, 18, 19, 25, 26, and 13.

7.5.2 CIRCUITRY

7.5.2.1 Over-all System

A functional block diagram of the reactor control system was shown in Figure 7.10. Figure 7.11 showed the functional code letters used in Figure 7.10. A functional block diagram of the safety system is shown in Figures 7.33a through 7.33d. The functional code lettering identified in Figure 7.11 also applies to Figure 7.33.

7.5.2.2 Alarm

The alarm system provided indication to the operator that an abnormal condition existed, by lighting a warning light to indicate the source of the alarm. These alarm lights were located on either the operator's console or the secondary panels; those on the operator's console were located either on an annunciator panel or near the meters that monitored the sensed parameter. An energized light was not de-energized until the individual alarm source cleared, at this time the light was self-clearing.

Alarm lights displayed on the operator's console are listed in Table 7.3. Alarm lights displayed on the secondary panels are listed in Table 7.4. Alarm lights for selected FET supplied services were also displayed on the secondary panels as listed in Table 7.5. Table 7.6 lists the ranges and alarm point settings for several parameters leading to alarm actions on the secondary panels.

7.5.2.3 Scram

Scram action was the rapid insertion of the control rods into the reactor, and resulted in abrupt reduction of reactor power level accompanied by the lighting of an indicating light that identified the cause of the safety action. A distinction was made between a reactor scram that occurred above a reactor power level of 3.5 percent of full power and one that occurred below this level in that complete engine shutdown was performed only when the reactor was scrammed from the higher level. The safety system supplied the logic that determined the shutdown procedure.

The events that occurred during reactor scram were:

1. Shutdown was initiated if the reactor power level was above 3.5 percent of full power.
2. Control rods were rapidly inserted.
3. Aftercooling blowers automatically advanced from idling to operating speed.
4. A light on the operator's console was energized, indicating the reason for the scram. Two master scram lights on the operator's console also were energized.

The safety violations and indicating lights causing reactor scram are listed in Table 7.7. All indicating lights were located on the operator's console.

7.5.2.4 Shutdown

The events that occurred during engine shutdown were as follows:

1. The reactor was scrammed.
2. Fuel flow was stopcocked.
3. The fuel pump was declutched.
4. The fuel circulating pump was stopped.
5. Bleed-speed valves were closed without overspeed.
6. The starter engaged when engine speed fell below approximately 1450 rpm. (The starter air supply was assumed to be on the line.)
7. Aftercooling blowers automatically advanced from idling to operating speed.
8. A light on the operator's console was energized, indicating the reason for the shutdown. Two master shutdown lights on the operator's console also were energized.

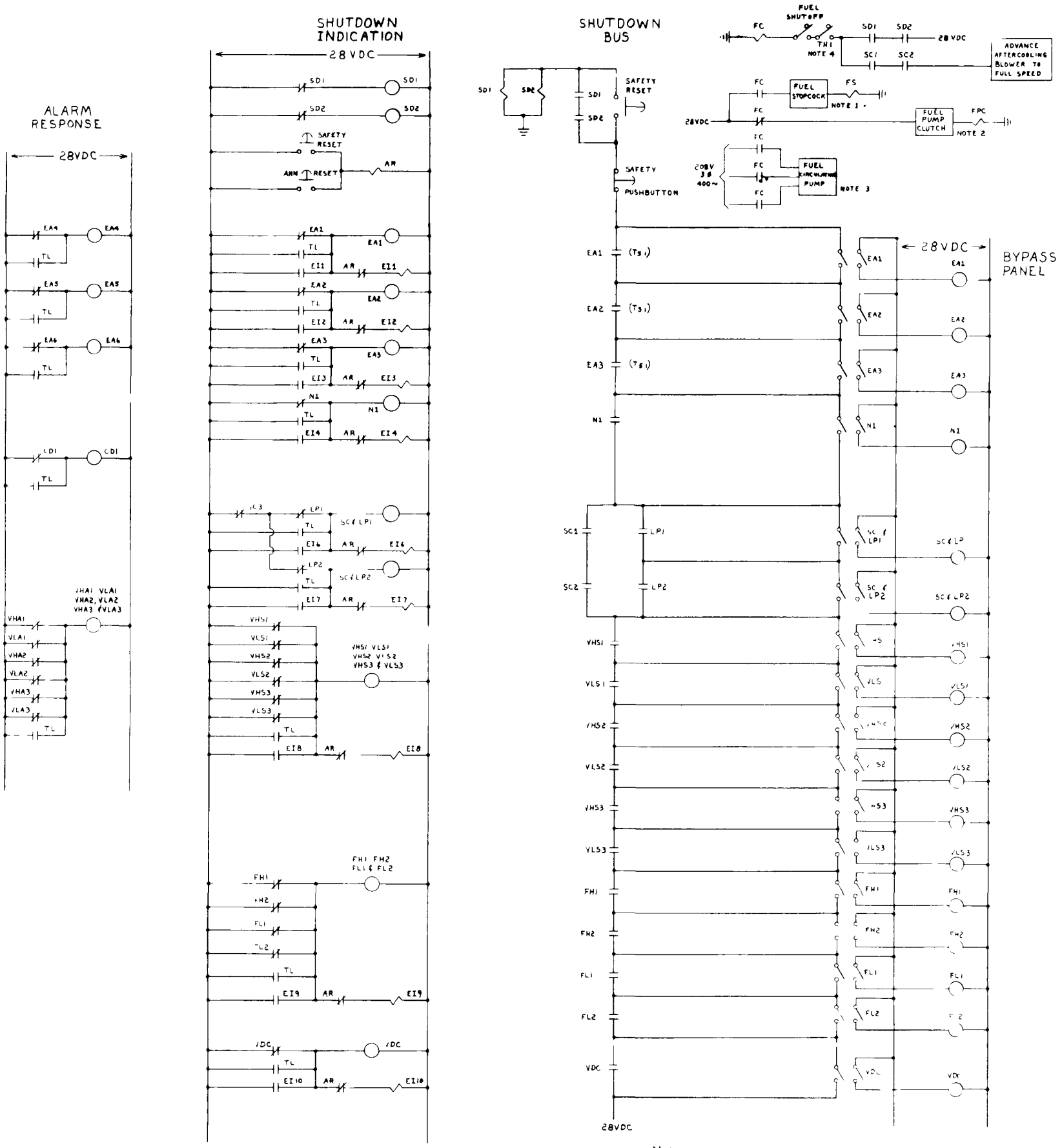

Notes:

1. Fuel is stopcocked when power is off
2. Fuel pump is declutched when power is on
3. Fuel circulating pump is off when power is off
4. Operator's initiation (throttle in off position – limit switch)

Fig. 7.33a – Safety system (Dwg. 682E862, Sh. 1)

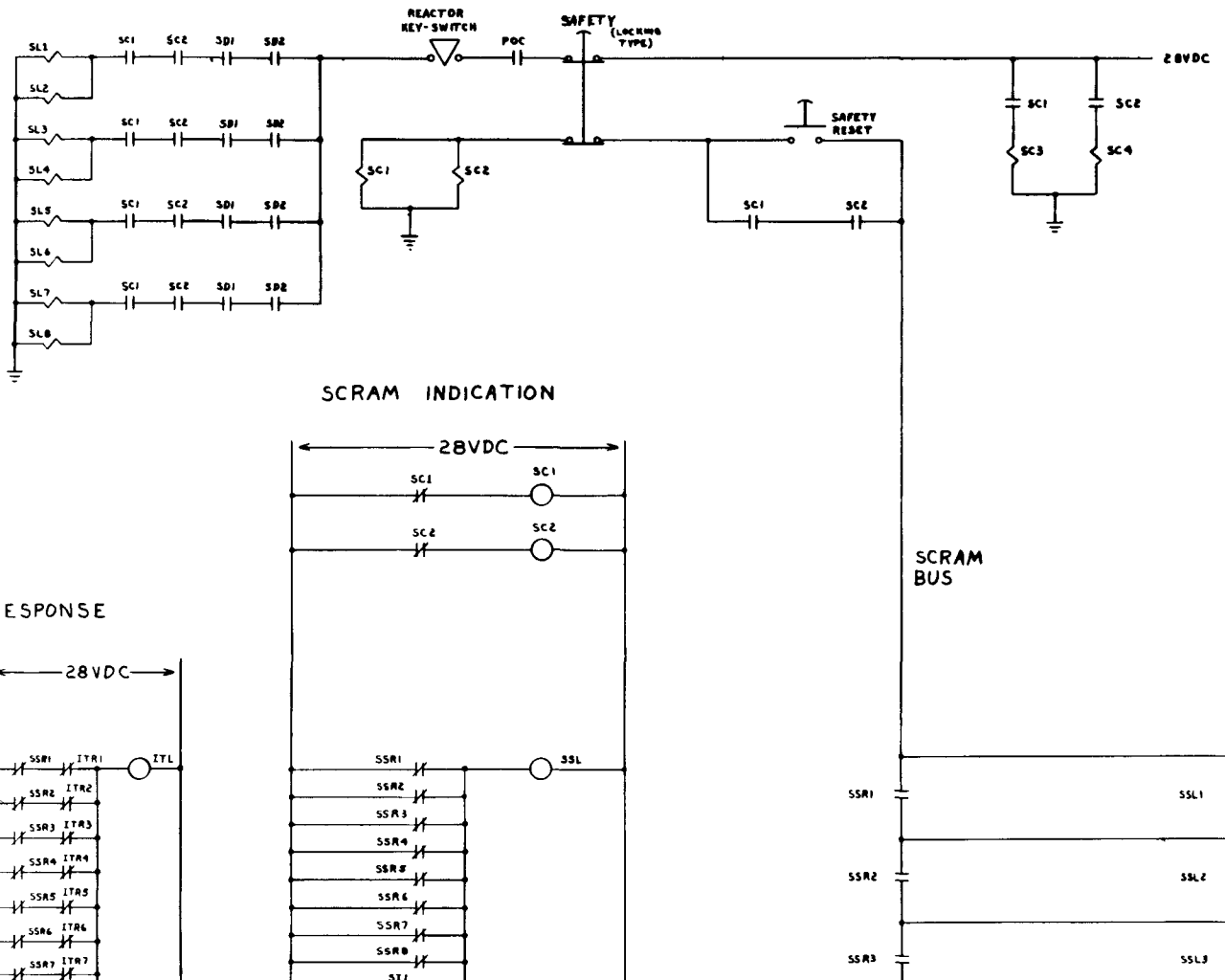

Fig. 7.33b – Safety system (Dwg. 682E862, Sh. 2)

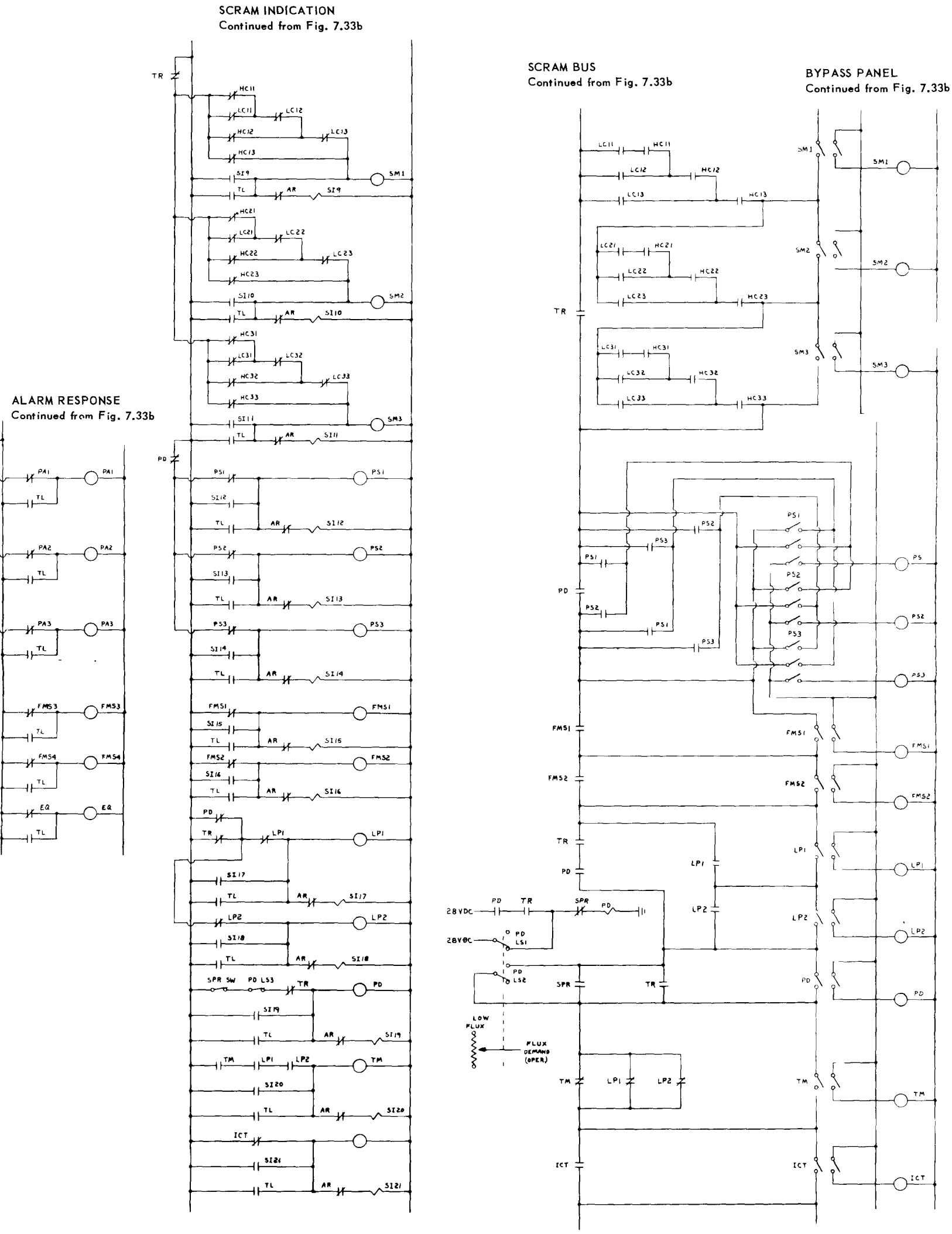

Fig. 7.33c – Safety system (Dwg. 682E862, Sh. 3)

ALARM RESPONSE
Continued from Fig. 7.33c

SCRAM INDICATION
Continued from Fig. 7.36c

SCRAM BUS
Continued from Fig. 7.33c

BYPASS PANEL
Continued from Fig. 7.33c

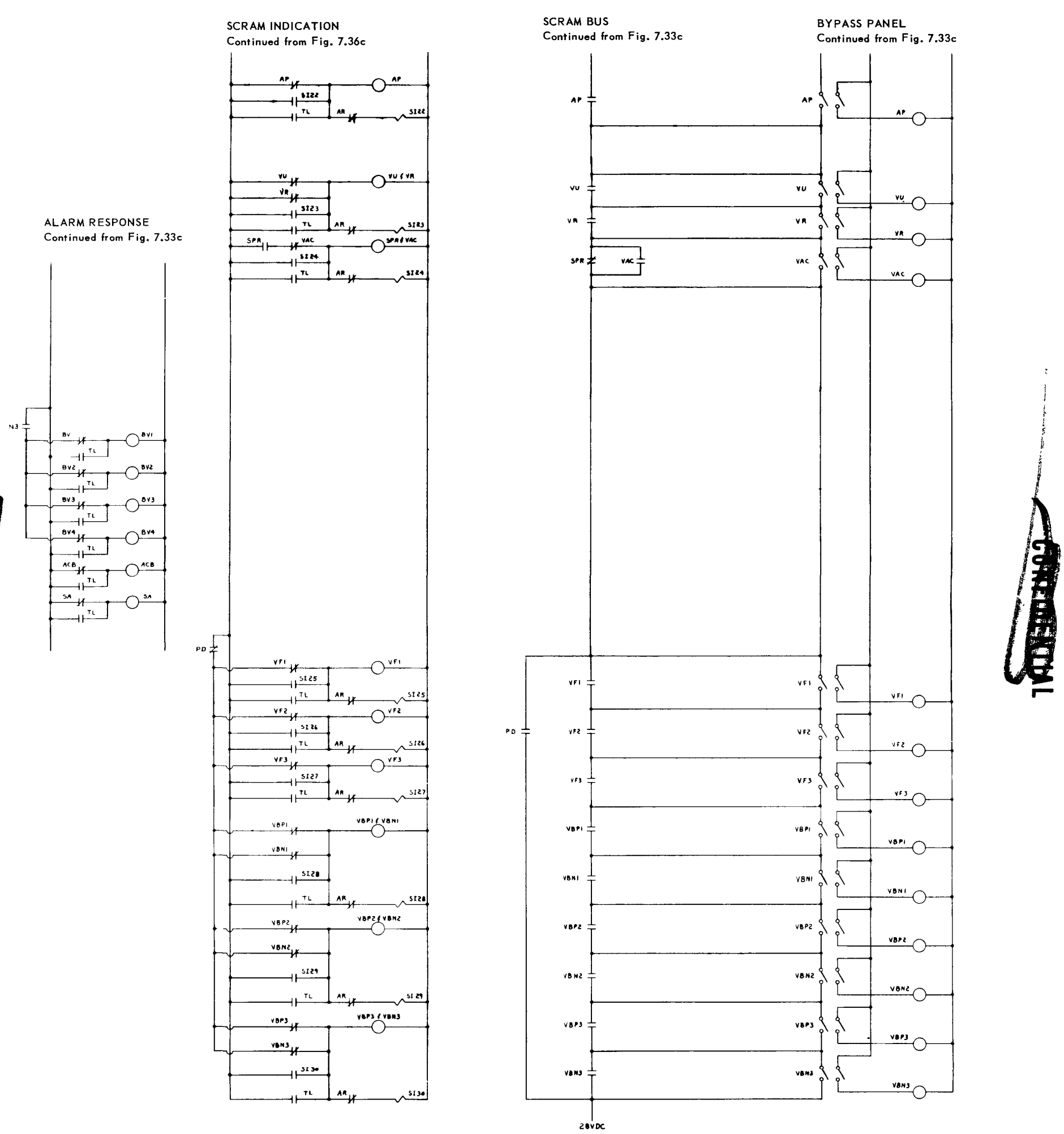

Fig. 7.33d – Safety system (Dwg. 682E862, Sh. 4)

TABLE 7.3

ALARMS INDICATED ON OPERATOR'S CONSOLE

Parameter	Violation Causing Alarm	Number Of Trips	Number Of Lights
1. Turbine discharge-air temperature ($T_{5.1}$)	$T_{5.1}$ within 50°F of shutdown trip level	3	3
2. Fuel element surface temperature (T_S)	T_S within 50°F of scram level	3	3
3. Engine bleed-speed valves	Bleed-speed valves open and speed below 1500 rpm	4	4
4. Aftercooling-air blowers	Not functioning properly	a	a
5. Starter air supply	Failure of air supply	1	1
6. Reactor period	Reactor period shorter than 10 seconds	3	3
7. 400-cps power supply voltage	Voltage on any phase deviated more than ±5% from nominal	6	1
8. Facility monitor	Excessive flux level or excessive effluent level	2	2
9. Reactor-control-system continuity	Any chassis removed from equipment racks	1	1
10. Control-rod-actuator withdrawal travel limits	Any actuator at withdrawal travel-limit stops	8	1
11. Control-rod-actuator insertion travel limits	Any actuator at insertion travel-limit stops with uncocked scram springs	8	1

[a]Not established at time of contract termination.

TABLE 7.4

ALARM LIGHTS DISPLAYED ON SECONDARY PANELS

1. B Racks
   Alarms indicated on the operator's console were repeated on racks B-3 and B-4, but with only one light for a group in a single parameter. Eight alarms in rack B-2 were made available to the limit switches on the 24 single-point recorders.
2. C Racks
   Temperature, reactor discharge air
   Temperature, control rod guide tube discharge air
   Temperature, aft-retainer assembly cooling air
3. D Racks
   Inlet temperature, nozzle actuator hydraulic-fluid heat exchanger
   Inlet temperature, stator and bleed-speed-valve actuators hydraulic fluid heat exchanger
   Temperature, engine shaft
   Discharge temperature, fuel pump
   Discharge pressure, lube oil pump
   Pressure differential, nozzle hydraulic-fluid pump
   Pressure differential, stator and bleed-speed valve hydraulic-fluid pump
   Fluid level, each of 2 hydraulic-fluid reservoirs
   Bearing temperature, as selected
   Axial position, turbine rotor
4. E Racks
   Discharge pressure, starter lube oil pump
   Discharge temperature, starter lube oil pump
   Pressure, starter clutch lube oil
   Discharge temperature, CSD fluid
   Discharge pressure, CSD fluid
   Discharge pressure, facility cooling-oil boost pump
   Oil level, lube oil reservoir
   Inlet temperature, lube oil system
   Discharge pressure, lube oil system boost pump
   Low voltage, 400 cps a-c supply

TABLE 7.5

FACILITY SERVICE ALARMS INSTALLED
IN SECONDARY PANELS

1. Rack CBE2
   - Contaminated waste tank, 2/3 full
   - Contaminated waste tank, full
   - Air compressor AC101, failure
   - Instrument air system, low pressure
   - Sump pump SP 103, on - off
   - Sump pump SP 105, on - off
   - Sump pump SP 108, on - off
   - Spare

2. Rack CBE3
   - Tunnels, combustible gas
   - Coupling station, combustible gas
   - Fuel pump room #1, combustible gas
   - Fuel pump room #2, combustible gas
   - Engine fuel tank Tk 113A, low level
   - Engine fuel tank Tk 113B, low level
   - Engine fuel system, low or high pressure
   - Spare

3. Rack CBE4
   - Spares (8)

4. Rack CBE5
   - Cooling water supply line, high temperature
   - Cooling water system, low pressure
   - Primary power, failure
   - Emergency power, failure
   - Diesel cooling water pump 108B, failure
   - Spares (3)

5. Rack F5
   - Area monitor system
   - Rupture detector, alarm
   - Rupture detector, scram
   - Spray water
   - Spares (4)

TABLE 7.6

RANGE AND SETTING OF SELECTED ALARM PARAMETERS DISPLAYED ON SECONDARY PANELS

Parameter	Light Setting		Audible Warning Point Setting	
Fuel element surface temperature	700°-2800°F	(3)[a]	50°F below scram	(3)
Turbine discharge-air	700°-1500°F	(3)	50°F below scram point	(3)
Flux level (high)	15-150%	(2)	None	
Flux level (high)	150%	(1)	None	
Flux level (low)	3-1/2% (if armed)	(2)	None	
Switching monitor	Any channel open	(3)	None	
Period (startup range only)	5 second - 2 out of 3 coincidence (if armed)	(3)	10 sec - any channel (if armed)	(3)
Engine speed	105% N	(1)	None	
Temperature mode (low power)	Both low-power trips unoperated	(1)	None	
Facility monitor	Provided by FET system	(2)	Provided by FET	(2)
Low rod actuator pneumatic pressure	70-90%	(1)	None	
Flux demand	Positioned above 1.5% FP with 1.5% FP transfer relay unoperated (if armed)	(1)	None	
400-cycle a-c voltage	±10%	(1)	±5%	(1)
400-cycle a-c frequency	±10%	(1)	None	
28v d-c bus	- 6 volts	(1)	None	
1500v d-c bus	- 300 volts	(1)	None	
±200v d-c bus (startup only)	20v decrease (if armed)	(3)		
280v d-c bus (startup only)	30 volts decrease (if armed)	(3)	None	
60-cycle a-c voltage	-10% (micromicroammeter operation only)	(1)	None	
Pre-operationan checkout	Connector plug uncovered	(1)	None	
Key switch	Unoperated	(1)	None	
Equipment continuity	None		Any interlock open	(1)
Control rod actuator	Unlatched	(8)	None	
Control rod actuator	None		Insert travel limit	(1)
Control rod actuator	None		Withdraw travel limit	(1)
AHR system	None		Failure of any after-cooling blower	(1)
Starter-air supply	None		Low air pressure	(1)
Bleed-speed valve	None		Bleed-speed valves open at low engine speed	(4)
Ion-chamber-cable continuity	Cable improperly connected	(1)	None	

[a]Numbers in parentheses indicate total number of circuits and signals for each parameter.

TABLE 7.7

VIOLATIONS CAUSING SCRAM[a]

Parameter	Violation	Number Of Trips	Number Of Lights
1. Operator initiation	Operate SCRAM pushbutton	1	0
2. Shutdown	Shutdown caused scram	2	2
3. Scram springs not fully cocked	Scram springs on any of eight actuators not fully cocked	8	1
4. Fuel element temperature	Temperature exceeds trip level, adjustable, 700° to 2800°F	3	3
5. Neutron flux level	Flux level exceeds trip level, adjustable, 15 to 150% of full power	2	2
	Flux level exceeds trip level, fixed trip at 150% of full power	1	1
	Flux level exceeds 3.5% of full power prior to movement of flux demand above 1.5% of full power	2	2
6. Reactor period	Period less than 5 seconds prior to movement of flux demand above 1.5% of full power	3	3
7. Switching monitor	Any of nine source-range instrumentation channels or control-ion-chamber channel open when in use	10	3
8. Facility monitor	Excessive flux level or excessive effluent level	2	2
9. Flux demand dial improperly positioned	Flux demand set above 1.5% of full power prior to achieving 1.5% full power	1	1
10. Control mode selector improperly positioned	Selector set on TEMPERATURE prior to achieving 3.5% of full power	2	1
11. Control-ion-chamber cable improperly positioned	Cable transfer switch and subpower-range switch not in agreement	1	1
12. Preoperational checkout device	Checker inserted into control circuitry	1	1
13. Control-rod-actuator air supply	Pressure drops 30% below nominal pressure	1	1
14. 400-cps power supply voltage	Voltage on any phase deviates more than ± 10% from nominal	6	1
15. 400-cps power supply frequency	Frequency deviates more than ± 10% nominal	4	1
16. 28-v d-c power supply	Voltage drops 6 volts below nominal	1	1
17. Ion-chamber power supply voltage	Voltage drops 300 volts below nominal	2	1
18. Fission-chamber power supply voltage	Voltage drops 30 volts below nominal prior to movement of flux demand above 1.5% of full power	3	3
19. Source-range reference power supplies	B+ drops 20 volts below nominal or B- drops 20 volts below nominal prior to movement of flus demand above 1.5% of full power	6	3
20. 60-cps power supply	Voltage drops 10% below nominal and subpower-range switch at ON position	1	1

[a]This tabulation was applicable when the subpower-range switch was in the OFF position. When the subpower-range switch was in the ON position, the above tabulation was applicable with the following exceptions:

1. Item 5, 3.5% of full power trips were effective at all times.
2. Item 6, period trips were effective at all times.
3. Item 9, operator could move flux demand dial at any time.
4. Items 18 and 19, voltage trips were effective at all times.

Safety violations causing engine shutdown and their indicating lights are listed in Table 7.8. All indicating lights were located on the operator's console.

7.5.2.5 Overspeed Limiting

This action was a safety feature during chemical operation of the engine and occurred at 101.5 percent N. No significant circuitry details were involved.

7.5.3 MECHANIZATION

Mechanization of the safety system was based on using state-of-the-art components in conventional applications, and is discussed in references 25 and 28. Several safety trip circuits are discussed below because of their specialized application.

7.5.3.1 Power Safety Circuits

The power safety circuits shown in Figure 7.34 included safety trips for low voltage a-c and d-c supplies, a-c frequency, and the reference voltage and current.

+28-Volt d-c Trip - The +28-volt d-c trip had its trip point set at 22 volts nominal with a possible deadband of 3 volts. The safety relay was energized when the voltage was above 22 volts. Experimental results showed that this circuit was overdesigned and some simplification could be effected to reduce cost and improve reliability. However, the zener-diode scale-expansion technique was removed and the circuit did not meet requirements. The complete circuit of this trip is shown in zone A4, Figure 7.34.

+200- and -100-Volt d-c Trips - These trip circuits were the same as the +28-volt d-c trip except that the control windings were reversed. The +200-volt d-c trip circuits were set at 180 volts nominal with a permissible deadband of 10 volts. Experimental results showed that a line variation of ± 10 percent changed the trip point by only 0.8 volt. The deadband maximum was found to be 2.1 volts, dc, and the time constant to trip was 50 milliseconds.

+280-Volt d-c Trip - This trip circuit is shown in zone A3, Figure 7.34. It was identical to the +28-volt and +200-volt d-c trips, with the exception of the voltage-dropping resistor. The trip point was set for +250 volts nominal and the permissible deadband was 15 volts. The relay was energized whenever the parameter was in the proper range. Experimental results showed that the error of the trip point was 0.8 volt for a voltage variation of ± 10 percent. The maximum deadband was 2.7 volts and the time constant to trip was 50 milliseconds.

TABLE 7.8

VIOLATIONS CAUSING SHUTDOWN

Parameter	Violation	Number Of Trips	Number Of Lights
1. Operator initiation	Throttle in OFF position	1	0
2. Reactor scram	Reactor scram initiated when flux level was above 3.5% of full power	2	2
3. Turbine discharge-air temperature ($T_{5.1}$)	$T_{5.1}$ exceeds trip level, adjustable from 700° to 1500°F	3	3
4. Engine overspeed	Engine speed exceeds 105% N	1	1
5. Compressor shutoff doors	Compressor shutoff doors closed when speed was above 1000 to 1500 rpm	1	1

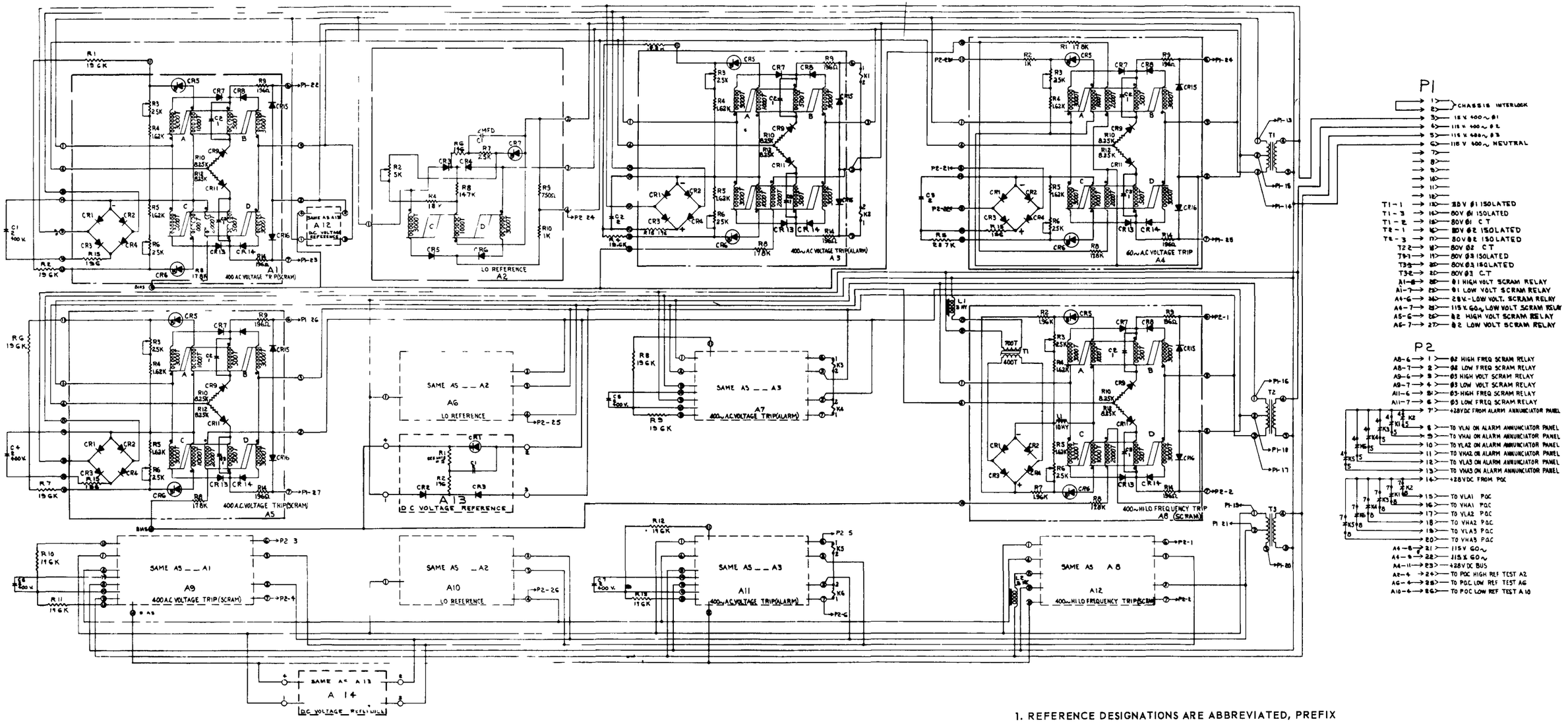

1. REFERENCE DESIGNATIONS ARE ABBREVIATED, PREFIX THE DESIGNATION WITH UNIT NUMBERS OF ASSEMBLY DESIGNATIONS OR BOTH
2. ALL DIODES IN 433B EXCEPT NOTED
3. ALL RESISTANCE VALUES ARE IN OHMS
4. ALL CAPACITY VALUES ARE IN MICROFARADS
5. FUNCTIONAL CODE LETTERS ARE SHOWN ON FIGURE 7.11

Fig. 7.34—Power safety circuits (Dwg. 207R327)

A-C Voltage Trips - The circuit of the 400-cycle-per-second voltage trip is shown in Figure 7.34, zone A1. The circuit of the 60-cycle-per-second voltage trip is shown in zone A4. These circuits were the same as the d-c trip circuits except that the input circuit used a full-wave bridge rectifier plus filters to convert the ac to dc. The 115-volt 400-cycle-per-second circuit contained dual trips, one set at ±5 percent and the other set at ±10 percent. The 10 percent trips were scram trips. The 115-volt 60-cycle-per-second circuit contained a single trip at ±10 percent; this was a scram trip.

The permissible deadband on the 400-cycle-per-second trips was 3.5 volts; the deadband on the 60-cycle-per-second trip was 5 volts. Experimental results showed that the error introduced by a 10-percent frequency variation was 1.8 volts for the 400-cycle-per-second trip circuit and 2.0 volts for the 60-cycle-per-second trip circuit. The deadband under the same conditions was 1.4 volts for the 400-cycle-per-second trip and 1.7 volts for the 60-cycle-per-second trip.

Frequency Trip - This trip circuit is shown in Figure 7.34, zone A8. It contained a full-wave bridge rectifier to convert the ac to dc, and also a saturable reactor that served as a frequency-sensitive component. (The output of a saturable reactor becomes frequency sensitive after the unit is saturated.) In this circuit, the zener diode was used to expand the range, and also to block out the unsaturated region in which the output of the saturable reactor was not purely frequency sensitive. Since a filtering capacitor could not be used in the bridge circuit because it would introduce a large voltage error, a choke in the control winding was used as a filter.

The trip points for the frequency trip circuits were a nominal ±10 percent. Experimental results showed that, with the input choke, the accuracy of the low-frequency trip for variations in line voltage of ±10 percent was 3 cycles, and the accuracy of the high frequency trip was 5 cycles. The error due to temperature was measured at -67°F only, and showed a change of +3 cycles in the trip point for the low-frequency trip and +4 cycles for the high-frequency trip.

7.5.3.2 High Voltage Trips

The high-voltage safety trips were built into the ion chamber voltage unit shown in Figure 7.35.

+1500-Volt d-c Trip - This trip circuit is shown in Figure 7.35, zone A1. The circuit was the same as the other trip circuits except for the values of the voltage-dropping resistors. It was nominally set for 1250 volts, and had a permissible deadband of 50 volts. Experimental results showed that the error due to 10-percent input line voltage variation was ±2.1 volts, and for ±10-percent input frequency variation the error was ±2.7 volts. The maximum deadband was ±17.4 volts for ±10-percent variations in line voltage, frequency, and the worst combinations.

HP1 Ionization Chamber Trip - Except for the high-low range switch, the complete circuit for the HP1 ionization chamber safety trip is shown on Figure 7.35, zone A1. The circuit was a compromise between complexity and response time since ionization chamber response was kept as fast as possible to adequately protect the reactor in case of a nuclear runaway. The best compromise was to have the low-range trip cover 13 to 30 percent of full power, and the high-range trip cover 26 to 135 percent of full power. This compromise corresponded to a range of approximately 0.3 to 4.0 milliamperes. The accuracy of both trip ranges, for a line variation of ±15-percent voltage and ±10-percent frequency, was ±1.25 percent of point. The maximum deadband was 10 percent of point. The time constant varied; for the low end of the low range, the time constant was 65 milliseconds, and for the high end of the low range the time constant was 55 milli-

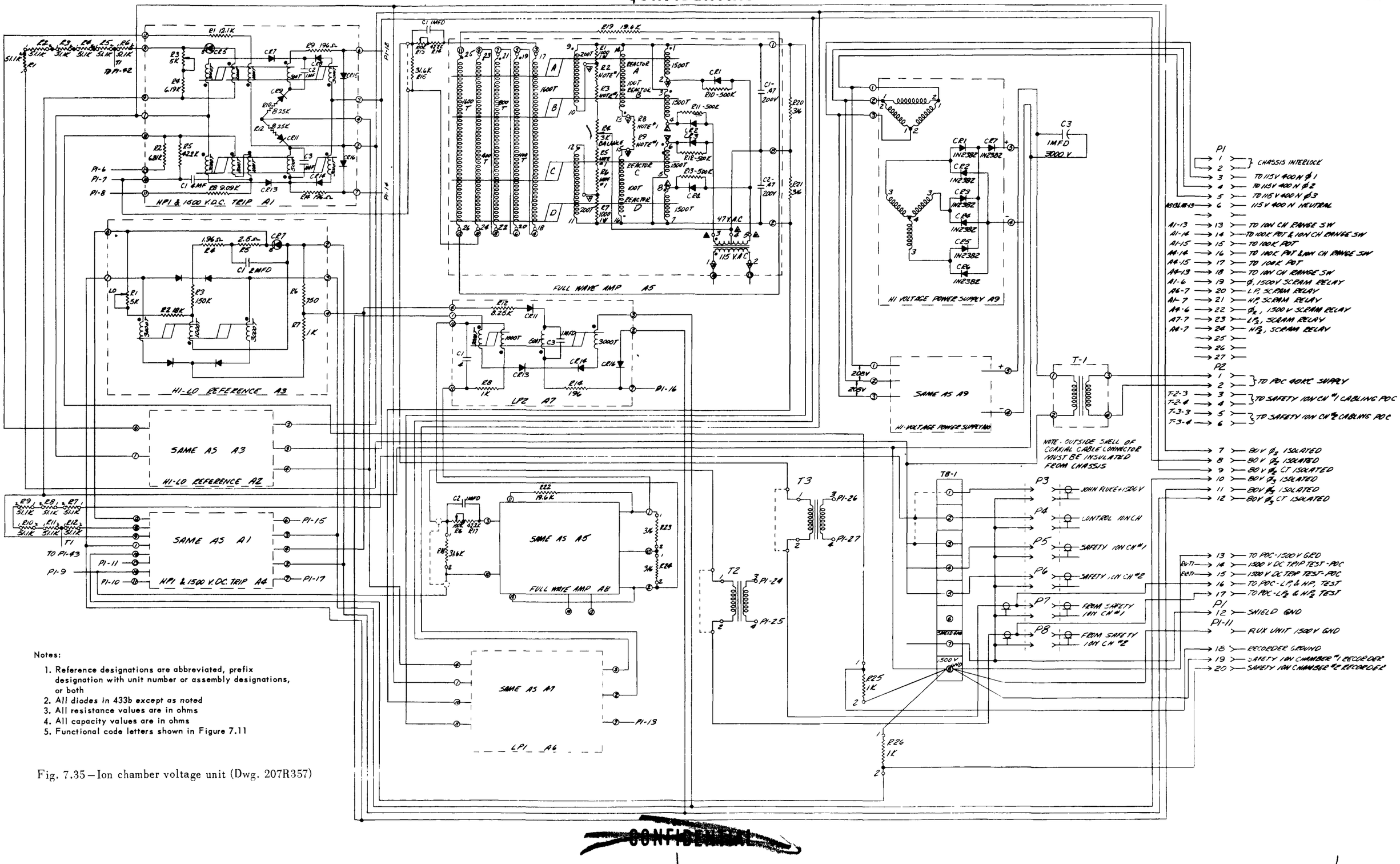

Notes:

1. Reference designations are abbreviated, prefix designation with unit number or assembly designations, or both
2. All diodes in 433b except as noted
3. All resistance values are in ohms
4. All capacity values are in ohms
5. Functional code letters shown in Figure 7.11

Fig. 7.35—Ion chamber voltage unit (Dwg. 207R357)

seconds. The input circuit was electrically isolated from the rest of the circuit since the low power relay was placed in series with the input. The maximum voltage developed across the circuit was less than 150 volts.

LP1 Ionization Chamber Trip - This circuitry is shown in Figure 7.35, zone A7. It was more sensitive than the HP1 trip circuit and required a preamplifier. The circuit was adjusted to trip (de-energize the relay) when the ionization chamber output current exceeded approximately 3.5 percent of full power, 0.1 milliampere. Experimental results showed that the error introduced by line voltage variations of ±10 percent was ±1.5 percent of point. The time constant was 50 milliseconds for a step input change from 30 percent below the trip point to 30 percent above the trip point.

7.5.3.3 High Temperature Trips

This circuitry is shown in Figure 7.36. Fuel element surface-temperature trips are shown in zones A10, A11, A12, and A13. Exit-air temperature trips are shown in zones A1 through A9. The temperature safety unit was designed to very close accuracy requirements, and used a second-harmonic amplifier as described in reference 17. Experimental results showed that the circuit error due to line voltage variations of ±15 percent and frequency variations of ±10 percent was equal to ±32 microvolts, approximately 1.5°F. The maximum deadband was approximately 30 microvolts. The time constant was 60 milliseconds when a step input from 50°F below the trip point to 50°F above the trip was applied. The accuracy of the voltage reference circuits was ±0.2 percent for a ±10-percent change in line voltage at the 1000°F trip point. The maximum error in the trip point, obtained by adding errors in the worst possible combination, was 3.95°F at the 1000°F trip point.

7.5.3.4 Period Trip

This circuit used only the basic bistable amplifier and derived its input from the period amplifier described in section 7.4.2.4. The period trip had two identical circuits; one was adjustable around a trip point of 10 seconds, and the other adjustable around a trip point of 5 seconds. Span adjustment was needed for calibration because, when the pulse equipment was changed (log-pump circuit), the slope of the log output changed and the over-all calibration could change. Experimental results showed that the trip point varied ±0.05 second for the 5-second trip, and ±0.2 second for the 10-second period trip, both values based on a ±15-percent line voltage change and a ±10-percent frequency change. The maximum deadband for the 5-second trip was 0.3 second, and 0.7 second for the 10-second trip.

7.5.3.5 Count-Rate Trip

This circuit used only the basic bistable amplifier. The low-count-rate trip energized the relay when the trip point was reached, and the high-count-rate trip was de-energized when the trip point was reached. The low-count-rate trip was the only trip circuit using the high reference voltage to maintain accuracy.

Tests wherein the count-rate amplifier was used as the input stage showed the following results for line voltage variations of ±15 percent, and frequency variations of ±10 percent. The low-count trip, when set at 10 counts per second, had an error of ±0.4 counts per second; when set at 150 counts, the error was ±5 counts per second. The high-count-rate trip had an error of ±50 counts per second when set at 3000 counts per second; when set at 200,000 counts per second, the error was ±10,000 counts per second. The response time of the count-rate trips for a step input of 30 percent below to 30 percent above the trip point was approximately 75 milliseconds. The deadband was approximately 17 percent for the low trip, and 6 percent for the high trip.

Notes:

1. Reference designations are abbreviated prefix designation with unit numbers or assembly designations or both.
2. All diodes in 443B except noted.
3. All resistance values are in ohms.
4. All capacity values are in microfarads.
5. Functional code letters are shown in Figure 7.11.

Fig. 7.36 – Temperature safety unit (Dwg. 207R370)

7.6 OPERATIONAL CHARACTERISTICS

7.6.1 OPERATING PROCEDURES

Operating procedures for testing the XNJ140E-1 engine in the FET were being developed at the time of program termination and are described in references 29 and 30. These procedures covered engine operation only: facility operation was treated separately. A single operator controlled the engine from the operator's console. These procedures, followed in the prescribed order, insured safe operation of the engine at all times.

Operating procedures unique to the nuclear heat source of the XNJ140E-1 turbojet engine involved power transfer, either way, between the chemical and nuclear heat sources, and the feasibility of starting and operating the engine in the all-nuclear regime. These operational characteristics are described below.

7.6.2 POWER TRANSFER

7.6.2.1 Cycle Characteristics

A general method for transferring from chemical to nuclear power, and from nuclear to chemical power was developed. The analog simulator was used to check the procedure. Manual fuel flow control was assumed and the following limitations were placed on the engine cycle.[31]

1. Maximum turbine inlet-air temperature (T_4) was 1600°F when the temperature rise across the chemical combustor (chemical ΔT) was less than 700°F (operating primarily on nuclear heat), and 1400°F when the chemical ΔT was greater than 700°F.
2. Minimum steady-state chemical ΔT was 400°F. Minimum transient chemical ΔT was 200°F.
3. Minimum fuel flow was 3,000 pounds per hour.

Initial analyses based on steady-state operating data left doubt that power transfer from chemical to nuclear was feasible under Idaho Hot Day (120°F) ambient conditions.[32] The reservations as to effecting successful power transfers, while maintaining the limitations identified above, were based on the following assumptions:

1. T_4 would not change during the speed transient.
2. Nozzle area would not change during the speed transient.
3. The bleed-speed valve would close instantaneously.

Supporting analog computer analyses showed that the first assumption was invalid when the full transient was considered. The second assumption was valid since the nozzle was very close to its full-open area at high engine speeds. Since flameout produced a large $T_{5.1}$ error signal in the reactor temperature control loop, a sharp increase in reactor power resulted, together with a slower increase in $T_{3.7}$ and T_4. The analyses showed that, during the first 6 percent speed change, T_4 increased by 50°F. Since the $T_{5.1}$ control loop always responded to a decrease in $T_{5.1}$, engine shutdown could occur only when the speed transient was so severe that engine speed decayed into the unstable operating region below 85 percent N. The bleed-speed valve area loop remained stable through the transient.

Subsequently, a procedure was developed that insured successful power transfer in minimum time while observing these limitations. The following control loops were assumed to be operative and used as needed:

1. Bleed-speed control, utilizing bleed reset
2. Automatic $T_{5.1}$ temperature control loop, as defined in reference 19
3. Manual reactor power control, as defined in reference 19
4. Manual fuel control, as defined in reference 33

In addition to operating procedures using manual fuel control, a study was completed on power transfers using an assumed automatic fuel control in which fuel flow was scheduled as a function of engine speed, T_2, P_3 and a $T_{5.1}$ override. The study did not consider integrating these additional control system requirements and procedures into the XNJ140E-1 thrust selector. Reference 34 describes power transfers based on an automatic fuel control loop.

The time allowed to effect power transfer was not critically limited by aircraft performance considerations. The problem of loss of altitude during power transfer was investigated by the Convair division, General Dynamics Corporation.[36] An XMA-1-type installation was assumed wherein zero thrust occurred on each power package during the transfer operation. One minute per engine was allowed for transfer. On a hot day, and using military power, a total altitude loss of 860 feet occurred, assuming transfer at 10,000 feet. On a standard day there was only a 30-foot change in altitude. In the case of power transfer at 20,000 feet prior to landing, the hot-day altitude loss was 1325 feet and the standard-day loss was 655 feet. None of the power transfers studied included afterburning.

This study considered two XMA-1 engines installed in the Convair airframe. Since each engine contained two sets of turbomachinery, the power transfers involved a 50-percent loss of thrust. The loss of altitude during a power transfer involving a 33-1/3-percent loss of thrust, as would occur with a three-engine XNJ140E installation, would be less.

7.6.2.2 Detailed Operational Requirements

The detailed requirements imposed on operating procedures to effect power transfers were as follows:

1. Chemical ΔT exceeded $200^{\circ}F$ at all times, and ΔT between $200^{\circ}F$ and $400^{\circ}F$ was of a transient nature (1 minute maximum).
2. Turbine inlet-air temperature (T_4) did not exceed $1600^{\circ}F$ when chemical ΔT was less than $700^{\circ}F$ (some heat being generated by the reactor), nor $1400^{\circ}F$ when chemical ΔT was greater than $700^{\circ}F$.
3. Minimum fuel flow was 3,000 pounds per hour.
4. Procedures must allow the control system to provide suitable protection against overspeeds due to chemical light-off.
5. Procedures must allow the control system to provide protection against possible nozzle failure (since turbine inlet-air temperature limitations necessitated removal of nozzle bound during chemical or chemical-assist operation).
6. Any possible tendency toward engine instability caused by chemical flame blowout must be completely eliminated.
7. Procedures meeting these requirements could differ, depending on whether transfer was desired in minimum time or by a slow, deliberate process.

Initial operating conditions for transfer from CHO to NHO were chosen as (1) 95-percent speed, (2) automatic speed control, (3) nozzle unbounded, and (4) manual fuel flow adjusted to give maximum turbine discharge-air temperature (assuming no turbine inlet-air temperature sensors were available). The selection of 95-percent speed permitted protection against nozzle failure during power transfer; the maximum turbine discharge-air or turbine inlet-air temperature, with unbounded nozzle, led to maximum utilization of the engine speed control subsystem during the flame blowout transient. The reactor was assumed to be operating on flux control at the lower limit of the power range (1.5% full power).

The operating conditions for transfer from NHO to CHO were the same as those for CHO to NHO except that the turbine discharge-air temperature ($T_{5.1}$) was adjusted to give nearly open nozzle area (1,750 sq. in.). This reduced the possibility of overtemperaturing during the light-off transient, and further minimized the effect of possible nozzle failure. The nozzle was unbounded, and automatic speed demand was set at 95 percent.

7.6.2.3 Procedures for Minimum-Time Transfers

Studies on the analog computer showed that the following procedures for minimum-time power transfers led to fully stable operation while meeting the detailed requirements listed in section 7.6.2.2. The power level of the reactor was made to change at its maximum rate by maintaining the maximum temperature-error signal in the reactor power range temperature control subsystem.

Power Transfer CHO to NHO - The following procedure was shown, by analog computer studies, to effect satisfactory transfers:

1. Initial Operating Conditions:
   a. Automatic speed control, speed demand at 95 percent N
   b. Manual flux control, set a lower limit of power range demand
   c. Manual fuel flow to give a turbine discharge-air temperature of 840°F
   d. Nozzle unbounded.
2. The temperature-loop error was nulled. Control was switched to the automatic temperature ($T_{5.1}$) loop.
3. Temperature demand was set at 985°F.
4. As turbine discharge-air temperature started to increase, $T_{5.1}$ was maintained at 800° to 860°F by adjusting fuel flow.
5. When minimum fuel flow was reached, the reactor was allowed to stabilize for 20 to 30 seconds, then fuel was stopcocked. Reactor power increased to maintain turbine discharge-air temperature at 985°F.
6. Nozzle bounds were applied.

Power Transfer NHO to CHO - The following procedure was shown, by analog computer studies, to effect satisfactory transfers:

1. The interburners were ignited at minimum fuel flow.
2. After stable burning was established, the fuel flow was increased to obtain and maintain turbine discharge-air temperature at 985°F.
3. When the reactor power level decreased to 4 megawatts, the reactor control was switched to the flux loop, and placed in standby.
4. Fuel flow was adjusted to obtain and maintain turbine discharge-air temperature at 840°F.

7.6.2.4 Procedures for Slow Transfers

These procedures involved slow, incremental steps using the engine speed control subsystem and reactor power range temperature loop. The values of turbine discharge-air temperature in these procedures were chosen, on the basis of analog computer analyses, to provide acceptable values of turbine inlet-air temperature (T_4) for any expected ambient air condition. All requirements listed in section 7.6.2.2 were satisfied.

Power Transfer CHO to NHO - The following procedure was shown, by analog computer studies, to effect satisfactory transfers.

1. Initial Operating Conditions:
   a. Automatic speed control, speed demand set at 95 percent N
   b. Manual flux control at lower limit of power range demand
   c. Manual fuel flow to give a turbine discharge-air temperature of 840°F
   d. Nozzle unbounded.
2. The reactor power range control subsystem, temperature loop, error was nulled. Control was switched to the temperature loop.
3. The temperature demand was increased to produce the desired transfer temperature (985°F maximum).

4. Fuel flow was adjusted to maintain turbine discharge-air temperature between 800° and 860°F, insuring that the bleed-speed valve did not close completely.
5. When fuel flow corresponding to 400°F chemical ΔT was reached, the engine was allowed to stabilize.
6. Fuel flow was reduced to a rate corresponding to a ΔT of 200°F within 30 seconds, insuring that the bleed-speed valve did not close completely.
7. 20 to 30 seconds were allowed for the reactor to stabilize, then the fuel was stop-cocked.
8. The temperature demand was set at 985°F and the nozzle was bound.

Power Transfer NHO to CHO - The following procedure was shown, by analog computer studies, to effect satisfactory transfers.

1. Initial Operating Conditions:
   a. Speed at 95 percent N
   b. Temperature loop demand adjusted to give A_8 = 1750 square inches
   c. Nozzle unbounded.
2. The interburners were ignited with the fuel flow set at the lesser of the rates required to provide (a) a chemical ΔT of 200°F across the interburners, or (b) a minimum flow of 3000 pounds per hour.
3. After stable burning was observed, the fuel flow was increased slowly until a rate corresponding to a 400°F chemical ΔT was reached. This was completed in one minute maximum.
4. Fuel flow was slowly increased until the reactor power level was reduced to 4 megawatts. The reactor was placed on standby.
5. Fuel flow was adjusted to maintain turbine discharge-air temperature at 840°F.

7.6.2.5 Transfer Procedures Using Fully Manual Control

Satisfactory procedures for manually controlled power transfers were demonstrated by analog computer studies. These procedures used the manual fuel control subsystem and the reactor control system manual control loop. All steps in the procedures were manually initiated and manually controlled.

Power Transfer CHO to NHO - The following procedure was shown, by analog computer studies, to effect satisfactory transfers.

1. Initial Operating Conditions:
   a. Engine speed control demand set at 95 percent N and speed stabilized
   b. Manual flux control at lower limit of power range demand
   c. Manual fuel flow adjusted to give a turbine discharge-air temperature of 840°F
   d. Nozzle unbounded.
2. The fuel flow was reduced and flux level increased by small increments until fuel flow corresponding to a ΔT of 700°F was reached. The bleed-speed valve did not close completely during fuel flow reductions, and the turbine discharge-air temperature did not exceed 840°F during the reactor power level increases.
3. When fuel flow corresponding to a ΔT of 700°F was reached, the flux level was slowly increased until the turbine discharge-air temperature was 985°F. During this increase in power level, the chemical ΔT was rechecked and fuel flowrate reduced if ΔT exceeded 700°F.
4. When the engine had stabilized with discharge-air temperature at 985°F and ΔT equal to or less than 700°F, the fuel flow was alternately reduced and flux level increased, insuring that the turbine discharge-air temperature did not exceed 985°F until fuel flow corresponding to a ΔT of 400°F was reached.

5. When the engine had stabilized with turbine discharge-air temperature at 985°F, and ΔT at 400°F, the fuel flow was reduced smoothly to that rate corresponding to a ΔT of 200°F, completing the operation within approximately 15 seconds.
6. The flux level was immediately increased to obtain a turbine discharge-air temperature of 985°F, completing this operation within approximately 45 seconds.
7. When the turbine discharge-air temperature was 985°F, or when 45 seconds had elapsed, whichever occurred first, the fuel flow was stopcocked.
8. When the engine had stabilized, the nozzle-bound system was actuated, and flux level increased until the turbine discharge-air temperature was 985°F.

Power Transfer NHO to CHO - The following procedure was shown, by analog computer studies, to effect satisfactory transfers.

1. Initial Operating Conditions:
   a. Engine speed control demand set at 95 percent N and speed stabilized
   b. Manual flux control set to produce A_8 = 1,750 square inches
   c. Nozzle unbounded.
2. The interburners were lighted off with the lesser fuel requirement to produce a 200°F temperature rise across the combustor, or a 3,000 pounds per hour fuel flow.
3. After light-off and stable burning was observed, the flux demand was reduced to one-half its original value, and the turbine discharge-air temperature started to decrease.
4. The fuel flow was adjusted to maintain turbine discharge-air temperature between 840° and 985°F, insuring that the bleed-speed valve did not close completely.
5. When the engine had stabilized, a ΔT of 400°F across the combustor was established. If ΔT was less than 400°F, fuel flow was increased to the rate required to maintain a ΔT of 400°F, observing the 985°F maximum turbine discharge-air temperature limit.
6. Flux demand was alternately reduced and fuel flow increased (maintaining between 840° and 985°F turbine discharge-air temperature and insuring that the bleed-speed valve did not close) until a ΔT of 700°F was reached.
7. When the engine had stabilized with ΔT equal to or less than 700°F, the flux demand was decreased to its minimum value and fuel flow was adjusted to obtain and maintain 840°F turbine discharge-air temperature.

7.6.2.6 Data From Power Transfer Analog Computer Studies

The results of the analog computer studies showed that power transfers, either way, could be performed successfully over the range of expected inlet conditions, even when an additional requirement of a maximum T_4 of 1400°F was imposed. Utilization of the procedures outlined in section 7.6.2.3 resulted in transfers in minimum time. If desired, a slow step-by-step process as outlined in section 7.6.2.4 could be used. Fully manually controlled power transfers, as outlined in section 7.6.2.5, were also studied.

The results of the analog computer study for a minimum-time power transfer are shown in Figures 7.37a and 7.37b for transfer from CHO to NHO. Figures 7.38a and 7.38b show the transfer from NHO to CHO. The horizontal time scale of these figures is 5 seconds per major division, and the ambient condition was ITS, hot day. All engine parameters remained within limits during both transfers.

Further results of studies for other inlet conditions and other modes of control are contained in reference 35.

7.6.3 NUCLEAR STARTS

Starting the XNJ140E-1 engine on nuclear power was desirable since it permitted elimination of the chemical interburners or, at least, confined their use to emergency opera-

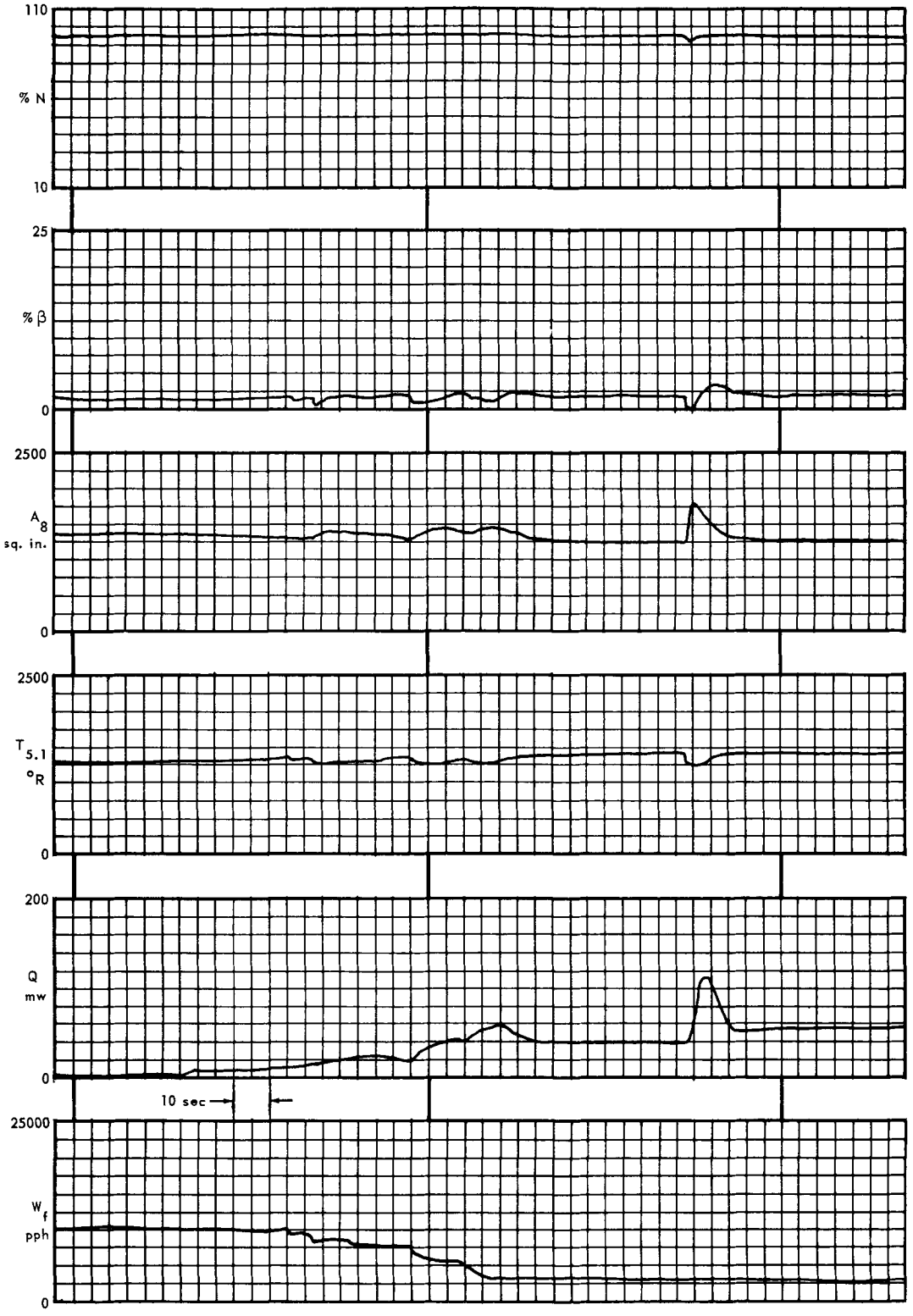

Fig. 7.37a – Analog computer study of power transfer CHO to NHO during ITS hot day conditions

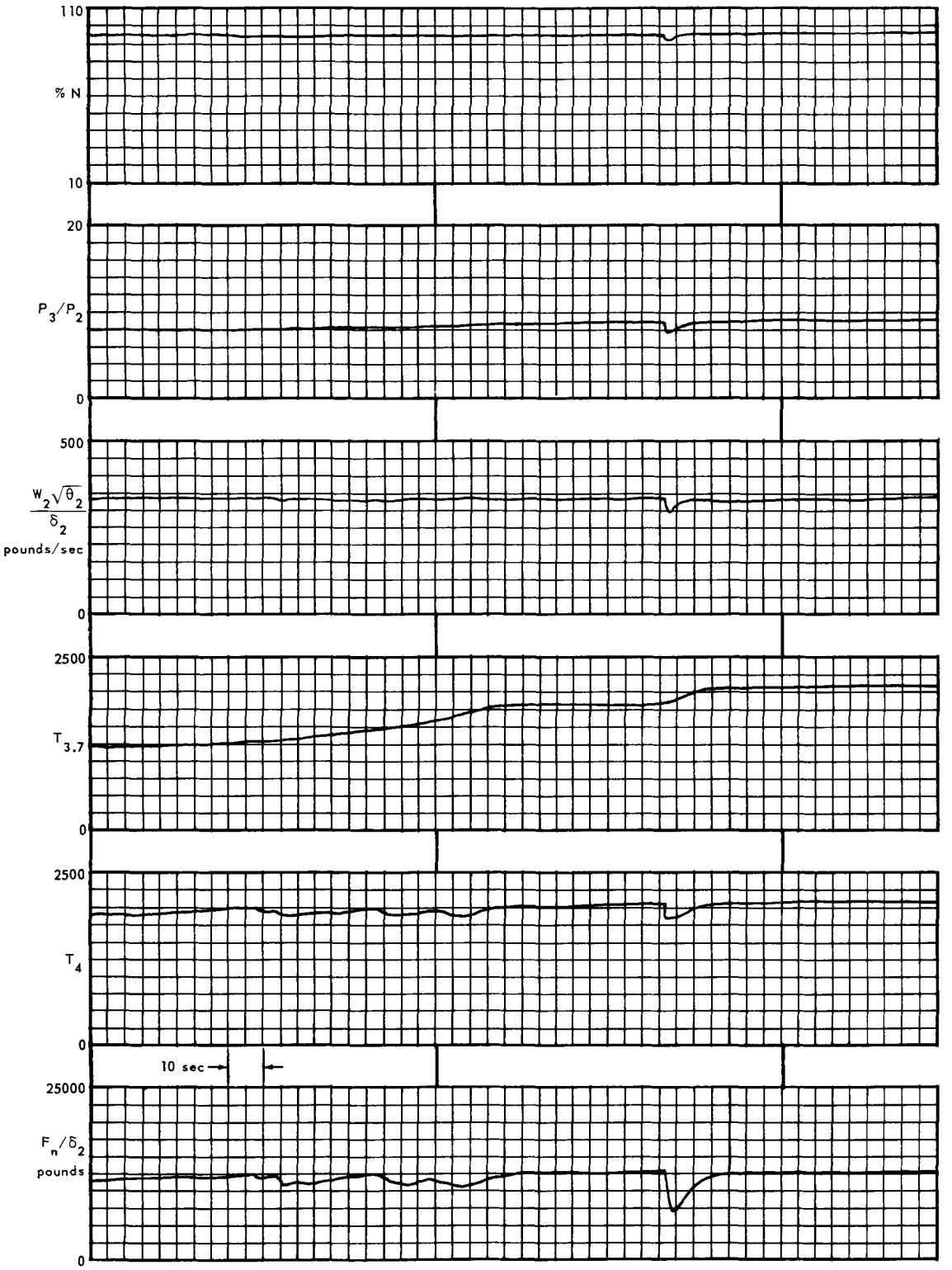

Fig. 7.37b – Analog computer study of power transfer CHO to NHO during ITS hot day conditions

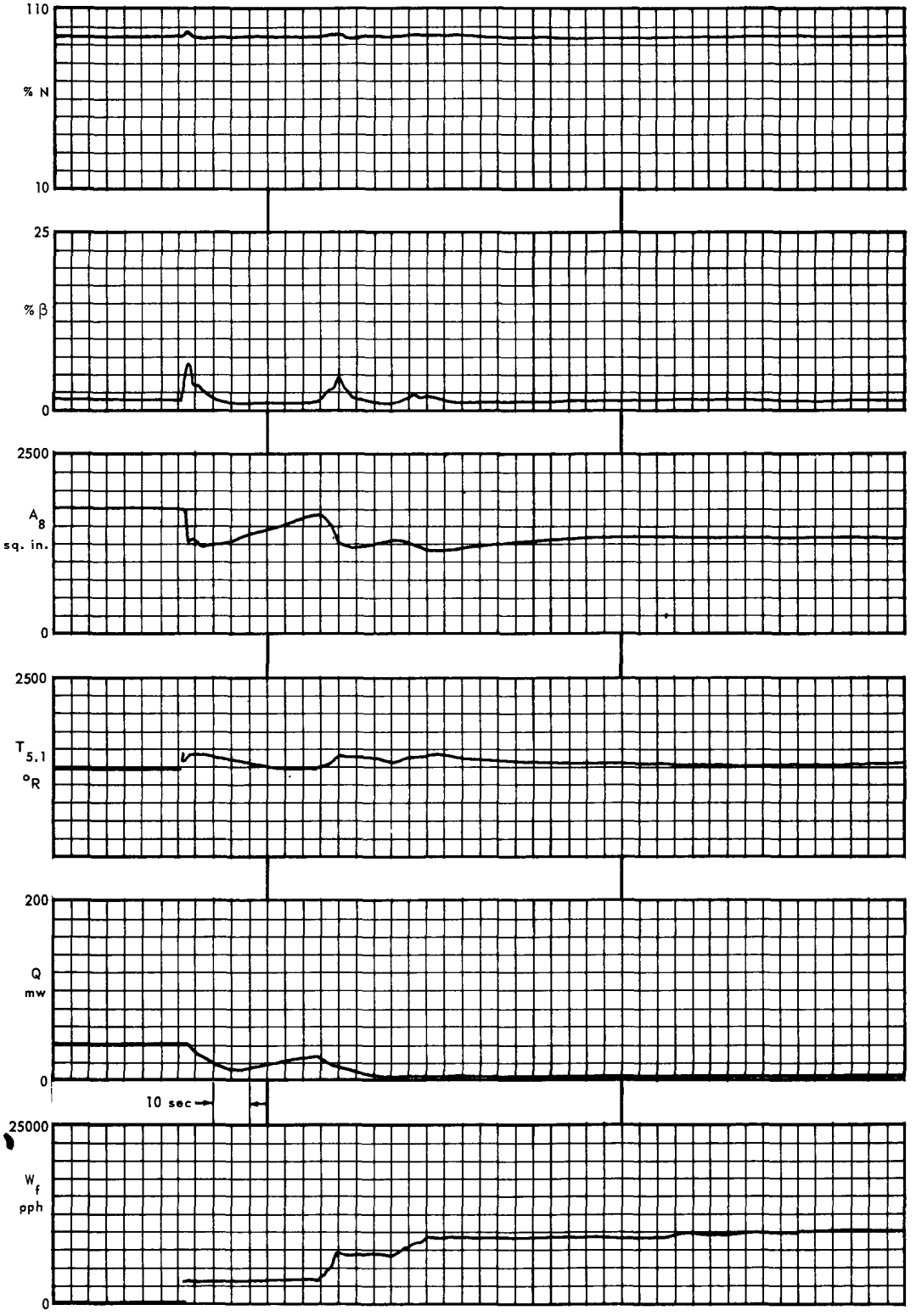

Fig. 7.38a – Analog computer study of power transfer NHO to CHO during ITS hot day conditions

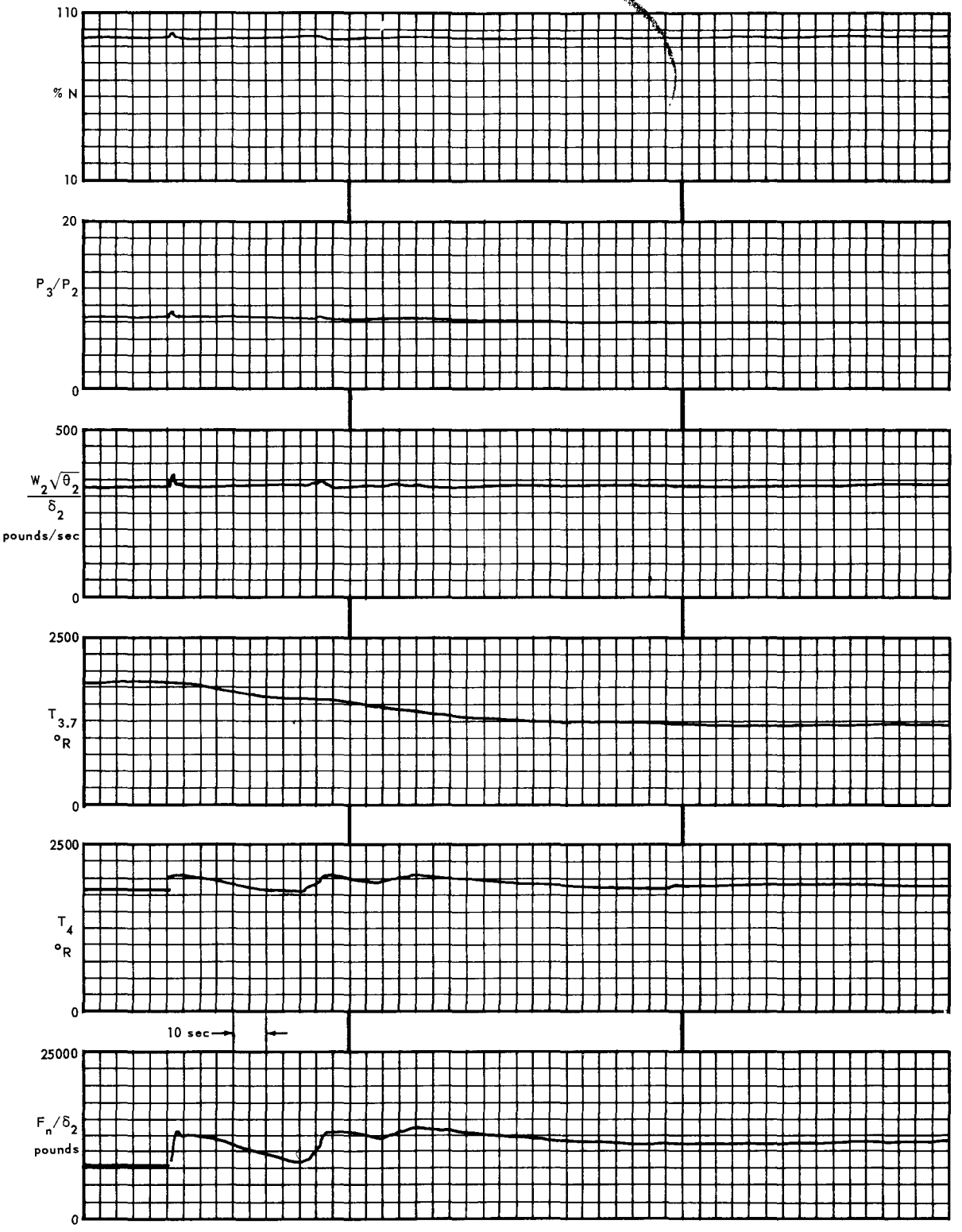

Fig. 7.38b – Analog computer study of power transfer NHO to CHO during ITS hot day conditions

tion. The feasibility of nuclear starts of the XNJ140E-1 power plant was investigated on the analog computer.

The problem involved was that of traversing an inherently unstable region of engine operation. Analysis of the dynamic characteristics of the XMA-1 power plant showed that the engine was unstable below the slope reversal in the curve of turbine inlet-air temperature versus speed; a stability analysis of this condition is reported in reference 37.

The HTRE No. 3 test assembly exhibited the same instability when an attempt was made to operate it in this region. As a result of this demonstration of instability, various methods of starting the HTRE No. 3 test assembly on nuclear power were investigated on the analog computer. The procedures developed during this study, and the successful demonstration of nuclear starting, are contained in reference 38. Analog computer simulator studies of the XNJ140E-1 power plant are contained in reference 39. A description of the analog computer simulator is contained in APEX-912, Controls and Instrumentation.

These studies showed that the basic requirements for traversing the unstable region involved the final power level and the rate of power increase. The optimum starting procedure initially increased power at a slow rate to reduce transient temperature variations while the rotor was accelerating rapidly. A rapid increase in power to the final power level was then required. If the rate of power increase was too slow, rotor acceleration increased, due to the stored reactor heat, until the stored energy was expended. The engine would then start to decelerate if the power level had not reached the energy level necessary to maintain steady-state conditions in the stable region. If the rate of increasing power was too high, large excursions in engine speed and reactor discharge-air temperature resulted. Consequently, a compromise was necessary to establish a rate of increase in power which would traverse the unstable region without cycle collapse, but would lead to minimum temperature and speed excursions. The final power level was of importance since the engine speed could not decelerate into instability. It was found that a power level which led to a high steady-state operating speed was necessary to preclude the speed decay. However, the final power level was restricted to a narrow range since overspeed was a limiting condition.

The XNJ140E-1 engine speed control subsystem provided an effective method of controlling speed at any operating point above engine starter cutout speed. It incorporated bleed-speed valve area and reset as well as nozzle area for controlling speed, and was effective at low engine speeds. Consequently, the restrictions on nuclear startup requirements were relaxed. In fact, studies showed that nuclear starts could be effected successfully if the speed increase was terminated at idle speed.

The following simulator studies are presented to show the trends of different power levels, effects of speed control, and different rates of power increase in nuclear starts of the XNJ140E-1 power plant. The ambient conditions for all studies were 5000-foot altitude and 41°F. Analog simulator plots of these, and other studies, are contained in reference 39.

One study investigated the effect of increasing the reactor power to an arbitrary level and maintaining it at that level. Reactor power was increased to 10 megawatts, then approximately 1 minute was spent resetting the controls before the power was further increased to 20 percent full power. The heat capacity of the reactor led to an appreciable time lag between the rate of power generation and the rate of heat release to the cooling air. The starter was set to automatically drop out and re-engage at approximately 66 percent N. During normal operation, once the starter was disconnected it would be manually re-engaged. The results showed that the power level used in this study, 20 percent of full power, was not high enough to traverse the unstable operating region. Since the starter was permitted to re-engage, the engine went into a speed cycle with a 110-second period. A higher power level, one that permitted steady-state operation in a stable region, was

programmed into the next study. The power level was set at 49 percent full power and the nozzle area was held fixed. The cycle stabilized at a fixed speed of 92 percent N; however, a transient overspeed of 8 percent occurred. If the power level had been set higher, engine overspeeds high enough to cause reactor scram would have resulted.

Another analog simulator study depended upon the bleed-speed control loop to limit the speed overshoot and the accuracy required for programming the final power level. The speed demand was set initially for a fixed value of 85 percent full power. The power increased to 49 percent full power. The speed overshoot was limited to 3 percent, and the improvement in speed control resulting from introduction of the bleed-speed control loop was demonstrated.

7.7 PRODUCT HANDBOOK

The Controls Handbook for $140E^3$ was identified in section 1.6. Material contained in this handbook is illustrated by the following Table of Contents:

SECTION	TITLE
A	Table of Contents
B	Distribution
C	Responsibility
D	Introduction
E	Control Product Breakdown Index
F	Additional Reference Report List
1-5000-0.0	Design
1-5000-8.0	Drawing Planning List
1-5000-1	Over-all Power Plant Control System
1-5001-1	Control Room Description and Requirements
1-5010-1	Reactor Control System Description and Requirements
1-5011-1	Control Rod Actuation System Description and Requirements
1-5012-1	Startup System Description and Requirements
1-5013-1	Power Range (Flux) System Description and Requirements
1-5014-1	Power Range (Temperature) System Description and Requirements
1-5020-1	Bleed-Speed Control System
1-5023-1	Manual Nozzle Control
1-5041-1	Manual Fuel Control System
1-5050-1	Stator Control System
1-5070-1	Safety Control System Description and Requirements
1-5091-1	Temperature Indication Description and Requirements
1-5092-1	Pressure Indication Description and Requirements
1-5100-1	Actuators Description and Requirements
1-5100-8	Actuators Drawing List
1-5110-1	Power Head Assembly Description and Requirements
1-5111-1	Servo Valve Description and Requirements
1-5111-2	Servo Valve Mechanical Design
1-5111-3	Servo Valve Electrical Design
1-5112-1	Solenoid Shut-off Valve Description and Requirements
1-5112-2	Solenoid Shut-off Valve Mechanical Design
1-5112-3	Solenoid Shut-off Valve Electrical Design
1-5112-7	Solenoid Shut-off Valve Dimensional Control Drawings
1-5112-8	Solenoid Shut-off Valve Drawing List
1-5113-1	Air Motor Description and Requirements

SECTION	TITLE
1-5286-1	Count Rate Switching Magnetic Amplifier and Switching Monitor Description and Requirements
1-5286-2	Count Rate Switching Magnetic Amplifier and Switching Monitor Mechanical Design
1-5286-3	Count Rate Switching Magnetic Amplifier and Switching Monitor Electrical Design
1-5297-1	150 Percent Power Trip Description and Requirements
1-5451-1	Thermocouple Reference Junction Box Description and Requirements
1-5451-2	Thermocouple Reference Junction Box Mechanical Design
1-5451-3	Thermocouple Reference Junction Box Electrical Design
1-5451-6	Thermocouple Reference Junction Box Instrumentation
1-5451-8	Thermocouple Reference Junction Box References
1-5452-1	Transducer Reference Junction Box Description and Requirements
1-5452-2	Transducer Reference Junction Box Mechanical Design
1-5452-3	Transducer Reference Junction Box Electrical Design
1-5452-5	Transducer Reference Junction Box Nuclear Design
1-5452-6	Transducer Reference Junction Box Instrumentation
1-5460-1	Power Plant Electric Power Supply Description and Requirements
1-5460-2	Power Plant Electric Power Supply Mechanical Design
1-5460-3	Power Plant Electric Power Supply Electrical Design
1-5460-8	Power Plant Electric Power Supply References and Drawings
1-5461-1	Constant Speed Drive Description and Requirements
1-5461-8	Constant Speed Drive Drawing List
1-5462-1	Alternator Description and Requirements
1-5463-1	Exciter-Regulator Package Description and Requirements
1-5464-1	A-C Protective Panel Description and Requirements
1-5464-3	A-C Protective Panel Electrical Design
1-5472-1	Oil Reservoir Description and Requirements
1-5472-2	Oil Reservoir Mechanical Design
1-5472-6	Oil Reservoir Instrumentation
1-5472-7	Oil Reservoir Control Drawing
1-5540-2	Accessories- Fuel Measurement Components Mechanical Design
1-5540-3	Accessories-Fuel Measurement Components Electrical Design
1-5541-2	Fuel Flow Transmitter Mechanical Design
1-5541-3	Fuel Flow Transmitter Electrical Design
1-5541-7	Fuel Flow Transmitter Control Drawing
1-5542-1	Fuel Flow Indicator Description and Requirements
1-5542-2	Fuel Flow Indicator Mechanical Design
1-5542-3	Fuel Flow Indicator Electrical Design
1-5542-7	Fuel Flow Indicator Control Drawing
1-5560-1	Accessories - Fire Detection and Control Components Description and Requirements
1-5561-1	Power Plant Fire Detection Description and Requirements
1-5562-1	Power Plant Fire Control Description and Requirements
1-5563-1	Refrigeration Description and Requirements
1-5564-1	Checkout Description and Requirements
1-5565-1	Blower Fire Protection Description and Requirements
1-5566-1	Fuel Tank Protection Description and Requirements
1-5567-1	Wind Screen Description and Requirements
1-5610-1	Transducers Description and Requirements
1-5611-1	Pressure Transducers Description and Requirements

SECTION	TITLE
1-5632-5	Chromel-Alumel Thermocouples Nuclear Design
1-5632-8	Chromel-Alumel Thermocouples Drawing List
1-5633-1	Copper-Constantan Thermocouples Description and Requirements
1-5634-1	Iron-Constantan Thermocouples Description and Requirements
1-5640-1	Nuclear Instrumentation Description and Requirements
2-5000-0.0	Materials Development
3-5000-0.0	Manufacture, Assembly, Shipment
4-5000-0.0	Component Testing
4-5011-1.1	Control Rod Actuation System Test Facility, Purpose, Description, Conditions
4-5011-1.2	Control Rod Actuation System Tests Results and Interpretations
4-5011-1.3	Control Rod Actuation System Test Reports and References
4-5012-1.1	Reactor Startup Control Test Facility, Purpose, Description, Conditions
4-5012-1.2	Reactor Startup Control Test Results and Interpretations
4-5012-1.3	Reactor Startup Control Test Reports and References
4-5013-1.1	Power Range (Flux) System Test Facility, Purpose, Description, Conditions
4-5013-1.2	Power Range (Flux) System Test Results and Interpretations
4-5013-1.3	Power Range (Flux) System Test Reports and References
4-5014-1.1	Power Range (Temperature) System Test Facility, Purpose, Description, Conditions
4-5014-1.2	Power Range (Temperature) System Test Results and Interpretations
4-5014-1.3	Power Range (Temperature) System Test Reports and References
4-5111-1.1	Servo Valve Test Facility, Purpose, Description, Conditions
4-5111-1.2	Servo Valve Test Results and Interpretations
4.5111-1.3	Servo Valve Test Reports and References
4-5111-2.1	Servo Valve Test Facility, Purpose, Description, Conditions
4-5111-2.2	Servo Valve Test Results and Interpretations
4-5111-2.3	Servo Valve Test Reports and References
4-5140-1.1	Drive Mechanism Test Facility, Purpose, Description, Conditions
4-5140-1.2	Drive Mechanism Test Results and Interpretations
4-5140-1.3	Drive Mechanism Test Reports and References
4-5211-1.1	Position Error Amplifier Test Facility, Purpose, Description Conditions
4-5211-1.2	Position Error Amplifier Test Results and Interpretations
4-5211-1.3	Position Error Amplifier Test Reports and References
4-5212-1.1	Demodulator Test Facility, Purpose, Description, Conditions
4-5212-1.2	Demodulator Test Results and Interpretations
4-5212-1.3	Demodulator Test Reports and References
4-5223-1.1	Pulse Amplifier and Discriminator Test Facility, Purpose, Description, Conditions
4-5223-1.2	Pulse Amplifier and Discriminator Test Results and Interpretations
4-5223-1.3	Pulse Amplifier and Discriminator Test Reports and References
4-5224-1.1	Startup Regulated Power Supply Test Facility, Purpose, Description, Conditions
4-5224-1.2	Startup Regulated Power Supply Test Results and Interpretations
4-5224-1.3	Startup Regulated Power Supply Test Reports and References
4-5225-1.1	Binary and Log Count Rate Computer Test Facility, Purpose, Description, Conditions
4-5225-1.2	Binary and Log Count Rate Computer Test Results and Interpretations
4-5225-1.3	Binary and Log Count Rate Computer Test Reports and References

SECTION	TITLE
4-5631-1.2	Platinum Platinum-Rhodium Thermocouples, Test Results and Interpretations
4-5631-1.3	Platinum Platinum-Rhodium Thermocouples, Test Reports and References
4-5636-1.1	Extensive Lead Wire, Purpose, Description, Facility and Test Condition
4-5636-1.2	Extensive Lead Wire, Test Results and Interpretations
4-5636-1.3	Extensive Lead Wire, Test Reports and References
5-5000-0.0	Operations
6-5000-0.0	Schedules
6-5000-6.0	Power Plant Control System Over-all Schedule
6-5010-6.0	Reactor Control System Over-all Schudule
6-5210-6.0	Actuator Position Control Circuits Over-all Schedule
6-5220-6.0	Reactor Startup Components Over-all Schedule
6-5240-6.0	Reactor Power Range Components (Flux) Over-all Schedule
6-5260-6.0	Reactor Power Range Components (Temperature) Over-all Schedule
6-5270-6.0	Pre-Operational Checkout Components Over-all Schedule
6-5280-6.0	Safety Components Over-all Schedule
6-5500-6.0	Accessories - Intransit Aftercooling - Over-all Schedule
6-5510-6.0	Accessories - Shield and Aftercooling System Control Components - Over-all Schedule
6-5560-6.0	Accessories - Fire Detection and Control Components - Over-all Schedule
6-5611-6.0	Pressure Transducers Over-all Schedule
6-5612-6.0	Vibration Pickups Over-all Schedule
6-5621-6.0	Calorimetric, Tube, Single-Element, Short Heat Rate Sensors CTS-1 Over-all Schedule
6-5622-6.0	Calorimetric, Tube, Multiple-Element, Heat Rate Sensors CTM-2 Over-all Schedule
6-5623-6.0	Calorimetric, Tube, Single-Element, Long Heat Rate Sensors CTS-2 Over-all Schedule
6-5624-6.0	Bragg-Gray Ionization Chambers Over-all Schedule
6-5641-6.0	External Side Shield Test Instrumentation Over-all Schedule

7.8 REFERENCES

1. "Handbook of Instructions for 140E1," GE-ANPD, DC 60-7-1, July 1960.
2. Lepisto, L. L., "P140B-1 Radiation Isodose Patterns," GE-ANPD, DCL 60-6-27, May 27, 1960.
3. Control Design Subsection, "Controls Handbook for 140E1," GE-ANPD, DC 60-9-24, September 1960.
4. "Turbomachinery Handbook for 140E1," GE-ANPD, DC 60-9-23, September 1960.
5. Hession, J. P., "X-211 Engine Control System Design Requirements, Models D140E1 and D140E2," (Issued 7-20-60 and Revised 10-3-60), GE-FPD.
6. Emmert, R. I., and Budenstein, D., "Analysis of Initial Proposal for a Power Range Reactor Control System for Project 103," GE-ANPD, DC 56-10-153, October 1956.
7. Hurd, D. E., and Budenstein, D., "Description and Analysis of the XMA-1 Reactor Power Range Control," GE-ANPD, DC 57-5-16, May 1957.
8. Maitland, R., "The Analysis of an Automatic Startup Control and the Design of a Logarithmic Counting Rate Meter and Period for the XMA-1 (D103A) Power Plant Reactor," GE-ANPD, DC 57-8-37, August 1957.
9. Control Systems Engineering, "140E1 Reactor Control System," GE-ANPD, DC 61-1-41, January 1961.
10. Malone, P. E., "Evaluation Report of the XMA-1A Startup Control Development Equipment," GE-ANPD, DC 59-6-262, June 1959.
11. Emmert, R. I., and Feldbaumer, W. C., "Evaluation of Developmental XMA-1A Power Range Reactor Control and Task 4564-1-1 Job 50915 Closing Report," GE-ANPD, DC 59-12-220, December 1959.
12. Cook-Yarborough, E. H., and Pulsford, E. W., "An Accurate Logarithmic Counting Rate Meter Covering a Wide Range," Institution of Electrical Engineers Proceedings, Volume 98, Part 2 (Power Engineering), Number 62, April 1951, pp. 196-203.
13. Hiser, P. K., "Close-Out Report for Safety Control System for 140E1 Power Plant Electrical Components," GE-ANPD, DC 61-7-41, July 1961.
14. General Electric Company, Schenectady, New York, General Engineering Laboratory Report, "Reactor Startup Control," 58GL225, pp. 28-69.
15. Tupman, L. M., et al., "XMA-1A Reactor Control Electrical Component Development Closing Report - Task 4564-1-1, Jobs 50916 and 50915," GE-ANPD, DC 60-2-171, February 1960.
16. Jackson, C. N., and Hamper, V., "Close-Out Report 140E1 Reactor Startup Components," GE-ANPD, DC 61-7-39, July 1961.
17. Russell, J. A., "Low Level Magnetic Temperature Error Amplifier," GE-ANPD, XDC 60-7-43, July 1960.
18. Arnold, K. W., Glover, D., and Miller, R. F., "Safety Control System for 140E1 Power Plant," GE-ANPD, DC 61-1-114, January 1961.
19. Emmert, R. I., Hurd, D. E., Miller, R. F., and Showalter, J. A., "The P140E1 Reactor Control System Description and Component Requirement," GE-ANPD, DC 60-7-17, July 1960.
20. White, L. C., "Design and Development of the D140E1 Reactor Control Pneumatic System," GE-ANPD, DC 61-7-47, July 1961.
21. Schnorr, F. W., "Design, Development and Testing of a 400°F Gear Type Air Motor," GE-ANPD, DC 61-6-17, June 1961.
22. DeWeese, J. L., "Final Report on the D140 Transfer Box, Radial Shaft and Mounting Pads," GE-ANPD, DC 61-7-30, July 1961.
23. Uebele, R. C., "Control Rod Chain Drive," GE-ANPD, DC 61-6-41, June 1961.
24. Sharr, P. C., and Been, J. F., "Reactor Control Electrical Power Range Components - 140E1 Closing Report," GE-ANPD, DC 61-8-12, August 1961.

25. Baker, J. K., and Miller, R. F., "140E1 Scram Requirement Study," GE-ANPD, DC 60-7-16, July 1960.
26. Humphrey, W. R., "Instrumentation Requirements for D140E1 Power Plant," GE-ANPD, DCL 60-11-75, November 1960.
27. DeWeese, J. L., "Report on Dynamics of E-140 Control Rod Actuator Assembly," GE-ANPD, DC 61-6-18, June 1961.
28. Layman, D. C., "XNJ140E-1 Safety System Mechanization," GE-NMPO, DC 62-1-1, January 1962.
29. Malone, P. E., "Preliminary Operating Procedures for the Advanced Core Test Power Plant," GE-ANPD, DC 60-11-53, November 1960.
30. Layman, D. C., "Documentation of Preliminary Operating Procedures for Testing the XNJ140E-1 Engine," GE-NMPO, DC 62-1-2, January 1962.
31. Campbell, R. L., Wakefield, D. A., and McCubbin, S. E., "Required Cycle Characteristics of the X-211 D 140E1 Advanced Core Test Engine," R60FPD428.
32. Dresser, J. B., "Power Transfer Problems on the X-211 D140-1 Engine," GE-FPD, X-211 SAT-M-067.
33. Roberts, J. H., "Design Specification; X-211 P140A-1 Ground Test Engine; Manual Fuel System," GE-FPD, M50T974S1.
34. Elbert, T. F., "Analysis of Automatic Power Transfer," GE-ANPD, DC 60-9-114, September 1960.
35. Elbert, T. F., "Analysis of Power Transfer for the Advanced Core Test Power Plant," GE-ANPD, DC 60-9-79, September 1960.
36. Savage, W. F., "Trip Report - Convair October 29 and 30, 1959," GE-ANPD, DCL 59-11-35, November 5, 1959.
37. Miller, R. F., and Buden, D., "XMA-1 Power Plant Stability Investigation," GE-ANPD, DC 59-1-223, January 1959.
38. Elbert, T. F., "HTRE No. 3 Stability and Nuclear Start Study," GE-ANPD, DC 60-5-114, May 1960.
39. Buden, D., "Analysis of Nuclear Starts on the Analog Power Plant Simulator," GE-ANPD, DC 60-3-162, March 1960.